N° d'ordre : 8725

UNIVERSITE PARIS XI
U.F.R. SCIENTIFIQUE D'ORSAY

THESE

présentée pour obtenir le grade de :

DOCTEUR EN SCIENCES
DE L'UNIVERSITE PARIS XI ORSAY

par

Anca Mihaela APETREI

Sujet :

Etude des pyrochlores géométriquement frustrés $R_2M_2O_7$ (M=Sn ou Mo). Influence des substitutions chimiques et/ou de la pression appliquée

Laboratoire d'accueil :
Laboratoire Léon Brillouin/ DRECAM/ DSM/ CEA Saclay

Soutenue : le 20 septembre 2007

Devant la commission d'examen :

M. Philippe MENDELS	Président
Mme. Claudine LACROIX	Rapporteur
M. Clemens RITTER	Rapporteur
M. Pierre BONVILLE	Examinateur
Mme. Isabelle MIREBEAU	Directrice de thèse

à mon mari Alin
et
à mes parents

Va mulțumesc!

Remerciements

Je tiens à remercier ici tous ceux qui ont contribué directement ou indirectement à la réalisation de ce travail de thèse, en mettant à ma disposition leurs compétences scientifiques et leur soutien humain. Si j'ai oublié quelqu'un, je m'en excuse.

Cette thèse a été effectuée au sein du Laboratoire Léon Brillouin (LLB), CEA Saclay. Je remercie tout d'abord, Pierre Monceau et Michel Alba, ainsi que Philippe Mangin et Susana Gota-Goldmann, successivement directeurs du laboratoire pendant les années de ma thèse, pour m'avoir chaleureusement accueillie au sein du laboratoire et m'avoir permis de réaliser ce travail dans d'excellentes conditions.

Mes remerciements à Philippe Mendels pour avoir bien voulu présider mon jury de thèse. Je remercie également Claudine Lacroix et Clemens Ritter pour avoir accepté d'être les rapporteurs de cette thèse et pour leurs commentaires et leurs suggestions pertinentes. Merci aussi à Pierre Bonville d'avoir accepté d'être examinateur lors de ma soutenance et pour l'intérêt qu'il a bien voulu porter à ce travail.

Je tiens à exprimer toute ma reconnaissance à Isabelle Mirebeau, ma directrice de thèse, pour m'avoir fait confiance, m'avoir tant appris, m'avoir soutenue pendant ces trois années. Je la remercie d'avoir su me féliciter quand je faisais bien et de m'avoir guidé quand je faisais moins bien. Je la remercie de tout mon cœur pour sa gentillesse à mon égard et aussi pour sa grande disponibilité.

Je remercie nos collaborateurs, qui ont beaucoup contribué à la réussite de cette thèse.

Au LLB, merci d'abord à Igor Goncharenko pour son aide dans le travail expérimental, notamment pour les mesures de diffraction de neutrons et de rayons X sous pression. Un grand merci aussi pour les discussions fructueuses que nous avons eues, pour ses commentaires et son esprit critique exceptionnel. Merci aussi à Gilles André, Juan Rodríguez-Carvajal, Françoise Bourée, Martine Hennion, Arsène Goukasov, José Teixeira pour leur disponibilité, leurs explications, leurs conseils pendant les expériences.

Merci à Anne Forget et Dorothée Colson du Service de Physique de l'Etat Condensé (SPEC), CEA Saclay, pour le travail de préparation des échantillons, sans lesquels ce travail n'aurait pas vu le jour. Merci également à Pierre Bonville, qui m'a permis d'effectuer les mesures de susceptibilité au SQUID du SPEC, dans le cadre d'une collaboration très sympathique, ainsi que pour son investissement au niveau de la discussion des résultats expérimentaux. Merci à François Ladieu et Gwen Lebras du même service pour les mesures d'aimantation et résistivité électrique.

Mes remerciements s'adressent également à nos collaborateurs extérieurs au CEA Saclay. Tout d'abord mes remerciements à Daniel Andreica de l'Institut Paul Scherrer (PSI), Suisse, pour les mesures de Rotation et Relaxation de Spin du Muon et aussi pour son extraordinaire patience et sa disponibilité. Merci à Olivier Isnard et Emanuelle Suard de l'Institut Laűe Langevin (ILL), Grenoble, pour les mesures de diffraction de neutrons et aussi

à Wilson Crichton et Mohamed Mezouar de l'European Synchrotron Radiation Facility (ESRF), Grenoble, pour les mesures de diffraction de rayons X sous pression. Merci aux théoriciens Claudine Lacroix et Benjamin Canals (Institut Louis Néel, Grenoble) et Roderich Moessner (Ecole Normale Supérieure, Paris) pour l'intérêt porter à ce travail et pour les discussions enrichissantes.

Je remercie Rémy Lautié, Christophe Person et Gaston Exil du service informatique du LLB d'avoir toujours pris le temps de m'aider lorsque j'avais un problème. Merci à Xavier Guillou, Philippe Boutrouille, Bernard Rieu, Sébastian Gautrot, Patrick Baroni pour leur aide pendant mes expériences au LLB et merci aussi à l'atelier de mécanique. Un grand merci au personnel administratif, à Chantal Marais pour m'avoir toujours aidé avec le sourire, à Claude Rousse d'avoir facilité mes différentes missions, à Chantal Pomeau, Anne Mostefaoui et Bernard Mailleret pour leur gentillesse.

J'adresse aussi des remerciements particuliers à tous mes camarades doctorants: Sophie, Hakima, Saâd, Benoît, Delphine, Gabriel, Pascale, Lydie, Stéphane, Karine, Clémence, Chloé, Thomas, Nicolas pour leur soutien et le bon temps passé ensemble au cours de ces trois années. Merci aussi à Alexandre Bataille, Sylvain Petit et Vincent Klosek pour leur soutien, pour m'avoir encouragé et partagé leur expérience.

Je remercie mes anciens professeurs, du collège jusqu'à l'université, pour tout ce qu'ils m'ont appris. En particulier, je tiens à remercier les professeurs Alexandru Stancu et Ovidiu Călțun de l'Université "Al. I. Cuza" Iasi, Roumanie, ainsi que François Varret et Jorge Linarés du Laboratoire de Magnétisme et d'Optique, Université de Versailles et Saint Quentin-en-Yvelines, de m'avoir fait confiance et offert la possibilité d'obtenir une bourse CEA.

Je remercie mes amis et collègues roumains Alice, Areta, Raluca, Radu, Mariana et Beatrice. Merci de tout mon cœur pour le bon temps passé ensemble à Paris ou à Orsay, pour leur compréhension, leur soutien, leurs encouragements.

Finalement, je voudrais exprimer ma plus profonde gratitude à ma famille, tout particulièrement à mon mari Alin et à mes parents, qui m'ont toujours soutenu au cours de mes longues études et sans qui ces dernières n'auraient pas été possibles.

Table des matières

Table of contents

Introduction

Ces dernières années, les oxydes pyrochlores $R_2M_2O_7$, où les ions de terre rare R^{3+} et les ions de métal sp ou de transition M^{4+} occupent deux réseaux tridimensionnels de tétraèdres jointifs par les sommets, ont suscité beaucoup d'intérêt. Dans ce type de réseau, les interactions magnétiques d'échange entre premiers voisins peuvent être géométriquement frustrées, c'est-à-dire que la géométrie particulière du réseau ne permet pas à toutes ces interactions d'être satisfaites simultanément. D'un point de vue microscopique, de tels systèmes possèdent une très grande dégénérescence de l'état fondamental, et donc ne peuvent s'ordonner magnétiquement comme des systèmes classiques. Ils présentent des ordres magnétiques à courte portée exotiques, qui ont reçu le nom de liquides, glaces ou verres de spin, par analogie avec les états correspondants de la matière condensée. En pratique, la dégénérescence de l'état fondamental peut être levée par une perturbation comme l'énergie dipolaire ou l'anisotropie de champ cristallin. L'application d'une pression, qui change l'équilibre énergétique entre les différents types d'interactions peut induire de nouvelles phases magnétiques, dont l'étude renseigne aussi sur l'état à pression ambiante.

Ce travail est structuré en six chapitres. Son objet est d'étudier comment la substitution chimique et/ou la pression influence l'ordre magnétique dans certains pyrochlores de terbium : (i) $Tb_2Sn_2O_7$ qui n'a qu'un seul type d'ion magnétique Tb^{3+} sur un réseau pyrochlore (Chapitre III) et (ii) la série de composés $(Tb_{1-x}La_x)_2Mo_2O_7$ avec x=0-0.2, où les deux types d'ions Tb^{3+} et Mo^{4+} sont magnétiques (Chapitres IV-VI). L'utilisation des techniques microscopiques nous a permis d'obtenir une description précise et détaillée à la fois des corrélations statiques de spins et de la dynamique de fluctuations de spins dans ces composés.

Le chapitre I constitue une introduction aux propriétés des pyrochlores géométriquement frustrés. Nous définissons d'abord les concepts de base de la frustration géométrique, et considérons les pyrochlores parmi les autres systèmes géométriquement frustrés. Ensuite nous présentons les composés qui n'ont qu'un seul ion R^{3+} magnétique sur un réseau pyrochlore et introduisons les concepts de liquide de spin, glace de spin et verre de spin. En regard des définitions de base, nous donnons pour chaque cas un exemple réel et représentatif, relié directement à l'objet de notre étude, pour illustrer les signatures expérimentales du comportement liquide, glace ou verre de spin. Puis, nous abordons les systèmes avec deux ions magnétiques R^{3+} et Mo^{4+} sur un réseau pyrochlore et nous détaillons les résultats expérimentaux les plus importants obtenus dans ce domaine avant notre étude. Nous donnons les détails de la structure cristalline, qui sont aussi valables pour les composés avec un seul type d'ion magnétique. Pour tous les systèmes ci-dessus nous présentons quelques modèles théoriques qui tentent d'expliquer leurs propriétés.

Le chapitre II présente les techniques expérimentales essentielles utilisées dans ce

travail : la diffraction de neutrons et de rayons X et la rotation et relaxation de spin du muon (μSR), à pression ambiante et sous pression. La diffraction de rayons X permet d'obtenir une description précise de la structure cristallographique des composés étudiés. Nous portons une attention spéciale aux techniques de diffraction de neutrons et de μSR, les plus utilisées dans ce travail, et qui sont aussi parmi les techniques le plus puissantes pour l'étude du magnétisme de la matière condensée. Nous donnons plus de détails concernant les instruments utilisés et les méthodes d'analyse.

Un des composés les plus étudiés ces dernières années est $Tb_2Ti_2O_7$. Il constitue un exemple classique de liquide de spin, où les moments magnétiques, corrélés antiferromagnétiquement sur les distances entre premiers voisins, fluctuent jusqu'aux températures les plus basses mesurées (70 mK suivant la Référence [Gardner'99]). Comme indiqué au Chapitre I, la compréhension théorique de son comportement est toujours sujette à discussion. Pour mieux comprendre l'équilibre énergétique qui induit cet état fondamental original, nous avons décidé de le perturber. Nous dilatons le réseau en remplaçant l'ion Ti^{4+} non magnétique par un ion plus gros Sn^{4+}, non magnétique également. Le Chapitre III présente les résultats expérimentaux dans $Tb_2Sn_2O_7$. L'ordre magnétique est tout d'abord étudié par susceptibilité magnétique, puis par diffraction de neutrons et chaleur spécifique. Nous montrons que, contrairement à $Tb_2Ti_2O_7$, à basse température, $Tb_2Sn_2O_7$ montre un ordre magnétique à longue portée original. Nous avons appelé ce type d'ordre "glace de spin ordonnée", car dans un tétraèdre donné il présente la structure locale d'une glace de spin, tout en conservant un ordre à longue portée ferromagnétique des tétraèdres. Dans le cadre des modèles théoriques existant dans la littérature, et en utilisant les valeurs des constantes d'interactions proposées pour $Tb_2Ti_2O_7$, nous étudions l'équilibre énergétique des deux composés et tentons de comprendre leurs différences de comportement.

Nous considérons ensuite les systèmes ayant deux ions magnétiques, R^{3+} et Mo^{4+}, chacun des types d'ions occupant un réseau pyrochlore. Par rapport au cas précédent, ces systèmes permettent d'étudier les interactions entre deux réseaux frustrés. Par l'introduction de l'ion magnétique Mo^{4+}, le système devient donc plus complexe, mais aussi plus riche, et plus facile à étudier, puisque la température d'ordre magnétique augmente de près de deux ordres de grandeurs, d'environ 1K pour $Tb_2Sn_2O_7$ jusqu'à 20-100K pour les composés $R_2Mo_2O_7$. Les pyrochlores de molybdène peuvent donc avoir des applications potentielles. Ces dernières années ils ont attiré beaucoup d'attention à cause de la variation anormale à la fois de leurs propriétés de conduction et de leurs propriétés magnétiques, qui sont gouvernées par la variation du paramètre de réseau. Celle-ci peut être pilotée en jouant sur le rayon ionique moyen de la terre rare R_i. Quand R_i augmente, les composés $R_2Mo_2O_7$ présentent une transition d'un état verre de spin isolant (SGI) (pour R=Y, Dy, Tb) vers un état ferromagnétique métallique (FM) (pour R=Gd, Sm, Nd). Dans ces systèmes, outre les moments localisés 4f des ions de terre rare, il y a aussi les moments 4d des ions de transition Mo^{4+}, qui ont un caractère partiellement itinérant. La transition isolant-métal résulte de la position spécifique des niveaux t_{2g} des ions Mo^{4+} près du niveau de Fermi. Les ions R^{3+} sont polarisés par le champ moléculaire des ions Mo^{4+}. Les mesures macroscopiques sur les séries substituées $(RR')_2Mo_2O_7$ [Katsufuji'00, Kim'03, Miyoshi'03, Moritomo'01, Park'03] et les calculs de structure de bande [Solovyev'03] suggèrent que la transition SG-F est gouvernée par le changement des interactions Mo-Mo d'un état antiferromagnétique (frustré par la géométrie du réseau) vers un état ferromagnétique. Notre idée est d'étudier au niveau microscopique l'évolution de l'ordre magnétique en traversant la région du seuil de transition.

Le Chapitre IV concerne de l'influence de la substitution chimique sur l'ordre magnétique. A partir de $Tb_2Mo_2O_7$, qui présente des propriétés verre de spin en dépit de

l'absence de désordre chimique, nous dilatons le réseau en substituant les ions Tb^{3+} par des ions La^{3+} (non magnétiques) et nous étudions la série $(Tb_{1-x}La_x)_2Mo_2O_7$ avec x=0-0.2. Par diffraction de rayons X, nous étudions les propriétés cristallographiques de la série. Puis nous nous consacrons aux propriétés magnétiques. Les mesures de susceptibilité magnétique permettent de déterminer la température d'ordre, tandis que les neutrons combinés aux muons donnent accès à la fois aux corrélations de spins et aux fluctuations. Nous montrons que la substitution Tb/La induit une transition d'un état verre de spin frustré vers un état original "réentrant" de type ferromagnétique, ordonné à longue portée, mais où existe une deuxième transition en dessous de la température d'ordre ferromagnétique observée par les muons.

Le Chapitre V concerne l'influence de la pression sur les propriétés structurales et magnétiques de la séries $(Tb_{1-x}La_x)_2Mo_2O_7$. Par diffraction de neutrons et μSR, nous analysons l'évolution des corrélations de spin et des fluctuations sous pression pour un composé ferromagnétique et un composé verre de spin. Nous montrons que sous pression appliquée, l'ordre ferromagnétique se transforme en verre de spin. La diffraction sous pression de rayons X utilisant le rayonnement synchrotron permet de déterminer la dépendance du paramètre de réseau avec la pression (l'équation d'état).

Le Chapitre VI fait la synthèse des résultats dans la série $(Tb_{1-x}La_x)_2Mo_2O_7$, x=0-0.2. En utilisant l'équation d'état, nous pouvons reporter toutes nos mesures des températures de transition à pression ambiante et appliquée sur un même diagramme. Nous proposons un nouveau diagramme de phase qui possède, outre la région paramagnétique, une région verre de spin, une région ferromagnétique, mais aussi une région mixte. Nous discutons en détail chacune de ces régions et tentons de déterminer leur origine. Nous comparons nos résultats dans la série $(Tb_{1-x}La_x)_2Mo_2O_7$ à ceux obtenus dans deux autres composés $Gd_2Mo_2O_7$ et $Nd_2Mo_2O_7$, composés ordonnés respectivement proches et loin du seuil de la transition ferromagnétique-verre de spin. Finalement, nous comparons les effets de la pression chimique et de la pression appliquée sur les propriétés magnétiques et électriques des pyrochlores de molybdène.

Nous terminons cette étude par une conclusion générale sur les principaux résultats obtenus et leur suite possible. Deux calculs spécifiques sont également reportés en Appendice.

Introduction

In the recent years there has been a great deal of interest in the pyrochlore oxides $R_2M_2O_7$, where both rare earth R^{3+} and transition or sp metal M^{4+} ions form three dimensional networks of corner sharing tetrahedra. In this type of network the first neighbour exchange magnetic interactions may be geometrically frustrated, *i.e.* the specific geometry of the lattice prevents these magnetic interactions from being satisfied simultaneously. From a microscopic point of view such systems possess an enormous degeneracy of the ground state and therefore they cannot order magnetically in a classical way. They show exotic types of short range magnetic orders, which are called spin liquids, spin ices or spin glasses due to their striking similarities with the states of the condensed matter. In practice the degeneracy of the ground state may be lifted by a perturbation like dipolar energy or crystal field anisotropy. The applied pressure, which changes the balance between different types of interactions, may induce new magnetic phases. The analysis of these new phases yields a better understating of the ambient pressure state.

This study is structured in six chapters and analyses how the chemical substitution and/or the applied pressure influences the magnetic order of some terbium pyrochlores: (i) $Tb_2Sn_2O_7$, having Tb^{3+} as unique magnetic ion on a pyrochlore lattice (Chapter III) and (ii) $(Tb_{1-x}La_x)_2Mo_2O_7$ series, with x=0-0.2, where both Tb^{3+} and Mo^{4+} ions are magnetic (Chapters IV-VI). Microscopic techniques allowed us a detailed and precise analyse of both spin statics and dynamics of the above compounds.

Chapter I is an introduction to the properties of the geometrically frustrated pyrochlores. We first define the main concept of geometrical frustration and consider the pyrochlores among other geometrically frustrated systems. Then we focus on systems having only R^{3+} as magnetic ions on pyrochlore lattice and define the concepts of spin liquid, spin ice and spin glass. Besides the basic concepts in each case we choose a real and representative example, directly related to the present study, to illustrate the experimental fingerprint of a spin liquid, spin ice and spin glass behaviour. Then we focus on systems with two magnetic ions, R^{3+} and Mo^{4+}, on pyrochlore lattices and detail the most important experimental results previously obtained in this field. We give some details about their crystal structure, which are also valid for the compounds with only one magnetic ion R^{3+}. For all the above systems we also present some theoretical models which try to explain their properties.

Chapter II presents the main experimental techniques used in this study: the neutron and X ray diffraction and the Muon Spin Rotation and Relaxation (μSR), at ambient and under applied pressure, and also the macroscopic magnetic susceptibility, at ambient pressure. X ray diffraction allows the determination of the crystallographic structure of the analysed compounds. We pay special attention to the neutron diffraction and μSR techniques, mainly used in this work and which are among the most powerful techniques used to investigate

magnetism in condensed matter physics, and give more details concerning both the instruments and data analysis.

One of the most studied compounds of the recent years is $Tb_2Ti_2O_7$. It is a text book example of spin liquid, where the magnetic spins antiferromagnetically correlated only on first neighbour distances fluctuate down to the lowest measured temperature (70 mK according to Ref. [Gardner'99]). As shown in Chapter I, at theoretical level its behaviour is still under discussion. In order to better understand the energy balance which induces its original ground state, we decided to perturb it. We expand the lattice by chemical substitution of the non-magnetic Ti^{4+} by the bigger non-magnetic Sn^{4+} ion. Chapter III presents the experimental results on $Tb_2Sn_2O_7$. The magnetic order is first studied by magnetic susceptibility measurements and then by neutron diffraction and specific heat measurements. We show that, contrary to $Tb_2Ti_2O_7$, at low temperature $Tb_2Sn_2O_7$ shows an original long range magnetic order. We called this type of order an "ordered spin ice", since in a given tetrahedron it possesses the local spin structure of a spin ice, together with a ferromagnetic long range order of the tetrahedra. Within the theoretical models given in the literature and using the interaction constants proposed for $Tb_2Ti_2O_7$, we analyse the energetic balance for the two compounds and try to understand their different behaviours.

We then consider the systems having two magnetic ions, R^{3+} and Mo^{4+}, each of them belonging to a pyrochlore lattice. This allows the study of the interaction of two frustrated lattices, with respect to the above case. By introducing the Mo^{4+} magnetic ion, the system becomes more complex, but also "richer" and easier to study experimentally since the transition temperatures increase by roughly two orders of magnitude, from ~ 1 K for $Tb_2Sn_2O_7$ to ~ 20-100 K for $R_2Mo_2O_7$. Therefore the Mo pyrochlores could have more potential applications. In the recent years they have attracted great attention due to an unusual variation of both their conduction and magnetic properties, which are governed by the variation of the lattice constant. The lattice constant may be tuned by varying the rare earth average ionic radius R_i: when R_i increases the $R_2Mo_2O_7$ pyrochlores undergo a transition from a spin glass insulating (SGI) state (R=Y, Dy and Tb) to a ferromagnetic metallic (FM) one (R=Gd, Sm and Nd). In these systems, besides the localized 4f rare earth magnetic moments, there are also the 4d Mo^{4+} moments, with partially itinerant character. The I-M transition comes from the specific position of the Mo^{4+} t_{2g} orbitals situated nearby the Fermi level. The R^{3+} ions are polarized by the molecular field of Mo^{4+} ions. Macroscopic measurements on substituted series $(RR')_2Mo_2O_7$ [Katsufuji'00, Kim'03, Miyoshi'03, Moritomo'01, Park'03] and band structure calculations [Solovyev'03] suggest that the SG-F transition is determined by a change of Mo-Mo interactions from antiferromagnetic (frustrated by the lattice geometry) to ferromagnetic. Our idea is to study at microscopical level the evolution of the magnetic order throughout the threshold region.

Chapter IV focuses on the influence of the chemical substitution on the magnetic order. Starting from $Tb_2Mo_2O_7$, which shows spin glass properties despite the absence of chemical disorder, we expand the lattice by chemical substitution of Tb^{3+} by the non-magnetic La^{3+} and study the series $(Tb_{1-x}La_x)_2Mo_2O_7$, with x=0-0.2. By X ray diffraction we analyse the crystallographic properties of the whole series. Then we focus on the magnetic properties. The magnetic susceptibility measurements allow the determination of the ordering temperature, while the neutron diffraction combined with μSR give access to both spin static correlations and spin dynamics. We show that the Tb/La substitution induces a transition from a frustrated spin glass state to an original "reentrant" ferromagnetic type order, long range ordered, where a second transition below the ferromagnetic one is probed by μSR.

Chapter V focuses on the effect of the applied pressure on the structural and magnetic properties of the $(Tb_{1-x}La_x)_2Mo_2O_7$ series. By neutron diffraction and μSR we analyse the evolution of spin correlations and fluctuations under applied pressure for a ferromagnetic and a spin glass compound. We show that under applied pressure the ferromagnetic order transforms to spin glass. X ray synchrotron diffraction under pressure allows the determination of the lattice parameter pressure dependence (the equation of state).

Chapter VI makes a synthesis of the results obtained for $(Tb_{1-x}La_x)_2Mo_2O_7$ x=0-0.2 series. Using the equation of state we put together all our measurements of the transition temperatures, at ambient and under applied pressure, and propose a new phase diagram having, besides the paramagnetic region, a spin glass, a ferromagnetic but also a mixed region. We discuss in more details each of these regions and try to determine their origin. We compare our results for $(Tb_{1-x}La_x)_2Mo_2O_7$ series with those for the ordered compounds $Gd_2Mo_2O_7$ and $Nd_2Mo_2O_7$, situated close and far from the threshold region, respectively. Finally, we compare the effects of chemical and applied pressure on the magnetic and conduction properties of Mo pyrochlores.

We close this study by a general conclusion about the main obtained results and the future perspectives. Two specific calculations are also quoted in the Appendix.

Chapitre I.

Le cadre de l'étude: les pyrochlores géométriquement frustrés – liquides de spin, glaces de spin et verres de spin sans désordre chimique

Ce chapitre est une introduction. Son premier but est de définir les concepts de base et le second de présenter les résultats les plus importants obtenus au préalable dans le domaine des pyrochlores géométriquement frustrés $R_2M_2O_7$, où R est une terre rare ou yttrium et M un métal de transition ou sp.

Nous définissons d'abord le concept de frustration géométrique, en soulignant la différence avec la frustration qui résulte de la compétition d'interaction et du désordre chimique (verres de spins classiques). Nous donnons aussi quelques exemples de réseaux géométriquement frustrés et parmi eux nous introduisons le réseau pyrochlore.

Puis nous considérons les systèmes ayant un seul ion magnétique sur un réseau pyrochlore et présentons quelques uns des états fondamentaux induits par la frustration géométrique : liquides de spins, glaces de spin et verres de spin sans désordre chimique. A coté de concepts de base, nous donnons chaque fois des exemples réels de systèmes pyrochlores caractérisés par de tels états magnétiques. Pour l'état liquide de spin et glace de spin, nous mentionnons aussi les approches théoriques qui tentent de décrire ces comportements. Parmi eux nous présentons $Tb_2Ti_2O_7$, qui est un exemple canonique de liquide de spin. Il est le point de départ de la première partie de ce travail, l'étude de $Tb_2Sn_2O_7$ (Chapitre III) dans lequel Tb^{3+} est aussi le seul ion magnétique, mais où la substitution de Ti^{4+} par l'ion plus gros Sn^{4+} dilate le réseau et modifie l'équilibre énergétique des interactions.

Ensuite nous considérons les systèmes ayant deux ions magnétiques, chacun sur un réseau pyrochlore. Les pyrochlores de molybdène $R_2Mo_2O_7$ attirent beaucoup d'intérêt car leurs propriétés électriques et magnétiques dépendent fortement des distances inter atomiques, et essentiellement du paramètre de réseau, dont la variation peut être pilotée en changeant le rayon moyen R_i de la terre rare. Une transition d'un état verre de spin isolant (SGI) vers un état ferromagnétique métallique (FM) a été observée quand R_i augmente. Nous présentons les résultats les plus importants sur ces composés. Nous décrivons de façon détaillée leur structure cristalline, qui influence directement leurs propriétés. Finalement, nous présentons un modèle de structure de bande qui sans être complet, explique les propriétés générales des pyrochlores de molybdène au seuil de transition verre de spin isolant - ferromagnétique métal. La deuxième partie de ce travail (Chapitres IV-VI) est consacrée à l'étude expérimentale microscopique du magnétisme de ces composés dans la région de transition verre de spin-ferromagnétique.

Chapter I.

The framework of this study: the geometrically frustrated pyrochlores - spin liquids, spin ices and chemically ordered spin glasses

The first chapter is an introduction to this study. Its first goal is to define the main concepts: the geometrical frustration and the original magnetic ground states which it generates, *i.e.* the spin liquids, the spin ices and the spin glasses. The second goal is to present some of the most important results previously obtained in the field of the geometrically frustrated pyrochlores $R_2M_2O_7$, with R= rare earth or yttrium and M=transition or sp metal.

We define first the concept of geometrical frustration underlying the difference in regard to the frustration which results from competing interactions and chemical disorder (classical spin glasses). We give few examples of geometrically frustrated lattices and among them we present the three dimensional pyrochlore lattice. In the pyrochlore compounds both R and M ions occupy pyrochlore lattices.

Then we focus on systems having R^{3+} as unique magnetic ion on the pyrochlore lattice and define the original magnetic ground states induced by the geometrical frustration, *i.e.* the spin liquids, the spin ices and the spin glasses. Besides the basic concept we give each time real and representative examples of pyrochlore systems characterized by such magnetic ground states and directly related to this study. For the spin liquids and spin ices we also mention the theoretical approaches that try to explain their behaviour.

Finally, we focus on systems having two magnetic ions on a pyrochlore lattice: the molybdenum pyrochlores $R_2Mo_2O_7$, which have attracted special attention since the discovery of a crossover transition from an insulating spin glass state to a ferromagnetic metallic one, which can be tuned by the rare earth average ionic radius. We present the most important experimental results in this field. We detail their crystallographic structure, since it is directly related to their properties. We also present a band structure model, which without being complete explains the general properties of Mo pyrochlores.

I.1. The geometrical frustration

The geometrical frustration is a central theme in contemporary condensed matter physics. The conditions for magnetic frustration are satisfied in many real materials. On a more fundamental level the geometrically frustrated systems have attracted a great deal of interest over the past few years due to their propensity to adopt unusual, even exotic magnetic ground states, which in some cases still remain poorly understood.

Magnetic frustration arises when the system is not able to find its classical ground state energy by minimizing the energy between pairs of interacting magnetic moments (spins), pair by pair.

When frustration is determined purely by the geometry (topology) of the lattice it is termed geometrical (topological) frustration. The canonical example is an equilateral triangular "plaquette", which depicts the situation for the three nearest neighbour spins (see Figure 1a). As the Hamiltonian for the exchange interaction between any two spins i and j can be written as the scalar product of the spin operators:

$$\mathcal{H}_{\text{ex}} = -2J\vec{S}_i \cdot \vec{S}_j \qquad \text{[I.1]}$$

the energy is minimized for collinear (parallel or antiparallel) spin alignments. Under the conditions that J is negative, which favours the antiparallel (antiferromagnetic) correlation and that J is equal for all nearest neighbours (n.n.) pairs, it is clear that only two of the three spin constrains can be satisfied simultaneously, *i.e.* the system is geometrically frustrated. This can be contrasted with the situation for the square planar plaquette (Figure 1b), which under the same constraints is clearly non-frustrated.

We note that in order to understand the concept of geometrical frustration it is important to emphasize the difference in regard to frustration due to competing interactions, which is schematically illustrated in Figure 1c for a square plaquette. In this case the frustration is determined by the insertion of randomly ferromagnetic (F) n.n. interaction in an antiferromagnetic (AF) matrix. This kind of frustration is usually put into light when speaking about spin glasses. In the spin glasses, both microscopic conditions of site disorder and competing interactions give rise to frustration. For examples and more details one may see the reviews from Ref. [Ramirez'94, Ramirez'01]. Here we only point out a diagram proposed in these references (Figure 2), with site disorder and frustration treated as independent control parameters, which depicts natural interrelationships between magnetic classes. The conventional magnetic ground states (ferromagnetic, antiferromagnetic, ferrimagnetic…) lie in the upper-left-hand quadrant and correspond to both weak frustration and low disorder. Introducing disorder without frustration, the phenomena of random field magnetism and percolation effects are found. Both high frustration and high disorder are exhibited by spin glasses. The subject of our study, geometrically frustrated systems, lies in the upper-right-hand quadrant.

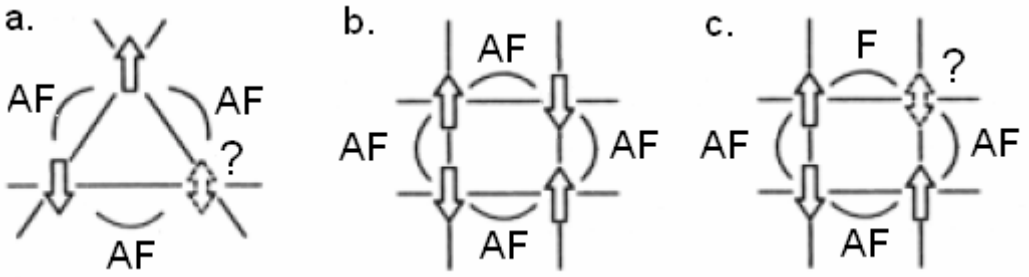

Figure 1. a. Equilateral triangle plaquette with antiferromagnetic (AF) nearest neighbours (n.n.) interactions showing geometrical frustration occurring among spins in a site-ordered system; b. Square lattice with AF n.n. interactions corresponding to non-frustrated case; c. Square lattice with one n.n. AF interaction replaced by a ferromagnetic (F) one showing the frustration induced by the site disorder common to the most spin glasses. Plots are from Ref. [Greedan'01, Ramirez'94, Ramirez'01].

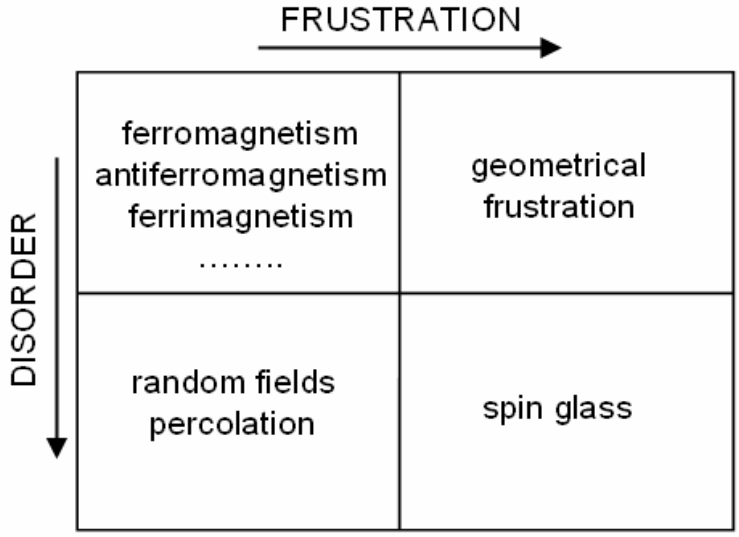

Figure 2. Different classes of magnetic ground states from the perspective of site disorder and frustration, as presented in Ref. [Ramirez'94, Ramirez'01].

The example shown in Figure 1a (AF n.n. spin coupling on triangular lattice) is just a convenient illustrative one. The geometrical frustration is not strictly confined to two dimensions, not even strictly to triangular plaquetts. The tetrahedron (Figure 3a), is a polyhedron comprised of four edge-sharing equilateral triangles and is also geometrically frustrated since in this case only two of the four equivalent AF n.n. interactions can be satisfied simultaneously. Even the square plaquette can be rendered frustrated if one goes beyond the nearest neighbour (n.n.) interactions, and also considers the next-nearest neighbour (n.n.n.) interactions which satisfy the condition $J_{nn} \sim J_{nnn}$ (Figure 3b).

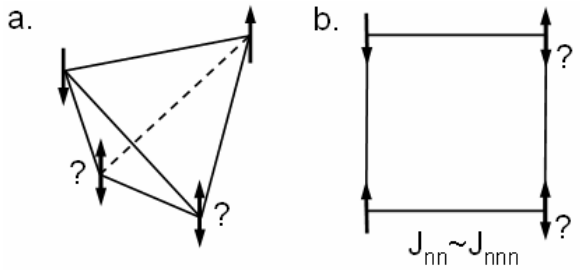

Figure 3. Other frustrated units (see Ref. [Greedan'01]): a. the tetrahedron; b. the square plaquette with $J_{nn} \sim J_{nnn}$.

The examples of geometrical frustration showed in Figure 1 and in Figure 3 can obviously be extended to infinite systems. We note that in addition to geometry, the sign of the interaction and its range are important. It is possible, in principle, to realize frustration on square lattice either with a mixture of precisely tuned AF and F n.n. interactions (Figure 1c) or with n.n.n. interactions (Figure 3b). However, compounds most likely to exhibit strong geometrical frustration possess triangle based lattices and AF n.n. interactions.

Figure 4 shows some examples of frustrated lattices that are based on the triangle (the two dimensional frustrating plaquette) or tetrahedron (the three dimensional frustrated plaquette): the edge shared triangular lattice, the corner shared triangular lattice (known as Kagome lattice), the edge shared tetrahedral lattice (face centered cubic lattice) and the corner sharing tetrahedral lattice. The last type is known as the pyrochlore lattice and occurs in

spinel, Lave phases and pyrochlore compounds. This is not an exhaustive listing but many real materials can be understood in terms of one or more of these lattices.

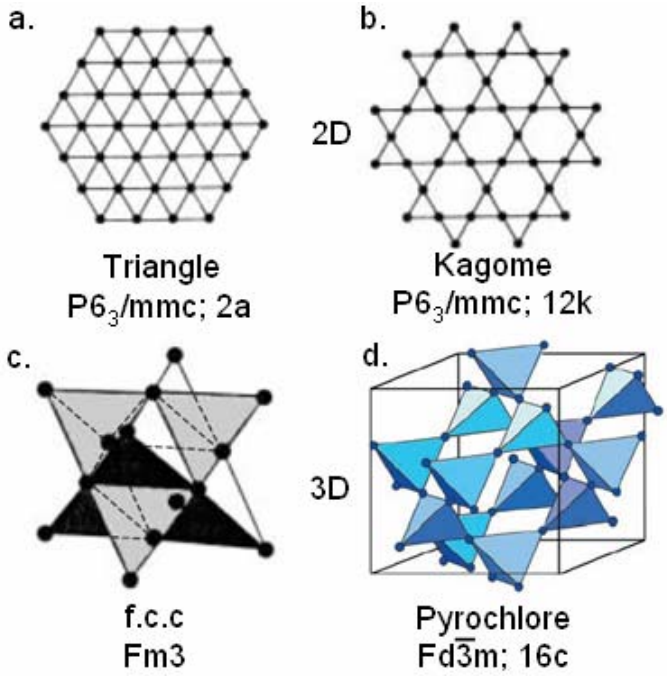

Figure 4. Magnetic lattices that are frustrated when occupied by spins (black dots) with AF n.n. interactions: a. the edge shared triangular lattice; b. the corner shared triangular lattice (Kagome); c. the edge sharing tetrahedral lattice (face centered cubic); d. the corner sharing tetrahedral lattice (pyrochlore). See Ref. [Greedan'01, Ramirez'94, Ramirez'01].

Since we are speaking about real systems, it is important to know a criterion which allows the identification of magnetic frustration from the experimentalist point of view. One knows that for all systems of interest the magnetic interactions are expected on an energy scale set by the exchange energy, $\mathcal{H}_{\text{ex}} \sim -2JS^2 \sim kT$, where $T >> 0$. A simple experimental measure of the exchange energy is provided by the Curie-Weiss constant θ_{CW}, given by the Curie-Weiss law:

$$\chi = \frac{C}{T - \theta_{CW}} \qquad \text{[I.2]}$$

where $C = N_A \mu_B^2 p^2 / 3k_B$ is the Curie constant with μ_B the Bohr magneton, N_A the Avogadro's number, k_B Boltzmann's constant and $p = g\sqrt{S(S+1)}$ the effective magnetic moment expressed in μ_B. From mean field theory it can be shown that:

$$\theta_{CW} = \frac{N_A}{3k_B} S(S+1) \sum z_n J_n \qquad \text{[I.3]}$$

with n the n^{th} neighbour and J_n the corresponding exchange constant, *i.e.* θ_{CW} is the algebraic sum of all exchange interactions in any magnetic system and therefore it sets the energy scale for the magnetic interactions. In the absence of frustration one expects the onset of strong deviations from the Curie-Weiss law for $T \sim |\theta_{CW}|$ and the establishment of a long

range order also near $|\theta_{CW}|$. For ferromagnetic order this is nearly realised, since $|\theta_{CW}|/T_c \sim 1$. T_c is the critical temperature below which sets the long range order. For antiferromagnetic order the situation is a little bit more complex, but typical values for non-frustrated lattices show $|\theta_{CW}|/T_C$ in the range of 2 to 4 or 5. Consequently, it was proposed that the somewhat arbitrary condition:

$$f = \frac{|\theta_{CW}|}{T_c} > 10 \qquad \text{[I.4]}$$

to be taken as a criterion for the presence of frustration, where f is the frustration parameter. For examples of f values for strongly geometrically frustrated compounds see the review References [Greedan'01, Ramirez'94, Ramirez'01] and the References therein.

It has long been recognized that the geometrically frustrated systems possess an enormous degeneracy of the ground state. However in reality this degeneracy can of course be lifted by a perturbation, which may have various origins: longer range interactions, as dipolar or exchange beyond n.n. interaction, and anisotropy. Thermal or quantum fluctuations, chemical or bond disorder may also relieve the degeneracy of the ground state, by selecting in this case a particular state in an order by disorder process, as well as pressure or applied magnetic fields.

The subject of this study is represented by the geometrically frustrated pyrochlores, which have the chemical composition $R_2M_2O_7$. These compounds crystallize in the cubic, face centered space group $Fd\bar{3}m$. The atomic sites are R *16d* [1/2,1/2,1/2], M *16c* [0,0,0], O1 *48f* [u,1/8,1/8] and O2 *8b* [3/8,3/8,3/8]. R-site is occupied by a trivalent element (rare earth or yttrium) and M-site by a tetravalent element (transition or *sp* metal). R^{3+} and M^{4+} ions form two interpenetrating three dimensional networks of corner sharing tetrahedra. Details on crystal structure of these compounds will be given in section I.3. There are three possibilities: (i) R-site occupied by a magnetic ion; (ii) M-site occupied by a magnetic ion; (iii) both sites so occupied. In most cases such systems are characterized by an enormous degeneracy of the ground state. Therefore they cannot order magnetically in a classical way and show original magnetic ground states, short range ordered, named spin liquids, spin ices and spin glasses [Greedan'01]. In the next sections we analyse first the geometrical frustrated pyrochlores having just one magnetic ion (R^{3+} or M^{4+}). Using real examples, directly related to this study, we give simple approaches for the concepts of spin liquid, spin ice and spin glass. Then, we focus on systems having two magnetic ions (R^{3+} and M^{4+}) on pyrochlore lattices.

I.2. The geometrical frustrated pyrochlores: systems with one magnetic ion

I.2.1. The spin liquids. Experimental results on $Tb_2Ti_2O_7$

The problem of antiferromagnetic n.n. exchange interactions on pyrochlore lattice was first considered in Ref. [Anderson'56], who predicted on qualitative grounds a very high ground state degeneracy and that no long range order would exist at any temperature for Ising spins. Villain [Villain'79] reached basically the same conclusion for Heisenberg spins and chose to describe such a system as a “cooperative paramagnet”. Through the years these ideas have been tested at many levels of theory. Both classical and quantum models ([Canals'01,

Canals'98, Moessner'98b, Moessner'98c, Reimers'92, Reimers'91]) show clearly that Heisenberg spins coupled with n.n. AF interactions on pyrochlore lattice do not support static long range Néel order. Nowadays these systems are referred to as either "cooperative paramagnets" or "spin liquids" by analogy with condensed matter liquids. Liquids are expected to crystallize at low temperature, but there is one exception, helium, which remains liquid down to $T = 0$, due to quantum fluctuations [Keeson'42, Simon'50]. Similarly, in magnetism the atomic magnetic moments (spins) are expected to order at a temperature scaled by the Curie-Weiss temperature θ_{CW}, but there are also the "spin liquids" which remain in an unusual state of short range correlated fluctuating spins down to very low temperatures. Actually, the Fourier transform of the spin correlations is quite similar to the pair correlation function of a casual liquid.

When analysing the ground state of geometrically frustrated systems, it is convenient to consider the basic unit/plaquette (triangle or tetrahedron in case of pyrochlores) [Reimers'91]. One may do that since such a system is formed by weakly connected units and hence its energy can be expressed as a sum of the unit's energies. For a base unit having p n.n. AF ($J < 0$) Heisenberg spins, the reduced energy per spin is:

$$\frac{E}{p|J|} = e = \frac{1}{p}\sum_{i,j=1}^{p} \vec{S}_i \cdot \vec{S}_j = \frac{1}{p}\left(\sum_{i=1}^{p} \vec{S}_i\right)^2 - \frac{1}{p}\sum_{i=1}^{p} \vec{S}_i^2 = \frac{1}{p}\left(\sum_{i=1}^{p} \vec{S}_i\right)^2 - 1 \qquad \text{[I.5]}$$

The ground state has the reduced energy $e_0 = -1$ and is determined by the condition:

$$\sum_{i=1}^{p} \vec{S}_i = 0 \qquad \text{[I.6]}$$

If generalizing for a pyrochlore lattice, this means that any configuration in which the spins of each tetrahedron satisfy the above criterion is a ground state. This can be obtained for the case wherein each tetrahedron has two pairs of antiparallel spins, but there is no correlation between tetrahedra.

The canonical example of spin liquid is considered the pyrochlore $Tb_2Ti_2O_7$.

Figure 5 presents few experimental results on $Tb_2Ti_2O_7$ (powder samples), which show a spin liquid behaviour. The dc susceptibility studies show no anomalies or history dependencies in the susceptibility, indicating the absence of a transition to a long range ordered Néel or spin glass like state above 2 K. A fit with the Curie-Weiss law (Figure 5a) gives a Curie-Weiss temperature $\theta_{CW} \simeq -19$ K, which indicates that the n.n. interactions between Tb^{3+} moments are antiferromagnetic [Gardner'99a, Gingras'00]. Neutron diffraction measurements show a magnetic diffuse scattering that starts to appear below around 50 K and develops down to at least 2.5 K (Figure 5b) [Gardner'99a, Gardner'01]. The fit with a cross section proposed in Ref. [Bertaut'67], $I(q) \sim \sin(qR_1)/qR_1$, with R_1 the n.n. spin distance, provides a relatively good description of the experimental data and shows that in $Tb_2Ti_2O_7$ spins are correlated over a single tetrahedron only. The low temperature paramagnetic behaviour of $Tb_2Ti_2O_7$ is confirmed by μSR measurements (Figure 5c) [Gardner'99a]. As one may see at all temperatures the decay of the muon spin polarisation is an exponential one, suggesting fluctuating internal fields. The muon spin relaxation rate λ is temperature independent at high temperatures, it then increases and finally it saturates at a finite value down to 70 mK. We note that 70 mK is well below the energy scale set by $\theta_{CW} = -19$ K, giving a significant frustration factor $f \geq 270$.

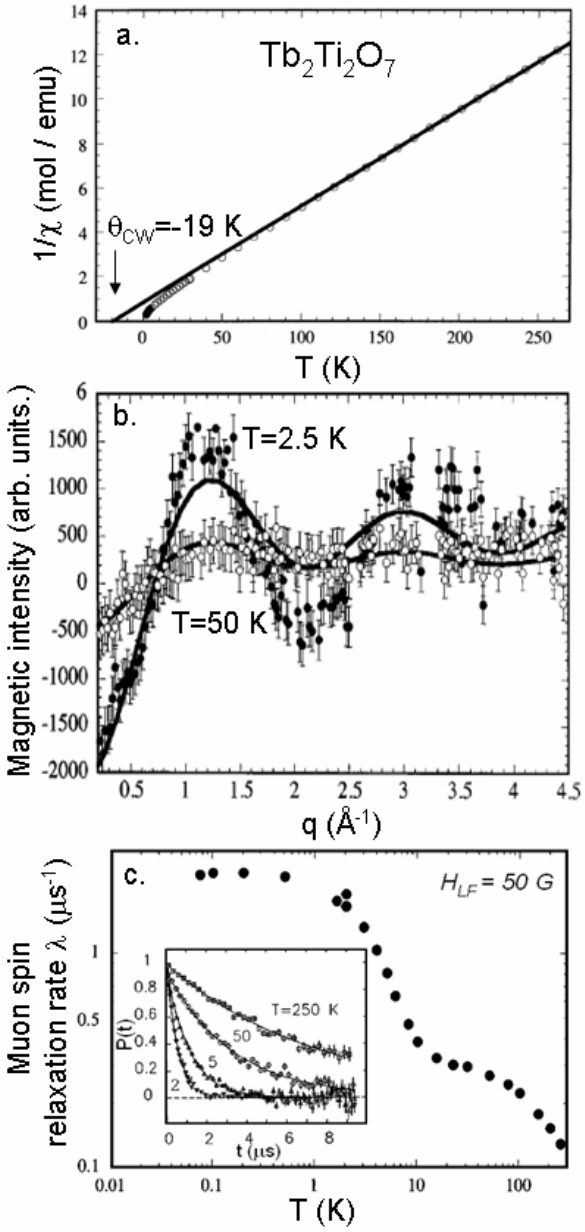

Figure 5. $Tb_2Ti_2O_7$: a. The temperature dependence of the inverse dc susceptibility along with a Curie-Weiss fit of the high temperature region giving $\theta_{CW} = -19\,K$ [Gardner'99a, Gaulin'98, Gingras'00]; b. Two magnetic neutron diffraction patterns at 2.5 and 50 K, respectively, showing short range spin correlations [Gardner'99a, Gardner'01, Gaulin'98]. $q = 4\pi \sin\theta / \lambda$ is the scattering vector. A spectrum at 100 K was each time subtracted and a correction for the Tb^{3+} form factor was made. Solid lines correspond to a calculation of the scattering expected from spin correlations extending over a single tetrahedron only; c. The temperature dependence of muon spin relaxation rate λ, in a small longitudinal applied field of 50 G, showing the persistence of spin fluctuations down to 70 mK. In inset the muon spin depolarisation function for several temperatures T= 2, 5, 50 and 250 K [Gardner'99a].

$Tb_2Ti_2O_7$ magnetic properties were also investigated by inelastic neutron scattering on single crystal in the temperature range 0.4-150 K [Yasui'02]. This study shows that when decreasing temperature below ~ 30 K the short range correlations become appreciable. Spins continue to fluctuate down to the lowest measured temperature. These results are in rather

good agreement with previous ones. However, an interesting behaviour is observed at low temperatures, where for a scattering vector $q=(0,0,2.1)$ a sharp upturn of intensity and hysteresis effects are observed below 1.5 K (Figure 6a). Other analyses bring also to light interesting low temperature features. DC susceptibility measurements on powder samples indicate substantial history dependence below 0.1 K [Luo'01]. The zero field cooled (ZFC) and field cooled (FC) curves diverge substantially below this temperature (Figure 6b). Furthermore, ac susceptibility $\chi^* = \chi' - i\chi''$ measurements on single crystal sample show that both real χ' and imaginary part χ'' are characterized by the presence of a peak at ~ 0.2 K (Figure 6c). The peak temperatures for both χ' and χ'' shift towards higher temperature when increasing frequency [Hamaguchi'04]. Specific heat anomalies are also see in this temperature region [Hamaguchi'04]. Despite the little differences concerning the temperature at which these effects are seen, all suggest a low temperature spin freezing corresponding to a spin glass or cluster glass state, which coexists with spin fluctuations.

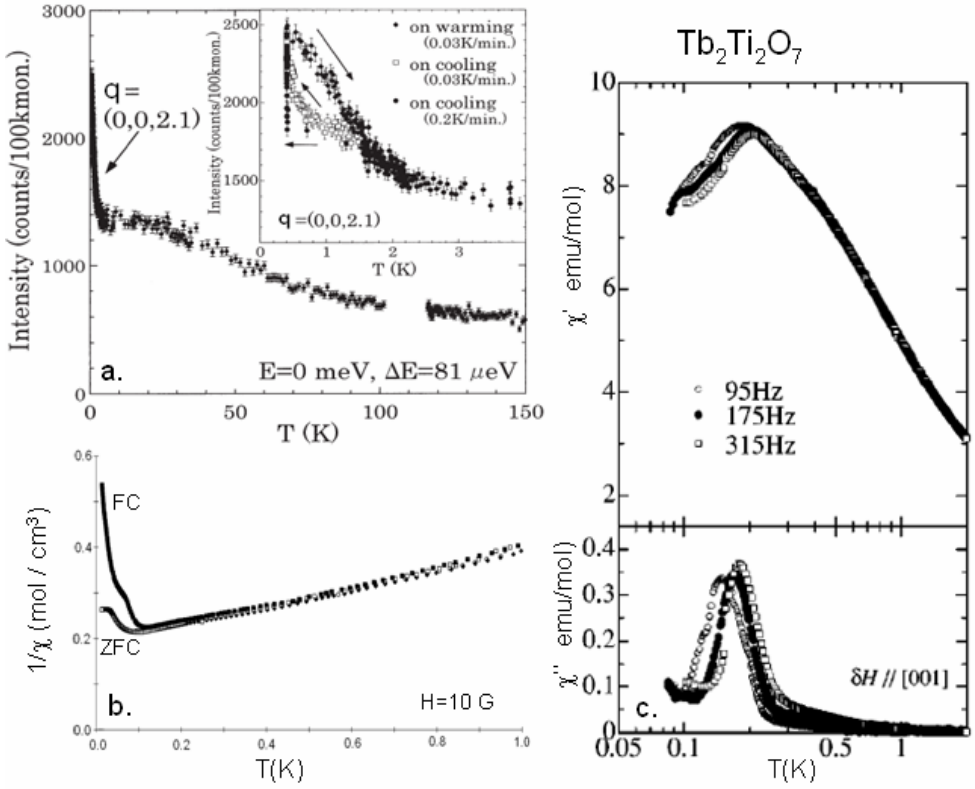

Figure 6. $Tb_2Ti_2O_7$: a. The temperature dependence of the scattered neutron intensity along the scattering vector q=(0,0,2.1), with E=0 meV and the energy resolution ΔE=81 μeV. The inset shows the hysteresis on intensity-temperature curves when warming and cooling. There is also a cooling rate dependency [Yasui'02]; b. Inverse dc susceptibility versus temperature below 1 K. History dependence is visible in the difference between zero field cooled (ZF) and field cooled (FC) data below about 0.1 K [Luo'01]; c. Temperature dependence of the ac susceptibilities $\chi^* = \chi' - i\chi''$ for several frequencies (95, 175 and 315 Hz) of the ac field δH applied along the [001] direction of the single crystal [Hamaguchi'04].

In order to understand better the ground state of $Tb_2Ti_2O_7$, its behaviour was analysed under the effect of a perturbation: the pressure. Figure 7 shows first results on powder neutron diffraction under high pressure [Mirebeau'04a, Mirebeau'02]. At $T=1.4$ K and $P=0$, the diffuse intensity arising from liquid like magnetic correlations shows no indication

of long range magnetic order. At $P = 1.5$ GPa small magnetic Bragg peaks start to emerge from the diffuse background and at $P = 8.6$ GPa the average intensity becomes much lower, but the magnetic peaks are clearly seen. Simultaneously, the diffuse intensity shows a stronger modulation (Figure 7a). The magnetic Bragg peaks start to appear below $T_N = 2.1$ K, whose value is almost pressure independent (Figure 7b). The analysis of the modulation amplitude $A(P,T) = I_{\max} - I_{\min}$, defined as the difference between the extremes of the diffuse intensity for a given pattern and expected to be proportional to the thermal average of the n.n. spin correlations [Gardner'99a], shed new light on the magnetic state below T_N. A is found to increase when decreasing temperature, showing the enhancement of the magnetic correlations in the spin liquid phase. This effect is more pronounced as pressure increases (Figure 7c). The onset of long range order at T_N coincides with a sharp kink of A. Below T_N, the decrease of A mirrors the increase of Bragg intensity, showing that long range ordered phase coexists with the spin liquid one in a mixed solid-liquid phase, with both static and dynamic character.

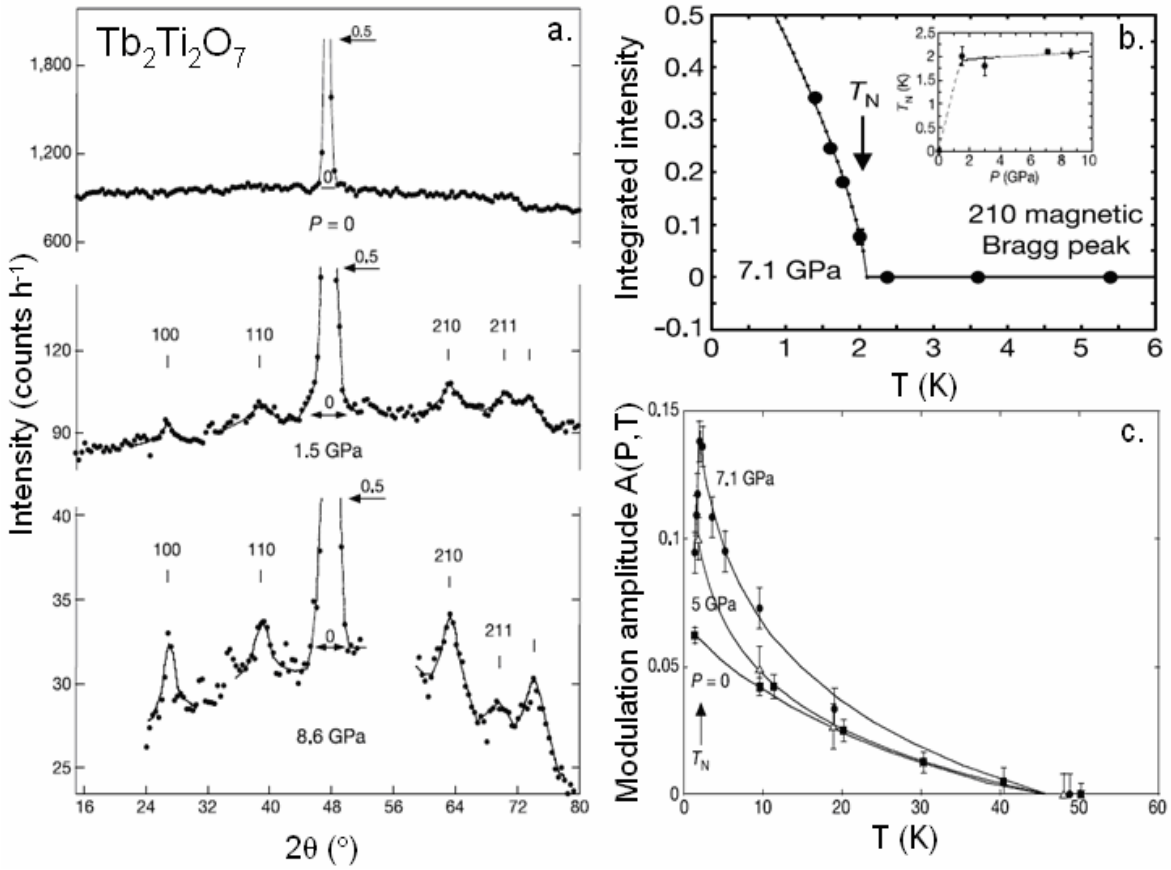

Figure 7. $Tb_2Ti_2O_7$ [Mirebeau'02]: a. The raw powder neutron diffraction spectra for three pressures P=0, 1.5 and 8.6 GPa at T=1.4 K. Intensity scales are chosen to show the magnetic peaks as compared with the (111) structural peak; b. The temperature variation of the integrated intensity of the (210) magnetic Bragg peak for P=7.1 GPa. In inset the pressure dependence of the Néel temperature T_N ; c. The temperature dependence of the modulation amplitude A(P,T) for P=0, 5 and 7.1 GPa, with $A(P,T)=I_{max}-I_{min}$ the difference between the extremes of the diffuse intensity.

Neutron diffraction measurements on single crystal allowed the comparison between the effects of a hydrostatic pressure P_i, an uniaxial stress P_u or a combination of both [Mirebeau'05, Mirebeau'04b]. It clearly shows that both components play a role in inducing

the long range order and that the Néel temperature and the ordered magnetic moment can be tuned by the direction of the stress. A stress along the [110] axis, namely along the n.n. distances between Tb^{3+} ions, is the most efficient in inducing the magnetic order.

Both powder and single crystal studies [Mirebeau'04a, Mirebeau'05, Mirebeau'02, Mirebeau'04b] show magnetic Bragg peaks of the simple cubic lattice which can be indexed from the crystal structure of the $Fd\bar{3}m$ symmetry, considering a propagation vector $\vec{k}$=(1,0,0). FULLPROF refinements [Rodríguez-Carvajal'93] of the single crystal data allowed the determination of the local spin structure within a Tb^{3+} tetrahedron. The main characteristics of the pressure induced magnetic structure are: (i) it is a non-collinear AF $\vec{k}$=(1,0,0) structure, meaning that in the unit cubic cell with four Tb^{3+} tetrahedra, two are identical and two have reversed moments; (ii) inside a tetrahedron, the magnetization is not compensated, namely the vectorial sum of the spins in non-zero (although it is of course compensated within the unit cell, since the magnetizations of the four tetrahedra cancels two by two). This means that in the pressure induced ground state, the local order does not correspond to any configuration which minimizes the energy in the spin liquid phase. In other words, pressure does not select any energy state among those belonging to the degenerated ground state of a spin liquid (ground state expected if one considers Heisenberg spins coupled via n.n. AF interactions only).

We note that in the literature there are several studies which also analyzed the behaviour of $Tb_2Ti_2O_7$ under an applied magnetic field (at ambient pressure or under pressure). We do not discuss these studies since the effect of the magnetic field is not the subject of this study.

I.2.2. The spin ices. Experimental results on $Ho_2Ti_2O_7$ and $Dy_2Ti_2O_7$

The antiferromagnetic n.n. Heisenberg spins on pyrochlore lattice is expected to form a fluctuating spin liquid state at low temperatures. On the contrary, n.n. Heisenberg spins on pyrochlore lattice and having a ferromagnetic coupling give rise to a long range ferromagnetic order. In this case there is a unique spin arrangement (collinear), which minimizes the energy. However, Ref. [Bramwell'01a, Bramwell'98, Harris'97] show that frustration can arise even for a ferromagnetic spin coupling, if there is a strong local single-ion anisotropy and the spin are constrained to orient along the <111> anisotropy axes.

Figure 8 shows that with simple “up-down” Ising spins the antiferromagnet is highly frustrated and the ferromagnet is not. Ising-like anisotropy (uniaxial) could be realized for systems having a unique privileged crystalline axis. In pyrochlore structures with cubic symmetry there is not such an axis. There are, however, local Ising anisotropy axes compatible with the cubic symmetry: the <111>-type directions which connect the center G of the tetrahedron to its vertices. The AF ground state is now unique, consisting of alternate tetrahedra with “all spins in” or “all spins out” (Figure 8d). The degeneracy is broken and there is a phase transition to an ordered state, observed in the pyrochlore FeF_3 [Ferey'86]. With the F coupling the ground state has the configuration “two spins in, two spins out” (Figure 8c).

This model maps exactly onto the ice model (Figure 9). In the low temperature phase of water ice (hexagonal or cubic ice) each oxygen atoms has four nearest neighbours. Bernal and Fowler [Bernal'33] and Pauling [Pauling'35] were the first to propose that the hydrogen atoms (protons) within the H_2O lattice are not arranged periodically, but are disordered. The

hydrogen atoms on the O-O bonds are not positioned at the mid-point between the two oxygen atoms, but rather each proton is near (covalently bonded) one oxygen and far (hydrogen bonded) from the other such that the water solid consists of hydrogen bonded H_2O molecules. In the Pauling model, the ice is established when the whole system is arranged according to the two ice rules: (i) precisely one hydrogen is on each bond that links two n.n. oxygen atoms; (ii) precisely two hydrogen atoms are near each oxygen and two are far from them (Figure 9). A consequence of this structure is that there is not a unique lowest energy state, but an infinitely large number of states that fulfil the ice rules. This degeneracy manifest itself by a residual entropy at zero temperature (called the zero-point entropy). Pauling [Pauling'35, Pauling'60] estimated theoretical the residual entropy as $(R/2)\ln(3/2) = 1.68$ J mol^{-1} K^{-1}.

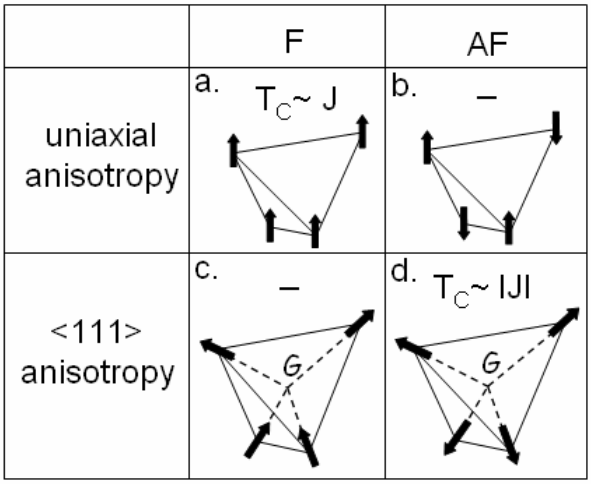

Figure 8. The ground state of a single tetrahedron of spins with various combinations of exchange coupling (F and AF) and uniaxial or local <111> anisotropy [Bramwell'98].

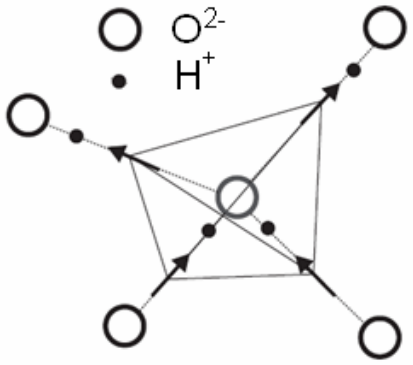

Figure 9. The local proton arrangement in ice, showing the oxygen atoms O^{2-} and the hydrogen atoms H^+ arranged to obey the "ice rules" [Bramwell'98]. The displacements of the hydrogen atoms from the mid-points of the oxygen-oxygen bond are represented as arrows, which translate into spins on one tetrahedron of the pyrochlore lattice represented in Figure 8c.

Returning to the magnetic Ising pyrochlores the analogy to the water ice arises if the spins are chosen to represent hydrogen displacements from the mid-points of the O-O bonds. The ice rule "two protons close, two protons further away" corresponds to the configuration "two spins in, two spins out" of each tetrahedron on the pyrochlore lattice. Because of this direct analogy with water ice the Ising pyrochlore is called "spin ice".

The best experimental realization of the spin ice is represented by the pyrochlore compounds $Ho_2Ti_2O_7$ and $Dy_2Ti_2O_7$. As $Tb_2Ti_2O_7$ (and all rare earth titanate pyrochlores), these compounds are chemically ordered insulators.

In $Ho_2Ti_2O_7$ the magnetic ion is Ho^{3+}, which has a $^5I_8$ free-ion ground state. Inelastic neutron scattering has been employed to study the crystal field parameters and the corresponding energy level scheme. It was found that the crystal field ground state is almost a pure $|\pm 8\rangle$ doublet well separated from the first excited state at ~ 240 K, with a strong <111> local Ising anisotropy axis [Rosenkrantz'00, Siddharthan'99]. Similar results were found for $Dy_2Ti_2O_7$ where the magnetic ion is Dy^{3+}, which has a $^6H_{15/2}$ free-ion ground state. Inelastic neutron scattering show that the crystal field ground state is almost a pure $|\pm 15/2\rangle$ doublet well separated from the first excited state by ~ 380 K, having also a strong <111> local Ising anisotropy axis [Rosenkrantz'00]. Bulk magnetization data analysis in a wide temperature range and variety of fields [Bramwell'00, Harris'97], confirms for both compounds the above ground states and the strong <111> single anisotropy. The assignment of Ho^{3+} in $Ho_2Ti_2O_7$ as a $|\pm 8\rangle$ doublet is the same as that reported by Ref. [Blöte'69] for Ho^{3+} in the related compound Ho_2GaSbO_7. Also based on heat capacity measurements the same Ref. [Blöte'69] confirms the $|\pm 15/2\rangle$ doublet ground state of $Dy_2Ti_2O_7$. The fit of inverse susceptibility with the Curie-Weiss law gives the Curie-Weiss temperatures $\theta_{CW} \sim$ 1-2 K for $Ho_2Ti_2O_7$ [Bramwell'00, Harris'97, Kanada'02, Matsuhira'00] and $\theta_{CW} \sim$ 0.5-1 K for $Dy_2Ti_2O_7$ [Bramwell'00, Ramirez'99], suggesting ferromagnetic interactions. Due to the presence of strong anisotropy along the <111> axes coupled with ferromagnetic interactions between the rare earth spins, both $Ho_2Ti_2O_7$ and $Dy_2Ti_2O_7$ would appear, at first sight, to be spin ice materials. A more detailed study of the exchange and dipolar interactions (see section I.2.3) will shed into light new information. We note the difference in regard to $Tb_2Ti_2O_7$, with Tb^{3+} having a $^7F_6$ free ion ground state, where the Ising anisotropy is reduced to much lower temperature due to narrowly spaced crystal field levels. Inelastic neutron scattering show a $|\pm 4\rangle$ ground state doublet followed by $|\pm 5\rangle$ doublet as first excited state, with a doublet-doublet energy splitting of only 18 K [Gardner'99a, Gardner'01, Gingras'00, Mirebeau'07a]. Contrary to $Ho_2Ti_2O_7$ and $Dy_2Ti_2O_7$ the Curie-Weiss constant $\theta_{CW} \sim$ -19 K [Gardner'99a, Gingras'00] shows antiferromagnetic interactions between Tb^{3+} spins.

For $Ho_2Ti_2O_7$ neutron diffraction measurements on single crystal sample show that there is no magnetic long range order down to temperatures of at least 0.35 K, but instead there is a diffuse scattering which develops when decreasing temperature [Harris'97, Harris'98]. Powder neutron diffraction confirm the appearance of the short range order when decreasing temperature (see Figure 11a) [Mirebeau'04a]. Low temperature muon spin relaxation analysis also finds no evidence for a magnetic transition down to at least 0.05 K [Harris'97, Harris'98].

In the case of $Dy_2Ti_2O_7$ specific heat measurements [Ramirez'99] give a direct experimental evidence that the similarity between water ice and spin ice goes beyond a simple analogy. The Figure 10a shows the temperature dependence of the magnetic specific heat $C(T)$, for a powdered sample $Dy_2Ti_2O_7$. The data shows no sign of a phase transition, as would be indicated by a sharp feature in $C(T)$. Instead, one observes a broad maximum at ~ 1.2 K, which is on the order of the energy scale of the magnetic interactions as measured by

θ_{CW}. The specific heat has the appearance of a Schottky anomaly, the characteristic curve for a system with two energy levels. At low temperature $C(T)$ falls rapidly to zero, suggesting a freezing of the magnetic moments. The most surprising aspect of these data is found when calculating the magnetic entropy by integrating $C(T)/T$ from 0.2 in the frozen regime to 12 K in the paramagnetic regime where the expected entropy should be $R\ln 2$ for a two state system. Figure 10b shows that the magnetic entropy recovered is about 3.9 J mol^{-1} K^{-1}, a number that falls considerably low in regard to the value $R\ln 2 \approx 5.76$ J mol^{-1} K^{-1}. The difference, 1.86 J mol^{-1} K^{-1} is quite close to Pauling's estimation for the entropy associated with the extensive degeneracy of water ice $(R/2)\ln(3/2) = 1.68$ J mol^{-1} K^{-1}, consistent with the existence of spin ice state in $Dy_2Ti_2O_7$.

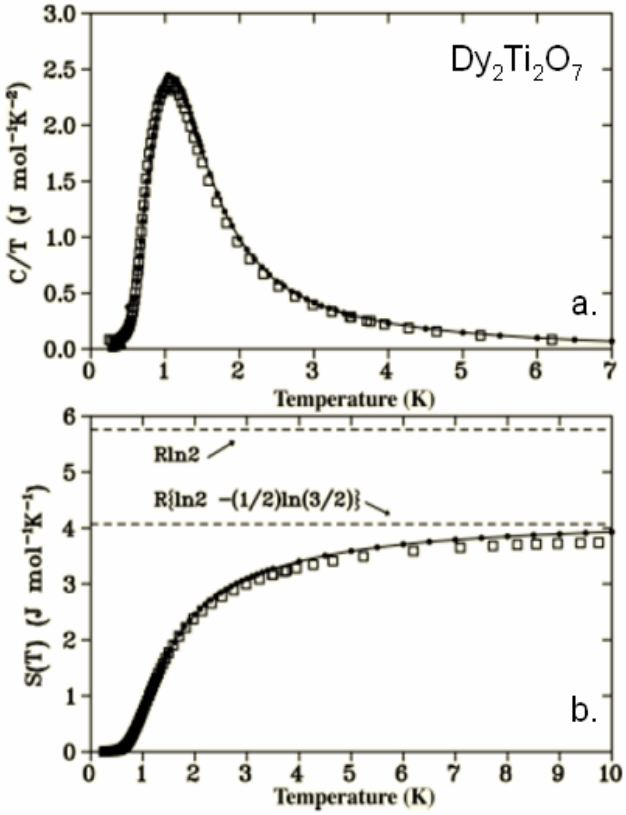

Figure 10. Specific heat and entropy of the spin ice compound $Dy_2Ti_2O_7$ showing the agreement with Pauling prediction for the entropy of the water ice I_h $(R/2)\ln(3/2) = 1.68$ J mol^{-1} K^{-1} [Ramirez'99]: a. Specific heat divided by temperature; b. The corresponding entropy found by integrating C/T from 0.2 to 12 K. The value $R(\ln 2 - (1/2)\ln(3/2))$ is that found for I_h and $R\ln 2$ is the full spin entropy. Lines are Monte Carlo simulations as described in the next section.

The behaviour of $Ho_2Ti_2O_7$ when analysing the effect of the applied pressure is different in regard to that of $Tb_2Ti_2O_7$. In Ref. [Mirebeau'04a] is shown that as at ambient pressure (Figure 11a), under pressure the diffuse magnetic scattering strongly increases when decreasing temperature. However there is no effect of pressure itself. Figure 11b shows the temperature dependence of the modulation amplitude $A(P,T)$ for three different pressures P=0, 5 and 6 GPa (in inset are shown the corresponding magnetic diffuse scattering for P=0 and 6 GPa). Its behaviour is clearly different from that observed for $Tb_2Ti_2O_7$ (Figure 7c). For $Ho_2Ti_2O_7$, A increases also when decreasing temperature showing the enhancement of the

magnetic correlations, but there is no indication of a low temperature transition to long range magnetic order. Additionally one may clearly see that there is no effect of the applied pressure to at least 6 GPa.

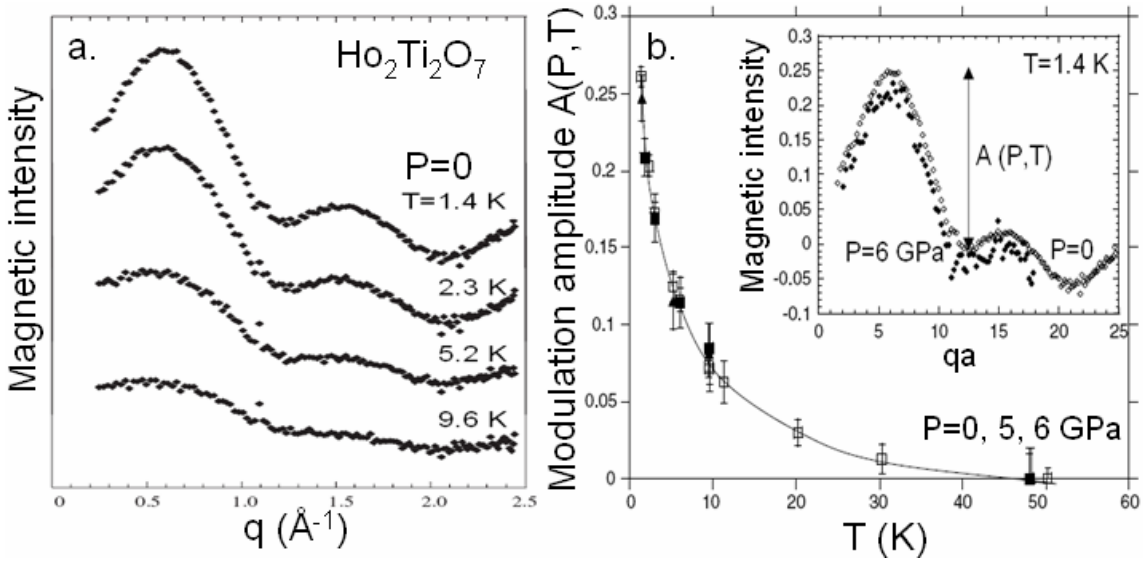

Figure 11. Powder neutron diffraction on $Ho_2Ti_2O_7$ [Mirebeau'04a]: a. Diffuse magnetic intensity for several temperatures T=1.4, 2.3, 5.2 and 9.6 K; b. The temperature dependence of the modulation amplitude A(P,T) for P=0, 5 and 6 GPa, with $A(P,T)=I_{max}-I_{min}$ the difference between the extremes of the diffuse intensity (see inset). In inset the magnetic scattering at P=0 and 6 GPa plotted versus the wave vector transfer qa in reduced units. This procedure allows all data to be compared qualitatively and to distinguish the effect of pressure from casual lattice contraction.

I.2.3. Theoretical approaches

After presenting few experimental results on $Tb_2Ti_2O_7$ (spin liquid), $Ho_2Ti_2O_7$ and $Dy_2Ti_2O_7$ (spin ices) we focus on some theoretical approaches that try to describe the magnetic behaviour of these compounds.

In all these systems the rare earth is the only magnetic ion and therefore the rare earth magnetism controls the ground state of the system. This ground state is determined by the special balance between the exchange, dipolar and crystal field energies. At the time being there are several theories that are trying to describe the magnetic ground state of pyrochlore magnets (some of them already mentioned when defining the concept of spin liquid and spin ice, respectively). They involve different combinations of the above mentioned energies: antiferromagnetic ($J_{nn} < 0$) or ferromagnetic ($J_{nn} > 0$) nearest neighbour exchange energy, ferromagnetic dipolar energy ($D_{nn} > 0$) and also the strength of the local anisotropy D_a.

First models [Canals'01, Canals'98, Moessner'98b, Moessner'98c, Reimers'92, Reimers'91] consider Heisenberg spins coupled via AF n.n. exchange interactions, where the Hamiltonian is defined as:

$$\mathcal{H}_{\text{ex}} = -J \sum_{i,j} \vec{S}_i \cdot \vec{S}_j \qquad \text{[I.7]}$$

with $J < 0$ for AF interactions. These models describe rather well the spin liquid behaviour of $Tb_2Ti_2O_7$ as shown in Figure 12.

Then there is the spin ice model [Bramwell'01a, Bramwell'98, Harris'97] that show how the local Ising anisotropy reverses the roles of ferromagnetic and antiferromagnetic exchange couplings with regard to the frustration, such that the ferromagnet is highly frustrated and the antiferromagnet is not. Almost in the same time Ref. [Moessner'98a] shows that a strongly anisotropic classical Heisenberg magnet on the pyrochlore lattice can be mapped onto an Ising model with an exchange constant of an opposite sign.

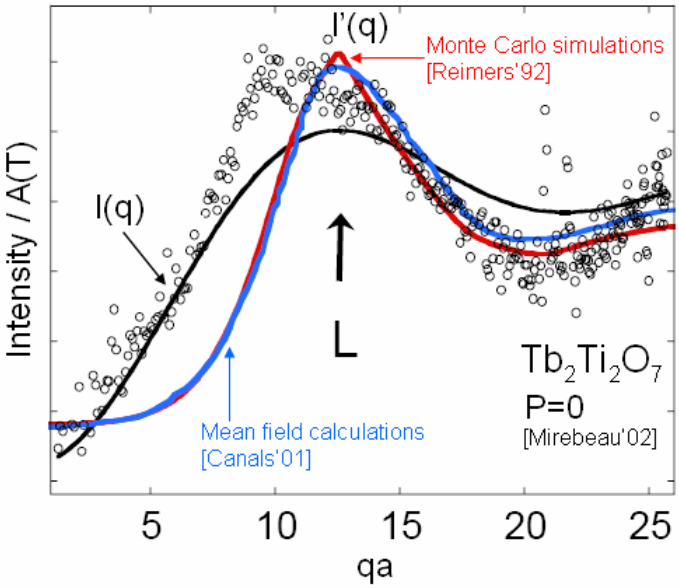

Figure 12. Magnetic diffuse scattering in $Tb_2Ti_2O_7$ at ambient pressure versus the reduced unities qa, with a the lattice parameter [Mirebeau'02]. A (T) is the modulation amplitude. Continuous lines represent fits with: (i) $I(q)$, representing a cross section proposed in Ref. [Bertaut'67], $I(q) \sim \sin(qR_1)/qR_1$, with R_1 the n.n. spin distance; (ii) $I'(q)$, calculated accordingly to Monte Carlo simulations [Reimers'92] and mean field calculation [Canals'01]. L marks the liquid peak position resulting from these models. For more details see [Cadavez-Peres'02].

However, the simple spin ice model raises some problems when analysing more carefully the two representative compounds $Ho_2Ti_2O_7$ and $Dy_2Ti_2O_7$. First we should mention that the nearest neighbour exchange coupling J_{nn} was determined by fitting the peak temperature of the electronic magnetic heat capacity. The obtained values are negative, indicating antiferromagnetic exchange interaction: $J_{nn}(Ho_2Ti_2O_7) \sim$ -0.52 K [Bramwell'01b] and $J_{nn}(Dy_2Ti_2O_7) \sim$ -1.24 K (see Figure 10) [denHertog'00]. According to the spin ice model, such a behaviour would by itself cause a phase transition to a Néel long range ordered state, which is not the case. Another interesting aspect is that the magnetic cations Ho^{3+} and Dy^{3+} carry a large magnetic moment μ of approximately 10 μ_B. Consequently, in these systems there should be strong long range dipolar interactions. Generally, the magnitude of the dipole interactions between nearest neighbours is given by: $D = (\frac{\mu_0}{4\pi})\frac{\mu^2}{r_{nn}^3}$, where μ is the magnetic moment and r_{nn} the nearest neighbour distance ($r_{nn} = (a/4)\sqrt{2}$, a being the unit cell dimension). Because the local anisotropy easy axes align along the <111> directions, the dipolar energy scale is $D_{nn} = \frac{5}{3}D$. In the same time for n.n. exchange interaction the energy

scale is $J_{nn} = \frac{1}{3} J$. The above relations allow the determination of the dipolar energy for $Ho_2Ti_2O_7$ and $Dy_2Ti_2O_7$: D_{nn} = 2.35 K > 0, indicating ferromagnetic dipolar interactions [Bramwell'01a, denHertog'00]. This value is comparable to that of the nearest neighbour exchange interaction and therefore in these systems this interaction can not be neglected.

In this context the dipolar spin ice model arrived naturally [Bramwell'01a, Bramwell'01b, denHertog'00, Gingras'01, Melko'04]. The corresponding Hamiltonian is defined as:

$$\mathcal{H} = -J \sum_{i,j} \vec{S}_i^{z_i} \cdot \vec{S}_j^{z_j} + D r_{nn}^3 \sum_{j>i} \frac{\vec{S}_i^{z_i} \cdot \vec{S}_j^{z_j}}{\left|\vec{r}_{ij}\right|^3} - \frac{3(\vec{S}_i^{z_i} \cdot \vec{r}_{ij})(\vec{S}_j^{z_j} \cdot \vec{r}_{ij})}{\left|\vec{r}_{ij}\right|^5} \qquad \text{[I.8]}$$

where the spin vector $\vec{S}_i^{z_i}$ represents the Ising moment of magnitude 1 at lattice site i and local Ising axis z_i.

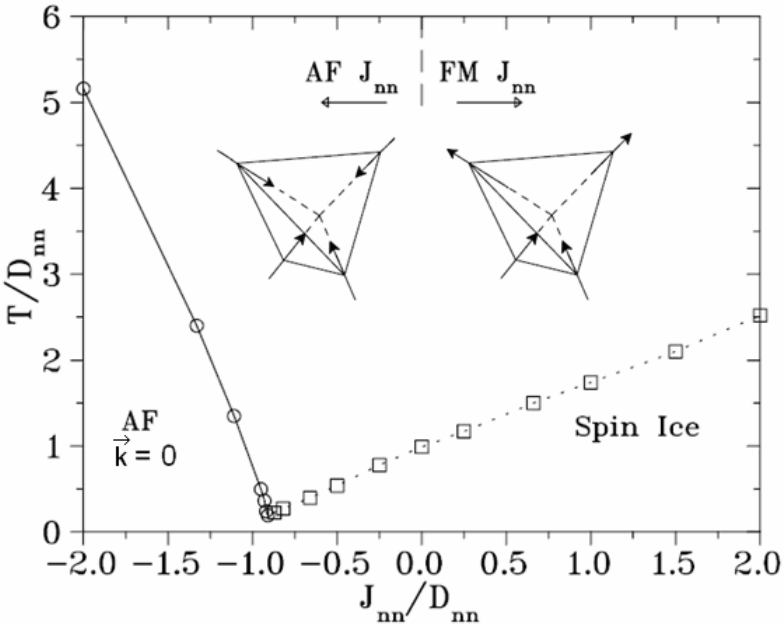

Figure 13. Phase diagram of Ising pyrochlore magnets with nearest neighbour exchange and long range dipolar interactions showing two phases of interest: the Néel long range ordered phase realized for $J_{nn} / D_{nn} < -0.91$ *and the spin ice phase, respectively .* J_{nn} *and* D_{nn} *are the parameters for the nearest neighbour exchange and dipole interaction as indicated in the text. The two insets represent the spin configurations corresponding to the two phases. Results are cited from Ref. [denHertog'00].*

In order to consider the combined role of the exchange and dipolar interactions, an effective nearest neighbour energy scale was defined for <111> Ising spins: $J_{nn}^{eff} = J_{nn} + D_{nn}$. This simple description predicts that a <111> Ising system could display spin ice properties, even for antiferromagnetic nearest neighbour exchange, $J_{nn} < 0$, as long as $J_{nn}^{eff} > 0$. And this is the case of the above systems, J_{nn}^{eff} being 1.83 K and 1.11 K for $Ho_2Ti_2O_7$ and $Dy_2Ti_2O_7$, respectively. The results of Monte Carlo simulations and mean field analysis [denHertog'00] show how the dipolar energy scale influences the ground state of the system: spin ice behaviour persists in the presence of antiferromagnetic exchange up to $J_{nn} / D_{nn} \sim -0.91$,

whereas for $J_{nn} / D_{nn} < -0.91$, there is a second order transition to a $\vec{k} = 0$ antiferromagnetic structure, where all the spins point either in or out of a given tetrahedron [Bramwell'98]. $Ho_2Ti_2O_7$ (J_{nn}^{eff} = 1.83 K, $J_{nn} / D_{nn} \sim -0.22$) and $Dy_2Ti_2O_7$ (J_{nn}^{eff} = 1.11 K, $J_{nn} / D_{nn} \sim -0.52$) are situated is the spin ice region of the phase diagram (see Figure 13). The sibling compound $Ho_2Sn_2O_7$ is also an dipolar spin ice (J_{nn}^{eff} = 2.7 K, $J_{nn} / D_{nn} \sim 0.14$) [Kadowaki'02].

In the case of $Ho_2Ti_2O_7$ [Bramwell'01a, Bramwell'01b] and $Ho_2Sn_2O_7$ [Kadowaki'02] it was shown that this dipolar spin ice model describes very accurately the diffuse magnetic neutron scattering, whereas the spin ice model represents only a more qualitative approximation. Figure 14a shows few examples of calculated magnetic intensities obtained by mean field analysis and taking into account different spin interactions: AF n.n. exchange interaction, F n.n. exchange interactions and long range dipolar interactions. The experimental magnetic neutron scattering of $Ho_2Sn_2O_7$ was well fitted with a combination of dipolar and a small exchange interaction as described in Ref. [Kadowaki'02].

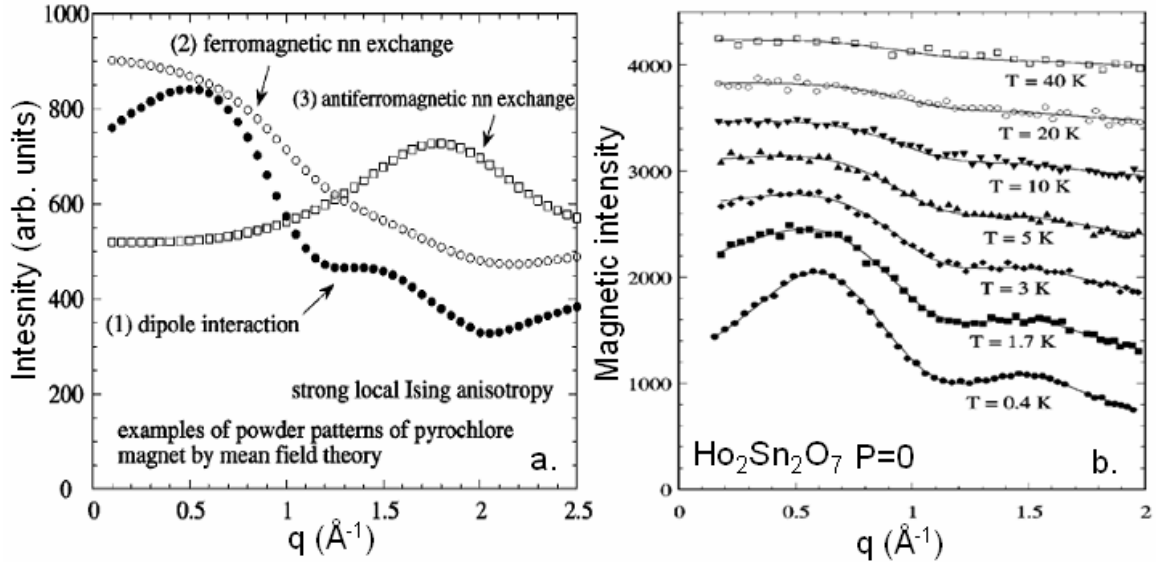

Figure 14. a. Examples of magnetic scattering calculated using the mean field theory. Spin interactions of the three curves are: (1) dipolar interaction D_{nn}= 1.4 K, J_{nn}=0; (2) F n.n. exchange interaction J_{nn}=2 K, D_{nn}=0; (3) AF n.n. exchange interaction J_{nn}=-2 K, D_{nn}=0; b. Elastic magnetic neutron scattering of $Ho_2Sn_2O_7$ as a function of the scattering vector q at various temperatures T=0.4, 1.7, 3, 5, 10, 20 and 40 K. For T≥ 1.7 K, data were shifted for clarity. Solid lines are fits using dipolar and a small exchange interaction as described in Ref. [Kadowaki'02].

A natural question arises: how about $Tb_2Ti_2O_7$? As Ho^{3+} and Dy^{3+}, Tb^{3+} cation also carries a large magnetic moment of approximately 9 μ_B and in its case it would be justified to take into account the dipolar interactions. In $Tb_2Ti_2O_7$, $J_{nn} \simeq$ - 0.88 K and $D_{nn} \simeq 0.8$ K [Enjalran'04, Gingras'00] and consequently $J_{nn}^{eff} = -0.08$ K < 0 and $J_{nn} / D_{nn} \sim -1.1$ and the effective interaction is antiferromagnetic. Therefore, within the phase diagram from Figure 13 [denHertog'00], since $Tb_2Ti_2O_7$ has $J_{nn} / D_{nn} < -0.91$, it should have a non-collinear Néel $\vec{q} = 0$ order below about 1 K, with all spins pointing into or out of each tetrahedron. However, in contrast, all experimental analyses show that $Tb_2Ti_2O_7$ remains a spin liquid down to the lowest measured temperature of 70 mK [Gardner'99a, Gardner'01]. First observation that one may get is that the dipolar spin ice model [denHertog'00] supposes an infinite anisotropy and

this is not the case for $Tb_2Ti_2O_7$. A key difference between $Tb_2Ti_2O_7$ and spin ices ($Ho_2Ti_2O_7$ and $Dy_2Ti_2O_7$) is that in the latter the first excited crystal field doublet lies above the ground state doublet at an energy which is several hundred times larger than the exchange and dipolar interactions and there is therefore little admixing between the excited crystal field states and the ground doublet induced by spin interactions. This is not the case for $Tb_2Ti_2O_7$ which has a splitting between the ground state doublet and first excited doublet of ~ 18 K, which is of the order of magnitude of the Curie-Weiss constant $\theta_{CW} = -19$ K. Hence the fluctuations between these two lowest lying doublets are allowed and non-negligible at low temperatures. Ref. [Kao'03] employ the random-phase approximation (RPA) to take into account the single-ion excitations from the ground state doublet to the first excited one and is able to describe qualitatively the experimental observed paramagnetic neutron scattering pattern and the energy dispersion of $Tb_2Ti_2O_7$. Even if a $\vec{q} = 0$ Néel order is still obtained at low temperature, this result indicate that the crystal fields effects are important. More recently Ref. [Malovian'07] used a model of non-interacting tetrahedra to describe the low temperature properties of $Tb_2Ti_2O_7$. They identify a new mechanism for dynamically induced frustration in a physical system, which proceeds via virtual crystal field excitations and quantum many-body effects. More specifically, they showed that due to the interaction-induced fluctuations among otherwise non-interacting single ion crystal field states $Tb_2Ti_2O_7$ does not act like an non-frustrated pyrochlore Ising antiferromagnet, but like a frustrated n.n. spin ice one. The remaining transverse fluctuations lift the classical ice-like degeneracy and at the single tetrahedron level, the system is in a quantum mechanically fluctuating spin ice state.

From experimental point of view a manner of better understating the ground state of this type of pyrochlore systems (spin liquids and spin ices) is to perturb it, for example, by applying pressure. The interest of pressure is that it varies the interatomic distances and, since the magnetic interactions depend in a way or another of these distances, it modifies the energy balance that defines the ground state. In current language, there are two types of pressures: (i) the applied pressure, which compresses the lattice and (ii) the chemical pressure, that can both expand (negative chemical pressure) and contract the lattice if the substitution is made by a bigger or a smaller atom, respectively. Additionally, the chemical pressure may induce disorder into the system and could affect its magnetic ground state.

I.2.4. The spin glasses. Experimental results on $Y_2Mo_2O_7$

Another example, in fact the most commonly observed, of systems with non-Néel magnetic state are the spin glasses. We recall and underline that the canonical spin glasses are disordered systems with competing interactions. Microscopically, the spin glass state represents a configuration of magnetic spins frozen into a more or less random state. There exists a characteristic freezing or glass temperature T_f (or T_{SG}), below which the random frozen state is established from a random fluctuating state. There will be a huge number of metastable frozen states, so that a given ground state found is determined by the experimental conditions and hysteresis will be observed. From experimental point of view, there are many signatures of the spin glass state and among the commonly observed are: (i) a field cooled (FC) / zero field cooled (ZFC) divergence below T_f, in the dc magnetic susceptibility; (ii) a strong frequency dependence of both real χ' and imaginary part χ'' below T_f, in the ac susceptibility; (iii) a T^1 dependence of the electronic contribution to the heat capacity at very low temperatures; (iv) the absence of the long range magnetic order from neutron diffraction

analysis; (v) a sharp decrease of the spin fluctuation or spin relaxation time as measured by inelastic neutron scattering, μSR or some other techniques sensitive to spin dynamics, below T_f [Greedan'01].

$Y_2Mo_2O_7$ shows spin glass characteristics. It is also an insulator which has one magnetic ion on the pyrochlore lattice. However, contrary to the systems presented before (the spin liquid $Tb_2Ti_2O_7$ and the spin ices $Ho_2Ti_2O_7$ and $Dy_2Ti_2O_7$, respectively), in this case the magnetic ion is the transition metal Mo^{4+}.

Figure 15 and Figure 16 show experimental results obtained for $Y_2Mo_2O_7$.

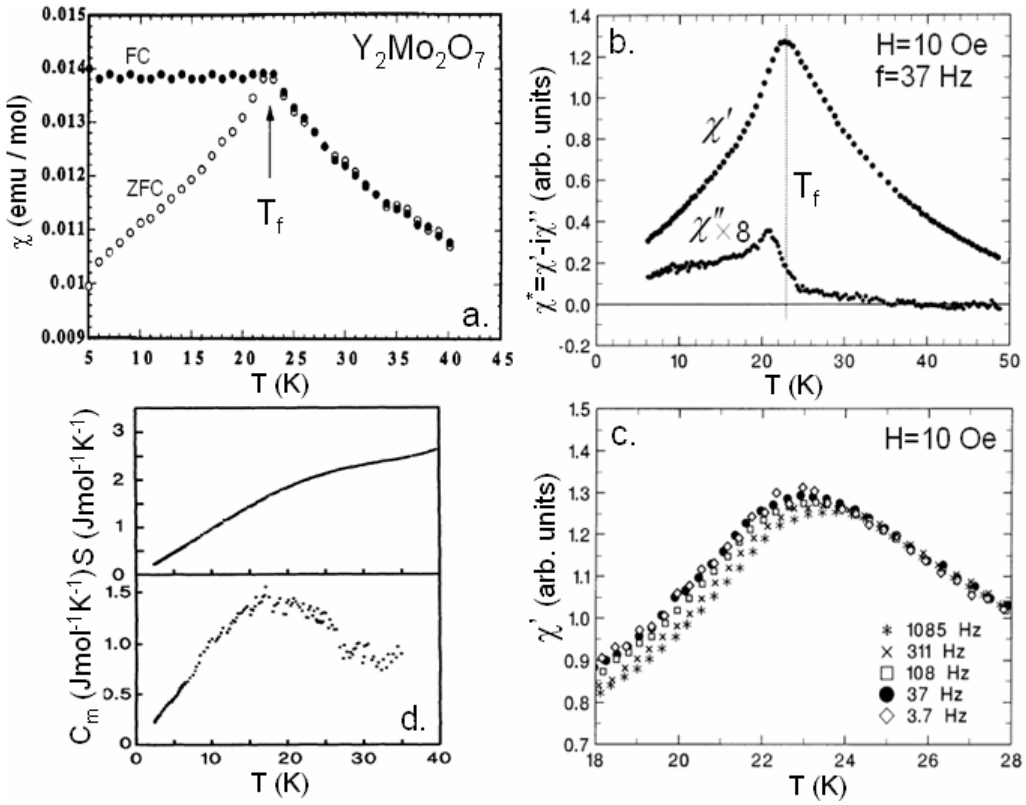

Figure 15. $Y_2Mo_2O_7$: a. Temperature dependence of the dc susceptibility measurements in zero field cooled (ZFC) and field cooled (FC) processes [Ali'92, Gaulin'98, Gingras'97]; b. Temperature dependence of the ac susceptibility $\chi^* = \chi' - i\chi''$, with χ' the real and χ'' the imaginary part, respectively, at H=10 Oe and f=37 Hz [Miyoshi'00a]; c. Temperature dependence of χ' at H=10 Oe and for several frequencies f=3.7, 37, 108, 311 and 1085 Hz [Miyoshi'00a]; d. Temperature dependence of the magnetic specific heat C_m and the corresponding magnetic entropy S [Raju'92].

The dc susceptibility shows the presence of irreversibilities between ZFC and FC curves (Figure 15a). The ZFC curve shows a sharp peak at $T_f \sim 22$ K, whereas the FC one remains constant below this temperature [Ali'92, Gaulin'98, Gingras'97]. The analysis of the nonlinear dc susceptibility χ_{nl}, close to and above the freezing temperature T_f, provides strong evidence that there is a phase transition at T_f, which is characterized by critical exponents $\gamma \approx 2.8$ and $\beta \approx 0.8$ [Gingras'96, Gingras'97]. These values are typical of those found in random spin glasses [Fisher'91]. Curie-Weiss analysis requires relatively high temperature susceptibility data in order to enter a truly paramagnetic state. Using data above

500 K, it was found that $\theta_{CW} \sim -200$ K, indicating strong antiferromagnetic interactions and an effective moment of ~ 2.3-2.5 μ_B [Gardner'99a, Gingras'97] close to the effective moment $g\sqrt{S(S+1)}\mu_B$ = 2.8 μ_B expected for S=1 Mo^{4+} ion. The ac susceptibility $\chi^* = \chi' - i\chi''$ shows, at a frequency $f = 37$ Hz and at a field amplitude H=10 Oe, a cusp in the real part χ' at ~ 23 K, while χ'' shows an abrupt increase at ~ 23 K and tails for lower temperatures. The cusp position of χ' appears to coincide with the inflexion point of χ'', indicating a spin freezing at T_f (Figure 15b). Figure 15c displays the temperature dependence of χ' for different frequencies down to 3.7 Hz and shows that it depends on the frequency below the maximum temperature, which becomes slightly lower with decreasing frequency showing again a spin freezing process [Miyoshi'00a]. Specific heat data show also features characteristic for spin glasses: (i) a broad anomaly in the magnetic specific heat C_m with a maximum at about the spin freezing temperature observed in the other measurements; (ii) a linear dependence of C_m below this temperature (see Figure 15d) [Raju'92].

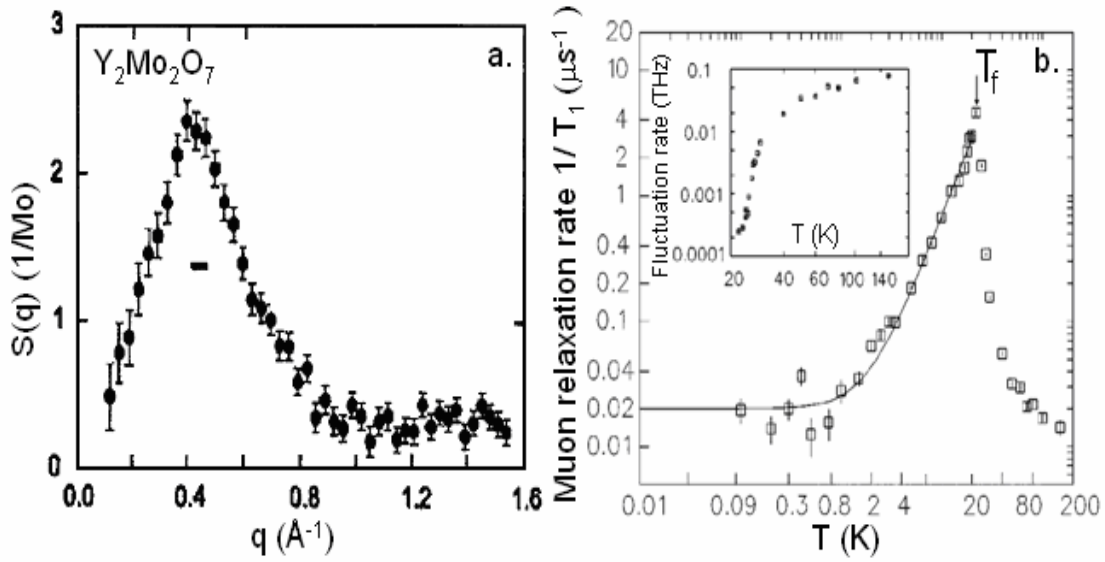

Figure 16. $Y_2Mo_2O_7$: a. The q dependence of the elastic magnetic scattering at T=1.4 K. Data taken at 50 K have been subtracted to account for the nuclear scattering [Gardner'99b]; b. The muon spin relaxation rate $1/T_1$ versus temperature, in a small applied field H=0.02 Tesla. In inset: the Mo^{4+} spin fluctuation rate versus temperature above T_{SG} [Dunsiger'96].

The neutron scattering shows no magnetic Bragg peaks [Gardner'99b]. Elastic neutron scattering were performed at 1.8 and 50 K. The difference between the two data sets, shown in Figure 16a, measures the low temperature elastic magnetic structure factor $S(q)$. The data show a peak for $q \approx 0.44$ Å^{-1}, indicating short range AF correlations. The correlation length was extracted from the half width half maximum (HWHM). Its value of about 5 Å implies correlated domains extending above a single tetrahedron. We note the difference in regard to $Tb_2Ti_2O_7$ where the Tb^{3+} spins are correlated over a single tetrahedron only.

The spin dynamics has been studied both by inelastic neutron scattering [Gardner'99b] and muon spin relaxation [Dunsiger'96]. The picture which emerges is as follows: dynamic short range order sets in a temperature as high as ~ 200 K (the θ_{CW} value), the spin fluctuation rate falls gradually to near T_f =22 K and below T_f there is a drop of two orders of

magnitude to attain a very low spin relaxation rate $1/T_1$ of 0.02 μs at 0.09 K (Figure 16b). Below T_f is therefore a disordered magnetic state similar to that found in a spin glass, but with a residual muon spin relaxation rate, temperature independent, which persists down to very low temperatures. Ref. [Dunsiger'96] suggests the existence well below T_f of a relatively large density of states for low energy magnetic excitations, much larger than in conventional randomly frustrated spin glasses.

Most experimental features of $Y_2Mo_2O_7$ correspond to the description of a canonical spin glass. This description is difficult to understand in the context of conventional, accepted ideas about spin glasses, wherein it is held that both frustration and either positional or bond disorder are necessary conditions [Ramirez'94, Ramirez'01]. For example, in insulating antiferromagnets, spin glass behaviour is observed, normally, only in actual glasses (amorphous materials) or in crystalline compounds in which the magnetic sites have been diluted by diamagnetic ions to a concentration below the percolation limit [Greedan'01].

It is not the case of $Y_2Mo_2O_7$, which is widely considered to be crystallographically well ordered, with a unique n.n. magnetic interaction J [Reimers'88]. Therefore, in the recent years, a special attention has been paid to the analysis of the structure of $Y_2Mo_2O_7$ in order to detect some kind of disorder of the system. By means of X-ray absorbtion fine-structure (XAFS) analysis as a probe of the Y and Mo environments, Ref. [Booth'00] suggests that there is a relatively large amount of bond length disorder that involves only the Mo-Mo pairs. The Mo tetrahedra are in fact distorted at the local level from their average, ideal structure. The distortion seems to act in a direction that is roughly parallel to the local Mo-Mo pairs and perpendicular to Mo-Y pairs. For example, one possible distortion is that obtained by displacing the Mo atoms towards or away from the tetrahedron body center as shown in Figure 17. The magnitude of this distortion may vary throughout the solid, creating a distribution of Mo-Mo pair distances and not severely altering the Mo-Y pairs.

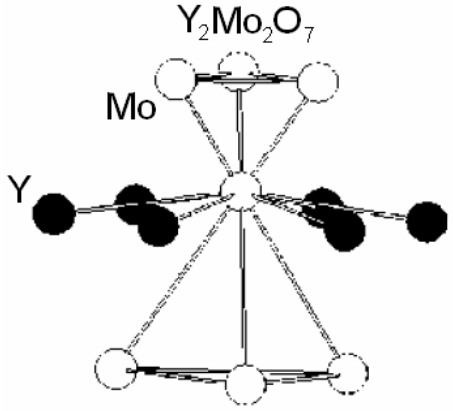

Figure 17. $Y_2Mo_2O_7$: one possible (exaggerated for clarity) distortion of the Mo tetrahedra as obtained from XAFS analysis [Booth'00].

Evidence of disorder was also revealed by the presence of regularly spaced peaks in ^{89}Y NMR measurements from Ref. [Keren'01], which claims the existence of many non-equivalent ^{89}Y sites due to a non-random distortion of the Mo sublattice. μSR analysis from Ref. [Sagi'05] sustains also the hypothesis of the presence of random lattice distortions, taking into account that the static muon relaxation rate is related to the lattice via the muon coupling to its neighbouring spins. Therefore the observed distribution of coupling constants is attributed to lattice disorder. One may notice that only local probes have revealed a

distribution of bond length, while usual diffraction techniques (X rays or neutrons) show no bond disorder, indicating that the average bulk structure is almost the perfect oxide pyrochlore lattice. More recently Ref. [Greedan'06] attempt to reconcile the average and local structure studies by applying neutron pair distribution function (NPDF) analysis to neutron diffraction spectra measured up to very high q values. With this technique both the local and average structures are determined simultaneously. Data were analysed by standard Rietveld methods for the average structure and with Fourier transformation $G(r)$ the pair distribution was obtained. According to Ref. [Greedan'06], Rietveld results show an anomalously large displacement ellipsoid for oxygen O1 and highly distorted displacements ellipsoids for Mo and Y. The fit of the $G(r)$ to the average structure results is satisfactory for the Mo-Mo and Mo-O1 pairs, but fails for the Y-O1 and O1-O1 pairs. This result apparently contradicts those obtained by local probe techniques. At the time being the existence in $Y_2Mo_2O_7$ of bond disorder involving Mo-Mo pairs is still under discussion.

I.3. The geometrical frustrated pyrochlores: systems with two magnetic ions

The last pyrochlore systems to be discussed are those with magnetic ions on both R and M sites and hence with two geometrically frustrated lattices. Among these systems, there is a class of compounds that attracted great deal of interest in the recent years: the molybdenum pyrochlores $R_2Mo_2O_7$, with R=rare earth or yttrium.

I.3.1. Experimental results on $R_2Mo_2O_7$

In these systems, besides the magnetism of the rare earth, there is also the contribution from the transition metal ion Mo^{4+}. The rare earth R^{3+} carries a large magnetic moment. The free ion values are 3.27 μ_B for Nd^{3+}, 7 μ_B for Gd^{3+}, 9 μ_B for Tb^{3+} and 10 μ_B for Dy and Ho, respectively. These values may be reduced by crystal field effects. However, these magnetic moments are localized showing weak R-R exchange interactions. Per contra, Mo^{4+} has a small magnetic moment (2 μ_B), but it is itinerant, suggesting strong Mo-Mo exchange interactions.

Ref. [Katsufuji'00] showed that both electric and magnetic properties of $R_2Mo_2O_7$ pyrochlores strongly depend on the rare earth mean ionic radius R_i (for the R_i values see Ref. [Shannon'76]). According to [Katsufuji'00], compounds with small ionic radius $R_i < R_{ic}$ (R=Y, Dy and Tb) are spin glass insulators (SGI), whereas those with $R_i > R_{ic}$ (R=Gd, Sm and Nd) are ferromagnetic metals (FM). The SG-F phase boundary and the M-I crossover correspond to a critical value $R_{ic} = 1.047$ Å. Taking into account a linear dependence of the lattice parameter a with the mean ionic radius, as suggested by Ref. [Katsufuji'00], the critical value of the lattice parameter is $a_c \sim 10.33$ Å. We note however that for $Gd_2Mo_2O_7$, which is the closest to the threshold, the transport properties strongly depend on the sample preparation. First measurements on powder samples showed a metallic conductivity [Greedan'87], while more recent data on high purity single crystals show an insulating ground state, very sensitive to the impurity doping [Kézsmárki'04]. The substitution of two different rare earths on the R site allows the variation of the lattice constant in a continuous way and the phase diagram from Figure 18 is obtained. It shows the transition temperature $T_{SG,C}$

variation with the average ionic radius R_i, obtained for mixed polycrystalline $(RR')_2Mo_2O_7$ series. As one may see all data points merge into a universal curve transition temperature against R_i. This result, obtained by means of macroscopic measurements, suggests that the SG-F transition is controlled by the interaction between Mo^{4+} magnetic moments, which changes its sign from AF (in the spin glass state) to F (in the ferromagnetic state).

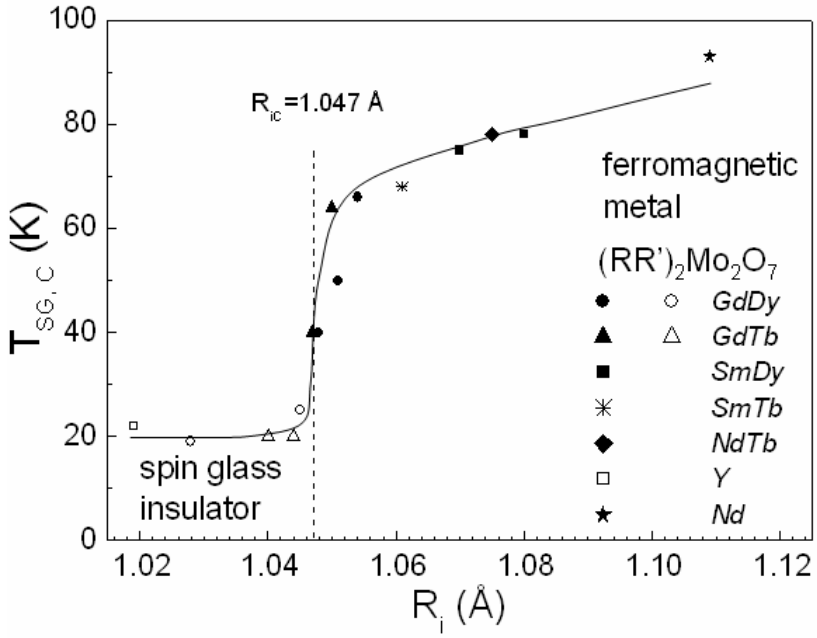

Figure 18. Phase diagram of $(RR')_2Mo_2O_7$ pyrochlores: transition temperature $T_{SG,C}$ versus the mean ionic radius R_i. The values for $Y_2Mo_2O_7$ are taken from Ref. [Gardner'99b], those for $(G_{1-x}Dy_x)_2Mo_2O_7$ (x=0, 0.1, 0.2, 0.4 and 1), $(G_{1-x}Tb_x)_2Mo_2O_7$ (x=0.25, 0.5, 0.75 and 1), $(Sm_{1-x}Dy_x)_2Mo_2O_7$ (x=0 and 0.2), $(Sm_{1-x}Tb_x)_2Mo_2O_7$ (x=0.5), $(Nd_{1-x}Tb_x)_2Mo_2O_7$ (x=0.5) from Ref. [Katsufuji'00] and those for $Nd_2Mo_2O_7$ from Ref. [Moritomo'01]. The dotted line shows the critical threshold of SGI-FM transition: R_{ic}=1.047 $Å^{-1}$ [Katsufuji'00]. The continuous line is a guide to the eye.

Macroscopic measurements show very interesting results if comparing the effect of chemical and applied pressure on the electric and magnetic properties of $R_2Mo_2O_7$ pyrochlores. Figure 19a shows the dc magnetization M versus temperature data at ambient pressure for single crystal $(Sm_{1-x}Tb_x)_2Mo_2O_7$ series, with x= 0, 0.4, 0.6, 0.7 and 0.8 [Miyoshi'03]. The zero field cooled (ZFC) and field cooled (FC) curves are measured in a static field H=100 Oe applied along the [111] direction. For $Sm_2Mo_2O_7$, the $M(T)$ data show a rapid increase as the temperature is lowered, indicating F ordering at ~ 90 K. With increasing Tb concentration, which compresses the lattice, T_C shifts towards a lower temperature gradually for $0 \le x \le 0.4$ but rapidly for $0.4 \le x \le 0.6$, although the FC magnetization M_{FC} for x=0.6 at low temperatures is still high (see right inset of Figure 19a). However, for x=0.8 the amplitude of magnetization is fairly low and the temperature at which the $M(T)$ curve exhibits the characteristic spin glass splitting is comparable to that of $Tb_2Mo_2O_7$ (according to the phase diagram from Figure 18). The plot of the amplitude of M_{FC} as a function of concentration situates the magnetic phase boundary in the interval x=0.7-0.8, in agreement with the results reported for polycrystalline samples in Ref. [Katsufuji'00]. Since the SG state is induced when compressing the lattice by chemical pressure, one may expect that the applied pressure, which also compresses the lattice, induces

the same magnetic ground state. The dc magnetization measurements under pressure (Figure 19b) shows that the amplitude of $M(T)$ for x=0.75 sample is systematically suppressed when increasing pressure, although the ordering temperature below which $M(T)$ exhibits an history dependent behaviour is almost pressure independent. Consequently, it is clear that the chemical and the applied pressure have similar effects on the magnetic properties of these systems: both induce the SG state. An applied pressure and doping-induced SG state was also reported by dc and ac measurements for a polycrystalline $(Gd_{1-x}Dy_x)_2Mo_2O_7$ series, with x=0, 0.1, 0.2 and 0.4 [Kim'05, Kim'03, Park'03].

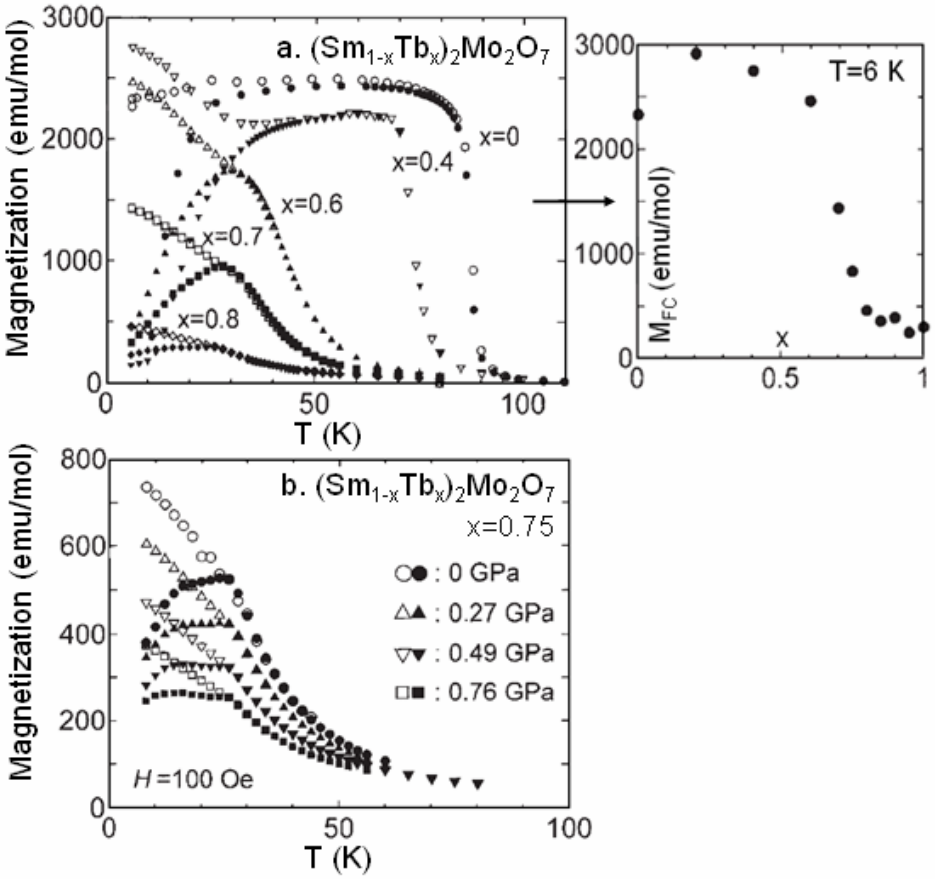

Figure 19. Temperature dependence of field cooled (FC) (open symbols) and zero field cooled (ZFC) (full symbols) dc magnetization under an applied magnetic field H=100 Oe along the [111] direction: a. $(Sm_{1-x}Tb_x)_2Mo_2O_7$, with x=0, 0.4, 0.6, 0.7 and 0.8. In the right inset: plots of the FC magnetization versus concentration x at T=6 K; b. $(Sm_{1-x}Tb_x)_2Mo_2O_7$, with x=0.75 under applied pressure up to 0.76 GPa. The results are from Ref. [Miyoshi'03].

The electrical properties of the same single crystal $(Sm_{1-x}Tb_x)_2Mo_2O_7$ series, with x= 0.7, 0.8, 0.9 and 1 were also analysed [Miyoshi'03]. Figure 20a shows the temperature variation of the electrical resistivity $\rho(T)$ at ambient pressure and measured along the [111] direction. The $\rho(T)$ curve for the samples with $0.8 \le x \le 1$ increases as the temperature is decreasing, showing an insulating behaviour and the resistivity at low temperatures decreases rapidly when decreasing Tb concentration x. The $\rho(T)$ for $x = 0.7$ displays a metallic behaviour. Briefly, the chemical substitution, compressing the lattice, induces an insulating behaviour. The M-I crossover is estimated to take place for x = 0.7-0.8. Accordingly, at ambient pressure, the M-I and F-SG phase boundaries situate in the same composition range, in agreement with earlier work of [Katsufuji'00]. Resistivity measurements under pressure

shed new light on the properties of $R_2Mo_2O_7$ pyrochlores. As one may clearly see in Figure 20b for $(Sm_{1-x}Tb_x)_2Mo_2O_7$, with x=0.8, at ambient pressure the $\rho(T)$ monotonically increases with decreasing temperature, showing an insulating behaviour. However at P=0.2 GPa the resistivity is significantly decreased at low temperatures and is further decreased for P=0.69 GPa. At P=1.1 GPa a metallic behaviour is observed for $T >$ 100 K. Similar results are also obtained for the $x = 0.75$ sample. Consequently, when decreasing the lattice dimensions by applying pressure a metallic state is induced and therefore the applied pressure disconnect the M-I and F-SG phase boundaries [Miyoshi'03].

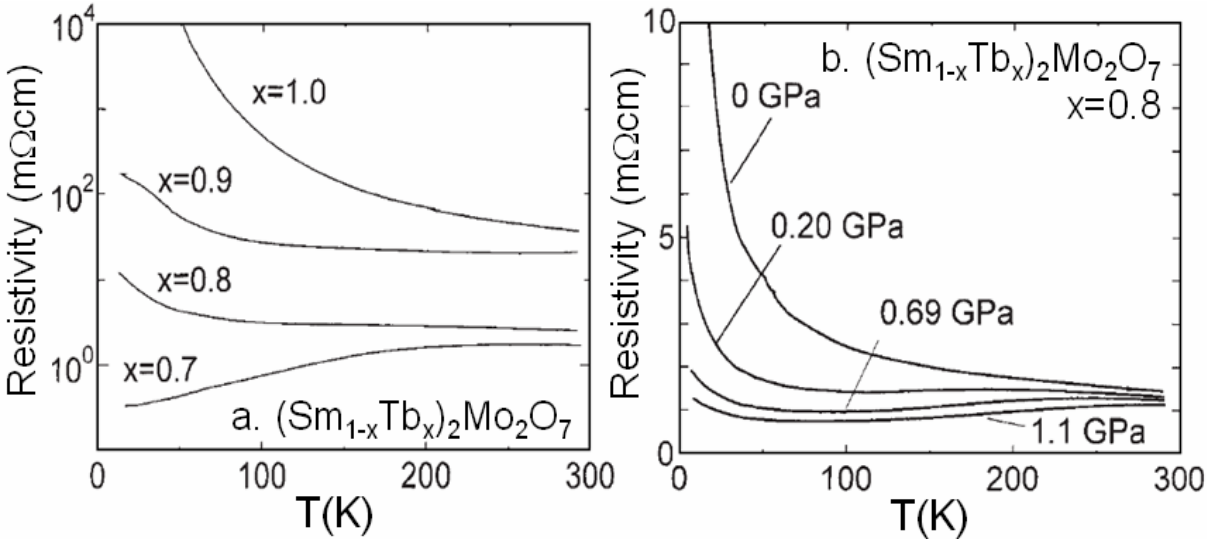

Figure 20. Temperature dependence of the electrical resistivity [Miyoshi'03]: a. $(Sm_{1-x}Tb_x)_2Mo_2O_7$, with x=0.7, 0.8, 0.9 and 1, measured along the [111] direction; b. $(Sm_{1-x}Tb_x)_2Mo_2O_7$, with x=0.8, measured along the [111] direction under several applied pressures: P=0, 0.2, 0.69 and 1.1 GPa.

Although the $R_2Mo_2O_7$ pyrochlores are well characterized from macroscopic point of view, there are only few studies of their microscopic properties. Up to this study only the compounds far from the threshold were studied: $Y_2Mo_2O_7$ and $Tb_2Mo_2O_7$, which are insulators with $R_i < R_{ic}$, and $Nd_2Mo_2O_7$, which is a metal with $R_i > R_{ic}$. $Y_2Mo_2O_7$ has already been described in section I.2. It shows spin glass characteristics, although the existence of chemical disorder is still under debate. In the following we summarize the results about $Tb_2Mo_2O_7$ and $Nd_2Mo_2O_7$.

- *$Tb_2Mo_2O_7$*

Figure 21 shows the principal experimental results describing the magnetic ground state of $Tb_2Mo_2O_7$. The dc magnetization (Figure 21a) is independent of the sample cooling history above ~ 25 K [Gaulin'94, Greedan'90, Greedan'91] (or 28 K [Ali'92]), but shows FC/ZFC irreversibilities below this temperature. Although this FC/ZFC splitting is similar to that observed in spin glasses, we underline the difference if comparing to $Y_2Mo_2O_7$, where below T_{SG} the FC magnetization saturates and ZFC one decreases towards zero (see Figure 15a). The linear ac susceptibility analysis shows that both real χ' and imaginary χ'' components present anomalies at temperatures that correlate quite well with the splitting of the dc FC/ZFC curves (Figure 21b) [Ali'89, Ali'92, Hill'89, Miyoshi'01]. A frequency dependence of the sharp peak seen in the non-linear ac susceptibility measurements was also observed [Miyoshi'00b].

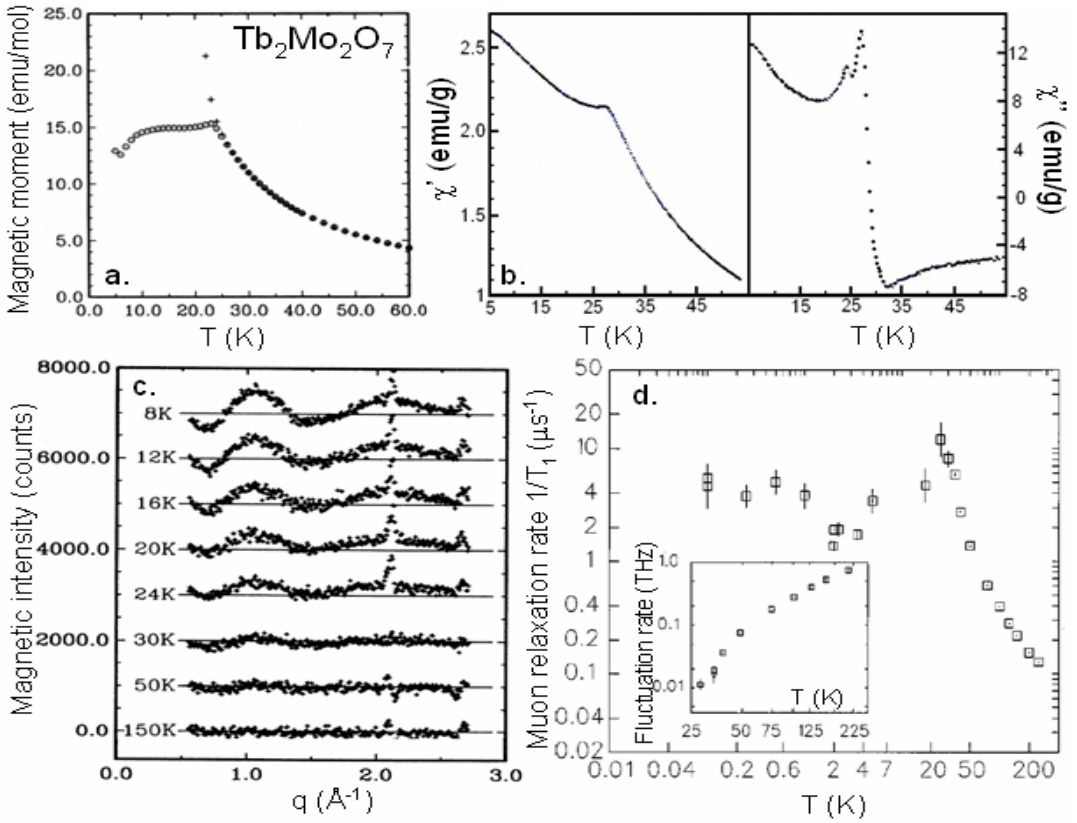

Figure 21. $Tb_2Mo_2O_7$: a. Magnetic moment versus temperature in the presence of an applied field H=0.002 Tesla, for ZFC (open circles) and FC (crosses) processes [Gaulin'94, Greedan'90, Greedan'91]; b. Temperature dependence of the real χ' and imaginary χ'' components of the ac susceptibility. Measurements were made using a magnetic field of 1.5 G with a frequency of 80 Hz [Ali'89, Ali'92, Hill'89]. The two-peak structure of χ'' was attributed to inomogeneities of the sample; c. Magnetic neutron scattering for several temperatures T=8, 12, 16, 20, 24, 30, 50 and 150 K. A spectrum from high temperature region (T= 300 K) was each time subtracted [Greedan'90, Greedan'91]; d. The dynamical muon spin relaxation rate $1/T_1$ versus temperature, in a small applied field H=0.005 Tesla. In inset: the Tb^{3+} magnetic moment fluctuation rate versus temperature above T_{SG} [Dunsiger'96].

At microscopical level, the neutron scattering measurements on $Tb_2Mo_2O_7$ show only a diffuse magnetic scattering (Figure 21c) [Greedan'90, Greedan'91]. It shows two broad peaks at 1.1 and 2.1 $Å^{-1}$ which develop continuously when decreasing temperature. There is also a small indication of peak below 0.5 $Å^{-1}$. We note the difference in regard to $Tb_2Ti_2O_7$ (Figure 5b), which shows also two peaks but near 1.1 and 3 $Å^{-1}$. Analysis of these results shows that while the $Tb_2Ti_2O_7$ behaviour can be explained if the magnetic correlations are extended only over the nearest neighbour distance (~ 3.59 Å), $Tb_2Mo_2O_7$ requires a longer correlation distance, corresponding to at least 4 coordination spheres (~7.3 Å) [Greedan'90, Greedan'91]. The spin dynamics of $Tb_2Mo_2O_7$ was analysed by both inelastic neutron scattering [Gaulin'92] and muon spin relaxation [Dunsiger'96]. The μSR (Figure 21d) indicates a behaviour rather similar to that of $Y_2Mo_2O_7$ (Figure 16b). As in $Y_2Mo_2O_7$, the spin fluctuation rate begins to slow down in 200 K range, well above T_{SG}. The muon spin relaxation rate $1/T_1$ shows a peak at T_{SG} ~ 25 K, then decreases and there is a residual muon spin relaxation rate of ~ 5 μs^{-1}, which persists down to the lowest measured temperature of 0.05 K. This relaxation rate is ~250 smaller than for $Y_2Mo_2O_7$, but has the same order of

magnitude as in $Tb_2Ti_2O_7$ (with $1/T_1 \sim 1\ \mu s^{-1}$ at low temperature as shown in Figure 5c). According to Ref. [Dunsiger'96] this suggests a more liquid like character of the ground state of $Tb_2Mo_2O_7$ than for $Y_2Mo_2O_7$. Additionally, the μSR shows that the static internal field seen by the muon is about 10 times larger in $Tb_2Mo_2O_7$ than in $Y_2Mo_2O_7$, as expected from the ratio of Tb^{3+} and Mo^{4+} magnetic moments.

All the above experimental results show that, although little different from $Y_2Mo_2O_7$, $Tb_2Mo_2O_7$ behaves as a spin glass, despite the apparent absence of disorder.

- *$Nd_2Mo_2O_7$*

Figure 22a shows the temperature dependence of the magnetization divided by the magnetic field M/H, obtained for a single crystal of $Nd_2Mo_2O_7$, where the magnetic field H =1 Tesla was applied along the [111] direction [Yasui'01]. The inset shows the $(M/H)^{-1}$ variation versus temperature. According to these dc measurements, the system undergoes the ferromagnetic transition at $T_C \sim 95$ K. Interestingly, with further decreasing of temperature, M/H is found to decrease below ~ 20 K.

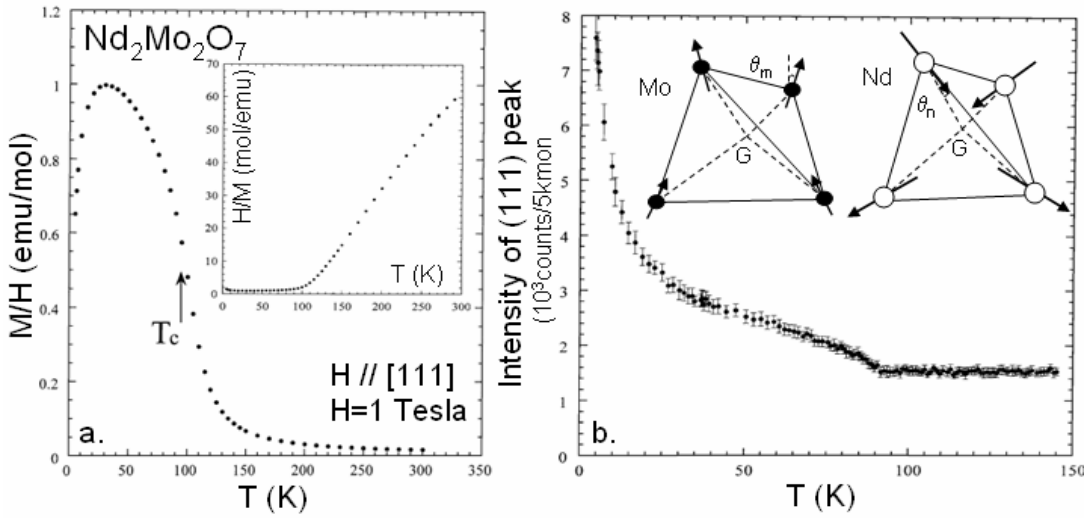

Figure 22. $Nd_2Mo_2O_7$ (single crystal) : a. Temperature dependence of M/H in an applied field H=1 Tesla along the [111] direction. The arrow indicates the Curie temperature. In inset: temperature dependence of $(M/H)^{-1}$; b. Temperature dependence of the neutron intensity of the (111) peak. In inset: the magnetic structure at T=4 K as determined from neutron diffraction analysis. Results are from Ref. [Yasui'01].

For the same single crystal, the temperature dependence of the intensity of the (111) peak as determined by neutron diffraction is shown in Figure 22b. The T_C value of ~ 93 K is consistent with the one determined by the magnetic measurements. Below ~ 20 K, the intensity strongly increases with decreasing temperature. From single crystal neutron diffraction measurements, two possible magnetic structures were proposed at low temperature (T=4 K). They are schematically represented in the inset of Figure 22b. The Mo^{4+} moments are found to have non-collinear structure in both cases, with a deviation from the [001] axis by an angle θ_m = 9.2° and 6.2 °, respectively. We note that if the Mo-Mo interaction is ferromagnetic and if the axial anisotropy is strong, each magnetic moment is expected to direct along the <111> axis and the magnetic structure is characterized by the arrangement "two spins in, two spins out". The present spin configuration shows that the Mo^{4+} anisotropy is not very significant. The Nd^{3+} moment is antiparallel to that of Mo^{4+}. For the two magnetic

models, Nd^{3+} magnetic moment makes an angle θ_n = 3.7° and 0°, respectively, with the <111> local anisotropy axis. This non-collinearity is a fingerprint of the strong Nd^{3+} axial anisotropy. One may note that in both magnetic structures, the Mo-Mo and Nd-Mo interactions seem to be F and AF, respectively. Further analysis at T=1.6 K confirm the second model, with θ_m ~ 4° and θ_n =0° [Yasui'03a]. Consequently, the same scenario explains both dc magnetization and neutron diffraction results: the ferromagnetic ordering at T_C is primarily associated with the ordering of the Mo^{4+} magnetic moments. When decreasing temperature, the ordering of Nd^{3+} moments develops gradually and becomes significant below ~ 20 K. The decrease of the magnetization below ~ 20 K is due to the antiferromagnetic coupling between Nd^{3+} and Mo^{4+} moments.

However, in the case of $Nd_2Mo_2O_7$ there are not the magnetic properties themselves that attracted the greatest interest, but its giant anomalous Hall effect. The main question concerning $Nd_2Mo_2O_7$ is: how are its magnetic properties related with this anomalous Hall effect?

A first result that attracted attention is the temperature dependence of the Hall coefficient R_H of a polycrystalline sample of $Nd_2Mo_2O_7$ (Figure 23a) [Yoshii'00]. When decreasing temperature, R_H starts to increase below ~ 100 K ($\sim T_C$). Then below ~ 20 K, *i.e.* the temperature where due to Nd moments ordering the magnetization is strongly suppressed, it shows a step increase. In order to further investigate this result, the Hall resistivity ρ_H of single crystals of $Nd_2Mo_2O_7$ was measured at several temperatures with the magnetic field along the [111] direction (Figure 23b) [Iikubo'01, Yoshii'00]. With decreasing temperature, the non-linear behaviour of the ρ_H - H curve appears at ~ T_C.

The Hall resistivity of ordinary ferromagnets can be divided into two contributions, the ordinary part and an anomalous one which is proportional to the magnetization:

$$\rho_H = R_0 H + 4\pi R_s M \qquad [I.9]$$

where R_0 and R_s are the ordinary and the anomalous Hall coefficients, respectively, and M the total magnetization.

As shown in Figure 23c, equation [I.9] fits well the high temperature region, but with decreasing temperature ρ_H starts to deviate from this simple relation below ~ 50 K. Therefore at low temperature (Figure 23d), where the ordering of Nd moments becomes significant, Ref. [Iikubo'01, Yoshii'00] propose another phenomenological equation which fits quite well the experimental data:

$$\rho_H = R_0 H + 4\pi R_s M_{Mo} + 4\pi R_s' M_{Nd} \qquad [I.10]$$

where M_{Mo} and M_{Nd}, and R_s and R_s' are the net magnetizations and the anomalous Hall coefficients corresponding to the Mo and Nd moments, respectively. The present analysis suggests that the anomalous part of ρ_H consists of two contributions from the Mo and Nd moments. The fit shows that: (i) R_s increases with decreasing temperature through T_C and seems to saturate at finite value at low temperatures; (ii) R_s' also remains non-zero and constant at low temperatures. These temperature independent and no-vanishing behaviour found not only in R_s but also in R_s' are in contradiction with those of ordinary ferromagnets,

where R_s are strongly suppressed below T_C and approaches zero as $T \to 0$. The same group [Iikubo'01, Yoshii'00] shows that unusual behaviour of the Hall resistivity was also obtained when applying a magnetic field along [001] and [110] directions.

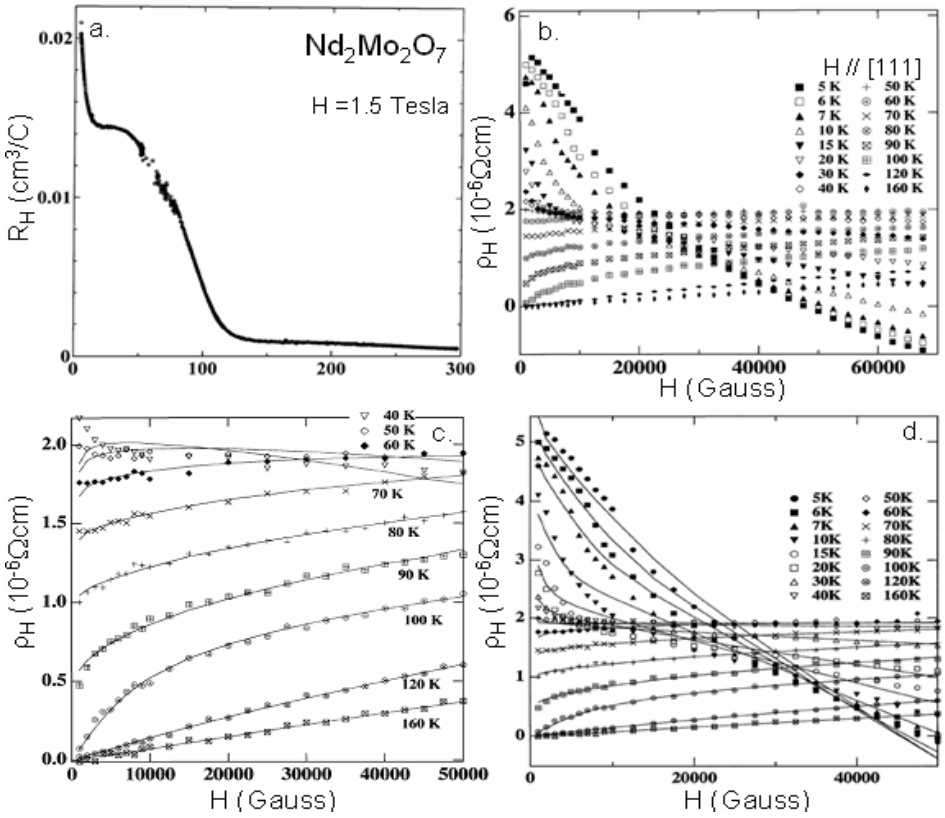

Figure 23. a. Temperature dependence of the Hall coefficient R_H, measured in a magnetic field H=1.5 Tesla for a polycrystalline sample of $Nd_2Mo_2O_7$; b. Magnetic field dependence of the Hall resistivity ρ_H of a single crystal $Nd_2Mo_2O_7$ at various temperatures. The magnetic field is applied along the [111] direction; c. Fits of $T \geq 40$ K data with function: $\rho_H = R_0 H + 4\pi R_s M$, with R_0 and R_s the ordinary and anomalous Hall coefficients and M the total magnetization; d. Low temperature data are fitted with the function: $\rho_H = R_0 H + 4\pi R_s M_{Mo} + 4\pi R_s' M_{Nd}$, with anomalous term divided into the two contributions from the net magnetizations M_{Mo} and M_{Nd} of the Mo and Nd moments, respectively. For details see ref. [Iikubo'01, Yoshii'00].

Beyond the proposed phenomenological approaches, it was interesting to investigate the relationship between the anomalous Hall resistivity and the non-collinear magnetic structure of $Nd_2Mo_2O_7$. The spin chirality mechanism was invoked, first for a Kagome lattice [Ohgushi'00]. The spin chirality is locally defined as $\chi = \vec{S}_1 \cdot \vec{S}_2 \times \vec{S}_3$, for three spins $\vec{S}_1$, $\vec{S}_2$ and $\vec{S}_3$, and hence a non-collinear and non-coplanar spin configuration corresponds to a non-zero spin chirality. A fictitious magnetic flux is then induced for each three spins situated on a triangular face of a tetrahedron. For a tetrahedron it acts like a fictitious magnetic field, finite and parallel to the total magnetization and hence leads to the anomalous Hall effect. The theory from Ref. [Ohgushi'00] proposes that the anomalous Hall conductivity σ_H ($= \rho_H / \rho$, with ρ the electrical resistivity) is proportional with this fictitious magnetic field. Taking into account the above theory, Ref. [Taguchi'01] calculates the Hall conductivity on the base of the spin chirality mechanism and proposes that the spin chirality of the Mo moments explains the

anomalous Hall effect observed for $Nd_2Mo_2O_7$. Briefly, at low temperature and in the low field regime, the tilting angles of the spins is relatively large, which gives rise to large spin chirality and hence large anomalous Hall term. Once a high field is applied the spins are aligned along the field direction, the spin chirality or the fictitious magnetic field is reduced and hence the anomalous Hall effect is reduced. Furthermore, Ref. [Taguchi'03] shows that the Hall resistivity ρ_H changes sign when the field is applied along [111] direction, but does not when applying along the [100] or [110] directions, and considers this fact as a evidence of the chirality mechanism of the ρ_H.

This proposal made by Taguchi *et al.* group raised lots of discussions. In contrast with their work, the group of Yasui, Iikubo, Yoshii *et al* . claims that the spin chirality χ does not consistently explain the behaviour of ρ_H [Yasui'03a, Yasui'03b, Yasui'06]. By means of neutron scattering data taken for a single crystal of $Nd_2Mo_2O_7$ they analysed in detail the evolution of the magnetic structure under applied magnetic field along different directions. Using this H-dependent magnetic structure, they calculate the spin chirality and the fictitious magnetic fields of the Mo and Nd moments, Φ_{Mo} and Φ_{Nd}, respectively. Supposing a direct proportionality between the ρ_H and these fictitious fields, they compared these quantities and show that neither Φ_{Mo}, nor a linear combination of Φ_{Mo} and Φ_{Nd} could explain the experimentally observed ρ_H.

There are more theoretical models, which studied the spin chirality mechanism in regard to anomalous Hall effect. In Ref. [Tatara'02] the anomalous Hall effect arising from the non-trivial spin configuration (chirality) is studied treating perturbatively the exchange coupling to localized spins. In the weak coupling limit it is shown that the Hall resistivity is proportional to a chirality parameter, with a sign that depends on details on the band structure. Recently, several groups confirmed such a behaviour in canonical AuFe spin glasses [Pureur'04, Taniguchi'04b]. More recently, Ref. [Taillefumier'06] proposes a model concerning the anomalous Hall effect due to spin chirality in a Kagome lattice. They put into light another idea, which seems to answer to the above debate: even if the spin chirality χ may be the origin of the anomalous Hall effect, it is not obvious that there should be a direct proportionality between the Hall resistivity and χ.

We put end to this introductive chapter, by giving few details concerning the crystallographic properties of Mo pyrochlores and a theoretical model, which without being complete, explains quite well the SGI-FM transition.

I.3.2. Crystallographic details on $R_2Mo_2O_7$

The $R_2Mo_2O_7$ pyrochlores crystallize in a face centered cubic (f.c.c.) structure with the space group $Fd\bar{3}m$, in which R and Mo occupy correspondingly *16d* [1/2,1/2,1/2] and *16c* [0,0,0] positions and form two interpenetrating sublattices of corner sharing tetrahedra. There are two types of oxygen sites O1 and O2, which occupy the *48f* [u,1/8,1/8] and *8b* [3/8,3/8,3/8] positions, respectively. Table I shows the Mo and R sites, expressed in units of the cubic lattice parameter. Each Mo site has a sixfold O1 48f coordination. The oxygen atoms specify the local coordinate frame around each Mo site, which depends of the coordinate u. u=5/16=0.3125 corresponds to the perfect octahedral environment, while for u>0.3125 there is an additional trigonal contraction of the local coordinate frame.

Mo sites	[0,0,0]	[0,1/4,1/4]	[1/4,0,1/4]	[0,1/4,1/4]
R sites	[0.5,0.5,0.5]	[0.25,0.25,0.5]	[0.25,0.5,0.25]	[0.5,0.25,0.25]

Table I. $R_2Mo_2O_7$ pyrochlores: Mo and R sites.

There are two crystallographic parameters of interest: the lattice parameter a and the coordinate of the oxygen O1 u. Based on these structural parameters, one may also calculate the Mo-O1 bond distance d and the Mo-O1-Mo bond angle θ. Table II shows the values of these parameters for the extreme compounds of the $R_2Mo_2O_7$ series: $Y_2Mo_2O_7$ ($a < a_c \sim 10.33$ Å) and $Nd_2Mo_2O_7$ ($a > a_c$). For comparison, we also give these parameters for $Tb_2Mo_2O_7$ ($a < a_c$), since it is one of the compounds that we analyse in this study. We underline that in all cases $u > 0.3125$ and hence all systems have a trigonal distortion of the Mo oxygen environment.

compound	a (Å)	u (units of a)	d (Å)	θ (°)
$Y_2Mo_2O_7$	10.21	0.3382	2.0171	127
$Tb_2Mo_2O_7$	10.3124(7)	0.3340	2.0159	129.1
$Nd_2Mo_2O_7$	10.4836(2)	0.3297	2.0332	131.4

Table II. Structural parameters of $Y_2Mo_2O_7$, $Tb_2Mo_2O_7$ and $Nd_2Mo_2O_7$: the cubic lattice parameter a (in Å), the oxygen parameter u (units of a), the distance Mo-O1 d (Å) and the angle Mo-O1-Mo θ (in degrees). The values for $Y_2Mo_2O_7$ and $Nd_2Mo_2O_7$ are taken from Ref. [Katsufuji'00, Moritomo'01, Reimers'88]. The values for $Tb_2Mo_2O_7$ are determined from our measurements (for details see Chapter IV) and given for comparison.

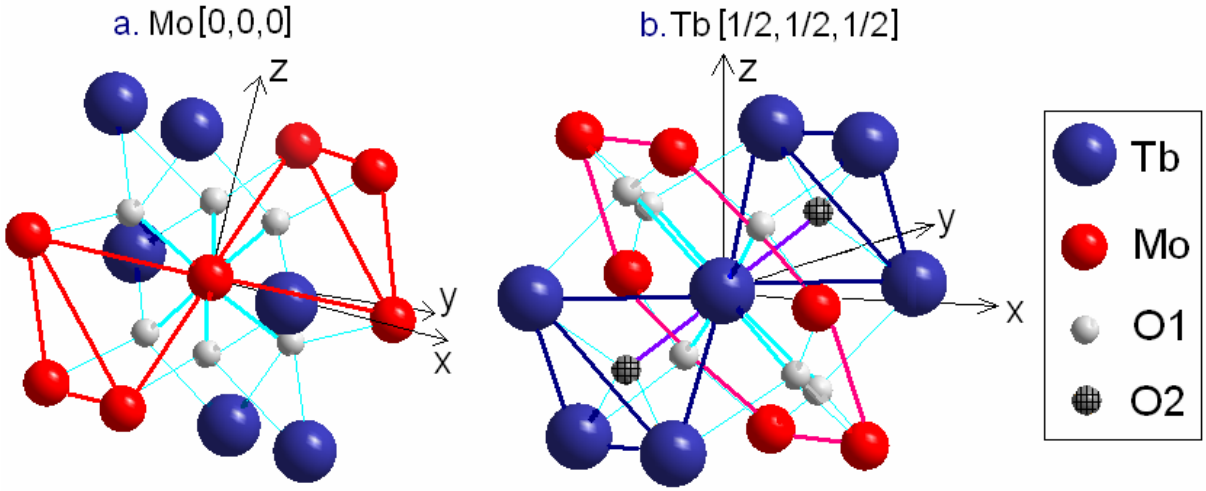

Figure 24. Crystallographic details on $Tb_2Mo_2O_7$ as obtained from our X ray and neutron diffraction analysis. The first coordination sphere of: a. Mo(0,0,0); b. Tb(1/2,1/2,1/2).

We also give few details on the crystallographic structure of $Tb_2Mo_2O_7$, as obtained from analysis of our X ray and neutron diffraction patterns (for details see Chapter IV). Figure 24a and Figure 24b show the crystallographic environment of Mo [0,0,0] and Tb [1/2,1/2,1/2], respectively. As one may see, Mo is octahedrally coordinated with six O1 (48f) oxygen atoms and has as nearest neighbours: six Mo (two corner sharing tetrahedra are formed) and six Tb magnetic ions, respectively. The oxygen environment of Tb is different from that of Mo: it is coordinated with six O1 oxygen atoms and also with two O2 (8b) oxygen atoms. For $u = 3/8$ Tb atom is coordinated with eight equally distant oxygen atoms (O1 and O2). Tb has also as

nearest neighbours six Mo and six Tb (two corner sharing tetrahedra are formed) magnetic ions. We note that each Tb ion is situated in the center of a hexagon formed by its six Mo first neighbours indicating a non-frustrated Tb-Mo lattice in contrast to the Tb and Mo pyrochlore frustrated lattices. Table III shows the first neighbours of both Mo and Tb atoms, with the corresponding distances and bond angles.

atom	n.n.	d (Å)	bond angles (°)
Mo	6 O1	2.01	Mo-O1-Mo ~ 129°
	6 Mo	3.64	Mo-O1-Tb ~ 107°
	6 Tb	3.64	
Tb	2 O2	2.23	Tb-O2-Tb ~ 109°
	6 O1	2.54	Tb-O1-Tb ~ 93°
	6 Mo	3.64	Tb-O1-Mo ~ 107°
	6 Tb	3.64	

Table III. $Tb_2Mo_2O_7$: first coordination cell of Mo and Tb atoms with the corresponding distances and bond angles, as obtained from X ray and neutron diffraction analysis. For details see Chapter IV.

I.3.3. Theoretical model on $R_2Mo_2O_7$

Having in mind the crystal structure of Mo pyrochlores, one natural question arises: which parameter, the lattice parameter a or the oxygen parameter u, controls the sign of the nearest neighbour magnetic interactions, which change from antiferromagnetic in the SG state to ferromagnetic? Another question is: in what way are the magnetic properties of these systems connected with the electronic ones?

Ref. [Solovyev'03] proposes band structure calculations on $R_2Mo_2O_7$ (with R=Y, Gd and Nd) and try to answer to both these questions.

Taking into account the structural parameters of $R_2Mo_2O_7$ (R=Y, Gd and Nd) the densities of states are obtained in the local-spin density approximation (LSDA), as shown in Figure 25 a and b for $Y_2Mo_2O_7$ and $Gd_2Mo_2O_7$, respectively. In the local coordinate frame, the Mo(4d) orbitals are split into the triply-degenerate t_{2g} and double-degenerate e_g states, with a splitting of ~ 4 eV. The t_{2g} bands are located near the Fermi level and well separated from the rest of the spectrum, consisting of a broad O(2p) band spreading from -8.5 to -2.5 eV and either Y(4d) or Gd/Nd (5d) bands located just above the t_{2g} states. The Mo(e_g) are situated in the higher part of the spectrum. Furthermore, the trigonal distortion and the difference in the hybridization with the O(2p) states spilt the Mo(t_{2g}) states into one-dimensional a_{1g} and the two-dimensional e'_g. As Ref. [Solovyev'03] recalls, the crystal structure affects the Mo(t_{2g}) band via two mechanisms: (i) the Mo-O1-Mo angle (see u), which controls the superexchange interactions between Mo(t_{2g}) orbitals mediated by the O(2p) states; the Mo-O1-Mo angle increases along the series Y→Gd→Nd and hence these interactions will also increase; (ii) the lattice parameter a and the Mo-Mo distance, which controls the direct exchange interactions between Mo(4d) orbitals; a increases along the series Y→Gd→Nd and hence the direct interactions will decrease. Consequently, the superexchange and exchange interactions should vary in opposite way in these series. LSDA calculations show that the width of e'_g band is practically the same for the all three compounds (Figure 26a). On the other hand, the a_{1g} orbitals, whose lobes are most distant from all neighbouring oxygen sites,

are mainly affected by the second mechanism and the a_{1g} bandwidth decreases within the series Y→Gd→Nd.

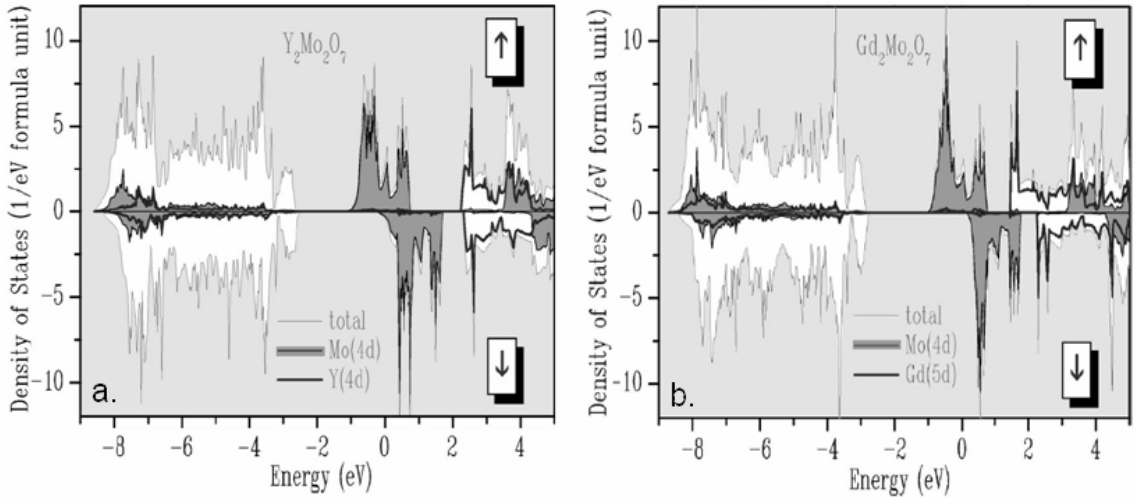

Figure 25. Total and partial densities of states of $Y_2Mo_2O_7$ (a) and $Gd_2Mo_2O_7$ (b) in the local density approximation. The Mo (t_{2g}) states are located near the Fermi level (chosen as zero for the energy), while the Mo (e_g) ones emerge around 4 eV. Results are taken from Ref. [Solovyev'03].

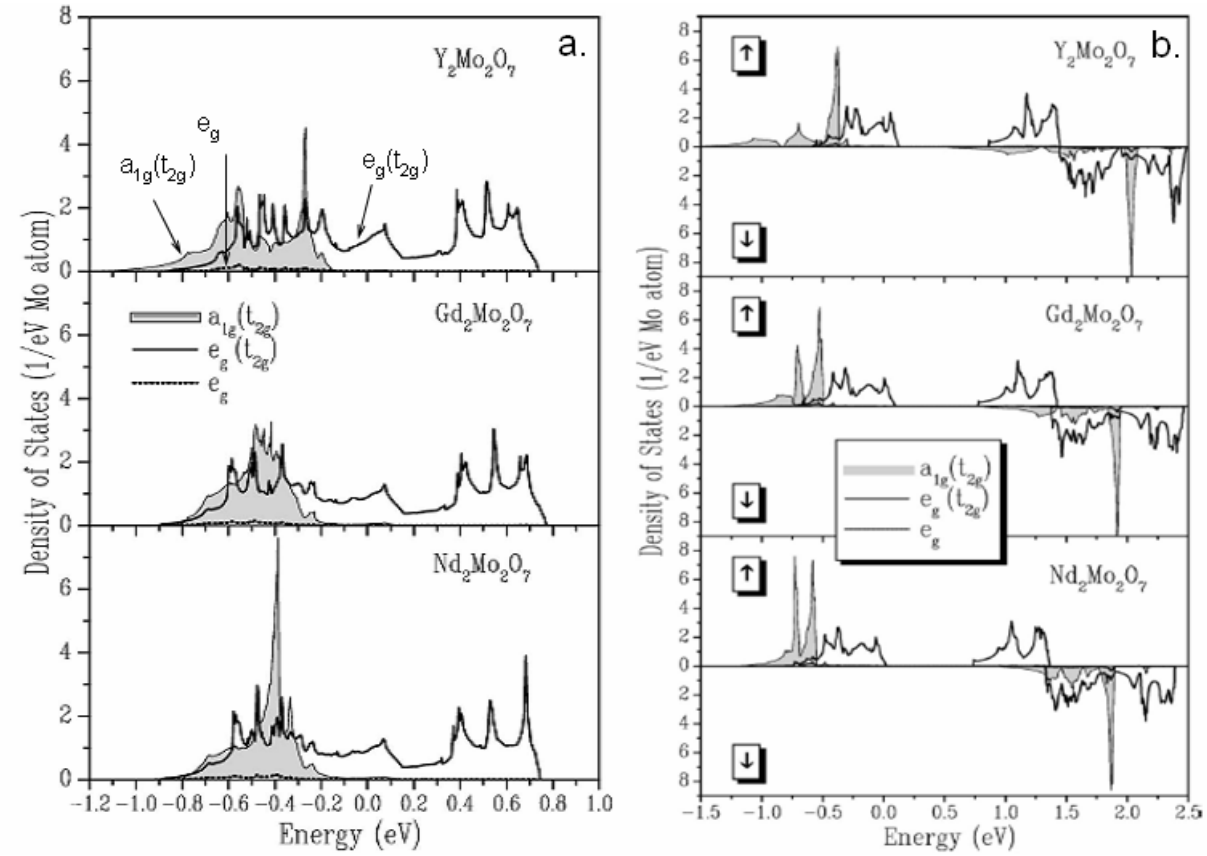

Figure 26. The distribution of Mo (4d) states: a. in the local coordinate frame, showing the splitting into one-dimensional a_{1g} and two-dimensional e_g (denoted $e_g(t_{2g})$) representations by the trigonal distortion; b. obtained in Hartree-Fock calculations for an Coulomb interaction U=3 eV. The Fermi level is at zero. Results are from Ref. [Solovyev'03].

The model proposed by Ref. [Solovyev'03] takes into account only the Mo(t_{2g}) bands and uses a mean field Hartree-Fock approach. It takes into account fine details of the electronic structure for these bands, extracted from the calculations in the LSDA approximation. The Coulomb interaction U is treated as a parameter, in order to consider different scenarios covering both metallic and insulating behaviour of $R_2Mo_2O_7$.

Assuming a F ordering between Mo spins, the LSDA calculations show that the majority (↑)-spin a_{1g} band is fully occupied and the Fermi level crosses the double-degenerate e_g' band (denoted $e_g(t_{2g})$ in Figure 26a). Consequently, at some point the Coulomb interaction U will split the e_g' band and induces an insulating state. Such a situation occurs between U=2 and 2.5 eV for all considered compounds, as shown in Figure 27a. In the metallic regime (small U) the densities of states are similar to those obtained in LSDA (Figure 26a). In this case, the major effect of U is the shift of the (↑)-spin a_{1g} band to the low energy of the spectrum relative to the e_g' band. Typical densities of states in the insulating state ($U > 2-2.5$ eV) are shown in Figure 26b. The a_{1g} band has a three-peak structure, while the distribution of the e_g' band is very similar for the three compounds.

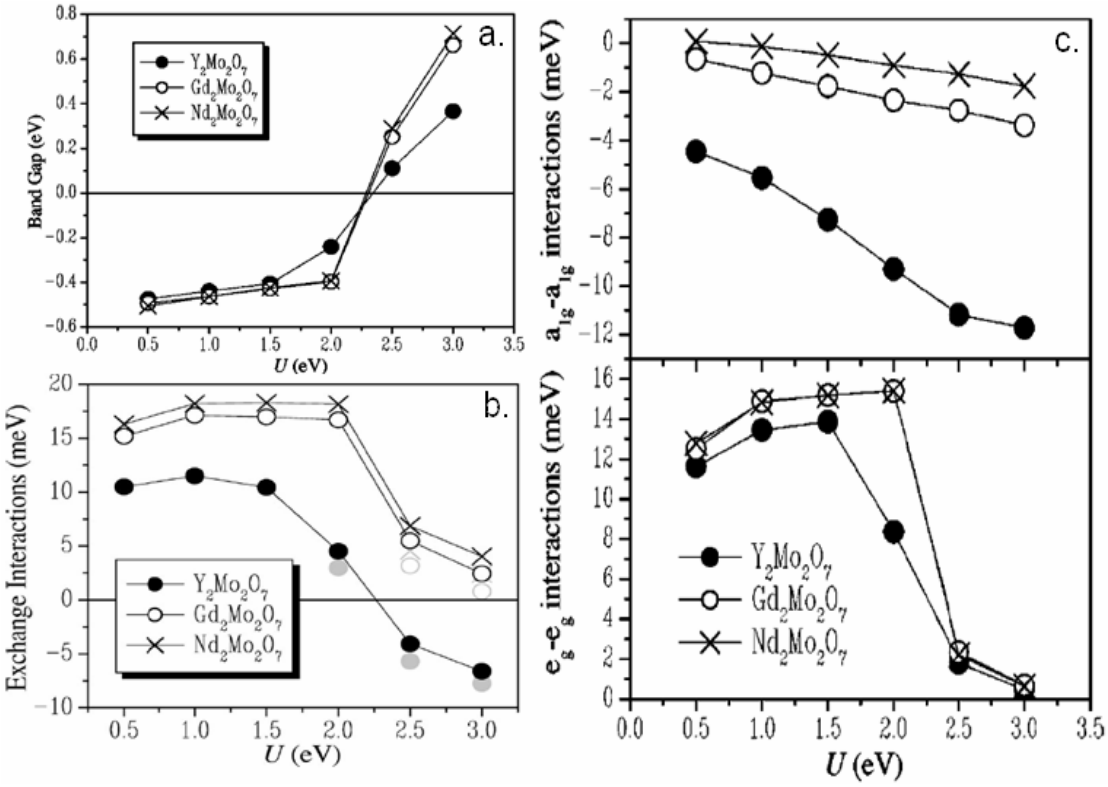

Figure 27. a. The band gap as a function of Coulomb interaction U; b. n.n. exchange interactions calculated in the ferromagnetic state; c. Contributions of a_{1g} and e_g' orbitals to the exchange interactions. Plots are from Ref. [Solovyev'03].

Then the nearest neighbour exchange interactions are calculated. Their variation with the Coulomb parameter is shown in Figure 27b. One may note two important aspects: (i) the n.n. exchange interactions are F for small U (metallic regime), but exhibit a sharp drop at the point of transition to the insulating state; (ii) there is a significant difference between Y and Nd/Gd compounds: in the Y case the exchange parameter is shifted towards negative values, so that the n.n. coupling becomes AF in the insulating phase, while the n.n. coupling remains

F for Gd/Nd. The behaviour of these systems may be understood in more details, if considering partial a_{1g} and e'_g contributions to the n.n. exchange coupling (Figure 27c). The main interactions are a_{1g}- a_{1g} and e'_g - e'_g (the a_{1g} - e'_g interaction is small and hence neglected). The model shows that the large e'_g - e'_g interaction in the metallic regime is related to the double exchange (DE) mechanism, which a measure of the kinetic energy for the itinerant ($\uparrow$)-spin e'_g electrons. As long as the system is metallic, the DE interactions are not sensitive to the value of U and the F coupling dominates. The transition into the insulating state is caused by the localization of the e'_g electrons. This reduces the kinetic energy and suppresses the DE interactions, which explains the sharp drop of e'_g - e'_g interaction. However, the main difference between Y and Gd/Nd is related to a_{1g}- a_{1g} interactions. Since the ($\uparrow$)-spin a_{1g} band is fully occupied and ($\downarrow$)-spin a_{1g} band is empty, the interactions are AF and the mechanism is the superexchange (SE). Since the SE coupling is proportional to the square of the a_{1g} bandwidth, this interaction is the largest in the case of Y. This explains the AF character of the total exchange coupling realized in this compound for large U.

As one may see, the model from Ref. [Solovyev'03] explains in a simple manner the magnetic and conduction properties of the Mo pyrochlores, taking into account only the electrons that populate the Mo(t_{2g}) levels, well separated from the rest of the spectrum. The electronic structures of $R_2Mo_2O_7$ have also been investigated by means of photoemission spectroscopy, which confirms that the electronic states near the Fermi level have mainly Mo(4d) character [Kang'04, Kang'02]. Solovyev shows how from a SG state with AF interactions, frustrated by the lattice and due to the SE mechanism, the system passes to a F state, due to the DE mechanism. This is obtained using a unique parameter, the Coulomb interaction U, which controls the levels splitting. When U increases a transition from a metal to a Mott insulator is induced. Experimental details on the M-I transition in Mo pyrochlores are given in Ref. [Kézsmárki'04, Taguchi'02] as obtained by optical spectroscopy. From the point of view of the structure parameters, this model also shows that the magnetic ground state of Mo pyrochlores is controlled by the cell parameter a, which directly controls the a_{1g} bandwidth and explains the stabilization of AF interactions in the case of $Y_2Mo_2O_7$. This result contradicts the widespread point of view that the magnetic ground state is controlled by the Mo-O1-Mo angle as suggested in Ref. [Katsufuji'00, Moritomo'01, Taniguchi'04a]. However, this model gives rise to few question marks. An important aspect that should also be taken into account is the presence of the rare earth, whose contribution it is not taken into account into these band structure calculations. It would also be interesting to connect the Coulomb interaction U with some other parameters which are accessible from experimental point of view.

I.4. Conclusions

In this chapter we presented some of the most interesting results concerning the geometrically frustrated pyrochlores $R_2M_2O_7$ in order to introduce our contribution.

We analysed first the systems having R^{3+} as unique magnetic ion on the pyrochlore lattice. We presented $Tb_2Ti_2O_7$, which at ambient pressure is a canonical example of spin liquid. This compound is the starting point of the first part of the present study: the analysis of $Tb_2Sn_2O_7$ (Chapter III), which has also Tb^{3+} as unique magnetic ion, but where the substitution of Ti^{4+} by the bigger Sn^{4+} ion expands the lattice and changes the energy balance.

Then we focused on the systems having two magnetic ions on pyrochlore lattice: the Mo pyrochlores. Up to now these systems have been well characterized at macroscopical level, while the microscopic studies concern just compounds far from the critical threshold of the spin glass - ferromagnetic transition. The second part of this study (Chapters IV-VI) concerns the microscopical analysis of the evolution of magnetism throughout the threshold region.

Chapitre II.

Les détails expérimentaux: la préparation des échantillons et les techniques expérimentales

Dans le Chapitre II, nous commençons par donner des informations sur la synthèse des échantillons : $Tb_2Sn_2O_7$ et la série $(Tb_{1-x}La_x)_2Mo_2O_7$, avec x=0, 0.05, 0.1, 0.15, 0.20 et récemment 0.25. Puis nous décrivons les principales techniques expérimentales utilisées dans cette étude et donnons des détails sur les instruments et le traitement des données:

(i) Diffraction de neutrons à pression ambiante et sous pression, que nous avons parfois utilisée pour déterminer la structure cristalline, mais surtout pour déterminer la structure magnétique et les corrélations de spin à courte portée.

(ii) Diffraction de rayons X. Nous l'avons utilisée pour déterminer la structure cristalline à pression ambiante, combinée à la diffraction de neutrons, et sous pression en utilisant le rayonnement synchrotron.

(iii) Rotation et relaxation de spin du muon (μSR), à pression ambiante et sous pression appliquée. Elle nous intéresse par sa complémentarité avec la diffraction de neutrons. Elle sonde à la fois les champs magnétiques statiques locaux et les fluctuations de spin.

(iv) Susceptibilité magnétique statique (mesurée au SQUID). L'analyse des courbes de susceptibilité dans l'état refroidi en champ nul (ZFC) et sous champ (FC) donne une information sur les températures d'ordres, préalable aux mesures de neutrons et de muons.

Chapter II.

Experimental details: sample preparation and experimental techniques

II.1. Sample preparation

For the sample preparation we are indebted to A. Forget and D. Colson from Service de Physique de l'Etat Condensé (SPEC), CEA-CNRS, CE-Saclay.

All samples studied in this thesis are polycrystalline samples (powders) and were prepared by solid state reaction at high temperature.

- *$Tb_2Sn_2O_7$ (Chapter III)*

In the first stage, Tb_2O_3 was prepared starting from Tb_4O_7 (Strem, with 99.9 % purity). The reaction was made in Ar atmosphere, with Ti/Zr chips to absorb the oxygen traces. The temperature of reaction is of 800-900 °C. Then, $Tb_2Sn_2O_7$ was synthesized using Tb_2O_3 and SnO_2 (Strem, with 99.9 % purity) oxides as starting materials. The reaction was made in air. The above oxides were heated (350 °C/h) up to 1425-1490 °C, where they were kept for 6 hours.

- *$(Tb_{1-x}La_x)_2Mo_2O_7$, x=0-0.25 (Chapters IV-VI)*

As above, the Tb_2O_3 was prepared starting from Tb_4O_7 (Strem, with 99.9 % purity), in Ar atmosphere, with Ti/Zr chips to absorb the oxygen traces. Then, the $(Tb_{1-x}La_x)_2Mo_2O_7$ was synthesized by reacting Tb_2O_3, La_2O_3 (Aldrich, with 99.999 % purity) and MoO_2 (Alfa, with 99 % purity). This reaction is also made in Ar atmosphere with Ti/Zr chips. The oxides were heated (350 °C/h) up to 1385 °C and kept at this temperature during 6 hours. Two annealings were necessary to obtain the sample in the pure form. First, five samples having x=0, 0.05, 0.1, 0.15 and 0.2 were prepared and their study represent the main part of the Chapters IV-VI. The substitution of Tb^{3+} by the bigger ion La^{3+} expands the lattice, but also increases the compacity (the occupied volume/the available volume). The La solubility limit situates at $\simeq 25\,\%$. The x=0.25 sample, much difficult to synthesize, was obtained latter (after the other five samples) and therefore it was studied in less details.

II.2. The neutron diffraction

The powder neutron diffraction is one of the most important techniques available to materials scientists. Since the wavelength of the incident neutrons has the same order of magnitude as the interatomic distances of solids (meaning the order of Å), it allows the study of properties of condensed matter at atomic level.

II.2.1. Theoretical principle

Although all diffraction experiments rest on Bragg's law, there are basically two ways of making them. In the first method the sample is bathed in a monochromatic beam of X rays or neutrons with a wavelength λ_0 and different d-spacings are measured by moving a detector to different angles:

$$\lambda_0 = 2d_h \sin\theta_h \qquad [II.1]$$

where h stands for the Miller indices (hkl) associated to that d-spacing. Experimental setups based on this method are called constant wavelength or steady state diffractometers. It is the method used in the present X ray and neutron diffraction experiments. An alternative method is to keep the detector fixed at an angle θ_0 and to vary the wavelength. This can be achieved by using a white spectrum with a wide range of wavelength and an energy dispersive detector. Then the d-spacings are obtained using the relation: $E_h \Rightarrow \lambda_h = 2d_h \sin\theta_0$.

The interaction of neutron with matter has two main terms: (i) the strong nuclear interaction, which corresponds to the interaction between the neutron and the sample nuclei and gives rise to the nuclear scattering; (ii) the magnetic interaction, which corresponds to the interaction between neutron spin and the atomic magnetic moments of the sample and gives rise to the magnetic scattering. The neutron diffraction has several advantages compared to the X ray diffraction. First, the scattering length which characterizes the nuclear interaction does not depend of the atomic number Z, contrary to the scattering length of X rays, which is proportional to Z. Therefore for X rays the light atoms are almost invisible (especially when heavy atoms are present), while for neutrons the light and heavy atoms may have comparable scattering length. Secondly, the neutron has a magnetic spin which interacts with the atomic magnetic moments and therefore it is an indispensable tool for the study of the magnetic structures.

The powder neutron diffraction characterizes the interaction between the incident neutron beam and the sample. The initial state is determined by $\vec{k}_i$ and E_i, representing the scattering wave vector of the incident neutrons and their energy, respectively, and also by $|\psi_i\rangle$, which characterizes the initial state of the sample. After the impact, both neutrons and sample are in a final state, characterized by $\vec{k}_f, E_f$ and $|\psi_f\rangle$, respectively. The interaction process is then characterized by the movement quantity transfer $\vec{q} = \vec{k}_f - \vec{k}_i$ (or the scattering vector) and an energy transfer $\hbar\omega = E_f - E_i$.

Considering the interaction between the neutron and the sample, one may define the total scattering cross section. It has two components: the coherent cross section and the incoherent one. The coherent cross section corresponds to an average response coming from all atoms of the system and gives access to the mean scattering potential. It gives rise to Bragg peaks in the case of the ordered structures. Per contra, the incoherent component corresponds to the individual response of each atom and gives the deviations from the mean scattering potential. In neutron diffraction measurements it yields a continuous background. We underline that the coherent term gives access to average quantities. For example, for a crystal, the thermal displacement of an atom with respect to the average position yield an attenuation of the coherent scattering length by a factor named Debye-Waller factor. For the case of fluctuating magnetic spins, the measured average quantity represents the mean ordered magnetic moment. In paramagnetic phase, for example, this mean ordered magnetic moment

is zero due to magnetic fluctuations in time and space. The coherent component is itself a sum of two terms: the elastic (corresponding to $\omega = 0$) and inelastic one ($\omega \neq 0$), respectively. In a diffraction experiment, there is no energy analysis of the scattered neutrons and therefore the two terms are not separated. In diffraction, the neutron cross section corresponds to an integration $\int_{-\omega_i}^{\infty} S(q,\omega)d\omega$ over the energies of the scattered neutron, where ω_i is the incident neutron energy. If ω_i is high enough, then the sum may be approximated to $\int_{-\infty}^{\infty} S(q,\omega)d\omega$ and one obtains $S(q,t=0)$, *i.e.* the neutron diffraction gives access to an instantaneous "picture" of the system at a given moment $t = 0$. Inelastic neutron scattering experiments allow one to analyse the energy of the scattered (out coming) neutrons and hence to separate the elastic and inelastic processes.

In neutron diffraction experiments using non-polarized neutrons, the nuclear and magnetic intensities are additive. The coherent elastic cross section is written as:

$$\left(\frac{d\sigma}{d\omega}\right)_{\substack{coherent \\ elastic}} = N\frac{(2\pi)^3}{v_0}\sum_{hkl}\left|F(\vec{q})\right|^2\delta(\vec{q}-\vec{Q}_{hkl}) \qquad [II.2]$$

where N is the unit cells number, v_0 is the unit cell volume, $\vec{Q}_{hkl}$ are the vectors of the crystal reciprocal space, which determine the diffraction peaks position, and $F(\vec{q})$ is the structure factor, which may be written in a similar manner for both nuclear and magnetic terms:

$$F(\vec{q}) = \sum_i \overline{b_i}\cdot e^{i\vec{q}\cdot\vec{r}_i} \qquad [II.3]$$

The summation is over the mean values of the nuclear scattering length b_N of the nuclei of the nuclear unit cell or over the mean values of the magnetic scattering length b_M of the atoms of the magnetic unit cell. The magnetic unit cell may be different from the crystallographic one. The nuclear scattering length b_N is independent of the scattering vector $\vec{q}$, since the characteristic dimension of a nucleus is much smaller than the neutron wavelength. Per contra, the magnetic scattering length b_M depends on $\vec{q}$, since the characteristic dimension of the electronic cloud is comparable to the neutron wavelength. The value of b_N change when changing the atom species. The magnetic scattering length b_M is given by:

$$b_M = 2\vec{\sigma}\cdot\left(\rho(\vec{q})\frac{\gamma r_e}{2}\frac{\vec{M}_\perp}{\mu_B}\right) \qquad [II.4]$$

where $\vec{\sigma}$ is the Pauli vectorial operator for the neutron spin, γ is the neutron gyromagnetic ratio, r_e is the neutron radius and μ_B is the Bohr magneton. $\rho(\vec{q})$ is the magnetic form factor, normalized in order that $\rho(0) = 1$. $\vec{M}_\perp$ is the projection of the atomic magnetic moment on the plane perpendicular to the scattering vector $\vec{q}$.

The information that one may obtain from a neutron diffraction spectra analysis:

- *the nuclear intensity*

The nuclear Bragg peak positions give access to the lattice parameter, while their

integrated intensities depend on the atom positions in the unit cell, on the occupation of different sites and on the scattering length values. In other words, the refinement of the nuclear phases of neutron diffraction spectra allows one to determine the crystalline structure of the compound.

- *the magnetic intensity*

First of all, the labelling of the magnetic peaks positions (peaks, which of course appear below the ordering temperature) gives access to the propagation vector, namely to the magnetic structure periodicity. In the reciprocal space the position of the magnetic reflections is given by

$$\vec{Q}_{hkl} = \vec{H}_{hkl} + 2\pi\vec{k} \qquad \text{[II.5]}$$

where $\vec{H}_{hkl}$ denotes the positions of the nuclear reflections and $\vec{k}$ is the propagation vector. If the magnetic peaks are superimposed on the nuclear ones, then $\vec{k} = 0$ and the magnetic unit cell is equal to the nuclear one. It is the case of ferromagnetic compounds or even compounds where there is also some antiferromagnetism. When new Bragg reflections appear in the reciprocal space, then $\vec{k} \neq 0$ and the magnetic unit cell is larger than the nuclear one. It is the case of many antiferromagnetic compounds.

Once the propagation vector is known, *i.e.* the periodicity of the magnetic structure, one has to analyse the intensities of the magnetic Bragg peaks. The comparison between the magnetic intensities calculated using a model of magnetic structure and those obtained experimentally allows the determination of the arrangement of the magnetic moments in the magnetic unit cell. In the most favourable case, one may determine the value and also the orientation of the magnetic moments.

Summarizing, the refinement of the magnetic phases of the neutron diffraction spectra allows the complete characterization of the magnetic structure of the analysed compounds, meaning both the periodicity and magnetic moments arrangement in the magnetic unit cell.

More details concerning the neutron diffraction may be found in Ref. [Bacon'75, HERCULES'05, JDN10'03].

II.2.2. Ambient pressure neutron diffraction

II.2.2.1. Diffractometers

The ambient pressure neutron diffraction measurements were carried out mainly in Léon Brillouin Laboratory (LLB), CEA Saclay. The following powder diffractometers were used: (i) 3T2, which is a high resolution, two-axis diffractometer. It has the typical incident neutron wavelength $\lambda = 1.225$ Å, which corresponds to thermal neutrons (coming from the Orphée reactor, CEA Saclay). It is well adapted for crystal structure analysis; (ii) G61, which is a high flux, two-axis diffractometer, with $\lambda = 4.741$ Å (cold neutrons guide). Due to its high flux, but limited scattering range ($q_{\max} \sim 2.5$ Å^{-1}), it is well adapted to the study of the magnetic order; (iii) G41, which is also a high flux, two-axis diffractometer, with $\lambda = 2.43$ Å (cold neutrons guide). It may be used for magnetic order analysis, having a wider scattering vector range than G61 ($q_{\max} \sim 4$ Å). Experiments were also performed in Laüe Langevin Institute (ILL), Grenoble, on: (i) D1B diffractometer having roughly similar characteristics to G41 ($\lambda = 2.52$Å and $q_{\max} \sim 3.3$ Å); (ii) the high flux diffractometer D20 ($\lambda = 2.419$ Å); (iii)

the high flux and high resolution diffractometer D2B ($\lambda = 1.594$ Å). When analysing crystal structures the experiments were made at room temperature (3T2 and D2B). When analysing magnetic structures the measurements were performed in the temperature range 1.4-100 K using an ILL cryostat and below 1.4 K, till to ~ 40-100 mK, with a dilution cryostat. For ambient pressure neutron diffraction measurements we thank to I. Goncharenko (LLB, G61), G. André (LLB, G41), F. Bourée (LLB, 3T2), O. Isnard (ILL, D1B) and E. Suard (ILL, D2B and D20).

Figure 1(left) shows the ambient pressure version of the G61 diffractometer. Briefly, a monochromatic neutron beam is selected by a graphite monochromator, giving λ=4.741 Å. The contamination of the higher order harmonics (λ/2, λ/3,…) is suppressed by inserting a beryllium filter (cooled down to liquid nitrogen temperature) in the incident beam path. The diffractometer is equipped with a linear (banana-type) 400-cells multidetector covering 80 degrees of scattering angle. The multidetector and its protection can rotate around the sample axis, covering a total angle of 150 degrees.

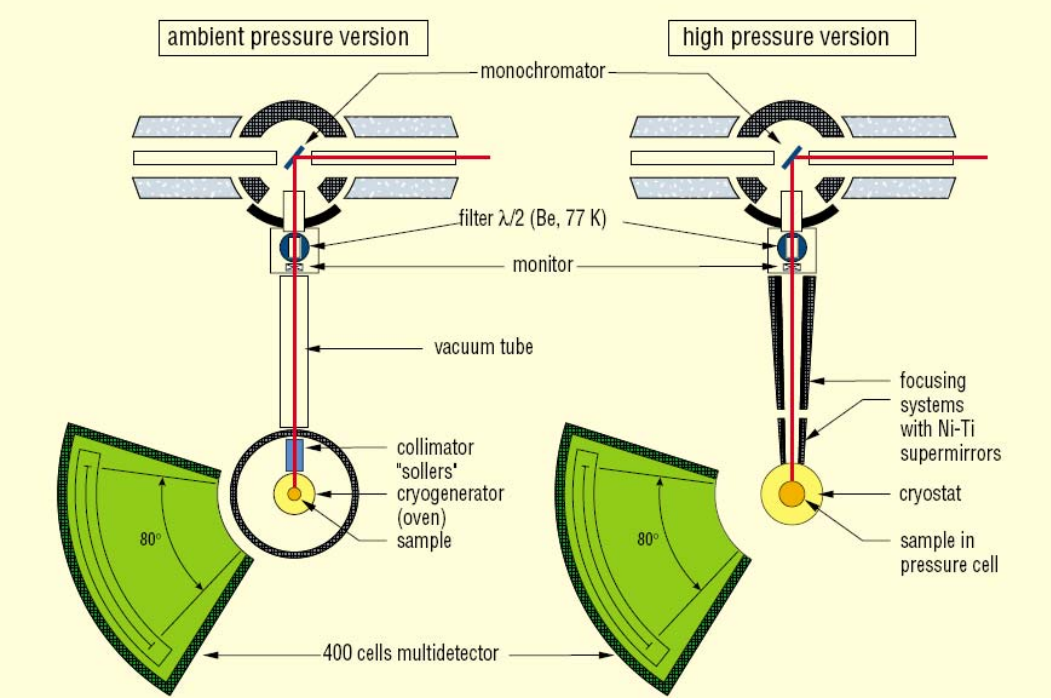

Figure 1. Schematic view of the cold-neutron, two-axis diffractometer G61 in ambient pressure version (left) and in the high pressure version (right).

II.2.2.2. Data analysis. The Rietveld method

The raw data obtained in a powder neutron experiment consist of a record of the intensity of diffraction (neutron counts) versus the diffraction angle 2θ. The 2θ dependence may be transformed in a q dependence, where $q = 4\pi \sin\theta / \lambda$ is the scattering vector. Then the neutron diffraction patterns are analyzed using the program FULLPROF [Rodríguez-Carvajal'93], which is based on a Rietveld analysis.

In numerical format, the raw data are given by a set of two arrays $\{2\theta_i, y_i\}_{i=1,\ldots,n}$, where y_i corresponds to the neutron counts at the scattering angle $2\theta_i$. After corrections and calibrations the data are given by a set of there arrays $\{2\theta_i, y_i, \sigma_i\}_{i=1,\ldots,n}$, where σ_i is the standard deviation of the profile intensity y_i. The profile can be modelled using the calculated

counts y_{ci} at the i^{th} step by summing the contribution from neighbouring Bragg reflections and the background:

$$y_{ci} = \sum_{\phi} S_{\phi} \sum_{h} I_{\phi,\vec{h}} \Omega(2\theta_i - 2\theta_{\phi,\vec{h}}) + b_i \qquad \text{[II.6]}$$

The vector $\vec{h}$ ($= \vec{H}_{hkl}$ or $\vec{H}_{hkl} + \vec{k}$) labels the Bragg reflections and ϕ labels the phase and varies from 1 up to the number of phases existing in the model. In FULLPROF the term phase reflects the same procedure for calculating the integrated intensities $I_{\phi,\vec{h}}$. This includes different crystallographic phases and also the magnetic contribution to the scattering coming from a single crystallographic phase in the sample. The general expression of the integrated intensity is:

$$I_{\phi,\vec{h}} = \left\{ L A P C F^2 \right\}_{\phi,\vec{h}} \qquad \text{[II.7]}$$

The meaning of the terms from equations [II.6] and [II.7] is the following: S_{ϕ} is the scale factor for the phase ϕ, $L_{\phi,\vec{h}}$ contains the Lorentz, polarisation and multiplicity factors, $A_{\phi,\vec{h}}$ is the absorbtion correction, $P_{\phi,\vec{h}}$ is the preferred orientation function, $C_{\phi,\vec{h}}$ includes, if necessary, special corrections (non-linearity, efficiencies, special absorbtion corrections *etc.*), $F_{\phi,\vec{h}}$ is the structure factor, Ω is the reflection profile function and b_i is the background intensity.

- *the Lorentz factor L*

For neutron diffraction, the Lorentz factor corresponding to a scattering angle θ is defined as: $L = 1/\sin\theta \sin(2\theta)$. In the case of X ray diffraction it also includes the polarization correction.

- *the absorption correction A*

The absorption correction for a given cylindrical sample holder of radius R, may be expressed using the Rouse and Cooper formula [Rouse'70]:

$$A(\theta) = \exp\left[-(a_1 + b_1 \sin^2\theta)\mu R - (a_2 + b_2 \sin^2\theta)(\mu R)^2 \right] \qquad \text{[II.8]}$$

where the numerical factors a_1, b_1, a_2 and b_2 are given in Ref. [Rouse'70].

μ is the linear absorption coefficient, which for a bulk crystal may be written as:

$$\mu = n \cdot \sigma_{total} \qquad \text{[II.9]}$$

n is the associated density defined as the number of formula units (moles) of the unit cell (8 for pyrochlore compounds) divided by the unit cell volume. σ_{total} is the total scattering cross section of one mole. It may be calculated as the summation of coherent, incoherent and absorbtion cross sections of each atom species of the formula unit: $\sigma_T = \sum_{atom} \sigma_c + \sigma_i + \sigma_a(\lambda)$.

The absorbtion cross section σ_a depends on the incident neutron wavelength and therefore, the absorbtion correction depends not only on sample but also on the used diffractometer. Consequently, one obtains:

$$\mu\left(cm^{-1}\right) = \frac{number\ of\ moles}{a^3}(cm^{-3}) \cdot \sigma_{total}(barn) \qquad [II.10]$$

where a is the lattice parameter.

Finally, we note that the linear absorbtion of a powder sample is inferior to that of a bulk sample. In order to take into account this aspect, when analysing the data, we considered a density coefficient of 0.5 and hence in formula [II.8] μR is replaced by $0.5\mu R$.

- *the reflection profile function Ω*

For a perfect sample, for example on ordered sample where the grain size is of order of micron ($>> \lambda$), the full width at half maximum of the Bragg peaks H corresponds to the experimental resolution, whose dependence on θ is described using three parameters U, V and W:

$$H^2 = U\tan^2\theta + V\tan\theta + W \qquad [II.11]$$

These three parameters are obtained by refining a pattern obtained for a reference sample, in some experimental conditions (incident beam, divergence, collimation).

One can also observe an intrinsic peak broadening. There are two profile functions that we used when analysing our data: the pseudo-Voigt and the modified Thomson-Cox-Hastings pseudo-Voigt function, respectively [Finger'94, Rodríguez-Carvajal'93]. In FULLPROF, the control variable is Npr.

The pseudo-Voigt peak-shape function ($Npr = 5$) is an approximation of the Voigt function, the latter being defined as a convolution of a Lorentzian and a Gaussian. The pseudo-Voigt function is a linear combination of a Lorentzian $L(2\theta)$ and a Gaussian $G(2\theta)$, having the same H:

$$\Omega(2\theta) = pV(2\theta) = \eta L(2\theta) + (1-\eta)G(2\theta) \qquad [II.12]$$

with $0 \le \eta \le 1$. $\eta = 0$ corresponds to a pure Gaussian, while $\eta = 1$ corresponds to a pure Lorentzian. In practice:

$$\begin{aligned} \Omega(2\theta) &= pV(2\theta) = pV(2\theta, \eta, H) \\ \eta &= \eta_0 + X \cdot 2\theta \end{aligned} \qquad [II.13]$$

and hence there are five parameters of interest: U, V, W, η_0 and X. U, V, W correspond to the experimental resolution and should be known and consequently the refinable parameters are η_0 and X. Generally, we used the pseudo-Voigt peak-shape function when analysing nuclear structures.

When analysing magnetic structures, we used the modified Thomson-Cox-Hastings pseudo-Voigt function ($Npr = 7$). When comparing to the pseudo-Voigt ($Npr = 5$) one, the only difference concerns the parametrisation of η and H. The modified Thomson-Cox-Hastings pseudo-Voigt function is defined as the convolution of a Lorentzian and a Gaussian, having different H:

$$\begin{aligned} H_G^2 &= U\tan^2\theta + V\tan\theta + W \\ H_L^2 &= \frac{Y}{\cos\theta} \end{aligned} \qquad [II.14]$$

If the instrumental resolution parameters U , V , W are known, then there is a unique refinable parameter: Y . When analyzing the peak broadening, the advantage of the modified Thomson-Cox-Hastings pseudo-Voigt function is that it allows the separation between the instrumental contribution and the contribution related to the physics of the sample. We considered a Lorentzian shape of peaks and hence the parameter Y is directly related to the size of the magnetic domains L_C of the analysed system:

$$L_C = \frac{360\lambda / \pi^2}{Y} \qquad \text{[II.15]}$$

For the used diffractometers, taking into account their different wavelength, we obtained: $L_C(G61) = 172.930/Y$, $L_C(G41) = 88.489/Y$ and $L_C(D1B) = 91.918/Y$.

- *the background*

This is normally the least interesting part of a powder neutron diffraction pattern and experimental set-ups are designed to minimize it and to enhance the peak/background ratio. However, we emphasize that the background is the sum of instrumental and sample contributions and, in specific cases, the latter part may provide useful information about the sample. The sample background arises from incoherent scattering as well as from local chemical or magnetic order. Therefore, when refining a structure (nuclear and/or magnetic), it is very important to specify what is the background and how it is defined. In FULLPROF we may define the background points or it may be created automatically by the program. In order to avoid systematic errors it is important to define the background for each temperature.

When analysing magnetic structures, we usually work with subtracted spectra: from the low temperature spectra we subtract a high temperature spectra. Hence we subtract the nuclear contribution (at high temperature the sample is in paramagnetic phase) and there is just the magnetic contribution that remains. In the same time, by making this subtraction, we suppress all contributions to the background coming from environment, incoherent scattering or phonons. Only the modulations of the background due to the local magnetic order remain.

Once all quantities of interest from equations [II.6] and [II.7] are known, the Rietveld method is applied. It consists of refining a structure (crystal and/or magnetic) by minimizing the weighted squared difference between the observed $\{y_i\}_{i=1,\ldots,n}$ and the calculated pattern $\{y_{ci}(\alpha)\}_{i=1,\ldots,n}$:

$$\chi^2 = \sum_{i=1}^{n} w_i \{y_i - y_{ci}(\alpha)\}^2 \qquad \text{[II.16]}$$

where $\alpha = (\alpha_1, \alpha_2, \alpha_3 \ldots \alpha_p)$ is a series of parameters corresponding to the angle $2\theta_i$. The statistical weight w_i is the inverse of the variance of the "observation" y_i ($w_i = 1/\sigma_i^2$). The parameters α may be of different types, related to the spectrometer (wavelength, initial position of the detector, experimental resolution), to the sample (the quantity of sample determines the scale factor) or to the structural model (peaks position, giving the parameters of the crystalline and magnetic cells, and their relative intensity, giving the structure factor). When the background is too high or the spectrum is polluted for some reason, the corresponding region may be excluded from the refinement.

The quality of the agreement between observed and calculated profiles is measured by the Bragg factor:

$$R_B = 100 \frac{\sum_h \left| I_{obs,\vec{h}} - I_{calc,\vec{h}} \right|}{\sum_h \left| I_{obs,\vec{h}} \right|} \qquad \text{[II.17]}$$

II.2.3. Neutron diffraction under pressure

Due to the low intensity of the neutron sources, a powder neutron diffraction experiment usually requires a large sample volume (typically of about 1 cm^3). Per contra, in order to apply very high pressures, one needs extremely low quantities of sample. That is why for a long time in neutron experiments the maximal pressures were limited to 2-3 GPa. The powder diffractometer G61 (LLB), briefly described in the previous section, is fully adapted for neutron diffraction studies under high pressures (see Figure 1 right). It allows the study of very small quantities of samples (~ 0.001 mm^3) and hence very high pressures of ~ 50 GPa may be obtained. This would not be possible without substantial instrumental progress concerning both neutron instrumentation and pressure cells. For details see Ref. [Goncharenko'04, Goncharenko'95, Goncharenko'98]. For the neutron diffraction measurements, especially for the pressure cells preparation, we are indebted to Igor Goncharenko.

Figure 2 shows the pressure cells used on G61, the so-called "Kurchatov-LLB" cells. In function of the needed pressure range, these pressure cells may be equipped with sapphire anvils, which provide a maximal pressure of ~ 10 GPa, or with diamond anvils providing higher pressures. In our experiments we used sapphire anvil cells, whose schematic view is presented in Figure 2. These pressure cells have seats for the anvils made from a non-magnetic Cu-Be bronze. The sample is placed between two sapphire anvils and inside an aluminium gasket (it yields a neutron transmission of about 95% and a low background). NaCl powder was used as pressure transmitting medium. The pressure is always applied at room temperature and its value is determined by measuring the fluorescence of a thin layer of ruby powder put on the sample.

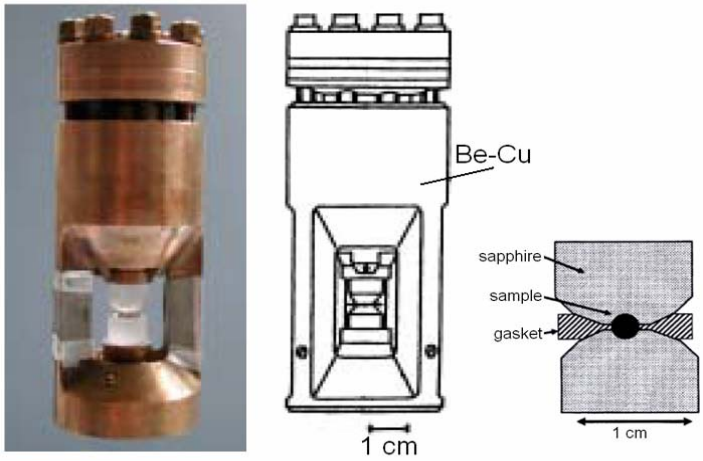

Figure 2. The "Kurchatov-LLB" pressure cell (photo and schematic view) with sapphire anvils (schematic view on the right) [Goncharenko'04].

The experimental device (diffractometer and pressure cell) is shown in Figure 3. The pressure cells are situated in a He-cryostat. In order to avoid any parasitic scattering from the cryostat walls and hence to reduce the background, a system of absorbing masks is placed

inside the cryostat. The multidetector and the monochromator are the same as in ambient pressure version. The main innovation of the high pressure version is constituted by the double stage focusing system, installed between the monochromator and the sample. The focusing systems are an essential part of the diffractometer and were developed especially to study small samples under pressure. Each of the focusing devices is made of four Ni-Ti supermirrors compressing the beam both in vertical and horizontal plane in order to choose the best compromise between intensity and angular resolution [Goncharenko'04]. This system (see photo from Figure 4) increases the scattered intensity by a factor ~7. We also note that the whole experimental device is screened with cadmium protections to reduce the background.

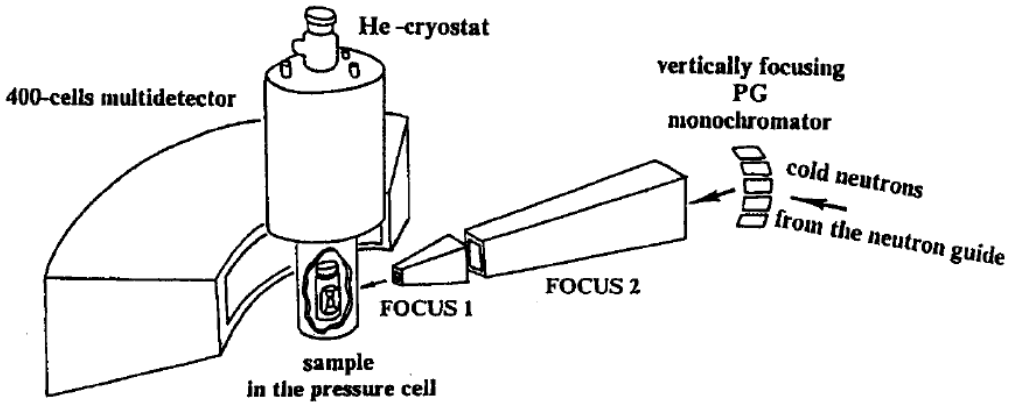

Figure 3. Schematic view of the G61 diffractometer (LLB) in the high pressure version.

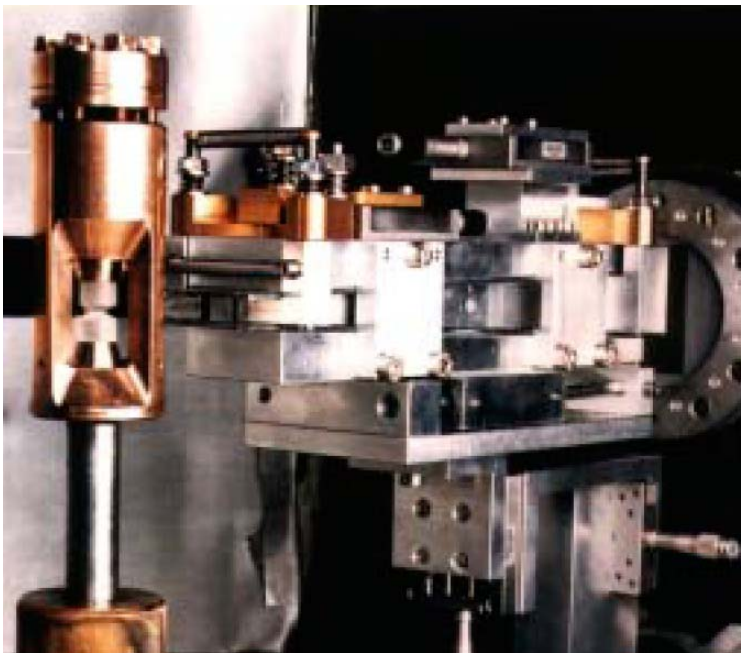

Figure 4. Focusing system and high pressure cell on specialized high-pressure diffractometer G61 of LLB [Goncharenko'04].

For a given pressure, we measured the diffraction pattern at different temperatures. In order to obtain reasonable statistics the counting times were typically of ~ 8-10 hours per temperature. We note the difference with regards to the ambient pressure measurements, where the typical counting time is about 1-2 hours per temperature. The neutron diffraction

patterns under pressure are analyzed using the same FULLPROF program and in the same manner as the ambient pressure data [Rodríguez-Carvajal'93].

II.3. X ray powder diffraction

II.3.1. Ambient pressure X ray diffraction

The ambient pressure X ray diffraction measurements were made using a Brüker D8 instrument (with Cu K_α = 1.5418 Å radiation), at Service de Physique de l'Etat Condensé (SPEC), CEA-CNRS, CEA Saclay, by A. Forget and D. Colson. The spectra were recorded at room temperature.

The ambient pressure X ray characterization allowed us to check the quality of our samples and showed that all are single phase. The raw data obtained in a powder X ray diffraction experiment consist of a record of the intensity of diffraction versus the diffraction angle 2θ. The analysis of X ray diffraction patterns using the program FULLPROF [Rodríguez-Carvajal'93] allowed us to determine the crystal structure of our samples.

II.3.2. X ray diffraction under pressure

Since the required sample volume is much less than for neutrons, the X ray diffraction measurements with a small wavelength of the incident beam and also a high resolution are very suitable to study crystal structures under pressure with a very high precision. These measurements represent a welcome complement for the neutron diffraction ones.

All experiments were performed on the ID27 beam line of European Synchrotron Radiation Facility (ESRF) specialized in high pressure measurements. We thank I. Goncharenko, W. A. Crichton, M. Mezouar and M. Hanfland for their help.

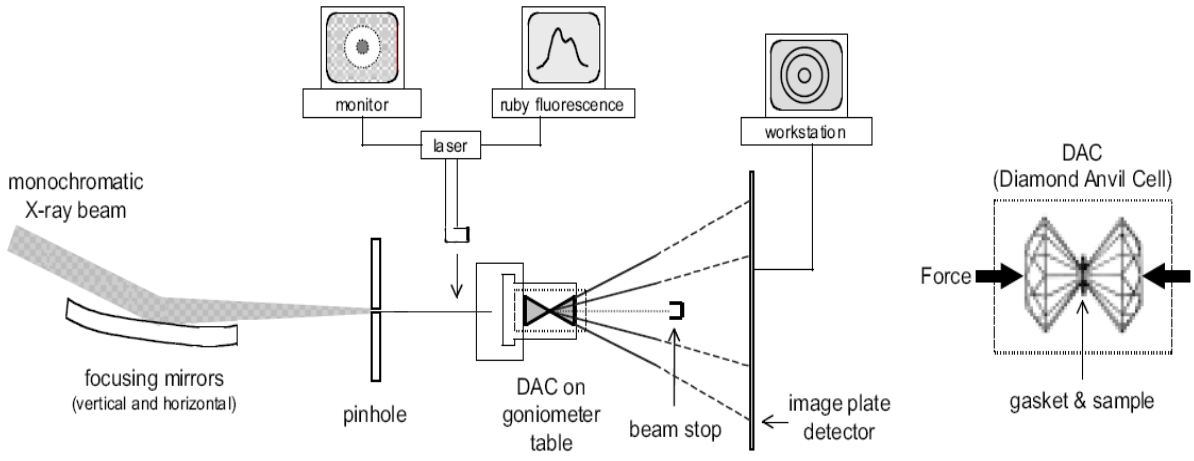

Figure 5. Schematic view of the X ray diffractometer ID27 (ILL)(left) and of a diamond anvil cell (right).

A schematic view of the X ray diffractometer ID27, including the pressure cell, is shown in Figure 5. We used powder samples in diamond anvil pressure cells. Depending of the pressure range, we used different transmitting mediums: nitrogen or neon for high pressures of 35-40 GPa and also an ethanol-methanol mixture, which provides hydrostatical

conditions till lower pressure values of about 10 GPa. Briefly, a monochromatic X ray beam is selected using a silicon monochromator, giving a wavelength λ=0.3738 Å. Then the beam is focalised using a double system of horizontal and vertical mirrors and sent to the sample through a pinhole of ~ 30 μm diameter. The scattered signal is recorded using a two-dimensional photo-sensible detector. The diamond pressure cell is situated on a two-axis goniometer together with the membrane press used to apply pressure. The pressure is measured by the ruby fluorescence technique.

The limiting factor for the X ray diffraction measurements is that the small quantity of sample (especially for experiments under applied pressure) does not provide a very good powder average and there are texture effects. In order to obtain diffraction images of high quality for each two-dimensional diffraction image, the contaminated regions were excluded and then an average on the diffraction cone was done. For this we used the program Fit2D, proposed by the ID27 scientific group [Hammersley], which provides the diffraction patterns: scattered intensity=f (2θ). For a given sample, we measured the room temperature X ray diffraction pattern at different pressures. The X ray diffractions patterns under pressure were analyzed using the FULLPROF program [Rodríguez-Carvajal'93].

II.4. The μSR

The acronym μSR stands for Muon Spin Rotation, Relaxation and Resonance. In this study we deal only with the first two techniques, actually the two most commonly used. To study magnetism, the μSR is complementary to other local techniques (such as Nuclear Magnetic Resonance, Mössbauer spectroscopy), to microscopic techniques (neutron diffraction) and to macroscopic ones (magnetic susceptibility or magnetization measurements). There are of course significant differences between these techniques, resulting in clear advantages of using more than one. The present study will clearly prove this aspect.

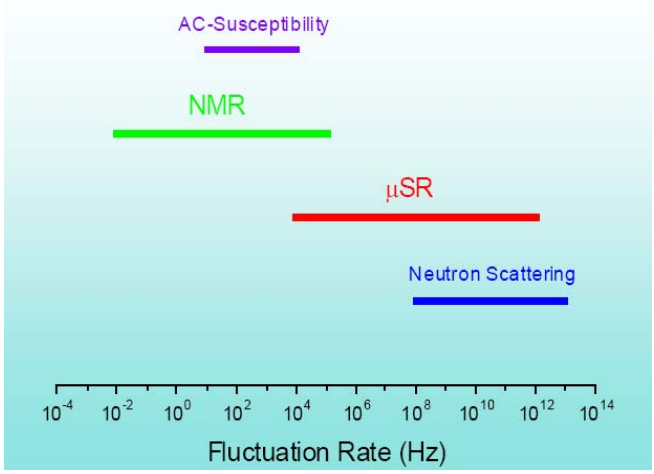

Figure 6. The time window of a μSR experiment compared with other methods [Sonier'02].

There are several advantages in using the μSR technique to study magnetic systems: (i) Due to the large muon magnetic moment (μ_μ=8.89 μ_N), μSR is sensitive to extremely small internal fields (down to about 10^{-5} Tesla) and therefore can probe local magnetic fields which can be nuclear or electronic in nature. (ii) μSR can measure magnetic fluctuation rates in the range 10^4-10^{12} Hz. This time window bridges the gap between fluctuation rates sensed with

NMR and neutron scattering techniques (see Figure 6). (iii) The local character of the muon probe makes μSR very sensitive to spatially inhomogeneous magnetic properties. μSR is a powerful tool when magnetic order is of short range and/or random nature. It also may be used to check the coexistence of different phases. (iv) Since no applied field is necessary to polarize the spin of the implanted muons, μSR measurements can be performed without external field. (v) The muon is a spin ½ particle and hence is free of quadrupolar interactions; (vi) The muon is an implanted guest in the host material and therefore μSR is not limited to specific target nuclei (as for NMR or Mössbauer spectroscopy) and may present an advantage when studying materials containing elements that strongly absorb neutrons.

Nevertheless, there are some limitations of this technique: (i) The muon diffusion at high temperature can mask the intrinsic magnetic behaviour by mimicking spin fluctuations. (ii) To extract quantitative information, the knowledge of the muon stopping-site is useful and it cannot always be known. (iii) The muon is not an "innocent" probe since it may induce local lattice distortions reflected by a small shift in the position of the nearest neighbour ions. (iv) Another disturbing effect of the implantation of a positive charge in the lattice is that the modification of the local charge density can affect the crystal electric field of the neighbouring atoms.

II.4.1. Theoretical principle

Polarized μ^+ muons are obtained via the two body decay of positive pions π^+ and implanted in the sample, where they localize at a particular site. The local magnetic field $\vec{B}_{loc}$ at this interstitial site induces a torque on the muon spin, so that the spin precesses around $\vec{B}_{loc}$, with a frequency $\omega = \gamma_\mu B_{loc}$. This is known as Larmor precession. $\gamma_\mu = 2\pi \times 1.3554 \times 10^8$ rad×s^{-1}×Tesla^{-1} is the gyromagnetic ratio of the muon. The average muon life time is $\tau_\mu \sim 2.2$ μs, after which the muon decays and a positron e^+ is emitted.

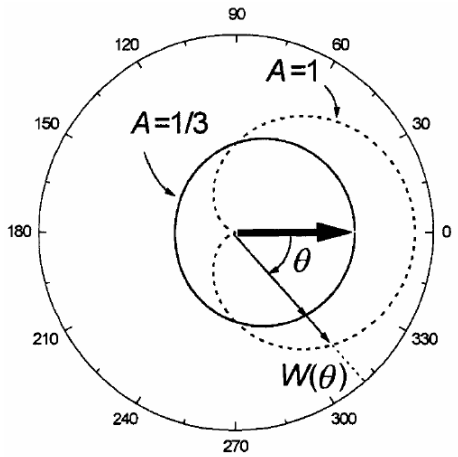

Figure 7. Polar diagram of the angular distribution of positrons from the muon decay: (dashed line, A=1) if only positrons with maximum energy are counted; (full line, A=1/3) if integrated over all positron energies. The bold arrow indicates the direction of the muon spin at the moment of the decay. The diagram is taken from Ref. [Andreica'01].

The decay positrons are emitted preferentially in the direction of the μ^+ spin. The angular distribution of the emitted positrons is given by:

$$W_{e^+}(E,\theta) = 1 + A(E)\cos\theta \qquad \text{[II.18]}$$

where θ is the angle between the muon spin at the moment of decay and the direction in which the positron is emitted. $A(E)$ is called the initial asymmetry and is strongly dependent on the positron energy. A increases monotonically with the positron energy and for the maxim positron energy $A = 1$. When integrating over all energies, one obtains $A = 1/3$ (see Figure 7).

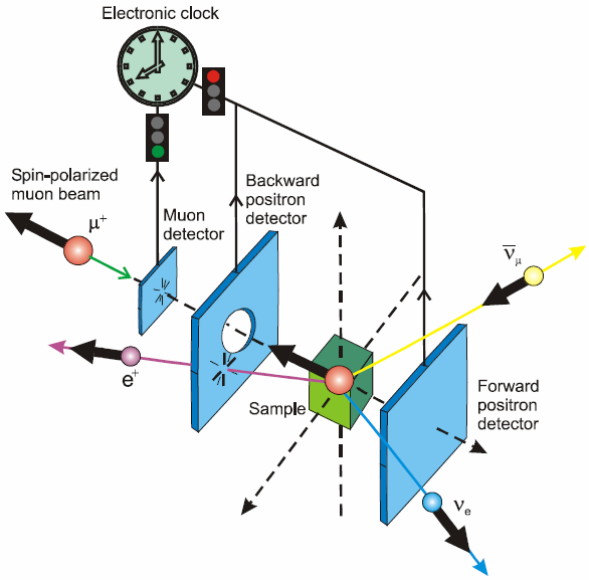

Figure 8. Schematic view of zero field μSR setup [Sonier'02].

When the μ^+ are submitted to magnetic fields, their polarization becomes time dependent $\vec{P}(t)$. The time evolution of the muon polarization, *i.e.* the μSR spectra, is obtained by recording the emitted positrons in different detectors placed nearby the sample (mostly forward F and backward B). Figure 8 shows a typical μSR experimental arrangement in zero applied magnetic field. Each incoming muon gives the start-clock signal and each emitted positron a stop-clock signal. The positrons are monitored and stored by detection electronics in a counts versus time histogram. The time histogram of the collected intervals has the form:

$$N_{e^+}(t) = B + N_0 e^{-\frac{t}{\tau_\mu}}\left[1 + A P_r(t)\right] \qquad \text{[II.19]}$$

where B is an independent background, N_0 is a normalization constant and the exponential e^{-t/τ_μ} accounts for the μ^+ decay. $P_r(t)$ reflects the time dependence of the μ^+ polarization, r indicating the direction of observation:

$$P_r(t) = \vec{n} \cdot \frac{\vec{P}(t)}{P(0)} \qquad \text{[II.20]}$$

$\vec{n}$ is an unit vector in the direction of observation.

For $\vec{P}(0) = \pm\vec{n}$, $P_r(t)$ is the normalized μ^+-spin auto-correlation function $G(t)$:

$$P_r(t) = \pm G(t), \quad with\ G(t) = \frac{\left\langle \vec{S}(t)\cdot\vec{S}(0)\right\rangle}{S(0)^2} \qquad \text{[II.21]}$$

which depends on the average value, distribution and time evolution of the internal fields and therefore contains all the physics of the magnetic interactions of the μ^+ inside the sample. In practice, $AP_r(t)$ is often called the μSR signal and $P_r(t)$ is known as the μ^+ depolarization function.

If the sample exhibits phase separation (for example magnetic domains with different orientations) or if the muons stop in magnetically non-equivalent sites in the same magnetic domain, then $P_r(t)$ is simply the sum of different contributions: $AP_r(t) = \sum_i A_i P_{ri}(t)$. If the muons are implanted uniformly into the sample, the relative amplitudes A_i of the different contributions are a direct measure of the volume fractions of the different phases.

A μSR experiment gives access to the distribution of the static local fields and/or to the spin fluctuations. Commonly, there are three types of experiments which give access to this information: zero field (ZF), longitudinal field (LF) and transverse field (TF) μSR (the latter two correspond to longitudinal and transverse fields with regards to the initial muon spin polarization). Since the ZF μSR is used in this study, in the following we focus on it and analyse the μ^+ depolarization in the presence of static and dynamic internal fields. We suppose that the direction of observation and that of the initial μ^+ polarization are the same and parallel to z axis.

- *static internal fields*

In the ZF μSR configuration, the muon feels only the internal magnetic field at the place where is comes to rest, the muon site. In the simplest case, all the muons see the same magnetic field $\vec{B}_{loc}$. The time dependence of the muon polarization as seen in the backward detector is:

$$P_Z(t) = \cos^2\theta + \sin^2\theta \cos(\gamma_\mu B_{loc} t) \qquad \text{[II.22]}$$

where θ is the angle between the magnetic field $\vec{B}_{loc}$ and $\vec{P}(0) \parallel$ Oz axis. All muon spins precess is the same magnetic field and their polarization describes a cone with the local field $\vec{B}_{loc}$ as axis of rotation. It is only the component of the muon spin perpendicular to $\vec{B}_{loc}$ which processes. The parallel one is time independent.

Clearly, the assumption of a single magnetic field direction for all muons throughout the sample is a very simple model. This situation might occur in an ideal single-domain single crystal having just one magnetically equivalent muon site. In the case of a polycrystalline sample, the average over all θ angles yields:

$$P_Z(t) = \frac{1}{3} + \frac{2}{3}\cos(\gamma_\mu B_{loc} t) \qquad \text{[II.23]}$$

The one third term in the above equation can be easily understood by considering that, since magnetic fields can have all orientations, in average one third of the muons will see fields parallel to their initial polarization and will not precess, while two thirds of them will see fields perpendicular to their initial polarization and will precess. Obviously, the next step is to assume a field distribution at the muon site.

The time dependence of the polarization can be determined by integrating equation [II.22] over the field distribution:

$$P_Z(t) = \int f(\vec{B}_{loc})(\cos^2\theta + \sin^2\theta \cos(\gamma_\mu B_{loc} t))\, d\vec{B}_{loc} \qquad \text{[II.24]}$$

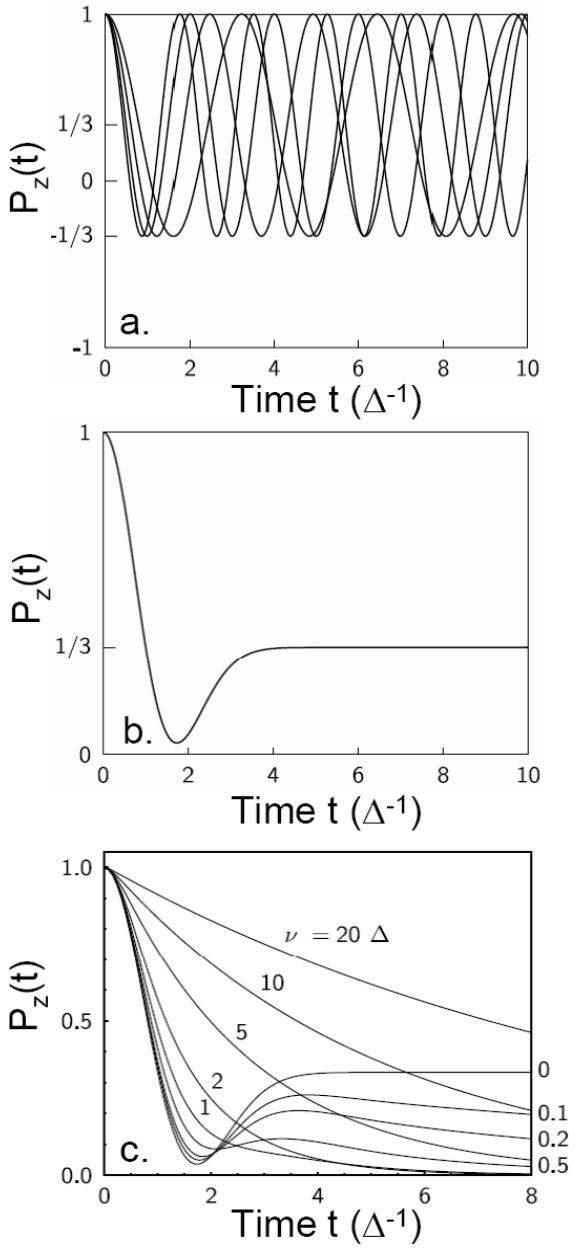

Figure 9. μSR analysis : a. The time evolution of the muon spin polarization corresponding to equation [II.23] with different values of the magnitude of B_{loc} ;b. The averaging of terms from (a) yields the Kubo-Toyabe relaxation function (equation [II.26]) with its characteristic dip and recovery to a value of 1/3; c. The relaxation function for a muon hopping at rate ν. After each hop the value of the internal field is taken from a Gaussian distribution around zero, with width Δ/γ_μ. The curve for ν=0 corresponds to the ZF Kubo-Toyabe relaxation function. The time is measured in units of Δ^{-1}. Plots are taken from Ref. [Blundell'02].

Assuming that the internal fields are Gaussian distributed in their values and randomly oriented, *i.e.*:

$$f(B_i) = \frac{1}{\sqrt{2\pi}} \frac{\gamma_\mu}{\Delta} \exp\left(-\frac{\gamma_\mu^2 B_i^2}{2\Delta^2}\right), \quad \text{with } i = x, y, z \qquad \text{[II.25]}$$

the field distribution has zero average value and no spontaneous frequency is observed. $P_Z(t)$ is expressed as:

$$P_Z(t) = \frac{1}{3} + \frac{2}{3}(1-\Delta^2 t^2)\exp(-\frac{\Delta^2 t^2}{2}) \qquad \text{[II.26]}$$

where Δ^2/γ_μ^2 represents the width of the field distribution along an axis perpendicular to the initial μ^+ polarization, *i.e.:* $\Delta^2/\gamma_\mu^2 = \langle B_x^2 \rangle = \langle B_y^2 \rangle = \langle B_z^2 \rangle$. Equation [II.26] represents the Kubo-Toyabe (KT) function, having as main features: (i) For early times ($t << \Delta^{-1}$) the KT function approaches a Gaussian and can be approximated by: $P_Z(t) = \exp(-\Delta^2 t^2)$. (ii) It has a minimum at $t_{\min} = \sqrt{3}/\Delta$. (iii) It saturates at a value $P_Z(t) = 1/3$. Figure 9b shows that the KT function is a strongly damped oscillation. Its origin is indicated schematically in Figure 9a, which shows a number of curves of equation [II.23] for different values of the internal magnetic field B_{loc}. One clearly sees that initially all oscillations are roughly in phase, yielding the minimum in the KT function, but after a short time they become out of phase. Therefore their average, the KT relaxation function, falls from unity to a minimum and then tends to an average value of 1/3.

- *time-dependent fields*

Generally, the magnetic field at the muon site is not static. Field fluctuations are due either to fluctuating magnetic moments or to muon diffusion. Since in both cases the effects on the muon depolarization rate are the same if described by a Markovian process (see below), in the following only the case of static field distribution and a hoping muon will be discussed. One considers a static magnetic field distribution described by Δ, which is identified by a $P_Z^0(t)$ depolarization function if the muons do not diffuse. Further, the muons are allowed to hop from one site to another, the hops being considered instantaneous events. τ_0 is the mean time spent by the muon in each site ($1/\tau_0 = \nu$, the jump or fluctuation rate). At each site the muon sees the local field (from the static field distribution), *i.e.* the equilibrium is reached et each transition (for details see Ref. [Andreica'01] and References therein). The time evolution of the muon depolarization between two hops is given by the static $P_Z^0(t)$ depolarization function. One assumes that the field at the muon site at the moment t has a value uncorrelated with that at the previous moment (Markovian process). The relaxation function $P_Z(t)$ involves contributions from muons that did not hop, performed 1 hop, …, n hops, up to the time t:

$$P_Z(t) = \sum_n P^n(t) \qquad \text{[II.27]}$$

with :

$$P^0(t) = P_Z^0(t)\exp(-\nu t) \qquad \text{[II.28]}$$

where a Poisson distribution of the hoping probabilities was considered, *i.e.* $\exp(-\nu t)$ is the probability that the muon did not hop until time t.

For example, if considering a KT static depolarization function:

$$P_Z^0(t) = \frac{1}{3} + \frac{2}{3}(1-\Delta^2 t^2)\exp(-\frac{\Delta^2 t^2}{2}) \qquad \text{[II.29]}$$

$P_Z(t)$ calculated for different values of the Δ/ν ratio are shown in Figure 9c. The resulting $P_Z(t)$ depolarization function is called dynamical Kubo-Toyabe (DKT) function. One may note that: (i) the effect of the fluctuating fields is to flatten the $P_Z(t)$ dependence, *i.e.* to reduce the muon depolarization. This effect is similar to the motional narrowing effect in NMR; (ii) for small ν/Δ values the DKT function is Gaussian at early times and only the 1/3 term is affected by the fluctuations; (iii) for high ν/Δ values the DKT becomes exponential. However, there is no simple analytical form for the DKT function, excepting in some limit cases:

(i) In the slow fluctuations limit ($\nu/\Delta << 1$) only the 1/3 term is affected by the fluctuations for quasistatic field distributions:

$$P_Z(t) = \frac{1}{3}\exp(-\frac{2}{3}\nu t) + \frac{2}{3}(1-\Delta^2 t^2)\exp(-\frac{\Delta^2 t^2}{2}) \qquad \text{[II.30]}$$

(ii) In the fast fluctuation limit the depolarization function becomes exponential:

$$P_Z(t) = \exp(-\lambda t) \qquad \text{[II.31]}$$

where $\lambda = 2\Delta^2/\nu$ is the depolarization rate involving spin-flip transitions induced by fluctuating magnetic fields with component perpendicular to $\vec{P}(0)$. It is the same as the spin relaxation rate from NMR ($1/T_1$ process with $1/T_1 = \lambda$).

For more details concerning the μSR technique one may see Ref. [Amato'97, Andreica'01, Blundell'02, DalmasdeRéotier'97, Schenck'85, Sekarya'07].

II.4.2. Ambient pressure μSR

Muon beams are produced either as a continuous beam or as pulsed one. For continuous beams every event is treated separately. The clock is started when the μ^+ enters the sample and stopped when the corresponding decay positron is detected. The elapsed time is stored in the counts versus time diagram that we have already spoken about. For pulsed beams all muons come in the same time t_0. This pulse has however a finite width distribution around t_0 and therefore the pulsed beams have a worst resolution than the continuous ones. Their advantage is their lower background.

The μSR measurements presented in this study have been carried out at Paul Scherrer Institute (PSI), Switzerland, in collaboration with D. Andreica. We also thank A. Amato and U. Zimmermann.

The ambient pressure μSR measurements have been performed on the GPS and DOLLY instruments, which use surface muons. They are called like this, since they are obtained from the decay of pions at rest near the surface of the production target. The produced beam is fully polarized and monochromatic, with a kinetic energy of 4.1 MeV. We used mainly the ZF geometry (see Figure 8) in a temperature range $T \sim$ 2-200 K (depending on the sample). For calibration, we used a transverse field geometry, with an applied transverse field of 50-70 G at a temperature situated in the paramagnetic region.

II.4.3. μSR under pressure

The μSR measurements under pressure have been performed on the GPD instrument, which is a high energy muon beam instrument. The pions that decay into muons leave the target at high energies. The penetration depth of the muons into the sample is larger for the high energy beam than for the surface beam and the former should therefore be used when studying samples within pressure cells. The polarization of the muon beam is limited to ~ 80 %. Muons are generated in bunches at a rate given by the frequency of the accelerator (50.63 MHz at PSI). Although the bunch structure is smeared out during the transport of the beam to the sample, it is still visible in the μSR spectra as an oscillating accidental background in the time dependence of the number of counts. Therefore, in the analysis of the spectra additional oscillating terms are required, with frequencies equal to the accelerator frequency and higher harmonics (101.26 MHz), multiplied by e^{t/τ_μ} ($1/\tau_\mu = 0.455$, with τ_μ the muon lifetime) to compensate for the muon decay. The μSR spectra are therefore fitted with:

$$\begin{aligned} AP_Z(t) = A_1 P_{Z\,sample}(t) + A_2 e^{0.455t}\cos(2\pi\cdot 50.63t + \phi_2) + \\ + A_3 e^{0.455t}\cos(2\pi\cdot 101.26t + \phi_3) + A_4 P_{Z\,pressure\,cell}(t) \end{aligned} \qquad \text{[II.32]}$$

The last term takes into account the contribution of the pressure cell, which is fitted by a Gaussian Kubo-Toyabe function (see equation [II.26]).

For more details concerning the pressure cells one may see Ref. [Andreica'01]. Briefly, the sample was mounted in a piston cylinder cell inserted in a cryostat. The pressure transmitting medium was a 1-1 mixture of isopropyl alcohol and N-pentane. The sample was first measured in the pressure cell at ambient pressure in the chosen temperature range. Then the cell was pressurized and the experiment repeated. The pressure was determined by measuring the superconducting transition of an indium wire situated inside the pressure cell.

II.5. Magnetic susceptibility measurements

The dc susceptibility measurements were recorded using a Superconducting Quantum Interference Device (SQUID) magnetometer, at Service de Physique de l'Etat Condensé (SPEC), CEA-CNRS, CEA Saclay, in collaboration with P. Bonville.

The sample, fixed on a mobile bar, is vertically moved such as to cross the detection coils parallel to the applied magnetic field. Basically, when the sample is moved it produces a magnetic flux variation and hence induces a current in the detection coil. The detection coil has 2N spires in the center and on both sides there is a coiling with N spires with opposite coiling sense. This system allows the screening of the currents induced by the applied magnetic fields and, eventually, by other external fields. The detection coils are coupled to the SQUID, a superconducting ring, which is a very sensitive quantum interferometer and may detect very small flux variation. This flux variation is proportional to the magnetization of the sample. The SQUID is inserted in a liquid ^{4}He cryostat and hence allows measurements in a wide temperature range, from 300 K down to ~ 5 K (for $(Tb_{1-x}La_x)_2Mo_2O_7$ series). In order to obtain lower temperatures ~ 0.1 K (for $Tb_2Sn_2O_7$ sample) a ^{4}He-^{3}He dilution cryostat was used.

For each sample, we measured the temperature dependence of its magnetization, in a small static applied field $H = 80$-100 G, in zero field cooled (ZFC) and field cooled (FC)

process. In ZFC process, the sample is first cooled from ambient temperature down to the lowest temperature and then the magnetic field is applied and the magnetization measured with increasing temperature. In the FC process the sample is cooled down to the lowest temperature under applied magnetic field and the FC magnetization is measured when increasing the temperature. The susceptibility is obtained from the raw experimental signal $S(A/m^2)$ using the relation:

$$\chi(emu/mol\ subst.) = \frac{1000 \cdot M(g)}{H(Gauss) \cdot m(g)} S(A/m^2) \qquad \text{[II.33]}$$

where M and m are the atomic mass and the mass of the sample, respectively.

Chapitre III.

$Tb_2Sn_2O_7$: une "glace de spin ordonnée" avec des fluctuations magnétiques

Le composé pyrochlore $Tb_2Sn_2O_7$ est caractérisé par la présence d'un seul ion magnétique Tb^{3+} qui occupe un réseau de tétraèdres jointifs par les sommets. Dans ce réseau les interactions magnétiques peuvent être géométriquement frustrées et l'état fondamental dégénéré. L'état fondamental dépend d'un équilibre subtil entre les interactions d'échange, les interactions dipolaires et l'énergie de champ cristallin et toutes les énergies d'interactions dépendent d'une façon ou d'une autre des distances inter atomiques. Dans ces conditions, une pression appliquée, qui modifie les distances inter atomiques peut modifier l'équilibre énergétique et favoriser un ordre magnétique particulier.

Le point de départ de cette étude est de considérer $Tb_2Ti_2O_7$ et de voir l'influence sur les propriétés magnétiques d'une dilatation de réseau, obtenue en remplaçant l'ion non magnétique Ti^{4+} par un ion non magnétique plus gros Sn^{4+}. $Tb_2Ti_2O_7$ est un exemple classique de liquide de spin : à pression ambiante, les moments magnétiques corrélés sur des distances de premiers voisins fluctuent jusqu'aux plus basses températures mesurées (70 mK), c'est-à-dire sur une échelle d'énergie 300 fois plus faible que celle donnée par la température de Curie-Weiss θ_{CW} du composé (~ -19K) [Gardner'99]. Nous étudions les propriétés magnétiques d'un composé qui ne diffère de $Tb_2Ti_2O_7$ que par la nature de l'ion non magnétique (Ti/Sn).

Nous étudions les propriétés structurales de $Tb_2Sn_2O_7$ par diffraction de rayons X et de neutrons à pression ambiante, mais ce chapitre est surtout consacré à l'étude de l'ordre magnétique par susceptibilité magnétique, diffraction de neutrons et chaleur spécifique, à pression ambiante. Nous comparons le comportement de $Tb_2Sn_2O_7$ à celui de $Tb_2Ti_2O_7$.

L'ajustement de la susceptibilité magnétique par une loi de Curie-Weiss, dans la gamme de température 100 K-300 K, donne une température de Curie–Weiss de -12.5 K, indiquant des corrélations antiferromagnétiques, plus faibles que celles de $Tb_2Ti_2O_7$. Contrairement à $Tb_2Ti_2O_7$, à basse température, la susceptibilité montre des irréversibilités entre l'état refroidi en champ nul (ZFC) et l'état refroidi sous champ (FC), associé à une augmentation de la susceptibilité FC qui suggère une transition vers un ordre de type ferromagnétique.

La diffraction de neutrons montre qu'à haute température $Tb_2Sn_2O_7$ a le comportement d'un liquide de spin, avec des corrélations antiferromagnétiques entre premiers voisins. Cependant, en accord avec les mesures de susceptibilité magnétiques, lorsque la température décroît en dessous d'environ 2 K, des corrélations ferromagnétiques apparaissent et dessous de 1.3 K se produit une transition en deux étapes (1.3 K et 0.87 K) vers un ordre magnétique à longue portée non colinéaire. Les caractéristiques principales de la structure magnétique sont

les suivantes : (i) c'est un ordre caractérisé par le vecteur de propagation $\vec{k}$=0, c'est-à-dire que les quatre tétraèdres de Tb^{3+} de la maille cubique sont identiques; (ii) l'ordre local dans un tétraèdre est voisin de celui d'une glace de spin ("deux spins in, deux spins out"); il existe une composante ferromagnétique, qui représente 37% du moment magnétique ordonné, et qui s'ordonne en domaines de taille ~190 Å orientés le long des axes <100>. Nous avons appelé cette structure originale "glace de spin ordonnée ".

Les mesures de chaleur spécifique confirment l'existence d'une transition en deux étapes. Nous avons comparé la valeur du moment magnétique déduit de la diffraction de neutrons (5.9(1) μ_B) à celle déduite de la chaleur spécifique (4.5(3) μ_B). Le moment magnétique plus faible déduit de la chaleur spécifique montre que les niveaux hyperfins du terbium sont hors équilibre, et suggère la présence de fluctuations magnétiques "lentes" (~10^{-8} s) de spins corrélés. Ces fluctuations non conventionnelles sont réminiscentes de l'état liquide de spin, dans la phase ordonnée. Leur existence a été récemment confirmée par des mesures de muons [Bert'06, DalmasdeRéotier'06], bien qu'on ne sache pas encore clairement comment des domaines magnétiques d'une telle taille peuvent fluctuer à de telles échelles de temps.

L'état magnétique fondamental que nous avons déterminé expérimentalement a été comparé à ceux prédits par les modèles théoriques existant à l'heure actuelle. La meilleure description est donnée par un modèle impliquant un échange ferromagnétique effectif (résultant de la somme des interactions d'échange direct et des interactions dipolaires) et d'une anisotropie finie, résultant de la faible séparation des premiers niveaux de champ cristallin. Finalement nous comparons les valeurs des énergies d'échanges, dipolaires et de champ cristallin dans $Tb_2Sn_2O_7$ et $Tb_2Ti_2O_7$ et tentons d'expliquer leur différence de comportement.

Chapter III.

$Tb_2Sn_2O_7$: an "ordered spin ice" with magnetic fluctuations

The pyrochlore system $Tb_2Sn_2O_7$ is characterized by the presence of a unique magnetic ion, Tb^{3+}, which occupies a network of corner sharing tetrahedra. In this lattice the first neighbour magnetic interactions may be geometrically frustrated and in this case the magnetic ground state is degenerated. In $Tb_2Sn_2O_7$ the ground state depends on the subtle balance between the exchange, dipolar and crystal field energy and all these types of energy depend, in a way or another, of interatomic distances. In these conditions a perturbation like pressure, which modifies the interatomic distances, can change the energy balance, lift the degeneracy of the ground state and hence favour a particular magnetic order.

The idea of this study starts from $Tb_2Ti_2O_7$ and is to see the influence on magnetic properties of the lattice expansion when replacing Ti^{4+} with a bigger ion Sn^{4+}. $Tb_2Ti_2O_7$ is a text book example of spin liquid: at ambient pressure the antiferromagnetic short range magnetic correlated moments fluctuate down to the lowest measured temperature of 70 mK, with typical energy scales almost 300 times lower than the energy scale given by the Curie-Weiss temperature θ_{CW} of -19 K [Gardner'99]. We study the magnetic properties of a system which differs from $Tb_2Ti_2O_7$ only by the nature of the non-magnetic ion (Ti/Sn).

We analyse the structural properties of $Tb_2Sn_2O_7$ by ambient pressure X ray and neutron diffraction, but mainly this chapter is dedicated to the analysis of the magnetic order by means of magnetic susceptibility, neutron diffraction and specific heat measurements. We observe at low temperature a new magnetic order, compare this experimental result to recent μSR experiments and to theoretical models. We also discuss the differences between $Tb_2Sn_2O_7$ and $Tb_2Ti_2O_7$.

III.1. Magnetic susceptibility measurements: transition to ferromagnetic type order

First studies of $Tb_2Sn_2O_7$ reveal the temperature dependence of the magnetic susceptibility χ (T) [Bondah-Jagalu'01, Matsuhira'02]. A fit of susceptibility by a Curie-Weiss law, in the temperature range 100 – 300 K, yields a Curie-Weiss temperature $\theta_{CW} \cong$ - 12.5 K. This indicates the presence of antiferromagnetic correlations, but weaker than in $Tb_2Ti_2O_7$ with $\theta_{CW} \cong$ -19 K [Gardner'99]. The effective magnetic moment μ_{eff} = 9.68 μ_B is in agreement with the value of 9.72 μ_B corresponding to the $^7F_6$ ground state of Tb^{3+} [Matsuhira'02]. This study also reports for the first time that the magnetic susceptibility shows a divergent behaviour at 0.87 K suggesting a ferromagnetic order.

We focus on the low temperature range as shown in Figure 1. The magnetic susceptibility measurements were recorded using a SQUID (Superconducting Quantum Interference Device) magnetometer, at SPEC (Service de Physique de l'Etat Condensé, CEA-CNRS, CE-Saclay).

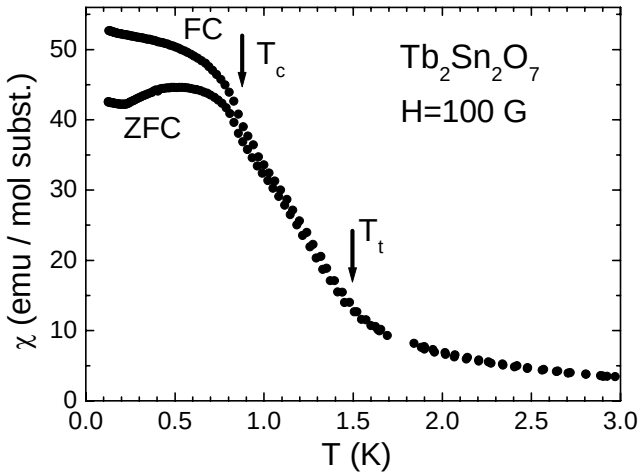

Figure 1. Magnetic susceptibility of $Tb_2Sn_2O_7$ measured in a static field of 100 G, in the zero field cooling (ZFC) and field cooling (FC) processes. The two transition temperatures T_C = 0.87 K and T_t ~ 1.5 K are indicated.

The temperature dependence of the magnetic susceptibility suggests a two step transition, with two characteristic temperatures. T_t ~ 1.5 K corresponds to the appearance of weak irreversibilities between the zero field cooled (ZFC) and field cooled (FC) curves. T_C = 0.87 K corresponds to inflection point of the FC curve and suggests a transition to a ferromagnetic type order.

III.2. X ray and neutron diffraction: crystal structure

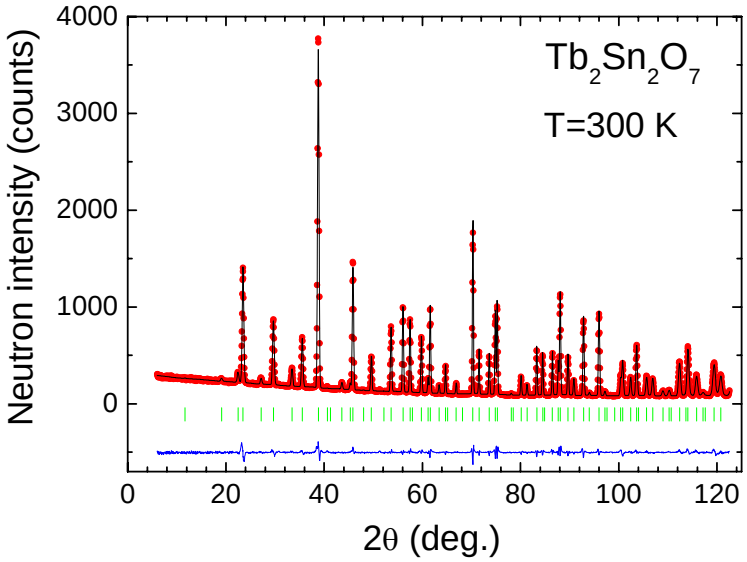

Figure 2. Neutron diffraction intensity of $Tb_2Sn_2O_7$ versus the scattering angle 2θ, measured at 300 K (paramagnetic phase) on the 3T2 powder diffractometer. The incident wavelength is λ = 1.225 Å. Solid lines show the best calculated pattern (R_B = 2.4 %) and the difference spectrum (bottom). Tick marks indicate the Bragg peaks positions.

The ambient pressure crystal structure of a powder sample $Tb_2Sn_2O_7$ is determined at 300 K by combining X ray and neutron diffraction. The neutron pattern was measured using the high resolution diffractometer 3T2 (λ = 1.225 Å) of the Laboratoire Léon Brillouin (LLB). Rietveld refinements performed with the program FULLPROF [Rodríguez-Carvajal'93] show that the compound crystallize in the face centred cubic space group $Fd\bar{3}m$, yielding a lattice parameter a = 10.426(2) Å and an oxygen position parameter u = 0.336(1) (in units of a). We note that Ti substitution by Sn enlarges the unit cell from a = 10.149(2) Å in $Tb_2Ti_2O_7$ [Mirebeau'02] to a =10.426(2) Å for $Tb_2Sn_2O_7$, with the corresponding expansion $\Delta a / a \sim 2.7$ %. The best refinement is shown in Figure 2 with an agreement Bragg factor R_B = 2.4 %.

III.3. Neutron diffraction: magnetic order

The magnetic diffraction patterns were recorded between 1.9 and 100 K on the diffractometer G61 (λ = 4.741 Å) of LLB and down to 0.1 K on D1B diffractometer (λ = 2.52 Å) of the Institute Laüe Langevin (ILL), respectively. In order to be able to compare spectra obtained with different diffractometers and with different quantities of sample, we calibrated the subtracted intensity by multiplying it with a factor $F = 1/(IntI_{(222)} \cdot L)$, with $IntI_{(222)}$ the integrated intensity of the nuclear (222) peak at 100 K and $L = 1/(\sin\theta \cdot \sin 2\theta)$ the Lorentzian factor (see Chapter II).

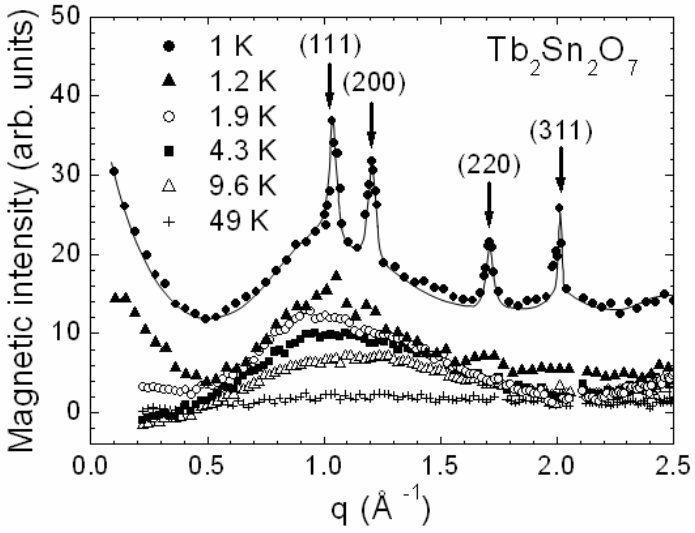

Figure 3. Magnetic intensity of $Tb_2Sn_2O_7$ versus the scattering vector $q = 4\pi \sin\theta / \lambda$. A spectrum in the paramagnetic region (100 K) was subtracted. The spectrum at 1 K has an offset of 10 for clarity. The solid line for 1 K spectra is a guide to the eye, Bragg peaks regions being fitted with a Lorentzian function. Arrows show the position of the Bragg peaks.

Figure 3 shows the evolution of magnetic neutron diffraction pattern for several temperatures. We clearly see that below 100 K the intensity of the magnetic diffuse scattering starts to grow. It narrows and slightly shifts to $q \sim 1$ Å^{-1} as temperature decreases. Additionally, below 2 K an intense magnetic signal appears at low q values ($q < 0.5$ Å^{-1}). This shows the onset of ferromagnetic correlations, which also progressively develop as the temperature decreases. Below 1.2 K magnetic Bragg peaks start to appear.

In the following we analyse first the long range ordered phase (the Bragg peaks)

present at low temperatures. Then we focus on the short range ordered phase (the diffuse scattering) clearly seen at high temperatures, but also present at low temperatures below the Bragg peaks. Finally we propose a two phases model which describes the low temperature coexistence of long and short range order.

III.3.1. Long range order: magnetic Bragg peaks

We analyse first the low temperature magnetic spectra (T < 1.2 K), where magnetic Bragg peaks are observed, showing the presence of long range magnetic order. In this analysis the diffuse magnetic scattering below the Bragg peaks is considered as background.

Like the nuclear Bragg peaks, the magnetic Bragg peaks belong to the face centred cubic lattice, showing that the magnetic structure is derived from the chemical one of $Fd\bar{3}m$ cubic symmetry by a propagation vector $\vec{k}$=0. Rietveld refinements of the magnetic diffraction patterns were performed using the program FULLPROF [Rodríguez-Carvajal'93]. The magnetic structure was solved by a systematic search, using the program BASIREPS [Rodríguez-Carvajal] and a symmetry representation analysis [Yzyumov'79, Yzyumov'91]. The basis states describing the Tb^{3+} magnetic moments were identified and the symmetry allowed structures were compared to experiment. Neither a collinear ferromagnetic structure nor the $\vec{k}$=0 antiferromagnetic structure allowed by the $Fd\bar{3}m$ symmetry group were compatible with the experimental data, yielding extinctions of several Bragg peaks. This result suggests the existence of a magnetic component, which breaks the $Fd\bar{3}m$ cubic symmetry. Consequently, we searched for solutions in the tetragonal space group $I4_1/amd$, the subgroup of $Fd\bar{3}m$ with the highest symmetry, which allows ferromagnetic and antiferromagnetic components simultaneously. We found that a linear combination of the two basis vectors of the irreducible representation Γ_7 yields a good fit of the experimental data. Details concerning this symmetry representation analysis are presented in Appendix B.

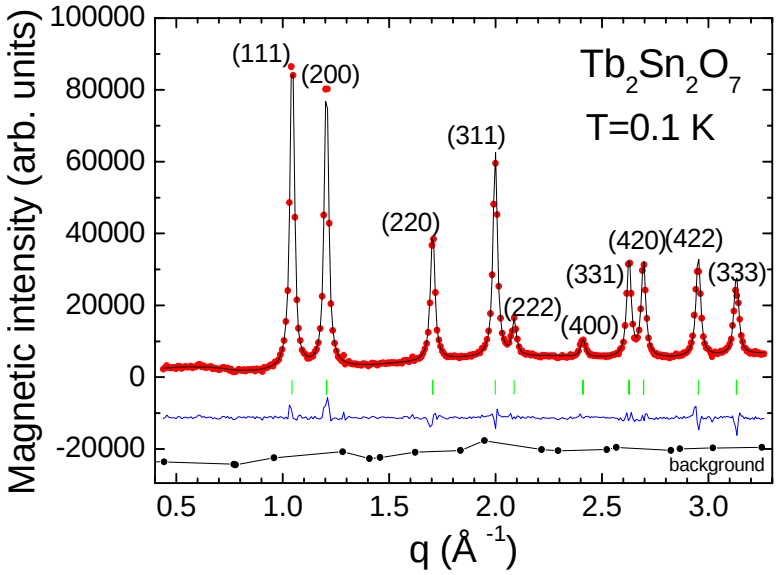

Figure 4. Magnetic diffraction pattern of $Tb_2Sn_2O_7$ versus the scattering vector $q = 4\pi \sin\theta / \lambda$ at 0.1 K. A spectrum at 1.2 K was subtracted. The incident wavelength is λ = 2.52 Å. Solid lines show the best refinement (R_B = 2.3 %) and the difference spectrum (bottom). Tick marks indicate the Bragg peaks positions. The background is also indicated.

The best refinement has an agreement Bragg factor R_B = 2.3 % and it is shown in Figure 4.

The fact that the Bragg peaks can be indexed with a propagation vector $\vec{k}$=0 in the $Fd\bar{3}m$ symmetry, shows that in the cubic unit cell the four tetrahedra are equivalent. As resulting from FULLPROF refinement, at 0.1 K in a given tetrahedron the Tb^{3+} magnetic moments make an angle α = 13.3° with the local <111> anisotropy axes connecting the center of the tetrahedron to the vertices as indicated in Figure 5 right. The components along these <111> axes are oriented in the configuration of the local spin ice structure: two spins are pointing into and two out of each tetrahedron, shortly named the "two in, two out" configuration [Harris'97]. The ferromagnetic component orders in magnetic domains oriented along <100> axes. It represents only 37% of the Tb^{3+} ordered magnetic moment. The perpendicular components make two couples of antiparallel vectors along <110> edge axes of the tetrahedron. Since in this compound the positions of spins in one tetrahedron are close to that of a spin ice and it undergoes long range order, we called it an "ordered spin ice". The magnetic structure, with both antiferromagnetic and ferromagnetic character, is indicated in Figure 5 (for the unit cell and for one tetrahedron, respectively).

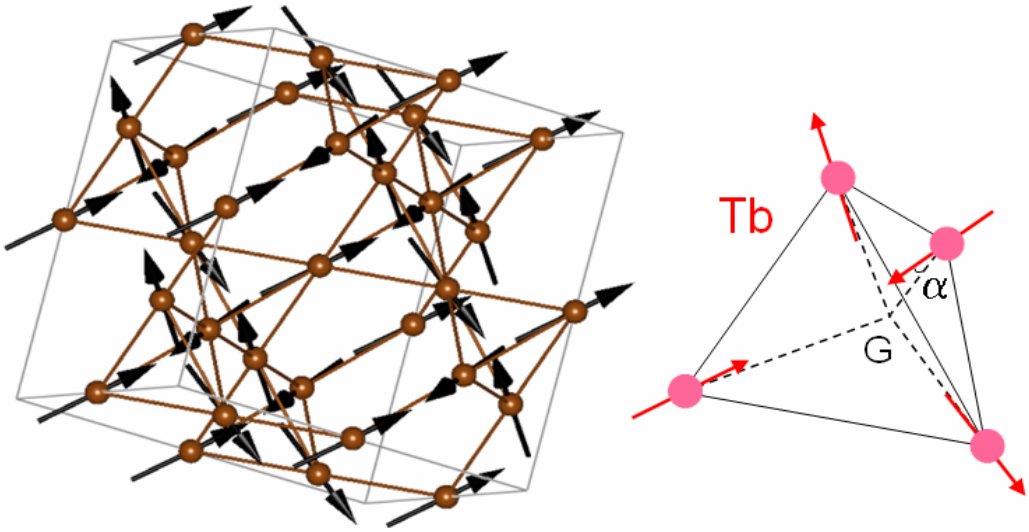

Figure 5. The magnetic structure corresponding to the best refinement shown in Figure 4: for the unit cell (left) and for one tetrahedron (right).

Table I shows the values of the magnetic moment components M_x, M_y and M_z of the four Tb^{3+} atoms of one tetrahedron at 0.1 K, as obtained from FULLPROF refinements. The corresponding value of the ordered magnetic moment of Tb^{3+} is M = 5.9(1) μ_B. It is reduced in comparison to the free ion value of 9 μ_B. This effect is expected due to crystal field effects.

Site	x	y	z	M_x (μ_B)	M_y (μ_B)	M_z (μ_B)
1	0.5	0.5	0.5	3.85(1)	3.85(1)	2.20(1)
2	0.25	0.25	0.5	-3.85(1)	-3.85(1)	2.20(1)
3	0.25	0.5	0.25	3.85(1)	-3.85(1)	2.20(1)
4	0.5	0.25	0.25	-3.85(1)	3.85(1)	2.20(1)

Table I. The magnetic moment components M_x, M_y and M_z of the four Tb^{3+} ions of one tetrahedron at 0.1 K. The atomic coordinates of the four Tb^{3+} ions expressed in unit cell units are also indicated.

Once the magnetic structure at the lowest temperature was known, we followed its evolution with temperature. When increasing temperature, the ordered magnetic moment of Tb^{3+} M remains almost constant up to 0.6 K. Then it steeply decreases showing an inflexion point at 0.87(2) K and finally at 1.3(1) K it vanishes as shown in Figure 6. Additionally, we followed the temperature evolution of the square root of the intensity of the (200) magnetic peak. When scaling this quantity to the magnetic moment at 0.1 K, we find as expected the same variation in temperature as the magnetic moment.

The neutron diffraction measurements allow the determination of the order parameter (the Tb^{3+} magnetic moment) and show that the magnetic order sets in two steps. First, the characteristic temperature T_t = 1.3(1) K corresponds to the appearance of Bragg peaks, whereas T_C =0.87(2) K corresponds to an inflection point of the curve shown below indicating a stronger increase of the magnetic moment.

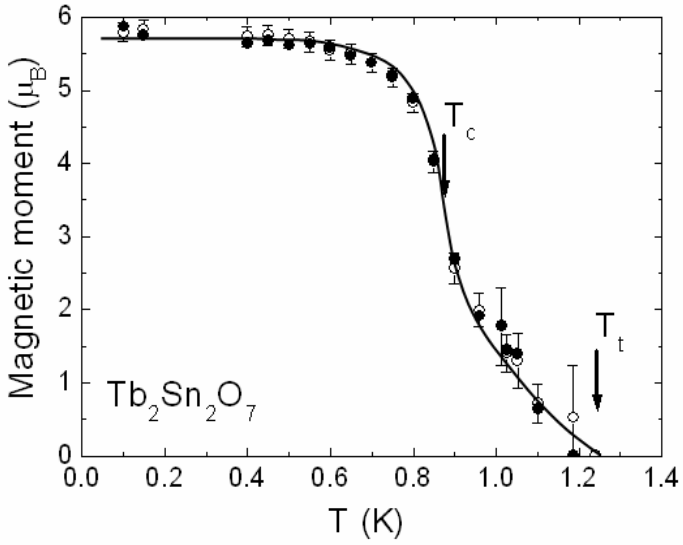

Figure 6. Tb^{3+} ordered magnetic moment M versus temperature (solid circles) and square root of the intensity of the (200) magnetic peak, scaled to the magnetic moment at 0.1 K (open circles). The solid line is a guide to the eye. The two transition temperatures are indicated.

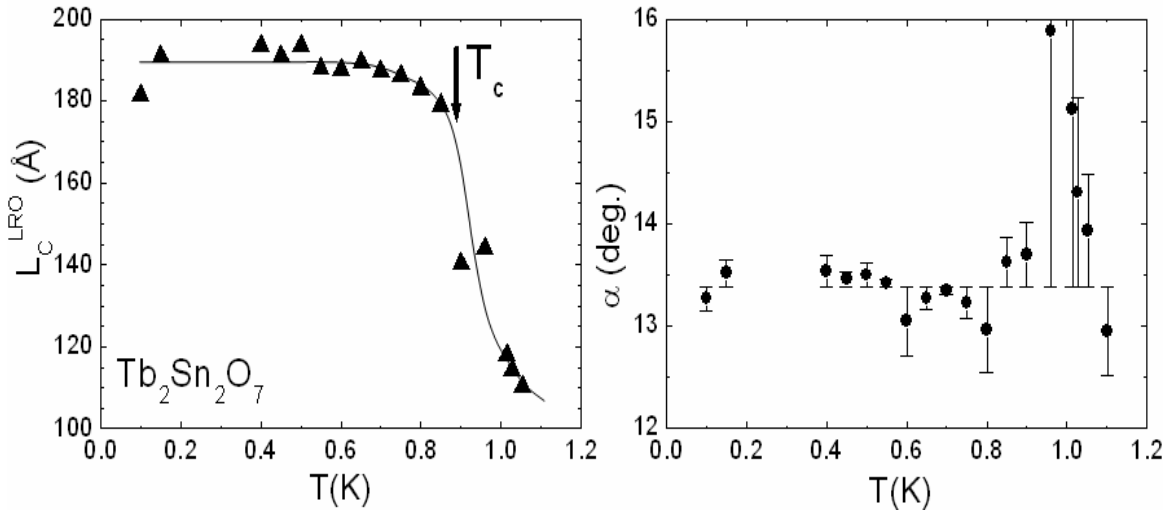

Figure 7. The temperature dependence of the correlation length L_C^{LRO}, deduced from the width of the magnetic Bragg peaks (left) and the angle α made by the magnetic moments with the local anisotropy axes (right) as obtained from the FULLPROF analysis.

In the FULLPROF analysis we used the Thompson-Cox-Hastings pseudo-Voigt peak shape function as presented in Chapter II (section II.2.2.2). The correlation length L_C^{LRO} was deduced from the intrinsic peak width. It shows a similar behaviour to that of the ordered magnetic moment (Figure 7 left): it remains constant and limited to about 190 Å, up to T_C, and then, above T_C, it decreases. Very interesting even far below T_C, L_C^{LRO} is much shorter than usually in ordered magnetic structures (see for comparison $(Tb_{0.8}La_{0.2})_2Mo_2O_7$ from Chapter IV).

The angle α between the magnetic moments and the local anisotropy axes remains constant in temperature, in the limit of error bars (Figure 7 right).

III.3.2. Short range order: diffuse magnetic scattering

In this section we focus first on the analysis of the diffuse magnetic scattering, which starts to grow below 100 K and shows the presence of short range magnetic correlations. When temperature decreases it narrows and slightly shifts (see Figure 8a).

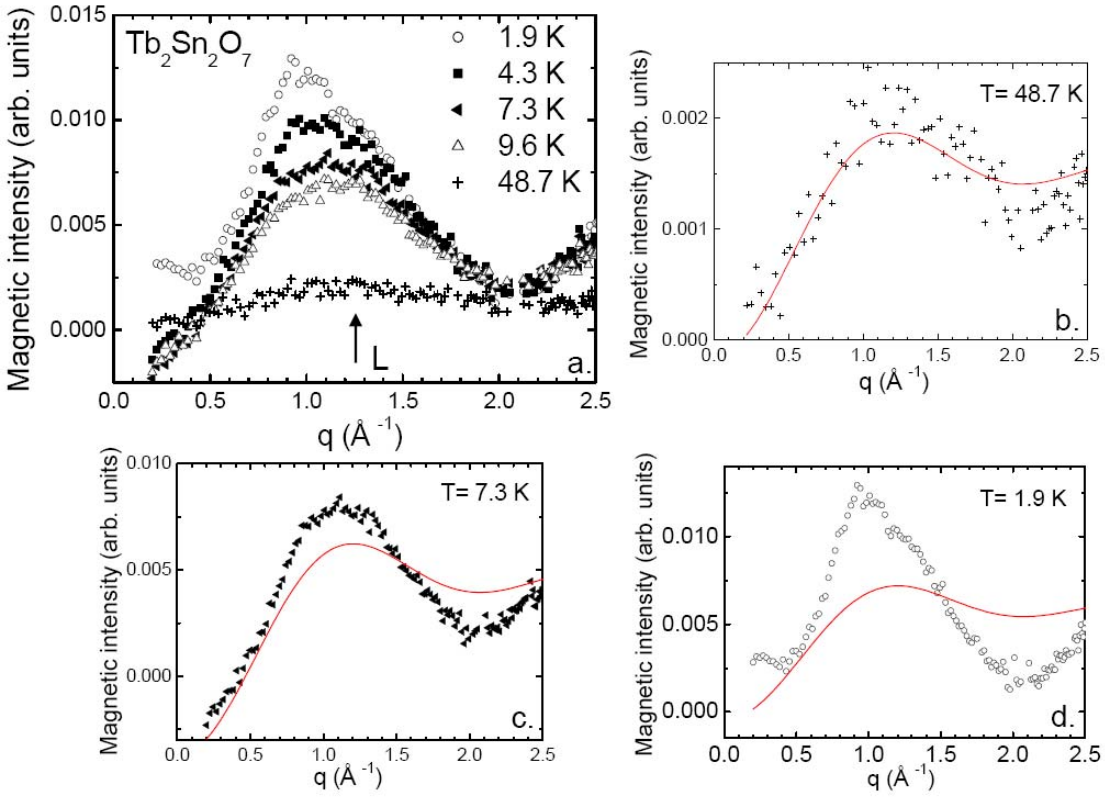

Figure 8. a. $Tb_2Sn_2O_7$: diffuse magnetic scattering versus the scattering vector $q = 4\pi \sin\theta / \lambda$, with λ=4.741 Å. A spectrum in the paramagnetic region (100 K) was subtracted. The arrow shows the near neighbour liquid peak (L) as calculated in Ref. [Canals'01] (see section I.2.3); b-d. Solid lines are data fits at different temperatures using the function $I(q)$, as described in the text.

To fit the experimental data we considered a cross section for magnetic scattering (when a spectrum in the paramagnetic region was subtracted) due to the short range spin - spin correlations, first proposed for spin glasses in Ref. [Bertaut'67, Wiedenmann'81] and then applied to the pyrochlore system in Ref. [Greedan'91]:

$$I(q) = N\left[\frac{1}{2} r_0 \gamma_0 f_m(q)\right]^2 \cdot \frac{2}{3}\sum_{i=1}^{n} c_i \gamma_i \frac{\sin(qR_i)}{qR_i} \qquad \text{[III.1]}$$

$\frac{1}{2} r_0 \gamma_0$ is the scattering length per Bohr magneton, $f_m(q)$ is the magnetic form factor of Tb^{3+}. The summation is over the coordination shells surrounding a central atom and c_i and R_i are the number of neighbours and the radius of the coordination cell (bond distance), respectively, known from crystallographic data. γ_i is the sum of spin correlations at each bond distance. For $Tb_2Sn_2O_7$ we took into account only the first neighbours, meaning: $n = 1$, $c_1 = 6$, $R_1 = a/\sqrt{8} = 3.6862$ Å and a spin–spin correlation function $\gamma_1 = <\mu_{Tb} \cdot \mu_{Tb}>$, with μ_{Tb} the Tb^{3+} magnetic moment. We fitted the subtracted data with:

$$I(q) = P(T) f_m^2(q) \frac{\sin(qR_1)}{qR_1} + b(T) \qquad \text{[III.2]}$$

where $P(T)$ and $b(T)$ are the adjustable parameters. $P(T)$ takes into account all the above quantities and $b(T)$ is a background factor.

Figure 8b-d shows the fits of the model to the data for three temperatures. At high temperature, ~49 K, we obtained a good description of the diffuse scattering, correctly accounting for the intensity and peak position. We obtained $P < 0$, which corresponds to a $\gamma_1 < 0$. Consequently, the peak is well described when taking into account first neighbour antiferromagnetic spin – spin correlations. This result recalls that reported in Ref. [Canals'01] (see section I.2.3.). Using an isotropic classical Heisenberg model, the spin correlations functions were computed and according to this model the antiferromagnetic nearest neighbour correlations give rise to a spin liquid like peak (L). Its position is indicated in Figure 8a. In this temperature region, $Tb_2Sn_2O_7$ in characterized by antiferromagnetic short range correlations limited to the first neighbour, like a spin liquid. It is similar to $Tb_2Ti_2O_7$ which has also antiferromagnetic correlated spins over a single tetrahedron only [Gardner'99]. Per contra, when temperature decreases the behaviour of $Tb_2Sn_2O_7$ differs from that of $Tb_2Ti_2O_7$: the calculated curve drifts away from the experimental data. The liquid peak narrows suggesting an increasing of the correlation length, but the inclusion of spin correlations beyond the first neighbour did not succeed to reproduce the experimental behaviour.

We analyzed then the intense small angle neutron scattering (SANS) (see Figure 9), which appears at low q values as indicated in inset. It corresponds to the onset of ferromagnetic Tb–Tb spin correlations. When temperature decreases from 2 K to 0.1 K the SANS progressively develops showing that the ferromagnetic correlations increase.

In order to obtain their correlation length, the SANS signal was fitted by a Lorentzian function:

$$I(q) = \frac{A}{\pi} \frac{k}{k^2 + q^2} \qquad \text{[III.3]}$$

A is the norm and k the half width half maximum of the Lorentzian curve, with: $k = 1/L_c$. At T= 0.1 K the correlation length was evaluated at 17(7) Å. Since it is situated between the values corresponding to the short range order given by first neighbours of 3.6862 Å and the long range order $L_c^{LRO} \sim 190$ Å, we call it a mesoscopic range order L_c^{MRO}. The temperature

dependence of L_c^{MRO} is shown in Figure 10a. Interestingly, its evolution when temperature increases from 0.1 to 1.2 K is quite similar to that observed for L_c^{LRO}: it remains constant up to T_C, and then, above T_C, it decreases. We note that the SANS signal is fitted by a Lorentzian function centered on $q = 0$. The large error bars take into account the fact that at low temperature the signal (which has a good statistics) deviates from a good Lorentzian. Figure 10b shows the temperature dependence of the norm A, as obtained from the Lorentzian fit. One may see that its temperature variation is roughly similar to that of the square of the Tb^{3+} ordered magnetic moment (the latter is scaled to A).

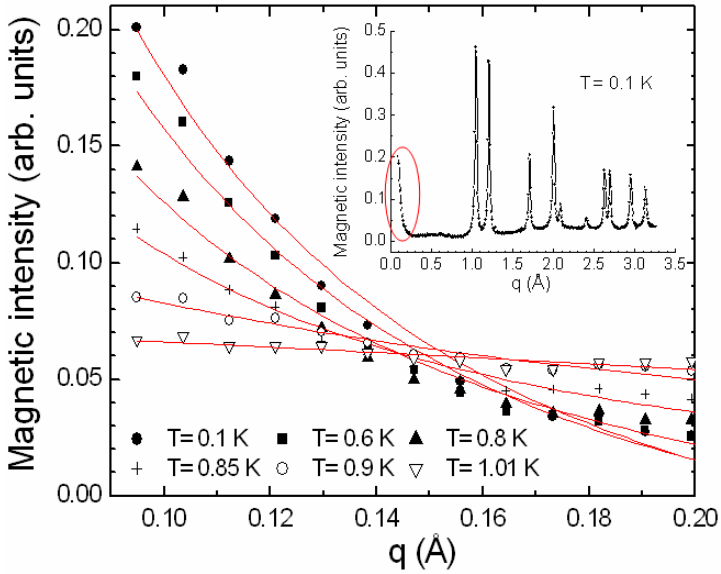

Figure 9. $Tb_2Sn_2O_7$: the small angle neutron magnetic intensity (SANS) versus the scattering vector q for several temperatures. The neutron wavelength is λ = 2.52 Å. Solid lines are fits as described in the text. In inset the magnetic spectra at T= 0.1 K for the whole q range. The interest q < 0.2 Å interval is marked.

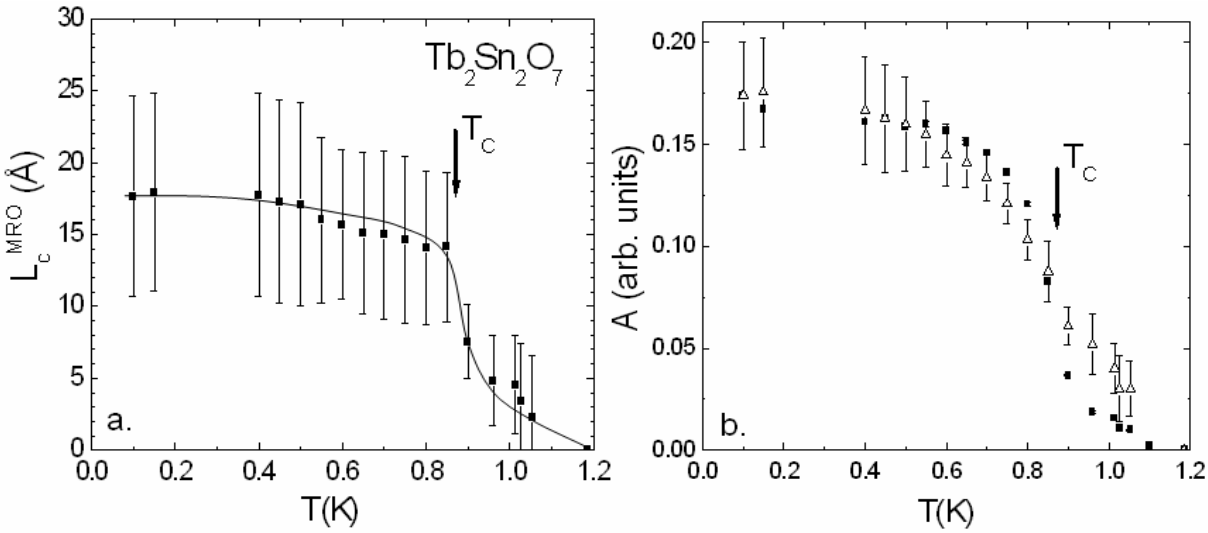

Figure 10. $Tb_2Sn_2O_7$, results of the Lorentzian fit: a. Temperature dependence of the mesoscopic correlation length L_c^{MRO}. The solid line is a guide to the eye; b. Temperature dependence of the norm A (open triangles) and of the square of the Tb^{3+} magnetic moment (scaled)(filled squares). The transition temperature to long range ferromagnetic type order, T_C = 0.87 K, is each time indicated.

III.3.3. Short and long range order: two phases model

In this paragraph we propose a two phases model, in order to take into account both long and short range phases in the same analysis. Contrary to the section III.3.1, where we included the diffuse scattering into the background, this time we consider it like a second magnetic phase with a linear background.

We assume that this short range order has the same symmetry as the long range one. The best Rietveld refinement with FULLPROFF [Rodríguez-Carvajal'93] of the T= 0.1 K spectrum is shown in Figure 11a. The agreement factors are: R_{B1} = 4.27 % and R_{B2} = 11.14 % for the long range and the short range phase, respectively. The contribution of the background, LRO and SRO phases to the calculated magnetic intensity are shown in Figure 11b-d.

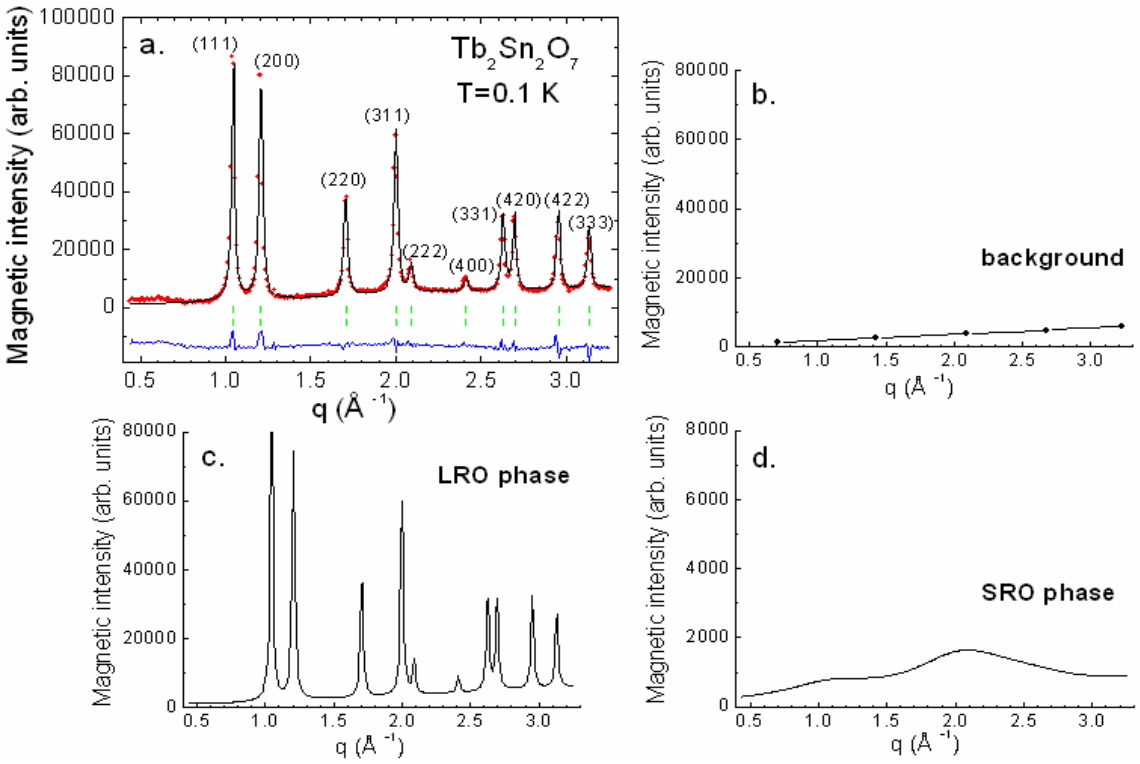

Figure 11. $Tb_2Sn_2O_7$: a. Magnetic diffraction pattern versus the scattering vector $q = 4\pi \sin\theta / \lambda$ at 0.1 K. Solid lines show the best refinement with the two phases model (R_{B1} = 4.27 % and R_{B2} = 11.14 %) and the difference spectrum. Tick marks indicate the two phases Bragg peaks positions; b. Background contribution; c-d. The calculated magnetic intensity, corresponding to the LRO and SRO phases, respectively. For clarity, the scale of SRO signal was reduced by 10.

The refinement shows that the long range phase is identical (in the error bars limit) with that obtained in one phase model (section III.3.1). In a given tetrahedron Tb^{3+} magnetic moments make an angle α_{LRO} = 13.4° with the <111> anisotropy axes and their components along these axes orient in "two in, two out" local spin ice configuration. For the second, short range ordered phase, we obtained that Tb^{3+} moments make an angle α_{SRO}= 18.3° with the [001] axis and they are coupled antiferromagnetically with the magnetic moments of the first phase. The values of the ordered moment are M_{LRO} = 5.8(1) μ_B and M_{SRO} = 3.3(1) μ_B, for the first and second phase, respectively. Calculating the total moment as: $M = \sqrt{M_{LRO}^2 + M_{SRO}^2}$,

we obtain a value of $M = 6.6(1)\ \mu_B$, which is still well reduced from the free ion value of 9 μ_B. The correlation length for the LRO phase was fixed at ~ 190 Å (like in the one phase model). For the SRO phase we obtained L_c^{SRO} = 4(1) Å. This value is very close to the first neighbour distance of 3.6862 Å, showing that the SRO phase corresponds to a first neighbours order. We note that this low temperature SRO phase has a ferromagnetic component in contrast with the high temperature behaviour described in the section III.3.2.

III.4. Specific heat measurements: magnetic fluctuations

The specific heat was measured in the temperature range 0.15 – 4.8 K by the dynamic adiabatic method. The measurements were done by V. Glazkov and J. P. Sanchez (Service de Physique Statistique, Magnétisme et Supraconductivité, CEA-Grenoble) and the analysis thanks to the program of P. Bonville (SPEC).

The temperature dependence of the specific heat C_p is shown in Figure 12. It starts to increase below $T_t \sim 1.5$ K and then shows a well defined peak at T_C = 0.87 K, in good agreement with the magnetic susceptibility and neutron diffraction data. The final increase of C_p below 0.38 K is attributed to a nuclear Schottky anomaly, as determined by the splitting of the energy levels of the ^{159}Tb nuclear spin (I = 3/2) by the hyperfine field due to the Tb^{3+} electronic moment. Experimentally, it appears like a peak in the specific heat, in the temperature range where the hyperfine interactions are noticeable. This nuclear peak has already been observed at very low temperature as a broad peak, thanks to specific heat measurements down to 0.07 K in Tb_2GaSbO_7 [Blöte'69].

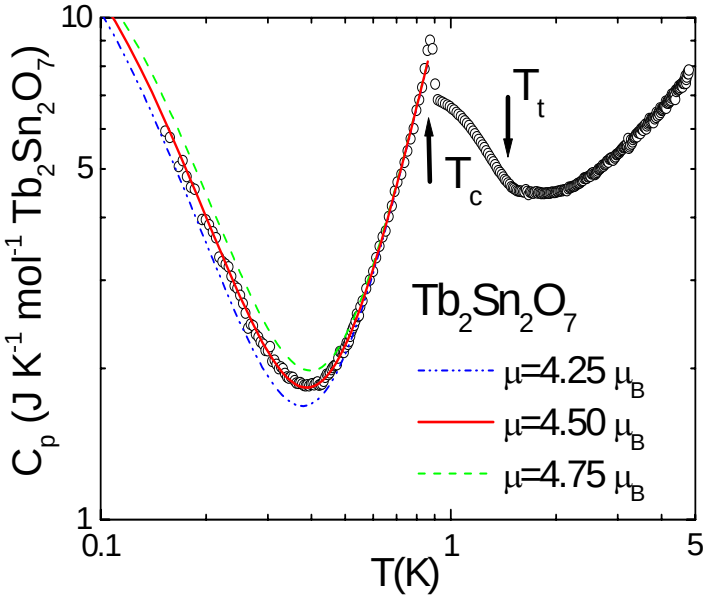

Figure 12. Specific heat C_p in $Tb_2Sn_2O_7$. The curves below T_C are computed using the expression: $C_p = C_{nucl} + C_m$. C_{nucl} is the standard expression of a nuclear Schottky anomaly and is computed for three values of the magnetic moment, whereas C_m is an empirical electronic magnon term (see text). The arrows indicate the two transition temperatures.

Below T_C the experimental data were fitted with the function:

$$C_p = C_{nucl} + C_m \qquad [III.4]$$

C_{nucl} corresponds to the nuclear Schottky anomaly observed below 0.38 K. $C_m = \beta T^3$ represents an empirical magnon term which fits well the rise of C_p above 0.4 K, with β = 12.5 J K^{-4} mol^{-1}.

The nuclear Schottky anomaly C_{nucl} was calculated as follows. First we calculated the full hyperfine Hamiltonian, which is the sum of two terms: the magnetic one due to the hyperfine field H_{hf} and an electric quadrupolar one. The quadrupolar term is the sum of a lattice contribution, extrapolated from that measured in another pyrochlore stannate $Gd_2Sn_2O_7$ [Bertin'01], and an estimated 4f term, both amounting to about 5% of the magnetic term. The angle between the hyperfine field and the local <111> anisotropy axis was fixed at the value of 13.3°, as obtained by neutron diffraction. Once all these quantities are known, only one parameter remains: the hyperfine field H_{hf} (Tesla), which is proportional to the Tb^{3+} magnetic moment $m\,(\mu_B)$:

$$H_{hf}\ (Tesla) = 40\ m\,(\mu_B) \qquad \text{[III.5]}$$

with 40(4) Tesla/ μ_B the hyperfine constant [Dunlap'71]. For more details concerning the calculus of the full hyperfine Hamiltonian see Appendix A. Then this Hamiltonian (4×4 matrix) was diagonalized and the hyperfine energies E_i $(i = \overline{1,4})$ were obtained. We calculated the nuclear specific heat, C_{nucl}, using the expression:

$$C_{nucl} = \frac{1}{k_B T^2}\left[\left\langle E^2\right\rangle - \left\langle E\right\rangle^2\right] \qquad \text{[III.6]}$$

where $\left\langle E\right\rangle = \sum_{i=1}^{4} E_i e^{-\frac{E_i}{k_B T}} / Z$ is the mean energy, $\left\langle E^2\right\rangle = \sum_{i=1}^{4} E_i^2 e^{-\frac{E_i}{k_B T}} / Z$ is the mean square energy and $Z = \sum_{i=1}^{4} e^{-\frac{E_i}{k_B T}}$ is the partition function.

As shown in Figure 12, the best fit of the experimental data is obtained when using a hyperfine field H_{hf} = 180 Tesla, which corresponds to a Tb^{3+} magnetic moment m = 4.5(3) μ_B.

The electronic entropy variation S between the temperatures $T_{\min} = 0.15$ K and $T_{\max} = 4.8$ K was calculated starting from the total measured specific heat from which the hyperfine contribution was subtracted. We used the thermodynamic relation:

$$S = \int_{T_{\min}}^{T_{\max}} \frac{C_p - C_{nucl}}{T} dT \qquad \text{[III.7]}$$

Current measurements of $Tb_2Ti_2O_7$ and $Tb_2Sn_2O_7$ by inelastic neutron scattering performed at LLB [Mirebeau'07a] show that the crystal field levels scheme of $Tb_2Sn_2O_7$ is only slightly modified with respect to that of $Tb_2Ti_2O_7$, whose ground state is a doublet followed by another doublet as first excited state, with the doublet-doublet energy gap of about 18 K [Gingras'00, Mirebeau'07a]. In case of $Tb_2Sn_2O_7$ the energy gap is around 15 K. For systems having a doublet as ground state, in the magnetically ordered state ($T < T_C$) the exchange energy lifts this degeneracy. At $T = 0$ K only the ground state is populated and

$S(T=0)=R\ln 1=0$, with $R=8.3145$ $Jmol^{-1}K^{-1}$ the molar gas constant. For $T>T_C$, the doublet is degenerated and $S(T=T_C)=R\ln 2$. When T keeps increasing, the excited energy levels become populated. For a first excited state doublet, as in this case, S should reach the value Rln4 when it becomes populated. In the case of $Tb_2Sn_2O_7$, as shown in Figure 13, the behaviour is different: the entropy released at T_C is only 25% of Rln2 and it reaches ~ 50% at 1.5 K. This reflects that above T_C and T_t there still are strong correlations of the magnetic moments. Above T_t, $Tb_2Sn_2O_7$ enters a geometrically frustrated spin liquid phase and not a paramagnetic one, as shown by neutron diffraction.

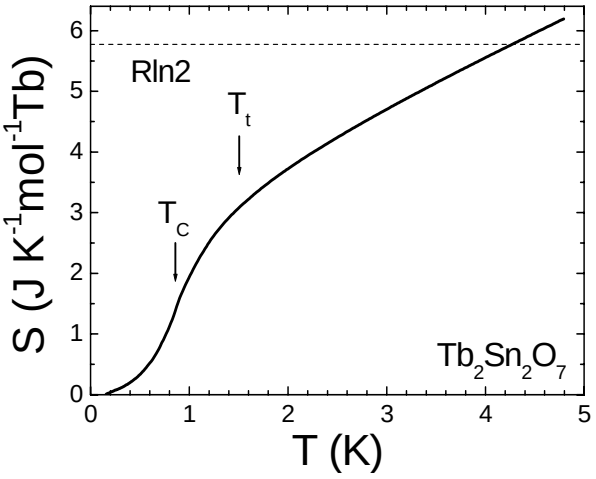

Figure 13. $Tb_2Sn_2O_7$: the temperature dependence of the electronic entropy. The arrows show the transition temperatures T_C and T_t, respectively. Rln2 is the entropy corresponding to the doublet ground state. $R=8.3145$ $Jmol^{-1}K^{-1}$ is the molar gas constant.

The value of Tb^{3+} magnetic moment deduced from nuclear specific heat m = 4.5(3) μ_B is well below the value obtained by neutron diffraction M = 5.9(1) μ_B. We explained such a remarkable reduction by the presence of electronic fluctuations, as suggested in Ref. [Bertin'01] for $Gd_2Sn_2O_7$. Considering the nuclear spins a two-level system driven by a randomly fluctuating field, a stochastic model was developed, which yields an analytical expression for the probability distribution of the level populations. This quantity depends on the ratio T_1/τ between the spin-lattice nuclear relaxation time T_1, which governs the thermalization of the hyperfine levels, and the electronic spin flip time τ. It is shown that an out of equilibrium distribution can occur when the electronic spin flips persist at low temperature and when the nuclear relaxation time T_1 is longer or of the same order of magnitude as the flipping time τ of the hyperfine field of the electronic spins. The very low temperature spin fluctuations were evidenced through the observation that the hyperfine levels the ^{155}Gd nuclei are populated out of thermal equilibrium.

The standard (static) two level Schottky anomaly is given by:

$$C_{nucl}^{Schottky}=k_B\left(\frac{\Delta}{k_BT}\right)^2\frac{e^{-\frac{\Delta}{k_BT}}}{\left(1+e^{-\frac{\Delta}{k_BT}}\right)^2} \qquad \text{[III.8]}$$

where $\Delta\sim H_{hf}$ is the mean hyperfine splitting. Within the model presented in Ref.

[Bertin'01], the nuclear specific heat is in fact reduced with respect to the standard (static) Schottky anomaly according to the expression:

$$C_{nucl} = g(\frac{T_1}{\tau})C_{nucl}^{Schottky} = \frac{1}{1+2\frac{T_1}{\tau}}C_{nucl}^{Schottky} \qquad \text{[III.9]}$$

with $g(T_1/\tau)$ the reduction function.

For $Tb_2Sn_2O_7$, the two values of Tb^{3+} magnetic moment, m = 4.5(3) μ_B and M = 5.9(1) μ_B deduced from specific heat and neutron diffraction, respectively, give an experimental reduction $m/M = 0.76$. Within the model [Bertin'01] we attributed it to a specific heat reduction. According to [III.5] and [III.8] $C_{nucl} \sim \Delta^2 \sim H_{hf}^2 \sim m^2$ and we calculated this specific heat reduction: $C_{nucl}/C_{nucl}^{Schottky} = (m/M)^2 = 0.58$ and using [III.9], we obtained a ratio: $T_1/\tau \simeq 0.36$. This value is comparable to that of $Gd_2Sn_2O_7$, with $T_1/\tau \simeq 0.85$, and supposing the same order of magnitude of T_1, in Ref. [Mirebeau'05] we first concluded that $Tb_2Sn_2O_7$ is characterized by low temperature fluctuations of the Tb^{3+} magnetic moments with a time scale of 10^{-4} – 10^{-5} s, as for Gd^{3+}. In fact, there are many systems where the nuclear relaxation is much more rapid and this seems to be the case of our system. As presented in the following section μSR experiments show that the spin fluctuations for $Tb_2Sn_2O_7$ are more rapid (~10^{-8} s).

III.5. Discussion

III.5.1. Magnetic ground state: theoretical models

The magnetic ground state of $Tb_2Sn_2O_7$ and $Tb_2Ti_2O_7$ is determined by the delicate balance between the nearest neighbour exchange energy, long range dipolar energy and anisotropy. At the time being there are several theories that are trying to describe the magnetic ground state of the pyrochlore magnets. They involve different combinations of the above mentioned energies: antiferromagnetic ($J_{nn} < 0$) or ferromagnetic ($J_{nn} > 0$) nearest neighbour exchange energy, ferromagnetic dipolar energy ($D_{nn} > 0$) and also the strength of the local anisotropy D_a.

In fact, the behaviour of the real system $Tb_2Sn_2O_7$ is best described by a combination of two models.

The first one is a continuous spin ice model, with classical Heisenberg spins replacing the Ising ones (see Ref. [Champion'02]). These spins populate a cubic pyrochlore lattice and are coupled to their nearest neighbours by a ferromagnetic exchange interaction and to the local <111> anisotropy axes by a single ion anisotropy term. The model is defined by the spin Hamiltonian:

$$\mathcal{H} = -J\sum_{i,j}\vec{S}_i \cdot \vec{S}_j - D_a\sum_i(\vec{S}_i \cdot \vec{d}_i)^2 \qquad \text{[III.10]}$$

where $\vec{S}_i$ are the classical vectors of unit length and $\vec{d}_i$ are the four directions <111>. There are involved two parameters: the strength of the exchange ferromagnetic interaction J and

that of the uniaxial anisotropy along the <111> axes D_a. The model describes the transition from an Heisenberg ferromagnetic behaviour, characterized by $D_a / J \to 0$, to a spin ice behaviour, when $D_a / J \to \infty$.

Figure 14 shows the temperature dependence of the magnetization per spin as obtained from Monte Carlo simulations [Champion'02]. According to this model, for finite values of D_a / J a transition to a long range ordered magnetic state is predicted and it disappears in the spin ice limit $D_a / J \to \infty$. The characteristics of this ordered state are: (i) the ground state is a $\vec{k}$ = 0 four sublattice structure; (ii) the local order within one tetrahedron is close to that of a spin ice, "two in, two out", with a canting of the spins towards the [001] axis in the present case, as indicated in Figure 14 right; (iii) the magnetic transition is of second order for $D_a = 0$ but changes clearly to first order for large D_a / J value.

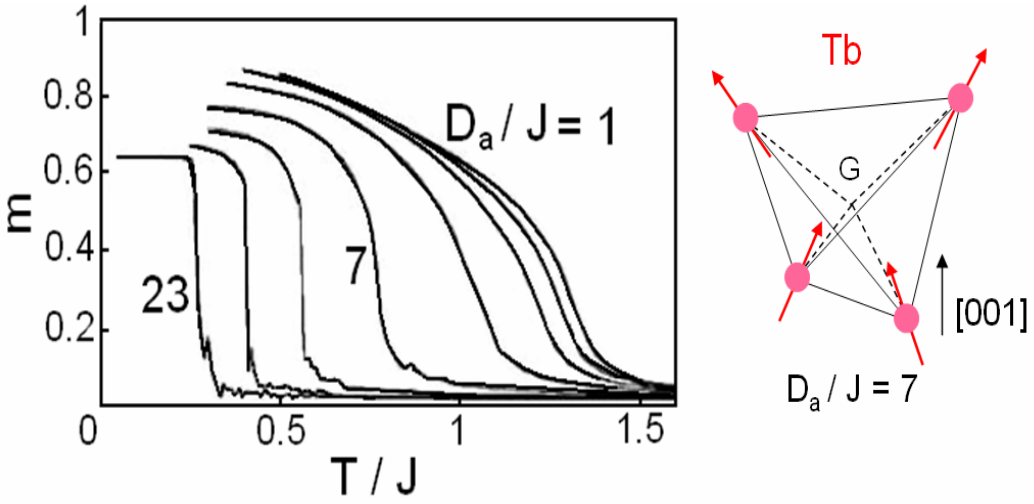

Figure 14. Magnetization per spin versus temperature (left) for different values of D_a / J. From left to the right $D_a / J \cong$ 22.9, 15.5, 10.5, 7, 4.8, 3.2, 2.1, 1. Spin structure (right) corresponding to D_a / J = 7. Results are presented in Ref. [Champion'02].

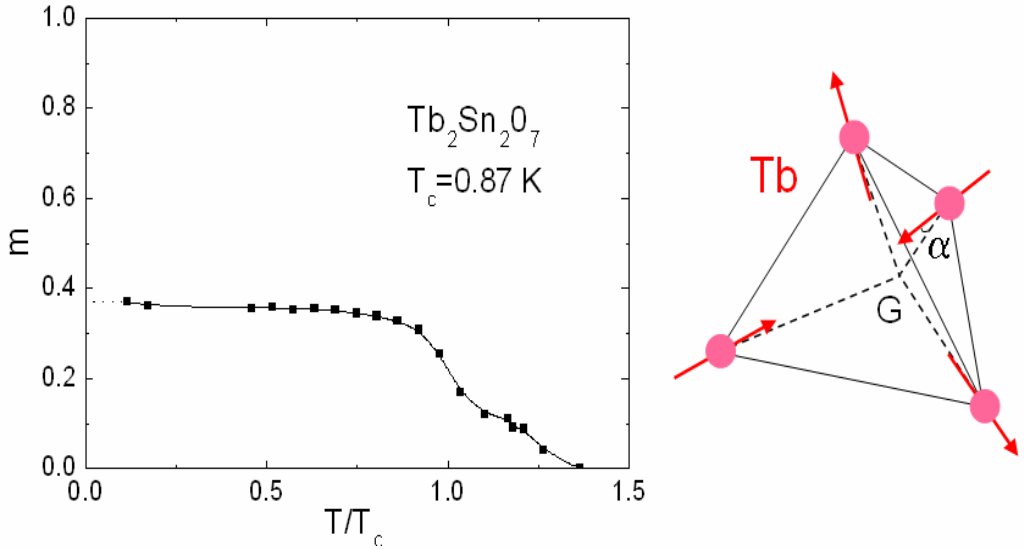

Figure 15. $Tb_2Sn_2O_7$: spontaneous magnetization versus temperature (left) and the low temperature magnetic structure (right).

If comparing the magnetic order obtained in the ferromagnetic finite anisotropy model, one may see that all its characteristics are found in our experimental data on $Tb_2Sn_2O_7$ (Figure 15).

Still, there is a question that arises: how could we justify a ferromagnetic exchange interaction, like in the finite anisotropy model, taking into account that in $Tb_2Sn_2O_7$ $\theta_{CW} \simeq -12$ K < 0 indicates the presence of antiferromagnetic interactions? Here interferers the second model: the dipolar spin ice model. We recall the unusual change with temperature of the short range correlations of $Tb_2Sn_2O_7$ from antiferromagnetic to ferromagnetic, which takes place just above the transition as clearly indicated by neutron diffraction measurements. This suggests a transition that is driven by an effective ferromagnetic interaction. Furthermore the magnetic ground state of the system is a non-collinear ferromagnetic one. These characteristics result naturally if one considers the combined role of exchange and dipolar interactions, as in dipolar spin ice model [Bramwell'01a, Bramwell'01b, denHertog'00, Melko'04], and defines an effective nearest neighbour ferromagnetic interaction: $J_{nn}^{eff} = J_{nn} + D_{nn} > 0$, where $J_{nn} = J/3$ and $D_{nn} = 5D/3$ are the exchange and dipolar energy scales, respectively.

Consequently, we may claim that the behaviour of $Tb_2Sn_2O_7$ is best described by an "effective ferromagnetic exchange and finite anisotropy" model, described by the Hamiltonian [III.10], having J replaced by $J^{eff} = 3J_{nn}^{eff}$, with $J_{nn}^{eff} = J_{nn} + D_{nn} > 0$.

However there is an important difference if comparing the finite anisotropy model with the real system: the deviations from the spin ice structure are different. In the model, the spins are uniformly canted towards the ferromagnetic direction. When decreasing D_a / J, the ground state magnetization relative to the local magnetic moment increases from $1/\sqrt{3}$, which is the average magnetization of a tetrahedron in the spin ice case, to 1, value which corresponds to simple ferromagnetic case. Per contra, in $Tb_2Sn_2O_7$ the deviations of the Tb^{3+} magnetic moments from the local <111> anisotropy axes, meaning the deviation from the spin ice arrangement, actually reduce the magnetization to about 0.37 in relative units (Figure 15). Consequently, the deviation of the magnetic moments in $Tb_2Sn_2O_7$ acts in an opposite way to that predicted by the finite anisotropy ferromagnetic model.

One could therefore think that another contribution to the energy is necessary. Besides this "effective ferromagnetic finite anisotropy model", recent discussions [Canals'06] shed into light another interesting idea: a Heisenberg model with antisymmetric Dzyaloshinsky-Moria interactions [Dzyaloshinski'58, Moria'60, Morya'60]. This interaction is compatible with pyrochlore lattice geometry. A first try [Canals'06] was done using a Hamiltonian with four terms: ferromagnetic first and third neighbour exchange interaction, finite locale anisotropy and antisymmetric interactions. This model seems to work, at T = 0 K a $\vec{k} = 0$ order state is predicted, with a canting angle close to 13° (as we obtained pour $Tb_2Sn_2O_7$) and a variation of magnetization in the right way (contrary to the ferromagnetic finite anisotropy model presented above). Still, there is a question that remains: how could one justify the existence of an antisymmetric Dzyaloshinsky-Moria interaction in a rare earth compound, since this type of interaction is generally negligible in the rare earth compounds?

- *comparison between $Tb_2Sn_2O_7$ and $Tb_2Ti_2O_7$*

We now focus on the difference between $Tb_2Ti_2O_7$, which remains spin liquid till to the lowest measured temperature, and $Tb_2Sn_2O_7$, which from a spin liquid becomes an

"ordered spin ice" at low temperature. We try to explain this difference by analysing the first neighbour exchange J_{nn}, the dipolar D_{nn} and crystal field D_a energies and hence the resulting energetic balance for the two compounds.

The estimation of the exchange constant is usually achieved through measurements of the paramagnetic Curie-Weiss temperature θ_{CW}. The usual method to determine θ_{CW} is to measure the inverse magnetic susceptibility and to fit its thermal linear variation (if any) to the Curie-Weiss law. However, in the Tb pyrochlores with a very large overall crystal field (CF) splitting (about 800 K for $Tb_2Ti_2O_7$ and 600 K for $Tb_2Sn_2O_7$) the Curie-Weiss law does not hold in the usual temperature range of measurements, *i.e.* below 300-400 K. A first approximation is to write the paramagnetic constant as the sum of two contributions, one due to the exchange/dipolar interactions and the other due to the crystal field splitting: $\theta_{CW} = \theta_{CW}^{exchange} + \theta_{CW}^{CF}$. Inelastic neutron scattering measurements and crystal field calculations allow the determination of the crystal field contribution θ_{CW}^{CF} and hence of $\theta_{CW}^{exchange}$ and one may determine the associated exchange constant $\mathcal{J}$ according to: $\theta_{CW}^{exchange} = \mathcal{J} z J(J+1)/3$, with $J = 6$ and $z = 6$ nearest neighbours for Tb^{3+} ion. Then the nearest neighbour exchange constant J_{nn} may be deduced from $\mathcal{J}$ according to: $J_{nn} = \frac{1}{3}\,\mathcal{J}\frac{\mu^2}{g_J^2\mu_B^2}$. μ is the ground state magnetic moment and $g_J = 3/2$ for Tb^{3+} [Mirebeau'07a].

Such a calculus was first done for $Tb_2Ti_2O_7$, having a high temperature paramagnetic Curie-Weiss temperature $\theta_{CW} = -19$ K [Gardner'99]. Ref. [Gingras'00] proposed initially a value of -13 K but then it was revised to $\theta_{CW}^{exchange} = -14$ K [Enjalran'04b, Kao'03, Molavian'07] and the corresponding nearest neighbour exchange is $\mathcal{J} = -0.167$ K. Starting from this value and supposing $|\pm 4\rangle$ as ground state: $J_{nn} = \frac{1}{3}\,\mathcal{J}4^2 = -0.88$ K [Enjalran'04a, Gingras'01]. As for the dipolar constant, the same research group gives $D_{nn} = 0.8$ K, considering a ground state magnetic moment of 5.1 μ_B [Enjalran'04a, Gingras'01, Gingras'00]. According to these values $J_{nn}^{eff} = J_{nn} + D_{nn} = -0.08$ K < 0 and $Tb_2Ti_2O_7$ would have an effective antiferromagnetic exchange interaction.

Without determining the values of J_{nn} and D_{nn} for $Tb_2Sn_2O_7$ and taking into account only that it is well described by the "effective ferromagnetic exchange and finite anisotropy" model, as we stated above, it would appear that there is an significant difference between the two compounds: for $Tb_2Ti_2O_7$ $J_{nn}^{eff} < 0$, while for $Tb_2Sn_2O_7$ $J_{nn}^{eff} > 0$. One may think that this could explain why $Tb_2Sn_2O_7$ orders and $Tb_2Ti_2O_7$ does not.

However, recent inelastic scattering measurements and crystal field analysis on both $Tb_2Ti_2O_7$ and $Tb_2Sn_2O_7$ shed new light on the differences between the two compounds [Mirebeau'07a]. According to Ref. [Mirebeau'07a], $\theta_{CW}^{exchange} = -7$ K and -6.3 K for $Tb_2Ti_2O_7$ and $Tb_2Sn_2O_7$, respectively. As one may see for $Tb_2Ti_2O_7$ the contribution to the paramagnetic Curie-Weiss temperature of the exchange interactions is about half of the value initially reported (of -14 K). The corresponding exchange integrals are $\mathcal{J} = -0.083$ K for $Tb_2Ti_2O_7$ and $\mathcal{J} = -0.075$ K for $Tb_2Sn_2O_7$.

Table II gives the new values of the nearest neighbour exchange and dipolar constants as reported in Ref. [Mirebeau'07a]. The dipolar constants are determined starting from that of

$Tb_2Ti_2O_7$ $D_{nn} = 0.8$ K [Gingras'01] and assuming that $D_{nn} \sim \mu^2 / a^3$, with μ the ground state magnetic moment and a the lattice parameter (see Chapter I, section I.2.3). Using $\mu = 5.1$ μ_B [Gingras'00, Mirebeau'07a] and $\mu = 5.95$ μ_B [Mirebeau'07a] for $Tb_2Ti_2O_7$ and $Tb_2Sn_2O_7$, respectively, we obtain: $D_{nn}(Ti) / D_{nn}(Sn) = 0.8$ (with $a(Tb_2Ti_2O_7) = 10.149$ Å [Mirebeau'02] and $a(Tb_2Sn_2O_7) = 10.426$ Å) and hence $D_{nn} = 1$ K for $Tb_2Sn_2O_7$.

	$Tb_2Ti_2O_7$	**$Tb_2Sn_2O_7$**	**$Dy_2Ti_2O_7$**	**$Ho_2Ti_2O_7$**
J_{nn}	- 0.32 K [Mirebeau'07a]	-0.39 K [Mirebeau'07a]	-1.24 K [Gingras'01]	-0.52 [Gingras'01]
D_{nn}	0.8 K [Gingras'01]	1 K [Mirebeau'07a]	2.35 K [Gingras'01]	2.35 K [Gingras'01]
$J_{nn}^{eff} = J_{nn} + D_{nn}$	0.48 K	0.61 K	1.11 K	1.83 K
J_{nn} / D_{nn}	-0.4	-0.39	-0.52	-0.22

Table II. New values of the first neighbour exchange and dipolar energies for $Tb_2Ti_2O_7$ and $Tb_2Sn_2O_7$ as reported in Ref. [Mirebeau'07a]. For comparison the corresponding values for the spin ices $Dy_2Ti_2O_7$ and $Ho_2Ti_2O_7$ are also given [Gingras'01].

As one may see, both $Tb_2Ti_2O_7$ and $Tb_2Sn_2O_7$ have now an effective ferromagnetic exchange interaction ($J_{nn}^{eff} > 0$), of comparable order of magnitude, and therefore their different experimental behaviour cannot be understood within the framework of the dipolar spin ice model. In the phase diagram from Ref. [denHertog'00] (see Chapter I, section I.2.3) both $Tb_2Ti_2O_7$ and $Tb_2Sn_2O_7$ are situated in the spin ice region ($J_{nn} / D_{nn} > -0.91$), but closer to the critical value in comparison to the canonical spin ices $Dy_2Ti_2O_7$ and $Ho_2Ti_2O_7$. For comparison $Dy_2Ti_2O_7$ and $Ho_2Ti_2O_7$ exchange and dipolar constants are also given in Table II.

The anisotropy for the two compounds may also be roughly determined if supposing only the uniaxial anisotropy term $D_a J_z^2$. $Tb_2Ti_2O_7$ has a $|\pm 4\rangle$ ground state and $|\pm 5\rangle$ as first excited state [Gingras'00, Kao'03, Mirebeau'07a], while $Tb_2Sn_2O_7$ has a $|\pm 5\rangle$ ground state and $|\pm 4\rangle$ as first excited state [Mirebeau'07a]. Then the gap between the ground state level and the first excited one may be expressed as $D_a = \Delta / |4^2 - 5^2|$, with the energy gap $\Delta = 18$ K for $Tb_2Ti_2O_7$ [Gingras'00, Mirebeau'07a] and $D_a = \Delta / |5^2 - 4^2|$, with $\Delta = 15$ K for $Tb_2Sn_2O_7$ [Mirebeau'07a] and gives $D_a(Tb_2Ti_2O_7) = 2$ K and $D_a(Tb_2Sn_2O_7) = 1.66$ K. The values of D_a change when changing the hypothesis on the ground state. Since we consider only the uniaxial anisotropy term $D_a J_z^2$, neglecting the others, maybe it is more realistic to consider for both compounds $|\pm 6\rangle$ as the ground state and $|\pm 5\rangle$ as first excited level. Within this hypothesis $D_a = \Delta / |6^2 - 5^2|$. With the same Δ as given above we obtain $D_a(Tb_2Ti_2O_7) = 1.63$ K and $D_a(Tb_2Sn_2O_7) = 1.36$ K. They have also comparable orders of magnitude and seem not to be able to modify the energy balance so that to explain the difference between the two compounds.

III.5.2. Magnetic fluctuations: μSR

The neutron diffraction allowed the study of the magnetic order. Above 1.3 K and to at least 50 K, the diffuse magnetic scattering corresponds to the short range order. $Tb_2Sn_2O_7$ has a spin liquid behaviour, where the magnetic correlated spins are fluctuating. Below 1.3 K, Bragg peaks appear and increase when decreasing temperature: the system orders at long range. The comparison between the values of the ordered magnetic moment clearly shows that: m = 4.5(3) μ_B (specific heat measurements) << M = 5.9(1) μ_B (neutron diffraction). Within the model of Ref. [Bertin'01], we explain this reduction by the presence of magnetic fluctuations. We show, in an indirect manner, that the Bragg peaks are not static: the ordered magnetic moments are fluctuating till to the lowest measured temperature.

This study attracted great deal of interest. Recently, in Ref. [Bert'06, DalmasdeRéotier'06], the dynamical nature of the ground state of $Tb_2Sn_2O_7$ was studied, in a direct manner this time, by μSR.

In Ref. [Bert'06], the time dependence of the muon spin depolarisation function was recorded from room temperature down to 30 mK in a small longitudinal field H_{LF} = 50 G. The inset of Figure 16 shows few relaxation curves below and above T_C= 0.87 K. The function used for fit is a stretched exponential:

$$P(t) = \exp(-\lambda t)^{\beta} \qquad \text{[III.11]}$$

where the exponent β is close to 1 in the whole temperature range. λ is the muon spin relaxation rate, which in the fast fluctuation limit and for a single time relaxation process is expressed as:

$$\lambda = \frac{2\gamma_\mu^2 H_\mu^2 \nu}{\nu^2 + \gamma_\mu^2 H_{LF}^2} \qquad \text{[III.12]}$$

with H_μ the magnitude of the local fluctuating field seen by the muon, ν the spin fluctuation rate and γ_μ the muon gyromagnetic ratio.

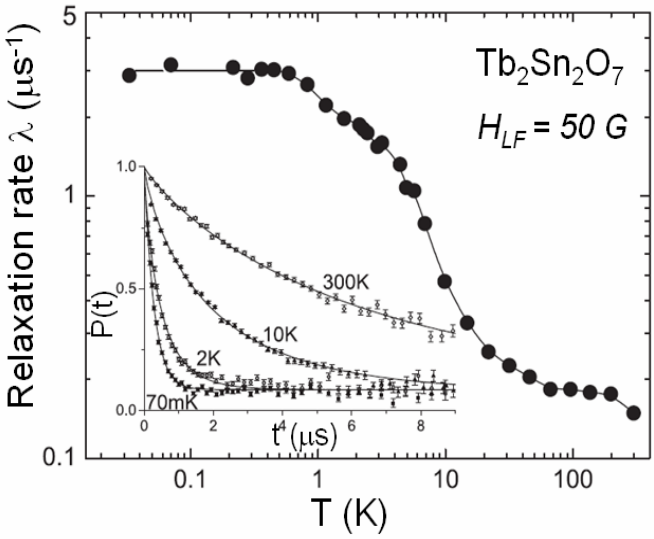

Figure 16. $Tb_2Sn_2O_7$: temperature dependence of the muon relaxation rate λ. In inset the corresponding muon spin depolarisation function $P(t)$ for several temperatures below and above T_C, in a small longitudinal field H_{LF}=50 G. Results are from Ref. [Bert'06].

As seen in Figure 16, at high temperatures the muon relaxation rate λ is almost temperature independent, as expected from paramagnetic fluctuations. Then in the interval 1 – 10 K it steeply increases indicating a strong slowing down of the spin fluctuations when approaching T_C. Below T_C and down to the lowest measured temperature the muon relaxation rate saturates at a constant value. Very interesting results are obtained from the depolarisation function $P(t)$ (see Figure 16 inset). First, there is no sign indicating a static magnetic ground state, meaning no long time tail $P(t)\,(t \to \infty, T \to 0)$ = 1/3. Secondly, there is no sign of long range order, meaning no oscillations of the polarisation due to a well defined internal field.

In order to determine the nature, static or dynamic, of the muon relaxation at low temperature, the magnetic field dependence $P(H_{LF},t)$ was analysed. Supposing that the relaxation is related to a static local field H_μ^s at the muon site or, in a more disordered scenario, that it is related to a distribution of static fields of width H_μ^s, H_μ^s could be approximated to λ/γ_μ. According to Ref. [Blundell'99], for an applied field satisfying the condition $H_{LF} \geq 5H_\mu^s$ the full muon polarisation should be restored. Or, as indicated in Ref. [Bert'06], the relaxation is still strong under applied fields which largely satisfy this condition. Consequently, the dynamical nature of the relaxation muon polarisation was stated. The field dependence $\lambda(H_{LF})$ is given by equation [III.12]. The fit of the experimental data (considering just high fields and long time relaxation) gives the local field on the muon site $H_\mu \simeq 200\,\mathrm{G}$ and the spin fluctuation rate ν = 0.2 GHz, corresponding to a time scale of order of 10^{-8} s.

In Ref. [DalmasdeRéotier'06] there is reported the same behaviour of the muon spin polarization function in zero applied field. Fits of experimental data with function [III.11], gave a relaxation rate with the same characteristics as in [Bert'06]. However, there is a difference that concerns the fluctuation time scale. Ref. [DalmasdeRéotier'06] reports that the dynamics in $Tb_2Sn_2O_7$ is characterized by a time scale of ~ 10^{-10} s, using the relation $\lambda = \gamma_\mu^2 H_\mu^2/\nu$. The difference comes from the intensity of the local field: referring to the spontaneous fields measured in $Gd_2Ti_2O_7$ and $Gd_2Sn_2O_7$, H_μ is estimated at 2000 G.

The absence of the oscillations of the muon spin polarisation, meaning no long range order, is quite intriguing, taking into account that neutron diffraction shows the presence of Bragg peaks. The correlation length obtained from neutron diffraction is about 190 Å and it is quite large compared to the length scale set by the dipolar coupling of the muon. The muon should sense therefore an internal field and an oscillation of polarization should be seen. The explanation given in Ref. [Bert'06] takes into account two aspects. First that the absence of oscillations means zero average field at the muon site, which supports the scenario: if at a given time the field at the muon spin is H_μ, then it has to fully reverse to $-H_\mu$ on the time scale $1/\nu$. For fast fluctuations $\nu \geq \gamma_\mu H_\mu$, an exponential decay of $P(t)$ is obtained. Secondly, they recall that the ordered spin ice state is six fold degenerate, meaning six possibilities of arranging the spins in the configuration "two in, two out" or equivalently the resulting magnetic moment for one tetrahedron may be parallel with one of the six (100) type directions (the degeneracy for one tetrahedron corresponds to the degeneracy of the magnetic domains mean orientation). Consequently, in the proposed scenario the ferromagnetic transition seen by neutron diffraction corresponds to the freezing of spin correlations on a large but finite length scale L_C, meaning long range order. This order has a dynamical

character in the sense that the domains of well ordered spins fluctuate between the six degenerate configurations allowed in the "ordered spin ice" structure.

Considering the results reported by the two μSR studies, a question arises: what is the mechanism which allows that domains of ~ 190 Å change their orientation with such high frequencies of 10^{-8}-10^{-10} s? A first mechanism would be a superparamagnetic relaxation, but this is very unlikely for such frequencies. A second one would be a change of orientation via a domain wall motion. This is a more realistic scenario, since there have already been observed such effects, with frequencies of comparable order of magnitude but under pulsed applied fields and not spontaneously [Bert'05]. Farther experiments [Bert'06] show how the longitudinal applied field breaks the symmetry: the field favours one of the six degenerate orientations and oscillations are restored. Frozen correlations are also evidenced by the presence of a field history dependence when comparing the filed cooled and zero field cooled muon relaxation below ~T_C.

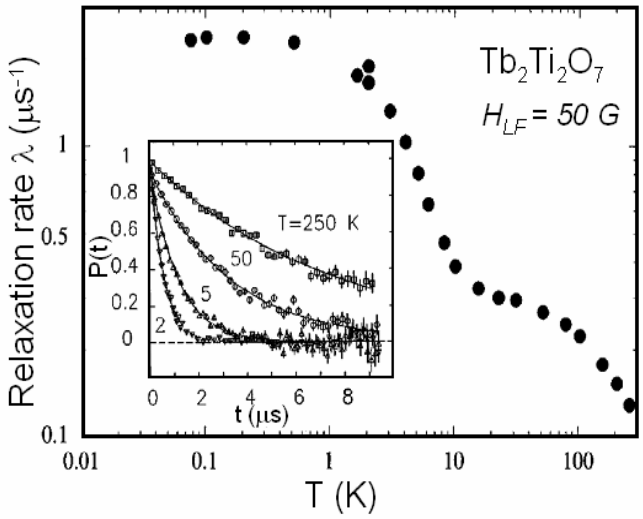

Figure 17. $Tb_2Ti_2O_7$: temperature dependence of muon relaxation rate λ. In inset: muon spin depolarisation function $P(t)$ for several temperatures in a small longitudinal field H_{LF}=50 G. Results are from Ref. [Gardner'99].

Similar results concerning the spin dynamics were reported in $Tb_2Ti_2O_7$ (see Ref. [Gardner'99]). As one may see in Figure 17, in low applied longitudinal field (H_{LF} = 50 G) and at all temperatures, the decay of muon polarisation is an exponential one, suggesting fluctuating internal fields. As for $Tb_2Sn_2O_7$, the relaxation rate λ is temperature independent at high temperature, it then increases and finally at low temperature it saturates at a finite value. The corresponding low temperature fluctuation rate is of 40 GHz, corresponding to a time scale of 10^{-10} s. The comparison of these two systems is very interesting: both show very similar behaviour of the fluctuation rate in μSR, but $Tb_2Sn_2O_7$ orders, while $Tb_2Ti_2O_7$ does not.

III.6. Conclusions

In this chapter we studied the structural and magnetic properties of the geometrically frustrated pyrochlore $Tb_2Sn_2O_7$.

At high temperature $Tb_2Sn_2O_7$ is a spin liquid, characterized by antiferromagnetic short range correlations. However low temperature neutron diffraction shows that around 2 K

ferromagnetic short range correlations start to appear and below 1.3 K there is a "two step transition" to a non-collinear ordered magnetic state. This transition is confirmed by magnetic susceptibility and coincides with a peak in the specific heat. The main characteristics of the magnetic structure are: (i) it is a $\vec{k}=0$ order; (ii) the local order is close to that of a spin ice, "two spins in, two spins out"; (iii) there is a ferromagnetic component, which represents 37 % of the ordered magnetic moment which orders in magnetic domains of ~ 190 Å and oriented along <100> axes. We called this original structure with both ferromagnetic and antiferromagnetic character an "ordered spin ice".

We then compared the value of the magnetic moment as obtained from neutron diffraction and specific heat analysis. The lower Tb^{3+} magnetic moment estimated from specific heat shows that the hyperfine levels are out of equilibrium and evidences the presence of slow magnetic fluctuations of correlated spins. These unconventional fluctuations are reminiscent of the spin liquid in the ordered phase. Their presence has been recently confirmed by μSR experiments, although it is no clear yet how magnetic domains having such a large size are able to fluctuate so rapidly.

The $Tb_2Sn_2O_7$ magnetic ground state obtained experimentally was compared to theoretical models existing at the time being. The best approximation of the real system is given by an "effective ferromagnetic exchange and finite anisotropy" model, where the effective exchange interaction is given by the sum of first neighbour exchange and dipolar interactions. Finally, we compare the first neighbour exchange, dipolar and crystal field energies, *i.e.* the energetic balance for $Tb_2Sn_2O_7$ and $Tb_2Ti_2O_7$ and discuss the differences between the two compounds.

III.7. Perspectives

Of course, there still remain open questions. At the end of this chapter we would like to mention several studies on $Tb_2Sn_2O_7$, already started or planned for the immediate future, which could give the answer to these questions. First, we mention the crystal field study of $Tb_2Sn_2O_7$ by inelastic neutron scattering, which allows one to determine the origin of the Tb^{3+} finite anisotropy. This analysis, performed in parallel for $Tb_2Ti_2O_7$, could exhibit more subtle differences between the two geometrically frustrated systems. Secondly, we mention a study by inelastic neutron scattering of the spin fluctuations, which persist in the "ordered spin ice" state. We saw that under the effect of the chemical pressure we modified the energy balance and passed from a spin liquid system ($Tb_2Ti_2O_7$) to a ferromagnetic "ordered spin ice" ($Tb_2Sn_2O_7$). Therefore, we mention finally a neutron diffraction study that could give the answer to a natural question: would $Tb_2Sn_2O_7$ become a spin liquid under the effect of the applied pressure?

Chapitre IV.

$(Tb_{1-x}La_x)_2Mo_2O_7$, x=0-0.2: une "glace de spin ordonnée" induite par la substitution Tb / La

A partir d'un système comprenant un seul ion magnétique Tb^{3+} (voir $Tb_2Sn_2O_7$, Chapitre III), avec un seul réseau frustré et où les propriétés magnétiques sont déterminées seulement par les ions Tb^{3+}, nous considérons maintenant des systèmes ayant deux types d'ions magnétiques. C'est les cas des pyrochlores de molybdène $R_2Mo_2O_7$, où les ions R^{3+} (terre rare ou Y) et Mo^{4+} occupent tous deux des réseaux géométriquement frustrés de tétraèdres jointifs par les sommets. Ces composés ont attiré l'attention depuis la découverte d'une transition verre de spin isolant (SGI) – ferromagnétique métal (FM), pilotée par le rayon ionique moyen de la terre rare R_i [Katsufuji'00, Moritomo'01]. Les composés de faible rayon ionique $R_i < R_{ic} = 1.047$ Å (R=Y, Dy, Tb) sont des SGI, ceux avec $R_i > R_{ic}$ (R=Gd, Sm, Nd) sont des FM.

Dans les séries $(RR')_2Mo_2O_7$, les mesures macroscopiques (aimantation et résistivité) ont montré une dépendance universelle de la température de transition en fonction de R_i, la même pour toutes les combinaisons (RR'), suggérant que les interactions Mo-Mo contrôlent la formation de l'état verre de spin ou ferromagnétique. Jusqu'à cette étude, toutes les études microscopiques concernaient des composés de rayon loin du seuil de transition : $Y_2Mo_2O_7$ et $Tb_2Mo_2O_7$ ($R_i < R_{ic}$) [Booth'00, Gardner'99, Gaulin'92, Gingras'97, Greedan'91], dont le comportement verre de spin reste surprenant compte tenu de l'absence de désordre chimique, et $Nd_2Mo_2O_7$ ($R_i > R_{ic}$) [Taguchi'01, Yasui'01] qui présente un effet Hall anormal géant.

L'idée de ce travail est d'étudier l'évolution microscopique du magnétisme dans la région de transition. A partir du verre de spin $Tb_2Mo_2O_7$, la dilution par un atome non magnétique plus gros La^{3+} dilate le réseau, modifie les distances inter atomiques et par conséquent l'état fondamental du système.

Ce chapitre est consacré à l'analyse de l'influence de la substitution chimique Tb/La dans la série $(Tb_{1-x}La_x)_2Mo_2O_7$ avec x=0-0.2 et récemment 0.25. Nous étudions les propriétés structurales de la série, mesurées par diffraction de rayons X et de neutrons à pression ambiante et aussi les propriétés électriques pour x=0 et 0.2. Mais ce chapitre est surtout consacré à l'étude de l'ordre magnétique par des mesures de susceptibilité, diffraction de neutrons et rotation et relaxation de spin du muon (μSR). La diffraction de neutrons montre comment les corrélations magnétiques changent graduellement avec la dilution Tb/La. Les mesures de muons montrent l'évolution des champs internes statiques et de la dynamique des fluctuations des spins.

D'un point de vue structural, nous montrons que la dilution Tb/La dilate le réseau sans induire de transition de phase. Le paramètre de réseau varie de a=10.312 Å (x=0) à a=10.378 Å (x=0.2), ce qui monte qu'on a traversé le seuil de transition ($a_c \sim 10.33$ Å). En conséquence, les propriétés magnétiques sont fortement modifiées.

Les mesures de susceptibilité magnétiques montrent un comportement verre de spin pour x=0 et 0.05, avec une susceptibilité indépendante de l'histoire thermique au dessus de T_{SG}, mais avec des irréversibilités entre les courbes de l'échantillon refroidi en champ nul (ZFC) et sous champ (FC) au-dessus de T_{SG}. Pour x=0.1-0.25, une forte augmentation de l'aimantation est observée suggérant une transition vers un état ferromagnétique.

La diffraction de neutrons permet d'étudier les changements microscopiques du magnétisme, quand la concentration en La augmente de 0 à 0.2. Les composés x=0 et 0.05 ($a < a_c$) montrent des corrélations à courte portée, comme dans les verres de spin. Les corrélations Tb-Tb sont ferromagnétiques, alors que les corrélations Tb-Mo et Mo-Mo sont antiferromagnétiques. En revanche, les composés x=0.15 et x=0.2 ($a > a_c$) sont caractérisés par la coexistence entre un ordre à courte portée et un ordre à longue portée non colinéaire (pics de Bragg) dominant. Les caractéristiques principales de la structure magnétique ordonnée sont: (i) un vecteur de propagation $\vec{k}$=0 (les quatre tétraèdres Tb^{3+} de la maille cubique sont identiques, ainsi que les quatre tétraèdres Mo^{4+}); (ii) les moments magnétiques de Tb^{3+} s'orientent près de leurs axes d'anisotropie <111> comme pour une glace de spin; (iii) les moments de Mo^{4+} s'orientent près de l'axe [001] avec un petit angle de "tilt"; (iv) toutes les corrélations (Tb-Tb, Tb-Mo, Mo-Mo) sont ferromagnétiques ; (v) la composante ferromagnétique résultante s'oriente le long d'un axe [001]. Nous avons appelé ce type d'ordre "glace de spin ordonnée". Le composé x=0.1 situé dans la région de transition a un comportement intermédiaire : (i) un ordre mésoscopique (à l'échelle de ~ 55-70 Å) qui coexiste avec l'ordre à courte portée; (ii) les angles de tilt sont plus grands et les corrélations ont un caractère antiferromagnétique plus prononcé que dans les composés x=0.15 et 0.2.

L'expérience de muons apporte un nouvel éclairage sur l'ordre magnétique en sondant les fluctuations et le champ local statique en dessous de T_C. Pour x=0.2, une deuxième transition de nature dynamique a été observée à $T^* = 15(5)\,\mathrm{K} < T_C = 57(1)\,\mathrm{K}$. L'origine de cette deuxième transition sera discutée au Chapitre VI. Quand la concentration de La décroît, les deux transitions semblent se confondre.

Chapter IV.

$(Tb_{1-x}La_x)_2Mo_2O_7$, x=0-0.2: an "ordered spin ice" induced by Tb / La substitution

From a system having Tb^{3+} as unique magnetic ion (see $Tb_2Sn_2O_7$, Chapter III), with only one frustrated lattice and where the magnetic properties are determined only by the Tb^{3+} magnetism, we now consider systems with two magnetic ions. It is the case of the molybdenum pyrochlores $R_2Mo_2O_7$, where both R^{3+} (rare earth and Y) and Mo^{4+} ions occupy geometrically frustrated lattices of corner sharing tetrahedra. Molybdenum and rare earth ions are both magnetic. These compounds have attracted special interest since the discovery of a transition from a spin glass insulating (SGI) state to a ferromagnetic metallic (FM) one, which can be tuned by the rare earth average ionic radius R_i [Katsufuji'00, Moritomo'01]. The compounds having a small ionic radius $R_i < R_{ic} = 1.047$ Å (R=Y, Dy and Tb) are SGI, whereas those with $R_i > R_{ic}$ (R=Gd, Sm and Nd) are FM.

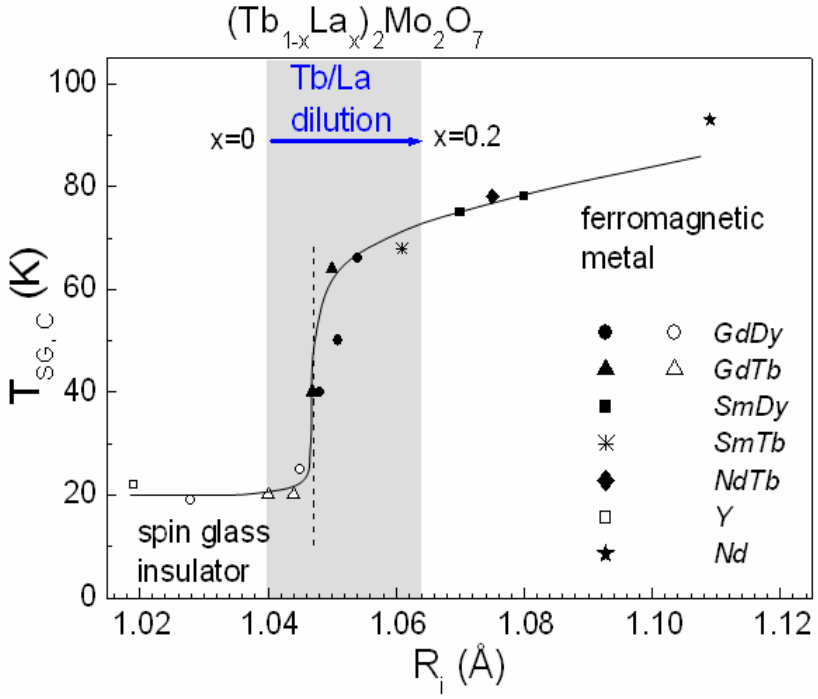

Figure 1. Phase diagram of $(RR')_2Mo_2O_7$ pyrochlores: transition temperature $T_{SG,C}$ against the average ionic radius R_i. The values are taken from Ref. [Gardner'99, Katsufuji'00, Moritomo'01]. The dotted line shows the SG-F phase boundary (R_{ic}=1.047 Å). The continuous line is a guide to the eyes. The grey region emphasizes the region of interest of our study.

The analysis of substituted series $(RR')_2Mo_2O_7$ shows a universal dependence of the transition temperature versus R_i (Figure 1), the same for all (RR') combinations, suggesting that the Mo-Mo interactions control the formation of a spin glass or a ferromagnetic state. Up to this study, all existing microscopic studies deal with compounds far from the threshold radius: $Y_2Mo_2O_7$ and $Tb_2Mo_2O_7$ ($R_i < R_{ic}$) [Booth'00, Gardner'99, Gaulin'92, Gingras'97, Greedan'91], where the SG behaviour is surprising with regards to their chemical order, and $Nd_2Mo_2O_7$ ($R_i > R_{ic}$) [Taguchi'01, Yasui'01], which shows a giant anomalous Hall effect.

The idea of this study is to investigate the microscopic evolution of magnetism throughout the threshold region. Staring from the spin glass $Tb_2Mo_2O_7$ the dilution by a bigger non-magnetic ion La^{3+} expands the lattice, modifies the interatomic distances and, consequently, the magnetic ground state of the system.

This chapter is dedicated to the analysis of the effect of Tb/La chemical substitution in $(Tb_{1-x}La_x)_2Mo_2O_7$ series, with x=0-0.2. We first study the structural properties for the whole series, measured by ambient pressure X ray and neutron diffraction and also the electrical properties for x=0 and 0.2, respectively. But mainly this chapter is dedicated to the investigation of the magnetic order, by means of magnetic susceptibility, neutron diffraction and Muon Spin Rotation and Relaxation (μSR). The neutron diffraction shows how the magnetic correlations gradually change with Tb^{3+} dilution with a non-magnetic ion La^{3+}. The μSR probes both statics (internal fields) and dynamics (spin fluctuations).

IV.1. Magnetic susceptibility measurements: ordering temperature

The magnetic susceptibility measurements were recorded using a SQUID (Superconducting Quantum Interference Device) magnetometer, at SPEC (Service de Physique de l'Etat Condensé), CEA-CNRS, CE-Saclay.

Figure 2 shows the field cooled (FC) and zero field cooled (ZFC) curves measured in a static field of 80 G for the whole series of samples (x=0-0.25). For $Tb_2Mo_2O_7$ the magnetic susceptibility is independent of sample cooling history above $T_{SG} \sim 22$ K, but there are irreversibilities between FC and ZFC curves below this temperature. Such a behaviour was already reported in Ref. [Ali'92, Greedan'91] with a slight different transition temperature of 25-28 K (see Chapter I, section I.3.1.). The real and imaginary part components of the ac susceptibility measurements show small peaks at the FC/ZFC splitting temperature [Ali'92]. These characteristics have been attributed to a spin glass like behaviour. We underline however the difference when comparing to a classical spin glass behaviour, where below T_{SG} the FC saturates and ZFC susceptibility decreases towards zero, as observed in $Y_2Mo_2O_7$ [Ali'92, Gaulin'98, Gingras'97] (see the inset of Figure 2a). This suggests the presence of a ferromagnetic component in the case of $Tb_2Mo_2O_7$, which is also present under lower applied fields (20 G as reported in [Greedan'91]). Similar characteristics are observed for x=0.05 sample, where the FC/ZFC splitting indicates a transition at $T_{SG} \sim 25$ K. For $x \geq 0.1$, a strong increase of magnetization is observed, suggesting a crossover towards ferromagnetism. For these compounds the transition temperature is defined as the inflection point of the FC curve. For x=0.1, 0.15, 0.2 and 0.25 samples we obtained the transition temperatures: $T_C \sim 51$, 61, 58 and 61 K, respectively. For comparison Figure 3a presents the FC and ZFC curves for x=0 and x=0.2 samples, showing the increase of both transition temperature and magnetization when doping with La^{3+}. Figure 3b summarizes the above results in a phase diagram: transition temperature versus La^{3+} concentration.

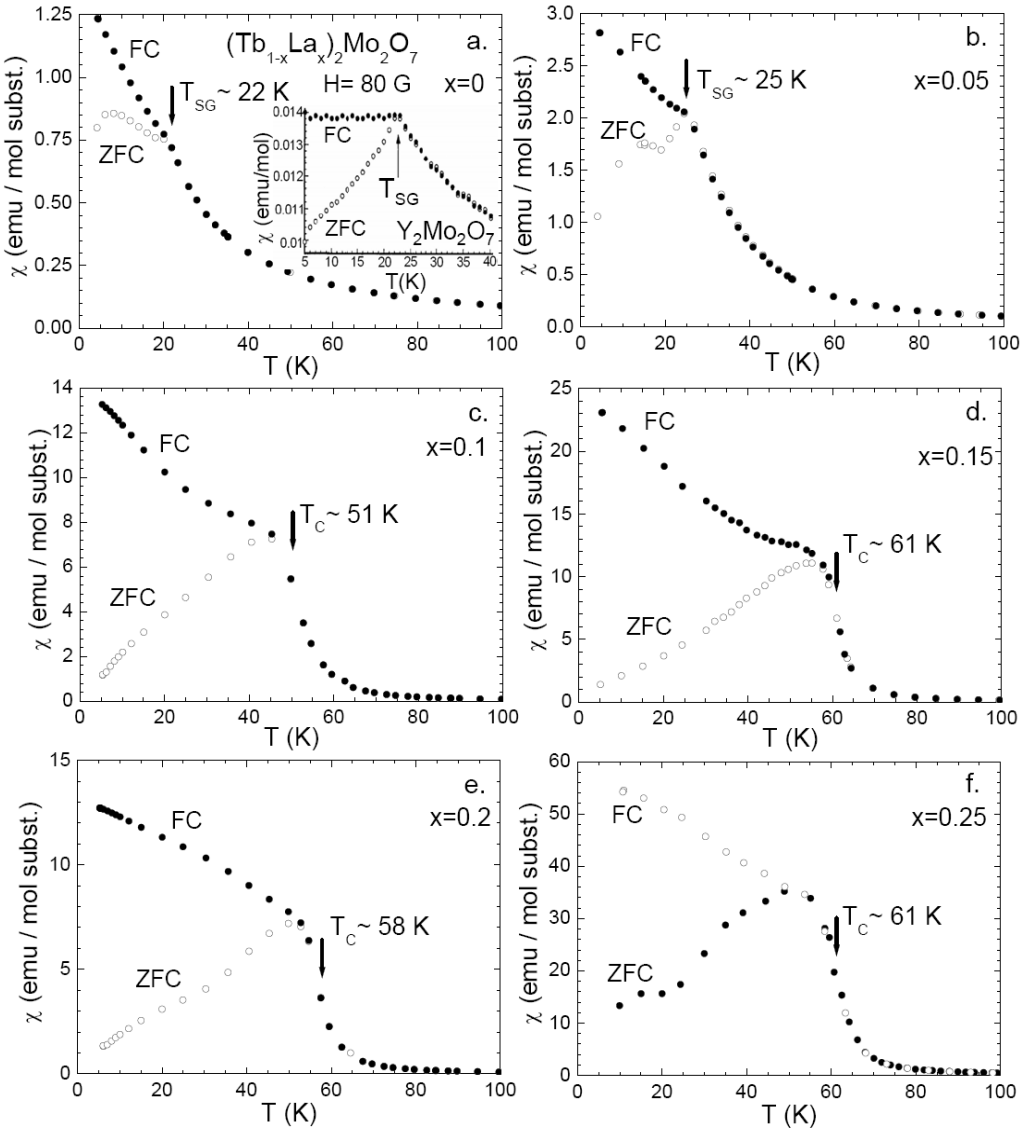

Figure 2. Magnetic susceptibility of $(Tb_{1-x}La_x)_2Mo_2O_7$, for x=0-0.25, measured in a static field of 80 G, in zero field cooled (ZFC) and field cooled (FC) processes .The temperatures of transition to a spin glass (T_{SG}) or to a ferromagnetic type order (T_C) are indicated . In inset of figure 2a: the magnetic susceptibility against temperature for $Y_2Mo_2O_7$ [Ali'92, Gaulin'98, Gingras'97], considered a canonical spin glass despite the absence of chemical disorder..

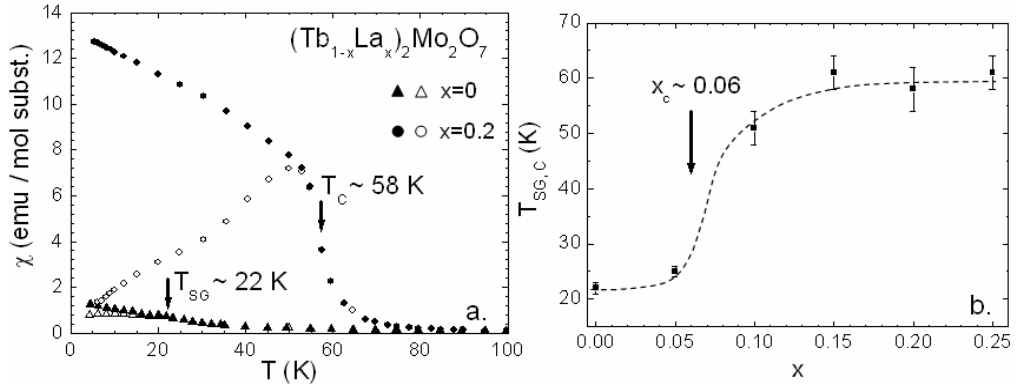

Figure 3. a. Comparison between the magnetic susceptibility of $(Tb_{1-x}La_x)_2Mo_2O_7$ for x=0 and 0.2; b. Phase diagram: transition temperature $T_{SG,C}$ against the La^{3+} concentration x. The dashed line is a guide to the eye.

IV.2. X ray and neutron diffraction: crystal structure

The ambient pressure crystal structure of powder samples $(Tb_{1-x}La_x)_2Mo_2O_7$ (x=0, 0.05, 0.1, 0.15 and 0.2) is determined by combining X ray and neutron diffraction measurements. The X ray patterns were measured using a Brüker D8 diffractometer (SPEC) (λ=1.5406 Å), while the neutron patterns were measured using the diffractometer G61 of the Laboratoire Léon Brillouin (LLB) (λ=4.741 Å).

Rietveld refinements of X ray and neutron diffraction patterns, performed with the crystallographic programs of the FULLPROFF suite [Rodríguez-Carvajal'93], show that Tb/La substitution does not induce a structural phase transition: all samples crystallize in the $Fd\bar{3}m$ cubic space group.

Few details concerning the crystallographic structure of $R_2Mo_2O_7$ pyrochlores and among them $Tb_2Mo_2O_7$ were given in Chapter I, section I.3.2. We recall that there are two parameters of interest: the lattice parameter a and the oxygen O1 position u.

The structural parameters derived from Rietveld analysis (lattice parameter a, oxygen position parameter u and also Mo-O1 bond length d and Mo-O1-Mo bond angles θ) for the whole $(Tb_{1-x}La_x)_2Mo_2O_7$ series are summarized in Table I. The lattice parameter was determined from the X ray diffraction analysis taking into account that the wavelength is precisely determined and also the higher resolution in comparison with that of G61 diffractometer (which is a high-intensity long wavelength diffractometer, used to study magnetic order and not a high-resolution one suitable for a crystal structure analysis). Per contra, the X ray diffraction is much less sensible to the presence of light atoms (like oxygen) and therefore the oxygen parameter u is determined from neutron diffraction analysis.

$(Tb_{1-x}La_x)Mo_2O_7$	R_i (Å)	a (Å)	u (units of a)	d (Mo-O1) (Å)	θ (Mo-O1-Mo)
x=0	1.040	10.3124(7)	0.3340(3)	2.0159	129.1
x=0.05	1.046	10.3313(1)	0.3330(3)	2.0178	129.7
x=0.1	1.052	10.3461(8)	0.3327(3)	2.0204	129.8
x=0.15	1.058	10.3621(8)	0.3321(3)	2.0228	130.1
x=0.2	1.064	10.3787(8)	0.3314(3)	2.0203	130.5

Table I. Structural parameters of $(Tb_{1-x}La_x)_2Mo_2O_7$, x=0-0.2: the cubic lattice parameter a (in Å), the positions u of oxygen O1 48f sites [u,1/8,1/8] (units of a), the distances Mo-O1 d (in Å) and the angle Mo-O1-Mo θ (in degrees). The mean ionic radius R_i are calculated starting from the values given for Tb^{3+} and La^{3+} ions in Ref. [Shannon'76] and using the relation: $R_i(x) = (1-x)R_i(Tb^{3+}) + xR_i(La^{3+})$.

Figure 4 shows the cell and oxygen position parameters variation with the mean rare earth ionic radius R_i. We clearly show that, as expected since La^{3+} ion is bigger than Tb^{3+}, a increases with R_i. The oxygen parameter u decreases with R_i. Our results are in good agreement with those reported for the series $R_2Mo_2O_7$, with R= Dy, Gd, Sm and Nd. The dashed line marks the critical threshold R_{ic}=1.047 Å. Taking into account the linear dependence $a = \alpha R_i + \beta$ (α, β fit parameters) between the lattice parameter a and the average ionic radius R_i as shown in Ref. [Katsufuji'00, Moritomo'01] for $(RR')_2Mo_2O_7$ series, we determined the corresponding critical lattice parameter $a_c \sim 10.33$ Å. We also show that by substitution of Tb by La, we cross the threshold region for a La concentration $x_c \sim 0.06$.

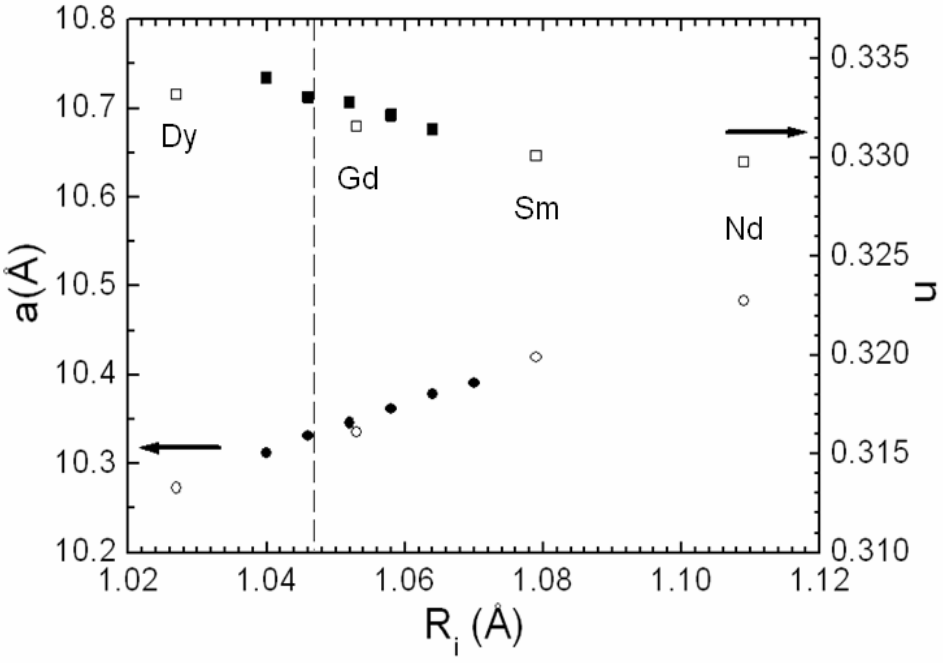

Figure 4. $(Tb_{1-x}La_x)_2Mo_2O_7$ with x=0-0.2 (filled symbols): lattice parameter a and the oxygen parameter u versus the mean ionic radius R_i (see Table I). For comparison $R_2Mo_2O_7$ (open symbols) , with R= Dy, Gd, Sm and Nd from Ref. [Katsufuji'00, Moritomo'01]. Vertical dashed line indicates the SG-F phase boundary (corresponds to critical value R_{ic}=1.047 Å [Katsufuji'00]).

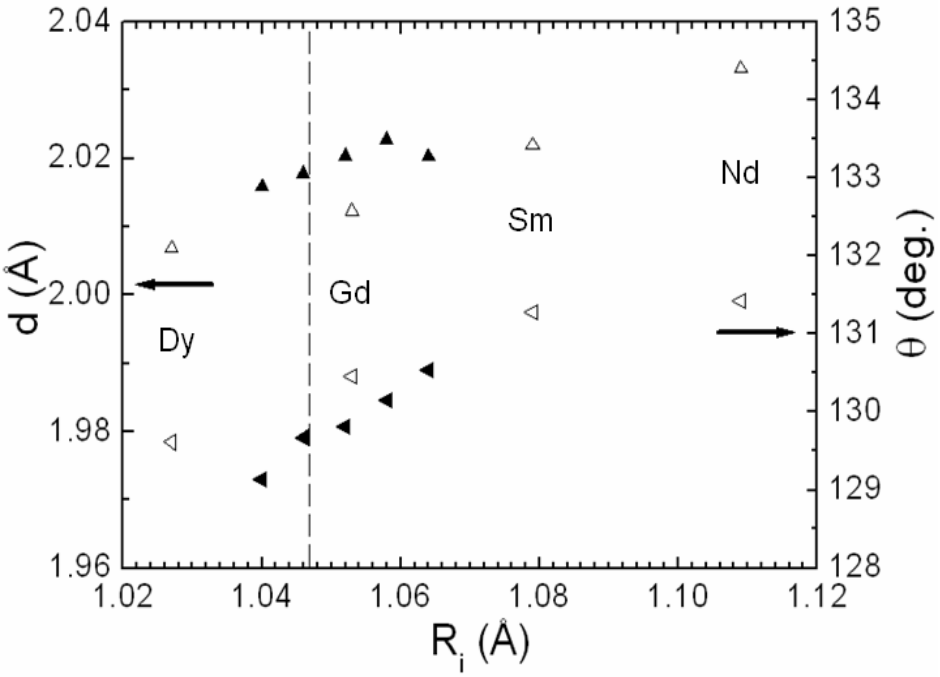

Figure 5. $(Tb_{1-x}La_x)_2Mo_2O_7$ with x=0-0.2 (filled symbols): Mo-O1 bond length d and Mo-O1-Mo bond angle θ against the average ion radius R_i (see Table I) . For comparison $R_2Mo_2O_7$, with R= Dy, Gd, Sm and Nd from Ref.[Katsufuji'00, Moritomo'01]. Vertical dashed line indicates the SG-F phase boundary (R_{ic}=1.047 Å [Katsufuji'00]).

Consequently, from the lattice structural point of view the x=0 and 0.05 samples are situated in the spin glass region of the phase diagram from Figure 1, while those with x≥0.1 are situated in the ferromagnetic region. *u* determines the Mo environment and

$u = 5/16 = 0.3125$ corresponds to an octahedral environment. We notice that for the whole series $(Tb_{1-x}La_x)_2Mo_2O_7$ x=0-0.2, $u > 0.3125$ showing that the octahedral environment is distorted, but this distortion diminishes when increasing La concentration. We also note that for the above series there is a small variation of u when increasing R_i of roughly 0.003 (in units of a) corresponding to a variation of only 1.4° of the superexchange angle θ. This result suggests that the important parameter is the lattice parameter a and not the oxygen position u (as already shown by the band structure model from section I.3.3).

We also calculated the Mo-O1 bond length d and the Mo-O1-Mo bond angle θ. As shown in Figure 5, the increase of R_i causes (i) the elongation of d, as well as (ii) the widening of θ, in agreement with results reported in Ref. [Moritomo'01] for the $R_2Mo_2O_7$ series (R= Dy, Gd, Sm and Nd).

IV.3. Neutron diffraction: magnetic structure

The ambient pressure powder neutron diffraction measurements on $(Tb_{1-x}La_x)_2Mo_2O_7$ were performed as follows: (i) for x=0-0.2, between 1.4 and 100 K, on the G61 diffractometer (LLB), which in the usual configuration has λ=4.741 Å and a limited scattering vector range with $q_{max} \sim 2.5$ Å^{-1}; (ii) for x=0.2, at 1.5 and 70 K, on the G41 diffractometer (LLB), having λ=2.426 Å and a wider scattering vector range $q_{max} \sim 4$ Å^{-1}; (iii) for x=0, down to 40 mK on the D1B diffractometer of the Institute Laüe Langevin (ILL), with λ=2.52 Å and $q_{max} \sim 3.3$ Å^{-1}. The magnetic intensity is obtained by subtracting a spectrum in the paramagnetic region (70 or 100 K). Then, in order to compare spectra obtained with different diffractometers and with different quantities of sample, we calibrated the subtracted spectra by multiplying it by a factor $F = 1/(IntI_{(222)} \cdot L)$, with $IntI_{(222)}$ the integrated intensity of the (222) nuclear peak (at 70 or 100 K) and $L = 1/(\sin\theta \cdot \sin 2\theta)$ the Lorentzian factor (see Chapter II).

Figure 6 shows the evolution of the magnetic neutron diffraction patterns for the series $(Tb_{1-x}La_x)_2Mo_2O_7$, with x=0, 0.05, 0.1, 0.15 and 0.2.

It is shown how the magnetic order changes when going through the critical threshold under the effect of Tb / La substitution. The x=0 and 0.05 samples, $a < a_c$ (Figure 6 a,b), are characterized by a diffuse magnetic scattering with maxima around q=1 and 2 Å^{-1}, corresponding to short range spin correlations. For x=0.1 sample, situated just above the threshold $a \sim a_c$ (Figure 6c), Lorentzian peaks start to grow at the position of the diffuse maxima revealing the onset of mesoscopic magnetic order. For x=0.15 and 0.2 samples, $a > a_c$ (Figure 6d,e), we clearly see magnetic Bragg peaks, that correspond to long range magnetic order. Additionally, we observe for all samples an intense small angle neutron scattering (SANS) for $q < 0.5$ Å^{-1}, which corresponds to the ferromagnetic correlations. The intensity of the SANS signal decreases, when x increases.

In the following we analyse in more details the magnetic correlations or/and the magnetic structure of three representative samples: the short range ordered $Tb_2Mo_2O_7$ ($a < a_c$), the long range ordered $(Tb_{0.8}La_{0.2})_2Mo_2O_7$ ($a > a_c$) and the mesoscopic range ordered $(Tb_{0.9}La_{0.1})_2Mo_2O_7$ (situated in the threshold region). Finally, we make a comparative study on the whole $(Tb_{1-x}La_x)_2Mo_2O_7$ series and discuss the effect of chemical substitution on the magnetic order.

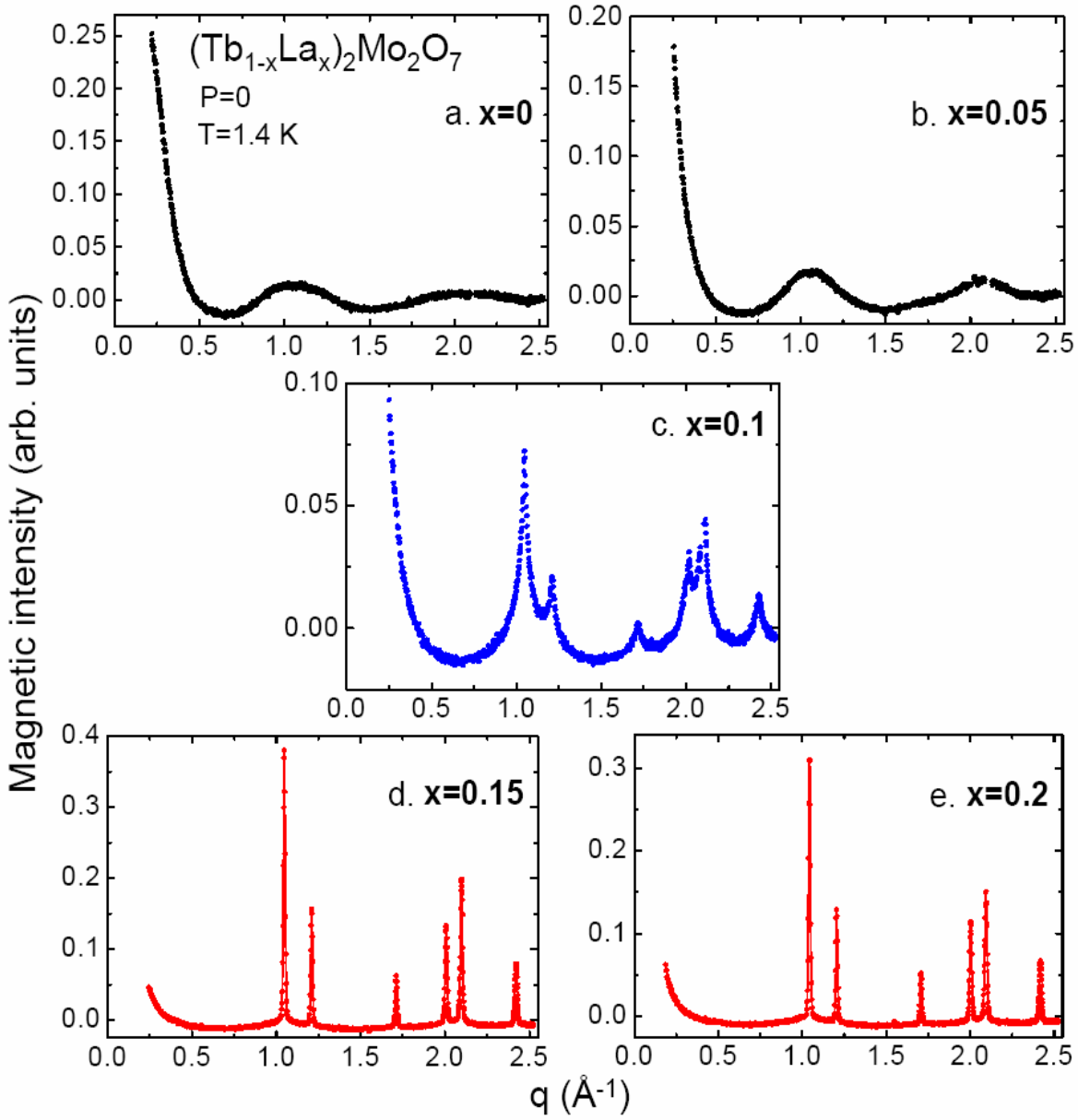

Figure 6 a-e. Magnetic intensity of $(Tb_{1-x}La_x)_2Mo_2O_7$ (x=0, 0.05, 0.1, 0.15 and 0.2) versus the scattering vector $q = 4\pi \sin\theta / \lambda$, at T= 1.4 K and ambient pressure. The incident neutron wavelength is λ=4.741 Å. A spectrum in the paramagnetic region (100 K) was subtracted.

IV.3.1. $Tb_2Mo_2O_7$: spin glass

We analyse the ambient pressure magnetic correlations in $Tb_2Mo_2O_7$ ($a \sim 10.312$ Å $< a_c \sim 10.33$ Å). This compound is considered a spin glass, with a spin glass transition at $T_{SG} \sim 22-27$ K (see Chapter I, section I.3.1.), despite the absence of chemical disorder. Besides the diffuse magnetic scattering observed for $q > 0.5$ Å^{-1}, already reported in Ref. [Gaulin'92, Greedan'91], we observed an intense SANS signal below this q value. It corresponds to the onset of ferromagnetic spin correlations. The temperature evolution of the magnetic correlations (Figure 7) clearly shows the increase of ferromagnetic correlations with decreasing temperature. By performing neutron diffraction measurements down to 40 mK (inset Figure 7), we show that the magnetic correlations saturate below 1.4 K. Their

observation down to 40 mK (0.002 T_{SG}) proves that the spin glass state is indeed the ground state of this compound.

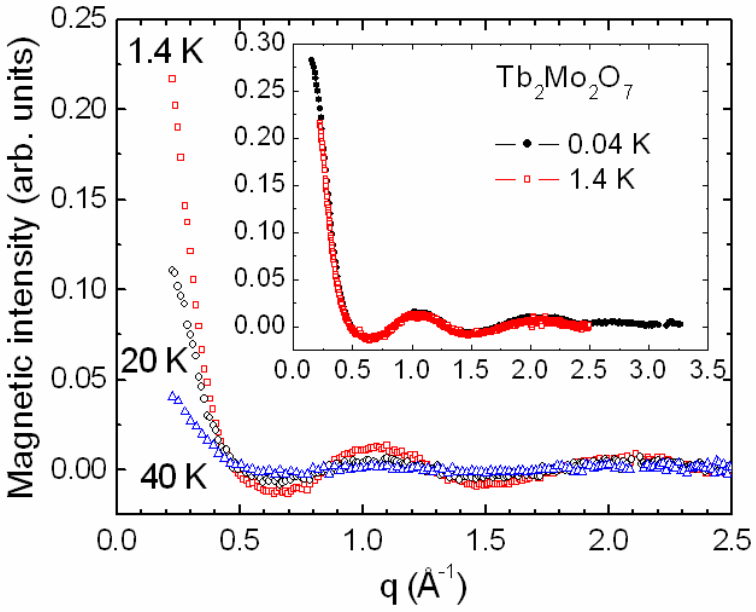

Figure 7. Magnetic intensity in $Tb_2Mo_2O_7$ against the scattering vector q for several temperatures: T= 1.4, 20 and 40 K (λ=4.741 Å) and for comparison T=0.04 K (λ=2.52 Å) in the inset. A pattern at 100 K was subtracted.

In the range q = 0.5-2.5 Å, we fitted the experimental data using a cross section for scattering due to the short range spin-spin correlations, first proposed for spin glasses in Ref. [Bertaut'67, Wiedenmann'81] and then applied to the pyrochlore system in Ref. [Greedan'90, Greedan'91]:

$$I(q) = N\left[\frac{1}{2}r_0\gamma_0 f_m(q)\right]^2 \cdot \frac{2}{3}\sum_{i=1}^{n} c_i\gamma_i \frac{\sin(qR_i)}{qR_i} \qquad \text{[IV.1]}$$

where $r_0\gamma_0/2$ is the scattering length per Bohr magneton and $f_m(q)$ is the magnetic form factor, assumed for simplicity to be the same for Tb^{3+} and Mo^{4+}. In equation [IV.1] we used the magnetic form factor of Tb^{3+}, calculated according to Ref. [Freeman'79]:

$$f_m(q) = -0.04 + 1.06\exp\left[-4.7(0.08q + 0.039)^2\right] \qquad \text{[IV.2]}$$

In [IV.1] the summation is over the coordination shells from a central atom and c_i and R_i are the number of neighbours and bond distances, respectively, known from the crystallographic data and shown in Table II.

i	c_i	R_i (Å)
1	6	3.646
2	6	5.156
3	12	6.315
4	12	7.292

Table II. Number of neighbours c_i and bond distances R_i for the first four coordination cells (n=4) as obtained from the crystal structure analysis.

It is the same SRO model used for $Tb_2Sn_2O_7$ (section III.3.2). The differences in the case of $Tb_2Mo_2O_7$: (i) there are two magnetic ions Tb^{3+} and Mo^{4+}; (ii) we take into account the spin correlations γ_i up to the fourth correlation shell (~ 7.3 Å), meaning $n=4$, and not $n=1$ as for $Tb_2Sn_2O_7$. In this case only the sum of correlations at each bond distance can be determined from the data:

$$\begin{aligned}
\gamma_1 &= 2\langle \mu_{Tb}\mu_{Mo}\rangle_{R_1} + \langle \mu_{Tb}\mu_{Tb}\rangle_{R_1} + \langle \mu_{Mo}\mu_{Mo}\rangle_{R_1} \\
\gamma_2 &= 2\langle \mu_{Tb}\mu_{Mo}\rangle_{R_2} \\
\gamma_3 &= 2\langle \mu_{Tb}\mu_{Mo}\rangle_{R_3} + \langle \mu_{Tb}\mu_{Tb}\rangle_{R_3} + \langle \mu_{Mo}\mu_{Mo}\rangle_{R_3} \\
\gamma_4 &= \langle \mu_{Tb}\mu_{Tb}\rangle_{R_4} + \langle \mu_{Mo}\mu_{Mo}\rangle_{R_4}
\end{aligned} \qquad \text{[IV.3]}$$

We focus on γ_2 and γ_4. γ_2 gives access only to the Tb-Mo correlations, while γ_4 takes into account the Tb-Tb and Mo-Mo correlations. Since the Tb^{3+} magnetic moment is roughly nine time larger than the Mo^{4+} moment, one would expect that γ_4 is determined by the Tb-Tb correlations, while the Mo-Mo correlations could be neglected (γ_1 and γ_3 should also be dominated by the Tb-Tb correlations, but their analysis is less evident). It is for the same reason (Tb moment nine time larger than the Mo) that the difference between the form factors for Tb^{3+} and Mo^{4+} was ignored when calculating the cross section.

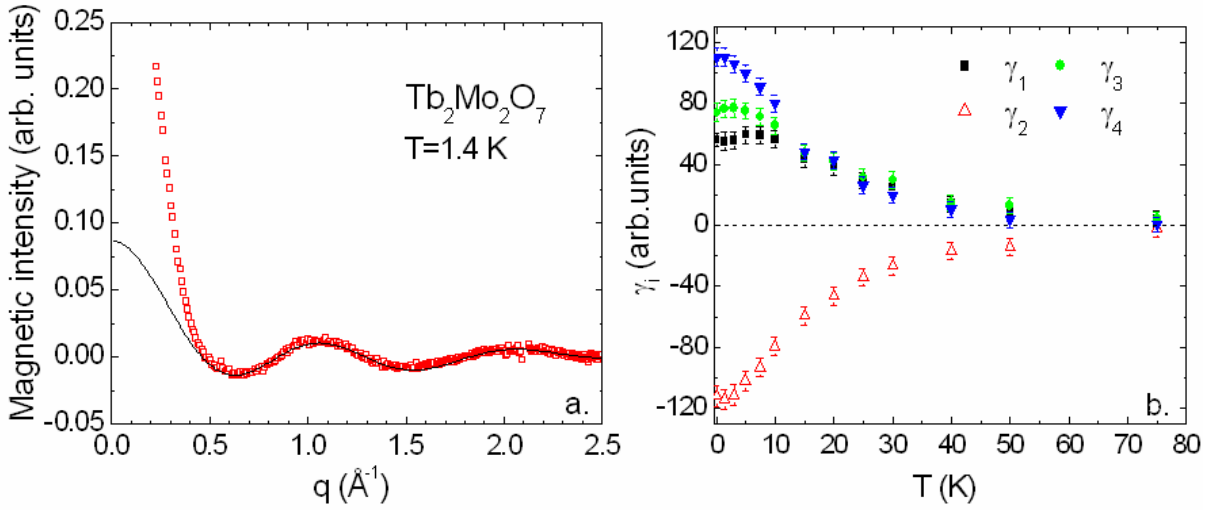

Figure 8. $Tb_2Mo_2O_7$: a. Magnetic intensity versus the scattering vector q at T= 1.4 K (λ=4.741 Å) and the fit with the SRO model (continuous line); b. Correlation parameters γ_i (i=1-4) obtained from the fit using the SRO model.

Figure 8a shows the fit of $Tb_2Mo_2O_7$ experimental data, at 1.4 K, using the expression [IV.1]. The corresponding spin correlations parameters are shown in Figure 8b. As one could clearly see $\gamma_{1,3,4} > 0$, while $\gamma_2 < 0$, *i.e.* the Tb-Tb correlations are ferromagnetic, while Tb-Mo correlations are antiferromagnetic in agreement with previous results [Greedan'91]. As stated above, the antiferromagnetic Mo-Mo correlations yielding the frustration in the spin glass state cannot be extracted from this model. Another disadvantage of the present SRO model is the fact that it cannot describe the SANS signal (as shown in Figure 8a). We mention that, in order to fit all q range (including the SANS signal), we also tried models which take into account not four but five, six and seven coordination cells, respectively, *i.e.* we tried to extend the correlation length till to $R_7 \sim 9.6$ Å. In all these cases ($n=5,6,7$) the fit quality is

similar to that obtained in the $n=4$ model. But, while the parameters $\gamma_{1,2,3,4}$ have a systematic variation, roughly the same as shown in Figure 8b, the parameters $\gamma_{5,6,7}$ strongly oscillate. And therefore, finally we chose the model with four coordination cells to describe the behaviour of $Tb_2Mo_2O_7$ for $q>0.5$ Å.

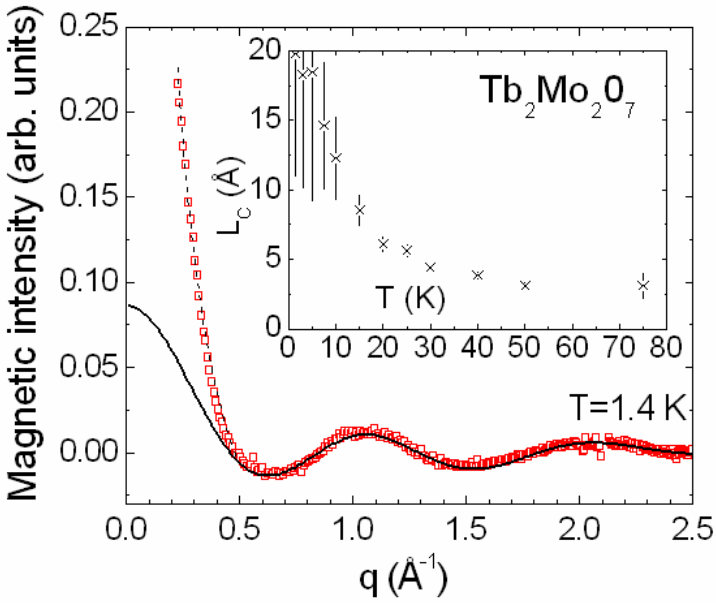

Figure 9. Magnetic intensity of $Tb_2Mo_2O_7$ versus the scattering vector q at T= 1.4 K (λ=4.741 Å), fit with the SRO model (the bottom continuous line), including the longer range ferromagnetic correlations (the upper dashed line). In inset the temperature dependence of correlation length L_C as obtained from Lorentzian fit of q=0 peak.

The SANS signal was fitted by a Lorentzian function:

$$I(q)=\frac{A}{\pi}\frac{k}{k^2+q^2} \qquad \text{[IV.4]}$$

where A and k are the norm and the half width at half maximum of the Lorentzian curve, with $k=1/L_C$. We evaluate the correlation length of these ferromagnetic correlations to 20(8) Å. Considering the relative magnitude of the Tb and Mo local moments and the fact that Tb-Mo and Mo-Mo correlations are antiferromagnetic, we attribute this signal to ferromagnetic Tb-Tb correlations. Figure 9 shows the fit with the SRO model including the longer range ferromagnetic correlations (upper dashed line). In inset we show the temperature evolution of L_c, showing that it decreases with temperature. We note that the important low temperature error bars are not due to the statistics (which is of course better at low temperatures), but they reflect a deviation of the experimental data from a Lorentzian function centered on $q=0$ as we considered. This may suggest that the magnetic intensity shows a peak not at $q=0$ but in $q\sim 0-0.22$ Å^{-1} interval, suggesting a small diffuse incommensurable phase.

IV.3.2. $(Tb_{0.8}La_{0.2})_2Mo_2O_7$: "ordered spin ice"

In this section we analyse the magnetic order observed in $(Tb_{0.8}La_{0.2})_2Mo_2O_7$. As one may see in Figure 6e, even for $a\sim 10.378$ Å$>a_c\sim 10.33$ Å, meaning that this system situates in the ferromagnetic region of the phase diagram from Figure 1, the Bragg peaks dominate but

still coexist with a diffuse magnetic scattering. This shows that the long range order coexist with short range order.

First we analyse only the long range magnetic order. Here the diffuse magnetic scattering below the Bragg peaks is considered as a background.

The magnetic Bragg peaks belong to the face centered cubic lattice, showing that the magnetic structure is derived from the chemical one of $Fd\bar{3}m$ symmetry by a propagation vector $\vec{k} = 0$. The presence of two magnetic peaks (200) and (220) forbidden in the pyrochlore structure, suggest a non-collinear ferromagnetic structure.

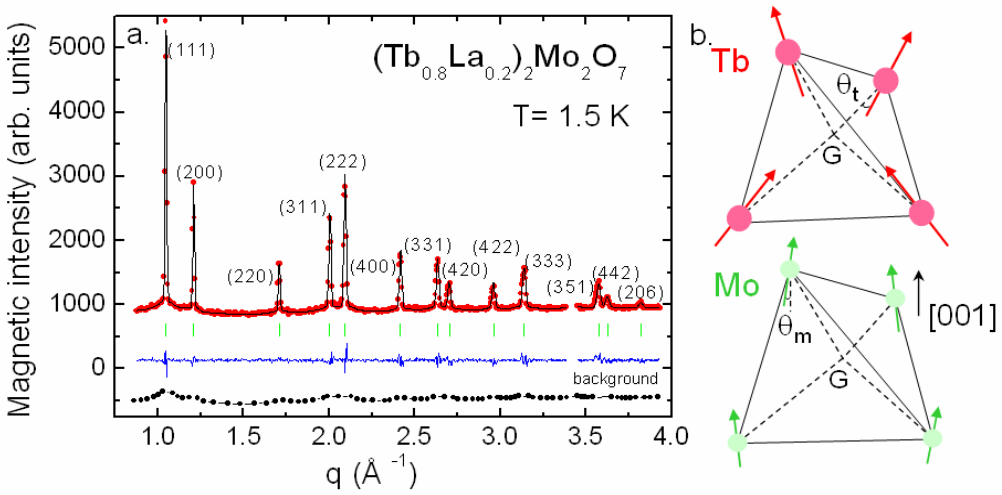

Figure 10. a: Magnetic diffraction pattern of $(Tb_{0.8}La_{0.2})_2Mo_2O_7$ versus the scattering vector $q = 4\pi \sin\theta / \lambda$ at 1.5 K, with the incident neutron wavelength λ = 2.426 Å. A spectrum in the paramagnetic region (70 K) was subtracted. The solid lines show the best refinement (R_B = 4 %) and the difference spectrum (bottom). Tick marks indicate the Bragg peaks positions. The background is also indicated; b: The magnetic structure corresponding to the best refinement: Tb and Mo tetrahedra.

Rietveld refinements of the magnetic diffraction patterns were performed using the program FULLPROF [Rodríguez-Carvajal'93]. The magnetic structure was solved by a systematic search, using the program BASIREPS [Rodríguez-Carvajal] and a symmetry representation analysis [Yzyumov'79, Yzyumov'91]. The basis states describing the Tb^{3+} and Mo^{4+} magnetic moments were identified and the symmetry allowed structures were compared to experiment. Neither a collinear ferromagnetic structure nor the $\vec{k}$=0 antiferromagnetic structure allowed by the $Fd\bar{3}m$ symmetry group were compatible with the experimental data, yielding extinctions of several Bragg peaks. This result suggests the existence of a magnetic component, which breaks the $Fd\bar{3}m$ cubic symmetry. Consequently, we searched for solutions in the tetragonal space group $I4_1/amd$, the subgroup of $Fd\bar{3}m$ with the highest symmetry, which allows ferromagnetic and antiferromagnetic components simultaneously. We found that a linear combination of the two basis vectors of the irreducible representation Γ_7, for both Tb and Mo, yields a good fit of the experimental data. Details concerning the symmetry representation analysis are presented in Appendix B.

The best refinement (having an agreement Bragg factor R_B = 4 %) is shown in Figure 10a. In the ordered structure with $\vec{k}$=0, the four tetrahedra of the unit cell are equivalent for both Tb and Mo lattices. At 1.5 K, in a given Tb tetrahedron (see Figure 10b), the Tb^{3+} magnetic moments orient close to the local <111> anisotropy axes connecting the center of

the tetrahedron to the vertices, with a small angle θ_t = 11.6 °. The components along these <111> axes are oriented in the configuration of the local spin ice structure "two in, two out" [Harris'97]. Their ferromagnetic component orders along a [001] axis. In a Mo tetrahedron (Figure 10b), the Mo magnetic moments align close to a [001] axis, with a slight tilting by an angle θ_m =6.8° at 1.5 K. All magnetic correlations are ferromagnetic: Tb-Tb, but also Tb-Mo and Mo-Mo, the last two in contrast with the spin glass $Tb_2Mo_2O_7$.

We underline that $(Tb_{0.8}La_{0.2})_2Mo_2O_7$ is characterized by a non-collinear ferromagnetic long range order and that the Tb^{3+} magnetic moment orientation within one tetrahedron is close to that of a spin ice. Therefore we also called $(Tb_{0.8}La_{0.2})_2Mo_2O_7$ an "ordered spin ice" like $Tb_2Sn_2O_7$ (see Chapter III.3.1), although it also involves the Mo^{4+} magnetism.

In Table III are shown the values of the magnetic moment components M_x, M_y and M_z of the four Tb^{3+} and Mo^{4+} atoms of one tetrahedron, at 1.5 K. The values of the ordered magnetic moments are: M_{Tb}^{LRO}=4.66(2) μ_B and M_{Mo}^{LRO}=0.64(3) μ_B, respectively. We notice that these values are reduced from the free ion values of 9 μ_B and 2 μ_B, respectively. For Tb, this strong reduction is partly explained by a change of Tb environment when diluted with the non-magnetic La ions, but it should also come from crystal field effects. As for Mo, it could arise either from quantum fluctuations due to the proximity of the threshold or from the frustration of the orbital component of the Mo moment [Solovyev'03].

Site	*x*	*y*	*z*	M_x (μ_B)	M_y (μ_B)	M_z (μ_B)
Tb1	0.5	0.5	0.5	2.25(1)	2.25(1)	3.40(1)
Tb2	0.25	0.25	0.5	-2.25 (1)	-2.25 (1)	3.40 (1)
Tb3	0.25	0.5	0.25	2.25 (1)	-2.25 (1)	3.40 (1)
Tb4	0.5	0.25	0.25	-2.25 (1)	2.25 (1)	3.40 (1)
Mo1	0	0	0	-0.05(1)	-0.05(1)	0.64(1)
Mo2	-0.25	-0.25	0	0.05(1)	0.05(1)	0.64(1)
Mo3	-0.25	0	-0.25	-0.05(1)	0.05(1)	0.64(1)
Mo4	0	-0.25	-0.25	0.05(1)	-0.05(1)	0.64(1)

Table III. The magnetic moment components M_x, M_y and M_z of the four Tb^{3+} and four Mo^{4+} atoms of one tetrahedron at 1.5 K. The atomic coordinates expressed in unit cell units are also given.

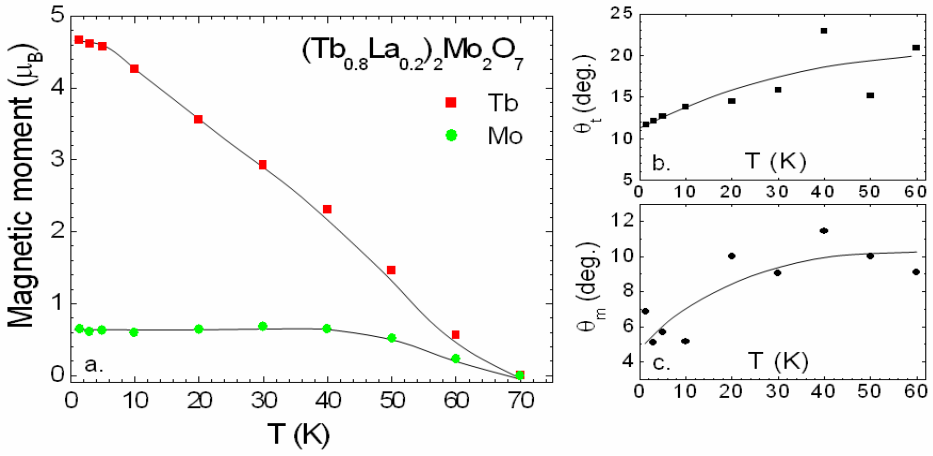

Figure 11. Tb^{3+} and Mo^{4+} ordered magnetic moments versus temperature (left) and the angles θ_t and θ_m made by Tb^{3+} and Mo^{4+} moments with the local anisotropy axes <111> and the [001] axes, respectively (right). Solid lines are guides to the eye.

The temperature dependence of Tb^{3+} and Mo^{4+} ordered magnetic moments deduced from refinements with the non-collinear ferromagnetic model is plotted in Figure 11a. Below T_C, M_{Tb}^{LRO} keeps increasing till to the lowest measured temperature of 1.5 K, while M_{Mo}^{LRO} starts to increase but below ~ 40 K is almost temperature independent. The two tilting angles seem to decrease when decreasing temperature (see Figure 11b,c). In FULLPROF analysis we used the Thompson-Cox-Hastings pseudo-Voigt peak shape function as presented in Chapter II. The correlation length L_C^{LRO} is deduced from the intrinsic peak width. At 1.5 K, $L_C^{LRO} \sim 3700$ Å.

As we have already noticed at the beginning of this section in $(Tb_{0.8}La_{0.2})_2Mo_2O_7$ the long range magnetic order coexists with a short range one corresponding to a diffuse scattering which appears below the Bragg peaks. This short range order appears below about 40 K. In the following, we analyse the system using a two phases model. This time the diffuse scattering is no more included in the background but considered as a second phase.

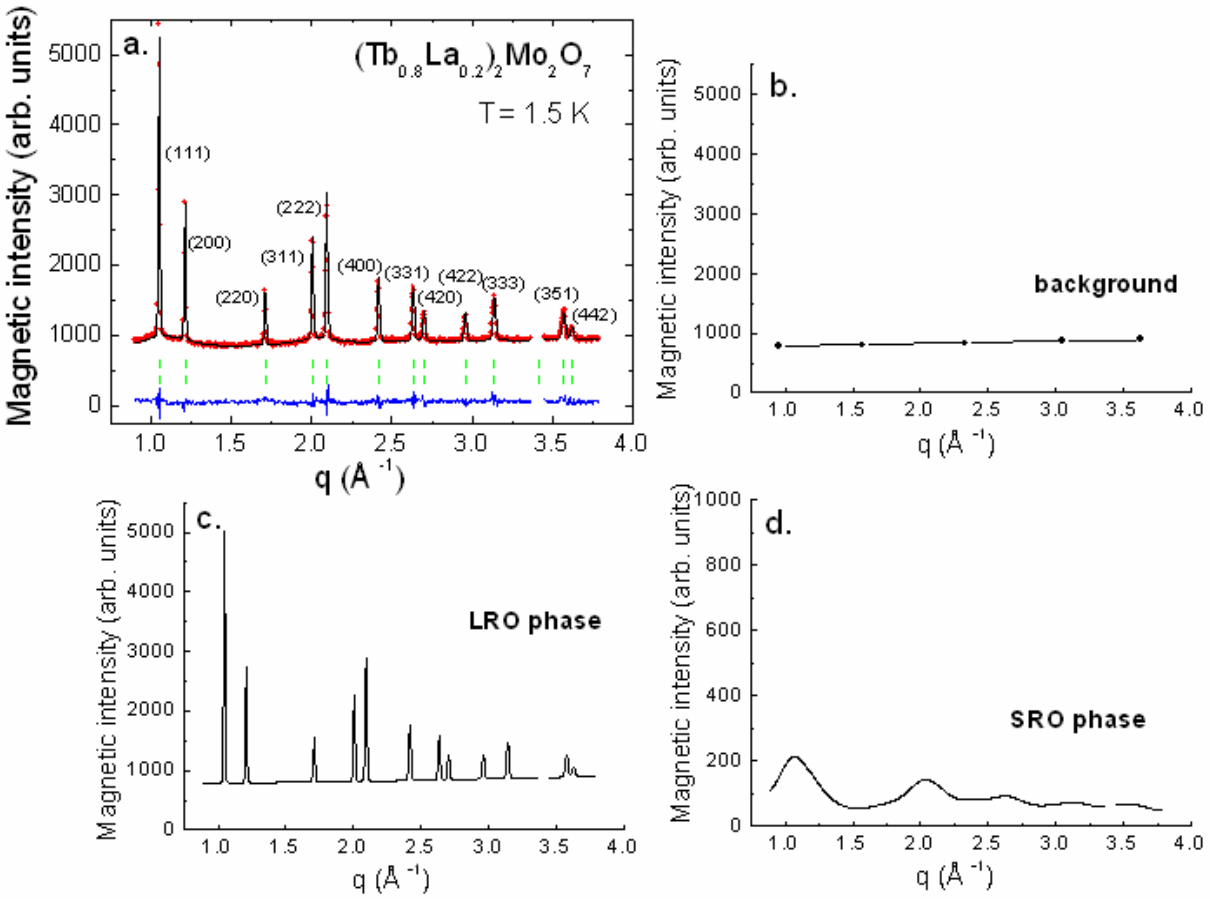

Figure 12. $(Tb_{0.8}La_{0.2})_2Mo_2O_7$: a. Magnetic diffraction pattern versus the scattering vector q at 1.5 K. Solid lines show the best refinement with the two phases model (R_{B1} = 2.42 % and R_{B2} = 10.31 %) and the difference spectrum. Tick marks indicate the two phases Bragg peaks positions; b. Background contribution; c-d. The calculated magnetic intensity corresponding to the LRO and SRO phases, respectively. For clarity, the scale of SRO signal was reduced by 5.

The short range order has the same symmetry as the long range order. The best Rietveld refinement with FULLPROFF [Rodríguez-Carvajal'93] of T = 1.5 K spectrum is shown in Figure 12a. The agreement factors are: R_{B1} = 2.42 % and R_{B2} = 10.31 % for the first

long range and the second short range phase, respectively. The contribution of background, LRO and SRO phases to the calculated total magnetic intensity are shown in Figure 12b-d.

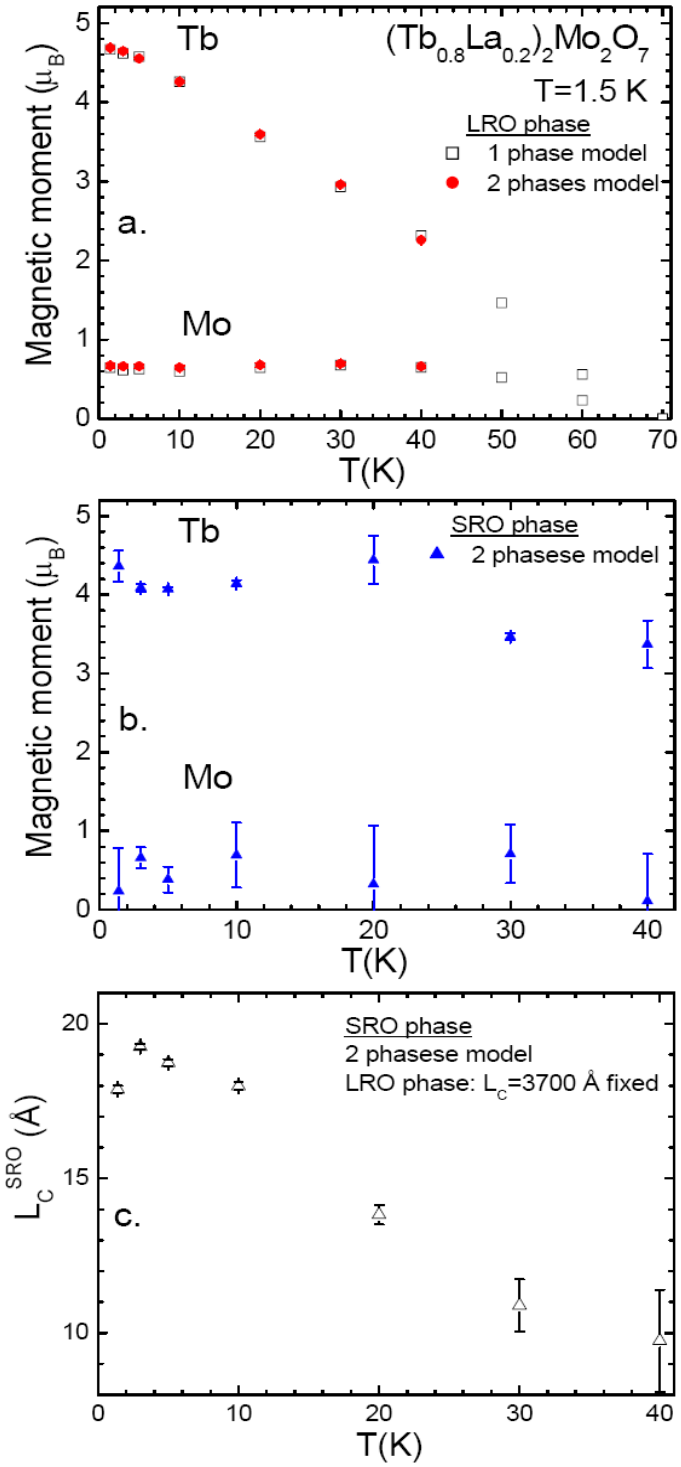

Figure 13. $(Tb_{0.8}La_{0.2})_2Mo_2O_7$: a-b. Temperature dependence of Tb^{3+} and Mo^{4+} ordered magnetic moments corresponding to the LRO and SRO phase, respectively, as obtained from 1 and 2 phases models; c. The temperature variation of the correlation length L_C^{SRO} as determined from the two phases model with L_C^{LRO} fixed at 3700 Å (see text).

We fixed the correlation length of the LRO moments at the value obtained in one phase model (3700 Å) and fitted the magnetic moments for the two phases and the correlation

length of the SRO moments. For 1.5 K we found that the LRO moments are close (in value and orientation) to those from the one phase model: (i) M_{Tb}^{LRO}=4.68(2) μ_B, with θ_t=11.5 ° and (ii) M_{Mo}^{LRO}=0.64(3) μ_B, with θ_m=6.6 °. We also evaluated the SRO magnetic moments: (i) M_{Tb}^{SRO}=4.3(2) μ_B, with θ_t~33 ° and (ii) M_{Mo}^{SRO}=0.2(5) μ_B, with θ_m~22 °. Their orientation roughly suggests that this SRO phase is much less ferromagnetic than the LRO one (where Tb-Tb, Tb-Mo and Mo-Mo correlations are all ferromagnetic). The total moments, calculated as $M = \sqrt{M_{LRO}^2 + M_{SRO}^2}$, are M_{Tb}=6.3(1) μ_B and M_{Mo}=0.7(2) μ_B, respectively. As one may see they are still well reduced from the free ion values of 9 μ_B and 2 μ_B, respectively. At T=1.5 K the SRO moments are correlated over ~ 17.9 Å.

Figure 13a shows for comparison the temperature evolution of the LRO magnetic moments as obtained from the two phases and one phase model, respectively. They have almost the same temperature evolution: M_{Mo}^{LRO} is almost T independent below 40 K, while M_{Tb}^{LRO} keeps increasing below T_C . M_{Tb}^{SRO} and M_{Mo}^{SRO} appear below 40 K and have a smoother temperature evolution (Figure 13b). Their correlation length decreases when increasing temperature (Figure 13c).

IV.3.3. $(Tb_{0.9}La_{0.1})_2Mo_2O_7$: threshold region

The $(Tb_{0.9}La_{0.1})_2Mo_2O_7$ with $a = 10.346$ Å is situated just above the critical threshold ($a_c \sim 10.33$ Å). As shown in Figure 6c, Lorentzian peaks start to grow at the position of the diffuse maxima.

The Rietveld analysis proved to be more complicated in this case. First, in contrast with the x=0.2 system where the magnetic Bragg peaks are well defined, for x=0.1 it is more difficult to separate the Lorentzian peaks from the diffuse scattering. Secondly, there is another problem that might appear when working with subtracted spectra: the temperature dependence of the lattice parameter. Considering the diffraction Bragg's law $2d\sin\theta = \lambda$, with the interplanar distance $d = a/\sqrt{h^2 + k^2 + l^2}$ for our cubic lattice (h,k,l are the Miller's indices): for $\lambda = const.$ a temperature evolution of the cell parameter a means a temperature variation of $\sin\theta$. A subtracted spectrum supposes that from a low temperature spectrum (a sum of nuclear and magnetic intensity) we subtract a high temperature one (in the paramagnetic region meaning only the nuclear intensity). When the contribution of the magnetic signal is important, we are able to subtract the two spectra without too much bother with the effect of temperature. It is the case of x=0.15 and 0.2 long range ordered samples. It is not the case of the other three x=0, 0.05 and 0.1 characterized by the presence of mesoscopic and short range magnetic order. Furthermore, for x=0 and 0.05 samples we can simply exclude the region with subtraction problems, without affecting significantly the short range correlations analysis. For x=0.1, it is the worst situation: for the peak (222) we are not able to make a correct subtraction. Therefore in first instance we exclude this peak and make the Rietveld analysis with only five peaks.

As for x=0.2 system, the magnetic Bragg peaks belong to the face centered cubic lattice and superimpose on the nuclear ones. Therefore, the propagation vector is $\vec{k}$=0. The presence of (200) and (220) magnetic peaks suggest also a non-collinear ferromagnetic structure. We performed Rietveld refinements with FULLPROF [Rodríguez-Carvajal'93] starting from the magnetic structure found for x=0.2 compound.

First we considered a one phase model (more reasonable taking into account the reduced number of peaks). First, we tried to fit the Lorentzian peaks and hence the diffuse scattering was included in the background. For T=1.4 K, the best refinement ($R_B = 7.89$ %) is shown in Figure 14a. In a Tb tetrahedron, the spin configuration is close to that of x=0.2 sample: (i) Tb^{3+} magnetic moments orient close to the local <111> anisotropy axes, with $\theta_t' \sim 10$ °; (ii) the components along <111> orient in the configuration "two in, two out" of a spin ice. The Mo moments make an angle $\theta_m' \sim 65°$ with the [001] axis. The correlation length, deduced from the intrinsic peak width, is ~ 70 Å showing a mesoscopic range order. The magnetic moments at 1.4 K are: $M_{Tb}^{MRO} = 4.4(1)$ μ_B and $M_{Mo}^{MRO} = 0.4(1)$ μ_B.

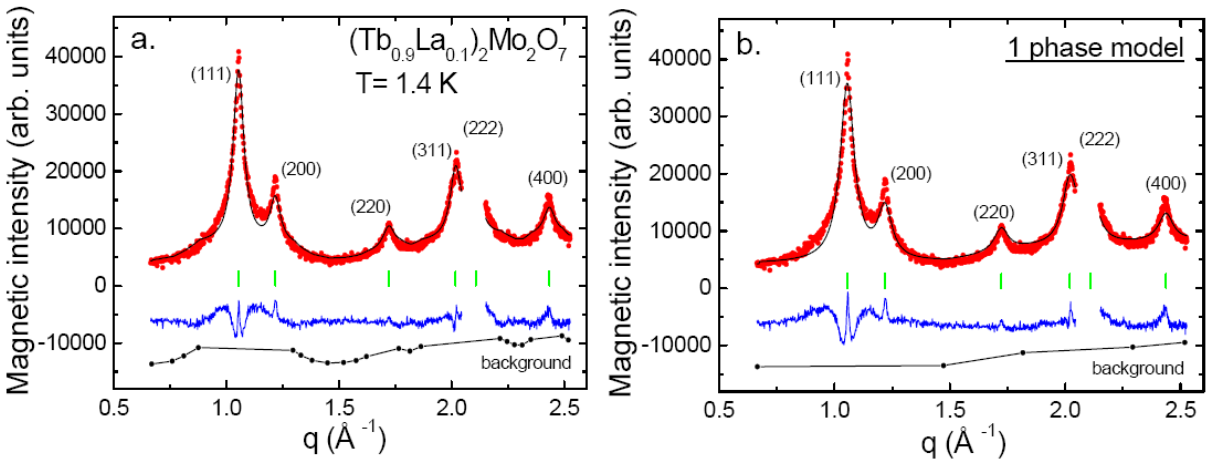

Figure 14. $(Tb_{0.9}La_{0.1})_2Mo_2O_7$: the magnetic intensity versus the scattering vector $q = 4\pi \sin\theta / \lambda$ at 1.4 K, with λ = 4.741 Å. A spectrum in the paramagnetic region (100 K) was subtracted. a and b correspond to the two possible magnetic structures resulted from Rietveld refinements using a one phase model with two different backgrounds as described in the text. The solid lines show the best refinement and the difference spectrum (bottom). Tick marks indicate the Bragg peaks positions. The background is also shown.

If for x=0.2 the Bragg peaks clearly dominate the SRO phase, it is not the case of this system. Here it is more difficult to consider the diffuse scattering as background. Therefore, we did a second analysis using also the one phase model, but this time we defined a non-modulated background. The best refinement ($R_B = 9.76$ %) is shown in Figure 14b. In a Tb tetrahedron, Tb^{3+} moments orient again close to the "two in, two out" configuration of a spin ice making an angle of $\theta_t'' \sim 20$ ° with the <111> axes. The Mo moments make an angle $\theta_m'' \sim 45°$ with the [001] axis. The correlation length is reduced at ~ 55 Å (this fact is expected since all short range order is taking into account in the fit). The magnetic moments are: $M_{Tb}^{MRO} = 5.0(2)$ μ_B and $M_{Mo}^{MRO} = 0.5(2)$ μ_B.

Finally, we tried a two phases model: MRO+SRO. To reduce the number of parameters we fixed the correlation length $L_C^{MRO} \sim 70$ Å and also the Tb^{3+} magnetic moments of both phases to the values corresponding to the magnetic structure from Figure 14a. The best refinement ($R_B = 3.3$ %) is shown in Figure 15a. The Mo^{4+} ordered magnetic moment is ~ 1.3 μ_B for both phases, while the angles made by Mo^{4+} moments with the [001] axis are ~ 13° and ~ 75° for the MRO and SRO phases, respectively. In Figure 15b, we show the best refinement ($R_B = 3$ %) with the two phases model, but with a "reconstructed" data file (we simulated the (222) peak using a Lorentzian function). Fixing the same parameters as above

we obtain comparable results: the Mo ordered magnetic moment is ~ 1.3 μ_B for both phases, while the Mo moments make angles of ~ 16 ° and ~ 80° with [001] axis in MRO and SRO phases, respectively. The correlation length of the short range phase: L_C^{SRO} ~ 15 Å (with or without (222) peak data).

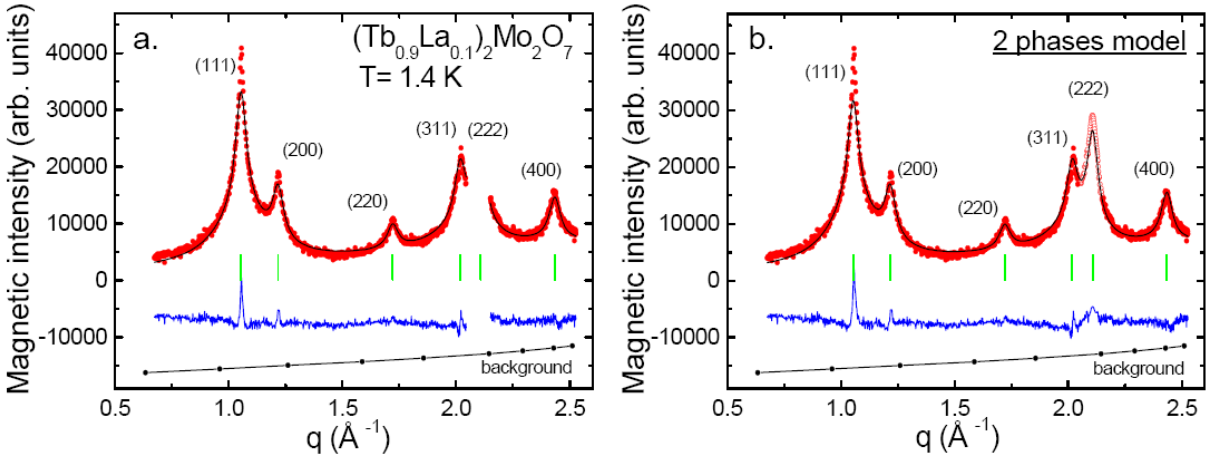

Figure 15. $(Tb_{0.9}La_{0.1})_2Mo_2O_7$: the magnetic intensity versus the scattering vector q at 1.4 K, with λ = 4.741 Å and a 100 K spectrum subtracted. a. The magnetic structure resulted from Rietveld refinements with a two phases model as described in the text; b. The same model tested when the (222) peak is taken into account. The solid lines show the best refinement and the difference spectrum (bottom). Tick marks indicate the Bragg peaks positions. The background is shown.

In consequence, with a one MRO phase model we use less parameters and the values of the magnetic moments are more realistic. We obtained two possible solutions. Within this model we determine: L_C^{MRO} ~ 55-70 Å. In the two MRO+SRO phases model the values of the Mo ordered magnetic moment are overestimated in comparison to those obtained for x=0.2: ~ 1.3 μ_B instead of ~0.6 μ_B. We underline however that they are still reduced with respect to the free ion value of 2 μ_B. The advantage of this model is that it gives: L_C^{SRO} ~ 15 Å.

The interesting result is that all these models suggest the same ideas: (i) the x=0.1 compound also has a non-collinear magnetic structure, but with more important canting angles showing a stronger antiferromagnetic character than for x=0.2 and (ii) shorter correlation lengths with regards to x=0.2: $L_C^{MRO}(x=0.1) \sim$ 55-70 Å << $L_C^{LRO}(x=0.2) \sim 3700$ Å.

IV.3.4. Discussion

After analysing in details three representative samples, x=0 ($x < x_c \sim 0.06$), x=0.1 (situated in the threshold region) and x=0.2 ($x > x_c$), we briefly present the results concerning the other two, x=0.05 and x=0.15.

As already shown in Figure 6b, the x=0.05 compound has a behaviour similar to that of x=0: a diffuse magnetic scattering for $q = 0.5 - 2.5$ Å^{-1} and an intense SANS signal for $q < 0.5$ Å^{-1}. We analysed this compound using the same short range model as in section IV.3.1. Figure 16 shows the temperature evolution of the correlation parameters. As for x=0, the Tb-Tb correlations are ferromagnetic ($\gamma_{1,3,4} > 0$), while Tb-Mo are antiferromagnetic ($\gamma_2 < 0$). However, we note that the absolute values of these parameters are all increasing

when passing from x=0 to x=0.05, indicating that both F and AF correlations increase by Tb/La substitution. This result is in agreement with the presence of more pronounced diffuse maxima for the x=0.05 sample (see Figure 6 a,b).

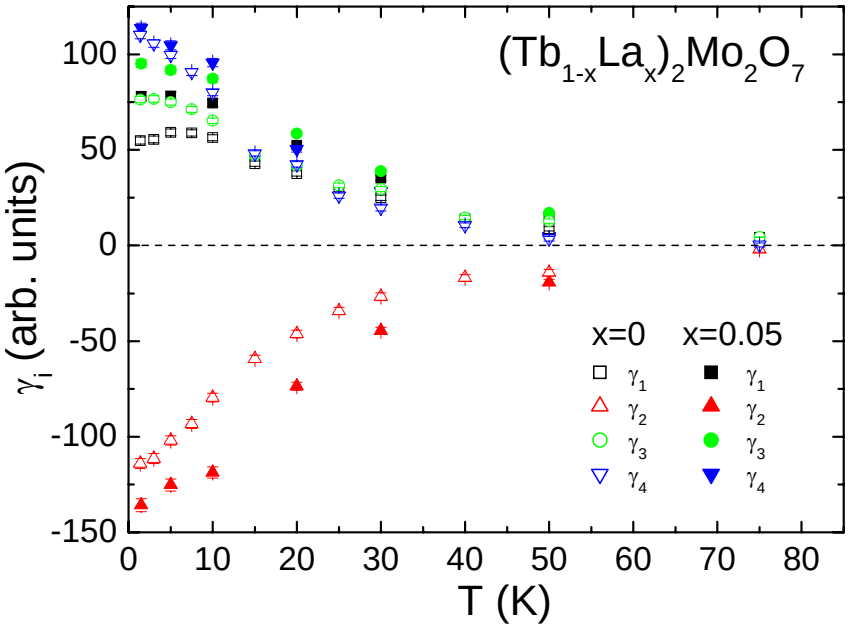

Figure 16. $(Tb_{1-x}La_x)_2Mo_2O_7$, x=0 and 0.05: comparison between the temperature evolution of the correlation parameters γ_i (i =1-4) as obtained from the SRO model.

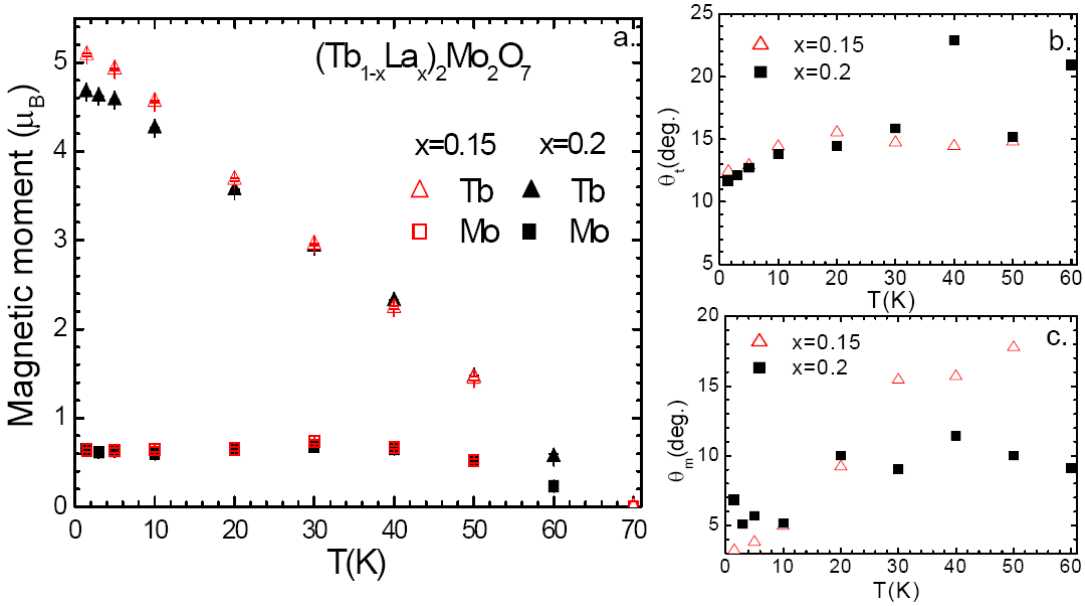

Figure 17. $(Tb_{1-x}La_x)_2Mo_2O_7$, x=0.15 and 0.2: a. Temperature evolution of the long range ordered magnetic moments of Tb^{3+} and Mo^{4+}; b-c. The angles θ_t and θ_m made by Tb^{3+} and Mo^{4+} moments with the local anisotropy axes <111> and the [001] axes, respectively.

Per contra, the x=0.15 compound has a behaviour similar to that of x=0.2 (see Figure 6d). It is characterized by the presence of Bragg peaks, which coexist with a diffuse magnetic scattering below ~ 40 K. The Rietveld analysis shows that x=0.15 is also an "ordered spin ice", where all magnetic correlations are ferromagnetic. The temperature evolution of the Tb^{3+} and Mo^{4+} long range ordered moments is shown in Figure 17, as well as the evolution of

angles made by Tb^{3+} and Mo^{4+} moments with the <111> and [001] axes, respectively. For comparison we plot also the x=0.2 results. One may clearly see the similarities. We note that, contrary to our expectations, at low temperature the Tb^{3+} magnetic moment is bigger in the case of x=0.15. However this result is in agreement with our magnetic measurements. As one may see in Figure 2d,e, the low temperature magnetization of x=0.15 exceeds that of x=0.2. At 1.4 K the correlation length of the long range ordered phase is $L_c^{LRO} \sim 1400$ Å. For the short range ordered phase, at 1.4 K, the correlation length is $L_c^{SRO} \sim 17.6$ Å and the magnetic moments are $M_{Tb}^{SRO} = 3.8(2)\ \mu_B$ and $M_{Mo}^{SRO} = 0.5(3)\ \mu_B$.

At the end of this section we summarize the results for the whole $(Tb_{1-x}La_x)_2Mo_2O_7$ series. As one can easily see the dilution of Tb by La expands the lattice and induces a change from a spin glass like state to a non-collinear ferromagnetic ("ordered spin ice") state. The neutron diffraction allows the microscopic study of this transition. It shows the spin-spin correlations evolution from only Tb-Tb ferromagnetic correlations in the spin glass state to all ferromagnetic. It also shows that the Tb^{3+} and Mo^{4+} ordered magnetic moments are almost constant, when increasing the amount of La (see Figure 18). We note that the latter result corresponds to a drop of the correlation length from 3700 Å (x=0.2) to 70 Å (x=0.1).

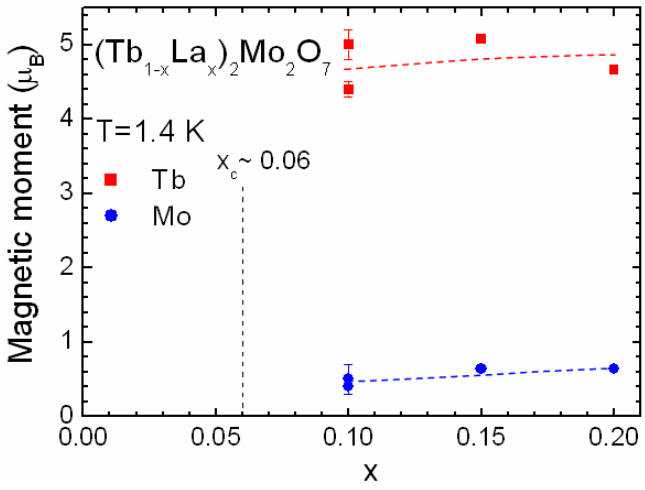

Figure 18. $(Tb_{1-x}La_x)_2Mo_2O_7$, x=0.1-0.2: Tb^{3+} and Mo^{4+} ordered magnetic moments versus La concentration x. For x=0.1 the two possible solutions obtained using the one phase model are indicated (the lower value corresponds to a background which takes into account the diffuse scattering; the upper value corresponds to a non-modulated background). $x_c \sim 0.06$ marks the critical threshold. The lines are guides to the eye.

$(Tb_{1-x}La_x)_2Mo_2O_7$	L_c^{SRO} (Å)	L_c^{MRO} (Å)	L_c^{LRO} (Å)
x=0	7.3	—	—
x=0.05	7.3	—	—
x=0.1	15	~55-70	—
x=0.15	17.6	—	~1400
x=0.2	17.9	—	~3700

Table IV. The correlation length L_c of all magnetic phases (short, mesoscopic and long range ordered) as obtained from the neutron diffraction analysis at 1.4 K and $q > 0.5$ Å^{-1}.

Table IV and Figure 19 summarize the results concerning the influence of La substitution on the correlation length L_c as deduced from the analysis of magnetic intensity

for $q > 0.5$ Å^{-1}: (i) for x=0 and 0.05 ($x < x_c$) there is only the diffuse scattering phase revealing correlations only up to the fourth coordination cell, *i.e.* 7.3 Å; (ii) for x=0.1 (situated in the threshold region) Lorentzian peaks reveal mesoscopic range order, which coexists with short range order; (iii) for x=0.15 and 0.2 ($x > x_c$), the coexistence of Bragg peaks and of the diffuse scattering shows the presence of two well separated phases, short and long range ordered, respectively.

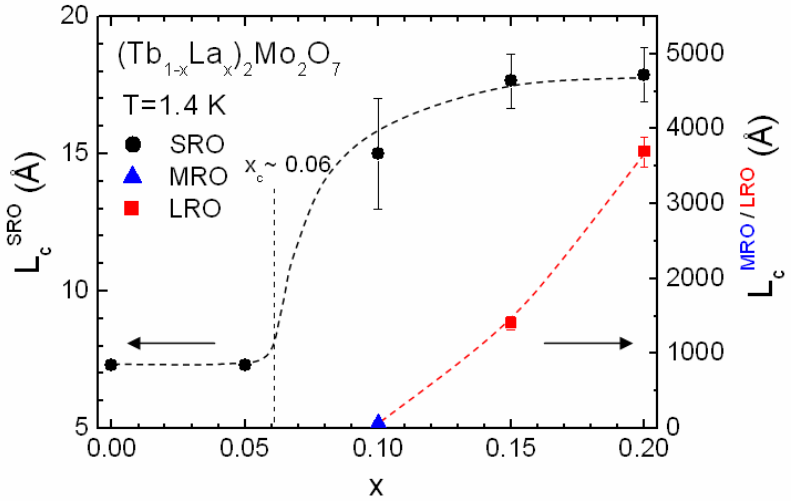

Figure 19. $(Tb_{1-x}La_x)_2Mo_2O_7$, x=0-0.2: the correlation length L_c evolution with the La concentration x, corresponding to short, mesoscopic and long range order as determined from neutron diffraction at 1.4 K for $q > 0.5$ Å^{-1}. The corresponding values are listed in Table IV. $x_c \sim 0.06$ marks the critical threshold. The lines are guides to the eye.

Of course, for all samples, there is also the SANS signal at $q < 0.5$ Å^{-1} indicating ferromagnetic correlations. Using a Lorentzian fit, we were able to evaluate the corresponding correlation length (~ 20 Å) for x=0. For the others samples a similar analysis was more difficult due to less experimental data points. It roughly suggests that in all cases these correlations persist to be short range ordered, above four neighbour distances, but we cannot discuss their evolution with the La concentration.

IV.4. μSR: spin dynamics

The neutron diffraction allowed the study of the magnetic order. We showed that for $(Tb_{1-x}La_x)_2Mo_2O_7$ series the Tb/La substitution expands the lattice and induces the transition from a spin glass (x=0, 0.05) to an "ordered spin ice" (x=0.15, 0.2), passing through a threshold region (x=0.1). The Muon Spin Rotation and Relaxation (μSR) measurements offer new information on the magnetic order by probing the spin fluctuations and the static field below T_C. The ambient pressure μSR measurements were performed on the GPS and DOLLY instruments of the Paul Scherrer Institute (PSI).

IV.4.1. $(Tb_{0.8}La_{0.2})_2Mo_2O_7$

For $(Tb_{0.8}La_{0.2})_2Mo_2O_7$ the time dependence of the muon spin depolarisation function was recorded in zero applied field, from 200 K down to 1.7 K. Figure 20 shows some relaxation curves below and above T_C, with the corresponding fit curves.

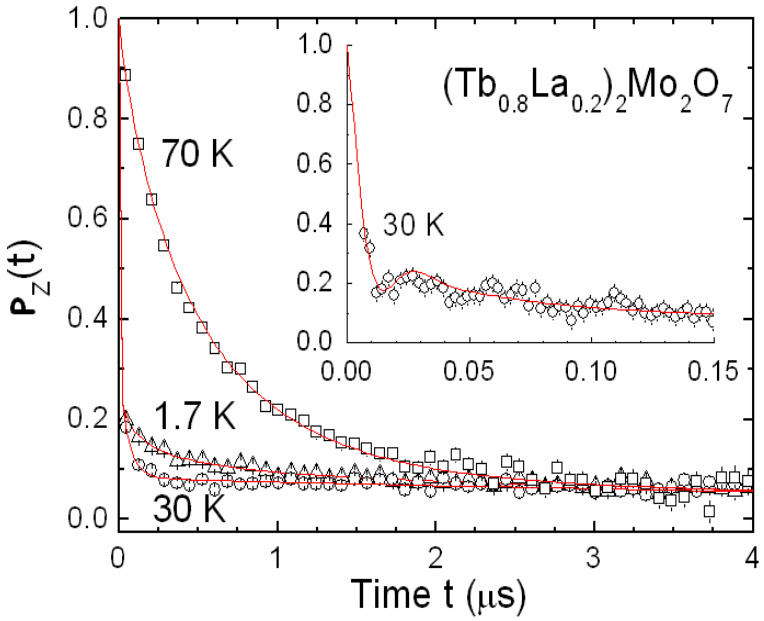

Figure 20. $(Tb_{0.8}La_{0.2})_2Mo_2O_7$ ambient pressure μSR results: the total muon spin depolarization function $P_Z(t)$ (the background term is taken into account) for three temperatures: 1.7 K, 30 K and 70 K. The inset shows the early time region (t< 0.15 μs) of the T=30 K spectrum, where the wiggle characteristic of static order is visible. Lines are fits as described in the text.

The total fit function is written as:

$$P_Z(t) = 0.9P_Z(t) + 0.1\exp(-0.1t) \qquad \text{[IV.5]}$$

where the exponential term corresponds to the background contribution from the cryostat walls. It was determined at 70 K in a transverse field of 50 G. $P_Z(t)$ is the muon spin depolarisation function corresponding to the sample. For $T > T_C$, the best fit corresponds to a stretched exponential:

$$P_Z(t) = \exp(-\lambda t)^{\beta}, \quad T > T_C \qquad \text{[IV.6]}$$

where λ is the muon spin relaxation rate. For $T < T_C$, the function chosen for fit is that expected for a magnetically ordered state of a powder sample as described in Ref. [Réotier'04, Réotier'97]:

$$P_Z(t) = \frac{1}{3}\exp(-\lambda_Z t)^{\beta} + \frac{2}{3}\exp(-\lambda_T t)\cos(\gamma_\mu \langle B_{loc} \rangle t), \quad T < T_C \qquad \text{[IV.7]}$$

In [IV.7], the first term governs the long-time relaxation and corresponds to the muon spin depolarisation by spin fluctuations perpendicular to the direction of the muon spin. There are two parameters of interest which reflect the spin dynamics: the longitudinal relaxation rate λ_Z and its exponent β. The second term takes into account the strong depolarisation and the wiggles seen in the early times region (t<0.15 μs, see Figure 20 inset) and reflects the precession of the muon spin in the average local field at the muon spin site. There are also two parameters of interest: the transverse relaxation rate λ_T and the average local field $\langle B_{loc} \rangle$. λ_T can have both static and dynamical character, but considering $\lambda_T >> \lambda_Z$ (see below) we associate it to the distribution of the static local field. γ_μ is the muon

gyromagnetic ratio ($\gamma_\mu = 2\pi \times 1.3554 \times 10^8$ rad×s^{-1}×Tesla^{-1}). The expressions [IV.6] and [IV.7] are expected to merge in the high temperature limit, when the dynamics of Tb^{3+} and Mo^{4+} moments is fast, yielding: $\lambda_Z = \lambda_T = \lambda$, $\langle B_{loc} \rangle = 0$ and $\beta = 1$.

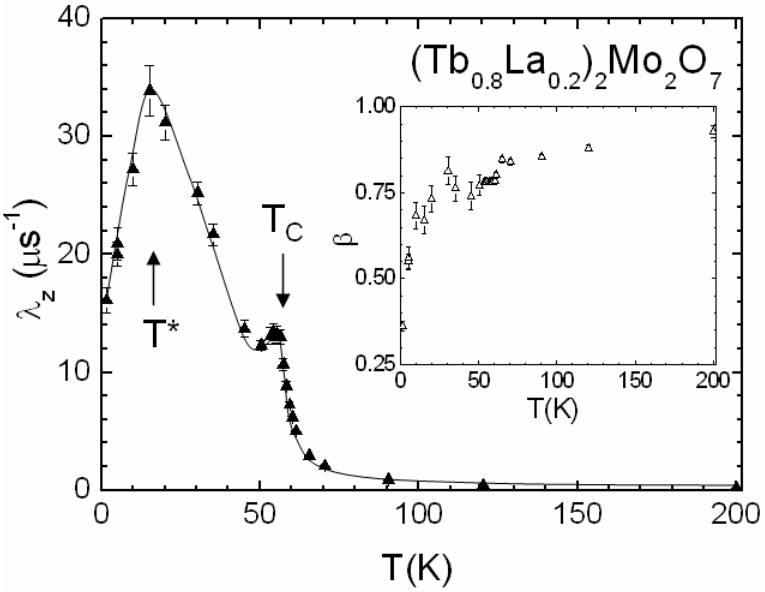

Figure 21. Ambient pressure μSR results for $(Tb_{0.8}La_{0.2})_2Mo_2O_7$: temperature dependence of the longitudinal relaxation rate λ_Z and its exponent β (in inset). The temperatures of interest are indicated: $T^* \simeq 15(5)$ K and $T_C = 57(1)$ K.

Figure 21 shows the temperature dependence of the dynamical parameters: λ_Z and β. With decreasing temperature the longitudinal relaxation rate λ_Z starts to increase when approaching T_C from the paramagnetic region, due to the slowing down of the spin fluctuations. It shows a clear cusp at $T_C = 57(1)$ K due to the onset of the magnetic order, in agreement with previous susceptibility and neutron diffraction measurements. In a standard ferromagnet, the contribution of the spin waves should yield a decrease of λ_Z below T_C down to zero as $T \to 0$. Per contra in our system, below 50 K λ_Z starts to increase and shows a broad maximum at $T^* = 15(5)$ K. This suggests a second transition. The exponent β is also temperature dependent: when decreases temperature it decreases from almost 1 at 200 K to 0.36 at 1.7 K.

Figure 22 shows the evolution in temperature of the transversal relaxation rate λ_T and of the local field at the muon site $\langle B_{loc} \rangle$. We first notice that at 1.7 K, $\lambda_T \sim 250$ μs^{-1} >> $\lambda_Z \sim 15$ μs^{-1}, showing that λ_T mostly has a static character. We assign λ_T mainly to the width of the distribution of the local fields. It smoothly increases below T_C in a way similar to the average local field $\langle B_{loc} \rangle$.

In first approximation, both λ_T and $\langle B_{loc} \rangle$ scale with the Tb^{3+} ordered magnetic moment $M_{Tb}^{LRO}(T)$ measured by neutron diffraction. This suggests that the local field seen by the muon comes mostly from the Tb^{3+} ions, which much larger magnetic moments, although more localized, than the Mo^{4+} ones. Previous μSR data (see Ref. [Dunsiger'96]) also show

that the static internal field is about 10 times larger in $Tb_2Mo_2O_7$ than in $Y_2Mo_2O_7$ spin glass. We recall that there is no anomaly of the long range ordered magnetic moments M_{Tb}^{LRO} at $\sim T^*$. At first sight it would appear that λ_T and $\langle B_{loc} \rangle$ do not show either such an anomaly, suggesting that the second transition seen in temperature dependence of λ_Z has a dynamical character.

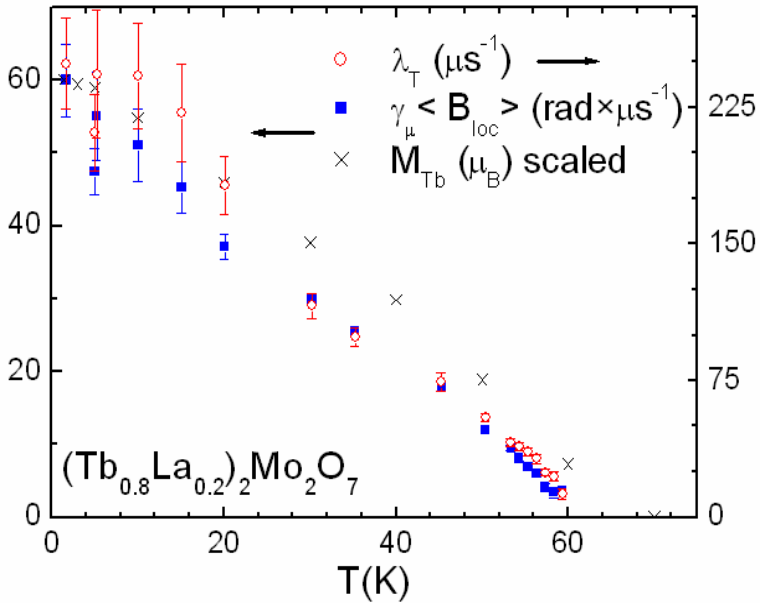

Figure 22. $(Tb_{0.8}La_{0.2})_2Mo_2O_7$: the transversal relaxation rate λ_T and the average local field $\langle B_{loc} \rangle$ as obtained from μSR measurements and the ordered magnetic moment M_{Tb}^{LRO} (scaled) as obtained from neutron diffraction measurements.

However, a closer insight into the temperature dependence of λ_T and $\langle B_{loc} \rangle$ (Figure 23) suggests a small inflection in the temperature range 20-30 K, *i.e.* roughly in the same temperature range where the short range magnetic correlations (M_{Tb}^{SRO}) become important. Such a behaviour may suggest a freezing of the short range correlated magnetic moments.

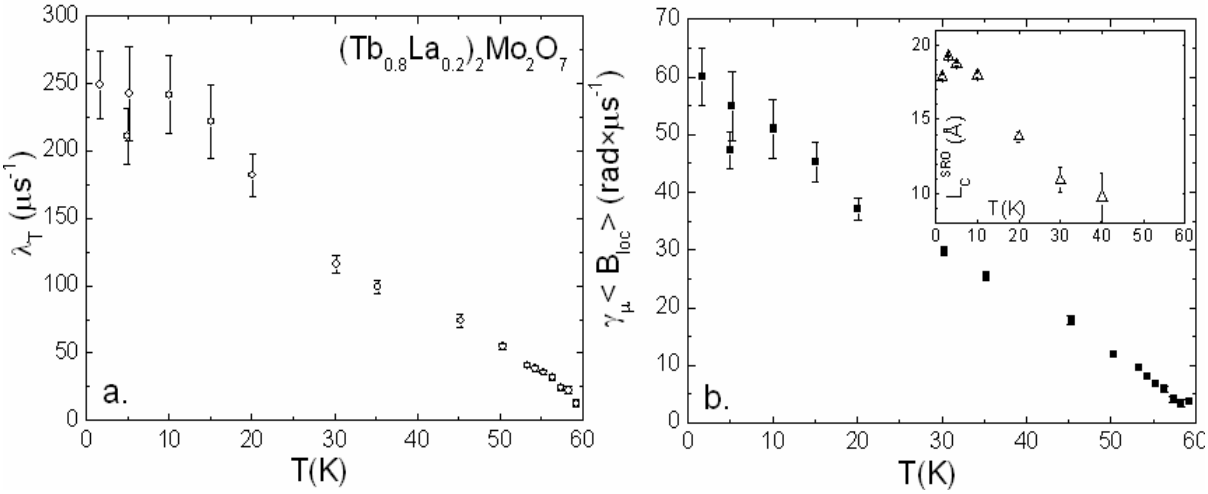

Figure 23. μSR results for $(Tb_{0.8}La_{0.2})_2Mo_2O_7$: the temperature dependence of the transversal relaxation rate λ_T (a) and of the average local field $\langle B_{loc} \rangle$ (with γ_μ the muon gyromagnetic ratio) (b).

IV.4.2. $(Tb_{1-x}La_x)_2Mo_2O_7$, x=0, 0.05 and 0.1

The ambient pressure μSR measurements for $(Tb_{1-x}La_x)_2Mo_2O_7$ series, with x=0, 0.05 and 0.1, were performed in the temperature range 1.5-120 K, on the GPS and DOLLY instruments of the Paul Scherrer Institute (PSI).

In all cases (x=0, 0.05 and 0.1) the muon spin depolarisation function $P_Z(t)$ was best fitted with a stretched exponential:

$$P_Z(t) = \exp(-\lambda t)^{\beta}, \quad T > T_C$$
$$P_Z(t) = \frac{1}{3}\exp(-\lambda t)^{\beta}, \quad T < T_C \qquad \text{[IV.8]}$$

where λ is the muon spin relaxation rate and β its exponent. We notice that for x=0.1 sample, where the neutron diffraction shows the presence of mesoscopic magnetic order and situates it in the threshold region of the spin glass-ferromagnetic transition, below T_C we also tried to fit using the function [IV.7] (the same as for x=0.2). The fit of the small times region is quite difficult. The fingerprint of the local field is less evident than for x=0.2 and we obtain important error bars for both λ_T and $\langle B_{loc} \rangle$. We chose therefore the same (simpler) function [IV.8], as for x=0 and 0.05. We notice that both functions [IV.7] and [IV.8] give a similar behaviour of the dynamical relaxation rate λ_Z.

Figure 24 shows the temperature dependence of λ_Z for the series $(Tb_{1-x}La_x)_2Mo_2O_7$, with x=0, 0.05, 0.1 and 0.2 (for comparison).

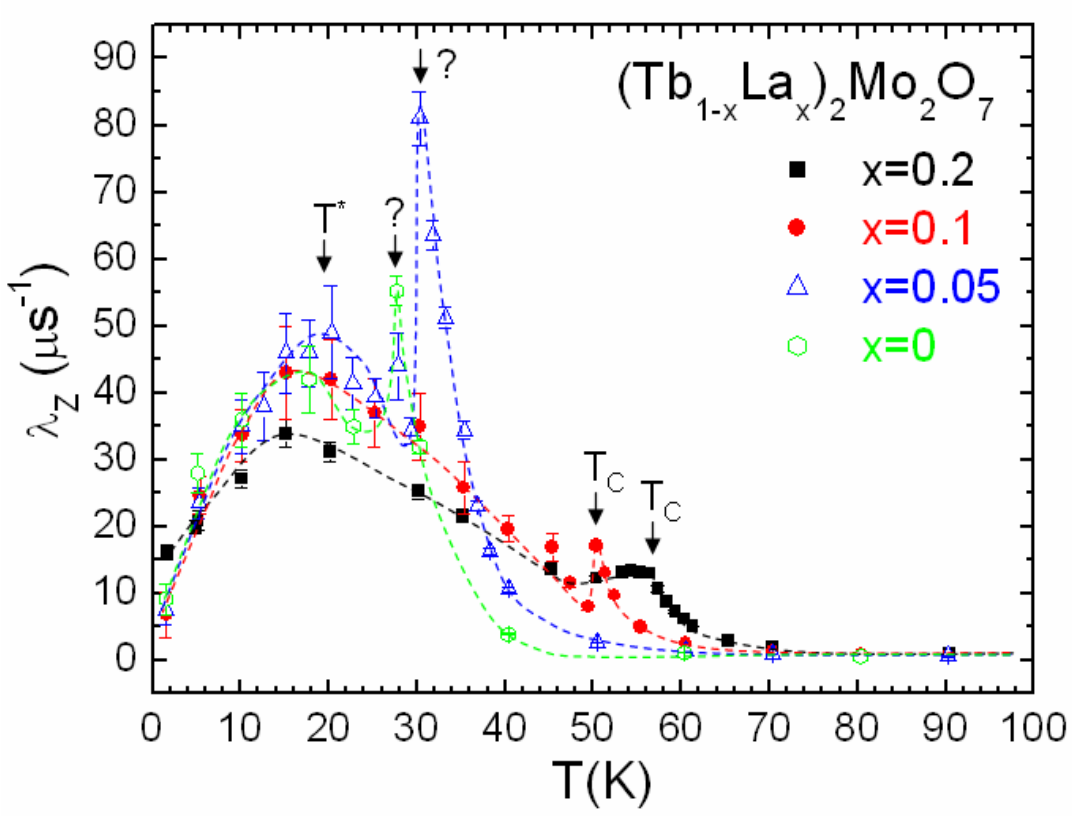

Figure 24. Ambient pressure μSR results for $(Tb_{1-x}La_x)_2Mo_2O_7$, with x=0, 0.05, 0.1 and 0.2 for comparison. Dashed lines are guides to the eye.

For the x=0.1 sample, λ_Z shows a cusp at $T_C = 50(2)$ K, followed by a second anomaly at $T^* = 18(5)$ K. It has as expected two transitions, as the x=0.2 sample. We note that the Tb/La substitution increases the Curie temperature.

Interesting results are obtained for the x=0 and 0.05 samples, which seem at first sight to have the same behaviour: a broad anomaly at $T^* = 18(5)$ K and 20(5), respectively, but also a second transition at higher temperatures, roughly 28 and 30 K, respectively, despite the spin glass behaviour shown by neutron diffraction. This may suggest the presence of some ferromagnetism, which may be related to the behaviour of ZFC/FC curves in the magnetic susceptibility measurements (different from that of the canonical spin glass $Y_2Mo_2O_7$) and also to the ferromagnetic correlations observed by neutron diffraction (the SANS signal). We note that for $Tb_2Mo_2O_7$, the spin dynamics has already been analysed by μSR measurements [Dunsiger'96], which show that the muon spin relaxation rate shows a peak unique at $T_{SG} \sim 25$ K, then decreases and shows a residual muon spin relaxation rate till to 0.05 K (see Chapter I, section I.3.1). Current analysis of the $Tb_2Mo_2O_7$ seems to suggest that a dynamical Kubo-Toyabe fit would be more appropriate and this fit function should also be tested on the x=0.05 sample.

IV.5. Resistivity measurements

We also tried to investigate the effect of Tb/La substitution on the transport properties. We chose two representative samples: $x = 0 < x_c \sim 0.06$ and $x = 0.2 > x_c$. The resistivity measurements of two fritted samples were recorded in the temperature range 4.4-264 K, using a four-probe technique, at SPEC (Service de Physique de l'Etat Condensé, CEA-CNRS, CE-Saclay) by G. Lebras and P. Bonville.

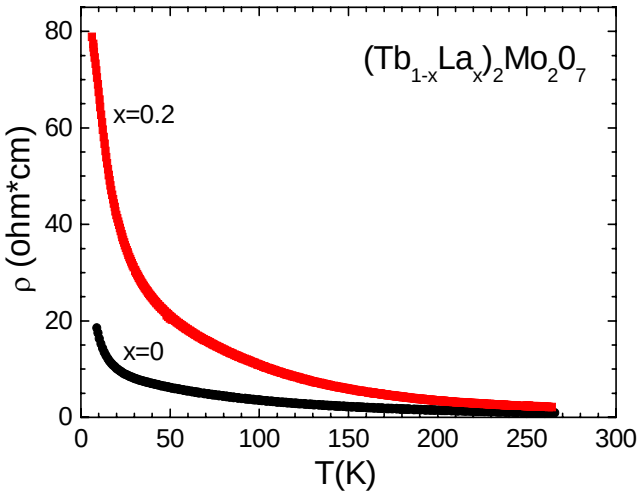

Figure 25. Temperature dependence of the electrical resistivity for two representative samples of $(Tb_{1-x}La_x)_2Mo_2O_7$ series: $x=0 < x_c \sim 0.06$ and $x=0.2>x_c$.

Figure 25 shows the temperature dependence of the electrical resistivity. For $x = 0$ sample the $\rho(T)$ curve increases when the temperature is decreasing showing an insulator type behaviour. Our result confirms that already reported in Ref. [Miyoshi'01]. Per contra, the result obtained for $x = 0.2$ is quite intriguing. Not only it also shows an insulator behaviour (surprising since $x > x_c$ so it should be a metal), but it has a more pronounced insulator behaviour even than $x = 0$: at 4.4 K $\rho(x = 0) \sim 23\,\Omega\times$cm, while $\rho(x = 0.2) \sim 85\,\Omega\times$cm. This

may be an artefact due to the powder effects or may be related to an real effect, proving that for the series $(Tb_{1-x}La_x)_2Mo_2O_7$ the spin glass-ferromagnetic transition is not coupled with the insulator-metal one.

IV.6. Conclusions

In this chapter we analysed the structural and magnetic properties of the geometrically frustrated $(Tb_{1-x}La_x)_2Mo_2O_7$ series having two magnetic ions, Tb^{3+} and Mo^{4+}, on pyrochlore lattices.

From structural point of view, we showed that without inducing a phase transition the Tb/La substitution expands the lattice. Consequently the magnetic properties are strongly modified.

The neutron diffraction allows the study of the microscopic changes of magnetism, when increasing the La concentration from 0 up to 0.2 . The x=0 and 0.05 compounds, $a < a_c$, have a spin glass like behaviour with short range correlated spins. Tb-Tb correlations are ferromagnetic, while Tb-Mo and Mo-Mo are antiferromagnetic. Per contra, x=0.15 and x=0.2 compounds, $a > a_c$, are characterized by the coexistence between short range order and a non-collinear ferromagnetic long range order which clearly dominates. The main characteristics of the low temperature magnetic structure are: (i) it is a $\vec{k}$=0 order; (ii) the Tb^{3+} magnetic moments orient close to their <111> anisotropy axes as for an "ordered spin ice"; (iii) the Mo^{4+} ones orient close to [001] axis with a small tilting angle; (iv) all correlations are ferromagnetic; (v) the resulting ferromagnetic component orients along the [001] axis. Situated in the threshold region the x=0.1 compound has an intermediate behaviour: (i) a mesoscopic range order, which also coexist with the short range one; (ii) the tilting angles being more important, the magnetic correlations have a more pronounced antiferromagnetic character with regard to the case of x=0.2 and 0.15.

The μSR experiments shed a new light on the magnetic order by probing the spin fluctuations and the static field below T_C. For x=0.2 a second transition of dynamical nature was observed at $T^* < T_C$. When decreasing the La concentration the two transitions seem to merge.

Chapitre V.

$(Tb_{1-x}La_x)_2Mo_2O_7$: une verre de spin induite sous pression

Dans le Chapitre IV nous avons analysé l'influence de la substitution chimique sur les propriétés structurales et magnétiques de la série $(Tb_{1-x}La_x)_2Mo_2O_7$. Dans le Chapitre V nous complétons cette étude par l'analyse de l'influence d'une pression appliquée.

Nous étudions d'abord l'effet de la pression sur les propriétés structurales par diffraction de rayons X sous pression en utilisant le rayonnement synchrotron. Nous avons étudié cinq composés $R_2M_2O_7$ et déterminé leur équation d'état. Tout d'abord, pour le même ion de transition $M=Mo^{4+}$, nous varions la terre rare R. Nous avons choisi d'étudier des composés situés dans les trois régions intéressantes du diagramme de phase magnétique: les deux concentrations extrêmes x=0 ($a < a_c \sim 10.33$ Å) et x=0.2 ($a > a_c$) de la série $(Tb_{1-x}La_x)_2Mo_2O_7$, et le composé $Gd_2Mo_2O_7$, voisin du seuil de transition ($a \sim a_c$). Puis, vice versa, nous fixons la terre rare $R=Tb^{3+}$ et nous étudions les changements structuraux sous pression en variant le métal M d'un état sp (Sn), 3d (Ti) et 4d (Mo).

Par diffraction de rayons X sous pression, nous montrons que jusqu'à la pression la plus élevée (10 ou 40 GPa selon les cas), aucun des cinq composés pyrochlores étudiés ne montre de transition structurale. Nous étudions la dépendance en pression du paramètre de réseau (*i.e.* l'équation d'état) et celle du paramètre de position de l'oxygène. L'équation d'état permet d'obtenir le module de compressibilité B_0. Dans $Tb_2M_2O_7$, (M=Mo, Ti, Sn), B_0 augmente quand on passe de l'ion de transition Mo à Ti, puis à Sn. Cette variation n'est pas en accord avec celle prédite *a priori* en considérant la variation des rayons ioniques. En revanche les pyrochlores $R_2Mo_2O_7$ sont tous décrits par la même équation d'état, quelque soit leur état électrique ou magnétique à basse température. Notons que les mesures X sont toutes faites à température ambiante, c'est-à-dire que tous les composés sont dans la phase paramagnétique. On peut s'attendre à ce que l'influence de la terre rare sur l'équation d'état soit beaucoup plus faible que celle du métal de transition.

Dans un deuxième temps, nous étudions l'effet de la pression sur l'ordre magnétique par diffraction de neutrons et µSR. Nous étudions le composé "glace de spin ordonnée" $(Tb_{1-x}La_x)_2Mo_2O_7$ x=0.2 par diffraction de neutrons sous pression (jusqu'à 3.7 GPa) et par µSR (jusqu'à 1.3 GPa), et le composé verre de spin $Tb_2Mo_2O_7$ par neutrons jusqu'à 5.3 GPa. Par diffraction de neutrons, nous montrons que sous pression l'état "glace de spin ordonnée" disparaît graduellement et que pour P=3.7 GPa, le composé $(Tb_{1-x}La_x)_2Mo_2O_7$ x=0.2 a un comportement verre de spin analogue à celui de $Tb_2Mo_2O_7$ à pression ambiante. Les corrélations Tb-Mo changent de ferro à antiferromagnétique, alors que les corrélations Tb-Tb restent ferromagnétiques. Les expérience de muons sous pression dans $(Tb_{1-x}La_x)_2Mo_2O_7$ x=0.2 montrent que la température de transition décroît de 57 K à 50 K entre la pression

ambiante et 1.3 GPa, alors que l'anomalie dynamique à T* semble inchangée. Dans le cas de $Tb_2Mo_2O_7$, qui est déjà verre de spin à pression ambiante, les mesures de diffraction de neutrons montrent que les corrélations ferromagnétiques Tb-Tb diminuent beaucoup sous pression.

Chapter V.

$(Tb_{1-x}La_x)_2Mo_2O_7$: a pressure induced spin glass state

In Chapter IV we analysed the effect of the chemical substitution on structural and magnetic properties in $(Tb_{1-x}La_x)_2Mo_2O_7$ series. In Chapter V we complete this study and analyse the effect of the applied pressure (see Figure 1).

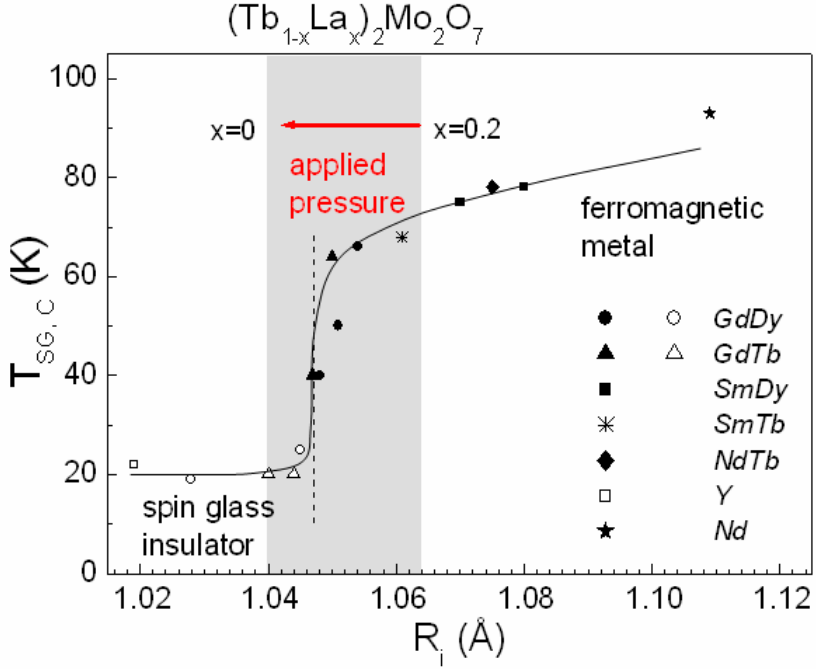

Figure 1. Phase diagram of $(RR')_2Mo_2O_7$ pyrochlores: transition temperature $T_{SG,C}$ against the average ionic radius R_i. The values are taken from Ref. [Gardner'99, Katsufuji'00, Moritomo'01]. The dotted line shows the SG-F phase boundary (R_{ic}=1.047 Å [Katsufuji'00]). The continuous line is a guide to the eyes. The grey region marks the region of interest of our study.

We focus first on the effect of pressure on the structural properties by means of high pressure X ray synchrotron diffraction measurements. We studied five compounds $R_2M_2O_7$ and determined their equation of state. First, for the same *4d* transition metal M=Mo, we varied the rare earth ion R. We chose to study there compounds situated in the three regions of interest of the above phase diagram: the two extreme concentrations x=0 ($a < a_c = 10.33\,\text{Å}$) and x=0.2 ($a > a_c$) of $(Tb_{1-x}La_x)_2Mo_2O_7$ series and also $Gd_2Mo_2O_7$ (located on the verge of the transition, $a \sim a_c$). Then, vice versa, we fix the rare earth R=Tb and analyse the changes when varying the M metal from *sp* (Sn), to *3d* (Ti) and *4d* (Mo). Then, by means of neutron diffraction under pressure, we analyze the effect of the applied pressure on the magnetic order

in the case of: (i) the ordered spin ice $(Tb_{0.8}La_{0.2})_2Mo_2O_7$ and (ii) the spin glass $Tb_2Mo_2O_7$. Finally, for $(Tb_{0.8}La_{0.2})_2Mo_2O_7$, by μSR, we probe the evolution of the spin dynamics under pressure.

V.1. Synchrotron X ray diffraction: crystal structure under pressure

The ambient pressure crystal structure was investigated by combining X ray and neutron diffraction. Neutron diffraction measurements were performed on: 3T2 ($Tb_2Sn_2O_7$ and $Tb_2Ti_2O_7$) and G61 ($Tb_2Mo_2O_7$ and $(Tb_{0.8}La_{0.2})_2Mo_2O_7$) diffractometers of LLB. Due to the natural huge absorbtion of Gd, neutron experiments on $Gd_2Mo_2O_7$ were done using an isotopically enriched ^{160}Gd and the high resolution-high flux diffractometer D2B of the Institute Laüe Langevin (ILL). Refinements of ambient pressure patterns show that all samples crystallize in $Fd\bar{3}m$ cubic space group. There are only two crystallographic parameters of interest: the lattice parameter a and the coordinate of the O1 48f sites, u. Their values are indicated in Table I. As one may see for some of the samples, we estimate these values with a larger error bar than presented in the other chapters. The reason is that this time we tried to take into account the differences between X ray and neutron diffraction and also between neutron diffraction results obtained on different diffractometers.

X ray synchrotron diffraction measurements under pressure at ambient temperature were performed on the ID27 beam line of European Synchrotron Radiation Facility (ESRF), with incident wavelength λ=0.3738 Å. We used a diamond-anvil cell. The transmitting medium and the maximal pressure are as follows: $Tb_2Mo_2O_7$ (nitrogen, P_{max}=35 GPa), $Gd_2Mo_2O_7$ (ethanol-methanol mixture, P_{max}=10 GPa), $(Tb_{0.8}La_{0.2})_2Mo_2O_7$ (ethanol-methanol mixture, P_{max}=10 GPa), $Tb_2Ti_2O_7$ (neon, P_{max}=42 GPa) and $Tb_2Sn_2O_7$ (ethanol-methanol mixture, P_{max}=35 GPa). For $Tb_2M_2O_7$ (M=Mo, Ti and Sn) we went to higher pressures in order to compare the effects of M substitution on the equation of state. Per contra, for the other two molybdenum pyrochlores ($Gd_2Mo_2O_7$ and $(Tb_{0.8}La_{0.2})_2Mo_2O_7$) we used a maximum pressure of 10 GPa, which goes well beyond the ferromagnetic-spin glass transition.

Under pressure, till to the highest pressure value, there is a peak broadening but neither additional peaks, nor a splitting of the existing ones. It shows that the crystal structure remains cubic with $Fd\bar{3}m$ space group in the whole pressure range.

Figure 1 shows the ambient temperature X ray diffraction patterns for $(Tb_{0.8}La_{0.2})_2Mo_2O_7$ (Figure 2a) and $Tb_2Sn_2O_7$ (Figure 2b), respectively. Each time two typical pressures were chosen: the lowest and the highest measured pressures. It clearly shows that in both cases there is no structural phase transition in the studied pressure interval.

The evolution of the structural parameters a and u with pressure was determined as follows. For each sample we made the following analysis. First we fitted some selected Bragg peaks, yielding the pressure dependence of a only but with high accuracy. Then we analyzed the whole patterns using FULLPROF in the profile matching mode, with no constraint on the peak intensities. Finally we performed a structure analysis with FULLPROF, allowing the determination of both a and u. The results are also shown in Figure 2, with the corresponding agreement Bragg factors in the legend. A Thompson-Cox-Hastings pseudo-Voigt peak shape function was used (for details see section II.2.2.2). The determination of a agrees for the three analysis. Its evolution with pressure is shown in Figure 3 for all samples.

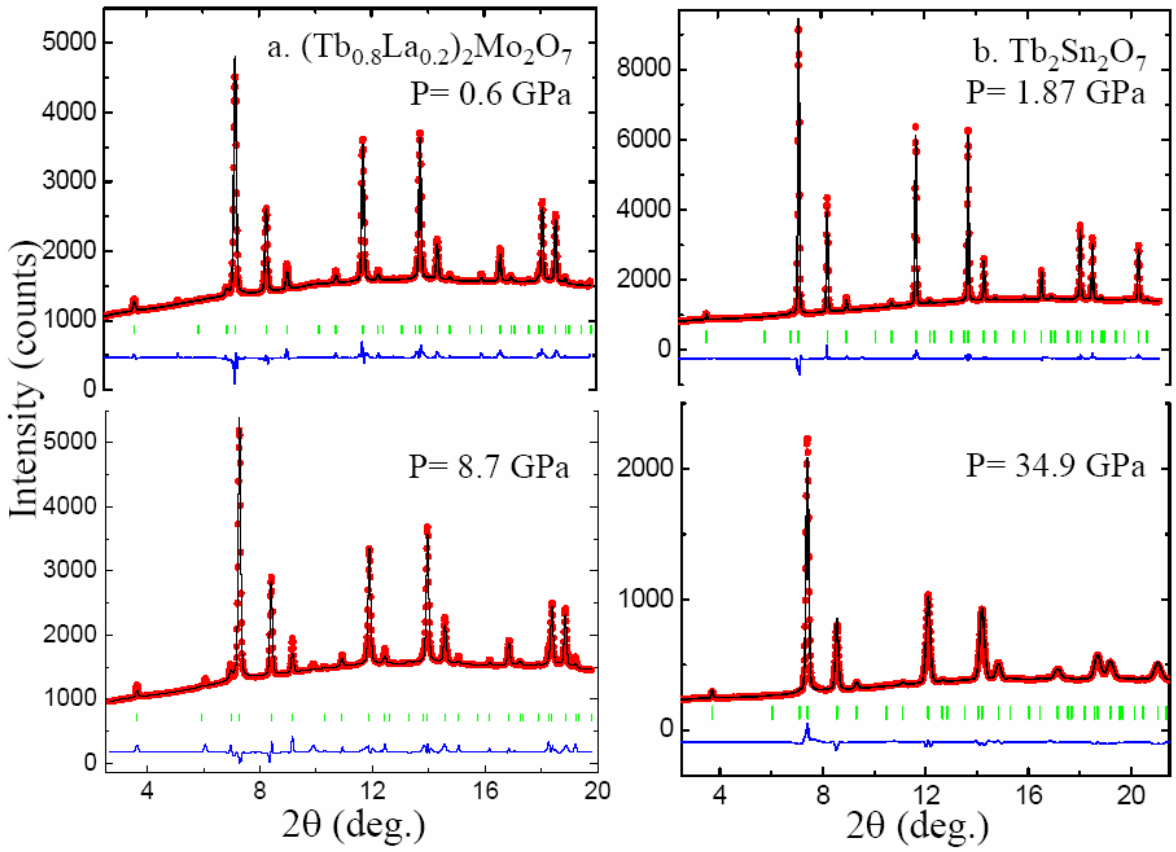

Figure 2. X ray diffraction intensity versus the scattering angle 2θ, with the incident X ray wavelength λ=0.3738 Å, at ambient temperature. a. $(Tb_{0.8}La_{0.2})_2Mo_2O_7$ at P= 0.6 GPa (R_B = 11.52 %) and 8.7 GPa (R_B = 10.41 %); b. $Tb_2Sn_2O_7$ at P=1.87 GPa (R_B = 6.09 %) and 34.9 GPa (R_B = 8.18 %). Solid lines show the best refinement with cubic $Fd\bar{3}m$ symmetry and the difference spectrum (bottom). Tick marks show the Bragg peaks positions.

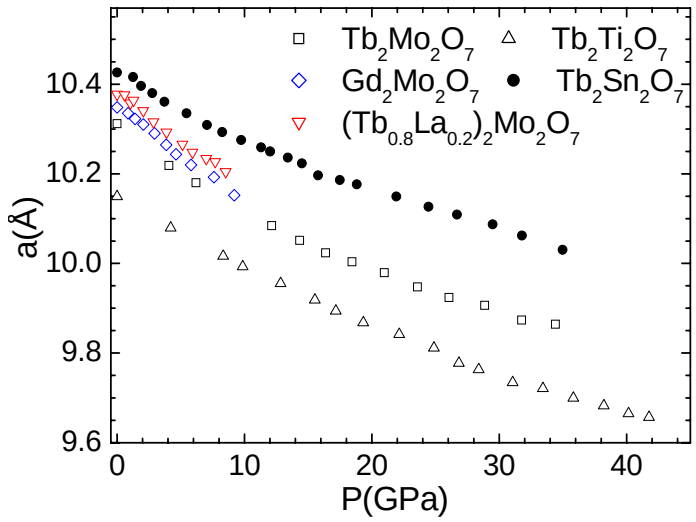

Figure 3. Pressure dependence of the lattice parameter a (deduced from the structure analysis), at ambient temperature, for the five samples: $Tb_2Mo_2O_7$, $Gd_2Mo_2O_7$, $(Tb_{0.8}La_{0.2})_2Mo_2O_7$, $Tb_2Sn_2O_7$ and $Tb_2Ti_2O_7$.

The equation of state was determined by fitting the experimental data to the Murnaghan equation (see Ref. [Strässle'05]):

$$\frac{V}{V_0} = \left(P\frac{B_1}{B_0} + 1 \right)^{-\frac{1}{B_1}} \qquad [V.1]$$

with V_0, B_0 and B_1 the volume at zero pressure, the bulk modulus and its first pressure derivative, respectively.

In a first step, when fitting, we took into account the whole experimental pressure range for all samples, no matter the pressure transmitting medium. We performed systematic fits using different values for the first pressure derivative of the bulk modulus, B_1. Then we fixed the value B_1=6, which allows a reasonable fit for all samples in the whole pressure range. As clearly seen in Figure 4, for $R_2Mo_2O_7$ the variation of V/V_0 versus pressure is independent of the mean ionic radius of the rare earth R_i. $Tb_2Mo_2O_7$ ($R_i < R_{ic}$), $Gd_2Mo_2O_7$ ($R_i \sim R_{ic}$) and $(Tb_{0.8}La_{0.2})_2Mo_2O_7$ ($R_i > R_{ic}$) are described by the same equation of state. The values of the bulk modulus B_0 deduced from this fit are listed in Table I.

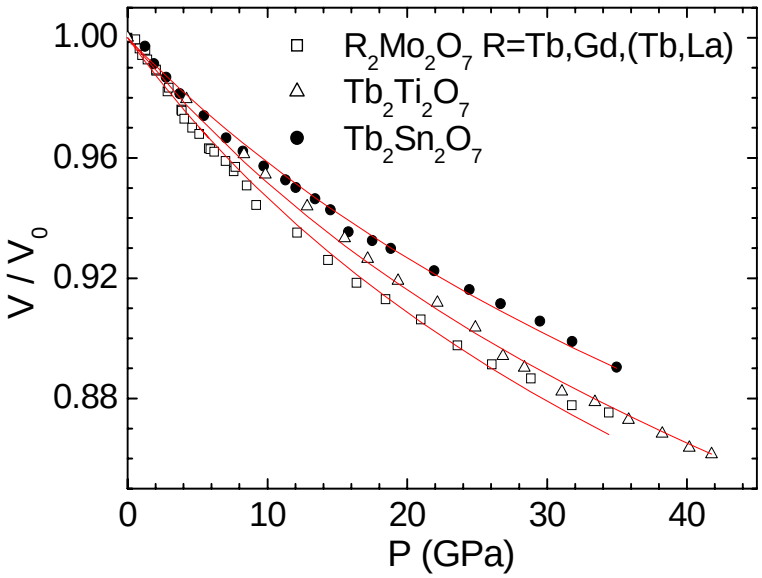

Figure 4. Pressure dependence of V/V_0, with V_0 the unit cell volume at ambient pressure. Lines correspond to fits using Murnaghan function, given by equation [V.1], with fixed B_1=6 in the whole pressure range for all samples. The corresponding values of B_0 are given in Table I.

The high B_1 value found in the above analysis may reflect some non-hydrostaticity above 10 GPa, considering the fact that different transmitting mediums were used, and only neon is believed to be fully hydrostatic at high pressure. The non-hydrostaticity of the ethanol-methanol mixture (used for $Tb_2Sn_2O_7$) and nitrogen (used for $Tb_2Mo_2O_7$) with regards to that of neon (used in $Tb_2Ti_2O_7$) is confirmed by a strong increase of the peak width above 10 GPa, as shown by the pressure dependence of the parameter Y (Figure 5) (as shown in section II.2.2.2, this parameter corresponds to the Lorentzian component of a modified Thomson-Cox-Hastings pseudo-Voigt function). This prevents to give a physical meaning to the high B_1 value.

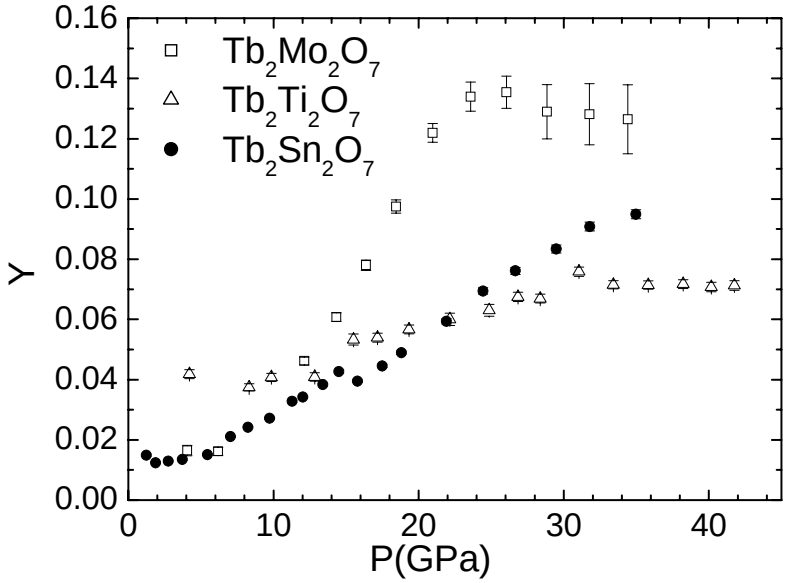

Figure 5. The variation of the parameter Y (related to the intrinsic peak width) with pressure.

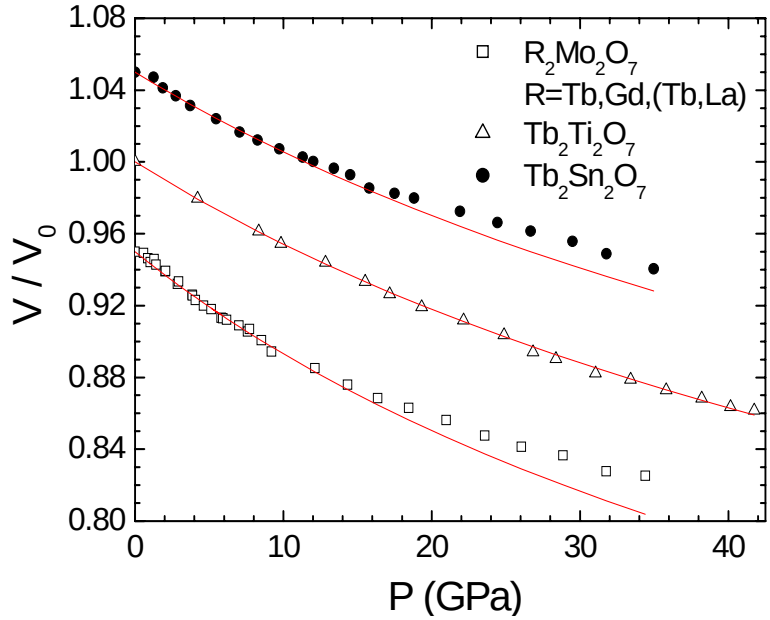

Figure 6. Pressure dependence of V/V_0. Lines correspond to fits using Murnaghan function. For clarity the $R_2Mo_2O_7$ and $Tb_2Sn_2O_7$ results were shifted with regard to $Tb_2Ti_2O_7$ with 0.05. The bulk modulus was fixed: B_1=4.5. For $Tb_2Ti_2O_7$ the fit was done considering the whole pressure range, while for $R_2Mo_2O_7$ and $Tb_2Sn_2O_7$ the fits correspond to the interval 0-10 GPa. The corresponding values of B_0 are also indicated in Table I, last column.

So in a second step, we took as reference $Tb_2Ti_2O_7$ measured with the neon transmitting medium. As shown in Figure 6, a good fit of the $Tb_2Ti_2O_7$ data can be obtained with a more reasonable value of the bulk modulus derivative, B_1=4.5. An independent fit of B_0 and B_1 yields the values B_0=187(3) GPa and B_1=4.8(3). We then fitted the data of the other samples, $R_2Mo_2O_7$ and $Tb_2Sn_2O_7$, by fixing B_1=4.5 and limiting the fitted pressure range to 10 GPa, an interval where ethanol-methanol mixture or nitrogen provide hydrostatical pressure conditions. The corresponding values of B_0 are listed in Table I, last column.

We consider these values as the most reliable, since they fit well the $Tb_2Ti_2O_7$ data in the whole pressure range and also the region of interest 0-10 GPa of pyrochlores of molybdenum. Therefore we used them in the following and obtained the equation of state:

$$a = \frac{a_0}{\left(0.0302\,P + 1\right)^{0.074}} \qquad [V.2]$$

or :

$$P = \frac{\left(\frac{a}{a_0}\right)^{13.5} + 1}{0.0302} \qquad [V.3]$$

with a_0 the ambient pressure lattice parameter.

As shown in Table I, when passing from Mo to Ti and then to Sn the bulk modulus increases: $B_0(Mo) < B_0(Ti) < B_0(Sn)$. This is not *a priori* expected from the variation of the ionic radius, evaluated in the periodic table to 0.68, 0.68 and 0.71 for Mo^{4+}, Ti^{4+} and Sn^{4+}, respectively. And this remains true whatever the value fixed for B_1.

compound	a (Å) ambient pressure	u (units of a) ambient pressure	B_0 (GPa) B_1=6	B_0 (GPa) B_1=4.5
$Tb_2Mo_2O_7$	10.312(1)	0.334(3)	154(4)	149(2)
$Gd_2Mo_2O_7$	10.348(1)	0.334(1)	154(4)	149(2)
$(Tb_{0.8}La_{0.2})_2Mo_2O_7$	10.378(2)	0.331(1)	154(4)	149(2)
$Tb_2Ti_2O_7$	10.149(2)	0.328(2)	173(3)	191(1)
$Tb_2Sn_2O_7$	10.426(2)	0.336(1)	207(5)	198(2)

Table I. Ambient pressure and temperature structural parameters of $R_2Mo_2O_7$ (R= Tb, Gd, (Tb,La)) and $Tb_2M_2O_7$ (M=Ti and Sn): the cubic lattice parameter a and oxygen positions of O1 48f sites [u, 1/8, 1/8]. The bulk modulus B_0 as obtained from the fits using the Murnaghan equation [V.1] is also indicated. The pressure derivative of the bulk modulus was first fixed at B_1=6, when the fit takes into account the whole pressure range for all samples. Then it was fixed at B_1=4.5 when we took into account the whole pressure range for $Tb_2Ti_2O_7$ and the 0-10 GPa interval for $R_2Mo_2O_7$ and $Tb_2Sn_2O_7$.

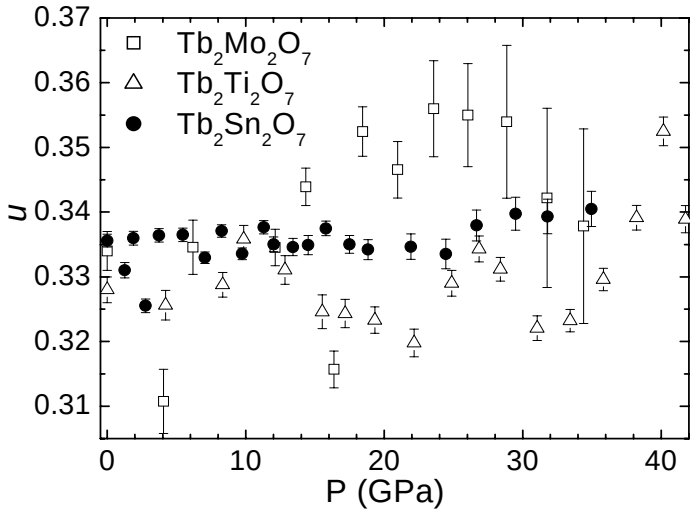

Figure 7. Oxygen position parameter u versus pressure at ambient temperature for Tb pyrochlores: $Tb_2Mo_2O_7$, $Tb_2Ti_2O_7$ and $Tb_2Sn_2O_7$.

The determination of the oxygen coordinate u is more intricate. It is directly related to the Bragg intensities, which may be partly affected by either texture effects or non isotropic powder averaging for very small samples. We still obtained reasonable values, with a scattering of about ± 5 %. In Figure 7, the u parameter is shown versus pressure when varying the transition metal, M= Mo, Ti and Sn. In each case u is independent of the applied pressure in the error bar limits. The u values for $Tb_2Ti_2O_7$ are systematically lower than for $Tb_2Sn_2O_7$ whereas the value for $Tb_2Mo_2O_7$ seems to be slightly higher. Our results for Ti and Sn samples agree with previous results [Kumar'06], which show that the cubic crystal structure is stable and u is independent of pressure in this pressure range.

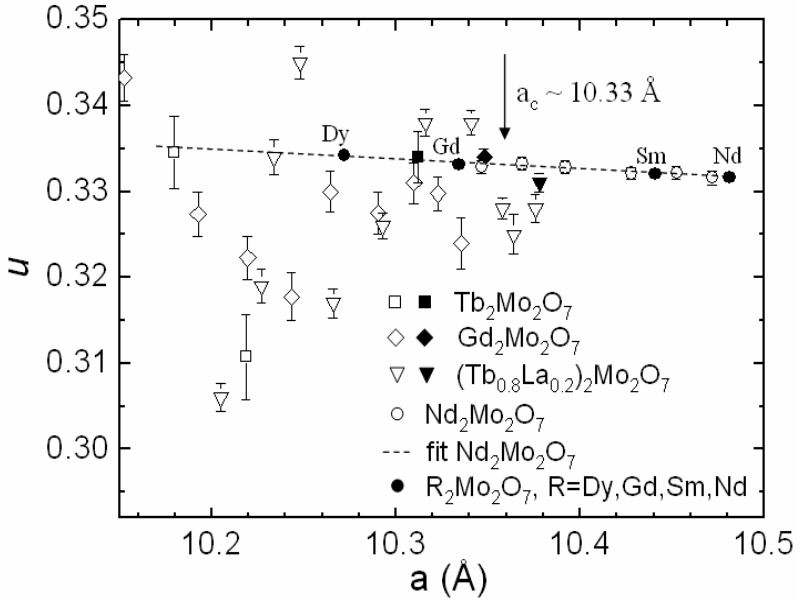

Figure 8. Oxygen coordinate u against the lattice parameter a for the Mo pyrochlores: $Tb_2Mo_2O_7$, $Gd_2Mo_2O_7$ and $(Tb_{0.8}La_{0.2})_2Mo_2O_7$. The open symbols correspond to data under pressure, while the solid ones indicate the ambient pressure data. For comparison the behaviour of $Nd_2Mo_2O_7$ under pressure is shown, as cited from Ref. [Ishikawa'04]. The dashed line is a linear fit of these data. The effect of rare earth chemical substitution as in Ref. [Moritomo'01] is also shown. $a_c \sim 10.33$ Å corresponds to the critical threshold.

Figure 8 shows the evolution of the oxygen coordinate u with the lattice constant for the Mo pyrochlore samples: $Tb_2Mo_2O_7$ ($a < a_c \sim 10.33$ Å), $Gd_2Mo_2O_7$ ($a \sim a_c$) and $(Tb_{0.8}La_{0.2})_2Mo_2O_7$ ($a > a_c$), in the pressure range 0-10 GPa. A pressure of 10 GPa is well beyond the values needed to induce the F-SG transition for both Gd and $(Tb_{0.8}La_{0.2})_2Mo_2O_7$ samples. The threshold pressures corresponding to the critical value of the lattice constant $a_c \sim 10.33$ Å are calculated using the equation of state [V.3]. For $(Tb_{0.8}La_{0.2})_2Mo_2O_7$ the critical pressure is around 2.1 GPa, while in the case of $Gd_2Mo_2O_7$ it lies in the pressure range 0.6-2.4 GPa according to different studies ([Mirebeau'06] and Refs. therein). Within the accuracy of our measurements we cannot evidence any systematic variation of u throughout the threshold. Our results are reported together with ambient pressure data on several samples with ionic radius encompassing the threshold, data from Ref. [Moritomo'01], as well as high pressure X ray data on $Nd_2Mo_2O_7$ performed up to 10 GPa [Ishikawa'04], where the powder averaging seems to be better than here. Our determination of u situates in the expected range. The very small increase observed under chemical pressure and in Ref. [Ishikawa'04] (the dashed line in Figure 8) corresponds to an increase from 0.3315 to 0.3348, namely about 1 % when a varies from 10.5 to 10.2 Å) is beyond the accuracy of the present pressure data.

V.2. Neutron diffraction: magnetic structure under pressure

The neutron diffraction measurements under pressure were performed on the diffractometer G61 of LLB (λ=4.741 Å) in the high pressure version (see Chapter II). The measurements were performed at 1.05, 1.9 and 3.7 GPa for $(Tb_{0.8}La_{0.2})_2Mo_2O_7$ and at 5.3 GPa in the case of $Tb_2Mo_2O_7$, in the temperature range 1.4-100 K. The magnetic intensity is obtained by subtracting a spectrum in the paramagnetic region (100 K) and then, in order to be able to compare diffraction patterns measured in different conditions, we calibrated it by multiplying by a factor $F = 1/(IntI_{(222)} \cdot L)$, with $IntI_{(222)}$ the integrated intensity of the (222) peak at 100 K and $L = 1/(\sin\theta \cdot \sin 2\theta)$ the Lorentzian factor (see Chapter II).

V.2.1. $(Tb_{0.8}La_{0.2})_2Mo_2O_7$: "ordered spin ice" under pressure

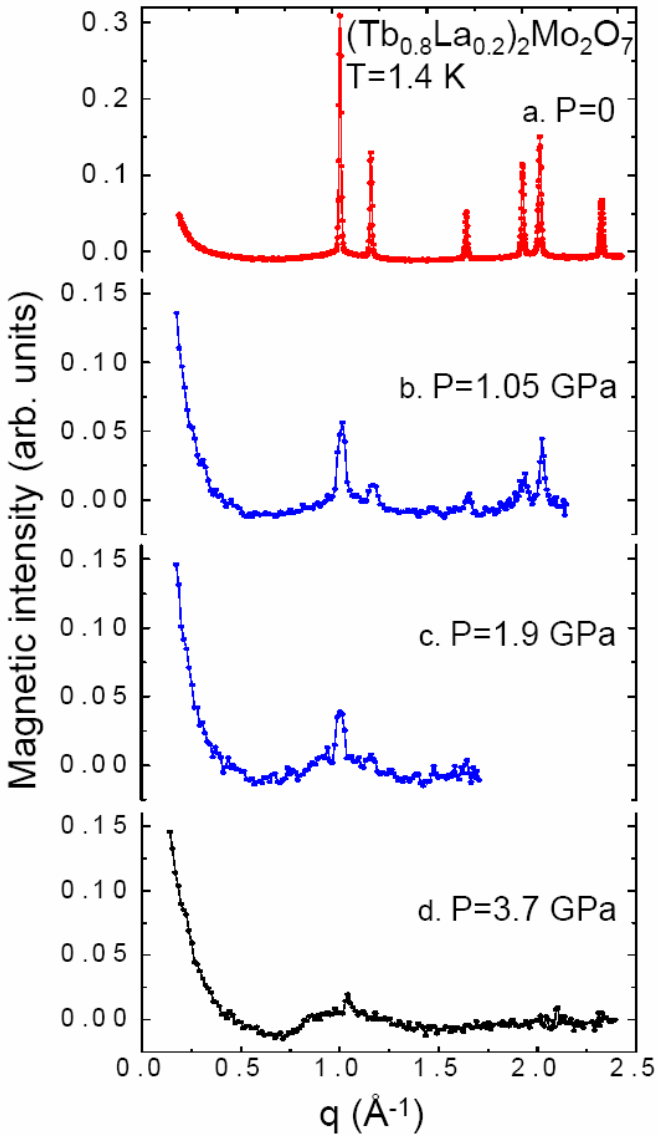

Figure 9. Magnetic intensity of $(Tb_{0.8}La_{0.2})_2Mo_2O_7$ versus the scattering vector $q = 4\pi \sin\theta / \lambda$, with the incident neutron wavelength λ=4.741 Å, at T= 1.4 K. A spectrum in the paramagnetic region (100 K) was subtracted. a. At ambient pressure; b-d. Under an applied pressure of 1.05, 1.9 and 3.7 GPa, respectively.

Figure 9 shows the evolution of the magnetic neutron diffraction patterns from ambient pressure (Figure 9a) to 1.05, 1.9 and finally to 3.7 GPa (Figure 9b-d). We note first that there are two magnetic phases which coexist: a short range magnetic order corresponding to the diffuse scattering and a long range one corresponding to the Bragg peaks. When increasing the applied pressure one may clearly observe that the contribution of the long range ordered phase (Bragg peaks) decreases gradually, while the disordered phase (diffuse scattering) increases. The magnetic pattern at 1.05 GPa is quite similar to that of $(Tb_{0.9}La_{0.1})_2Mo_2O_7$ at ambient pressure, while at 3.7 GPa the long range order is practically destroyed and the spectrum is similar to that of $Tb_2Mo_2O_7$ at ambient pressure (see Chapter IV, Figure 6). This result confirms our expectations: at 3.7 GPa > $P_c \sim 2.1$ GPa (corresponding to $a_c \sim 10.33$ Å and calculated using the equation of state) the system passed into the spin glass region of the phase diagram from Figure 1. We also notice that the intensity of the SANS signal, observed for $q < 0.5$ Å^{-1} and corresponding to ferromagnetic correlations, increases under applied pressure.

We analyse in more details the evolution of the magnetic order under applied pressure.

- *P=1.05 GPa* (the corresponding lattice parameter is $a \sim 10.354$ Å, according to the equation of state determined in section V.1)

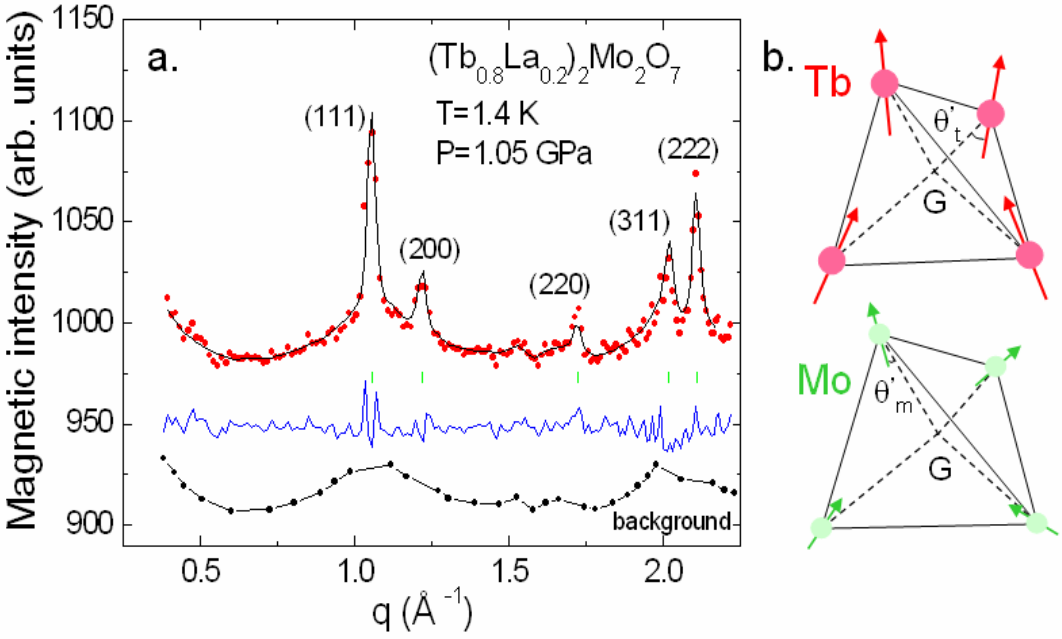

Figure 10. a. Magnetic diffraction pattern for $(Tb_{0.8}La_{0.2})_2Mo_2O_7$ versus the scattering vector q, at T= 1.4 K and P= 1.05 GPa, with λ=4.741 Å. A spectrum at 100 K was subtracted. The solid lines show the best refinement (R_B =20 %) and the difference spectrum (bottom). Tick marks indicate the Bragg peak positions. The background is also indicated; b. The corresponding magnetic structure: Tb and Mo tetrahedra.

As for the ambient pressure case, for P=1.05 GPa the magnetic Bragg peaks belong to the $Fd\bar{3}m$ symmetry group and superimpose on the nuclear ones, indicating a propagation vector $\vec{k}$ =0. The presence of (200) and (220) peaks indicates also a non-collinear magnetic structure. The Rietveld analysis was made with a one phase model which fits well the magnetic peaks (the long range phase). The diffuse scattering was included into the background. At T=1.4 K, the best refinement ($R_B \sim 20$ %) is shown in Figure 10a, with the corresponding spin arrangements in Figure 10b. The LRO Tb^{3+} magnetic moments keep the

local spin ice configuration, but with a different angle $\theta_t' = 28.3°$ with regards to ambient pressure. The Mo^{4+} also turn to a local spin ice order, making an angle $\theta_m' = 7.3°$ with the local anisotropy axes or an angle $\theta_m' = 62°$ with the [001] axis. The values of the ordered magnetic moments are: M_{Tb}^{LRO}=3.8(8) μ_B and M_{Mo}^{LRO}=0.4(9) μ_B, respectively. The correlation length, deduced from the intrinsic peak width, is roughly $L_C^{LRO} \sim 180$ Å. Table II shows for comparison the values and canting angles of Tb^{3+} and Mo^{4+} magnetic moments as well as the long range order correlation length at ambient and under pressure.

	$M_{Tb}^{LRO}(\mu_B)$	$\theta_t(°)$	$M_{Mo}^{LRO}(\mu_B)$	$\theta_m(°)$	L_C^{LRO} (Å)
$P = 0$	4.66(2)	11.6	0.64(3)	6.8	~ 3700
$P = 1.05$ GPa	3.8(8)	28.3	0.4(9)	62	~ 180

Table II. $(Tb_{0.8}La_{0.2})_2Mo_2O_7$, comparison between the ambient pressure and P=1.05 GPa magnetic order: values and canting angles of Tb^{3+} and Mo^{4+} magnetic moments, respectively, as well as the long range order correlation length. We recall that θ_t is the angle made with the local anisotropy axes <111>, while θ_m is the angle made with the [001] axes.

One may easily see that under the effect of pressure the magnetic order diminishes. If taking as reference the ambient pressure state, under applied pressure the canting angle of Tb^{3+} increases, Mo^{4+} becomes less ferromagnetic and both ordered magnetic moments and correlation length are reduced. Of course a two phases model, which takes into account the coexistence of LRO and SRO phases with the same symmetry, would be preferable. But this would suppose an important number of parameters, which is not compatible with the quality of the spectrum and the reduced number of peaks.

- *P=1.9 GPa* ($a \sim 10.336$ Å)

In this case a Rietveld analysis with a model with Tb^{3+} and Mo^{4+} magnetic moments and peak width as parameters was not possible. The q range is reduced and there is just one magnetic peak. However we tried to do some simulations, starting from P=1.05 GPa magnetic moments and fixing and/or refining the Tb^{3+} and/or Mo^{4+} magnetic moments, with different correlation length. The final result (see Figure 12) takes into account all these simulations and of course there are important error bars.

- *P=3.7 GPa* ($a \sim 10.298$ Å)

At this pressure the magnetic Bragg peaks disappear and we observe a diffuse magnetic scattering for $q > 0.5$ Å^{-1} and a SANS signal for $q < 0.5$ Å^{-1}, as for $Tb_2Mo_2O_7$ at ambient pressure. In the range $q = 0.5 - 2.5$ Å^{-1} we analyse the magnetic correlations by the short range model proposed in Ref. [Greedan'90, Greedan'91] and also applied for $Tb_2Mo_2O_7$ (section IV.3.1). The fit by the sum of radial correlation functions (see Figure 11 bottom continuous line) yields the spin correlation parameters γ_i up to the fourth coordination shell (~ 7.3 Å). The Tb-Tb correlations are ferromagnetic ($\gamma_{1,3,4} > 0$), while the Tb-Mo are antiferromagnetic ($\gamma_2 < 0$). If comparing to ambient pressure results, one may see the similitude with $Tb_2Mo_2O_7$ and the difference with regard to $(Tb_{0.8}La_{0.2})_2Mo_2O_7$, where all correlations are ferromagnetic. The evolution of spin correlation parameters $\gamma_{1,2,3,4}$ with temperature is shown in inset of Figure 11. Again Mo-Mo correlations are not seen, due to the smaller magnetic moment of Mo^{4+} in regard to that of Tb^{3+}. The intense signal below 0.5 Å^{-1}

corresponds to Tb-Tb ferromagnetic correlations. A Lorentzian fit (Figure 11 upper dotted line) gives a correlation length of ~ 18(7) Å, comparable to that found for $Tb_2Mo_2O_7$.

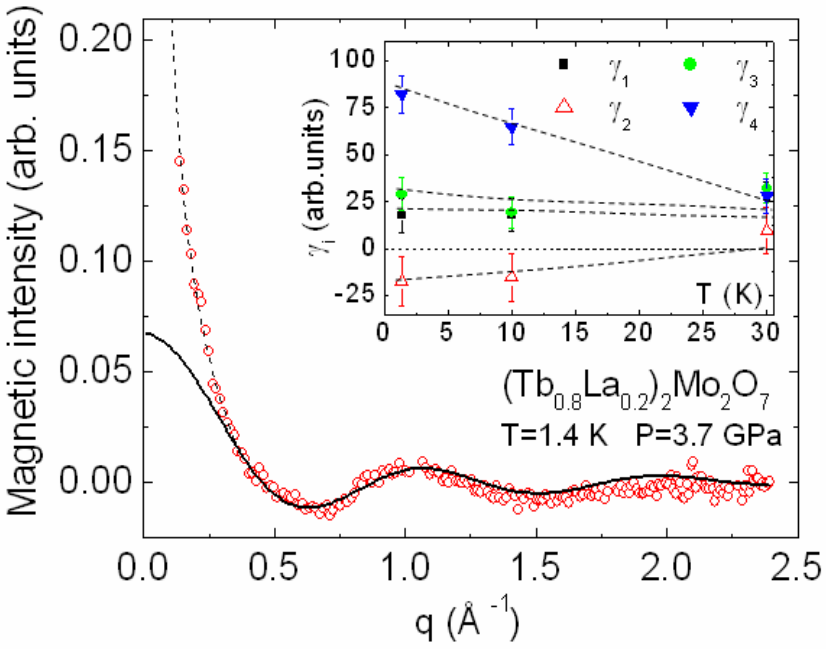

Figure 11. Magnetic intensity of $(Tb_{0.8}La_{0.2})_2Mo_2O_7$ against the scattering vector q, at T= 1.4 K and P= 3.7 GPa. λ=4.741 Å. A spectrum at 100 K was subtracted. The solid line (bottom) represents the fit with the SRO model, including the longer range ferromagnetic correlations (the upper dashed line). In inset the temperature dependence of the correlation parameters γ_i (i =1-4) from the fit using the SRO model. Dashed lines are guides to the eye.

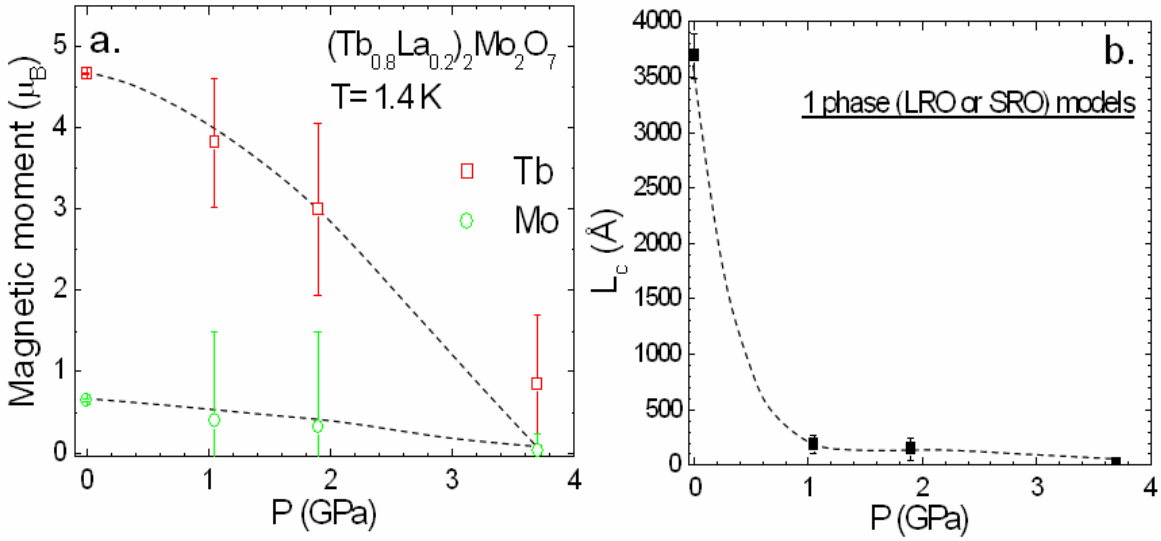

Figure 12. $(Tb_{0.8}La_{0.2})_2Mo_2O_7$ at T=1.4 K: a. Tb^{3+} and Mo^{4+} ordered magnetic moments versus pressure; b. Correlation length versus pressure as obtained from Rietveld analysis with 1 phase models (P=0, 1.05 and 1.9 GPa) or SRO model fit (P.3.7 GPa). Dashed lines are guides to the eye.

Figure 12 gives a summary of the evolution of the magnetic order under the effect of applied pressure. When increasing pressure, the magnetic order is gradually destroyed: the ordered magnetic moments and the correlation length are both decreasing towards zero.

V.2.2. $Tb_2Mo_2O_7$: spin glass under pressure

After showing that an "ordered spin ice" becomes a spin glass under the effect of applied pressure, we analyse the effect of pressure on a system which is already a spin glass at ambient pressure: $Tb_2Mo_2O_7$.

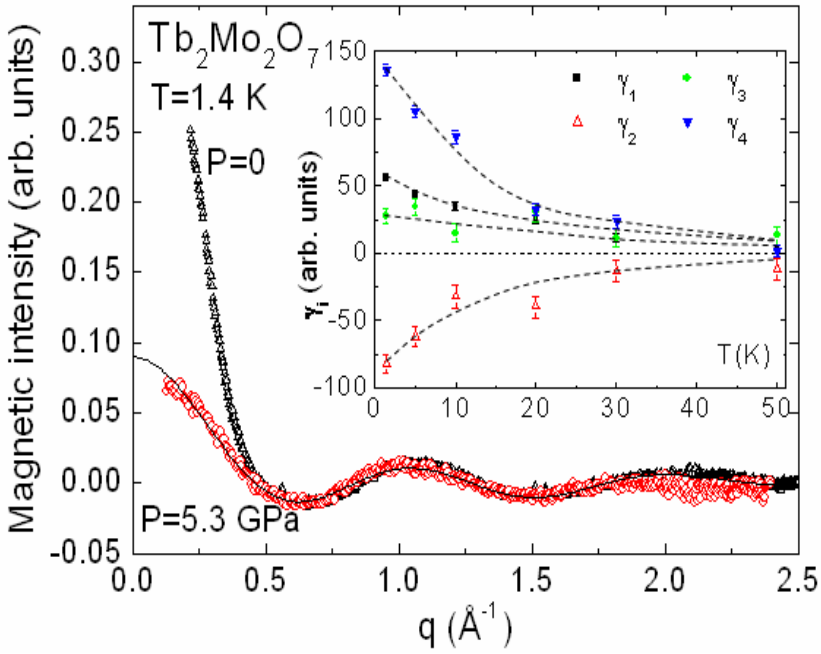

Figure 13. Magnetic scattering in $Tb_2Mo_2O_7$ at T=1.4 K: ambient and applied pressure P=5.3 GPa. A pattern at 100 K was subtracted. The fit of the P=5.3 GPa data is made using the SRO model. The temperature dependence of the correlation coefficients is shown in the inset, with dashed lines as guides to the eye.

Figure 13, which compares magnetic spectra at P=0 and 5.3 GPa (the corresponding lattice parameter is $a \sim 10.201$ Å), clearly shows that the diffuse scattering above 0.5 $Å^{-1}$ is almost unchanged by pressure. The correlation parameters keep the same sign as at ambient pressure ($\gamma_{1,3,4} > 0$ and $\gamma_2 < 0$, as shown in inset), yielding ferromagnetic Tb-Tb and antiferromagnetic Tb-Mo correlations, respectively. The values at ambient and under pressure are similar in the limit of the error bars. Per contra, the SANS signal and hence the corresponding ferromagnetic Tb-Tb correlations are pressure dependent: they decrease with increasing pressure. The correlation length decreases under pressure and the SRO model yields now a good fit for the whole q interval. Under the effect of pressure the correlations length decreases from ~ 20(7) Å at ambient pressure to ~ 7.3 Å (corresponding to the fourth order neighbours).

V.3. μSR: spin dynamics under pressure

In Chapter IV we showed how the spin dynamics evolves when substituting Tb by La. In this chapter we analyse the effect of the applied pressure. μSR experiments under pressure were performed on the GPD instrument of the Paul Scherrer Institute in the temperature range 3.1-122.5 K.

The μSR spectra under pressure are fitted with:

$$AP_Z(t) = A_1 P_{Z\,sample}(t) + A_2 e^{0.455t}\cos(2\pi\cdot 50.63t + \phi_2) + \\ + A_3 e^{0.455t}\cos(2\pi\cdot 101.26t + \phi_3) + A_4 P_{Z\,pressure\,cell}(t) \qquad [V.4]$$

As stated in Chapter II, the first term corresponds to the sample, the second and third terms correspond to an oscillating accidental background, while the fourth term corresponds to the pressure cell. Figure 14 represents a fit with the equation [V.4], where only the contribution from sample and pressure cell, respectively, are shown.

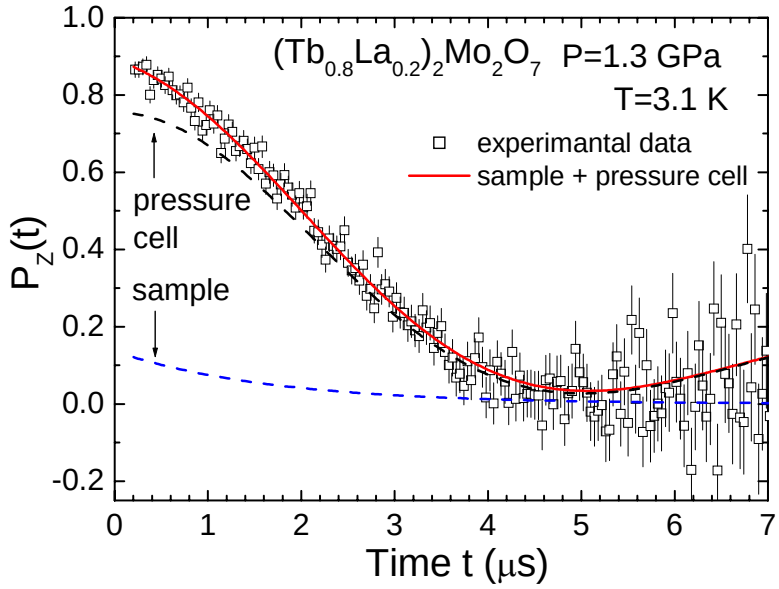

Figure 14. μSR spectra for $(Tb_{0.8}La_{0.2})_2Mo_2O_7$ recorded under pressure P=1.3 GPa and at T=3.1 K. The contribution of the sample and of the pressure cell are indicated.

Speaking about the sample, under pressure and for $T < T_C \sim 50$ K, it was difficult to extract any information from the μSR spectra at small times (meaning the 2/3 term of equation IV.7, Chapter IV). This is due to the large background of the pressure cell and also to the fast depolarisation of the 2/3 term. Consequently, below T_C we fitted the experimental data using only the 1/3 term, with an exponential depolarisation function, and skipping the first 0.2 μs of the μSR spectrum:

$$P_{Z\,sample}(t) = \frac{1}{3}\exp(-\lambda t) \qquad [V.5]$$

For $T > T_C$ we also used an exponential function:

$$P_{Z\,sample}(t) = \exp(-\lambda t) \qquad [V.6]$$

where λ is the muon spin depolarisation rate.

The pressure cell contribution was fitted by a Gaussian Kubo-Toyabe function (see Chapter II, section II.4.1.):

$$P_{Z\,pressure\,cell}(t) = \frac{1}{3} + \frac{2}{3}\left(1-\Delta^2 t^2\right)\exp\left(-\frac{\Delta^2 t^2}{2}\right) \qquad [V.7]$$

Figure 15b shows the temperature dependence of the muon depolarization rate λ, for P=1.3 GPa. It is compared to that obtained at ambient pressure (Figure 15a). As one may see under the effect of pressure $T_C = 57(1)$ K decreases to $T_C' \sim 50$ K. The anomaly seen at ambient pressure at $T^* = 15(5)$ K is strongly suppressed but seems to be present and located roughly in the same temperature range $T^{*'} \sim 20$ K. Under the effect of pressure T_C decreases towards $T^{*'}$.

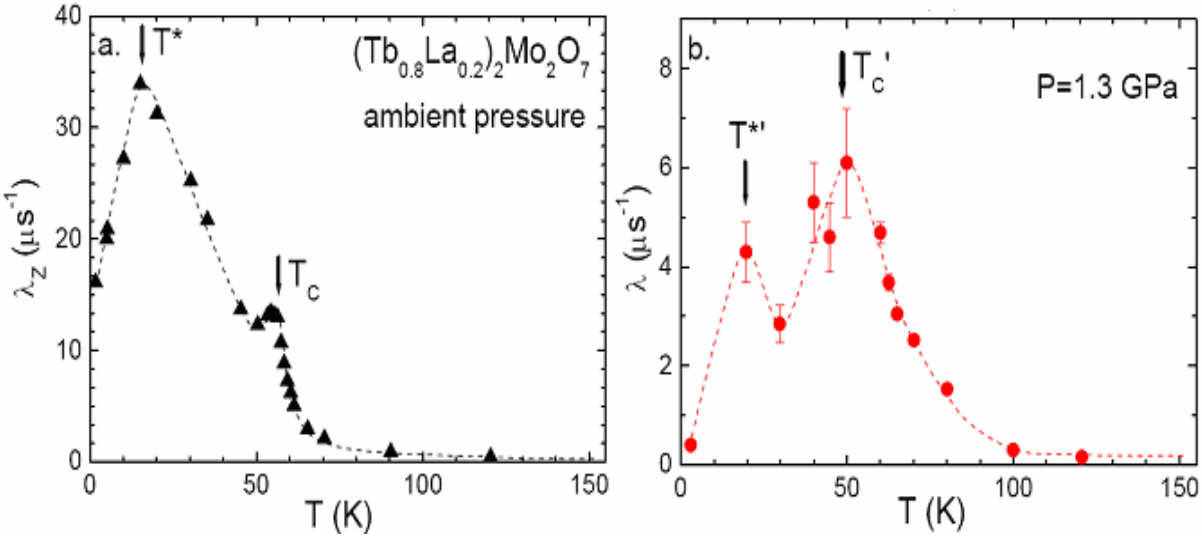

Figure 15. μSR results on $(Tb_{0.8}La_{0.2})_2Mo_2O_7$: the muon relaxation rate versus temperature at ambient (a) and under applied pressure P=1.3 GPa (b). The two transition temperatures are indicated.

V.4. Conclusions

In this chapter we focused first on the high pressure X ray synchrotron diffraction measurements. We have studied the crystal structure of five pyrochlore compounds: $Tb_2Mo_2O_7$ ($a < a_c$), $Gd_2Mo_2O_7$ ($a \sim a_c$), $(Tb_{0.8}La_{0.2})_2Mo_2O_7$ ($a > a_c$) and also $Tb_2Ti_2O_7$ and $Tb_2Sn_2O_7$. We have shown that there is no structural phase transition till to the highest applied pressure. We analysed the pressure dependence of the lattice parameter a and of the oxygen position parameter u. The dependence $a(P)$, *i.e.* the equation of state, yields the bulk modulus. In $Tb_2M_2O_7$ (M=Mo, Ti and Sn) the bulk modulus increases when varying the transition metal from Mo to Ti and then to the *sp* metal Sn. In contrast, the $R_2Mo_2O_7$ pyrochlores are all described by the same equation of state, whatever their electric/magnetic state. In the analysed pressure range, the oxygen parameter u is independent of pressure.

We analysed then the effect of the applied pressure on the magnetic properties, for both statics (by neutron diffraction) and dynamics (by μSR). We showed that when compressing the lattice under applied pressure the magnetic order of the "ordered spin ice" $(Tb_{0.8}La_{0.2})_2Mo_2O_7$ disappears gradually and for P=3.7 GPa the system has a spin glass like behaviour similar to that of $Tb_2Mo_2O_7$. Tb-Mo correlations change from ferro- to antiferromagnetic, while Tb-Tb ones rest ferromagnetic. In the case of $Tb_2Mo_2O_7$, which is already a spin glass at ambient pressure, the pressure decreases the ferromagnetic Tb-Tb correlations. The μSR experiments under pressure on $(Tb_{0.8}La_{0.2})_2Mo_2O_7$ show the dynamical anomaly at roughly the same temperature as at ambient pressure $T^* \sim 20$ K, while T_C decreases from ~ 57 K to ~ 50 K.

Chapitre VI.

$(Tb_{1-x}La_x)_2Mo_2O_7$, x=0-0.2. Discussion

Dans les Chapitres IV et V, nous avons analysé respectivement l'influence d'une pression chimique et appliquée sur les propriétés structurales et magnétiques de la série $(Tb_{1-x}La_x)_2Mo_2O_7$, x=0-0.2. L'étude de ces composés fournit la première description microscopique des corrélations et fluctuations de spin au seuil de la transition ferromagnétique –verre de spin. Dans ce chapitre nous faisons la synthèse de ces résultats et nous les discutons par rapport aux autres pyrochlores de molybdène.

Les mesures de rayons X sous pression fournissent l'équation d'état des pyrochlores de molybdène. En utilisant cette équation, nous pouvons combiner toutes nos données expérimentales sur les températures de transition magnétiques obtenues par susceptibilité magnétique, diffraction de neutrons et μSR, à pression ambiante et sous pression, et tracer un diagramme de phase complet pour la série $(Tb_{1-x}La_x)_2Mo_2O_7$. Ce diagramme de phase, qui reporte les températures de transition en fonction du paramètre de réseau, constitue le point central de ce chapitre. Il peut être comparé aux diagrammes de phase précédemment déterminés par des mesures macroscopiques pour les pyrochlores de molybdène. De façon intéressante, il montre en dessous de la phase paramagnétique, non seulement deux phases magnétiques, ferromagnétique et verre de spin, mais aussi une troisième phase mixte.

Les mesures macroscopiques et les calculs de structure de bande suggèrent que la transition verre de spin- ferromagnétique est due à un changement du signe des interactions Mo-Mo, qui passent d'un état antiferromagnétique frustré par la géométrie à un état ferromagnétique. Bien que le molybdène semble jouer un rôle dominant, notre étude met en valeur le rôle important joué par la terre rare. Nous comparons la "glace de spin ordonnée" $(Tb_{1-x}La_x)_2Mo_2O_7$ x=0.2 avec deux autres composés ordonnés situés dans la même région du diagramme de phase : $Gd_2Mo_2O_7$ ($a \sim a_c$, où l'ion Gd^{3+} est isotrope) et $Nd_2Mo_2O_7$ ($a > a_c$, où l'ion Nd^{3+} possède une anisotropie uniaxiale comme Tb^{3+}). Nous montrons que l'ordre à longue portée ferromagnétique non colinéaire "glace de spin ordonnée" est induit par l'anisotropie de la terre rare. En comparant la série $(Tb_{1-x}La_x)_2Mo_2O_7$ à la série $(Y_{1-x}La_x)_2Mo_2O_7$, où les interactions Mo-Mo deviennent aussi ferromagnétiques par dilatation du réseau, mais ne suffisent pas à induire l'ordre à longue portée, nous montrons que le magnétisme de la terre rare est nécessaire pour induire l'ordre à longue portée. Ceci peut venir des interactions Tb-Mo, qui ne sont pas frustrées par la géométrie.

En dessous de la température d'ordre ferromagnétique, les mesures de muons et plus récemment de diffusion inélastique de neutrons montrent que dans le composé $(Tb_{1-x}La_x)_2Mo_2O_7$ x=0.2 existe une transition "réentrante" vers une phase mixte, dans laquelle l'état "glace de spin ordonnée" coexiste avec des composantes de spins corrélées à courte portée gelées (comportement "verre de spin"), mais aussi avec des fluctuations lentes (comportement "liquide de spin"). Nous comparons de nouveau $(Tb_{1-x}La_x)_2Mo_2O_7$ x=0.2

avec $Gd_2Mo_2O_7$ et $Nd_2Mo_2O_7$, qui possèdent des ions Gd^{3+} et Nd^{3+} respectivement isotrope et anisotrope, mais sans le désordre induit par la substitution chimique. Nous montrons que l'origine de la phase mixte vient de l'anisotropie de la terre rare, mais que ses caractéristiques dépendent du désordre induit par la substitution chimique.

Finalement, en considérant les tendances générales prédites par le modèle de Hubbard et les calculs de structure de bande publiés pour les pyrochlores de molybdène, nous tentons d'expliquer qualitativement pourquoi la pression chimique et la pression appliquée sont équivalentes d'un point de vue magnétique (les deux favorisent un état "verre de spin"), alors que leur effet sur les propriétés de conduction est différent (la pression chimique favorise l'état isolant, la pression appliquée favorise l'état métallique).

Chapter VI.

$(Tb_{1-x}La_x)_2Mo_2O_7$, x=0-0.2. Discussion

In Chapters IV and V we analysed the effect of the chemical and the applied pressure, respectively, on the structural and magnetic properties of the $(Tb_{1-x}La_x)_2Mo_2O_7$ (x=0-0.2) series, which belong to the molybdenum geometrically frustrated pyrochlores. The analysis of this particular series provided the first microscopic picture of spin correlations and fluctuations in the region of the spin glass-ferromagnetic threshold.

The whole set of data determines a phase diagram, which represents the central point of this chapter. Interestingly, this phase diagram has not just two magnetic phases (beside the paramagnetic one), spin glass and ferromagnetic, as shown in the literature [Gardner'99, Katsufuji'00, Moritomo'01], but also a third mixed one. In the following we discuss the regions of interest of this phase diagram. We analyse the non-collinear ferromagnetic region and the spin glass one and also determine the origin of the mixed region. We compare our compounds with other Mo pyrochlores (or other systems with similar properties) and discuss the role of Mo^{4+} and R^{3+} magnetism. Finally, taking into account the existing theoretical models, we try to understand how the structural parameters of Mo pyrochlores determine their conduction and magnetic properties and underline the differences between the effect of chemical and applied pressure on these properties.

VI.1. Phase diagram

The X ray synchrotron diffraction measurements under pressure provide the equation of state $a(P)$ for the Mo pyrochlores (see chapter V, equations V.2 and V.3). This result allows the construction of a phase diagram, the temperature of transition against the lattice parameter, which contains all experimental data for $(Tb_{1-x}La_x)_2Mo_2O_7$ (x=0-0.2) series: magnetic susceptibility, neutron diffraction and μSR measurements at ambient and under applied pressure.

Figure 1 shows this phase diagram. Open symbols correspond to the ambient pressure data (chemical pressure), while the filled ones correspond to data taken under applied pressure. Magnetic susceptibility data (open circles) show an evolution from a spin glass with irreversibilities below $T_{SG} \sim 22-25$ K (x=0 and 0.05, with $a < a_C \sim 10.33$ Å) towards a ferromagnetic behaviour with strong increase of magnetisation below $T_C \sim 50-60$ K (x=0.1, 0.15, 0.2 and 0.25, with $a > a_C$). Neutron diffraction (open squares) and μSR (open down triangles) confirm these T_C values. Additionally, the μSR shows below T_C a broad maximum indicating a second transition at T^* (open up triangles). For x=0 and 0.05 $T^* \sim T_{SG}$. As one may clearly see the phase diagram shows the presence of three regions of interest. The

experiments under pressure show T_C and T^* values which situate roughly on the same phase boundaries, showing the equivalence between the chemical and the applied pressure.

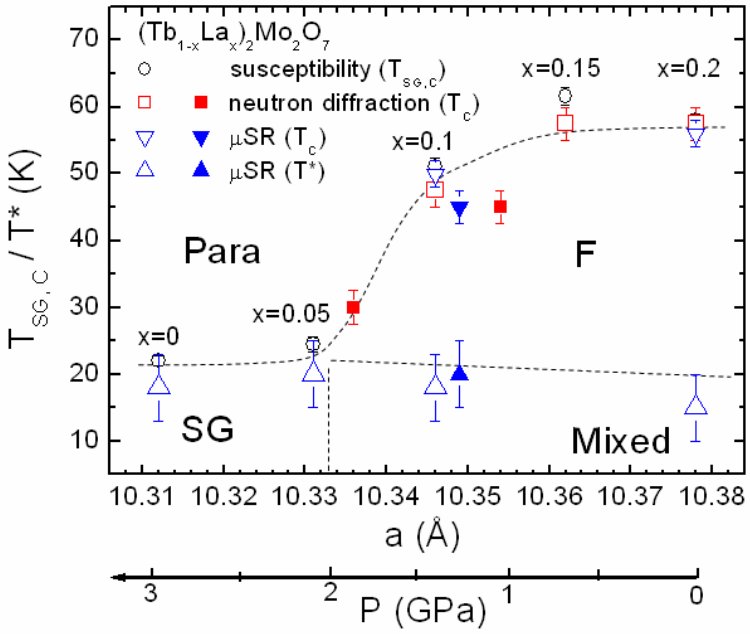

Figure 1. Phase diagram for $(Tb_{1-x}La_x)_2Mo_2O_7$: transition temperatures T_{SG}, T_C and T versus the lattice parameter a. The equation of state a(P) was taken into account in order to show all experimental results, obtained by means of susceptibility, neutron diffraction and μSR measurements at ambient and/or under applied pressure. The dashed lines are guides to the eye and point out the presence of three regions of interest (beside the paramagnetic one): spin glass, ferromagnetic and mixed.*

Figure 2 compares the phase diagram obtained for (Tb,La) substituted series with the general curve drawn accordingly to [Gardner'99, Katsufuji'00, Moritomo'01].

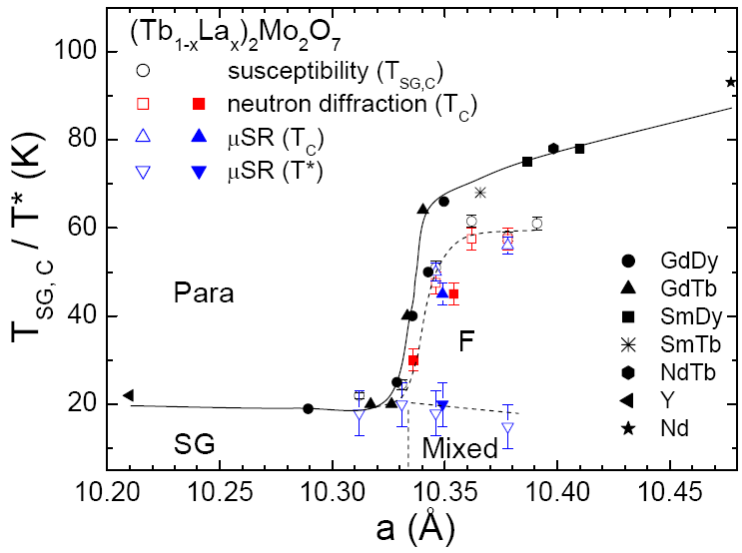

Figure 2. Phase diagram for $(Tb_{1-x}La_x)_2Mo_2O_7$: transition temperatures T_{SG}, T_C and T versus the lattice parameter a. For comparison the general curve for pyrochlores of molybdenum is represented (see Ref. [Gardner'99, Katsufuji'00, Moritomo'01]). Lines are guides to the eye.*

In the case of the general curve we passed from a mean ionic radius R_i to a lattice parameter a using a linear dependence deduced according to Ref. [Katsufuji'00]: $a = 7.9 + 2.32R_i$. It is the same equation as when we determined the correspondence $a_c \sim 10.33$ Å $\leftrightarrow$ $R_{ic} = 1.047$ Å. We notice that it was determined for (Gd,Dy), (Gd,Tb), (Sm,Dy), (Sm,Tb) and (Nd,Tb) substituted series. For Y it gives a lattice parameter of 10.268 Å, which is quite different from the value of 10.21 Å used in the literature [Gardner'99] and represented in Figure 2.

As one may see our curve slightly deviates from the general one: the T_C of x=0.15, 0.2 and x=0.25 samples are of about 60 K, instead of ~ 70 K. There are two possible explications. First we notice that the substitution of Tb^{3+} by the bigger ion La^{3+} expands the lattice and, in the same time, increases the compacity (the volume occupied by the ions/ the volume of the unit cell). This gives a solubility limit for La, close to 25% as stated in Chapter II, which may induce structural changes (phase separation, disorder). However, first analysis shows that it is not the case for x=0.25 sample. The second explication is that the lower value of T_C obtained for the $(Tb_{1-x}La_x)_2Mo_2O_7$ ($x > x_c \sim 0.06$) series is due to the substitution of Tb^{3+} by the non-magnetic ion La^{3+}.

We showed in this study that the Tb/La substitution induces long range magnetic order. However in Ref. [Sato'87], it is shown that in $(Y_{1-x}La_x)_2Mo_2O_7$ series (x=0-0.5) the substitution of Y^{3+} by La^{3+} does not induce a transition to long range magnetic order, although the critical threshold ($a_c \sim 10.33$ Å) is crossed. For $(Y_{1-x}La_x)_2Mo_2O_7$ series the Curie-Weiss constant changes sign as the rare earth ion average size increases: from negative $\theta_{CW} = -61$ K for x=0 to positive $\theta_{CW} = 41$ K for x=0.5 ($a = 10.461$ Å). This indicates a change from antiferromagnetic to ferromagnetic correlations. In spite of this, there is no transition to the ferromagnetic long range order as in $Sm_2Mo_2O_7$ or $Nd_2Mo_2O_7$ with similar lattice constants. All $(Y_{1-x}La_x)_2Mo_2O_7$ compounds behave like spin glasses. The only difference in regard to $(Tb_{1-x}La_x)_2Mo_2O_7$ is that Tb^{3+} is magnetic, while Y^{3+} is not. This underlines the importance of the role played by the Tb^{3+} magnetism. Furthermore, taking into account that both Tb-Tb and Mo-Mo interactions may be frustrated by the lattice (both form pyrochlore lattices), there rests the Tb-Mo interaction non- or less frustrated (see VI.4.). Returning to the phase diagram one could imagine the following scenario, forgetting the existence of the La solubility limit and supposing that it is possible to obtain $La_2Mo_2O_7$: (i) Starting from the spin glass $Tb_2Mo_2O_7$ the dilution with La induces LRO. (ii) At one point, the increasing of La concentration will determine the weakening of the Tb-Mo interaction. (iii) The long range order and the critical temperature will decrease. (iv) Finally, for $La_2Mo_2O_7$ one would obtain a spin glass behaviour with T_{SG} having the same order as for $Tb_2Mo_2O_7$. Consequently, one should imagine a ferromagnetic region (including x=0.2-0.25 interval) between two spin glass regions (x=0 and x=1, respectively). In this scenario the critical temperature increases from T_{SG} to $T_C \sim 60$ K, but it will not reach the 70 K before starting to decrease again towards T_{SG}.

In the following we analyse in more details the three regions of the phase diagram: the non-collinear ferromagnetic state, the origin of the third region and also the spin glass state.

VI.2. Non-collinear ferromagnetic state

The analysis of $(Tb_{0.8}La_{0.2})_2Mo_2O_7$ shows the coexistence between short and long range non-collinear ferromagnetic order which dominates. The main characteristics of the low

temperature magnetic structure are: (i) it is a $\vec{k}=0$ order; (ii) the Tb^{3+} magnetic moments orient close to their <111> anisotropy axes, with a small canting $\theta_t = 11.6°$; the components along these axes recall the local spin configuration of a spin ice; (iii) the Mo^{4+} ones orient close to [001] axis with also a small tilting angle $\theta_m = 6.8°$; (iv) all correlations are ferromagnetic; (v) the resulting ferromagnetic component orients along the [001] axis (see Figure 3a). The $(Tb_{0.85}La_{0.15})_2Mo_2O_7$ has a similar behaviour with slightly different canting angles.

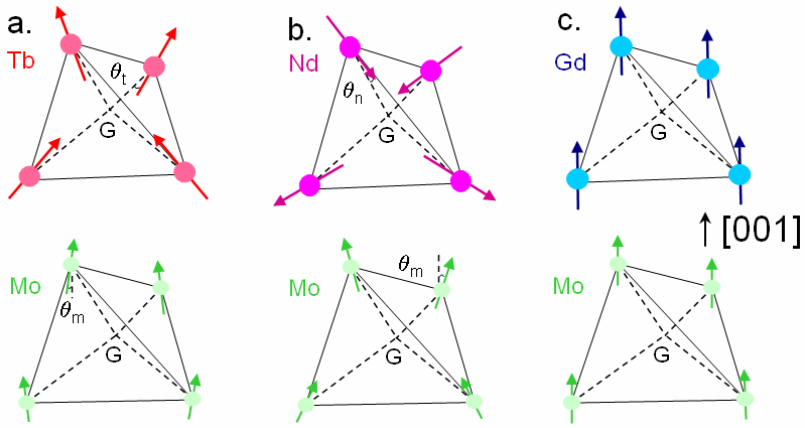

Figure 3. Magnetic ground state for three Mo pyrochlores situated in the ferromagnetic region of the general phase diagram: a. $(Tb_{0.8}La_{0.2})_2Mo_2O_7$ (1.5 K); b. $Nd_2Mo_2O_7$ (4K, see Ref. [Yasui'03, Yasui'01]); c. $Gd_2Mo_2O_7$ (1.7 K, see Ref. [Mirebeau'06]).

As stated in chapter I, for the Mo pyrochlores, the ground state is determined by the change of sign of the Mo-Mo exchange interactions (Ref. [Kang'02, Solovyev'03]). When increasing the rare earth ionic radius, the first neighbour Mo-Mo interactions change from antiferromagnetic, frustrated by the lattice and dominated by the superexchange mechanism, to ferromagnetic, due to the double exchange mechanism. Besides the magnetism of Mo^{4+}, there is also that of the rare earth ion. The rare earth crystal field anisotropy plays an important role, since it represents a possible source of frustration in the ferromagnetic region.

The magnetic structure obtained for $(Tb_{0.8}La_{0.2})_2Mo_2O_7$ is a direct proof of the influence of Tb^{3+} anisotropy, responsible of the canting of the magnetic moments. A similar orientation of Tb^{3+} magnetic moments was observed in the ordered spin ice: $Tb_2Sn_2O_7$. However, for $Tb_2Sn_2O_7$ the ground state is determined by an effective Tb-Tb ferromagnetic interaction, due to both exchange and dipolar interactions (see Chapter III) and not by the ferromagnetic Mo-Mo exchange interaction. The presence of Mo molecular field explains the transition temperatures which are in the 20-100 K range for Mo pyrochlores, well above those of Sn pyrochlores, with non-magnetic Sn, which are around 1-2 K.

The role of the rare earth anisotropy becomes more obvious if comparing our $(Tb_{0.8}La_{0.2})_2Mo_2O_7$ with two other pyrochlores of Mo situated in the ferromagnetic region of the general phase diagram: $Nd_2Mo_2O_7$ and $Gd_2Mo_2O_7$. For $Nd_2Mo_2O_7$, neutron diffraction carried out on single crystal sample provided two possible low temperature spin arrangements (Ref. [Yasui'01]), rather similar to that of $(Tb_{0.8}La_{0.2})_2Mo_2O_7$. A first model gives the canting angles of $\theta_n = 3.7°$ (in regard to <111> axes) and $\theta_m = 9.2°$ (in regard to [001] axis) for Nd^{3+} and Mo^{4+} spins (see Figure 3b), while the second one proposes the values of $\theta_n = 0°$ and $\theta_m = 6.2°$, respectively. The Nd^{3+} uniaxial anisotropy is responsible for this non-collinear structure. A first comparison shows that there is a difference between the two compounds: for

$(Tb_{0.8}La_{0.2})_2Mo_2O_7$ all correlations (Mo-Mo, Tb-Mo and Tb-Tb) are ferromagnetic, while for $Nd_2Mo_2O_7$ the Mo-Mo and Nd-Mo are ferromagnetic and antiferromagnetic, respectively. More details concerning the differences between these two compounds will be given in the next section. As for $Gd_2Mo_2O_7$, with Gd^{3+} isotropic ion, there is no canting: the Gd^{3+} and Mo^{4+} moments orient along the same [001] direction, with a ferromagnetic coupling (Figure 3c) [Mirebeau'06].

VI.3. Origin of the T^* transition

We focus now on the origin of the T^* transition in $(Tb_{1-x}La_x)_2Mo_2O_7$, brought to light by μSR measurements and which delimitates a third and new region on the phase diagram of Mo pyrochlores. We recall (see section IV.4.1) that this transition corresponds to a broad anomaly at $T^* < T_C$ seen in the muon spin dynamic relaxation. The static local field seen by the muon seems also to have an anomaly at this temperature, but much less evident. The neutron diffraction analysis shows no anomaly of the ordered magnetic moments. The long range magnetic order does not break at T^*, it persists down to the lowest temperature. All these characteristics suggest a transition of dynamical nature.

We discuss two possible aspects that could explain the origin of the T^* transition: the rare earth anisotropy and the chemical disorder of the system.

VI.3.1. The rare earth anisotropy

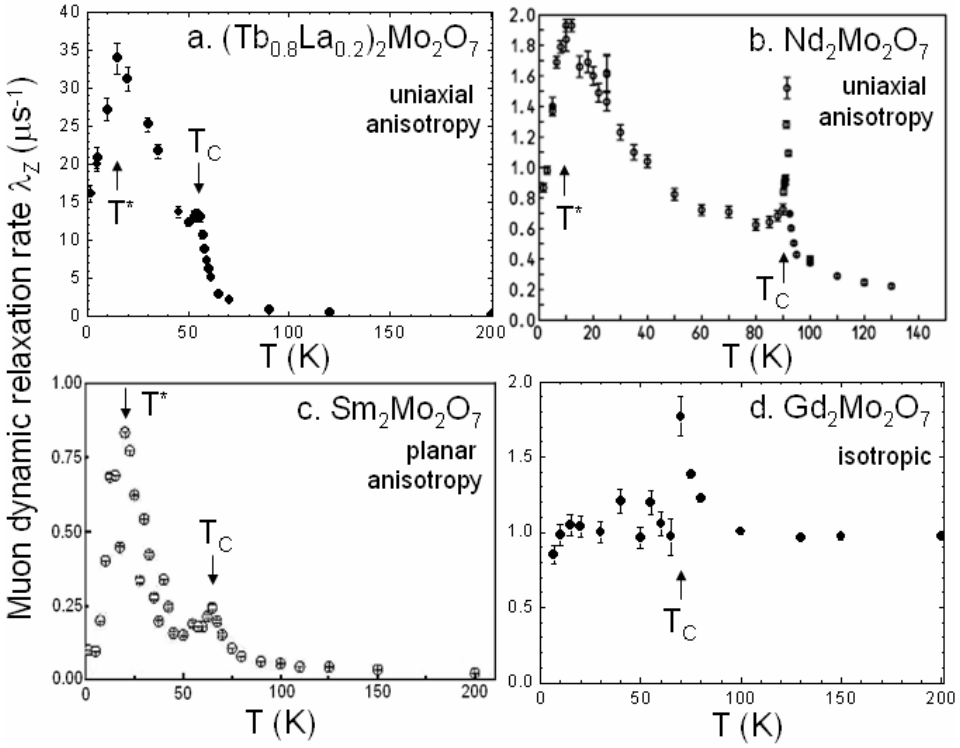

Figure 4. Muon spin dynamic relaxation rate versus temperature for four Mo pyrochlores situated in the ferromagnetic region of the general phase diagram: a. $(Tb_{0.8}La_{0.2})_2Mo_2O_7$; b. $Nd_2Mo_2O_7$ (from Ref.[Mirebeau'07b]); c. $Sm_2Mo_2O_7$ (from Ref. [Jo'05]); d. $Gd_2Mo_2O_7$ (from Ref. [Mirebeau'06]). The rare earth (Tb, Nd, Sm and Gd) anisotropy type is indicated in each case. T_C and T are the two transition temperatures seen by μSR.*

We first notice that for the Mo pyrochlores this transition seems to be related, as the canted ferromagnetic order, with the rare earth anisotropy. We have observed it for $(Tb_{0.8}La_{0.2})_2Mo_2O_7$ and more recently for $Nd_2Mo_2O_7$ [Mirebeau'07b], compounds where both Tb^{3+} and Nd^{3+} have uniaxial anisotropy. It was also observed for $Sm_2Mo_2O_7$, having Sm^{3+} with planar anisotropy [Jo'05]. However, it is absent in the case of $Gd_2Mo_2O_7$, with Gd^{3+} isotropic ion [Mirebeau'06]. Figure 4 shows the muon spin dynamic relaxation rate for all these compounds: for $(Tb_{0.8}La_{0.2})_2Mo_2O_7$, $Nd_2Mo_2O_7$ and $Sm_2Mo_2O_7$ it shows a cusp at $T_C \sim$ 60, 90 and 70 K, respectively, followed by a broad maximum at a lower temperature $T^* \sim$ 15, 15 and 18 K, while for $Gd_2Mo_2O_7$ the broad maximum seems to be suppressed and there is only a transition at $T_C \sim 70$ K.

VI.3.2. The influence of the chemical disorder

- *comparison to the reentrant spin glasses*

This transition has been observed not only for the Mo pyrochlores, but it also recalls the behaviour of the reentrant spin glasses (RSG's). These systems are characterized by the competition between dominant ferromagnetic interactions and the chemical disorder. Accordingly to mean field theory of weakly randomly frustrated Heisenberg ferromagnets [Binder'86, Fisher'91, Gabay'81] they present an interesting phase diagram: temperature of transition as a function of the concentration of the constituents. For some concentrations several magnetic phases are observed when decreasing temperature: paramagnetic, ferromagnetic and mixed. Upon cooling, a transition from a paramagnetic phase to a ferromagnetic one first occurs at T_C, below which the system develops a non-zero magnetization M. At a lower temperature, T_{xy}, the transverse XY spin components perpendicular to M freeze in random directions, with longitudinal spin components that remain ferromagnetically ordered. There is no increase of M at T_{xy}. Finally, strong irreversibilities develop at a third temperature $T_F < T_{xy}$, with again no increase of M. In the mean field theory of Heisenberg spin glasses T_F is a remnant of the longitudinal freezing seen below Almeide-Thouless line in weakly frustrated Ising spin glasses [Binder'86, Fisher'91]. Both transitions occur without any destruction of the ferromagnetic order. All these transition temperatures merge at a critical concentration, leading to a single paramagnetic-spin glass transition. In real materials there is a question that arises: are T_F and T_{xy} really two distinct transitions or are they the same one?

By studying the a-$Fe_{1-x}Mn_x$, Ref. [Gingras'97, Mirebeau'97] suggest that T_F and T_{xy} are due to distinct thermodynamic "features" intrinsic to the system and not simply arising from a transition observed at different time and length scale when comparing results obtained from different experimental techniques. The T_C and T_F are most easily observed through magnetic susceptibility measurements, as shown in Figure 5 for several concentrations x [Mirebeau'90]. T_C and T_F are associated to the sharp increase and decrease, respectively, of the low field magnetization. The $x = 0.07$ sample behaves as a usual ferromagnet ($T_C > 500$ K), the x=0.22-0.26 samples correspond to rather weakly frustrated alloys ($T_C \sim 200$ K far from $T_F \sim 20$ K), x=0.3, 0.32 are very frustrated, close to the tricritical point ($x_c = 0.35$), and finally $x = 0.41$ is a true spin glass. The weak irreversibilities between ZFC and FC

curves, that occur well above T_F, are thought to be related to the freezing of the transverse spin components (T_{xy} predicted by the mean field theory).

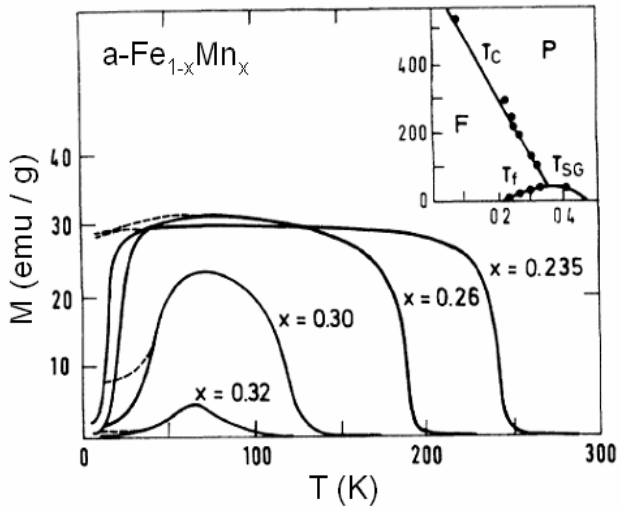

Figure 5. Low field magnetization (20 Oe) as a function of temperature for several a-$Fe_{1-x}Mn_x$ alloys (from Ref. [Mirebeau'90]). The magnetization is measured in the zero field cooled (ZFC) and field cooled (FC) processes. In inset the corresponding typical phase diagram.

However, for studying these type of compounds, the μSR is a more suitable technique, since it allows to extract simultaneously the amount of static order and the level of spin dynamics and therefore to show the possible difference between T_F and T_{xy}. The zero-field muon data are fitted with a dynamical Kubo-Toyabe relaxation (product) function:

$$G(t) = G_s(t) \cdot G_d(t)$$
$$G_s(t) = \frac{1}{3} + \frac{2}{3}(1-(\Delta t)^{\alpha})\exp(-\frac{(\Delta t)^{\alpha}}{\alpha}) \qquad \text{[VI.1]}$$
$$G_d(t) = \exp(-(\lambda t)^{\beta})$$

where $G_s(t)$ describes the depolarization arising from the static field at the muon site and $G_d(t)$ describes the depolarization due to the fluctuating field [Gingras'97, Mirebeau'97]. We underline the difference between a-$Fe_{1-x}Mn_x$ and $(Tb_{0.8}La_{0.2})_2Mo_2O_7$. a-$Fe_{1-x}Mn_x$ is an amorphous material and the muon may be located at numerous non-equivalent magnetic sites. Consequently, the average dipolar magnetic field seen by the muon spin is equal to zero in this case and no oscillatory behaviour is observed, even in the ferromagnetic phase. The relaxation rate Δ (mostly determined by the short time behaviour of muon depolarization) corresponds to the width of the local field distribution. It may be compared to λ_T of our study. α and β are temperature dependent fitting parameters.

Figure 6 shows the μSR results for a-$Fe_{1-x}Mn_x$, as presented in Ref. [Gingras'97, Mirebeau'97]. For x=0.26 and 0.3, one may observe a well defined peak at T_C, due to the critical fluctuations. When decreasing T, λ starts to increase when approaching T_C from the paramagnetic region, due to the slowing down of the spin fluctuations. It tends to diverge at T_C and decreases below, as the amplitude of the fluctuating fields decreases. A second broader peak is observed at a lower temperature (40 K), indicating a considerable slowing down of the spin dynamics. The two peaks situate at temperatures that correspond reasonably

well to T_C and T_F, as determined by magnetization measurements (see disorder-temperature phase diagram from inset Figure 6a). For x=0.41 sample there is a single peak, whose temperature coincides with the spin glass transition found in magnetization measurements. For the reentrant samples, x=0.26 and 0.3, there seems to be no dynamical signature of freezing of the transverse spin components at an intermediate temperature $T_F < T_{xy} < T_C$. Despite the absence of critical dynamics at T_{xy}, [Gingras'97, Mirebeau'97] show that an extra magnetic moment which does not contribute to the magnetization, develops smoothly below a temperature T_{xy}. The temperature dependence of the static relaxation rate Δ (Figure 6b) for the reentrant sample x=0.26 starts to increase from zero below $T_C \sim 200$ K, as expected from the onset of the magnetic order. In 100-200 K interval Δ scales with the internal field B deduced from neutron depolarization measured in low field and also with the magnetization M (excepting near T_C). Below 100 K, Δ continues to increase, while B and M saturate. This is considered the fingerprint of the onset of transverse spin freezing.

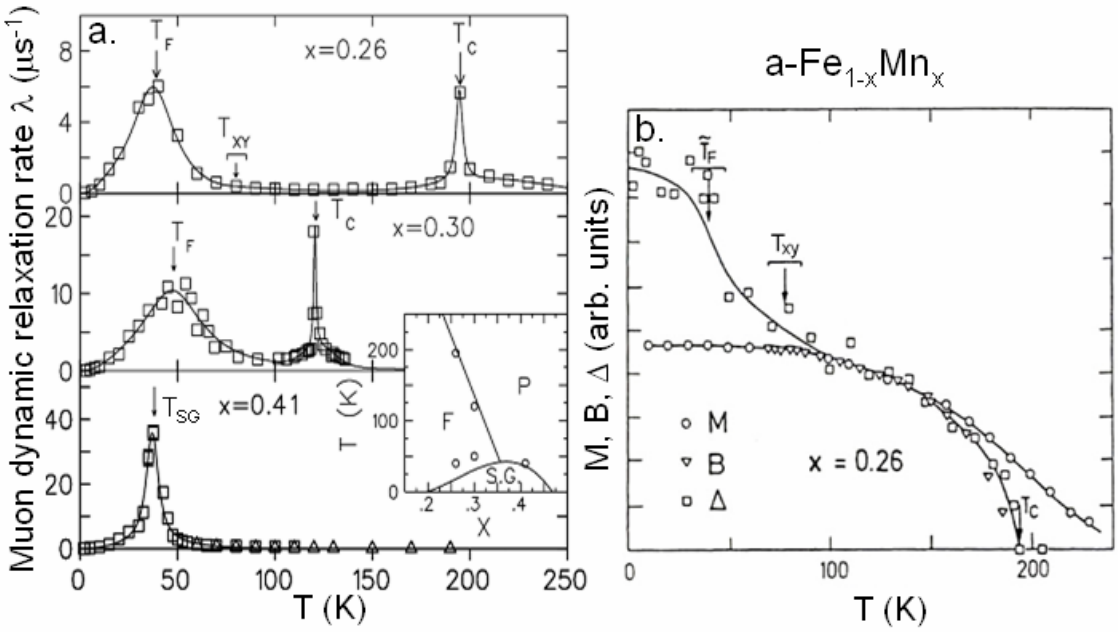

Figure 6. μSR for reentrant spin glasses a-$Fe_{1-x}Mn_x$ (from Ref. [Gingras'97, Mirebeau'97]): a. The muon dynamic relaxation rate λ against temperature for three different concentrations x=0.26, 0.3 and 0.41. In inset the T-x phase diagram: solid lines correspond to dc susceptibility results and symbols to μSR experiment; b. x=0.26: the temperature dependence of the static muon spin relaxation rate Δ (open squares), the internal field estimated from neutron diffraction measurements B (open triangles), as well as the dc magnetization of the sample M, in arbitrary units (open circles). The three transition temperatures T_F, T_{xy} and T_C are identified.

By studying the spin freezing of a-Fe_xZr_{100-x}, Ref. [Ryan'00, Ryan'04] argue that μSR provides a clear evidence of only two transitions, at T_{xy} and T_C, observed in both dynamic and static behaviour of the muon polarization decay (Figure 7). The dynamic relaxation rate shows the evolution from a ferromagnet (x=89) to a spin glass (x=93) (Figure 7a). T_C is marked by a clear cusp, that moves down in the temperature as the frustration level increases. At the same time a broader feature develops at a much lower temperature for x=90-92. This peak grows in amplitude and moves to higher temperatures with increasing x and hence frustration. Finally the two features merge at x=93 and the system becomes a spin glass. The

temperature dependence of the static relaxation rate Δ clearly shows the onset of the magnetic order at T_C (Figure 7b). For x=90-92 there is a distinct break in slope at the same temperature at which the lower maximum in λ is observed. When increasing frustration, the size of this break increases and moves to higher temperatures. $\Delta(T)$ was very well fitted by using a combination of a modified Brillouin function with a linear term to allow an additional increase associated with the ordering of the transverse spin components. Consequently, this second transition at T_{xy} is attributed to the freezing of the transversal spin components.

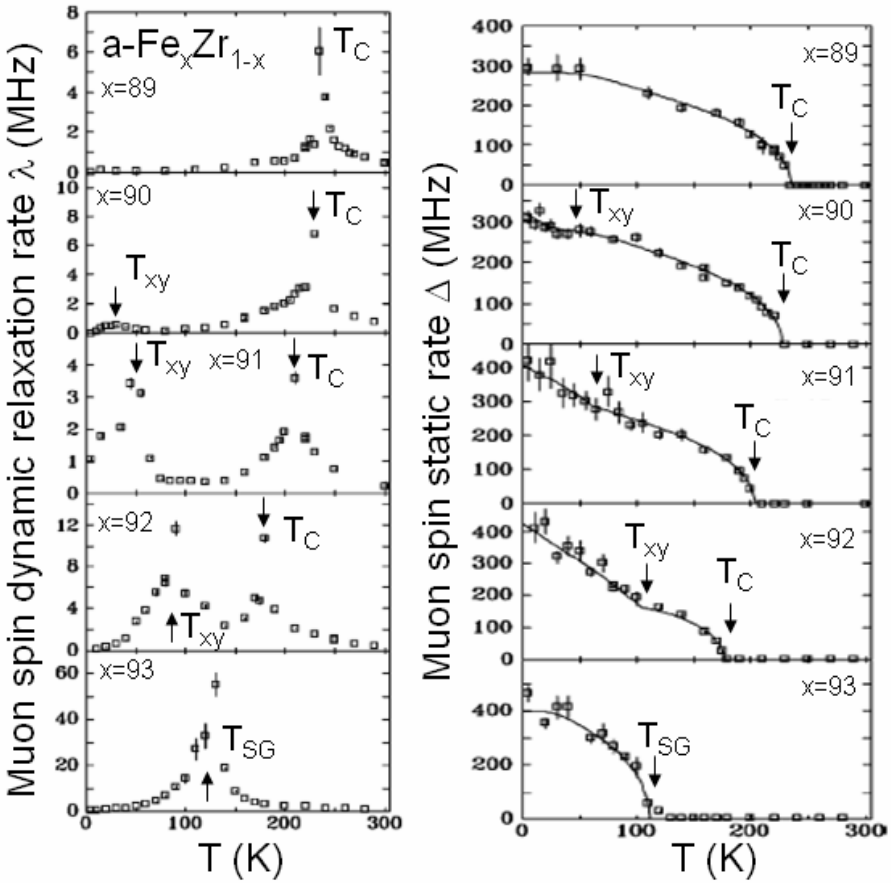

Figure 7. μSR for reentrant spin glasses a-Fe_xZr_{100-x} (see Ref. [Ryan'00, Ryan'04]), for five different concentrations x=89, 90, 91, 92 and 93: a. The muon dynamic relaxation rate λ against temperature; b. The temperature dependence of the static muon relaxation rate Δ. Lines are fits to a modified Brillouin function with a linear term to include the ordering of the transverse spin components. The transition temperatures are identified as: T_C and T_{xy}, which merge for x=0.93 into T_{SG}.

All these experiments yield the same idea: in RSG's the paramagnetic-ferromagnetic transition is followed by a freezing of the transverse spin component, which does not break down the long range order. The differences only concern the process of the freezing dynamics: either there is a unique event, frequency dependent [Ryan'00, Ryan'04] or there are two different transitions, which can be observed in the same time window at two different temperatures [Gingras'97, Mirebeau'97].

Taking into account the two examples of reentrant spin glasses presented above, we may do a correspondence between their behaviour and the behaviour of our series $(Tb_{1-x}La_x)_2Mo_2O_7$. A first aspect would be the fact that both types of systems are disordered. The RSG's are amorphous compounds, while in $(Tb_{1-x}La_x)_2Mo_2O_7$ there is chemical disorder produced by the substitution of Tb by La. Secondly, in the RSG's there is a freezing of the

transverse spin components ferromagnetically correlated on a scale of roughly 10-100 Å according to Ref. [Mirebeau'90], while for (Tb,La) pyrochlores we also observe short range correlations. In both cases the short range correlations do not destroy the long range order. One may speculate that the dynamic anomaly seen in μSR for (Tb,La) may be related to the freezing of these short range correlated spins. Therefore, we decided to investigate the spin dynamics by performing an energy analysis of the diffuse scattering.

- *analysis of spin dynamics by inelastic neutron scattering*

The inelastic neutron scattering (INS) experiments on $(Tb_{0.8}La_{0.2})_2Mo_2O_7$ were performed on the 4F1 could neutron three axis spectrometer of the LLB, with an incident wave-vector $k_i = 1.35$ Å^{-1}. We performed an analysis in energy of the diffuse signal, which persists, as shown by neutron diffraction, under the Bragg peaks and also close to $q = 0$. The energy analysis was done for temperatures between 1.5 and 150 K and for five q values (0.25, 0.3, 0.5, 0.7 and 1 Å^{-1}), whose position on a neutron diffraction spectra are indicated by bold arrows in Figure 8.

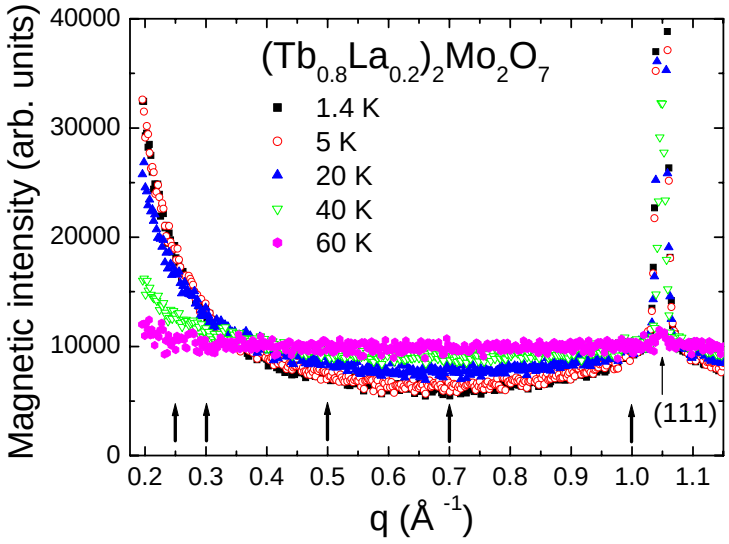

Figure 8. $(Tb_{0.8}La_{0.2})_2Mo_2O_7$: magnetic intensity versus the scattering vector q as obtained from neutron diffraction measurements, with λ=4.741 Å. A spectrum in the paramagnetic region was subtracted. The bold arrows mark the q values for which the diffuse signal was analysed in energy by INS. The position of the (111) peak is also indicated.

In an INS experiment, the magnetic fluctuations yield a quasielastic signal, which may be separated from the elastic one. The experimental data are fitted with a cross section given by:

$$\frac{d\sigma}{d\omega} = \omega n(\omega)\chi(q)\cdot\frac{1}{\pi}\frac{\Gamma}{\Gamma^2+\omega^2} + I_{elastic}\delta(\omega) \qquad \text{[VI.2]}$$

where the first term corresponds to the quasielastic signal and the second term to the elastic one. $n(\omega) = 1/(1-e^{-\omega/kT})$ is the Bose factor, $\chi(q)$ is the static susceptibility, Γ is the half width half maximum of the quasielastic peak and $I_{elastic}$ is the elastic intensity. There are three independent parameters of interest obtained from the fit: (i) the static susceptibility $\chi_{quasielastic}$, (ii) the half width half maximum $\Gamma \sim 1/\tau$, with τ the spin relaxation time, and (iii) the elastic

intensity $I_{elastic}$. In the limit $\omega << kT$: $\omega n(\omega) = kT$ and one may also determine another parameter: (iv) the quasielastic intensity, defined as $I_{quasielastic} = kT\chi(q)$.

Figure 9 shows two examples of fits, for $q = 0.25$ Å^{-1}, at the two extreme temperatures: T=5 and 150 K, respectively. The elastic peak was fitted with a Gaussian function, with a width fixed at 0.0035 (corresponding to the resolution limit) and the quasielastic one with a Lorentzian function. The elastic and quasielastic peaks are indicated by dashed line, as well as the background.

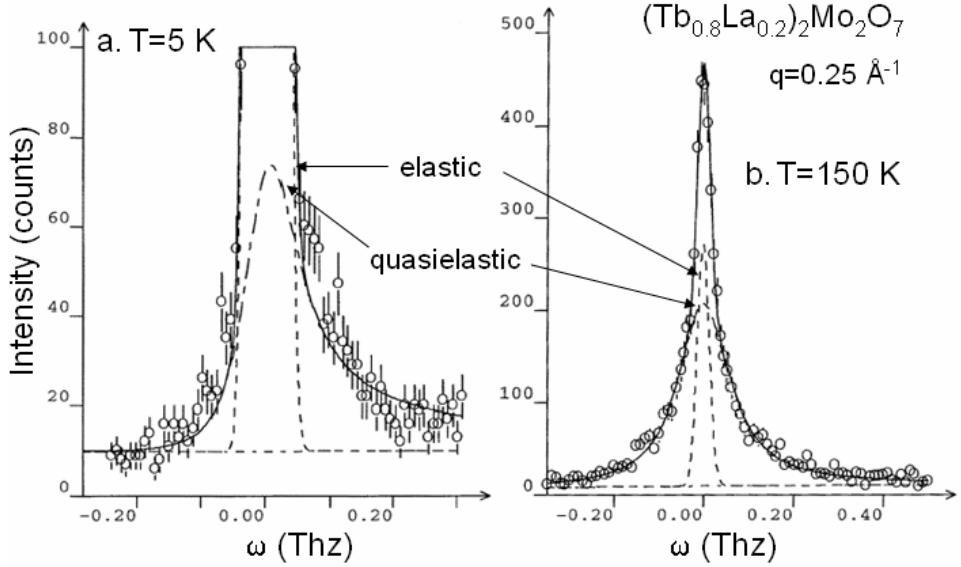

Figure 9. $(Tb_{0.8}La_{0.2})_2Mo_2O_7$: the neutrons intensity against energy for a scattering vector q=0.25 Å^{-1}, as obtained from INS. The elastic and quasielastic intensities (upper dotted lines) are shown for two extreme temperatures T= 5 and 150 K, respectively. The continuous lines represent the total intensity and the bottom dotted lines the background. Note at T=5 K the deformation of the Lorentzian quasielastic peak related to the Bose factor.

We analysed the temperature evolution of the four parameters: Γ, $\chi_{quasielastic}$, $I_{elastic}$ and $I_{quasielastic}$, for $q = 0.25$ and 0.5 Å^{-1}, respectively. Each time the two transition temperatures seen by μSR ($T^* = 15$ K and $T_C = 57$ K) are indicated. We chose these values of q since they are situated in regions with different behaviour. As one may see in Figure 8, for $q = 0.25$ Å^{-1} the neutron diffraction shows ferromagnetic correlations having a strong temperature dependence, while for $q = 0.5$ Å^{-1} there is a smaller change with the temperature.

The results obtained for $q = 0.25$ Å^{-1} are shown in Figure 10. We observe that well above T_C Γ starts to decrease when decreasing temperature. At ~ 40 K (between T_C and T^*), it shows a minimum, which situates well above the resolution limit of 0.0035 THz indicating a real effect. Then, below ~ 40 K, Γ starts to increase, while temperature is decreasing till to 5 K (Figure 10a). We recall that Γ represents the inverse of the spin relaxation time. Its high temperature behaviour shows a slowing down of the spin fluctuations (Γ decreases and hence τ increases), *i.e.* a spin freezing process. At high temperature the system is characterized by excitations between different well defined ground states (potential pots): the temperature is high enough and the energetic barriers may me passed. It is an Arrhenius type process. Then, below 40 K, Γ starts to increase. This behaviour may not anymore be explained by the above mechanism of excitation. In fact, it corresponds to a modification of the nature of the

excitations. At low temperature the system is submitted to diffusive excitations with a frozen state as metastable ground state. One may therefore explain why these excitations are so rapid. These are spin glass like excitations. The quasielastic susceptibility (Figure 10b) shows a behaviour which recalls that of the muon spin dynamical relaxation rate seen by μSR: an increasing till to T_C, followed when decreasing temperature by a well defined minimum between T_C and T^* and finally another increasing. We also note that the temperature interval where both Γ and the static susceptibility $\chi_{quasielastic}$ start to increase (roughly 20-40 K) corresponds to the temperature range where the neutron diffraction measurements show the appearance of the short range magnetic order (corresponding to a diffuse scattering below the Bragg peaks as shown in Chapter IV, section IV.3.2.). In this temperature range the short range magnetic moments (M_{Tb}^{SRO} and M_{Mo}^{SRO}) and also the corresponding correlation length (L_C^{SRO}) start to increase. The freezing process may also be seen in the behaviour of elastic and quasielastic intensities (Figure 10c). One may see that, when decreasing temperature from T_C or even above T_C (the temperature where the decreasing starts depends on the time window, on the q value), there is a transfer between $I_{quasielastic}$ and $I_{elastic}$: $I_{quasielastic}$ decreases, while concomitantly $I_{elastic}$ increases. Very interesting for $T \to 0$ K, the quasielastic intensity does not decrease to zero as expected in a spin glass. This behaviour suggests that at low temperature there still remain spin fluctuations like in a spin liquid; *i.e.* the system is characterized as at high temperature by excitations between different potential pots, which this time are separated by tiny energy barriers.

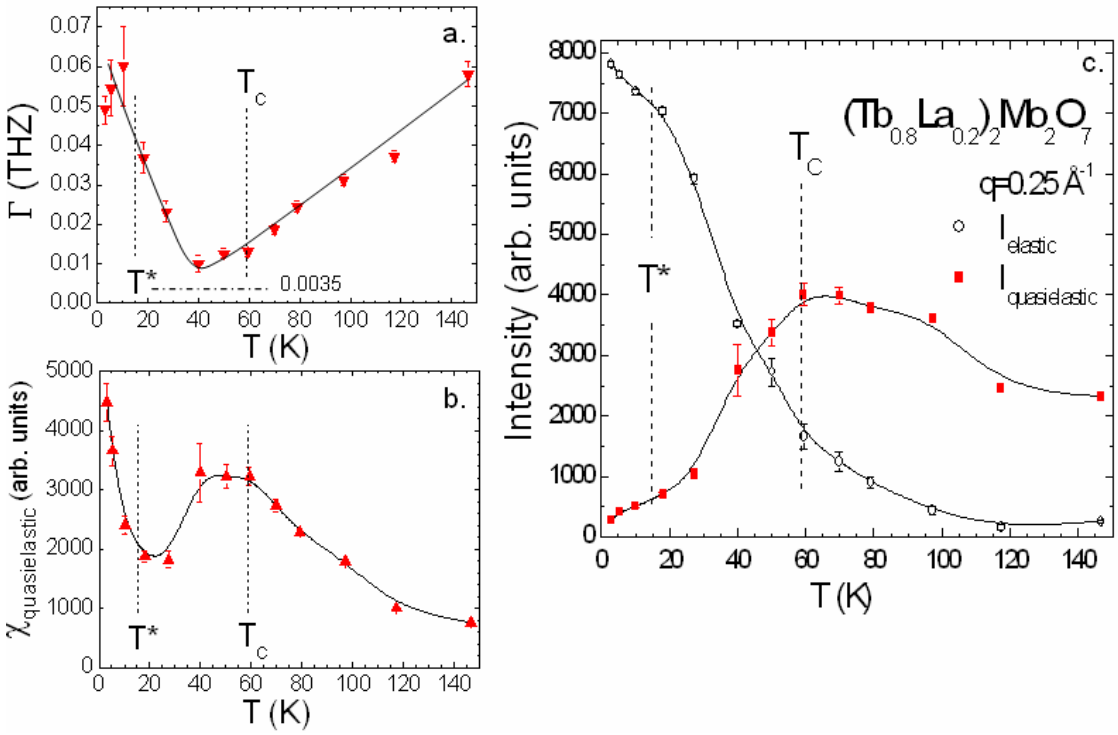

Figure 10. INS results on $(Tb_{0.8}La_{0.2})_2Mo_2O_7$ for q=0.25 Å^{-1}. The temperature evolution of the four parameters of interest: a. The half width half maximum Γ of the quasielastic peak. The resolution limit of 0.0035 THz is also indicated; b. The static susceptibility $\chi_{quasielastic}$; c. Elastic and quasielastic intensities. The dashed lines indicate the two transition temperatures seen by μSR ($T^* = 15$ K and $T_C = 57$ K). Continuous lines are guides to the eye.

The temperature evolution of these four parameters shows the same anomalies for all investigated q values: (i) Γ decreases, has a minimum and increases again at low temperature; (ii) $\chi_{quasielastic}$ shows a maxima, decreases, has a minimum between T_C and T^* and increases again below T^*; (iii) increasing of $I_{elastic}$ and decreasing of $I_{quasielastic}$, but for $T \to 0$ $I_{quasielastic} \neq 0$. Figure 11 shows the q=0.5 Å^{-1} case.

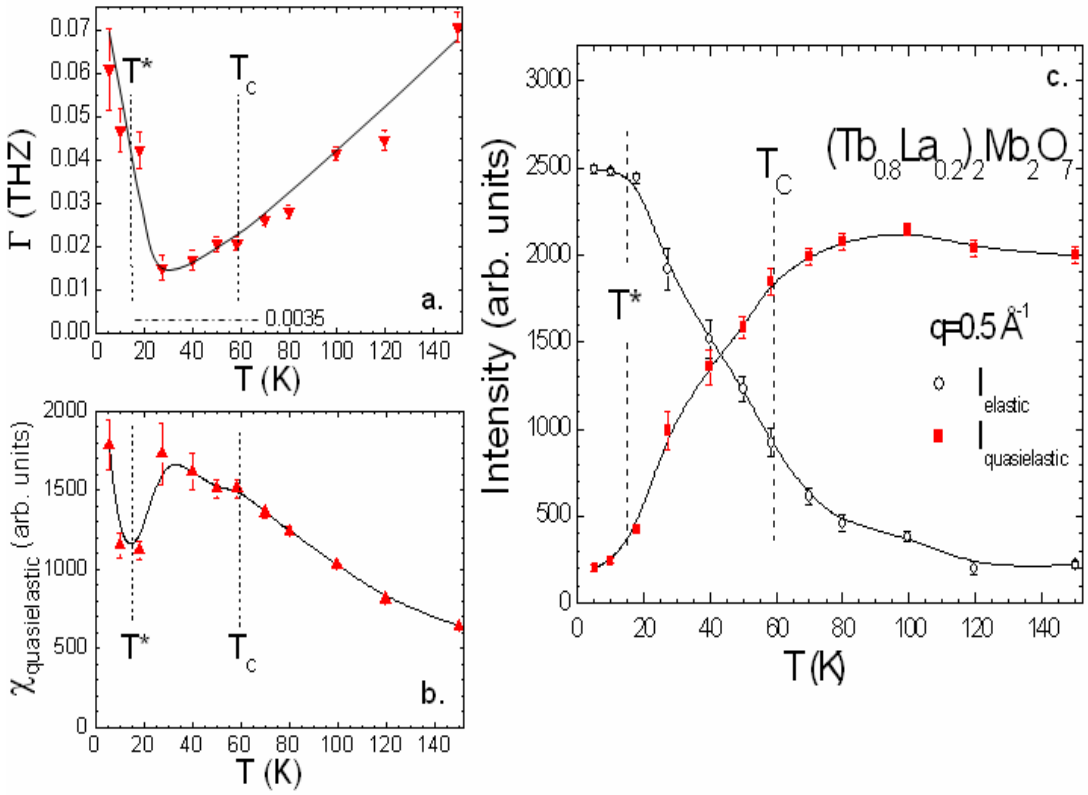

Figure 11. INS results on $(Tb_{0.8}La_{0.2})_2Mo_2O_7$ for q=0.5 Å^{-1}. The temperature evolution of the four parameters of interest: a. Γ (the resolution limit of 0.0035 THz is indicated); b. $\chi_{quasielastic}$; c. $I_{elastic}$ and $I_{quasielastic}$. The dashed lines indicate the two transition temperatures seen by μSR ($T^* = 15$ K and $T_C = 57$ K). Continuous lines are guides to the eye.

For comparison, Figure 12 shows the inelastic neutron scattering results on the a-$Fe_{1-x}Mn_x$, with x=0.41 [Bellouard'92]. As shown in Figure 5 and Figure 6 [Gingras'97, Mirebeau'97], magnetic susceptibility measurements situate this sample is the spin glass region of the temperature-disorder phase diagram and μSR shows a unique peak at T_{SG}. The INS results from Ref. [Bellouard'92] confirm the spin freezing process: (i) the quasielastic line width decreases showing the freezing of the spin fluctuations, it shows an minimum and than it increases due to diffusive excitations from a frozen ground state as in spin glasses; (ii) the signal is transferred from quasielastic to elastic contribution: $I_{quasielastic}$ decreases, while $I_{elastic}$ increases (see Figure 12 inset).

The similarities between the temperature evolution of the INS parameters for $(Tb_{0.8}La_{0.2})_2Mo_2O_7$ and a-$Fe_{1-x}Mn_x$ (x=0.41) show that in both cases at low temperature the spin freezing process coexists with spin fluctuations.

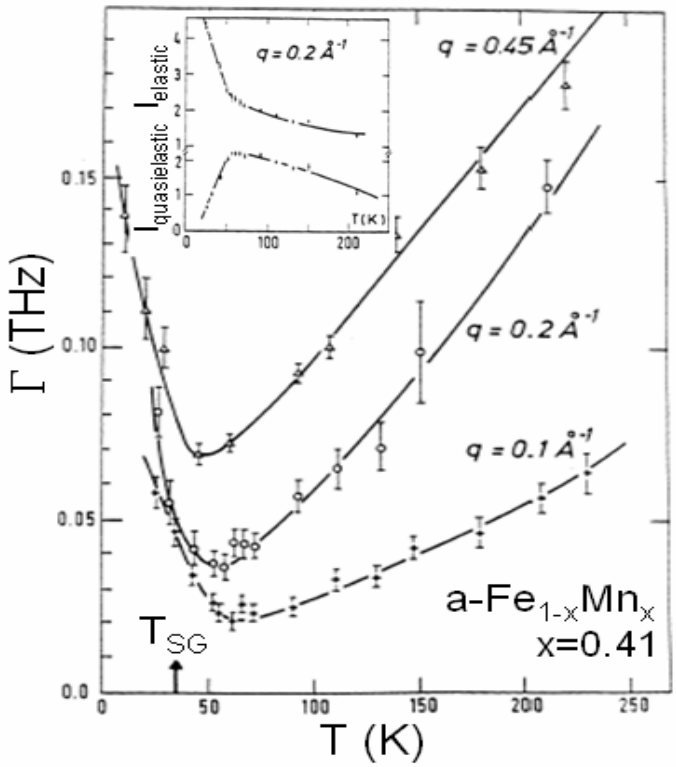

Figure 12. a-$Fe_{1-x}Mn_x$, x=0.41 (from Ref. [Bellouard'92]): temperature dependence of the quasielastic line-width Γ for several q values (0.1, 0.2 and 0.45 $Å^{-1}$). The spin glass temperature is indicated. In inset is plotted the temperature dependence of the elastic and quasielastic intensities expressed in arbitrary units.

We are now able to conclude that the third region of the phase diagram from Figure 1 corresponds to a mixed phase: (i) there is a non-collinear ferromagnetic long range order ("ordered spin ice"); (ii) there are also short range correlated magnetic spins, which start to freeze below T_C; (iii) at low temperatures these short range correlated spins are still fluctuating (spin liquid). In other words there is a reentrant spin glass transition in $(Tb_{0.8}La_{0.2})_2Mo_2O_7$ pyrochlore, which seems to be induced by the anisotropy of the rare earth and also by the disorder of the system.

- *comparison with $Nd_2Mo_2O_7$*

In this context, it is natural to compare $(Tb_{0.8}La_{0.2})_2Mo_2O_7$ and $Nd_2Mo_2O_7$, with both rare earth having uniaxial anisotropy. The difference between the two compounds: $Nd_2Mo_2O_7$ is chemically ordered, while $(Tb_{0.8}La_{0.2})_2Mo_2O_7$ is disordered due to the Tb substitution by La. The question that naturally arises: is there a reentrant spin glass transition also in the ordered system? The μSR experiments (see Figure 4b) show similar behaviour of the muon spin dynamical relaxation rate, *i.e.* a second transition at $T^* < T_C$, and therefore suggest an affirmative answer. However magnetization and neutron diffraction measurements show that at low temperatures there are important differences between the magnetic behaviour of the two compounds.

Figure 13 shows the dc magnetization curves for the two systems. $(Tb_{0.8}La_{0.2})_2Mo_2O_7$ was measured just in the low field regime, while $Nd_2Mo_2O_7$ [Mirebeau'07b] was measured in both low and high field. For $(Tb_{0.8}La_{0.2})_2Mo_2O_7$ the magnetization has a typical ferromagnetic behaviour, with the Curie temperature $T_C = 58$ K, corresponding to an abrupt and strong increase of the magnetization with decreasing temperature, which is also close to the onset of

FC/ZFC irreversibilities. For magnetic fields of the same magnitude (10 and 100 Gauss), $Nd_2Mo_2O_7$ shows also a transition to a ferromagnetic order with $T_C = 93$ K, defined as above and also close to FC/ZFC irreversibilities. However at low temperatures $Nd_2Mo_2O_7$ has a different behaviour. Below T_C, the magnetization does not continue to increase as for $(Tb_{0.8}La_{0.2})_2Mo_2O_7$. In temperature range ~ 30-90 K it increases very smoothly (almost constant) and below ~ 28 K it starts to decrease. Furthermore, when increasing the magnetic field (500 Gauss - 1 Tesla), the decrease of the magnetization at low temperatures becomes more pronounced. This low temperature decreasing of the magnetization, which accentuates when increasing the applied magnetic field, suggests an antiferromagnetic coupling between Nd and Mo magnetic moments. Similar results on the magnetization of $Nd_2Mo_2O_7$ have already been reported for single crystals [Taguchi'01, Taguchi'03, Yasui'01] and powder samples [Iikubo'01] and the ferrimagnetic order of the Nd and Mo ordered magnetic moments was also invoked.

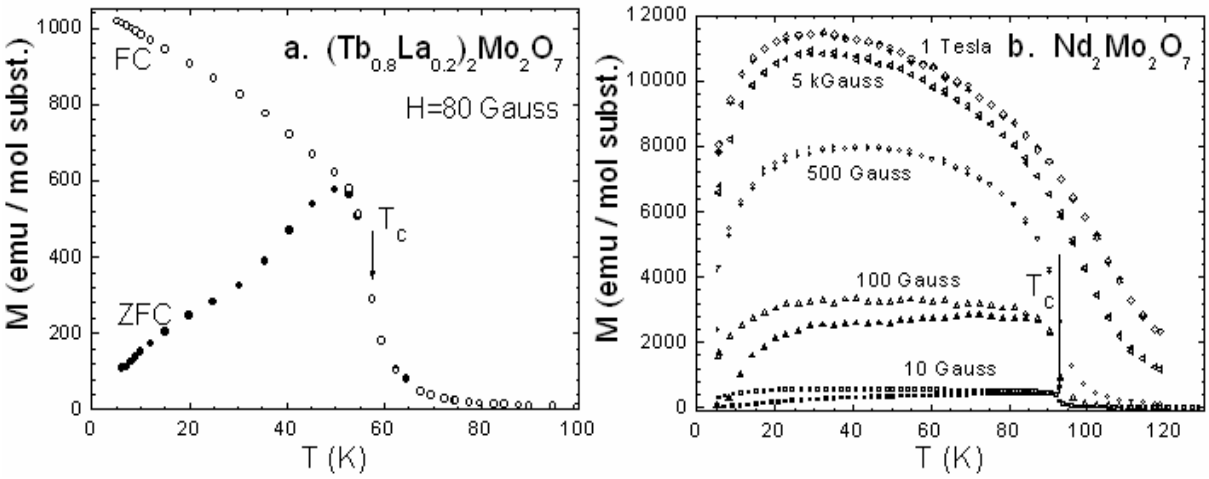

Figure 13. Temperature dependence of ZFC (filled symbols) and FC (open symbols) dc magnetization for: a. $(Tb_{0.8}La_{0.2})_2Mo_2O_7$, in low field: H=80 Gauss; b. $Nd_2Mo_2O_7$, in low and high fields: H=10, 100, 500, 5000 and 10000 Gauss. The Curie temperatures of 58 and 93 K for $(Tb_{0.8}La_{0.2})_2Mo_2O_7$ and $Nd_2Mo_2O_7$ [Mirebeau'07b], respectively, are indicated.

The neutron diffractions analysis also shows important differences between the two compounds. If comparing the small angle neutron scattering (SANS) ($q < 0.5$ Å^{-1}) corresponding to mesoscopic ferromagnetic correlations (see Figure 14a and c), one may see that for $(Tb_{0.8}La_{0.2})_2Mo_2O_7$ these correlations increase when decreasing temperature, while per contra for $Nd_2Mo_2O_7$ they disappear at low temperature [Mirebeau'07b]. Therefore for $Nd_2Mo_2O_7$ we show the low temperature non-subtracted spectra, with both magnetic and nuclear intensities (at 1.4 K there is roughly only the nuclear contribution). Passing to higher q values, we observe that for $(Tb_{0.8}La_{0.2})_2Mo_2O_7$ both intensities of (111) and (200) peaks are decreasing gradually when increasing temperature and at 60 K ($\sim T_C$) both vanish. The behaviour of $Nd_2Mo_2O_7$ is different: (i) the peak (200) appears below 28 K ($<< T_C$) and then increases when temperature is decreasing; (ii) the (111) appears below 95 K ($\sim T_C$), then it increases when decreasing temperature (we note that it decreases more slowly from 95 to 28 K than below 28 K). These results are in agreement with single crystal analysis [Taguchi'01, Yasui'01].

The low temperature magnetic structure of $(Tb_{0.8}La_{0.2})_2Mo_2O_7$ is that from Figure 3a, while for $Nd_2Mo_2O_7$ the recent powder neutron diffraction analysis [Mirebeau'07b] shows a

magnetic structure which is quite similar to that obtained for single crystals in Ref. [Yasui'01] and shown in Figure 3b. The temperature evolution of the magnetic moments intensifies the difference between the two compounds. For $(Tb_{0.8}La_{0.2})_2Mo_2O_7$, below $T_C \sim 60$ K M_{Tb}^{LRO} keeps increasing till to 1.4 K, while M_{Mo}^{LRO} starts to increase but below ~ 40 K is almost temperature independent (see section IV.3.2). For $Nd_2Mo_2O_7$, below $T_C \sim 95$ K, M_{Nd}^{LRO} starts slowly to increase. When temperature is decreasing from 80 to 30 K, it is almost constant. Then suddenly, below 30 K, it strongly increases (almost four times more than in 30-95 K interval). M_{Mo}^{LRO} increases slowly below T_C. These results show that for $(Tb_{0.8}La_{0.2})_2Mo_2O_7$ the Tb-Mo coupling is strong: both magnetic moments increase with decreasing temperature, without any anomaly. Per contra, in $Nd_2Mo_2O_7$ the Nd-Mo coupling is small: Mo starts to order below T_C, while Nd is still almost paramagnetic. Below ~ 30 K, the ordered antiferromagnetic component of Nd increases drastically.

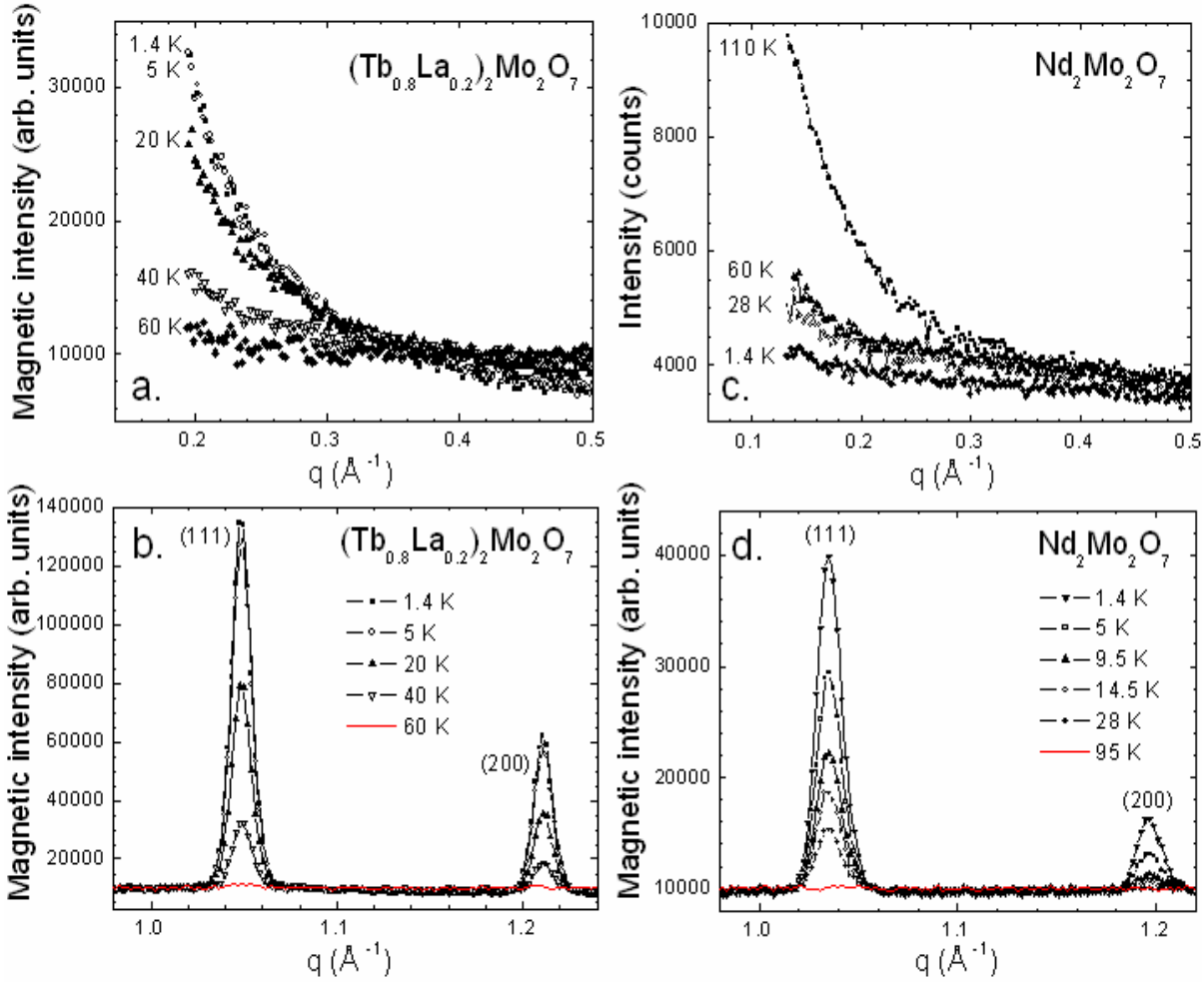

Figure 14. Neutron diffraction intensity versus the scattering vector $q = 4\pi \sin\theta / \lambda$, with the incident neutron wavelength λ=4.741 Å. The small angle ferromagnetic correlations and the region of (111) and (200) peaks are shown for several temperatures. a-b. Magnetic intensity of $(Tb_{0.8}La_{0.2})_2Mo_2O_7$. A spectrum in the paramagnetic region was subtracted; c-d: Total intensity (magnetic and nuclear) of $Nd_2Mo_2O_7$ [Mirebeau'07b].

The neutron diffraction shows that the T^* transition seen by μSR does not have the same microscopic description for both compounds. For $(Tb_{0.8}La_{0.2})_2Mo_2O_7$, the long range

magnetic order (the Bragg peaks) coexists with a short range order (the diffuse scattering as shown in section IV.3.2 and less clear in Figure 14 and also the SANS signal; for clarity, due to its slightly higher correlation length, the latter may be considered as corresponding to a mesoscopic order). All increase when decreasing temperature. For this system T^* is a transition to disorder. This behaviour is probably due to the Tb/La chemical substitution. Per contra, for $Nd_2Mo_2O_7$, when decreasing temperature the Bragg peaks increase, while the SANS signal decreases. T^* represents a transition to long range order, which becomes more significant with decreasing temperature below T^* (there is an unique magnetic ground state).

Finally, we underline that the broad maximum seen in the dynamical muon relaxation rate at T^*,well below T_C, may have different significations: (i) a spin freezing in a completely chemically disordered system in amorphous RGS's; (ii) a freezing of the disordered component (short range correlated magnetic spins) in $(Tb_{0.8}La_{0.2})_2Mo_2O_7$, with chemical disorder induced by Tb/La substitution; (iii) a freezing of the ordered spin component in the chemically ordered $Nd_2Mo_2O_7$.

VI.4. Spin glass state

The analysis of the spin glass type order which characterizes the Mo pyrochlores having $a < a_c \sim 10.33$ Å, puts into light other interesting question marks. It is considered that the spin glass state is determined by the antiferromagnetic Mo-Mo interactions, due to the superexchange mechanism and frustrated by the lattice geometry [Kang'02, Solovyev'03].

We have already made in section VI.1. the comparison between $(Tb_{1-x}La_x)_2Mo_2O_7$ series (x=0-0.2), where the Tb/La substitution induces the transition from a spin glass type to a non-collinear ferromagnetic order, and the $(Y_{1-x}La_x)_2Mo_2O_7$ series (x=0-0.5), where the Y/La substitution does not induce a transition to long range magnetic order, although the critical threshold ($a_c \sim 10.33$ Å) is crossed [Sato'87]. All the compounds of the latter series remain spin glasses, although the Curie-Weiss constant changes its sign when passing the critical threshold, indicating a change from antiferromagnetic to ferromagnetic correlations. The only difference between the two series is that Tb^{3+} is magnetic and Y^{3+} it is not.

A question arises: besides the molybdenum magnetism, what is the exact role of the rare earth magnetism?

Our analysis of $Tb_2Mo_2O_7$ ($a = 10.312$ Å) by a short range model shows the presence of antiferromagnetic Tb-Mo correlations and ferromagnetic Tb-Tb correlations, in good agreement with previous results [Greedan'90, Greedan'91] . This analysis cannot probe the Mo-Mo correlations in the spin glass phase, since the Mo^{4+} moment is too small with regards to that of Tb^{3+}. However the Mo-Mo correlations can be directly evidenced in $Y_2Mo_2O_7$ ($a = 10.21$ Å), where only Mo^{4+} ions are magnetic. Elastic scattering measurements show that in $Y_2Mo_2O_7$ [Gardner'99] the Mo-Mo antiferromagnetic correlations with a length scale of about 5 Å yield a peak in the diffuse scattering at $q = 0.44$ Å^{-1}. A similar behaviour to that of $Y_2Mo_2O_7$ is also observed in $Yb_2Mo_2O_7$ ($a = 10.168$ Å), where the contribution of Yb^{3+} magnetic moments (around 1 μ_B) is much lower than that of Tb^{3+} [Mirebeau'06].

Figure 15a-c shows how in the $(Tb_{1-x}Y_x)_2Mo_2O_7$ series (with x=0, 0.4 and 1) the decrease of the concentration of Tb^{3+} magnetic ion by chemical substitution with the non-magnetic Y^{3+} favours the antiferromagnetic correlations. As shown in section V.2.2, the effect of the applied pressure on $Tb_2Mo_2O_7$ is similar: the ferromagnetic Tb-Tb correlations are reduced and hence the antiferromagnetism is also favoured.

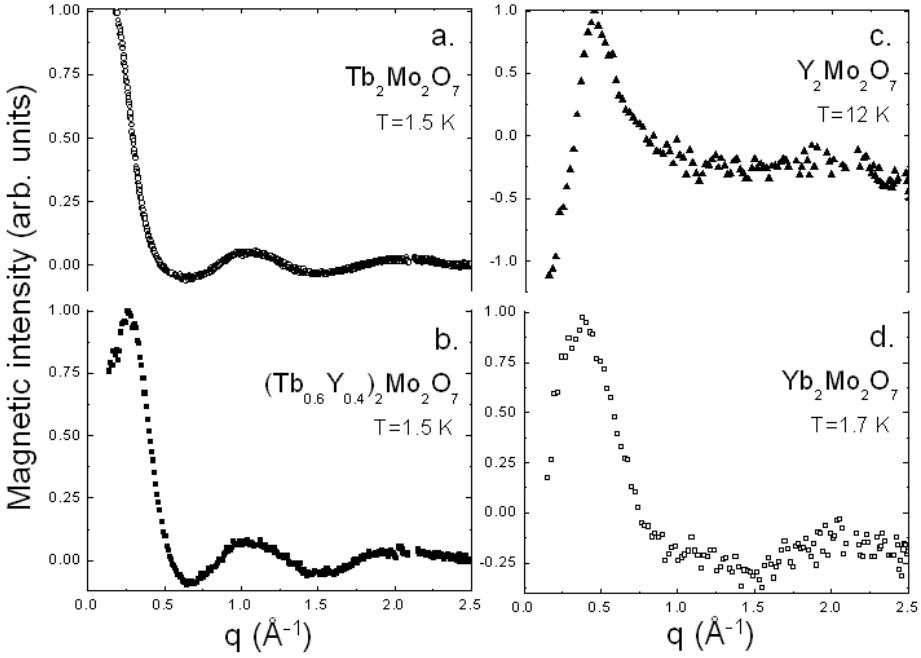

Figure 15. Magnetic intensity versus the scattering vector q for four Mo pyrochlores situated in the spin glass region of the phase diagram: a. $Tb_2Mo_2O_7$ (a=10.312 Å); b. $(Tb_{0.6}Y_{0.4})_2Mo_2O_7$ (a=10.278 Å); c. $Y_2Mo_2O_7$ (a=10.21 Å)[Mirebeau'06]; d. $Yb_2Mo_2O_7$ (a=10.168 Å) [Mirebeau'06]. A pattern in the paramagnetic region was subtracted and the magnetic intensity was normalised to the maximal value.

How the magnetic interactions determine such behaviour? The Tb-Tb interactions are weak (interactions between f ions). We do not know their sign, but if additionally they are frustrated by the geometry (corner sharing tetrahedra lattice) they are not able to induce the long range magnetic order. Per contra, the Tb-Mo interactions are not or are less frustrated because of the Tb-Mo lattice, which is not a pyrochlore one (each Tb atom situates in the center of a hexagon formed by its six Mo first neighbours). The interaction Tb-Mo could therefore mediate the long range order. The substitution of Tb^{3+} with La^{3+}, weakens this interaction, so that at high La^{3+} concentrations we should obtain again a spin glass state. The substitution of Tb^{3+} by Y^{3+} should also weaken the Tb-Mo interaction. Under pressure the Tb-Mo and/or Mo-Mo interactions seem to become more antiferromagnetic.

VI.5. Spin glass insulator- ferromagnetic metallic transition: chemical pressure versus applied pressure

When speaking about crystal structure of the molybdenum pyrochlores, there are two parameters that could influence their electronic and magnetic properties: the lattice parameter a, which controls the strength of the direct Mo-Mo interactions, and the Mo-O1-Mo bond angle, which governs the interactions between Mo(t_{2g}) orbitals mediated by oxygen (2p). However, band structure calculations [Solovyev'03] (for details see Chapter I) argue that the key parameter is the Mo-Mo distance directly related to a. Experimental results confirm this hypothesis: our crystal analysis at ambient and under applied pressure on $(Tb_{1-x}La_x)_2Mo_2O_7$ series (x=0-0.2), as well as those reported in Ref. [Moritomo'01] on $R_2Mo_2O_7$ (with R=Dy, Gd, Sm and Nd) or in Ref. [Ishikawa'04] on $Nd_2Mo_2O_7$ under pressure show that the variation of the bond angle is very small when crossing the threshold.

The microscopic analysis of $(Tb_{1-x}La_x)_2Mo_2O_7$ series (x=0-0.2) or the macroscopic ones on $(Gd_{1-x}Dy_x)_2Mo_2O_7$ (x=0-0.4) [Kim'03, Park'03] or $(Sm_{1-x}Tb_x)_2Mo_2O_7$ series (x=0-0.8) show that from the point of view of magnetic properties both chemical and applied pressure have the same effect: the decrease of the lattice parameter a yields a spin glass behaviour. Per contra, as shown for $(Sm_{1-x}Tb_x)_2Mo_2O_7$ series (x=0-0.8) by resistivity measurements [Miyoshi'03], the decrease of a by chemical pressure yields an insulation behaviour, while the applied pressure favours the metallic state.

A comparison between the effects of chemical and applied pressure on conduction and magnetic properties of the Mo pyrochlores is possible in the framework of the Hubbard model, whose Hamiltonian has only two terms: one corresponding to the electrons kinetic energy (parametrized by the transfer integrals t between two sites or by the electronic bandwidth W) and the other one corresponding to the on-site Coulomb energy (parametrized by U).

At ambient pressure, when the decreases of a is induced by chemical substitution, the ferromagnetic-spin glass and metallic-insulator transitions are quite well explained taking into account the behaviour of the $Mo(t_{2g})$ levels situated near the Fermi level and well separated from the rest of the spectrum, as shown by band structure calculations [Solovyev'03] and confirmed by photoemission spectroscopy [Kang'02]. When a decreases, the on-site Coulomb U interaction increases and it opens a gap at the Fermi level: the metal becomes insulator through a Mott transition. In the same time the antiferromagnetic superexchange interactions exceed the ferromagnetic ones due to double exchange mechanism and the spin glass state is stabilized. In this process, only the size of the R^{3+} ion varies, while the changes of the bandwidth of Mo orbitals are supposed to be quite small [Solovyev'03]. In the framework of Hubbard model: under chemical pressure U increases, while t is roughly constant.

The effect of the applied pressure is different. It increases the on-site Coulomb repulsion energy U, but one expects that the variation of U with pressure is less important than that of the bandwidth of Mo orbitals and the kinetic energy of electrons t. The Mott transition does not take place in this case and if the system is metallic at ambient pressure it remains metallic when applying pressure. The transition from ferromagnetic to spin glass state under the effect of the applied pressure may be explained within the same Hubbard model. Since the superexchange interaction is proportional to t^2/U [Auerbach'94], for an on-site Coulomb interaction which does not vary significantly and important variations of t, it dominates.

VI.6. Conclusions

All experimental data on $(Tb_{1-x}La_x)_2Mo_2O_7$ (x=0-0.2) series provide a phase diagram: temperature of transition versus the lattice parameter. In this chapter we showed that on this phase diagram there are three regions of interest (beside the paramagnetic one): non-collinear ferromagnetic, spin glass and mixed. We analysed the nature of each region.

It was well established that the spin glass-ferromagnetic transition corresponds to a change of sign of the Mo-Mo exchange interactions, but the role of the rare earth has not been discussed up to now (most experimental and theoretical studies assumed that it was negligible). In this chapter we discussed the role of the rare earth in regard to this transition, which is seen only for systems having two magnetic ions (Mo^{4+} and R^{3+}) on pyrochlore lattices. We showed that the non-collinear ferromagnetic long range order ("ordered spin ice")

is due to the rare earth anisotropy. At low temperature μSR and inelastic neutron scattering show that there is a reentrant spin glass transition to a mixed phase, where the "ordered spin ice" coexists with a freezing of the short range correlated spins (spin glass behaviour) and also with slow spin fluctuations (spin liquid behaviour). The origin of this mixed phase is the anisotropy of the rare earth and also the disorder of the system induced by chemical substitution. We also show that the rare earth magnetism is necessary to induce the long range order when the lattice is expanded.

Finally, within Hubbard model and band structure calculations, we tried to explain why chemical and applied pressure favours both the same magnetic state (spin glass), while their behaviour is different in regard to the conduction properties (chemical pressure favours the insulating state and applied pressure the metallic one).

VI.7. Perspectives

As perspectives, we mention first that would be interesting to develop a microscopic theory of the spin glass – ferromagnetic transition, which should take into account not only the Mo magnetism, but also that of the rare earth, which, as we showed, cannot be negligible. Secondly, we mention the study of the nature of the "reentrant" transition seen in the $Nd_2Mo_2O_7$, characterized by the absence of chemical disorder and which presents a giant anomalous Hall effect.

Conclusion générale

Cette étude a été consacrée à l'analyse des propriétés structurales et magnétiques de deux types de pyrochlores : (i) $Tb_2Sn_2O_7$, où les ions Tb^{3+} occupent un réseau pyrochlore frustré et où l'état fondamental résulte essentiellement de l'influence des interactions d'échange, dipolaires et de l'anisotropie des ions Tb^{3+} et (ii) la série $(Tb_{1-x}La_x)_2Mo_2O_7$ (x =0-0.2) où deux types d'ions magnétiques Tb^{3+} et Mo^{4+} occupent des réseaux frustrés et où l'état fondamental est déterminé à la fois par les moments localisés des ions Tb^{3+} et par le magnétisme partiellement itinérant des ions Mo^{4+}. Notre premier but a été de caractériser à un niveau microscopique le comportement magnétique de ces systèmes. Nous avons utilisé plusieurs techniques microscopiques : (i) la diffraction de rayons X à pression ambiante et sous pression, pour déterminer la structure cristalline et (ii) la diffraction de neutrons et la rotation et relaxation de spin des muons (μSR), qui grâce à leur complémentarité fournissent une information précise sur les corrélations statiques et la dynamique de spin. Notre deuxième but a été de tenter de déterminer dans chaque cas le rôle exact de la terre rare et/ou du métal de transition et de déterminer comment les interactions magnétiques favorisent un état magnétique spécifique.

L'analyse de $Tb_2Sn_2O_7$, a montré qu'à haute température il a le comportement d'un liquide de spin, comme $Tb_2Ti_2O_7$, mais qu'à basse température (T <1.3 K) il se comporte comme une "glace de spin ordonnée". Autrement dit, à cause de l'anisotropie de Tb^{3+}, l'arrangement des spins dans un tétraèdre est proche de celui d'une glace de spin, mais contrairement aux glaces de spins classiques, il existe une composante ferromagnétique ordonnée à longue portée (les quatre tétraèdres de la maille sont identiques). En combinant la diffraction de neutrons et les mesures de la chaleur spécifique, nous avons montré que dans $Tb_2Sn_2O_7$, l'état "glace de spin ordonnée" coexiste avec des fluctuations réminiscentes de l'état liquide de spin. Dans le cadre des modèles théoriques proposés dans la littérature, nous avons montré que dans $Tb_2Sn_2O_7$, ce type d'ordre magnétique peut s'expliquer par une interaction d'échange effective ferromagnétique (somme de l'interaction d'échange directe et de l'interaction dipolaire) couplée à une anisotropie finie. Ce comportement diffère de celui de $Tb_2Ti_2O_7$, où l'interaction d'échange effective est supposée antiferromagnétique, ou faiblement ferromagnétique. La substitution chimique de Ti^{4+} par Sn^{4+}, qui dilate le réseau et modifie les poids respectifs des différentes interactions dans l'équilibre énergétique, offre donc non seulement la possibilité d'étudier un nouveau type d'ordre magnétique, mais aussi aide à comprendre le composé parent $Tb_2Ti_2O_7$.

L'étude de la série $(Tb_{1-x}La_x)_2Mo_2O_7$ constitue la première étude microscopique des corrélations et fluctuations de spin dans la région du seuil de transition ferromagnétique – verre de spin et fournit une information nouvelle sur la physique des pyrochlores de molybdène. La substitution chimique Tb/La dilate le réseau et induit, comme le montre la diffraction de neutrons, une transition d'un état verre de spin vers un état ferromagnétique non

colinéaire ordonné à longue portée. Cette transition correspond à un changement des corrélations de spin (Mo-Mo et Tb-Mo antiferromagnétiques dans l'état verre de spin, toutes les corrélations ferromagnétiques dans l'état ordonné). L'état ferromagnétique est dominé par l'interaction ferromagnétique Mo-Mo, mais reste frustré par l'anisotropie du Tb^{3+}. A cause de cette anisotropie, les moments de Tb^{3+} s'orientent dans une configuration voisine de celle d'une glace de spin. Ce type de ferromagnétisme peut donc aussi s'intituler "glace de spin ordonnée". Nous remarquons que, compte tenu du fort champ moléculaire du Mo^{4+}, la température d'ordre augmente de près de deux ordres de grandeur par rapport à celle de $Tb_2Sn_2O_7$. En dessous de la température d'ordre, les mesures de muons et récemment de diffusion inélastique de neutrons révèlent l'existence d'une seconde transition. Elle correspond à une transition "réentrante" vers une phase mixte, dans laquelle l'état "glace de spin ordonnée" coexiste avec un gel de composantes de spin corrélées à courte portée, mais aussi avec des fluctuations de spin. Cette phase mixte est induite par l'anisotropie du Tb^{3+}, mais aussi par le désordre lié à la substitution Tb/La. La comparaison avec les composés sans désordre $Gd_2Mo_2O_7$ (isotrope) et $Nd_2Mo_2O_7$ (anisotrope) permet de déterminer les influences respectives du désordre et de l'anisotropie sur cette nouvelle transition.

Sous pression appliquée, l'état "glace de spin ordonnée" est détruit et un état verre de spin est stabilisé. Nous montrons donc l'équivalence entre l'effet d'une pression chimique et celui d'une pression appliquée sur le changement des propriétés magnétiques de ces composés. Bien que le rôle dominant dans cette transformation soit joué par les interactions Mo-Mo, notre étude montre aussi le rôle important du magnétisme du Tb^{3+}. La comparaison entre la série $(Tb_{1-x}La_x)_2Mo_2O_7$ et la série $(Y_{1-x}La_x)_2Mo_2O_7$, dans laquelle les interactions Mo-Mo deviennent aussi ferromagnétiques par dilatation du réseau mais n'induisent pas d'ordre à longue portée, suggère que le magnétisme de la terre rare est nécessaire pour induire l'ordre à longue portée. Ceci peut venir de la présence des interactions Tb-Mo, qui ne sont pas frustrées par la géométrie. En combinant toutes nos données sur les températures d'ordre à pression ambiante et sous pression, nous proposons un nouveau diagramme de phase pour les pyrochlores de molybdène, qui comporte non pas deux mais trois phases hors la phase paramagnétique : verre de spin, ferromagnétique et mixte.

Cette étude met donc en valeur l'intérêt des techniques microscopiques, combinées à celui de la pression, pour l'étude du comportement complexe des systèmes géométriquement frustrés.

Pour terminer, nous mentionnons quelques perspectives pour ce travail, qui correspondent pour la plupart à des études en cours. Pour $Tb_2Sn_2O_7$: (i) l'étude du champ cristallin par diffusion inélastique de neutrons, permet de déterminer l'origine de l'anisotropie finie du Tb^{3+} en comparaison avec celle dans $Tb_2Ti_2O_7$; (ii) l'étude des fluctuations de spin qui persistent dans la phase ordonnée par diffusion inélastique de neutrons ; (iii) l'étude de l'état "glace de spin ordonnée" sous pression par diffraction de neutrons. Pour les pyrochlores $R_2Mo_2O_7$: (i) il serait intéressant de développer une théorie microscopique du seuil de transition ferromagnétique-verre de spin, prenant en compte non seulement le magnétisme du Mo^{4+} mais aussi celui de la terre rare, dont nous avons montré qu'il ne peut pas être négligé ; (ii) l'étude de la nature de la transition "réentrante" dans le composé sans désordre $Nd_2Mo_2O_7$, qui présente un effet Hall anormal géant.

General conclusion

This study was dedicated to the analysis of the structural and magnetic properties of two types of pyrochlore systems: (i) $Tb_2Sn_2O_7$, where the rare earth ions Tb^{3+} occupy a frustrated pyrochlore lattice and the magnetic ground state mostly results from the influence of Tb^{3+} exchange, dipolar and crystal field energies and (ii) $(Tb_{1-x}La_x)_2Mo_2O_7$ x=0-0.2 series, where both Tb^{3+} and Mo^{4+} ions occupy frustrated pyrochlore lattices and the magnetic ground state is determined by both the localized Tb^{3+} and the partially itinerant transition metal Mo^{4+} magnetism. The first goal was to characterize at microscopical level the magnetic behaviour of these systems. We used several microscopical techniques: (i) X ray diffraction at ambient and under pressure, to determine the crystal structure and (ii) neutron diffraction and μSR at ambient and under pressure, which due to their complementarity offered precise information on both spin statics and dynamics. The second goal was to try to understand in each case the exact role of the rare earth and/or transition metal ions and to determine how the magnetic interactions favour a specific ground state.

The analyse of $Tb_2Sn_2O_7$ showed that at high temperature it has a spin liquid behaviour, like $Tb_2Ti_2O_7$, but at low temperature (T <1.3 K) it is an "ordered spin ice", *i.e.* due to the Tb^{3+} anisotropy the spin arrangement on one tetrahedron is close to that of a spin ice configuration, but contrary to the usual spin ices it has a long range ferromagnetic component (the four tetrahedra of the unit cell are identical). Combining neutron diffraction and specific heat measurements we showed that in $Tb_2Sn_2O_7$ the "ordered spin ice" coexists with spin fluctuations reminiscent of a spin liquid behaviour. Within the models existing in the literature we showed that in $Tb_2Sn_2O_7$ this type of magnetic order may be explained by a ferromagnetic effective exchange interaction (which summarizes both direct exchange and dipolar interactions) coupled with a finite rare earth anisotropy. Its behaviour differs from that of $Tb_2Ti_2O_7$, where the effective exchange interaction is assumed to be antiferromagnetic or weakly ferromagnetic. The chemical substitution of Ti^{4+} by Sn^{4+}, which expands the lattice and modifies the contribution of the involved interactions to the energetic equilibrium, offers therefore not only the possibility of studying a new type of magnetic order but could also help to understand its parent compound $Tb_2Ti_2O_7$.

The study of $(Tb_{1-x}La_x)_2Mo_2O_7$ series provides the first microscopic picture of spin correlations and fluctuations in the threshold region of the spin glass-ferromagnetic transition and gives new information on the physics of the molybdenum pyrochlores. The Tb/La chemical substitution expands the lattice and induces, as probed by neutron diffraction, a transition from a spin glass to a non-collinear long range ordered ferromagnetic state. This transition corresponds to a change of the magnetic spin correlations (from antiferromagnetic Mo-Mo and Tb-Mo in the spin glass state to all ferromagnetic in the ordered state). The ferromagnetic state is dominated by the ferromagnetic Mo-Mo interaction, but remains frustrated by the Tb anisotropy. Due to this anisotropy, the magnetic moments orient in a

configuration close to that of a spin ice. This type of ferromagnetism can also be called an "ordered spin ice". We notice that, due to the strong Mo molecular field, the ordering temperature increases by roughly two orders of magnitude comparing to $Tb_2Sn_2O_7$. Below the ordering temperature, the μSR and recent inelastic neutron scattering measurements show a second transition. It corresponds to a "reentrant" transition to a mixed phase, where the "ordered spin ice" coexists with a freezing of the short range correlated spins and also with slow spin fluctuations. This mixed phase is induced by Tb^{3+} anisotropy, but also by the chemical disorder due to Tb/La substitution. The comparison with the ordered compounds $Gd_2Mo_2O_7$ (isotropic) and $Nd_2Mo_2O_7$ (anisotropic) allows the determination of the influence on this transition of the disorder and rare earth anisotropy, respectively.

Under applied pressure the long range "ordered spin ice" phase is destroyed and a spin glass like state is recovered. We showed therefore the equivalence between the effect of chemical and applied pressure on the change of magnetic properties of these systems. Although the Mo-Mo interactions seem to play the main role in this change, our study also shows the important role played by Tb^{3+} magnetism. The comparison of $(Tb_{1-x}La_x)_2Mo_2O_7$ with $(Y_{1-x}La_x)_2Mo_2O_7$ series, where Mo-Mo interaction also becomes ferromagnetic when expanding the lattice but which does not induce long range order, suggests that the rare earth magnetism is necessary to induce long range order. This may come from the presence of Tb-Mo interaction, which is not frustrated by the geometry. Using all our data on the ordering temperatures, at ambient and under applied pressure, we propose a new phase diagram for Mo pyrochlores, which has not only two but three regions beside the paramagnetic one: spin glass, ferromagnetic and mixed.

This study underlines the interest in microscopical techniques, at ambient and especially under applied pressure, when studying the complex behaviour of the geometrically frustrated systems.

Finally, we mention few perspectives, most of them corresponding to current studies. For $Tb_2Sn_2O_7$: (i) the crystal field study by inelastic neutron scattering, which allows to determine the origin of Tb^{3+} finite anisotropy in comparison to that found in $Tb_2Ti_2O_7$; (ii) the study of spin fluctuations, which persist in the "ordered spin ice" state, by inelastic neutron scattering and (iii) the study of the "ordered spin ice" under applied pressure, by neutron diffraction. For $R_2Mo_2O_7$ pyrochlores: (i) it would be interesting to develop a microscopic theory of the spin glass – ferromagnetic transition, that should take into account not only the Mo magnetism, but also that of the rare earth, which, as we showed, cannot be negligible and (ii) the study of the nature of the "reentrant" transition seen in the $Nd_2Mo_2O_7$, characterized by the absence of chemical disorder and which presents a giant anomalous Hall effect.

Appendix A

Analysis of the nuclear specific heat C_{nucl} in $Tb_2Sn_2O_7$

The nuclear specific heat of $Tb_2Sn_2O_7$, which is dominant below 0.38 K, as presented in section III.4, was calculated starting from the full hyperfine Hamiltonian. This Hamiltonian has two terms: the magnetic one due to the hyperfine field $\vec{H}_{hf}$ and an electric quadrupolar one, respectively:

$$\mathcal{H}_{hf} = -\vec{\mu}_I \cdot \vec{H}_{hf} + \alpha_Q[I_z^2 - \frac{I(I+1)}{3}] \qquad \text{[A.1].}$$

In equation [A.1]: $\vec{\mu}_I = g_I \mu_N \vec{I}$ is the nuclear magnetic moment, with g_I the nuclear g factor, μ_N the nuclear magneton, $\vec{I}$ the nuclear spin, $\vec{H}_{hf}$ is the hyperfine field and α_Q corresponds to the quadrupolar term.

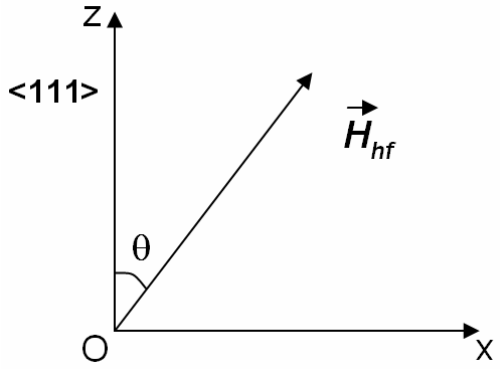

Figure 1.

If one considers the xOz plane, where the anisotropy axis [111] is parallel to Oz, and notes with θ the angle between this axis and the hyperfine field as indicated in Figure 1, then the Hamiltonian has the expression:

$$\mathcal{H}_{hf} = -g_I \mu_N H_{hf}[I_z \cos\theta + I_x \sin\theta] + \alpha_Q[I_z^2 - \frac{I(I+1)}{3}] \qquad \text{[A.2].}$$

Taking into account that for ^{159}Tb I =3/2, we calculated the matrices associated to the nuclear spin operators I_z, I_+, I_-:

$$I_z = \hbar\begin{pmatrix} 3/2 & 0 & 0 & 0 \\ 0 & 1/2 & 0 & 0 \\ 0 & 0 & 1/2 & 0 \\ 0 & 0 & 0 & 3/2 \end{pmatrix}, I_+ = \hbar\begin{pmatrix} 0 & \sqrt{3} & 0 & 0 \\ 0 & 0 & 2 & 0 \\ 0 & 0 & 0 & \sqrt{3} \\ 0 & 0 & 0 & 0 \end{pmatrix}, I_- = \hbar\begin{pmatrix} 0 & 0 & 0 & 0 \\ \sqrt{3} & 0 & 0 & 0 \\ 0 & 2 & 0 & 0 \\ 0 & 0 & \sqrt{3} & 0 \end{pmatrix} \quad [A.3]$$

and then $I_x = (I_+ + I_-)/2$.

The Hamiltonian [A.2] becomes:

$$\mathcal{H}_{hf} =$$

$$\begin{pmatrix} -\frac{3}{2}g_I\mu_N H_{hf}\cos\theta + \alpha_Q & -\frac{\sqrt{3}}{2}g_I\mu_N H_{hf}\sin\theta & 0 & 0 \\ -\frac{\sqrt{3}}{2}g_I\mu_N H_{hf}\sin\theta & -\frac{g_I\mu_N H_{hf}}{2}\cos\theta - \alpha_Q & -g_I\mu_N H_{hf}\sin\theta & 0 \\ 0 & -g_I\mu_N H_{hf}\sin\theta & \frac{g_I\mu_N H_{hf}}{2}\cos\theta - \alpha_Q & -\frac{\sqrt{3}}{2}g_I\mu_N H_{hf}\sin\theta \\ 0 & 0 & -\frac{\sqrt{3}}{2}g_I\mu_N H_{hf}\sin\theta & \frac{3}{2}g_I\mu_N H_{hf}\cos\theta + \alpha_Q \end{pmatrix} \quad [A.4]$$

As one may see, in [A.4] there are three parameters: (i) the hyperfine filed H_{hf}; (ii) the angle θ made by $\vec{H}_{hf}$ with the local <111> anisotropy axis; (iii) the quadrupolar term α_Q. We expressed these parameters accordingly to Ref. [Abragam'70, Dunlap'71, Goldanskii'68] and taking into account the quantities to which we have access experimentally.

(i) the hyperfine field H_{hf}

The hyperfine field was determined accordingly to Ref. [Abragam'70, Dunlap'71, Goldanskii'68]:

$$\vec{H}_{hf} = -2\mu_B \left\langle r^{-3} \right\rangle_{4f} \left\langle J \left\| N \right\| J \right\rangle \left\langle \vec{J} \right\rangle \quad [A.5]$$

where μ_B is the Bohr magneton, $\left\langle r^{-3} \right\rangle_{4f}$ is the mean inverse third power of the $4f$ electron distance from the nucleus averaged over the electronic wave functions, $\left\langle J \left\| N \right\| J \right\rangle$ is an multiplicative factor for $4f$ ions and $\vec{J}$ is the total angular momentum. Since the electronic magnetic moment $\vec{\mu} = -g_J\mu_B\vec{J}$, with g_J the Landé factor, [A.5] becomes:

$$\vec{H}_{hf} = \frac{2}{g_J}\left\langle r^{-3} \right\rangle_{4f} \left\langle J \left\| N \right\| J \right\rangle \left\langle \vec{\mu} \right\rangle \quad [A.6]$$

For Tb^{3+} $g_J = \frac{3}{2}$, $\left\langle r^{-3} \right\rangle_{4f} = 8.53\, a_0^{-3}$, with Bohr radius $a_0 = 5.292\cdot 10^{-9}$ cm, $\left\langle J \left\| N \right\| J \right\rangle = \frac{5}{9}$ and therefore:

$$H_{hf}\ (Tesla) = 40\ \mu\ (\mu_B) \qquad [A.7]$$

(ii) the angle θ made by $\vec{H}_{hf}$ with the local <111> anisotropy axis was fixed at the value obtained by neutron diffraction analysis:

$$\theta = 13.3° \qquad [A.8]$$

(iii) the quadrupolar term α_Q has an electronic $4f$ and a lattice term:

$$\alpha_Q = \alpha_Q^{4f} + \alpha_Q^{lattice} \qquad [A.9]$$

- the $4f$ quadrupolar interaction α_Q^{4f} was expressed accordingly to Ref. [Abragam'70, Goldanskii'68]:

$$H_Q = \frac{3eQV_{zz}}{4I(2I-1)}\left[I_Z^2 - \frac{I(I+1)}{3}\right] \qquad [A.10]$$

With $I = \frac{3}{2}$ for Tb^{3+}: $\quad H_Q = \frac{1}{4}eQV_{zz}\left[I_z^2 - \frac{5}{4}\right] = \alpha_Q^{4f}\left[I_z^2 - \frac{5}{4}\right]$ [A.11]

e is the electron charge magnitude and Q the nuclear quadrupolar moment. $V_{zz} = \partial^2 V / \partial z^2$ represents the electric field gradient at the nucleus, which for $4f$ electrons is expressed:

$$V_{zz}^{4f} = -e(1-R_Q)\left\langle r^{-3}\right\rangle_{4f}\left\langle J\left\|\alpha\right\|J\right\rangle\left\langle 3J_Z^2 - J(J+1)\right\rangle \qquad [A.12]$$

R_Q is the atomic Sternheimer shielding factor, $\left\langle J\left\|\alpha\right\|J\right\rangle$ is an multiplicative factor. $R_Q \cong 0.2$ for the rare ions and for Tb^{3+}: $Q = 1.3$ b, $\left\langle r^{-3}\right\rangle_{4f} = 8.53\ a_0^{-3}$, $\left\langle J\left\|\alpha\right\|J\right\rangle = -1/99$ and $J = 6$.

From [A.11] and [A.12], using the above values and making the approximation $\left\langle J_z^2\right\rangle \approx \left\langle J_z\right\rangle^2 \approx (\mu / g_J\mu_B)^2$, we obtain:

$$\alpha_Q^{4f} = 0.2517\left[3\left(\frac{H_{hf}}{40}\frac{2}{3}\right)^2 - 42\right]\ (mK) \qquad [A.13]$$

- the lattice quadrupolar interaction $\alpha_Q^{lattice}$ was extrapolated from the value

measured in another pyrochlore stannate, $Gd_2Sn_2O_7$, by Mössbauer spectroscopy [Bertin'01]. Since for ^{155}Gd $eQV_{zz}^{lattice} = -26.76\,(mK)$, we expressed for ^{159}Tb : $\alpha_Q^{lattice}(^{159}Tb)$ = $\frac{1}{4}eQ(^{159}Tb)V_{zz}^{lattice} = \frac{1}{4}e\frac{Q(^{159}Tb)}{Q(^{155}Gd)}Q(^{155}Gd)V_{zz}^{lattice}$. With $\frac{Q(^{159}Tb)}{Q(^{155}Gd)} \simeq 1$, it results:

$$\alpha_Q^{lattice}\left(^{159}Tb\right) = -6.69\,(mK) \qquad [A.14]$$

Considering [A.8], [A.9], [A.13] and [A.14], the Hamiltonian [A.4] depends only on the hyperfine magnetic field H_{hf}. This means according to [A.7] that it depends only on Tb^{3+} magnetic moment $\mu\,(\mu_B)$. We notice that in the thesis text the magnetic moment was noted with $m\,(\mu_B)$ for consistency reasons.

Appendix B

Symmetry representation analysis

As already stated in Chapter II, when solving a magnetic structure there are two steps: (i) the identification of the propagation vector (or vectors) $\vec{k}$ and (ii) the determination of the magnetic moments.

In general, the magnetic structure has a distribution of magnetic moments that can be expanded as a Fourier series:

$$\vec{m}_{jl} = \sum_{\vec{k}} \vec{S}_k^j \exp\left[-2\pi i(\vec{k}\cdot\vec{R}_l)\right] \qquad \text{[B.1]}$$

$\vec{m}_{jl}$ is the magnetic moment corresponding to the atom j ($j = 1, 2, \ldots n_a$) of the cell l (having its origin at $\vec{R}_l$). $\vec{S}_k^j$ are the Fourier coefficients. The sum is extended to all propagation vectors $\vec{k}$. We note that if there is an unique propagation vector, then [B.1] becomes:

$$\vec{m}_{jl} = \vec{S}_k^j \exp\left[-2\pi i(\vec{k}\cdot\vec{R}_l)\right] \qquad \text{[B.2]}$$

and, furthermore, supposing $\vec{k} = (0,0,0)$ (it is the case of all magnetic structures analysed in this study) the Fourier coefficients are real and equal to the magnetic moments.

Starting from the principle that, in first approximation, there is a conservation of the crystalline symmetry between the low temperature ordered magnetic state and the high temperature paramagnetic state, one may determine the propagation vector group G_k. It is the so-called "little group". G corresponds to the space group of the nuclear structure.

The symmetry approach in the theory of magnetic structures rests on the idea that any magnetic structure with a prescribed propagation vector $\vec{k}$ may be expanded in basis functions of irreducible representations of the space group of the crystal having this $\vec{k}$. The determination of the Fourier coefficients $\vec{S}_k^j$ for different irreducible representations of G_k group involves several steps: (i) the symmetry operators of the "little group" G_k are determined; (ii) the magnetic reducible representation Γ_{magn} of the G_k group is determined by working with the symmetry operators of G_k acting on the atoms coordinates and components of the axial vectors; (iii) the magnetic reducible representation Γ_{magn} is then decomposed in irreducible representations Γ_ν of the G_k group; (iv) finally, the basis

functions of the irreducible representations Γ_ν of G_k, corresponding to the magnetic sites, are deduced using projection operators.

Taking into account the symmetry, the vectors $\vec{S}_k^j$ may be written as a linear combination of the basis functions of the irreducible representations of the propagation vector group G_k:

$$\vec{S}_k^j = \sum_{nd} C_{nd}^\nu \vec{V}_{nd}^{\vec{k}\nu}(j) \qquad [B.3]$$

where ν labels the irreducible representation of the propagation vector group G_k, d varies from 1 to the dimension of Γ_ν ($d = 1, 2, \ldots, \dim(\Gamma_\nu)$) and the index n varies from 1 to the number of times the irreducible representation Γ_ν is contained in the magnetic reducible representation Γ_{magn} ($n = 1, 2, \ldots, a_\nu$). C_{nd}^ν are the coefficients (that may be real or pure imaginary). Finally, $\vec{V}_{nd}^{\vec{k}\nu}(j)$ are the basis vectors, obtained by applying the projection operator formula to unity vectors along the directions of the cell parameters.

The symmetry analysis allows, for a given representation, to define the list of the independent basis vectors $\vec{V}_{nd}^{\vec{k}\nu}(j)$, the coefficients C_{nd}^ν and the number of free parameters to describe the magnetic structure, $n_f = a_\nu \times \dim(\Gamma_\nu)$.

The advantage of the symmetry analysis is that it allows an important reduction of the number of free parameters. This reduction is facilitated by selecting only those magnetic structures which are allowed by the symmetry of the crystal. When the constraints induced by the symmetry analysis are not enough to simplify the problem, one should consider other restrictions, imposed by a preliminary knowledge of the analysed magnetic system (as, for example, the constant amplitude of the magnetic moments or constraints of parallelism or antiparallelism of the magnetic moments).

For more details on the symmetry representation analysis of the magnetic structures see the following References: [Bertaut'63, Bertaut'68, Bertaut'81, Giot'06, Izyumov'80, Izyumov'79a, Izyumov'91, Izyumov'79b, Izyumov'79c, Izyumov'79d].

The calculus of the Fourier coefficients $\vec{S}_k^j$ for different irreducible representations of the group G_k, for each atomic site, starting from the propagation vector $\vec{k}$ and from the space group of the paramagnetic phase G, is made by the program BASIREPS of the FULLPROF suite [Rodríguez-Carvajal].

The main information contained by the input file of BASIREPS program are the following: (i) the Hermann-Mauguin symbol of the space group [ITC'83]; (ii) the components of the propagation vector $\vec{k}$; (iii) the atoms coordinates. Speaking about the atoms coordinates, there are two possibilities: one gives just one atom and the program generates itself the rest of the atoms of the unit cell or one gives explicitly the sublattices (this option offers a better control to the user).

The present study contains two examples of magnetic structures solved using the program BASIREPS and the symmetry representation analysis: (i) $Tb_2Sn_2O_7$, with Tb^{3+} as unique magnetic ion and (ii) $(Tb_{0.8}La_{0.2})_2Mo_2O_7$, where both Tb^{3+} and Mo^{4+} ions are

magnetic. We choose the system having two magnetic ions and give in the following a concrete example of symmetry representation analysis.

- cubic $Fd\bar{3}m$ space group

We first looked for the solution in the cubic $Fd\bar{3}m$ space group. The input information of BASIREPS program is indicated in Table I.

Space group	$Fd\bar{3}m$
Propagation vector $\vec{k}$	(0, 0, 0)
Number of atoms	8
Tb_1	(0.5, 0.5, 0.5)
Tb_2	(0.25, 0.25, 0.5)
Tb_3	(0.25, 0.5, 0.25)
Tb_4	(0.5, 0.25, 0.25)
Mo_1	(0, 0, 0)
Mo_2	(-0.25, -0.25, 0)
Mo_3	(-0.25, 0, -0.25)
Mo_4	(0, -0.25, -0.25)

Table I. BASIREPS input information corresponding to $Fd\bar{3}m$ group.

In output, BASIREPRS gives three possible irreducible representations, with real coefficients, identical for both Tb and Mo sites: (i) Γ_3 (with 1 basis function); (ii) Γ_8 (with 6 basis functions) and (iii) Γ_{10} (with 3 basis functions). For each representation, taking into account the basis functions and the corresponding coefficients, we determined the Fourier coefficients $\vec{S}_k^j$ (see below). As already stated, for a unique propagation vector $\vec{k}=(0, 0, 0)$ they are equal to the magnetic moments: $\vec{S}_k^j = \vec{m}_j$. Then, the magnetic structure allowed by the symmetry was introduced in the FULLPROF program and compared to the experiment.

The conclusion was that the $\vec{k}=0$ antiferromagnetic structures allowed by the cubic space group were not compatible with the experimental data. Taking into account that neither a collinear ferromagnetic structure fitted the experimental pattern (we also tried this possibility, since according to the literature we expected for our compound to have a ferromagnetic behaviour), we decided to look for the solution in a space group that allows both ferromagnetic and antiferromagnetic components.

- tetragonal $I4_1/amd$ space group

We therefore looked for the solution in the tetragonal $I4_1/amd$ space group, the subgroup of $Fd\bar{3}m$ with the highest symmetry, which allows ferromagnetic and antiferromagnetic components simultaneously. The input information for BASIREPS is indicated in Table II. When passing from the $Fd\bar{3}m$ cubic space group to the tetragonal one, we used the transformation [Giacovazzo'02]:

$$\begin{pmatrix} x' \\ y' \\ z' \end{pmatrix} = \left(P^T\right)^{-1} \left[\begin{pmatrix} x \\ y \\ z \end{pmatrix} - p \right] \qquad \text{[B.4]}$$

(x, y, z) and (x', y', z') are the atomic coordinates in cubic and tetragonal space group, respectively, while P and p are the rotation and translation matrices defined as:

$$P = \begin{pmatrix} 1 & \bar{1} & 0 \\ 1 & 1 & 0 \\ 0 & 0 & 1 \end{pmatrix} \quad , \quad p = \begin{pmatrix} 1/4 \\ 1/4 \\ 0 \end{pmatrix} \qquad [B.5]$$

Consequently, we obtained:

$$\begin{pmatrix} x' \\ y' \\ z' \end{pmatrix} = \begin{pmatrix} x - y \\ x + y - 0.5 \\ z \end{pmatrix} \qquad [B.6]$$

and calculated the atomic coordinates values given in Table II. The unit cell parameters in the tetragonal symmetry group are: $a\sqrt{2}/2, a\sqrt{2}/2, c$.

Space group	$I4_1/amd$
Propagation vector $\vec{k}$	(0, 0, 0)
Number of atoms	8
Tb_1	(0, 0.5, 0.5)
Tb_2	(0, 0, 0.5)
Tb_3	(-0.25, 0.25, 0.25)
Tb_4	(0.25, 0.25, 0.25)
Mo_1	(0, -0.5, 0)
Mo_2	(0, -1, 0)
Mo_3	(-0.25, -0.75, -0.25)
Mo_4	(0.25, -0.75, -0.25)

Table II. BASIREPS input information corresponding to $I4_1/amd$ group.

```
--------------------------------
Output of BasIREPS for FullProf
--------------------------------
                    X       Y       Z          for site:  1
 -> TB_1     :    0.0000  0.5000  0.5000  : (x,y,z) + ( 0  , 0  , 0  )
 -> TB_2     :    0.0000  0.0000  0.5000  : (-x+1/2,-y,z+1/2) + (-1/2, 1/2,-1/2)
 -> TB_3     :   -0.2500  0.2500  0.2500  : (-y+1/4,-x+1/4,-z+3/4) + ( 0  , 0  , 0  )
 -> TB_4     :    0.2500  0.2500  0.2500  : (y+1/4,x+3/4,-z+1/4) + (-1/2,-1/2, 1/2)

 => Basis functions of Irreducible Representation 7
    dimension 1 contained 2 times in the reducible representation
    Representation number    :  7 for Site:  1
    Number of basis functions:  2
SYMM x,y,z
BASR   0  1  0   0  0  1
BASI   0  0  0   0  0  0
SYMM -x,-y+1/2,z
BASR   0 -1  0   0  0  1
BASI   0  0  0   0  0  0
SYMM -y+1/4,-x+1/4,-z+3/4
BASR   1  0  0   0  0  1
BASI   0  0  0   0  0  0
SYMM y-1/4,x+1/4,-z+3/4
BASR  -1  0  0   0  0  1
BASI   0  0  0   0  0  0
```

Figure 1. BASIREPS output information for Tb site (site 1), showing the information on the irreducible representation Γ_7. BASR and BASI represent the real and imaginary part of the basis functions. In this case the basis functions are real.

In output, BASIREPRS gives five possible irreducible representations, with real coefficients, identical for both Tb and Mo sites: (i) Γ_1 (with 1 basis function), (ii) Γ_3 (with 1 basis function), (iii) Γ_5 (with 2 basis functions), (iv) Γ_7 (with 2 basis functions) and (v) Γ_{10} (with 6 basis functions). Figure 1 shows the output information given by BASIREPS on the irreducible representation Γ_7. We note that in this case the number of free parameters needed to describe the magnetic structure is $n_f = a_\nu \times \dim(\Gamma_\nu) = 1 \times 2 = 2$ for Tb atom and also 2 for Mo one.

Starting from the basis functions given by the program for Γ_7, we may determine the Fourier coefficients, *i.e.* the magnetic moments:

$$\begin{array}{cccc} \text{Tb\_1} & \text{Tb\_2} & \text{Tb\_3} & \text{Tb\_4} \\ \begin{pmatrix} 0 & 1 & 0 \\ 0 & 0 & 1 \end{pmatrix} & \begin{pmatrix} 0 & \bar{1} & 0 \\ 0 & 0 & 1 \end{pmatrix} & \begin{pmatrix} 1 & 0 & 0 \\ 0 & 0 & 1 \end{pmatrix} & \begin{pmatrix} \bar{1} & 0 & 0 \\ 0 & 0 & 1 \end{pmatrix} \end{array} \qquad [B.7]$$

$$\begin{cases} \vec{S}_k^1 = C_1(0,1,0) + C_2(0,0,1) \\ \vec{S}_k^2 = C_1(0,\bar{1},0) + C_2(0,0,1) \\ \vec{S}_k^3 = C_1(1,0,0) + C_2(0,0,1) \\ \vec{S}_k^4 = C_1(\bar{1},0,0) + C_2(0,0,1) \end{cases} \qquad [B.8]$$

and hence:

$$\begin{cases} \vec{S}_k^1 = (0, C_1, C_2) = (m_{1x}, m_{1y}, m_{1z}) \\ \vec{S}_k^2 = (0, -C_1, C_2) = (m_{2x}, m_{2y}, m_{2z}) \\ \vec{S}_k^3 = (C_1, 0, C_2) = (m_{3x}, m_{3y}, m_{3z}) \\ \vec{S}_k^4 = (-C_1, 0, C_2) = (m_{4x}, m_{4y}, m_{4z}) \end{cases} \qquad [B.9]$$

As one may see this representation allows a ferromagnetic component along the [001] axis. Similar results are also obtained for the Mo site, but with two different coefficients C_3 and C_4 corresponding to the basis functions.

The magnetic structure (calculated according to [B.9] for Tb site and with a similar relation for Mo) was then introduced in the input file of FULLPROF program and compared to the experimental pattern. There are four refinable parameters: C_1, C_2 (corresponding to Tb atom) and C_3, C_4 (corresponding to Mo). Once the solution within the tetragonal symmetry group was determined (*i.e.* C_1, C_2, C_3, C_4 were determined) we reconverted it in the cubic space group using the inverse transformation of [B.4].

The solution given in Chapter IV, section IV.3.2, for $(Tb_{0.8}La_{0.2})_2Mo_2O_7$ corresponds to the linear combination of the two basis vectors of the irreducible representation Γ_7, for both Tb and Mo. The solution for $Tb_2Sn_2O_7$ (Chapter III, section III.3.1) corresponds to the irreducible representation Γ_7 calculated for the Tb site.

References

[Abragam'70] A. Abragam, and B. Bleaney, *Electronic paramagnetic resonance of transition ions* (Claredon press Oxford, 1970).

[Ali'89] N. Ali, M. P. Hill, S. Labroo, and J. E. Greedan, J. Solid State Chem. **83**, 178 (1989).

[Ali'92] N. Ali, P. Hill, X. Zang, and F. Willis, J. Alloys and Compounds **181**, 281 (1992).

[Amato'97] A. Amato, Rev. Mod. Phys. **69**, 1119 (1997).

[Anderson'56] P. W. Anderson, Phys. Rev. **102**, 1008 (1956).

[Andreica'01] D. Andreica, *PhD Thesis* (Swiss Federal Institute of Technology Zurich, Switzerland, 2001).

[Bacon'75] G. E. Bacon, *Neutron diffraction* (Clarendon Press, Oxford, UK, 1975).

[Bellouard'92] C. Bellouard, M. Hennion, I. Mirebeau, and B. Hennion, J. Magn. Magn. Mat. **104-107**, 1627 (1992).

[Bernal'33] J. D. Bernal, and R. H. Fowler, J. Chem. Phys. **1**, 515 (1933).

[Bert'05] F. Bert, private communications (2005).

[Bert'06] F. Bert, P. Mendels, A. Olariu, N. Blanchard, G. Collin, A. Amato, C. Baines, and A. D. Hiller, Phys. Rev. Lett. **97**, 117203 (2006).

[Bertaut'63] E. F. Bertaut, *Spin Configurations of Ionic Structures. Theory and Practice in Magnetism, vol. 3* (Ed. G. T. Rado and H. Suhl, Academic Press, New York, 1963).

[Bertaut'68] E. F. Bertaut, Acta Cryst. A **24**, 217 (1968).

[Bertaut'81] E. F. Bertaut, J. Magn.Magn. Mat. **24**, 267 (1981).

[Bertaut'67] E. F. Bertaut, and P. Burlet, Solid State Commun. **5**, 279 (1967).

[Bertin'01a] E. Bertin, P. Bonville, J. P. Bouchaud, J. A. Hodges, J. P. Sanchez, and P. Vuillet, Eur. Phys. J. B **27**, 347 (2001a).

[Bertin'01b] E. Bertin, P. Bonville, J. P. Bouchaud, J. A. Hodges, J. P. Sanchez, and P. Vulliet, Eur. Phys. J. B **27**, 347 (2001b).

[Binder'86] K. Binder, and A. P. Young, Rev. Mod. Phys. **58**, 801 (1986).

[Blöte'69] H. W. J. Blöte, R. F. Wielinga, and W. J. Huiskamp, Physica (Amsterdam) **43**, 549 (1969).

[Blundell'99] S. J. Blundell, Contemp. Phys. **40**, 175 (1999).

[Blundell'02] S. J. Blundell, cond-mat **0207699** (2002).

[Bondah-Jagalu'01] V. Bondah-Jagalu, and S. T. Bramwell, Can. J. Phys. **79**, 1381 (2001).

[Booth'00] C. H. Booth, J. S. Gardner, G. H. Kwei, R. H. Heffner, F. Bridges, and M. A. Subramanian, Phys. Rev. B **62**, R755 (2000).

[Bramwell'00] S. T. Bramwell, M. N. Field, M. J. Harris, and I. P. Parkin, J. Phys.: Condens. Matter **12**, 483 (2000).

[Bramwell'01a] S. T. Bramwell, and M. J. P. Gingras, Science **294**, 1495 (2001a).

[Bramwell'98] S. T. Bramwell, and M. J. Harris, J. Phys.: Condens. Matter **10**, L215 (1998).

[Bramwell'01b] S. T. Bramwell, M. J. Harris, B. C. d. Hertog, M. J. P. Gingras, J. S. Gardner, D. F. McMorrow, A. R. Wildes, A. L. Cornelius, J. D. M. Champion, R. G. Melko, and T. Fennel, Phys. Rev. Lett. **87**, 047205 (2001b).

[Cadavez-Peres'02] P. Cadavez-Peres, *PhD Thesis* Paris XI University 2002).

[Canals'06] B. Canals, private communications (2006).

[Canals'01] B. Canals, and D. A. Garanin, Can. J. Phys. **79**, 1323 (2001).

[Canals'98] B. Canals, and C. Lacroix, Phys. Rev. Lett. **80**, 2933 (1998).

[Champion'02] J. D. M. Champion, S. T. Bramwell, P. C. W. Holdsworth, and M. J. Harris, Europhys. Lett. **57**, 93 (2002).

[DalmasdeRéotier'06] P. DalmasdeRéotier, A. Yaouanc, L. Keller, A. Cervellino, B. Roessli, C. Baines, A. Forget, C. Vaju, P. C. M. Gubbens, A. Amato, and P. J. C. King, Phys. Rev. Lett. **96**, 127202 (2006).

[DalmasdeRéotier'97] P. DalmasdeRéotier, and Y. Yaouanc, J. Phys.:Condens. Matter **9**, 9113 (1997).

[denHertog'00] B. C. denHertog, and M. J. P. Gingras, Phys. Rev. Lett. **84**, 3430 (2000).

[Dunlap'71] B. D. Dunlap, *"Relativistic effects in hyperfine interactions" in Mössbauer effect methodology 7* (I. J. Gruverman, Plenum Press, 1971).

[Dunsiger'96] S. R. Dunsiger, R. F. Kiefl, K. H. Chow, B. D. Gaulin, M. J. P. Gingras, J. E. Greedan, A. Keren, K. Kojima, G. M. Luke, W. A. MacFarlane, N. P. Raju, J. E. Sonier, Y. J. Uemura, and W. D. Wu, Phys. Rev. B **54**, 9019 (1996).

[Dzyaloshinski'58] I. Dzyaloshinski, J. Phys. Chem. Solids **4**, 241 (1958).

[Enjalran'04a] M. Enjalran, and M. J. P. Gingras, Phys. Rev. B **70**, 174426 (2004a).

[Enjalran'04b] M. Enjalran, M. J. P. Gingras, Y.-J. Kao, A. delMaestro, and H. R. Molavian, J. Phys.: Condens. Matter **16**, S673 (2004b).

[Ferey'86] G. Ferey, R. dePape, M. Leblanc, and J. Pannetier, Rev. Chim. Miner. **23**, 474 (1986).

[Finger'94] L. W. Finger, D. E. Cox, and A. P. Jephcoat, J. Appl. Cryst. **27**, 892 (1994).

[Fisher'91] K. H. Fisher, and J. A. Hertz, *Spin glasses* (Cambridge Universy Press, Cambridge, England, 1991).

[Freeman'79] A. J. Freeman, and J. P. Desclaux, J. Magn. Magn. Mat. **12**, 11 (1979).

[Gabay'81] M. Gabay, and G. Toulouse, Phys. Rev. Lett. **47**, 201 (1981).

[Gardner'99a] J. S. Gardner, S. R. Dunsiger, B. D. Gaulin, M. J. P. Gingras, J. E. Greedan, R. F. Kiefl, M. D. Lumsden, W. A. MacFarlane, N. P. Raju, J. E. Sonier, I. Swainson, and Z. Tun, Phys. Rev. Lett. **82**, 1012 (1999a).

[Gardner'04] J. S. Gardner, G. Ehlers, S. T. Bramwell, and B. D. Gaulin, J. Phys.: Condens. Matter **16**, S643 (2004).

[Gardner'01a] J. S. Gardner, G. Ehlers, R. H. Heffner, and F. Mezei, J. Magn. Magn. Mat. **226**, 460 (2001a).

[Gardner'01b] J. S. Gardner, B. D. Gaulin, A. J. Berlinsky, P. Waldron, S. R. Dunsiger, N. P. Raju, and J. E. Greedan, Phys. Rev. B **64**, 224416 (2001b).

[Gardner'99b] J. S. Gardner, B. D. Gaulin, S.-H. Lee, C. Broholm, N. P. Raju, and J. E. Greedan, Phys. Rev. Lett. **83**, 211 (1999b).

[Gaulin'94] B. D. Gaulin, Hyperfine Interact. **85**, 159 (1994).

[Gaulin'98] B. D. Gaulin, J. S. Gardner, S. R. Dunsiger, Z. Tun, M. D. Lumsden, R. F. Kiefl, N. P. Raju, J. N. Reimers, and J. E. Greedan, Physica B **241**, 511 (1998).

[Gaulin'92] B. D. Gaulin, J. N. Reimers, T. E. Mason, J. E. Greedan, and Z. Tun, Phys. Rev. Lett. **69**, 3244 (1992).

[Giacovazzo'02] C. Giacovazzo, H. L. Monaco, D. Viterbo, F. Scordari, G. Gilli, G. Zanotti, and M. Catti, *Fundamentals of Crystallography* (C. Giacovazzo, IUCr, Oxford Science Publications, Oxford, 2002).

[Gingras'01] M. J. P. Gingras, and B. C. denHertog, Can. J. Phys. **79**, 1339 (2001).

[Gingras'00] M. J. P. Gingras, B. C. D. Hertog, M. Faucher, S. R. Dunsiger, L. J. Chang, B. D. Gaulin, N. P. Raju, and J. E. Greedan, Phys. Rev. B **62**, 6496 (2000).

[Gingras'97a] M. J. P. Gingras, M. Larkin, I. Mirebeau, W. D. Wu, K. Kojima, G. M. Luke, B. Nachumi, and Y. J. Uemura, cond-mat, 9709190 (1997a).

[Gingras'96] M. J. P. Gingras, C. V. Stager, B. D. Gaulin, N. P. Raju, and J. E. Greedan, J. Appl. Phys. **79**, 6170 (1996).

[Gingras'97b] M. J. P. Gingras, C. V. Stager, N. P. Raju, B. D. Gaulin, and J. E. Greedan, Phys. Rev. Lett. **78**, 947 (1997b).

[Giot'06] M. Giot, *PhD Thesis* Caen University 2006).

[Goldanskii'68] V. I. Goldanskii, and R. H. Herber, *Chemical Applications of Mössbauer Spectroscopy* (Academic Press, New York & London, 1968).

[Goncharenko'04] I. N. Goncharenko, High Press. Res. **24**, 193 (2004).

[Goncharenko'95] I. N. Goncharenko, J.-M. Mignot, G. Andre, O. A. Lavrova, I. Mirebeau, and V. A. Somenkov, High Press. Res. **14**, 41 (1995).

[Goncharenko'98] I. N. Goncharenko, and I. Mirebeau, Rev. High Press. Sci. Technol. **7**, 475 (1998).

[Greedan'01] J. E. Greedan, J. Mater. Chem. **11**, 37 (2001).

[Greedan'06] J. E. Greedan, A. D. Lozano-Gorrin, T. Proffen, S. J. L. Billinge, H.-J. Kim, and E. S. Bozin, *Abstract in: (i) "American Conference on Neutron Scattering", 18-22*

June, St. Charles, Illinois, USA; (ii) "International Conference on Highly Frustrated Magnetism", 15-19 August, Osaka, Japan 2006).

[Greedan'90] J. E. Greedan, J. N. Reimers, S. L. Penny, and C. V. Stager, J. Appl. Phys. **67**, 5967 (1990).

[Greedan'91] J. E. Greedan, J. N. Reimers, C. V. Stager, and S. L. Penny, Phys. Rev. B **43**, 5682 (1991).

[Greedan'87] J. E. Greedan, M. Sato, A. Naushad, and W. R. Datars, J. Solid State Chem. **68**, 300 (1987).

[Greedan'86] J. E. Greedan, M. Sato, X. Yan, and F. S. Razavi, Solid State Comun. **59**, 895 (1986).

[Hamaguchi'04] N. Hamaguchi, T. Matsushita, N. Wada, Y. Yasui, and M. Sato, Phys. Rev. B **69**, 132413 (2004).

[Hammersley] A. Hammersley, *Computer program Fit2D* ESRF, Grenoble.

[Harris'97] M. J. Harris, S. T. Bramwell, D. F. McMorrow, T. Zeiske, and K. W. Godfrey, Phys. Rev. Lett. **79**, 2554 (1997).

[Harris'98] M. J. Harris, S. T. Bramwell, T. Zieske, D. F. McMorrow, and P. J. C. King, J. Magn. Magn. Mat. **177**, 757 (1998).

[HERCULES'05] HERCULES, *Neutron and synchrotron radiation for condensed matter physics* (Les Editions de Physique_Springer-Verlag, Grenoble, France, 2005).

[Hill'89] P. Hill, S. Labroo, X. Zhang, and N. Ali, J. Less-Common Metals **149**, 327 (1989).

[Iikubo'01] S. Iikubo, S. Yoshii, T. Kageyama, K. Oda, Y. Kondo, K. Murata, and M. Sato, J. Phys. Soc. Jpn. **70**, 212 (2001).

[Ishikawa'04] H. Ishikawa, S. Xu, Y. Moritomo, A. Nakamura, Y. Ohishi, and K. Kato, Phys. Rev. B **70**, 104103 (2004).

[ITC'83] ITC, *International Tables for Crystallography, volume A: Space Group Symmetry* (Edited by Theo Hahn, published by the IUCr, D. Reidel Publishing Company, 1983).

[Izyumov'80] Y. A. Izyumov, J. Magn.Magn. Mat. **21**, 33 (1980).

[Izyumov'79a] Y. A. Izyumov, and V. E. Naish, J. Magn.Magn. Mat. **12**, 239 (1979a).

[Izyumov'91] Y. A. Izyumov, V. E. Naish, and R. P. Ozerov, *Neutron diffraction of magnetic materials* (consultants Bureau, Plenum Publishing Corporation, New York, 1991).

[Izyumov'79b] Y. A. Izyumov, V. E. Naish, and S. B. Petrov, J. Magn.Magn. Mat. **13**, 275 (1979b).

[Izyumov'79c] Y. A. Izyumov, V. E. Naish, and S. B. Petrov, J. Magn.Magn. Mat. **13**, 267 (1979c).

[Izyumov'79d] Y. A. Izyumov, V. E. Naish, and V. N. Syromiatnikov, J. Magn.Magn. Mat. **12**, 249 (1979d).

[JDN10'03] JDN10, Journal de Physique **103** (2003).

[Jo'05] Y. Jo, J.-G. Park, J. Park, H. C. Kim, H.-C. Ri, S. Xu, Y. Moritomo, A. D. Hillier, and S. H. Kilcoyne, J. Korean. Phys. Soc. **47**, 123 (2005).

[Kadowaki'02] H. Kadowaki, T. Ishii, K. Matsuhira, and Y. Hinatsu, Phys. Rev. B **65**, 144421 (2002).

[Kanada'02] M. Kanada, Y. Yasui, Y. Kondo, S. Iikubo, M. Ito, H. Harashina, M. Sato, H. Okumura, K. Kakurai, and H. Kadowaki, J. Phys. Soc. Jpn. **71**, 313 (2002).

[Kang'04] J.-S. Kang, Y. Moritomo, C. G. Olson, and B. I. Min, J. Magn. Magn. Mat. **272**, 221 (2004).

[Kang'02] J. S.-. Kang, Y. Moritomo, S. Xu, C. G. Olson, J. H. Park, S. K. Kwon, and B. I. Min, Phys. Rev. B **65**, 224422 (2002).

[Kao'03] Y.-J. Kao, M. Enjalran, A. delMaestro, H. R. Molavian, and M. J. P. Gingras, Phys. Rev. B **68**, 172407 (2003).

[Katsufuji'00] T. Katsufuji, H. Y. Hwang, and S.-W. Cheong, Phys. Rev. Lett. **84**, 1998 (2000).

[Keeson'42] W. H. Keeson, *Helium* (Elsevier, Amsterdam, 1942).

[Keren'01] A. Keren, and J. S. Gardner, Phys. Rev. Lett. **87**, 177201 (2001).

[Kézsmárki'04] I. Kézsmárki, N. Hanasaki, D. Hashimoto, S. Iguchi, Y. Taguchi, S. Miyasaka, and Y. Tokura, Phys. Rev. Lett. **93**, 266401 (2004).

[Kim'05] H. C. Kim, Y. Jo, J.-G. Park, S. W. Cheong, M. Uhlarz, C. Pfleiderer, and H. V. Löhneysen, Physica B **359**, 1246 (2005).

[Kim'03] H. C. Kim, Y. Jo, J.-G. Park, H.-C. Ri, and S.-W. Cheong, Acta Physica Polonica B **34**, 1429 (2003).

[Kumar'06] R. S. Kumar, A. L. Cornelius, M. F. Nicol, K. C. Kam, K. Cheetham, and J. S. Gardner, Appl. Phys. Lett. **88**, 031903 (2006).

[Luo'01] G. Luo, S. T. Hess, and L. R. Corruccini, Phys. Lett. A **291**, 306 (2001).

[Matsuhira'02] K. Matsuhira, Y. Hinatsu, K. Tenya, H. Amitsuka, and T. Sakakibara, J. Phys. Soc. Jpn. **71**, 1576 (2002).

[Matsuhira'00] K. Matsuhira, Y. Hinatsu, K. Tenya, and T. Sakakibara, J. Phys.: Condens. Matter **12**, L649 (2000).

[Melko'04] R. K. Melko, and M. J. P. Gingras, J. Phys.: Condens. Matter **16**, R1227 (2004).

[Mirebeau'06] I. Mirebeau, A. Apetrei, I. Goncharenko, D. Andreica, P. Bonville, J. P. Sanchez, A. Amato, E. Suard, W. A. Crichton, A. Forget, and D. Colson, Phys. Rev. B **74**, 174414 (2006).

[Mirebeau'05a] I. Mirebeau, A. Apetrei, J. Rodríguez-Carvajal, P. Bonville, A. Forget, D. Colson, V. Glazkov, J. P. Sanchez, O. Isnard, and E. Suard, Phys. Rev. Lett. **94**, 246402 (2005a).

[Mirebeau'07a] I. Mirebeau, P. Bonville, and M. Hennion, to be published (2007a).

[Mirebeau'04a] I. Mirebeau, and I. Goncharenko, J. Phys.: Condens. Matter **16**, S653 (2004a).

[Mirebeau'07b] I. Mirebeau, I. Goncharenko, D. Andreica, P. Bonville, and A. Apetrei, to be published (2007b).

[Mirebeau'04b] I. Mirebeau, and I. N. Goncharenko, Physica B **350**, 250 (2004b).

[Mirebeau'05b] I. Mirebeau, and I. N. Goncharenko, J. Phys.: Condens. Matter **17**, S771 (2005b).

[Mirebeau'02] I. Mirebeau, I. N. Goncharenko, P. Cadavez-Peres, S. T. Bramwell, M. J. P. Gingras, and J. S. Gardner, Nature **420**, 54 (2002).

[Mirebeau'04c] I. Mirebeau, I. N. Goncharenko, G. Dhalenne, and A. Revcolevschi, Phys. Rev. Lett. **93**, 187204 (2004c).

[Mirebeau'97] I. Mirebeau, M. Hennion, M. J. P. Gingras, A. Keren, K. Kojima, M. Larkin, G. M. Luke, B. Nachumi, W. D. Wu, Y. J. Uemura, I. A. Chambell, and G. D. Morris, Hyperfine Interact. **104**, 343 (1997).

[Mirebeau'90] I. Mirebeau, S. Itoh, S. Mitsuda, T. Watanabe, Y. Endoh, M. Hennion, and R. Papoular, Phys. Rev. B **41**, 11405 (1990).

[Miyoshi'01] K. Miyoshi, K. Honda, T. Yamashita, K. Fujiwara, and J. Takeuchi, J. Magn. Magn. Mat. **226**, 898 (2001).

[Miyoshi'00a] K. Miyoshi, Y. Nishimura, K. Honda, K. Fujiwara, and J. Takeuchi, J. Phys. Soc. Jpn. **69**, 3517 (2000a).

[Miyoshi'00b] K. Miyoshi, Y. Nishimura, K. Honda, K. Fujiwara, and J. Takeuchi, Physica B **284**, 1463 (2000b).

[Miyoshi'06] K. Miyoshi, Y. Takamatsu, and J. Takeuchi, J. Phys. Soc. Jpn. **75**, 065001 (2006).

[Miyoshi'03] K. Miyoshi, T. Yamashita, K. Fujiwara, and J. Takeuchi, J. Phys. Soc. Jpn. **72**, 1855 (2003).

[Moessner'98a] R. Moessner, Phys. Rev. B **57**, R5587 (1998a).

[Moessner'98b] R. Moessner, and J. T. Chalker, Phys. Rev. B **58**, 12049 (1998b).

[Moessner'98c] R. Moessner, and J. T. Chalker, Phys. Rev. Lett. **80**, 2929 (1998c).

[Molavian'07] H. R. Molavian, M. J. P. Gingras, and B. Canals, Phys. Rev. Lett. **98**, 157204 (2007).

[Moria'60] T. Moria, Phys. Rev. Lett. **4**, 228 (1960).

[Moritomo'01] Y. Moritomo, S. Xu, A. Machiada, T. Katsufuji, E. Nishibori, M. Takata, M. Sakata, and S.-W. Cheong, Phys. Rev. B **63**, 144425 (2001).

[Morya'60] T. Morya, Phys. Rev. **91**, 129 (1960).

[Ohgushi'00] K. Ohgushi, S. Murakami, and N. Nagaosa, Phys. Rev. B **62**, R6065 (2000).

[Park'03] J.-G. Park, Y. Jo, J. Park, H. C. Kim, H.-C. Ri, S. Xu, Y. Moritomo, and S.-W. Cheong, Physica B **328**, 90 (2003).

[Pauling'35] L. Pauling, J. Am. Chem. Soc. **57**, 2680 (1935).

[Pauling'60] L. Pauling, *The nature of the chemical bond* (Cornell University Press, Ithaca, 1960), p. 465.

[Pureur'04] P. Pureur, F. W. Fabris, J. Schaf, and I. A. Campbell, Europhys. Lett. **67**, 123 (2004).

[Raju'92] N. P. Raju, E. Gmelin, and R. K. Kremer, Phys. Rev. B **46**, 5405 (1992).

[Ramirez'94] A. P. Ramirez, Annu. Rev. Mater. Sci. **24**, 453 (1994).

[Ramirez'01] A. P. Ramirez, Handbook of Magnetic Materials **13**, 423 (2001).

[Ramirez'99] A. P. Ramirez, A. Hayashi, R. J. Cava, R. Siddharthan, and B. S. Shastry, Nature **399**, 333 (1999).

[Reimers'92] J. N. Reimers, Phys. Rev. B **46**, 193 (1992).

[Reimers'91] J. N. Reimers, A. J. Berlinsky, and A.-C. Shi, Phys. Rev. B **43**, 865 (1991).

[Reimers'88] J. N. Reimers, J. E. Greedan, and M. Sato, J. Solid State Chem. **72**, 390 (1988).

[Réotier'04] P. D. d. Réotier, P. C. M. Gubbens, and A. Yaouanc, J. Phys.: Condens. Matter **16**, S4687 (2004).

[Réotier'97] P. D. d. Réotier, and A. Yaouanc, J. Phys.: Condens. Matter **9**, 9113 (1997).

[Rodríguez-Carvajal] J. Rodríguez-Carvajal, (ftp://ftp.cea.fr/pub/llb/divers.BasIReps.

[Rodríguez-Carvajal'93] J. Rodríguez-Carvajal, Physica B **192**, 55 (1993).

[Rosenkrantz'00] S. Rosenkrantz, A. P. Ramirez, A. Hayashi, R. J. Cava, R. Siddharthan, and B. S. Shastry, J. Appl. Phys. **87**, 5914 (2000).

[Rouse'70] K. Rouse, M. Cooper, E. York, and A. Chakera, Acta Cryst. A **26**, 682 (1970).

[Ryan'00] D. H. Ryan, J. M. Cadogan, and J. vanLierop, Phys. Rev. B **61**, 6816 (2000).

[Ryan'04] D. H. Ryan, J. vanLierop, and J. M. Cadogan, J. Phys.:Condens.Matter **16**, S4619 (2004).

[Sagi'05] E. Sagi, O. Ofer, and A. Keren, Phys. Rev. Lett. **94**, 237202 (2005).

[Sato'87] M. Sato, and J. E. Greedan, J. Solid State Chem. **67**, 248 (1987).

[Schenck'85] A. Schenck, *Muon Spin Spectroscopy: Principles and Applications in Solid State Physics* (Adam Hilger Ltd, Bristol, UK, 1985).

[Sekarya'07] S. Sekarya, *PhD Thesis* (Delft Technical University, Holland, 2007).

[Shannon'76] R. D. Shannon, Acta Cryst. A **32**, 751 (1976).

[Siddharthan'99] R. Siddharthan, B. S. Shastry, A. P. Ramirez, A. Hayashi, R. J. Cava, and S. Rosenkranz, Phys. Rev. Lett. **83**, 1854 (1999).

[Simon'50] F. E. Simon, and C. A. Swenson, Nature **165**, 829 (1950).

[Solovyev'03] I. V. Solovyev, Phys. Rev. B **67**, 174406 (2003).

[Sonier'02] J. E. Sonier, *brochure: Muon Spin Rotation/Relaxation/Resonance* (Simon Fraser University, British Columbia, 2002).

[Strässle'05] T. Strässle, S. Klotz, J. S. Loveday, and M. Braden, J. Phys.:Condens. Matter **17**, S3029 (2005).

[Taguchi'02] Y. Taguchi, K. Ohgushi, and Y. Tokura, Phys. Rev. B **65**, 115102 (2002).

[Taguchi'01] Y. Taguchi, Y. Oohara, H. Yoshizawa, N. Nagaosa, and Y. Tokura, Science **291**, 2573 (2001).

[Taguchi'03] Y. Taguchi, T. Sasaki, S. Awaji, Y. Iwasa, T. Tayama, T. Sakakibara, S. iguchi, T. Ito, and Y. Tokura, Phys. Rev. Lett. **90**, 257202 (2003).

[Taillefumier'06] M. Taillefumier, B. Canals, C. Lacroix, V. K. Dugaev, and P. Bruno, Phys. Rev. B **74**, 085105 (2006).

[Taniguchi'04a] K. Taniguchi, T. Katsufuji, S. Iguchi, Y. Taguchi, H. Takagi, and Y. Tokura, Phys. Rev. B **70**, 100401 (2004a).

[Taniguchi'04b] T. Taniguchi, K. Yamanaka, H. Sumioka, T. Yamazaki, Y. Tabata, and S. Kawarazaki, Phys. Rev. Lett. **93**, 246605 (2004b).

[Tatara'02] G. Tatara, and H. Kawamura, J. Phys. Soc. Jpn. **71**, 2613 (2002).

[Villain'79] J. Villain, Z. Phys. B **33**, 31 (1979).

[Wiedenmann'81] A. Wiedenmann, P. Burlet, H. Scheuer, and P. Convert, Solid State Commun. **38**, 129 (1981).

[Yasui'03a] Y. Yasui, S. Iikubo, H. Harashina, T. Kageyama, M. Ito, M. Sato, and K. Kakurai, J. Phys. Soc. Jpn. **72**, 865 (2003a).

[Yasui'03b] Y. Yasui, T. Kageyama, S. IIkubo, K. Oda, M. Sato, and K. Kakurai, Physica B **329**, 1036 (2003b).

[Yasui'06] Y. Yasui, T. Kageyama, T. Moyoshi, M. Soda, M. Sato, and K. Kakurai, J. Phys. Soc. Jpn. **75**, 084711 (2006).

[Yasui'02] Y. Yasui, M. Kanada, M. Ito, H. Harashina, M. Sato, H. Okumura, K. Kakurai, and H. Kadowaki, J. Phys. Soc. Jpn. **71**, 599 (2002).

[Yasui'01] Y. Yasui, Y. Kondo, M. Kanada, M. Ito, H. Harashina, M. Sato, and K. Kakurai, J. Phys. Soc. Jpn. **70**, 284 (2001).

[Yoshii'00] S. Yoshii, S. Iikubo, T. Kageyama, K. Oda, Y. Kondo, K. Murata, and M. Sato, J. Phys. Soc. Jpn. **69**, 3777 (2000).

Papers

- **Ordered spin ice and magnetic fluctuations in $Tb_2Sn_2O_7$**, I. Mirebeau, A. Apetrei, J. Rodríguez-Carvajal, P. Bonville, A. Forget, D. Colson, V. Glazkov, J.P. Sanchez, O. Isnard and E. Suard, Phys. Rev. Lett. **94**, 246402 (2005).
- **Two geometrically frustrated magnets studied by neutron diffraction**, I. Mirebeau, A. Apetrei, I. N. Goncharenko and R. Moessner, Physica B **385-386**, 307 (2006).
- **Microscopic study of a pressure-induced ferromagnetic-spin-glass transition in the geometrically frustrated pyrochlore $(Tb_{1-x}La_x)_2Mo_2O_7$**, A. Apetrei, I. Mirebeau, I; Gongharenko, D. Andreica and P. Bonville, Phys. Rev. Lett. **97**, 206401 (2006).
- **Study of ferromagnetic-spin glass threshold in $R_2Mo_2O_7$ by high-pressure neutron diffraction and μSR**, A. Apetrei, I. Mirebeau, I. Goncharenko, D. Andreica and P. Bonville, J. Pys.: Condens. Matter **19**, 145214 (2007).
- **Pressure induced ferromagnet to spin-glass transition in $Gd_2Mo_2O_7$**, I. Mirebeau, A. Apetrei,I. Goncharenko, D. Andreica, P. Bonville, J. P. Sanchez, A. Amato, E. Suard, W. A. Crichton, A. Forget and D. Colson, Phys. Rev. B **74**, 174414 (2006).
- **Magnetic transition induced by pressure in $Gd_2Mo_2O_7$ as studied by neutron diffraction and μSR**, I. Mirebeau, A. Apetrei, I. Goncharenko, D. Andreica and P. Bonville, J. Magn. Magn. Mat. **310**, 919 (2007).
- **Crystal structure under pressure of geometrically frustrated pyrochlores,** A. Apetrei, I. Mirebeau, I. Goncharenko and W. A. Crichton, J. Phys: Condens. Matter **19**, 376208 (2007).

PRL 94, 246402 (2005) PHYSICAL REVIEW LETTERS week ending 24 JUNE 2005

Ordered Spin Ice State and Magnetic Fluctuations in $Tb_2Sn_2O_7$

I. Mirebeau,[1] A. Apetrei,[1] J. Rodríguez-Carvajal,[1] P. Bonville,[2] A. Forget,[2] D. Colson,[2] V. Glazkov,[3] J. P. Sanchez,[3] O. Isnard,[4,5] and E. Suard[5]

[1]*Laboratoire Léon Brillouin, CEA-CNRS, CE-Saclay, 91191 Gif-sur-Yvette, France*
[2]*Service de Physique de l'Etat Condensé, CEA-CNRS, CE-Saclay, 91191 Gif-Sur-Yvette, France*
[3]*Service de Physique Statistique, Magnétisme et Supraconductivité, CEA-Grenoble, 38054 Grenoble, France*
[4]*Laboratoire de Cristallographie, Université J. Fourier–CNRS, BP 166, 38042 Grenoble, France*
[5]*Institut Laüe Langevin, 6 rue Jules Horowitz, BP 156X, 38042 Grenoble, France*

(Received 17 January 2005; published 21 June 2005)

We have studied the spin liquid $Tb_2Sn_2O_7$ by neutron diffraction and specific heat measurements. Below about 2 K, the antiferromagnetic liquidlike correlations mostly change to ferromagnetic. Magnetic order settles in two steps, with a smeared transition at 1.3(1) K, then an abrupt transition at 0.87(2) K. A new magnetic structure is observed, akin to an ordered spin ice, with both ferromagnetic and antiferromagnetic character. It suggests that the ordered ground state results from the influence of dipolar interactions combined with a finite anisotropy along $\langle 111 \rangle$ axes. The moment value of $3.3(3)\mu_B$ deduced from the specific heat is well below that derived from the neutron diffraction of $5.9(1)\mu_B$, which is interpreted by the persistence of slow collective magnetic fluctuations down to the lowest temperatures.

DOI: 10.1103/PhysRevLett.94.246402 PACS numbers: 71.27.+a, 61.12.Ld, 75.25.+z

Geometrically frustrated pyrochlores $R_2Ti_2O_7$ show exotic magnetic behaviors [1–4] such as dipolar spin ice ($R = Dy, Ho$) and spin liquid (Tb) phases, a first order transition in the spin dynamics (Yb), or complex antiferromagnetic (AFM) orders (Er, Gd). The type of magnetic order depends on the balance between antiferromagnetic exchange, dipolar, and crystal field energies [5,6]. $Tb_2Ti_2O_7$ is a unique case of a spin liquid where short-ranged correlated magnetic moments fluctuate down to 70 mK, with typical energies 300 times lower than the energy scale given by the Curie-Weiss constant θ_{CW} of -19 K. The fact that $Tb_2Ti_2O_7$ does not order at ambient pressure [2], but can order under applied pressure, stress, and magnetic field [7,8], is still a challenge to theory, since recent models predict a transition towards antiferromagnetic long range order at about 1 K [9,10].

With respect to titanium, substitution by tin yields a lattice expansion. It also modifies the oxygen environment of the Tb^{3+} ion and therefore the crystal field. The stannates $R_2Sn_2O_7$ show the same crystal structure [11] as the titanates, and susceptibility data [12,13] also suggest a great variety of magnetic behaviors. $Dy_2Sn_2O_7$ and $Ho_2Sn_2O_7$ are dipolar spin ices [14,15] like their Ti parent compounds, whereas $Er_2Sn_2O_7$ does not order down to 0.15 K [13], and $Gd_2Sn_2O_7$ undergoes a transition to AFM order [16]. In $Tb_2Sn_2O_7$, magnetic measurements suggest an original and complex behavior. Antiferromagnetic interactions are observed at high temperature, yielding a Curie-Weiss constant θ_{CW} of -11 to -12 K [12,13], but a ferromagnetic (FM) transition is seen around 0.87 K [13].

We have performed neutron diffraction and specific heat measurements in $Tb_2Sn_2O_7$. With decreasing temperature, a spin liquid phase is shown to transform into a new type of ordered phase, not predicted by theory, which could be called an "ordered spin ice." Just above the transition, an abnormal change in the spin correlations shows the influence of dipolar interactions. By comparing the ordered Tb^{3+} moment values from neutron diffraction and nuclear specific heat, we also indirectly observe slow fluctuations of correlated spins, which persist down to the lowest temperature.

The crystal structure of $Tb_2Sn_2O_7$ with space group $Fd\bar{3}m$ was studied at 300 K by combining powder x-ray and neutron diffraction, the neutron pattern being measured in the diffractometer 3T2 of the Laboratoire Léon Brillouin (LLB). Rietveld refinements performed with FULLPROF [17] confirmed the structural model ($R_B = 2.4\%$), yielding the lattice constant $a = 10.426$ Å and oxygen position parameter $x = 0.336$. The magnetic diffraction patterns were recorded between 1.4 and 300 K and down to 0.1 K in the diffractometer G6-1 (LLB) and D1B of the Institut Laüe Langevin (ILL), respectively. The specific heat was measured by the dynamic adiabatic method down to 0.15 K.

Figure 1 shows magnetic neutron diffraction patterns for several temperatures. The liquidlike peak corresponding to AFM first neighbor correlations [18] starts to grow below 100 K. Below 2 K, it narrows and slightly shifts, and an intense magnetic signal appears at low q values. This shows the onset of ferromagnetic correlations, which progressively develop as the temperature decreases. Below 1.2 K, a magnetic contribution starts to appear on the Bragg peaks of the face centered cubic (fcc) lattice, which steeply increases at 0.87(2) K. This shows the onset of an ordered magnetic phase with a propagation vector $\mathbf{k} = 0$.

Rietveld refinements of the magnetic diffraction patterns (Fig. 2) were performed with FULLPROF [17]. The magnetic

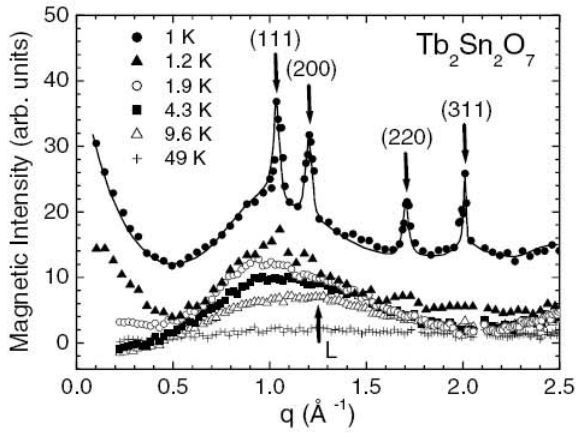

FIG. 1. Magnetic intensity of $Tb_2Sn_2O_7$ versus the scattering vector $q = 4\pi \sin\theta/\lambda$. A spectrum in the paramagnetic phase (100 K) was subtracted. Intensities at 1.0 K have an offset of 10 for clarity. Arrows show the position of the Bragg peaks and near neighbor liquid peak (L) calculated in Ref. [18].

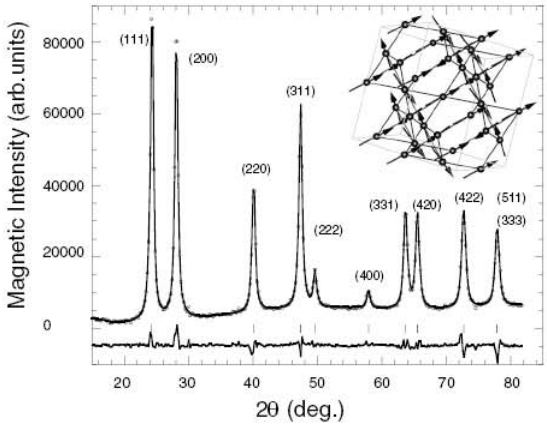

FIG. 2. Magnetic diffraction pattern of $Tb_2Sn_2O_7$ at 0.10 K versus the scattering angle 2θ. A spectrum at 1.2 K was subtracted. The neutron wavelength is 2.52 Å. Solid lines show the best refinement and the difference spectrum (bottom). In the inset, the magnetic structure is shown.

structure was solved by a systematic search, using the program BASIREPS [19] and symmetry-representation analysis [20]. The basis states describing the Tb^{3+} magnetic moments were identified and the symmetry allowed structures were compared to experiment. Neither a collinear ferromagnetic structure nor the $\mathbf{k} = 0$ AFM structures allowed by $Fd\bar{3}m$ symmetry were compatible with the data, yielding extinctions of several Bragg peaks. This suggests a magnetic component breaking the $Fd\bar{3}m$ symmetry. Then we searched for all solutions in the space group $I4_1/amd$, the highest subgroup allowing FM and AFM components simultaneously. The best refinement [21] ($R_B = 2.3\%$) is shown in Fig. 2 and Table I.

In the ordered structure with $\mathbf{k} = 0$, the four tetrahedra of the cubic unit cell are equivalent. In a given tetrahedron, the Tb^{3+} moments make an angle $\alpha = 13.3°$ with the local $\langle 111 \rangle$ anisotropy axes connecting the center to the vertices. The components along these $\langle 111 \rangle$ axes are oriented in the "two in, two out" configuration of the local spin-ice structure [1]. The ferromagnetic component, which represents 37% of the Tb^{3+} ordered moment, orders in magnetic domains oriented along $\langle 100 \rangle$ axes. The perpendicular components make two couples of antiparallel vectors along $\langle 110 \rangle$ edge axes of the tetrahedron. The ordered moment [$M = 5.9(1)\mu_B$ at 0.1 K] is reduced with respect to the free ion moment of $9\mu_B$ as expected from crystal field effects. With increasing temperature, M remains almost constant up to 0.6 K. Then it steeply decreases, showing an inflection point which coincides with the T_c value of 0.87(2) K determined from the peaks in the specific heat and susceptibility [13], and finally vanishes at 1.3(1) K (Fig. 3). The magnetic correlation length L_c was deduced from the intrinsic peak linewidth [17]. L_c remains constant and limited to about 190 Å up to T_c, and then starts to decrease above T_c. The angle α is constant within the experimental error.

The magnetic ground state results from a delicate balance between exchange, dipolar, and anisotropy energies. Several theories were developed involving the AFM nearest neighbor exchange J_{nn}, the FM nearest neighbor dipolar coupling D_{nn}, and the strength of the local anisotropy D_a (all taken in absolute values). A spin liquid ground state is predicted for AFM exchange only and Heisenberg spins [22], namely, for $J_{nn} \gg D_{nn}, D_a$. The dipolar spin-ice state is stabilized for Ising spins when dipolar interactions overcome the AFM exchange [23,24], namely, for $D_a \gg D_{nn} > J_{nn}$. Its local spin structure is similar to the present one, but spins keep the orientational disorder allowed by the "ice rules." When either a finite anisotropy [25] ($J_{nn} \geq D_a \gg D_{nn}$) or a small dipolar coupling [6] ($D_a \gg J_{nn} > D_{nn}$) is considered, a $\mathbf{k} = 0$ structure is predicted, but with a different local order, where all spins of a tetrahedron point either "in" or "out." For Heisenberg spins when dipolar interactions dominate ($D_{nn} > J_{nn} \gg D_a$) a $\mathbf{k} = 0$ structure is predicted, but the local spin structure consists of antiparallel moments along the $\langle 110 \rangle$ edge axes of the

TABLE I. Magnetic components M_x, M_y, and M_z of the four Tb^{3+} moments (in μ_B) in one tetrahedron at 0.1 K. The atomic coordinates x, y, z and the magnetic components are expressed in the cubic unit cell.

Site	x	y	z	M_x	M_y	M_z
1	0.5	0.5	0.5	3.85 (1)	3.85 (1)	2.20 (1)
2	0.25	0.25	0.5	−3.85 (1)	−3.85 (1)	2.20 (1)
3	0.25	0.5	0.25	3.85 (1)	−3.85 (1)	2.20 (1)
4	0.5	0.25	0.25	−3.85 (1)	3.85 (1)	2.20 (1)

PRL 94, 246402 (2005) PHYSICAL REVIEW LETTERS week ending 24 JUNE 2005

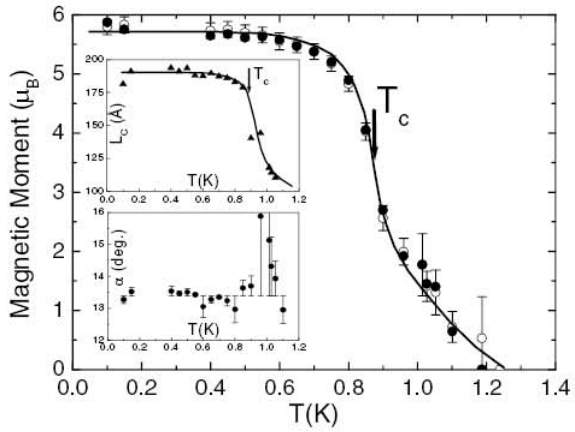

FIG. 3. Ordered magnetic moment M versus temperature (filled circles) and squared intensity of the (200) magnetic peak, scaled to the moment at 0.10 K (open circles). T_c is determined from the peak in the specific heat. The correlation length L_c, deduced from the width of the magnetic Bragg peaks, and the angle α with the local anisotropy axis are plotted in the insets.

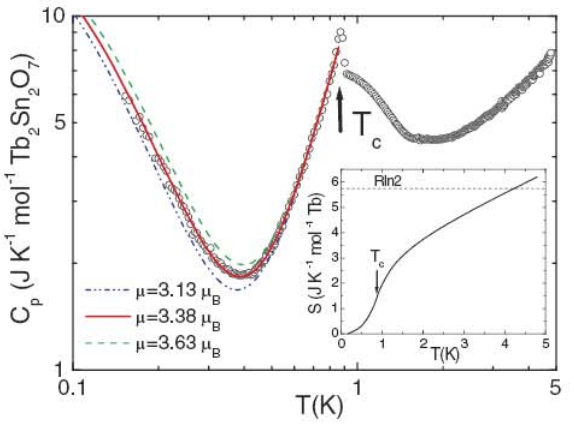

FIG. 4 (color online). Specific heat C_p in $Tb_2Sn_2O_7$. The curves below 0.8 K are the sum of a T^3 magnon contribution and of a nuclear Schottky anomaly, the latter being computed for 3 moment values (see text). The electronic entropy variation is shown in the inset. The arrows label the transition at $T_c = 0.87$ K.

tetrahedron [26]. For an easy plane anisotropy ($D_a < 0$), the local order selected for the $\mathbf{k} = 0$ structure, which is actually observed in $Er_2Ti_2O_7$, is also different [4]. The ordered state of $Tb_2Sn_2O_7$ rather resembles that predicted for a *ferromagnetic* first neighbor exchange interaction combined with a finite anisotropy along ⟨111⟩ axes [27]. It suggests that in $Tb_2Sn_2O_7$ the magnetic order results from an effective ferromagnetic interaction resulting from AFM exchange and FM dipolar coupling, the strength of the uniaxial anisotropy tuning the angle α. This may happen if $D_{nn} > D_a > J_{nn}$. The unusual change with temperature in the short range correlations from AFM to FM, which occurs just above the transition, also suggests that it is driven by an effective ferromagnetic interaction, which should naturally result from the influence of dipolar coupling [28] as in dipolar spin ices.

The temperature dependence of the specific heat C_p is shown in Fig. 4. In good agreement with neutron diffraction data, the specific heat C_p starts to increase below about 1.5 K, and then shows a well defined peak at 0.87 K. The final increase of C_p below 0.38 K is attributed to a nuclear Schottky anomaly, resulting from the splitting of the energy levels of the ^{159}Tb nuclear spin ($I = 3/2$) by the hyperfine field due to the Tb^{3+} electronic moment. The whole nuclear Schottky peak was observed in Tb_2GaSbO_7 [29]. The nuclear Schottky anomaly C_{nuc} was calculated as follows: the full hyperfine Hamiltonian, i.e., the Zeeman part due to the hyperfine field H_{hf} and a quadrupolar term, was diagonalized to obtain the four hyperfine energies. The small quadrupolar term is the sum of a lattice contribution, extrapolated from that measured in $Gd_2Sn_2O_7$ [30] and of an estimated $4f$ term, both amounting to about 5% of the magnetic term. The angle the hyperfine field is at the local ⟨111⟩ axis was fixed at the value 13.3°. The H_{hf} value then is the only parameter for the calculation of C_{nuc}, which was obtained using the standard expression for a Schottky anomaly. The lines in Fig. 4 below 0.8 K represent $C_p = C_{nuc} + C_m$, where $C_m = \beta\, T^3$ is an empirical electronic magnon term which fits well the rise of C_p above 0.4 K, with $\beta = 12.5\ \mathrm{J\,K^{-4}\,mol^{-1}}$. The best fit to the data is obtained with a hyperfine field of 135 T, which corresponds to a Tb^{3+} moment value of $3.3(3)\mu_B$, using the hyperfine constant of 40(4) T/μ_B. The electronic entropy variation S was computed by integrating $(C_p - C_{nuc})/T$ (inset of Fig. 4). In $Tb_2Sn_2O_7$, our current measurements show that the crystal field level scheme is only slightly modified with respect to that in $Tb_2Ti_2O_7$, where the lowest states are two doublets separated by 18 K [31]. Therefore S should reach the values R ln2 and R ln4 when T increases above T_c, as the first two doublets become populated. In fact, the entropy released at the transition is only 25% of R ln2, and it reaches 50% of R ln2 at 1.5 K. This reflects the strong correlations of the magnetic moments in the spin liquid phase above 1.5 K.

The value $m_{eff} = 3.3(3)\mu_B$ for the Tb moment deduced from the nuclear specific heat is therefore well below the neutron value $M = 5.9(1)\mu_B$. Such a remarkable reduction can be explained by the presence of electronic fluctuations, if their characteristic time τ is comparable to the spin-lattice nuclear relaxation time T_1 which governs the thermalization of the hyperfine levels, as in $Gd_2Sn_2O_7$ [30]. Within this model [30], the reduction factor of the nuclear Schottky anomaly is $1 + 2T_1/\tau$, to be compared with the experimental reduction proportional to $(m_{eff}/M)^2 \simeq 0.3$. Then a ratio $T_1/\tau \simeq 1$ can be inferred in $Tb_2Sn_2O_7$. This

implies low temperature fluctuations of the Tb^{3+} moments with a time scale 10^{-4}–10^{-5} s, much slower than for paramagnetic spins (10^{-11} s), which means that these fluctuations involve correlated spins, as previously noticed in geometrically frustrated magnets [23]. Here, they occur in magnetically ordered domains and may be connected with their finite size. They could be probed by muon spin relaxation experiments.

Why does $Tb_2Sn_2O_7$ order and not $Tb_2Ti_2O_7$? The weaker AFM exchange of $Tb_2Sn_2O_7$ may not be the only reason. Our current crystal field study of the two compounds by high resolution neutron scattering points out another fact. In $Tb_2Sn_2O_7$ only, we have observed a small splitting (1.5 K) of a low energy excitation. It shows a lifting of the degeneracy of a crystal field doublet, possibly due to the higher value of the oxygen parameter which controls the local distortion around the Tb^{3+} ion. Assuming that the spectral density of the spin fluctuations decreases with energy, this lifting could weaken in $Tb_2Sn_2O_7$ the quantum fluctuations responsible for the persistence of the spin liquid state in $Tb_2Ti_2O_7$, and allow long range order to set in.

In conclusion, we observed a new magnetic structure in the spin liquid $Tb_2Sn_2O_7$. This unpredicted structure with both ferromagnetic and antiferromagnetic character could be called an "ordered dipolar spin ice." It arises below 1.3(1) K with a low ordered moment and strong fluctuations. Then at 0.87 K a steep increase of the ordered moment coincides with a peak in the specific heat. In the spin liquid phase, ferromagnetic correlations start to replace antiferromagnetic ones below about 2 K. In the ground state, the lower Tb^{3+} moment estimated from specific heat shows that the hyperfine levels are out of equilibrium and evidences the persistence of slow magnetic fluctuations of correlated spins. These unconventional fluctuations are reminiscent of the spin liquid in the ordered phase.

We thank F. Bourée for the neutron measurement on the diffractometer 3T2, as well as R. Moessner and M. J. P. Gingras for interesting comments. We also thank F. Thomas and the cryogenic team of the ILL.

[1] M. J. Harris *et al.*, Phys. Rev. Lett. **79**, 2554 (1997).
[2] J. S. Gardner *et al.*, Phys. Rev. Lett. **82**, 1012 (1999).
[3] J. A. Hodges *et al.*, Phys. Rev. Lett. **88**, 077204 (2002).
[4] J. D. M. Champion *et al.*, Phys. Rev. B **64**, 140407(R) (2001); **68**, 020401(R) (2003).
[5] R. Siddharthan *et al.*, Phys. Rev. Lett. **83**, 1854 (1999).
[6] B. C. den Hertog and M. J. P. Gingras, Phys. Rev. Lett. **84**, 3430 (2000).
[7] I. Mirebeau, I. N. Goncharenko, P. Cadavez-Peres, S. T. Bramwell, M. J. P. Gingras, and J. S. Gardner, Nature (London) **420**, 54 (2002).
[8] I. Mirebeau, I. N. Goncharenko, G. Dhalenne, and A. Revcolevschi, Phys. Rev. Lett. **93**, 187204 (2004).
[9] Y. J. Kao *et al.*, Phys. Rev. B **68**, 172407 (2003).
[10] M. Enjalran *et al.*, J. Phys. Condens. Matter **16**, S673 (2004).
[11] B. J. Kennedy, B. A. Hunter, and C. J. Howard, J. Solid State Chem. **130**, 58 (1997).
[12] V. Bondah-Jagalu and S. T. Bramwell, Can. J. Phys. **79**, 1381 (2001).
[13] K. Matsuhira *et al.*, J. Phys. Soc. Jpn. **71**, 1576 (2002).
[14] K. Matsuhira, H. Hinatsu, K. Tenya, and T. Sakakibara, J. Phys. Condens. Matter **12**, L649 (2000).
[15] H. Kadowaki, Y. Ishii, K. Matsuhira, and Y. Hinatsu, Phys. Rev. B **65**, 144421 (2002).
[16] P. Bonville *et al.*, J. Phys. Condens. Matter **15**, 7777 (2003).
[17] J. Rodríguez-Carvajal, Physica (Amsterdam) **192B**, 55 (1993).
[18] B. Canals and D. A. Garanin, Can. J. Phys. **79**, 1323 (2001).
[19] J. Rodríguez-Carvajal, BASIREPS, ftp://ftp.cea.fr/pub/llb/divers/BasIreps.
[20] Y. A. Izyumov, V. E. Naish, and R. P. Ozerov, *Neutron Diffraction on Magnetic Materials* (Consultants Bureau, New York, 1991).
[21] The magnetic structure is obtained for a state described as a linear combination of the two basis vectors of the irreducible representation Γ_7. To obtain the list of irreducible representations and basis functions for the case $I4_1/amd$ and $\mathbf{k} = 0$, one has to run the program BASIREPS using the coordinates of Tb atoms (0, 0.5, 0.5), (0, 0, 0.5), (−0.25, 0.25, 0.25), (0.25, 0.25, 0.25).
[22] J. N. Reimers, A. J. Berlinsky, and A. C. Shi, Phys. Rev. B **43**, 865 (1991).
[23] S. T. Bramwell *et al.*, Phys. Rev. Lett. **87**, 047205 (2001).
[24] S. T. Bramwell and M. J. P. Gingras, Science **294**, 1495 (2001).
[25] R. Moessner, Phys. Rev. B **57**, R5587 (1998).
[26] S. E. Palmer and J. T. Chalker, Phys. Rev. B **62**, 488 (2000).
[27] J. D. M. Champion, S. T. Bramwell, P. C. W. Holdsworth, and M. J. Harris, Europhys. Lett. **57**, 93 (2002).
[28] R. G. Melko and M. J. P. Gingras, J. Phys. Condens. Matter **16**, R1277 (2004).
[29] H. W. J. Blöte, R. F. Wielinga, and W. J. Huiskamp, Physica (Amsterdam) **43**, 549 (1969).
[30] E. Bertin, P. Bonville, J. P. Bouchaud, J. A. Hodges, J. P. Sanchez, and P. Vuillet, Eur. Phys. J. B **27**, 347 (2002).
[31] M. J. P. Gingras *et al.*, Phys. Rev. B **62**, 6496 (2000).

Available online at www.sciencedirect.com
ScienceDirect
Physica B 385–386 (2006) 307–312
PHYSICA B
www.elsevier.com/locate/physb

Two geometrically frustrated magnets studied by neutron diffraction

I. Mirebeau[a,*], A. Apetrei[a], I.N. Goncharenko[a], R. Moessner[b]

[a]*Laboratoire Léon Brillouin, CEA/CNRS UMR12, Centre d'Etudes de Saclay, 91191 Gif sur Yvette, France*
[b]*Laboratoire de Physique théorique de l'Ecole Normale Supérieure, CNRS-UMR8549, 75005 Paris, France*

Abstract

In the pyrochlore compounds, $Tb_2Ti_2O_7$ and $Tb_2Sn_2O_7$, only the Tb^{3+} ions are magnetic. They exhibit quite abnormal—and, in view of their chemical similarity, strikingly different—magnetic behaviour, as probed by neutron diffraction at ambient and applied pressure. $Tb_2Ti_2O_7$ is a cooperative paramagnet ("spin liquid"), without long-range order at ambient pressure; however, it does become ordered under pressure. By contrast, $Tb_2Sn_2O_7$ enters an "ordered spin ice" state already at ambient pressure. We analyse a simple model which already clearly exhibits some of the qualitative features observed experimentally. Overall, comparing these two compounds emphasizes the power of small perturbations in selecting low-temperature states in geometrically frustrated systems.

PACS: 71.27.+a; 61.12.Ld; 75.25.+2

Keywords: Spin liquid; Spin ice; Neutron diffraction

1. Introduction

Geometrical frustration (GF) [1] is now widely studied in solid state physics, as it seems to play a key role in original phenomena recently observed in new materials. Examples include the large anomalous Hall effect in ferromagnetic pyrochlores or spinels [2], the unconventional superconductivity observed in water substituted Na_xCoO_2 with triangular Co sheets [3], or the interaction between electric and magnetic properties of multiferroics materials [4].

What is GF? Most simply, it occurs when the specific geometry of the lattice prevents magnetic interactions from being satisfied simultaneously. In insulating systems such as the rare earth pyrochlores, the impossibility of a simple Néel ground state due to GF offers the possibility of finding a large variety of alternative, magnetic and non-magnetic, short-or long-ranged ordered states. In the most extreme case, paramagnetic behaviour persists down to the lowest temperatures, leading to an extended cooperative paramagnetic, or spin liquid, regime, in which only short-range correlations result [5].

Ferromagnetic interactions on the pyrochlore lattice may also be frustrated, namely when the exchange is dominated by a strong anisotropy which forces the spins in a tetrahedron to point along their local, non-collinear easy axes [6]. This leads to the spin ice state, whose degeneracy can be mapped onto that of real ice [6], leading to approximately the same entropy in the ground state [7].

In real compounds, the eventual choice of the stable magnetic state depends on a subtle energy balance between the frustrated first neighbour exchange energy term and perturbation terms of various origins (longer range interactions, anisotropies, quantum fluctuations, etc.). It is of course also determined by thermodynamic parameters, such as temperature, pressure or magnetic field. Counter intuitively, thermal fluctuations can even induce order when ordered states permit softer fluctuations than generic disordered ones. This effect is known as order by disorder [8] and is commonly encountered in frustrated magnetism. It has been well studied by Monte-Carlo simulations, and also received some experimental confirmation [9]. Pressure can change the nature of, and balance between different terms in the Hamiltonian, as they can depend on interatomic distances in different ways. An applied field adds Zeeman energy, and can, for

*Corresponding author.
E-mail address: mirebea@dsmmail.saclay.cea.fr (I. Mirebeau).

0921-4526/$ - see front matter © 2006 Elsevier B.V. All rights reserved.
doi:10.1016/j.physb.2006.05.026

example, stabilize a subset of the original ground states, at times resulting in magnetization plateaus.

In this paper, we study a well-known pyrochlore $Tb_2Ti_2O_7$, which we investigated by neutron diffraction under extreme conditions of temperature (down to 0.1 K) and applied pressure (up to 8.7 GPa). We review one of its most fascinating properties, namely its ability to "crystallize" or order magnetically under pressure and we propose a new theoretical approach which accounts for some important peculiarities of this effect. We also compare $Tb_2Ti_2O_7$ to its sibling compound $Tb_2Sn_2O_7$, very recently studied, which behaves as an "ordered spin ice". Both compounds have a fully chemically ordered structure, the pyrochlore structure of cubic $Fd\bar{3}m$ space group, where the Tb^{3+} magnetic ions occupy a GF network of corner sharing tetrahedra. Although they differ only by the nature of the non-magnetic ion (Ti/Sn), they show very different magnetic ground states. The comparison sheds some light on how to select the ground state through very small perturbations, one of the most prominent characteristics of GF.

2. $Tb_2Ti_2O_7$: a spin liquid orders under applied pressure

$Tb_2Ti_2O_7$ is a famous example of a spin liquid, investigated by numerous groups, where short-range correlated Tb spins fluctuate down to 70 mK at least [10], that is more than 300 times below the typical energy scale of the magnetic interactions (the Curie–Weiss constant θ_{CW} of −19 K, where the minus sign corresponds to AF interactions). The persistence of these fluctuations was checked by muon relaxation [10], at the timescale of the muon probe of about 10^{-6} s. At shorter timescales, inelastic neutron scattering showed a quasielastic signal, whose energy linewidth strongly decreases below about 1 K, indicating a stronger slowing down in this temperature range [11]. Coexisting with the spin liquid phase, spin glass-like irreversibilities and anomalies of the specific heat were recently observed in the range 0.1–0.8 K [12]. Using high-pressure powder neutron diffraction [13], we observed two interesting phenomena induced by pressure [14]: (i) the onset of antiferromagnetic long-range order below a Néel temperature T_N of about 2 K; (ii) the enhancement of the magnetic correlations in the spin liquid phase above T_N. Just below T_N, the ordered phase coexists with the spin liquid in a mixed solid–liquid phase, whose relative contributions vary with pressure and temperature. The magnetic Bragg peaks of the simple cubic lattice can be indexed from the crystal structure of $Fd\bar{3}m$ symmetry, taking a propagation vector $\mathbf{k} = (1, 0, 0)$. It means that in the cubic unit cell with four Tb tetrahedra, two tetrahedra are identical and two have reversed moment directions. A longer wavelength modulation of this structure, involving a much larger unit cell, was also observed in the powder data.

What is the pressure induced ground state? More fundamentally what is the role of pressure? To answer these questions, we performed single crystal neutron diffraction down to very low temperatures (0.14 K), combining hydrostatic pressure with anisotropic stress [15]. We showed that both components play a role in inducing the long-range order, and that the ordered moment and Néel temperature can be tuned by the direction of the stress. A stress along a [1 1 0] axis, namely along the direction of the first neighbour distances between Tb^{3+} ions, is the most efficient in inducing magnetic order (Fig. 1).

FullProf refinements of the single crystal data allowed a determination of the magnetic structure with better precision, especially the local spin structure within a Tb tetrahedron. The structure corresponding to the best refinement ($R_F = 14\%$ is given in Table 1). The bond 1–4 along the axis of the stress, which should be reinforced, has AF collinear spins. This corresponds to a natural expectation for AF first neighbour exchange. The orientation of

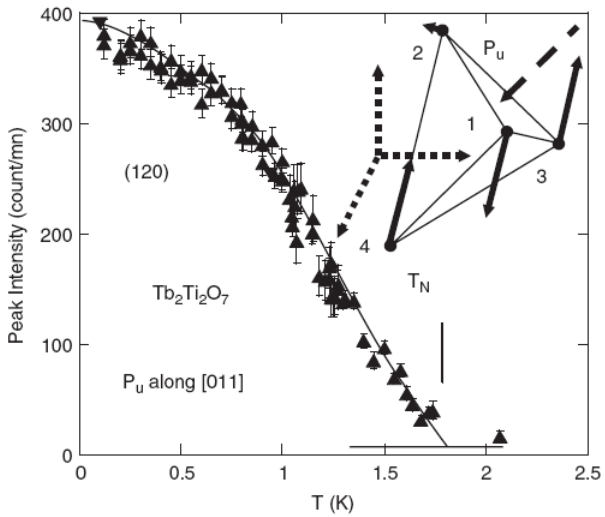

Fig. 1. $Tb_2Ti_2O_7$: an antiferromagnetic ordered state with $\mathbf{k} = (1, 0, 0)$ propagation vector is induced under pressure. Here an isotropic pressure $P_i = 2.0$ GPa is combined with uniaxial pressure $P_u = 0.3$ GPa along [0 1 1] axis. The variation of the peak intensity of the magnetic Bragg peak (1 2 0) shows the Néel temperature. The local spin structure in a tetrahedron has non-compensated magnetization.

Table 1
Orientation of the magnetic moments in one tetrahedron in the pressure induced state of Fig. 1, deduced from the refinement of the magnetic structure

Site	x	y	z	M
1	0.5	0.5	0.5	[1 0 −1]
2	0.25	0.25	0.5	[1 0 1]
3	0.25	0.5	0.25	[−1 0 1]
4	0.5	0.25	0.25	[−1 0 1]

The stress component is along [0 1 1]. The atomic coordinates x, y, z, are expressed in the cubic unit cell containing four tetrahedra. Two tetrahedra are identical and two have reversed spin orientations.

the spin 2 (orthogonal to the three others) is more surprising since with three collinear spins, the exchange field on the fourth one should be also collinear. Since no collinear structure gave a good fit to the data, it suggests that the real spin structure may be even more complex than the proposed one. In any case, both powder and single crystal data yield an important conclusion: we found that inside a tetrahedron, the magnetization is not compensated, namely the vectorial sum of the four spins is non-zero, (although it is of course compensated within the cubic cell, since magnetizations of the four tetrahedra cancel two by two). This means that in the pressure induced ground state, the local order does not correspond to any configuration which mimimizes the energy in the spin liquid phase. In other words, pressure does not select any energy state among those belonging to the ground state degeneracy of the spin liquid (the ground state expected if one considers Heisenberg spins coupled via first neighbour AF exchange interactions only). The anisotropic component (stress) relieves the frustration in a more drastic way, by creating uncompensated bonds, associated with a very small distortion of the pyrochlore lattice. In addition the isotropic component shortens all distances in the same way, increasing the frustrated exchange interaction. This effect could also contribute to the increase of T_N.

The prominent role of stress in inducing magnetic order raises a subsequent question. Could it be stabilized spontaneously by internal stresses? To answer this question, we have now checked the magnetic order at ambient pressure by neutron diffraction in two $Tb_2Ti_2O_7$ samples with different heat treatments, down to about 0.1 K. In an "as-cast" powder sample, we observe at 0.07 K broad magnetic peaks close to the positions expected for the pressure-induced magnetic order (Fig. 2). The Lorentzian lineshape corresponds to a finite correlation length of about 25 Å (2–3 cubic cells). The peaks disappear around 0.3 K. We also studied a single crystal, which was annealed at 1150 °C for 25 h to relieve internal stresses. In the second case, the mesoscopic magnetic order is absent and only the liquid-like correlations are observed, down to the minimum temperature of 0.15 K. Since both samples are chemically ordered and stoichiometric within the accuracy of neutron diffraction, it means that the mesoscopic order is induced by internal stresses. The onset of this mesoscopic order may strongly influence the spin glass irreversibilities and anomalies of the specific heat observed in the same temperature range [12], which seem to depend on the heat treatment.

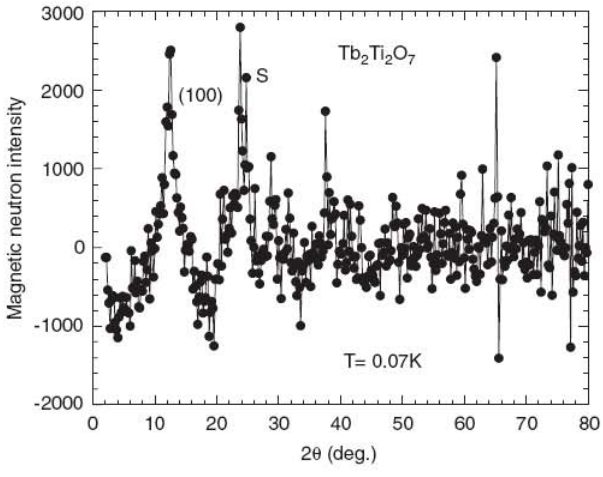

Fig. 2. $Tb_2Ti_2O_7$: a mesoscopic order is induced by spontaneous strains at very low temperature. Magnetic neutron diffraction spectra at 0.07 K, showing broad peaks close to the positions of the (1 0 0) magnetic peak and secondary magnetic phase (S) of the pressure-induced state [14]. The spectrum of the spin liquid regime at 1.2 K has been subtracted. The incident neutron wavelength is 2.52 Å. The broad magnetic peaks disappear at about 0.3 K.

3. $Tb_2Sn_2O_7$: an ordered spin ice state

In contrast to $Tb_2Ti_2O_7$, $Tb_2Sn_2O_7$ undergoes a transition to an ordered state already at ambient pressure. The magnetic structure, very recently determined by powder neutron diffraction experiments [16], was called an "ordered spin ice". The local order within one tetrahedron is close to the "two in–two out" configuration of spin ice, taking into account a small deviation of 13° of the magnetic moments with respect to the local ⟨1 1 1⟩ easy anisotropy axes. In the canonical spin ice state, individual tetrahedra keep the mutual orientational disorder allowed by the "ice rules", leading to short-range order and ground state entropy [17]. Here the four tetrahedra of the unit cell are identical, leading to an ordered structure with $\mathbf{k} = 0$ propagation vector (Fig. 3). The resulting magnetic structure is non-collinear, but exhibits a ferromagnetic component, which represents about 37% of the Tb^{3+} ordered moment. This explains the ferromagnetic character of the transition, previously observed by magnetization [18].

Together with the non-collinear magnetic structure, the original effects of the frustration persist in the ordered phase of $Tb_2Sn_2O_7$. The magnetic order is stabilized in two steps (1.3 K and 0.87 K) corresponding to anomalies of the specific heat. Such behavior is not observed in a classical second order transition. The correlation length increases throughout the transition region, and remains limited to 180 Å even at very low temperature. The ordered state coexists with slow collective fluctuations, in the time scale of 10^{-4}–10^{-8} s. They were probed by comparing the Tb^{3+} moment value of 5.9(1) μ_B deduced from neutron diffraction to the smaller value of 4.5(3) μ_B deduced from the nuclear specific heat [16,19].

The magnetic order in $Tb_2Sn_2O_7$ may be compared to that found by Champion et al. [20], who considered the competition between first neighbour exchange and uniaxial anisotropy in a pyrochlore *ferromagnet*. The model involves two parameters, the strength of the ferromagnetic interaction J and that of the uniaxial anisotropy D_a along ⟨1 1 1⟩ axes. Ferromagnetic and spin ice states correspond

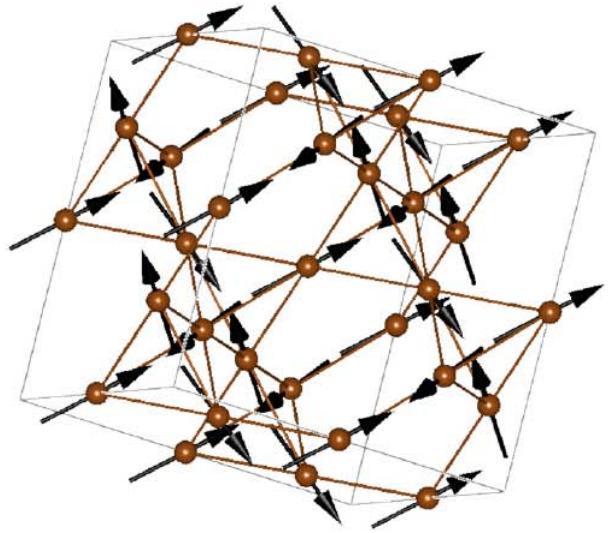

Fig. 3. $Tb_2Sn_2O_7$: an ordered spin ice structure: the local spin structure in a tetrahedron is close to the "two in–two out" structure of a spin ice, but individual tetrahedra are identical, leading to an ordered structure with $\mathbf{k} = 0$ propagation vector and ferromagnetic character.

to the cases $D_a/J = 0$ and ∞, respectively. For finite D_a/J values, the magnetic order shows many similarities with the observed one. Namely: (i) the ground state is ordered in a $\mathbf{k} = 0$ four sublattice structure; (ii) the local order within one tetrahedron may also be deduced from the spin ice structure; (iii) the magnetic transition is of first order, changing to second order with decreasing D_a/J.

However, the deviations from the local spin ice structure are different in the model and in the real system. In the model, spins are uniformly canted towards the ferromagnetic direction. The ground state magnetization relative to the local moment increases from $0.578 = \frac{1}{\sqrt{3}}$ (the average magnetization of a tetrahedron in the spin ice case) to 1 (the ferromagnetic case) with decreasing D_a/J. By contrast, in $Tb_2Sn_2O_7$, the deviations of the magnetic moments from the local $\langle 1\,1\,1\rangle$ axes actually reduce the magnetization (to about 0.37 in relative units). So the deviations of the magnetic moments from the local spin ice structure act in an opposite way to that predicted by the finite anisotropy ferromagnetic model.

Finally, in $Tb_2Sn_2O_7$, the neutron and magnetic data together with the comparison with theory, suggest that here the effective first neighbour interaction becomes ferromagnetic, although the physics of the system cannot be simply reduced to the energy scheme assumed in Ref. [20].

4. A simple model for the influence of stress

An analysis of the effect of pressure applied to an individual tetrahedron already manifests qualitatively two basic experimental results observed in $Tb_2Ti_2O_7$: the much stronger influence of an anisotropic stress along a [1 1 0] axis (as opposed to hydrostatic pressure or to a stress along the [1 0 0] direction), and the presence of an uncompensated magnetization.

In the isotropic problem, all six bonds of the tetrahedron are equivalent. Application of stress in the [1 1 0] direction lowers this symmetry, as shown in Fig. 4. In symmetry terms, the bonds form a six-dimensional representation of the tetrahedral group T_d, which decomposes into three irreducible representations. A singlet, A amounts to a uniform change of all bonds together. Furthermore, there is a doublet, E, the components of which correspond (a) to strengthening two opposite bonds, and weakening the four others (or vice versa) or (b) to weakening an opposite pair of those four bonds, and strengthening the other pair. Finally, each component of the triplet, T, implies a strengthening/weakening (by an equal amount) of an opposite pair of bonds [21].

The crucial point is that the uniaxial [1 1 0] stress can couple to all three representations. In its presence, there are three (instead of only one) symmetry-inequivalent bond strengths (see Fig. 4). In other words, the Hamiltonian including the uniaxial [1 1 0] stress has a lower symmetry than the isotropic one. The case of [1 0 0] pressure is intermediate: here only two representations are present, the triplet being absent, as illustrated in the left panel of Fig. 4.

Whereas the initial degeneracy of the isotropic system is a signature of the different possible compromises between which bonds to frustrate and which to satisfy, some of these choices have become forbidden as it is not possible to trade off inequivalent bonds against one another.

For simplicity, let us consider a classical, isotropic Heisenberg antiferromagnet at $T = 0$ under stress. We have considered the spin configurations which minimize the energy for different orientations of the stress. We find that these configurations have a compensated magnetization for a stress along [1 0 0]. By contrast, a non-compensated

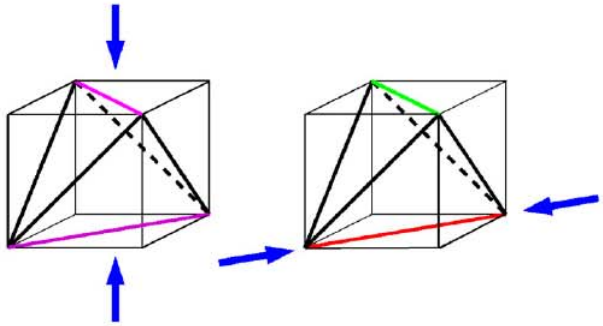

Fig. 4. Tetrahedron under uniaxial stress, denoted by the arrows. Left (right) panel: stress applied in the [1 0 0] ([1 1 0]) direction. This splits the six bonds into the following symmetry-inequivalent groups: the bond along the [1 1 0] direction (bottom), the one perpendicular to it (top)—which remain equivalent for [1 0 0] but not for [1 1 0] stress—and the four remaining ones.

magnetic moment can arise for a stress along a [1 1 0] axis. A summary of the calculation is given below.

The results for an ice-type model (i.e. a ferromagnet in the presence of anisotropy D_a) can be obtained along similar lines. It needs to be borne in mind, however, that (a) the strict ice model ($D_a/J = \infty$) does not permit small deviations of the spins from their preferred axes, and that (b) a ferromagnet will generically exhibit a non-compensated moment even in the absence of stress. By contrast, an anisotropic (but strain-free) antiferromagnet has a momentless ground state, which, however, is the simple FeF_3-type "all-in" or "all-out" ground state.

This classical isotropic Hamiltonian has a continuous two-parameter family of degenerate ground states in the isotropic case [1]. This degeneracy is reduced by the strain. For example, in the presence of an E-distortion weakening the average strength of the top/bottom pair of bonds with respect to the other two pairs, a collinear state will be selected. In this state, each spin is parallel to its partner at the other end of the coloured bond, and antiparallel to the other pair of spins. The total spin of the tetrahedron thus remains compensated at zero. For an E distortion of the opposite sign, the top (and bottom) pair of spins will be antialigned; for the full pyrochlore lattice, this generates decoupled chain states. In contrast to this situation, the presence of a T distortion does not change the energy of the isotropic ground states relative to one another to first order. This happens because it couples to a difference in the expectation value of opposing bonds, a difference which vanishes in the unperturbed ground states.

However, in higher order, a difference in relative bond strength can induce a difference between the expectation values of the scalar product $S_i \cdot S_j$ across the bottom and top bonds. Such a difference is equivalent to an uncompensated total moment of the tetrahedron (as a tetrahedron with zero moment necessarily has equal expectation values of $S_i \cdot S_j$ on opposite bonds). The ground states in the presence of stress are thus close to—but not a subset of—those of the isotropic system.

5. Discussion

In this section we briefly comment about the relevance of the above model to $Tb_2Ti_2O_7$, and then focus on the origin of the differences between the two compounds.

At ambient pressure, the fact that $Tb_2Ti_2O_7$ does not order but remains "liquid" down to 70 mK, is still a challenge to theory. Sophisticated calculations taking into account the crystal field energy [22] together with dipolar interactions, predict an Ising-like behaviour for the Tb ion moment in the ground state (with the moment reduced with respect to the free ion value) and an effective AF first neighbour interaction [23]. These calculations predict at ambient pressure a transition to an AF order similar to that found in FeF_3 (a $\mathbf{k} = 0$ structure with an "all in–all out" local configuration) below 1–2 K, which is however not what is observed experimentally.

The simple model discussed above, already proposed on a more empirical basis in Ref. [16], reproduces the main characteristics of the pressure-induced state in $Tb_2Ti_2O_7$, namely the stronger effect of degeneracy lifting of the [1 1 0] over the [1 0 0] stress, and the appearance of an uncompensated magnetization in the former case. This is presumably the case because it incorporates the most fundamental property of the stress, namely the explicit symmetry breaking it induces. This effect should occur in qualitatively the same way in a much larger class of models.

These results are therefore rather robust but, by the same token, they are also only qualitative: the model in its current form yields little information on the detailed Hamiltonian of the system, nor the origin of the effective nearest-neighbour interaction J and of its sensitivity to pressure. In particular, we have not been able to reproduce the detailed finite-temperature spin structure.

We now turn to $Tb_2Sn_2O_7$, which behaves as an ordered spin ice. Neutron data as compared with theory strongly suggest that the effective first neighbour interaction has now become ferromagnetic. What is the reason for this change? We can propose the following explanation. In the "true" spin ices $Ho_2Ti_2O_7$ or $Dy_2Ti_2O_7$ with stronger uniaxial anisotropy), it was shown that the effective ferromagnetic interaction results from the influence of the dipolar coupling which overcomes the weak AF superexchange [17]. Taking the same conventional notations, the effective first neighbour interaction J_{eff} is expressed as $J_{eff} = J_{nn} + D_{nn}$, where $J_{nn} = J/3$ and $D_{nn} = 5D/3$ are the superexchange and dipolar energy scales, respectively. In $Tb_2Ti_2O_7$ ($J_{nn} = -0.88$ K, $D_{nn} = 0.8$ K from Ref. [23]), this effective interaction remains AF. In $Tb_2Sn_2O_7$, Sn substitution enlarges the unit cell (from $a = 10.149$ to 10.426 Å in Ti and Sn compounds, respectively). This expansion $\Delta a/a \sim 2.7\%$, equivalent to a negative chemical pressure of about 12–15 GPa, should strongly decrease the AF superexchange interaction J. Assuming roughly a decrease of J_{nn} in the ratio of the Curie–Weiss constants (-19 and -12 K in Ti and Sn compounds, respectively) without big changes in the dipolar constant, we get $J_{eff} = 0.18\,\text{K} > 0$ for $Tb_2Sn_2O_7$. Therefore, the expansion in the unit cell induced by Sn substitution might be enough to switch the compound to the spin ice region of the phase diagram [24].

To go further, microscopic models should take into account the exact nature of the anisotropy, which is not simply uniaxial in the Tb compounds [22]. This involves a reinvestigation of the crystal field levels, currently in progress. It could exhibit more subtle differences between the two compounds than the simple effect of a chemical pressure discussed above.

In conclusion, the two compounds studied here clearly show the rich variety of behaviour exhibited by geometrically frustrated magnets. Comparing them allows one to understand better the key role played by small perturbations in selecting one peculiar state among the many potential magnetic states.

Acknowledgements

We thank A. Gukasov and O. Isnard for their help in the neutron measurements at LLB and ILL, respectively. We also thank G. Dhalenne, A. Revcolevschi, A. Forget and D. Colson, who provided the single crystal and powdered samples. R.M. thanks S. Sondhi and O. Tchernyshyov for collaboration on related work. He was supported in part by the Ministère de la Recherche with an ACI grant.

References

[1] For an introduction to frustrated magnets, see R. Moessner, Can. J. Phys. 79 (2001) 1283; reviews of exact diagonalizations and experiments, respectively, are C. Lhuillier, P. Sindzingre, J.-B. Fouet, Can. J. Phys. 79 (2001) 1525; P. Schiffer, A.P. Ramirez, Comments Condens. Matter Phys. 18 (1996) 21.
[2] Y. Taguchi, Y. Oohara, H. Yoshisawa, N. Nagaosa, Y. Tokura, Science 291 (2001) 2573.
[3] K. Takada, et al., Nature 422 (2003) 53.
[4] G.R. Blake, et al., Phys. Rev. B 71 (2005) 214402.
[5] J. Villain, Z. Phys. B 33 (1979) 31.
[6] M.J. Harris, et al., Phys. Rev. Lett. 79 (1997) 2554.
[7] A.P. Ramirez, A. Hayashi, R.J. Cava, R. Siddhartan, B.S. Shastry, Nature 399 (1999) 333.
[8] J. Villain, R. Bidaux, J.P. Carton, R. Coute J. Phys. (Paris) 41 (1980) 1263;
E.F. Shender, Sov. Phys. JETP 56 (1982) 178.
[9] A.G. Gukasov, et al., Europhys. Lett. 79 (1997) 2554;
J.D.M. Champion, et al., Phys. Rev. B 68 (2003) 020401R.
[10] J.S. Gardner, et al., Phys. Rev. Lett. 82 (1999) 1012.
[11] Y. Yasui, et al., J. Phys. Soc. Japan 71 (2002) 599.
[12] N. Hamaguchi, T. Matsushita, N. Wada, Y. Yasui, S. Masatoshi, Phys. Rev. B 69 (2004) 132413.
[13] I.N. Goncharenko, High Pressure Res. 24 (2004) 193.
[14] I. Mirebeau, I.N. Goncharenko, P. Cadavez-Peres, S.T. Bramwell, M.J.P. Gingras, J.S. Gardner, Nature 420 (2002) 54.
[15] I. Mirebeau, I.N. Goncharenko, G. Dhalenne, A. Revcolevschi, Phys. Rev. Lett. 93 (2004) 187204;
I. Mirebeau, I. Goncharenko, J. Phys.: Condens. Matter 17 (2005) S771.
[16] I. Mirebeau, et al., Phys. Rev. Lett. 94 (2005) 246402.
[17] S.T. Bramwell, M.J.P. Gingras, Science 294 (2001) 14.
[18] K. Matsuhira, et al., J. Phys. Soc. Japan 71 (2002) 1576.
[19] The value of the Tb moment deduced from the nuclear specific heat has been erroneously stated to be 3.3(3) μ_B in Ref. [16].
[20] J.D.M. Champion, S.T. Bramwell, P.C.W. Holdsworth, M.J. Harris, Europhys. Lett. 57 (2002) 93.
[21] Y. Yamashita, K. Ueda, Phys. Rev. Lett. 85 (2000) 4960;
O. Tchernyshyov, R. Moessner, S.L. Sondhi, Phys. Rev. Lett. 88 (2002) 067203.
[22] M.J.P. Gingras, et al., Phys. Rev. B 62 (2000) 6496.
[23] Y. Kao, M. Enjalran, A. Del Maestro, H. Molavian, M.J.P. Gingras, Phys. Rev. B 68 (2002) 172407;
M. Enjalran, M.J.P. Gingras, Phys. Rev. B 70 (2004) 174426.
[24] B.C. Den Hertog, M.J.P. Gingras, Phys. Rev. Lett. 84 (2000) 3430.

PRL 97, 206401 (2006) PHYSICAL REVIEW LETTERS week ending 17 NOVEMBER 2006

Microscopic Study of a Pressure-Induced Ferromagnetic–Spin-Glass Transition in the Geometrically Frustrated Pyrochlore $(Tb_{1-x}La_x)_2Mo_2O_7$

A. Apetrei,[1] I. Mirebeau,[1] I. Goncharenko,[1] D. Andreica,[2,3] and P. Bonville[4]

[1]*Laboratoire Léon Brillouin, CEA-CNRS, CE-Saclay, 91191 Gif-sur-Yvette, France*
[2]*Laboratory for Muon-Spin Spectroscopy, Paul Scherrer Institut, 5232 Villigen-PSI, Switzerland*
[3]*Faculty of Physics, Babes-Bolyai University, 400084 Cluj-Napoca, Romania*
[4]*Service de Physique de l'Etat Condensé, CEA-CNRS, CE-Saclay, 91191 Gif-Sur-Yvette, France*

(Received 24 April 2006; published 15 November 2006)

We have studied $(Tb_{1-x}La_x)_2Mo_2O_7$ pyrochlores by neutron diffraction and μSR at ambient and under applied pressure. (Tb, La) substitution expands the lattice and induces a change from a spin-glass-like state ($x = 0$) to a noncollinear ferromagnet ($x = 0.2$). In the ferromagnetic structure, the Tb moments orient close to their local anisotropy axes as for an ordered spin ice, while the Mo ones orient close to the net moment. The temperature dependence of the μSR relaxation rates and static local fields suggests a second transition of dynamical nature below the Curie transition. Under pressure, the long range order breaks down and a spin-glass-like state is recovered. The whole set of data provides a microscopic picture of the spin correlations and fluctuations in the region of the ferromagnetic–spin-glass threshold.

DOI: 10.1103/PhysRevLett.97.206401 PACS numbers: 71.30.+h, 71.27.+a, 75.25.+z

In the pyrochlore compounds $R_2M_2O_7$, both the rare earth R^{3+} and the M^{4+} transition metal form a three-dimensional network of corner-sharing tetrahedra. The pyrochlore lattice is geometrically frustrated for both antiferromagnetic (AF) and ferromagnetic (F) nearest-neighbor exchanges, leading to intriguing magnetic states such as spin liquids, spin ices, or chemically ordered spin glasses [1,2].

In $R_2Mo_2O_7$ pyrochlores, electrical and magnetic properties strongly depend on the rare earth ionic radius r. Compounds with a small ionic radius (Y, Dy, and Tb) are spin-glass (SG) insulators, whereas those with Gd, Sm, and Nd are F metals. The $(RR')_2Mo_2O_7$ series shows a universal dependence [3,4] of the transition temperature versus r, suggesting that the sign of Mo-Mo interactions controls the formation of the spin-glass–ferromagnetic state. Photoemission experiments and band structure calculations [5,6] point out that the concomitant changes of the transport and magnetic properties come from strong electron correlations in the Mo(t_{2g}) band near the Fermi level.

Up to now, there has been no microscopic investigation of the SG-F threshold, so as to follow the changes in the magnetic correlations and spin fluctuations. All microscopic studies deal with compounds far from the threshold radius r_c. $Y_2Mo_2O_7$ and $Tb_2Mo_2O_7$ with $r < r_c$ were intensively studied [7–10], since the SG transition is surprising with regards to their chemical order. $Nd_2Mo_2O_7$ with $r > r_c$ showing a giant abnormal Hall effect was also much studied [11,12]. F compounds near the threshold (Sm and Gd) are difficult to study by neutrons due to their strong absorption. So the microscopic evolution of magnetism throughout the threshold was not clarified so far.

To understand the role of interatomic distances in the SG-F transition, the most direct way is to combine applied pressure and chemical pressure. In $Gd_2Mo_2O_7$, magnetic measurements showed that an applied pressure as well as (Gd, Dy) substitution could suppress the ferromagnetic transition and induce spin-glass-like anomalies [13,14]. Here we have studied the $(Tb_{1-x}La_x)_2Mo_2O_7$ system by neutron diffraction and μSR at ambient and applied pressure. Starting from the spin glass $Tb_2Mo_2O_7$, the dilution by a *nonmagnetic* La ion induces long range magnetic order. By neutron diffraction, we follow this evolution at a microscopic level. For $x = 0.2$, we observe a new ordered magnetic structure, involving noncollinear ferromagnetic arrangement of both Tb and Mo moments. Under pressure, the $x = 0.2$ sample transforms into a spin glass similar to $Tb_2Mo_2O_7$. While neutron diffraction probes magnetic correlations, the μSR technique allows one to study spin fluctuations. For $x = 0.2$, we observe by μSR a dynamical anomaly at a temperature $T^\star$ well below the Curie temperature T_C. Under pressure, the two temperatures seem to merge. The whole data provide the first and complete microscopic picture of the F-SG threshold.

The crystal structure of $(Tb_{1-x}La_x)_2Mo_2O_7$ powders ($x = 0$, 0.05, 0.1, 0.15, and 0.2) was characterized at 300 K by combining x-ray and neutron diffraction. FULLPROF refinements [15] show that all samples crystallize in the $Fd\bar{3}m$ space group, with a lattice constant a between 10.3124(7) ($x = 0$) and 10.3787(8) Å ($x = 0.2$). The $x = 0.1$ sample [$a = 10.3461(8)$ Å] is above the critical threshold ($a_c \sim 10.33$ Å). The lattice constant was measured under pressure for $x = 0$ and 0.2 on the ID27 beam line of the European Synchrotron Radiation Facility (ESRF). Susceptibility data show an evolution from a spin glass with irreversibilities below $T_{SG} \sim 22$ K ($x = 0$) towards a ferromagnetic state with a strong increase of magnetization below $T_C \sim 58$ K ($x = 0.2$).

Magnetic diffraction patterns were recorded on the powder diffractometers G61 and G41 of the Laboratoire Léon

Brillouin (LLB) at ambient pressure and under pressure on G61 in its high pressure version [16]. They show the evolution of the magnetic order when going through the critical threshold by substitution of Tb for La [Fig. 1(a)] and by applied pressure [Fig. 1(b)]. It is clear evidence that magnetic changes induced by chemical and applied pressures are microscopically equivalent.

In $Tb_2Mo_2O_7$ ($x = 0$), short range order yields diffuse maxima around $q = 1$ and 2 $Å^{-1}$. An intense signal at low q values reveals ferromagnetic correlations. For $x = 0.1$, Lorentzian peaks start to grow at the position of the diffuse maxima, revealing the onset of mesoscopic magnetic order. For $x = 0.2$, the low q signal almost disappears, and we clearly see magnetic Bragg peaks showing long range magnetic order. When we apply pressure on the $x = 0.2$ sample, the intensity of the Bragg peaks decreases, and the ferromagnetic correlations and diffuse maxima start to grow. The magnetic pattern for $x = 0.2$ at 1.05 GPa (3.7 GPa) is very similar to that for $x = 0.1$ ($x = 0$) at ambient pressure.

In the range $q = 0.5$–2.5 $Å^{-1}$, we analyzed the magnetic correlations in $Tb_2Mo_2O_7$ by a short range magnetic model as in Ref. [8]. A fit of the diffuse magnetic intensity by the sum of radial correlation functions yields the spin correlation parameters γ up to the fourth coordination shell (~ 7.3 Å). The Tb-Tb correlations are F ($\gamma_{1,3,4} > 0$), while the Tb-Mo are AF ($\gamma_2 < 0$) in agreement with previous results [8]. The AF Mo-Mo correlations yielding the frustration in the SG state are not seen, being about 50 times smaller than the Tb-Tb ones due to the smaller Mo moment. The intense signal below 0.5 $Å^{-1}$ was not detected in previous patterns measured in a higher q range [8,9]. It cannot be accounted for by the short range magnetic model, even when increasing the correlation range up to the seventh coordination shell. We attribute it to Tb-Tb ferromagnetic correlations and evaluate their length scale to 20(8) Å.

The magnetic Bragg peaks observed for $x = 0.2$ belong to the face centered cubic lattice, showing that the magnetic structure is derived from the chemical one of $Fd\bar{3}m$ symmetry by a propagation vector $\mathbf{k} = \mathbf{0}$. The two magnetic peaks (200) and (220), forbidden in the pyrochlore structure, suggest a noncollinear F structure.

The magnetic structure was solved by a systematic search, using the program BASIREPS [17] and symmetry-representation analysis [18] combined with FULLPROF [15]. Since neither a collinear F structure nor the $\mathbf{k} = \mathbf{0}$ AF structure allowed by $Fd\bar{3}m$ symmetry were compatible with the data, we searched for a solution in the space group I_{41}/amd, the highest subgroup allowing F and AF components simultaneously. The best refinement ($R_B = 4\%$) is shown in Fig. 2(a). In the ordered structure with $\mathbf{k} = \mathbf{0}$, the four tetrahedra of the unit cell are equivalent, for both Tb and Mo lattices. In a given Tb tetrahedron [inset in Fig. 2(a)], the Tb^{3+} moments orient in the local spin ice structure [1] with a small angle $\theta_t = 11.6°$ at 1.4 K with the local ⟨111⟩ anisotropy axes connecting the center to the vertices. Their F component orders along a [001] axis. The Mo moments align close to a [001] axis [inset in Fig. 2(a)], with a slight tilting by the angle $\theta_m = 6.8°$ at 1.4 K towards the local ⟨111⟩ axes. Both Mo-Mo and Tb-Mo correlations are F, in contrast with the spin glass.

As a striking feature, long range order (LRO) is induced by diluting the Tb lattice with a nonmagnetic ion. It proves that the main effect of dilution is the lattice expansion. From the lattice constant, a small La content ($x \sim 0.06$) should induce the SG-F transition. We notice that Tb magnetism should play a role in this transition together

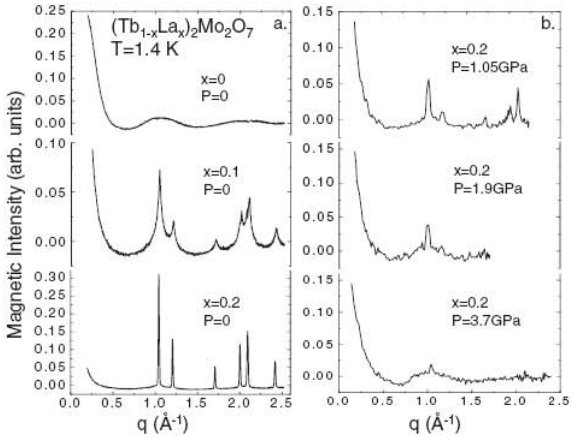

FIG. 1. Magnetic intensity of $(Tb_{1-x}La_x)_2Mo_2O_7$ at 1.4 K versus the scattering vector $q = 4\pi \sin\theta/\Lambda$. The neutron wavelength is $\Lambda = 4.741$ Å. A spectrum in the paramagnetic phase (70 K) was subtracted, and the magnetic intensity was scaled to the (222) nuclear peak intensity.

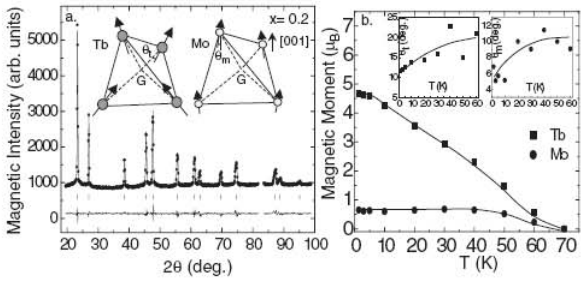

FIG. 2. (a) Magnetic intensity in the $x = 0.2$ sample at 1.5 K versus the scattering angle 2θ, with $\Lambda = 2.426$ Å. A spectrum at 70 K was subtracted. The solid lines show the best refinement ($R_B = 4\%$) and the difference spectrum (bottom). In the inset is the magnetic structure of the Tb and Mo tetrahedra. (b) Ordered magnetic moments versus temperature. In the inset are the angles θ_t and θ_m made by Tb and Mo moments with the local anisotropy ⟨111⟩ and the [001] axes, respectively. The solid lines are guides to the eye.

with the change in sign of the Mo-Mo interaction, since $(Y_{1-x}La_x)_2Mo_2O_7$ compounds do not show LRO [19]. At higher dilution ($x = 0.2$), the Bragg peaks are better defined, but they still coexist with short range order (SRO), as shown by a diffuse scattering which increases below 40 K. The SRO has the same symmetry as the LRO. It likely arises from the different local (Tb, La) environments.

As for the LRO moments [Fig. 2(b)], M_{Mo} is almost T-independent below 40 K while M_{Tb} keeps increasing below T_C. At 1.4 K, we obtain $M_{Tb} = 4.66(2)\mu_B$ and $M_{Mo} = 0.64(3)\mu_B$. The SRO moments are correlated over about 20 Å and evaluated to $4.3(2)\mu_B$ (Tb) and $0.2(5)\mu_B$ (Mo). The total moments of $6.3(1)\mu_B$ (Tb) and $0.7(2)\mu_B$ (Mo) are still well reduced from the free ion values of $9\mu_B$ and $2\mu_B$, respectively. For Tb, this strong reduction could be explained mainly by crystal field effects. As for Mo, it could arise from orbital frustration or the proximity of the threshold leading to quantum fluctuations. The two tilting angles slightly decrease with decreasing temperature [inset in Fig. 2(b)].

The noncollinear structure for both Tb^{3+} and Mo^{4+} originates from the uniaxial anisotropy of the Tb^{3+} ion, which brings spin ice frustration to the ferromagnetic phase. The ground state is determined by Mo-Mo F exchange interactions like in $Nd_2Mo_2O_7$ [11], while in the "ordered spin ice" $Tb_2Sn_2O_7$ with similar orientation of Tb^{3+} moments [20] it results from F dipolar interactions between the Tb^{3+} ions.

Under pressure, the ordered moments ($x = 0.2$) decrease and reorient (Fig. 3). For $P = 1.05$ GPa, we observe the coexistence of LRO and SRO phases of the same symmetry. The LRO Tb moments keep the local spin ice configuration with a different $\theta'_t = 28.3°$. Mo moments also turn to a local spin ice order, making an angle $\theta'_m = 7.3°$ with the local $\langle 111 \rangle$ axes. The ordering temperature decreases with increasing pressure. At 3.7 GPa, the Bragg peaks disappear. From our fits, we obtain short range F Tb-Tb ($\gamma_{1,3,4} > 0$) and AF Tb-Mo correlations ($\gamma_2 < 0$), with a ferromagnetic correlation length of 18(7) Å. These parameters are similar to those of $Tb_2Mo_2O_7$. Our recent results also reveal the same behavior in $Gd_2Mo_2O_7$ under pressure [21].

μSR measurements (Fig. 4) shed new light on the magnetic order by probing the spin fluctuations and the static local field below T_C. The recent availability of μSR under pressure allows us to probe them on both sides of the threshold. We measured the $x = 0.2$ sample at ambient pressure on the GPS and GPD instruments of the Paul Scherrer Institut (PSI) and under a pressure of 1.3 GPa on GPD.

Sample μSR spectra above T_C were best fitted with a stretched exponential function $P_Z(t) = \exp(-\lambda t)^\beta$. Below T_C, $P_Z(t)$ was fitted by the function $P_Z(t) = [\exp(-\lambda_Z t)^\beta + 2\exp(-\lambda_T t)\cos(\gamma_\mu \langle B_{loc} \rangle t)]/3$, expected for the magnetically ordered state of a powder sample

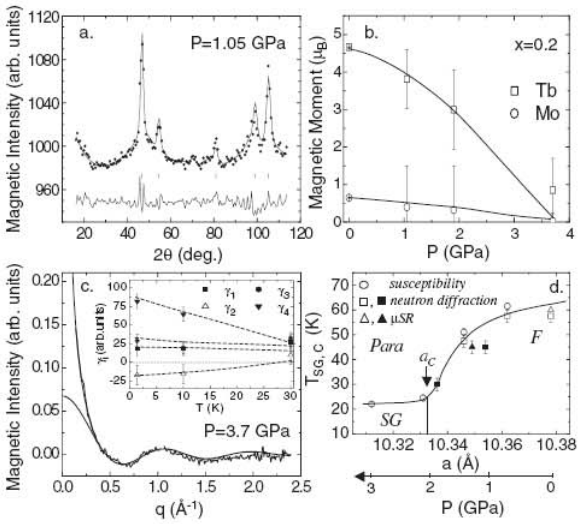

FIG. 3. (a) Magnetic intensity in $x = 0.2$ sample at 1.4 K and $P = 1.05$ GPa, with $\Lambda = 4.741$ Å. The solid lines show the best refinement ($R_B = 20\%$) and the difference spectrum; (b) magnetic moment versus pressure; (c) magnetic intensity of $x = 0.2$ at 1.4 K and $P = 3.7$ GPa versus scattering vector. The fit is made with the short range model (bottom line), including longer range F correlations (upper line). In the inset is the temperature dependence of the correlations coefficients; (d) phase diagram for $(Tb_{1-x}La_x)_2Mo_2O_7$ in the threshold region. The open symbols are measured at ambient pressure for several x contents. The solid symbols are for $x = 0.2$ under pressure, taking into account ESRF data to determine $a(P)$.

[22]. The first term of the function relevant for temperatures below T_C corresponds to the depolarization by spin fluctuations perpendicular to the direction of the muon spin, whereas the second term reflects the precession of the muon spin in the average local field $\langle B_{loc} \rangle$ at the muon site. The transverse relaxation rate λ_T can have both static and dynamical character. Both expressions of $P_Z(t)$ are expected to merge in the high temperature limit, when the dynamics of Tb^{3+} and Mo^{4+} moments is fast, yielding $\lambda_Z = \lambda_T$, $\langle B_{loc} \rangle = 0$, and $\beta = 1$. We notice that a fit with a dynamical Kubo-Toyabe function is possible for a small temperature range below T_C, but the function used above gives better results at low temperature and close to T_C. The background contribution from the cryostat walls was determined at 70 K in a transverse field of 50 G. The total function is written as $P_Z(t) = 0.9P_Z(t) + 0.1\exp(-0.1t)$. Spectra are shown in Fig. 4(a).

The longitudinal relaxation rate λ_Z shows a cusp at $T_C \sim 60$ K, then a broad maximum at $T^\star \sim 25$ K. The transverse relaxation rate λ_T is about 10 times larger than $\lambda_Z(T)$. It smoothly increases below T_C in a way similar to the average local field $\langle B_{loc} \rangle$. This leads us to assign λ_T mainly to the width of the distribution of local fields. Both quantities scale with the ordered moment $M_{Tb}(T)$ measured by

PRL 97, 206401 (2006) PHYSICAL REVIEW LETTERS week ending 17 NOVEMBER 2006

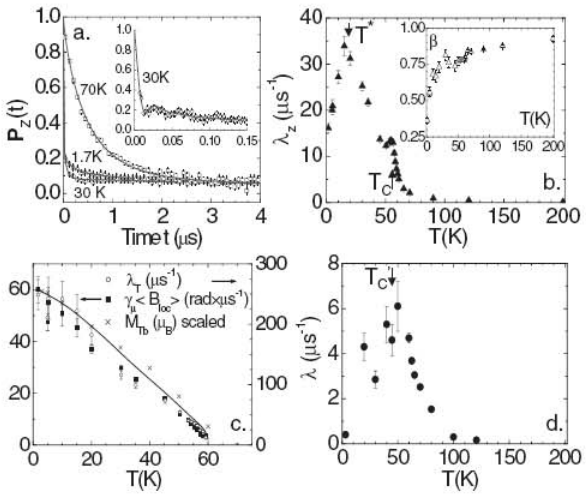

FIG. 4. μSR results for $x = 0.2$. (a) Muon depolarization function $P_Z(t)$ at ambient pressure for several temperatures, taking into account the background term. (b) Temperature dependence of λ_Z and β at ambient pressure; (c) $\langle B_{\rm loc}\rangle$, λ_T, and $M_{\rm Tb}$ (scaled) at ambient pressure; (d) λ at $P = 1.3$ GPa.

neutron diffraction. It suggests that the local field seen by the muon comes mostly from the Tb^{3+} ions with much larger moments, although more localized, than the Mo^{4+} ones. Previous μSR data [7] also show that the static internal field is about 10 times larger in $Tb_2Mo_2O_7$ than in $Tb_2Mo_2O_7$ spin glass.

Under pressure and below T_C, it was difficult to extract any information from the μSR spectra at small times (the 2/3 term), due to the large background of the pressure cell and the fast depolarization of the 2/3 term. Therefore, below T_C we fitted the data only to the 1/3 term, with an exponential depolarization function, skipping the first 0.2 μs of the μSR spectra. The T_C value decreases under pressure, in agreement with the neutron data, and the anomaly at $T^\star$ is strongly suppressed. The results at 1.3 GPa suggest that T_C will tend to merge with $T^\star$ as pressure increases further, so that a single spin-glass transition will occur.

The anomaly at $T^\star$ is akin to that observed by μSR in $Sm_2Mo_2O_7$ [23]. It also recalls observations [24,25] in reentrant spin glasses (RSG's). In contrast, it does not seem to exist in $Gd_2Mo_2O_7$ with the isotropic Gd ion, where the ground state is a collinear ferromagnet [21]. This shows that, in $R_2Mo_2O_7$ compounds, the occurrence of the $T^\star$ anomaly does not require chemical disorder like in RSG's. It may be induced by the crystal field anisotropy of the R ion, either uniaxial (Tb and Nd) or planar (Sm), and the consecutive frustration of the ferromagnetic state.

We notice that the long range magnetic order does not break at $T^\star$ and that there is no anomaly in the ordered moments or canting angles. The static field seen by the muon shows no anomaly either. It suggests a dynamical effect, possibly connected with the freezing of the short range correlated moments. We could check it in the future by inelastic neutron scattering.

In conclusion, in $(Tb_{1-x}La_x)_2Mo_2O_7$ we showed that long range magnetic order can be induced by diluting the Tb lattice with a nonmagnetic La ion and then be destroyed under pressure. We could study the microscopic changes of magnetism when crossing the F-SG threshold, for both statics and dynamics.

We thank A. Amato and U. Zimmermann for μSR measurements on GPS and GPD (PSI), W. Crichton for x-ray measurements on ID27 (ESRF), F. Bourée and G. André for neutron measurements on 3T2 and G41 (LLB), and A. Forget and D. Colson for the sample preparation (SPEC).

[1] S. T. Bramwell and M. J. P. Gingras, Science **294**, 1495 (2001).
[2] J. E. Greedan, J. Mater. Chem. **11**, 37 (2001).
[3] T. Katsufuji *et al.*, Phys. Rev. Lett. **84**, 1998 (2000).
[4] Y. Moritomo *et al.*, Phys. Rev. B **63**, 144425 (2001).
[5] J. S. Kang *et al.*, Phys. Rev. B **65**, 224422 (2002).
[6] I. V. Solovyev, Phys. Rev. B **67**, 174406 (2003).
[7] S. R. Dunsiger *et al.*, Phys. Rev. B **54**, 9019 (1996).
[8] J. E. Greedan *et al.*, Phys. Rev. B **43**, 5682 (1991).
[9] B. D. Gaulin *et al.*, Phys. Rev. Lett. **69**, 3244 (1992).
[10] J. S. Gardner *et al.*, Phys. Rev. Lett. **83**, 211 (1999).
[11] Y. Yasui *et al.*, J. Phys. Soc. Jpn. **70**, 284 (2001).
[12] Y. Taguchi *et al.*, Science **291**, 2573 (2001).
[13] H. C. Kim *et al.*, Acta Phys. Pol. B **34**, 1429 (2003); Physica (Amsterdam) **359B**, 1246 (2005).
[14] J.-G. Park *et al.*, Physica (Amsterdam) **328B**, 90 (2003).
[15] J. Rodríguez-Carvajal, Physica (Amsterdam) **192B**, 55 (1993).
[16] I. Goncharenko, High Press. Res. **24**, 193 (2004).
[17] J. Rodríguez-Carvajal, BASIREPS, ftp://ftp.cea.fr/pub/llb/divers/BasIreps.
[18] Y. A. Izyumov *et al.*, *Neutron Diffraction on Magnetic Materials* (Consultants Bureau, New York, 1991).
[19] M. Sato and J. E. Greedan, J. Solid State Chem. **67**, 248 (1987).
[20] I. Mirebeau *et al.*, Phys. Rev. Lett. **94**, 246402 (2005).
[21] I. Mirebeau *et al.*, cond-mat/0606420.
[22] P. Dalmas de Réotier, P. C. M. Gubbens, and A. Yaouanc, J. Phys. Condens. Matter **16**, S4687 (2004).
[23] Y. Jo *et al.*, J. Korean Phys. Soc. **47**, 123 (2005).
[24] I. Mirebeau *et al.*, Hyperfine Interact. **104**, 343 (1997).
[25] D. H. Ryan *et al.*, Phys. Rev. B **61**, 6816 (2000).

IOP Publishing Journal of Physics: Condensed Matter

J. Phys.: Condens. Matter **19** (2007) 145214 (9pp) doi:10.1088/0953-8984/19/14/145214

Study of ferromagnetic–spin glass threshold in $R_2Mo_2O_7$ by high-pressure neutron diffraction and μSR

A Apetrei[1], I Mirebeau[1], I Goncharenko[1], D Andreica[2,3] and P Bonville[4]

[1] Laboratoire Léon Brillouin, CEA-CNRS, CE-Saclay, 91191 Gif-sur-Yvette, France
[2] Laboratory for Muon-Spin Spectroscopy, Paul Scherrer Institut, 5232 Villigen-PSI, Switzerland
[3] Babes-Bolyai University, Faculty of Physics, 400084 Cluj-Napoca, Romania
[4] Service de Physique de l'Etat Condensé, CEA-CNRS, CE-Saclay, 91191 Gif-Sur-Yvette, France

E-mail: mirebea@llb.saclay.cea.fr

Received 12 December 2006
Published 23 March 2007
Online at stacks.iop.org/JPhysCM/19/145214

Abstract

We present a comparative study of $(Tb_{0.8}La_{0.2})_2Mo_2O_7$ and $Gd_2Mo_2O_7$ situated at the verge of a Mott transition from ferromagnetic metal to insulating spin glass, which can be tuned by the rare-earth ionic radius. We probe the spin correlations and fluctuations versus temperature and pressure thanks to neutron scattering and μSR. The ambient pressure state of ferromagnetic character shows striking differences between the two compounds, both in the static and dynamic properties, showing the influence of the Tb crystal field anisotropy. Under pressure, both compounds transform into a spin glass state. We also studied the chemically ordered spin glass $Tb_2Mo_2O_7$ with pressure and temperature. We observe mesoscopic ferromagnetic correlations between Tb moments, together with short-range correlations. All persist down to very low temperature (40 mK), showing that the spin glass order corresponds to the magnetic ground state. Under pressure, the lengthscale of the mesoscopic correlations is strongly reduced, whereas the short-range correlations are unchanged.

1. Introduction

$R_2T_2O_7$ pyrochlores, where R^{3+} is a rare-earth ion and T^{4+} is a transition-metal ion, form a large family of oxides with many unusual magnetic and conduction properties. The geometrical frustration of the pyrochlore lattice, which can exist in both R and T sublattices, yields the possibility of exotic magnetic states, such as spin liquids, spin ices, spin glasses with chemical order, as well as complex ordered magnetic structures. On the other hand, the strong intra-site Coulomb interaction between the electrons of the transition metal offers the possibility of inducing many anomalous conduction properties. Generally speaking, the trends are as follows. 3d transition-metal pyrochlores (like $R_2Ti_2O_7$) are insulating due to the strong

electron correlations and small electron transfer along O–T–O bonds. 4d transition-metal pyrochlores show an intermediate behaviour. They may be insulating ($R_2Sn_2O_7$), metallic ($R_2Mn_2O_7$ or $R_2Bi_2O_7$), or display an insulating–metal transition ($R_2Mo_2O_7$). 5d transition-metal pyrochlores are generally metallic, since the 5d orbitals are more extended than the 3d or the 4d orbitals, and hybridize more strongly with the oxygen p states. For some 5d ions, the influence of electrons correlations remains important, for example in $Cd_2Os_2O_7$ and $Cd_2Re_2O_7$, which behave as semi-metals with a Fermi level lying in a pseudogap [1] and show spectacular resistivity anomalies.

Within the pyrochlores, the 4d transition-metal $R_2Mo_2O_7$ are especially suitable for studying the interplay between magnetic and conduction properties. The Mo^{4+} 4d t_{2g} orbitals, situated nearby the Fermi level and well separated from the other bands [2, 3], play a dominant role in the band structure and the magnetic properties. As a direct probe of the influence of the Mo molecular field, the magnetic transition temperatures in $R_2Mo_2O_7$ are in the range 25–100 K, well above the transition temperatures of $R_2Sn_2O_7$ with non-magnetic Sn, which are around 1–2 K. Interestingly, the Mo magnetism can be tuned by the R ionic radius [4, 5]. Compounds with small ionic radius (R = Y, Tb) behave as insulating spin glasses with chemical order [6–8]. Compounds with large ionic radius (Sm, Nd) behave as ferromagnetic metals. $Nd_2Mo_2O_7$ was intensively studied, due to its giant abnormal Hall effect [9]. Although the exact mechanism is still debated [3, 10], the Nd crystal field anisotropy leading to spin ice frustration seems to play a key role. The chirality mechanism invoked recalls that proposed for metallic spin glasses [11–13].

Band structure calculations [3] and detailed investigations of many substituted $(RR')_2Mo_2O_7$ compounds show that the ferromagnetic–spin glass transition observed versus ionic radius in $R_2Mo_2O_7$ comes from a change in the sign of the Mo–Mo interactions. Ferromagnetic interactions in the metallic side become antiferromagnetic and thus geometrically frustrated on the insulating side of the phase diagram. The origin of this effect is the aperture of a Mott–Hubbard gap in the t_{2g} band due to intra-site electron correlations. The trigonal distortion of the Mo oxygen environment splits the t_{2g} band into a_{1g} and e'_g sub-bands. As the lattice constant decreases, the increasing Coulomb energy localizes the itinerant e'_g electrons, ferromagnetically coupled by a double exchange mechanism. Their contribution to the magnetic exchange interaction decreases at the expense of the a_{1g} ones, which interact antiferromagnetically by a superexchange mechanism mediated by oxygen 2p orbitals. The band structure calculation therefore closely correlates the dominant antiferromagnet (AF) interaction to the insulating character. Coming back to the real systems, some questions arise. Do the ferro-spin glass and insulating–metal transitions always coincide? What is the role of the rare-earth magnetism? How is an external pressure compared with the chemical pressure induced by the rare-earth ion? One should also understand how the ferromagnetic order transforms into the spin glass order. What is the evolution of the spin correlations and fluctuations? Do the spin glass (SG) and ferromagnet (F) orders coexist in some region of the phase diagram?

To find the answers to these questions, we studied two compounds in the ferromagnetic region close to the F–SG threshold. We used neutron diffraction, μSR and x-ray synchrotron radiation, at ambient and under applied pressure. In $(Tb_{0.8}La_{0.2})_2Mo_2O_7$, we have induced ferromagnetism by expanding the lattice through Tb/La substitution [14]. $Gd_2Mo_2O_7$ has been widely studied using various techniques [15–18], but never by neutrons due to its huge absorption, nor by muons. Our detailed results on $Gd_2Mo_2O_7$ are reported in [19]. In contrast with Tb, the Gd ionic moment has no orbital component. Here we present a comparative study of the two compounds, as well as new results on $Tb_2Mo_2O_7$ spin glass, studied by neutrons down to 40 mK and under applied pressure.

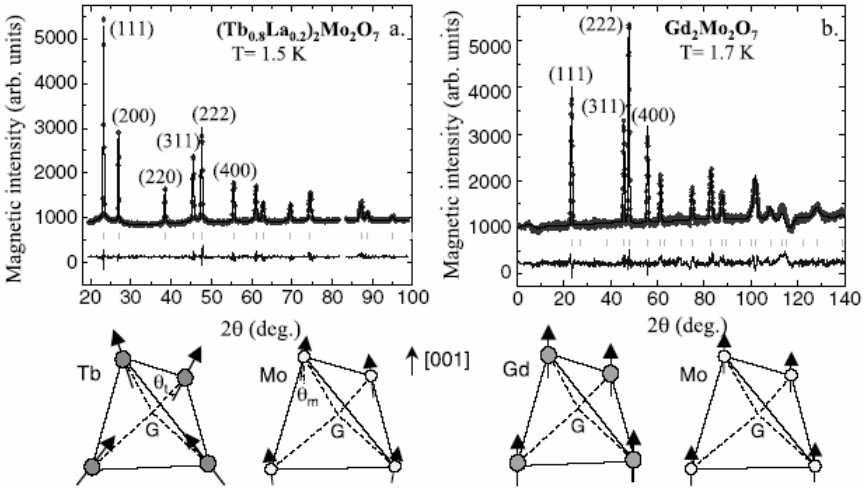

Figure 1. Magnetic neutron intensity versus the scattering angle 2θ: (a) TbLa sample at $T = 1.5$ K, ambient pressure and neutron incident wavelength $\lambda = 2.426$ Å. (b) Gd sample at $T = 1.7$ K, ambient pressure and $\lambda = 2.419$ Å. A pattern in the paramagnetic range (70 and 90 K for TbLa and Gd samples, respectively) was subtracted. Solid lines show the best refinement and the difference spectrum. At the bottom are the corresponding spin arrangements of Tb, Gd and Mo tetrahedra.

2. Experimental details

Ambient pressure powder neutron diffraction measurements on $(Tb_{1-x}La_x)_2Mo_2O_7$ ($x = 0$ and 0.2) were performed on G61 and G41 diffractometers of the Laboratoire Léon Brillouin (LLB) down to 1.4 K and down to 40 mK on the D1B diffractometer of the Institute Laüe Langevin (ILL). As for $Gd_2Mo_2O_7$, we used isotopically enriched ^{160}Gd and the high-flux diffractometers D20 and D2B of the ILL. High-pressure neutron diffraction patterns were recorded on the G61 (LLB) in the high-pressure version [20]. μSR measurements were performed at the Swiss Muon Source at the Paul Scherrer Institute (PSI) on GPS (ambient pressure) and GPD (under pressure). The equation of state was determined by x-ray diffraction under pressure using the synchrotron radiation at the ID27 beam line of the European Synchrotron Radiation Facility (ESRF).

3. Comparison of two compounds: $(Tb_{0.8}La_{0.2})_2Mo_2O_7$ and $Gd_2Mo_2O_7$

Both compounds are situated in the ferromagnetic region of the phase diagram ($a > a_c$) with lattice constants of $a = 10.3787(8)$ Å and 10.3481(2) Å for TbLa and Gd samples, respectively. From [4], we get $a_c \sim 10.33$ Å. The Curie temperatures T_C, deduced from susceptibility data, are 58 K (TbLa sample) and 70 K (Gd sample).

To compare their magnetic ground states, we consider the magnetic diffraction patterns well below T_C (figure 1), at 1.5 and 1.7 K respectively. The magnetic Bragg peaks belong to the face-centred cubic lattice, showing that in both cases the magnetic structure is derived from the chemical structure of the $Fd\bar{3}m$ symmetry by a propagation vector $\mathbf{k} = 0$. Therefore one R/Mo tetrahedron describes the magnetic structure. As a striking feature, for the TbLa sample we observe two magnetic peaks (200) and (220), which cannot be observed for the Gd sample. These peaks are forbidden by the chemical structure of the pyrochlore lattice. Their observation in the TbLa sample means that the spin arrangement is non-collinear.

By refining the magnetic structures, we see that for the TbLa sample the Tb moments are close to the local ⟨111⟩ anisotropy axis (with an angle $\theta_t \sim 11.5°$). They are oriented in the 'two in, two out' configuration of the local spin ice structure [21], which yields F components along [001]. The Mo moments align close to a [001] axis, with a slight tilting angle $\theta_m \sim 7°$. In the Gd sample, the magnetic structure corresponds to a collinear ferromagnet. For both compounds, the R and Mo moments are ferromagnetically coupled, in contrast with $Nd_2Mo_2O_7$. All ordered moments are strongly reduced (by about 50% for the Tb, 30% for the Gd ions, and up to 70% for Mo) with respect to the free ion values (9 μ_B for Tb, 7 μ_B for Gd and 2 μ_B for Mo). For Tb this reduction is partly explained by a change of Tb environment when diluted with non-magnetic La ions, but it should also come from crystal field effects. For Gd and Mo, it may arise either from quantum fluctuations due to the proximity of the threshold, or from the frustration of the orbital component of the Mo moment [3].

In both cases the ground state is determined by the Mo–Mo F exchange interaction. The difference in spin arrangements emphasizes the role of the strong uniaxial anisotropy of the Tb^{3+} ion compared to the Gd^{3+} ion, which is isotropic. The anisotropy of Tb^{3+} brings spin ice frustration into the ferromagnetic state.

With increasing temperature, the ordered spin ice structure found for the TbLa sample at low temperature is kept up to the Curie point, with a decrease in the canting angles. On the contrary, in the Gd sample, the ferromagnetic model does not fully account for the T dependence of the Bragg peaks, but no better magnetic structure could be found.

Looking at the magnetic fluctuations using μSR, we observed important new differences between the two compounds. The fit of the μSR depolarization function $P_Z(t)$ measured below T_C involves four parameters [14, 19]. The first two, which govern the long-time relaxation, are the longitudinal relaxation rate λ_Z and its exponent β. They reflect the spin dynamics. The others, which account for the strong depolarization at early times and the wiggles respectively, are the transverse relaxation rate, λ_T, and the average local field, $\langle B_{loc} \rangle$, at the muon site. Considering that $\lambda_T \gg \lambda_Z$, we associate λ_T with the distribution of *static* local fields.

As shown in figure 2 (right), the temperature dependence of the 'static' terms is similar in the two compounds and shows no anomaly with temperature. $\langle B_{loc} \rangle$ and λ_T scale with each other and with the R ordered moment (Tb or Gd) determined by neutron diffraction. It shows that the local magnetic field on the muon site is dominated by the R moment, much more than that of Mo.

Striking differences appear in the dynamic terms (figure 2, left). The T dependence of λ_Z shows a critical peak at T_C due to the onset of magnetic order. In a standard ferromagnet, the contribution of spin waves should yield a decrease of λ_Z below T_C, down to zero at $T = 0$. Here two types of abnormal behaviours are observed. In TbLa sample, λ_Z shows a broad maximum at $T^\star \sim 25$ K. It suggests a second transition of dynamical nature since there is no anomaly in the static terms. In Gd sample, the broad maximum is either strongly reduced or completely suppressed. λ_Z remains almost constant within the accuracy of the measurements, and close to its value above T_C down to 6 K. Finally, in TbLa sample, the β exponent (not shown) is strongly temperature dependent whereas it remains constant and equal to 1 in Gd sample.

Under pressure, the ferromagnetic order in both compounds is gradually destroyed [14, 17, 19]. We can follow this evolution both by μSR and by neutrons. T_C decreases under pressure and the two transitions observed for TbLa sample seem to merge. The Bragg peak intensity decreases under pressure and short range correlations arise. Figure 3 shows the spin correlations in TbLa at 3.7 GPa ($a \sim 10.298$ Å) and Gd sample at 2.7 GPa ($a \sim 10.289$ Å). The short range order modulations are akin to that in $Tb_2Mo_2O_7$ at ambient pressure (see below).

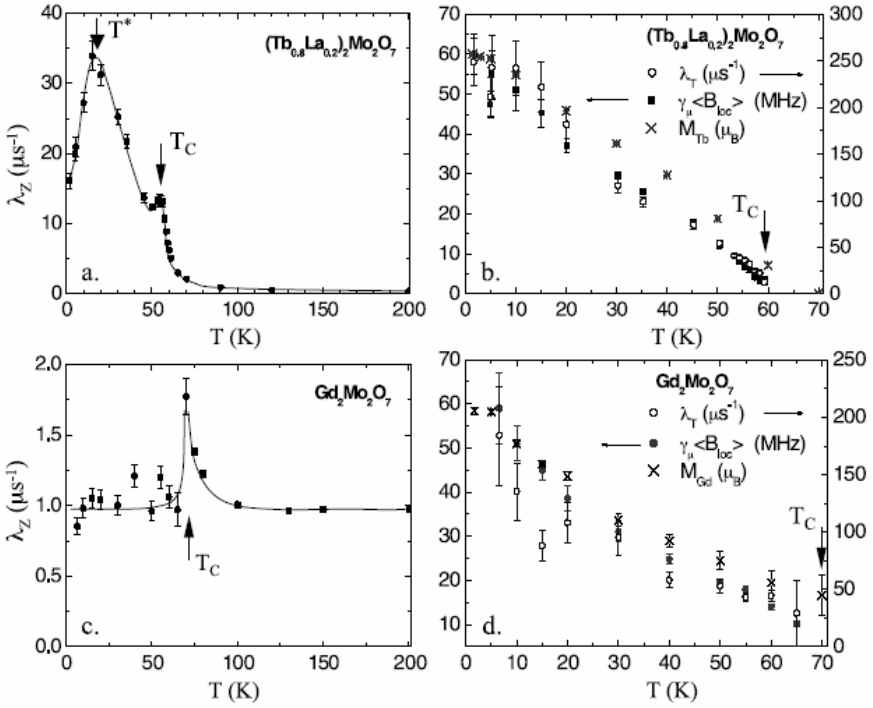

Figure 2. μSR ambient pressure results: TbLa sample, temperature dependence of (a) λ_Z; (b) λ_T, $\langle B_{loc}\rangle$ (with γ_μ being the muon gyromagnetic ratio) and ordered magnetic moment M_{Tb} (scaled); Gd sample, temperature dependence of (c) λ_Z; (d) λ_T, $\langle B_{loc}\rangle$, M_{Gd} (scaled). Lines are guides to the eye.

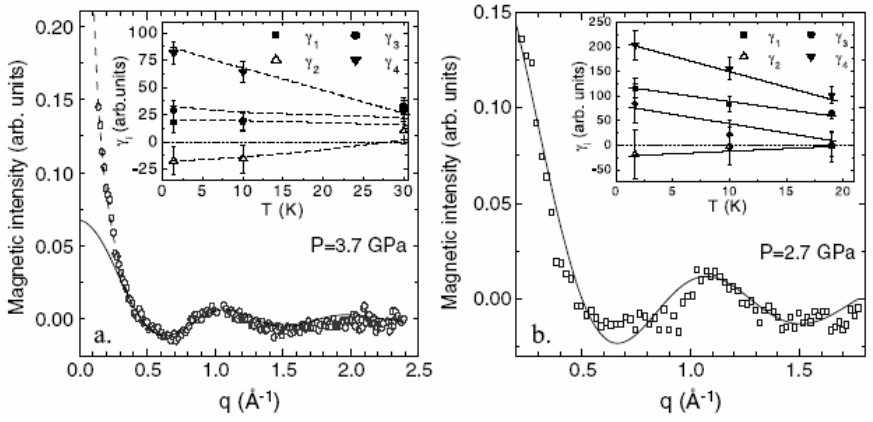

Figure 3. Magnetic intensity versus the scattering vector $q = 4\pi \sin\theta/\lambda$, with $\lambda = 4.741$ Å. A pattern in the paramagnetic region (100 K) was subtracted. (a) TbLa sample, at $T = 1.4$ K and $P = 3.7$ GPa. (b) Gd sample, at $T = 1.5$ K and $P = 2.7$ GPa. Lines are fits as described in the text. In the inset are the temperature dependence of the correlations coefficients. Dashed lines are guides to the eye.

The magnetic correlations were analysed with the short-range order (SRO) model described in [6]. This allows the determination of spin correlation parameters γ up to the fourth coordination cell, as seen in the two insets. For both samples, $\gamma_{1,3,4} > 0$ and $\gamma_2 < 0$. Considering the relative amplitude of the magnetic moments, it means that the R–R correlations

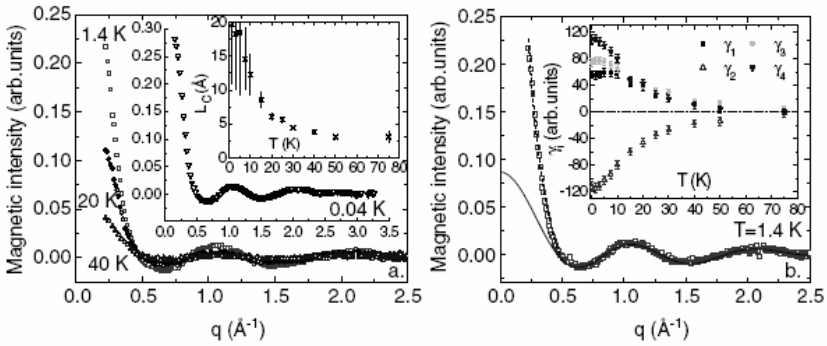

Figure 4. (a) Magnetic intensity in $Tb_2Mo_2O_7$: $T = 1.4, 20, 40$ K ($\lambda = 4.741$ Å) and $T = 0.04$ K ($\lambda = 2.52$ Å) in the first inset. A pattern at 100 K was subtracted. Second inset: temperature dependence of correlation length L_C. (b) Fit of 1.4 K spectrum with the SRO model (bottom line) including the longer-range F correlations (upper dashed line) with the corresponding correlation parameters in the inset.

(which control the $\gamma_{1,3,4}$ terms) are F, while the R–Mo correlations (γ_2) become AF under pressure.

The R–R ferromagnetic correlations are shown by intense scattering at low angles ($q < 0.5$ Å^{-1}). In the Gd sample at 2.7 GPa, they can be fitted by the SRO model (figure 3(b)), showing that they extend to four neighbours only (∼7 Å). In the TbLa sample at 3.7 GPa, the SRO model cannot account for them (figure 3(a)), since they extend to a longer length scale (about 18 Å).

4. $Tb_2Mo_2O_7$

We first analyse the ambient pressure magnetic correlations in $Tb_2Mo_2O_7$ ($a \sim 10.31$ Å), which is a well-known spin glass without chemical disorder and with a spin glass transition at $T_F \sim 25$ K. Besides the diffuse magnetic scattering observed for $q > 0.5$ Å^{-1}, denoting SRO as reported in [6, 7], we also observe intense small-angle neutron scattering (SANS) below this q value. This corresponds to the onset of F correlations with a mesoscopic length scale. The temperature evolution of magnetic correlations (figure 4(a)) clearly shows the increase in F correlations with decreasing temperature. By performing neutron diffraction measurements down to 40 mK, we show that the magnetic correlations saturate below 1.4 K. Their observation down to 40 mK (0.002 T_F) proves that the spin glass state is indeed the ground state of this compound.

Figure 4(b) shows the fits of $Tb_2Mo_2O_7$ magnetic spectra at 1.4 K. For $q > 0.5$ Å^{-1} we used the same model as in [6] (see figure 4(b) bottom line). The correlation parameters are plotted in the inset. As for the TbLa and Gd samples under pressure, we get $\gamma_{1,3,4} > 0$ and $\gamma_2 < 0$, which show F R–R and AF R–Mo correlations. As for TbLa, the SRO model cannot describe the SANS signal, which was fitted by adding a Lorentzian function (upper dashed line). The correlation length of the Lorentzian ($L_C \sim 20$ Å at 1.4 K) decreases with increasing temperature (second inset figure 4(a)).

Figure 5, which compares magnetic spectra at $P = 0$ and 5.3 GPa ($a \sim 10.201$ Å), clearly shows that the SANS signal and hence the corresponding F R–R mesoscopic correlations decrease with increasing pressure. The correlation length decreases under pressure and the SRO model now yields a good fit in the whole q interval, as for the Gd sample under pressure.

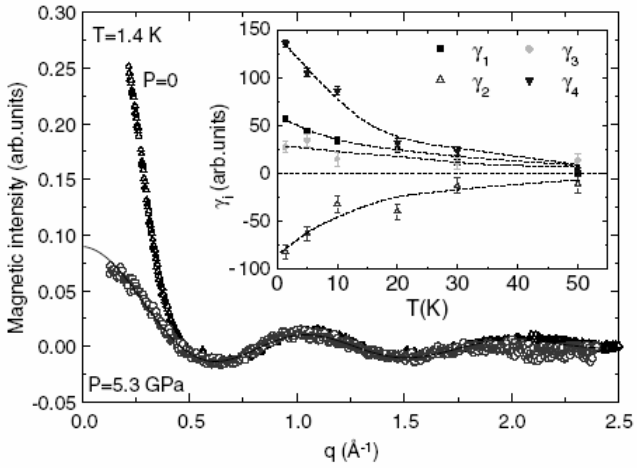

Figure 5. Magnetic intensity in $Tb_2Mo_2O_7$ at 1.4 K, $\lambda = 4.741$ Å: ambient (△) and applied pressure (○). A pattern at 100 K was subtracted. The fit of the $P = 5.3$ GPa data is made using the SRO model. The temperature dependence of correlation coefficients is shown in the inset, with dashed lines as guides to the eye.

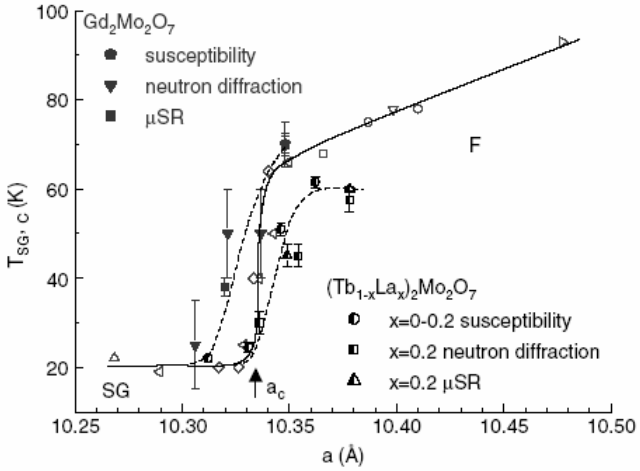

Figure 6. Phase diagram in the threshold region: general curve from [4, 5, 8] (open symbols), $(Tb_{1-x}La_x)_2Mo_2O_7$ (half filled symbols) and GdMo (filled symbols). Lines are guides to the eye.

The modulations above 0.5 $Å^{-1}$ are almost unchanged by pressure. The correlation parameters keep the same sign as at ambient pressure (inset of figure 5), yielding F R–R and AF R–Mo correlations, respectively. Their values at ambient and under pressure are similar in the limit of the error bars.

5. Discussion

5.1. The threshold region

An experimental phase diagram of the $R_2Mo_2O_7$ transition temperature against the cell parameter is shown in figure 6. At ambient pressure, our starting points for the Gd and TbLa samples slightly deviate from the general curve drawn according to [4, 5]. This could be due

to sample preparation. The Gd sample is very sensitive to it, with a T_C variation between 40 and 70 K reported in the literature. As for the TbLa sample, it may be due to La dilution close to the solubility limit. Besides these initial offsets, our results show the same behaviour under applied pressure as the general curve obtained under chemical pressure. They show how the LRO transforms in SRO passing through a region where the two signals coexist, providing a microscopic description of the F–SG threshold region (for details, see [14, 19]).

5.2. Dynamical transition in the ferromagnetic regime

In the TbLa sample, where the uniaxial Tb anisotropy yields a non-collinear ground state, we have observed a second transition using μSR, akin to that previously observed in re-entrant spin glasses [22, 23]. Recent μSR measurements [24] show that it also exists in $Sm_2Mo_2O_7$, where the magnetic structure is unknown but the Sm anisotropy is supposed to be planar. The temperature variation of the β exponent in the TbLa sample and in $Sm_2Mo_2O_7$ suggests a large distribution of relaxation rates, as in spin glasses [25]. In contrast, in $Gd_2Mo_2O_7$, where the Gd moment is isotropic and the ground state is collinear, there seems to be no second transition (or at least it is strongly suppressed) and we get $\beta = 1$. It is therefore tempting to connect the second transition with magnetic frustration on the R site induced by R anisotropy. In re-entrant spin glasses, the second transition was attributed to the freezing of transverse spin components with a mesoscopic length scale, which agrees with mean field theory [26]. In the TbLa sample, we have observed, below the Bragg peaks of the spin ice ordered structure, a magnetic background coming from short-range ordered moments, having the same type of correlations as the LRO. These moments start to correlate at around 40 K, namely between T_C and $T^\star$. It could be assumed that they remain paramagnetic at T_C, and start to correlate and freeze when T decreases further. An energy analysis of the SRO by inelastic neutron scattering should allow us to check the occurrence of this freezing on the neutron time scale. The neutron time scale ($\tau \sim 10^{-11}$ s) is much shorter than the muon time scale, so the freezing transition should occur above the $T^\star$ value probed by muons.

5.3. Spin glass state under pressure

As has already been stated, the F–SG transition is controlled by the Mo–Mo interactions. At ambient pressure, the magnetic interactions are ferromagnetic in both the TbLa and Gd samples. Their magnetic structures show that all correlations (Mo–Mo, R–Mo and R–R) are ferromagnetic. Under pressure the distances Mo–Mo are reduced and hence the balance between the double exchange F and superexchange AF interactions is changed: the AF Mo–Mo interactions are favoured. In both systems the ferromagnetic phase transforms into a spin glass state characterized by short-range correlations similar to that observed for $Tb_2Mo_2O_7$. Our observations provide a microscopic description of the pressure-induced spin glass state recently inferred from magnetic measurements [17, 27]. Besides the change in the Mo–Mo interactions which induce the spin glass frustration, the SRO model shows that, under pressure, the R–Mo correlations change to AF. The R–R correlations remain F, but they are strongly reduced under pressure, as shown by our study of $Tb_2Mo_2O_7$. What is the origin of the R–Mo and R–R correlations and why do they change with pressure? Our present study of the three compounds shows that these correlations do not arise from the rare-earth anisotropy and persist under La doping. Previous simulations of the diffuse scattering in $Tb_2Mo_2O_7$ [6, 28] show that correlations are not very sensitive to Mo–Mo interaction due to the small Mo moment. The R–Mo and R–R correlations could arise from R–Mo interaction, which involves the Mo t_{2g} band together with the 4f levels of the R ion. This interaction may be sensitive to pressure, though less than the Mo–Mo interaction.

In conclusion, neutron diffraction and μSR combined with high-pressure techniques are a useful tool to study the ferro-spin glass threshold in $R_2Mo_2O_7$ pyrochlores. The changes in the spin correlations can be studied in detail when encompassing the threshold, as well as the anomalous fluctuations at the verge of the Mott transition.

Acknowledgments

We thank O Isnard, E Suard and G André for their help in the neutron measurements on D1B, D20 and G41, respectively. We also thank A Amato and U Zimmermann for the μSR measurements on GPS and GPD and W Crichton for the x-ray measurements on ID27. We thank A Forget and D Colson for the sample preparation and J P Sanchez for providing the ^{160}Gd isotope and for useful discussions.

References

[1] Singh D H, Blaha P, Schwartz K and Sofo J O 2002 *Phys. Rev.* B **65** 155109
[2] Kang J S *et al* 2002 *Phys. Rev.* B **65** 224422
[3] Solovyev I V 2003 *Phys. Rev.* B **67** 174406
[4] Katsufuji T, Hwang H Y and Cheong S-W 2000 *Phys. Rev. Lett.* **84** 1998
[5] Moritomo Y *et al* 2001 *Phys. Rev.* B **63** 144425
[6] Greedan J E *et al* 1991 *Phys. Rev.* B **43** 5682
[7] Gaulin B D *et al* 1992 *Phys. Rev. Lett.* **69** 3244
[8] Gingras M J P *et al* 1997 *Phys. Rev. Lett.* **78** 947
[9] Taguchi Y *et al* 2001 *Science* **291** 2573
[10] Yasui Y *et al* 2006 *Preprint* cond-mat/0603045
[11] Kawamura H 2003 *Phys. Rev. Lett.* **90** 47202
[12] Pureur P *et al* 2004 *Europhys. Lett.* **67** 123
[13] Taniguchi T *et al* 2004 *Phys. Rev. Lett.* **93** 246605
[14] Apetrei A, Mirebeau I, Goncharenko I, Andreica D and Bonville P 2006 *Phys. Rev. Lett.* **97** 206401
[15] Hodges J A *et al* 2003 *Eur. Phys. J.* **33** 173
[16] Kézsmárki I *et al* 2004 *Phys. Rev. Lett.* **93** 266401
[17] Park J G *et al* 2003 *Physica* B **328** 90
[18] Hanasaki N *et al* 2006 *Phys. Rev. Lett.* **96** 116403
[19] Mirebeau I *et al* 2006 *Phys. Rev.* B **74** 174414
(Mirebeau I *et al* 2006 *Preprint* cond-mat/0606420)
[20] Goncharenko I 2004 *High Pressure Res.* **24** 193
[21] Bramwell S T and Gingras M J P 2001 *Science* **294** 1495
[22] Mirebeau I *et al* 1997 *Hyper. Interface* **104** 343
[23] Ryan D H *et al* 2000 *Phys. Rev.* B **61** 6816
Ryan D H *et al* 2004 *J. Phys.: Condens. Matter* **16** S4619
[24] Jo Y *et al* 2005 *J. Korean Phys. Soc.* **47** 123
[25] Campbell I A *et al* 1994 *Phys. Rev. Lett.* **72** 1291
[26] Gabay M and Toulouse G 1981 *Phys. Rev. Lett.* **47** 201
[27] Miyoshi K, Takamatsu Y and Takeuchi J 2006 *J. Phys. Soc. Japan* **75** 065001
[28] Reimers J N 1992 *Phys. Rev.* B **46** 193

PHYSICAL REVIEW B 74, 174414 (2006)

Pressure-induced ferromagnet to spin-glass transition in $Gd_2Mo_2O_7$

I. Mirebeau,[1] A. Apetrei,[1] I. Goncharenko,[1] D. Andreica,[2,3] P. Bonville,[4] J. P. Sanchez,[5] A. Amato,[2] E. Suard,[6] W. A. Crichton,[7] A. Forget,[4] and D. Colson[4]

[1]*Laboratoire Léon Brillouin, CEA-CNRS, CE-Saclay, 91191 Gif-sur-Yvette, France*
[2]*Laboratory for Muon Spin Spectroscopy, Paul Scherrer Institute, 5232 Villigen-PSI, Switzerland*
[3]*Faculty of Physics, Babes-Bolyai University, 400084 Cluj-Napoca, Romania*
[4]*Service de Physique de l'Etat Condensé, CEA-CNRS, CE-Saclay, 91191 Gif-Sur-Yvette, France*
[5]*Service de Physique Statistique, Magnétisme et Supraconductivité, CEA-Grenoble, 38054 Grenoble, France*
[6]*Institut Laüe Langevin, 6 rue Jules Horowitz, Boîte Postale 156X, 38042 Grenoble, France*
[7]*European Synchrotron Radiation Facility, Boîte Postale 220, 38043 Grenoble, France*

(Received 24 May 2006; published 13 November 2006)

$R_2Mo_2O_7$ compounds show a ferromagnetic metal-insulator spin-glass transition tuned by the radius of the rare earth ion R^{3+}. We have studied $Gd_2Mo_2O_7$ located on the verge of the transition, by neutron diffraction on a ^{160}Gd isotopic sample, μSR and x-ray diffraction using the synchrotron radiation. All measurements were done both at ambient and under applied pressure. At ambient pressure, a ferromagnetic state is observed below the Curie temperature (T_C=70 K). The ordered magnetic moments at 1.7 K are parallel and equal to 5.7(5) μ_B and 0.8(2) μ_B for Gd and Mo, respectively. The relaxation rate measured by μSR evidences strong spin fluctuations below T_C and down to the lowest temperature (6.6 K). A spin reorientation occurs in the range $20\ K < T < T_C$. The ferromagnetic state is strongly unstable under pressure. T_C sharply decreases (down to 38 K at 1.3 GPa) and Bragg peaks start to coexist with mesoscopic ferromagnetic correlations. The ordered moments decrease under pressure. At 2.7 GPa long range magnetic order completely breaks down. In this spin-glass state, Gd-Gd spin correlations remain ferromagnetic with a correlation length limited to the fourth neighbor, and Gd-Mo spin correlations turn to antiferromagnetic. The unique combination of three microscopic probes under pressure provides a detailed description of the magnetic transition, crucial for further theories.

DOI: 10.1103/PhysRevB.74.174414 PACS number(s): 71.30.+h, 71.27.+a, 75.25.+z

I. INTRODUCTION

Pyrochlores compounds $R_2T_2O_7$, where R^{3+} and T^{4+} are rare earth and transition or *sp* metal ions, respectively, show geometrical frustration of the first neighbor interactions. This occurs not only for antiferromagnetic interactions between first neighbor Heisenberg moments, but also for ferromagnetic interactions if the neighboring moments are constrained to lie along their local Ising anisotropy axes. This peculiarity of the pyrochlore lattice leads to exotic types of short range magnetic orders, such as spin liquids, spin ices or chemically ordered spin glasses, which are intensively studied.[1,2]

Among the pyrochlores, rare earth molybdenum pyrochlores $R_2Mo_2O_7$ have attracted special attention since the discovery of a crossover transition from an insulating spin-glass state to a metallic ferromagnetic state, which can be tuned by the rare earth ionic radius.[3,4] The variation of the transition temperature which shows a universal curve for all compounds with mixed rare earth ions, suggests that the dominant mechanism comes from a change in the sign of the Mo-Mo interactions. This change is connected with a change in the band structure, due to the specific energy of Mo t_{2g} orbitals, situated nearby the Fermi level and well separated from the other bands.[5,6] The insulating state observed at low rare earth ionic radius is attributed to the opening of a Mott-Hubbard gap at the Fermi level, due to strong electronic intrasite interactions.[6] With increasing rare earth ionic radius, Mo-Mo first neighbor interactions seem to evolve from antiferromagnetic, dominated by a superexchange mechanism and frustrated by the geometry, to ferromagnetic, due to a double exchange mechanism.

In the ferromagnetic region, the ferromagnetic alignment of the neighboring Mo moments favors the electronic kinetic energy and leads to a metallic conductivity, with a mechanism similar to that observed in the manganites. The rare earth crystal field anisotropy also plays a role, since it yields a possible source of frustration in the ferromagnetic region. This frustration seems to have important consequences on the conductivity properties. Namely, the $Nd_2Mo_2O_7$ compound shows a giant abnormal Hall effect at low temperature[7,8] which cannot be explained by the spin-orbit coupling. It is generally admitted that this effect is induced by the spin ice frustration of the 4*f* Nd^{3+} spins, transferred to itinerant Mo electrons through *f*-*d* interaction.

$Gd_2Mo_2O_7$ is especially interesting since the Gd ionic radius is situated just above the threshold for the metal insulator transition. This compound was thoroughly investigated by many techniques. Magnetic measurements[9,10] suggest a ferromagneticlike transition at T_C, with magnetic irreversibilities occurring below. The T_C values reported by various groups are in the range 40–70 K. Mössbauer measurements[10] show a hyperfine field below the transition and the hyperfine populations are found to be out of thermal equilibrium at 27 mK, indicating that Gd and Mo spin fluctuations are present in the magnetic phase and persist down to very low temperature. Heat capacity measurements[12] show two steplike anomalies, suggesting two magnetic transitions, one at T_C (70 K) and the other well below (11 K). The transport properties strongly depend on sample preparation. First measurements on powdered samples[11] show a metallic conductivity, with anomalies at T_C and in the 10–20 K temperature

range. However, more recent data on high purity single crystals[13] show an insulating ground state, which is very sensitive to impurity doping. In contrast with $Nd_2Mo_2O_7$, the Hall conductivity[8] shows the behavior of a conventional ferromagnet, as expected for Heisenberg-like Gd^{3+} moments ($4f^7$) without orbital angular momentum. An investigation by infrared (IR) spectroscopy[13] shows the presence of a very small Mott-Hubbard gap of 20 meV, about ten times smaller than in the neighboring insulating compounds (170 and 250 meV for Dy and Ho, respectively). The concomitant changes in the optical, magnetic, and transport properties suggest a quantum phase transition around $Gd_2Mo_2O_7$, opening the possibility to tune the transition by pressure and/or magnetic field. Magnetic measurements under pressure[14,15] and recent resistivity measurements[16] demonstrated this possibility at a macroscopic level.

Up to now, there was no characterization of the type of magnetic order and magnetic fluctuations in $Gd_2Mo_2O_7$. This is especially due to the huge absorption of natural Gd, which makes neutron scattering experiments extremely difficult. We present here an investigation of the magnetic order and magnetic fluctuations in $Gd_2Mo_2O_7$, by combining neutron diffraction on a ^{160}Gd isotopic sample with μSR experiments. We show that a ferromagnetic collinear order is indeed stabilized well below T_C, but that it coexists with low temperature fluctuations. At intermediate temperatures ($20\ K < T < T_C$) a reorientation of the magnetic moments occurs.

We also studied the sensitivity of the magnetic state in $Gd_2Mo_2O_7$ to applied pressure by neutron diffraction and μSR. The pressure induced changes of the crystal structure and lattice constant were checked by x-ray diffraction using the synchrotron radiation. We observe a pressure induced magnetic transition, which can be fully characterized using this unique combination of three microscopic probes. We show that the ferromagnetic state is highly unstable under pressure: a rather small pressure of 1.3 GPa yields a decrease of the Curie temperature by a factor of two. At 2.7 GPa, long range ferromagnetic order has fully disappeared. Our results demonstrate that the changes in magnetism induced by pressure are equivalent to those induced by chemical pressure (R substitution). They confirm at a microscopic level the conclusions inferred from the magnetization.[14] Therefore, keeping the same sample, a quantitative analysis of the neutron and muon data allows us to follow the evolution of the spin correlations and fluctuations throughout the transition.

The paper is organized as follows. In Sec. II, we describe the sample characterization, bulk magnetic properties, and crystal structure. In Sec. III, we describe the magnetic state at ambient pressure, studied by neutron diffraction and μSR as a function of temperature. In Sec. IV, we describe the evolution of the magnetic state under pressure from x-ray, neutron and μSR experiments. In Sec. V, we discuss the results in comparison with other experimental data and current theories.

II. CRYSTAL STRUCTURE AND BULK MAGNETIC PROPERTIES

Powdered $Gd_2Mo_2O_7$ samples were synthesized following the procedure given in Ref. 3. We used Gd_2O_3 and MoO_2 oxides as starting materials. The synthesis was made in an argon atmosphere without any excess of Mo, but with Ti/Zr chips to absorb oxygen traces. Samples were heated up to 1370 °C during 6 h. Two annealings at least were necessary to obtain the sample in pure form. A sample of 1 g with natural Gd was prepared for synchrotron and μSR experiments and a sample of 0.5 g with isotopically enriched ^{160}Gd was used for the neutron experiments. Both samples were characterized by x-ray diffraction, showing that they are single phase.

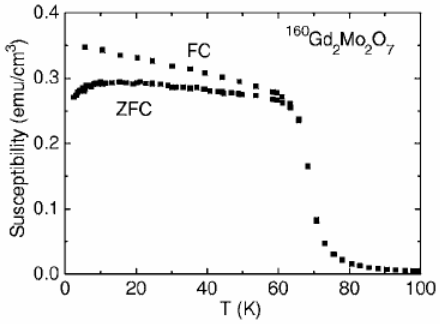

FIG. 1. Magnetic susceptibility measured in a static field of 50 G, in the zero field cooling (ZFC) and field cooling (FC) processes.

The dc magnetization of the two samples were recorded in a superconducting quantum interference device (SQUID) magnetometer with a static field of 50 G. Both show a rather broad Curie transition, as already reported in the literature. In the ^{160}Gd sample (Fig. 1), the transition occurs in a temperature range $\Delta(T) = \pm 7$ K, with a T_C value of 70 K defined as the inflexion point in the susceptibility curve. In the sample with natural Gd, we get $T_C = 72$ K and $\Delta(T) = \pm 5$ K. Below the transition we observe irreversibilities of the susceptibility depending on the cooling process, zero field cooling (ZFC) or field cooling (FC). In both samples they occur just below the Curie transition. The FC susceptibility linearly increases with decreasing temperature, whereas the ZFC susceptibility flattens and starts to drop below about 14 K. This drop suggests a blocking of domain walls mobility, possibly related to the spin reorientation discussed below.

The crystal structure of $Gd_2Mo_2O_7$ was investigated at 300 K by combining powder x-ray and neutron diffraction, the neutron pattern being measured in the high resolution-high flux diffractometer D2B of the Institute Laüe Langevin with an incident wavelength of 1.594 Å in the high intensity version. In order to decrease the residual absorption, the sample was placed in a hollow vanadium cylindrical container. In the refinement, we made a specific absorption correction, taking into account the container geometry,[17] the neutron wavelength, and the isotopic composition of the sample. The linear absorption coefficients were estimated to $\mu = 6.3$ and 4.1 cm^{-1} for D2B and D20, respectively.

The Rietveld refinement of the D2B diffraction pattern (Fig. 2) was made using the crystallographic programs of the Fullprof suite.[18] We took the diffraction pattern from the vanadium container into account as a second phase. The refinement ($R_B = 8.9\%$, $R_F = 5.9\%$) confirmed the structural model

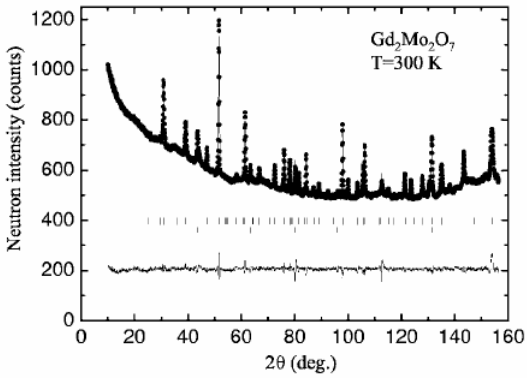

FIG. 2. Neutron diffraction pattern of $Gd_2Mo_2O_7$ measured at 300 K (paramagnetic phase) on the D2B powder diffractometer, with an incident neutron wavelength of 1.594 Å. Upper and lower tick marks show the Bragg peak positions of the sample and vanadium sample holder, respectively. Solid lines show the calculated pattern (R_B=8.9%) and the difference spectrum.

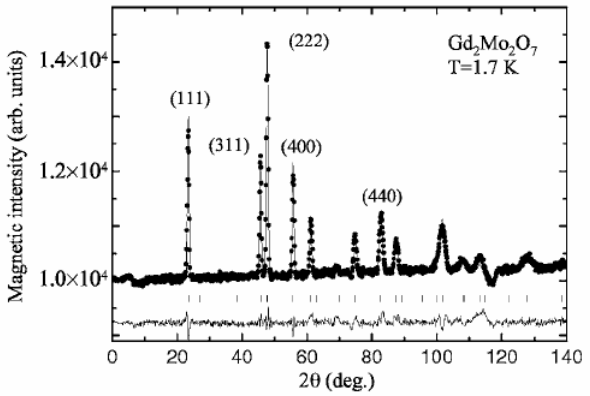

FIG. 3. Magnetic neutron diffraction pattern of $Gd_2Mo_2O_7$ measured at 1.7 K on the D20 powder diffractometer, with an incident neutron wavelength of 2.419 Å. A pattern measured at 90 K (above T_C) was subtracted. Tick marks show the Bragg peak positions. Solid lines show the pattern calculated with the collinear ferromagnetic model (R_B=11.3%) and the difference spectrum.

for a stoichiometric pyrochlore with space group $Fd\bar{3}m$, yielding a lattice constant a=10.3481(2) Å and an oxygen position parameter u=0.3342(2) at room temperature. These results agree with previous determinations from synchrotron radiation x-ray powder diffraction.[4]

III. MAGNETIC STATE AT AMBIENT PRESSURE

A. Magnetic neutron diffraction

Neutron diffraction patterns were recorded between 1.7 and 90 K on the high flux diffractometer D20 of the Institute Laüe Langevin with an incident wavelength 2.419 Å, with the same sample and sample holder as for D2B. Absorption corrections were made as above. Magnetic diffraction patterns were obtained by subtracting a spectrum at 90 K just above the transition. The magnetic pattern at 1.7 K is shown in Fig. 3. The magnetic peaks have *hkl* indices of the face centered cubic lattice. The (200) and (220) peaks, where there is no chemical contribution from Gd and Mo ions in the pyrochlore structure (due to extinction from the $Fd\bar{3}m$ space group and special Gd-Mo positions, respectively) are also absent in the magnetic pattern. We refined the magnetic patterns using the Fullprof suite.[18] At 1.7 K, we obtain a good refinement assuming a collinear ferromagnetic structure (magnetic factor R_B=11.3%, Fig. 3). The Mo and Gd moments orient along the same direction, with a ferromagnetic coupling. According to the ^{155}Gd Mössbauer measurements,[10] the angle between the Gd moment and the ⟨111⟩ axis is close to 54°. This strongly suggests that the Gd and Mo moments lie along a ⟨100⟩ axis.

With increasing temperature the intensities of the magnetic Bragg peaks start to decrease, but the (111) peak decreases much more rapidly than the high angle peaks (Fig. 4). It disappears around 50 K whereas the other peaks persist up to 70 K. Concomitantly, the magnetic intensities calculated within the collinear ferromagnetic model start to disagree with the experimental data (inset Fig. 4, R_B=39% at 40 K).

The refinements exclude a zero ordered moment on either the Gd or Mo sublattice. A global change of orientation of both Gd and Mo sublattices is also excluded since it would not change the magnetic diffraction pattern of a powdered cubic structure. The observed anomaly is therefore attributed to a decoupling of Gd^{3+} and Mo^{4+} moments above 20 K, yielding noncollinear moments in the Gd (and possibly Mo) sublattice. Unfortunately, a precise determination of this noncollinearity is hampered by the high symmetry of the crystal structure, the presence of eight independent moments in the unit cell, and the dominant ferromagnetic character.

To search for noncollinear structures, we first performed a symmetry analysis[19,20] using the program BasIreps,[21] searching for all $\mathbf{k}$=0 structures corresponding to irreducible representation of the $I4_1/amd$ space group, the highest symme-

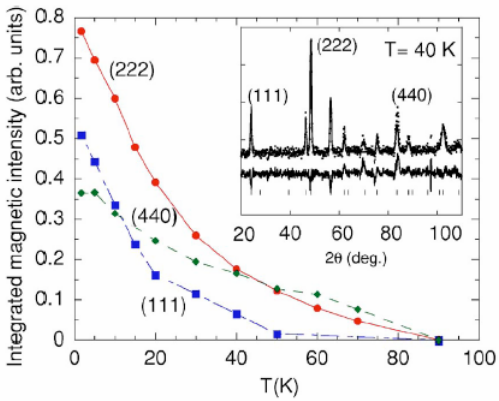

FIG. 4. (Color online) Integrated intensity of several magnetic Bragg peaks in $Gd_2Mo_2O_7$, measured versus temperature on D20. The intensities are scaled to the intensity of the (222) nuclear peak at 90 K. In the inset the magnetic diffraction pattern at 40 K.

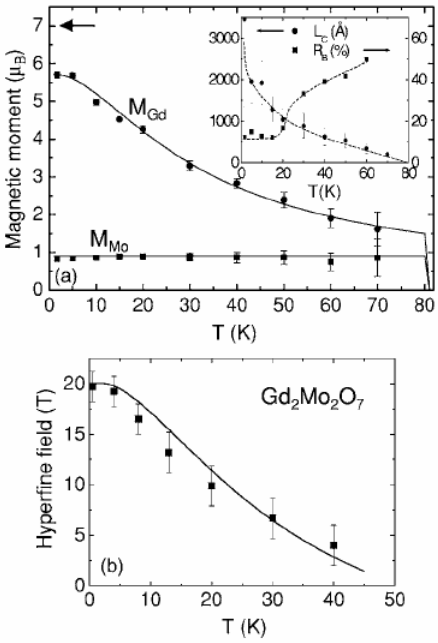

FIG. 5. (a) Temperature dependence of the ordered moments M_{Gd} (circles) and M_{Mo} (squares) in $Gd_2Mo_2O_7$ deduced from refinements of the neutron data in the collinear ferromagnetic model. Errors bars are given by Fullprof. The arrow shows the Gd free ion value of 7 μ_B. The solid line for Gd is a fit with a Brillouin function (see text). In the inset, the magnetic correlation length L_c deduced from the peak linewidth (dots, see text) and the magnetic factor R_B (squares) versus temperature. Dashed lines are guides to the eye. (b) Thermal variation of the ^{155}Gd hyperfine field in $Gd_2Mo_2O_7$, from Ref. 10. The line is a fit to the sum of a contact hyperfine field, proportional to the Gd moment, and of a transferred field, proportional to the Mo moment, and thus temperature independent.

try group allowing ferromagnetism. We also checked noncollinear structures predicted by theory, assuming either anisotropic or dipolar interactions.[22,23] Finally, we explored small deviations from the ferromagnetic collinear case using the simulated annealing process available in Fullprof.[18] Whatever the procedure, we could not improve the quality of the refinement significantly with respect to the collinear ferromagnetic model. We conclude that a noncollinearity of the Gd/Mo ordered moments indeed occurs above 20 K, although we cannot determine its nature presently. We also notice a slight change of the peak linewidth, showing that the magnetic correlation length increases with decreasing T in this temperature range [inset Fig. 5(a)]. The correlation length was deduced from the Fullprof refinement of the Lorentzian contribution to the peak profile, taking into account the instrumental resolution parameters, and using a Thompson-Cox-Hastings pseudo-Voigt profile function for the lineshape.[18]

The temperature dependence of the ordered magnetic moments deduced from refinements in the collinear ferromagnetic model is plotted in Fig. 5(a). At 1.7 K, the moment values deduced from the refinement are 5.70(8) μ_B and 0.82(5) μ_B for Gd and Mo, respectively. Considering the uncertainty on the scale factor between nuclear and magnetic scattering due to the absorption correction, we estimate the ordered magnetic moments in absolute scale with a larger error bar, namely 5.7(5) μ_B and 0.8(2) μ_B for Gd^{3+} and Mo^{4+} ions, respectively. The ordered Gd^{3+} moment is reduced with respect to the free ion value of 7 μ_B. The ordered Mo^{4+} moment is also much smaller than the value of 2 μ_B expected assuming a ionic description ($4d^2$ t_{2g} state with $S=1$ and $g=2$). The calculated ordered moment per formula unit of 13(1) μ_B is significantly smaller than the saturated value of 16.8 μ_B obtained at 2 K in a high field of 14 T.[16] Since we do not expect any strong reduction of the free ion values from crystal field effects (the Gd^{3+} moment has no orbital contribution), the reduced moment values should be associated with the low temperature fluctuations. This is also supported by the μSR experiments, as discussed in the next section.

In Fig. 5(a), we show $M_{Gd}(T)$ fitted by a Brillouin function $B_{7/2}$, assuming that the Gd ions are submitted to a molecular field coming from the Mo ions. As the Mo spontaneous moment is practically temperature independent up to T_C, we assumed the molecular field H_{ex} is constant up to 80 K and vanishes above. The fit in Fig. 5(a) is obtained with $H_{ex}=10.8$ T.

The thermal variation of the Gd moment has also been inferred from the ^{155}Gd Mössbauer data in $Gd_2Mo_2O_7$ in Ref. 10, assuming that the Gd moment is proportional to the hyperfine field. Comparison with the present neutron data shows a clear disagreement: the Mössbauer derived values fall much more rapidly than the neutron values as temperature increases. So we propose another interpretation of the Mössbauer data: the measured hyperfine field H_{hf} is assumed to be the sum of a contact hyperfine field, proportional to the Gd moment, and of a transferred hyperfine field H_{tr} coming from the polarization of the conduction band by the Mo moments (Refs. 24 and 25):

$$H_{hf}(T) = |AM_{Gd}(T) + H_{tr}|. \quad (1)$$

The sign of H_{hf} cannot be obtained by the Mössbauer data. The transferred field is proportional to the Mo moment, and it is thus temperature independent up to T_C. In Fig. 5(b), we have represented the hyperfine field data from Ref. 10 and the fit to the above formula, where $M_{Gd}(T)$ is calculated using the Brillouin function as above. The fit yields a contact hyperfine constant $A=5.8$ T/μ_B and a transferred field $H_{tr}=-13$ T. The sign of the latter is opposite to that of the contact term, which can occur in intermetallic Gd compounds with $3d$ or $4d$ metals.[24,25] Above 40 K, the measured hyperfine field is below 4 T, with a large error bar. The above law predicts that $H_{hf}(T)$ shows a minimum at 50 K (not shown), which could not be observed due to the small hyperfine field values. According to this picture, $Gd_2Mo_2O_7$ is an example where the measured ^{155}Gd hyperfine field is not proportional to the spontaneous Gd moment.

B. μSR measurements

μSR measurements at ambient pressure were performed at the Swiss Muon Source at the Paul Scherrer Institute (Vil-

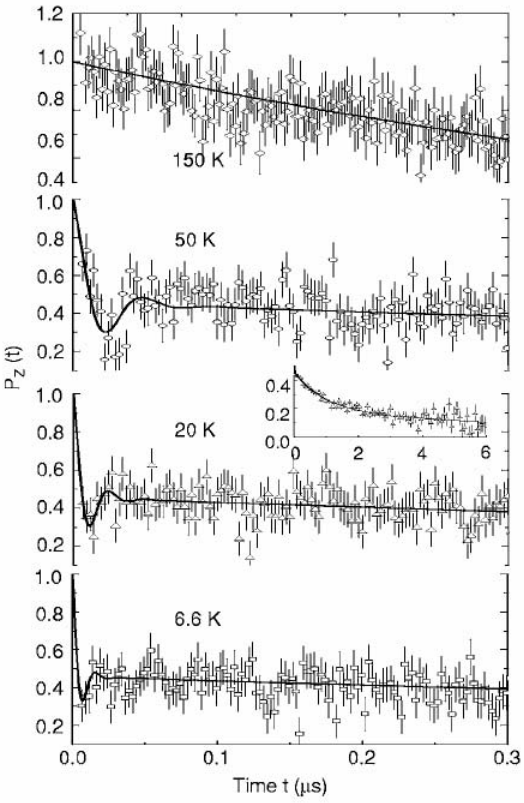

FIG. 6. Muon spin depolarization function $P_Z(t)$ in $Gd_2Mo_2O_7$ measured on the GPS beam line at several temperatures (ambient pressure). Lines are fits as described in text. The inset shows the depolarization function in an extended time range for $T=20$ K. The apparent oscillations at 6.6 K arise from noise in the data.

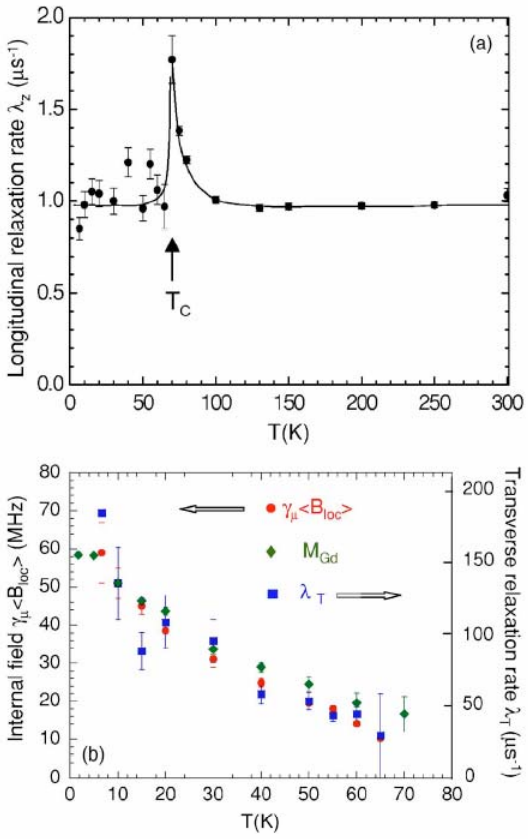

FIG. 7. (Color online) From μSR measurements in $Gd_2Mo_2O_7$. (a) Temperature dependence of the longitudinal relaxation rate λ_Z. The solid line is a guide to the eye. (b) Temperature dependence of $\gamma_\mu\langle B_{loc}\rangle$ (with γ_μ the muon gyromagnetic ratio), λ_T and M_{Gd} (scaled).

ligen, Switzerland) on the GPS instrument in the temperature range 6.6–300 K. Selected μSR spectra are shown in Fig. 6. Above T_C, the relaxation function $P_Z(t)$ shows an exponential like decay: $P_Z(t)=\exp(-\lambda_Z t)$. Below T_C, $P_Z(t)$ shows a rapidly damped oscillation at early times which is readily attributed to the presence of magnetic order. An exponential decay is also observed at long time scales in the ordered phase, showing that spin fluctuations persist down to the lowest temperature.

Below T_C, the relaxation function $P_Z(t)$ was fitted by the equation:

$$P_Z(t) = [\exp(-\lambda_Z t) + 2\exp(-\lambda_T t)\cos(\gamma_\mu\langle B_{loc}\rangle t)]/3. \quad (2)$$

This equation is expected to hold in the magnetically ordered phase of a powder sample.[26] The first term corresponds to the depolarization by spin fluctuations with the longitudinal relaxation rate λ_Z, whereas the second term reflects the precession of the muon spin in the average local field $\langle B_{loc}\rangle$ at the muon site. γ_μ is the muon gyromagnetic ratio. The transverse relaxation rate λ_T can have both static and dynamical character. In the high temperature limit, when the rate of fluctuations of Gd^{3+} and Mo^{4+} moments is much larger than the coupling between the muon spin and the electronic spins, one gets $\langle B_{loc}\rangle=0$ and $\lambda_T=\lambda_Z$. Then the above equation reduces to a simple exponential $P_Z(t)=\exp(-\lambda_Z t)$. This simple function was used to fit the data above T_C.

In a standard ferromagnet, the longitudinal relaxation rate λ_Z shows a cusp at the critical temperature, then decreases with decreasing temperature below T_C and tends to zero as $T\to 0$ (a T^2 behavior is expected for instance from Raman two magnon processes).[27] In $Gd_2Mo_2O_7$, λ_Z shows a cusp at T_C, but does not decrease below [Fig. 7(a)]. It keeps a high value close to that in the paramagnetic region down to the lowest measured temperature of 6.6 K, with possibly a very small bump below T_C, which needs to be confirmed. This abnormal behavior reflects the presence of strong spin fluctuations coexisting with the magnetic order, which seem to persist as $T\to 0$ in contrast with standard spin waves. Such peculiar fluctuations have already been observed by μSR in several geometrically frustrated magnets with a pyrochlore lattice. They were seen in spin liquids[28,29] like $Tb_2Ti_2O_7$ and $Yb_2Ti_2O_7$, as well as in ordered compounds[29–31] like $Gd_2Sn_2O_7$ and $Tb_2Sn_2O_7$. In all cases, the longitudinal relaxation rate saturates in the lowest T range (to values around 1 μs^{-1}), as here for $Gd_2Mo_2O_7$.

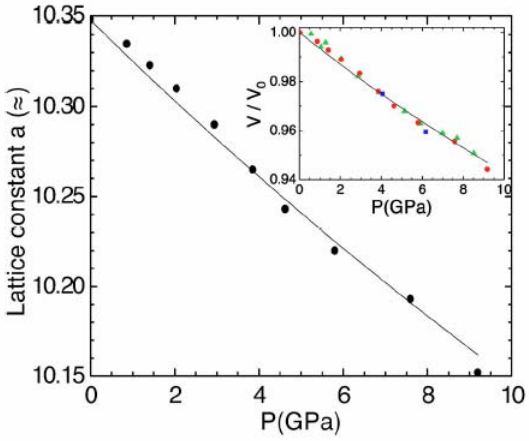

FIG. 8. (Color online) Variation of the lattice constant a versus pressure at ambient temperature. In the inset the relative volume V/V_0 is plotted versus pressure up to 10 GPa for three samples: $Gd_2Mo_2O_7$ (circles), $Tb_2Mo_2O_7$ with $a_0<a_c$ (squares), and $(Tb_{0.8}La_{0.2})_2Mo_2O_7$ with $a_0>a_c$ (triangles). Solid lines are fits to the Murnaghan equation.

The transverse relaxation rate λ_T is up to two orders of magnitude larger than $\lambda_Z(T)$. It smoothly increases below T_C and scales with the average local field $\langle B_{loc}\rangle$ as temperature varies. This leads us to assign λ_T mainly to the width of the distribution of local fields. We notice that both quantities also scale with the ordered moment $M_{Gd}(T)$ determined by neutron diffraction [Fig. 7(b)]. This suggests that the local field seen by the muon mostly comes from the Gd^{3+} ions with much larger moments, although more localized, than the Mo^{4+} ones. Our current neutron and μSR data in the $(Tb,La)_2Mo_2O_7$ series[33] as well as previous μSR data in $Tb_2Mo_2O_7$ and $Y_2Mo_2O_7$ spin glasses[32] support this interpretation, showing that the static internal field is about ten times higher in $Tb_2Mo_2O_7$, with both Tb^{3+} and Mo^{4+} moments, than in $Y_2Mo_2O_7$ where only Mo^{4+} moments are involved.

IV. THE PRESSURE INDUCED STATE

A. Crystal structure under pressure: X-ray diffraction

X-ray diffraction under pressure using the synchrotron radiation was performed at room temperature on the ID27 beam line of ESRF, in the pressure range 0–10 GPa, with an incident wavelength of 0.3738 Å. We used a diamond anvil cell and an ethanol-methanol mixture as the pressure transmitting medium. The crystal structure remains cubic with a $Fd\bar{3}m$ space group in the whole measured pressure range.

The evolution of the lattice constant a versus pressure is shown in Fig. 8. From Ref. 3, one estimates the critical lattice constant for the ferromagnetic spin-glass transition to be $a_c=10.327(5)$ Å (critical ionic radius $r_c=1.047$ Å). Besides $Gd_2Mo_2O_7$, we also studied two samples under pressure for comparison, namely $Tb_2Mo_2O_7$, an insulating spin glass with $a_0=10.3124(7)$ Å, smaller than a_c, and $(Tb_{0.8}La_{0.2})_2Mo_2O_7$ with $a_0=10.3787(8)$ Å greater than a_c. In the studied pressure range, we found the same variation of the relative volume V/V_0 (where V_0 is the unit cell volume at ambient pressure) for all compounds. The equation of state was fitted to the Murnaghan equation $V/V_0=(PB_1/B_0+1)^{-1/B_1}$, yielding a bulk modulus $B_0=148(3)$ GPa. The pressure derivative of the bulk modulus was fixed at a reasonable value ($B_1=4.5$).

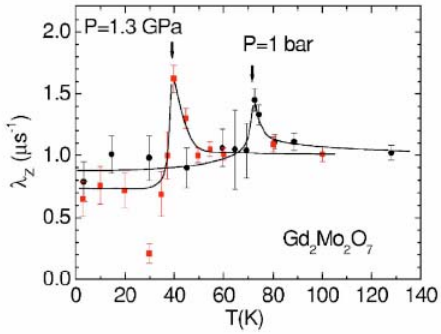

FIG. 9. (Color online) Temperature dependence of the relaxation rate λ_Z, with the $Gd_2Mo_2O_7$ sample in the pressure cell. Data were measured on the GPD instrument: ambient pressure (circles) and $P=1.3$ GPa (squares). Solid lines are guides to the eye.

Knowing the evolution of the lattice constant under pressure enables us to compare the pressure induced state in $Gd_2Mo_2O_7$ with the ambient pressure state in $R_2Mo_2O_7$ compounds with a smaller lattice constant. As discussed in the last section, the different experimental determinations of the critical pressure for $Gd_2Mo_2O_7$ lie in the pressure range 0.6–2.4 GPa.

We notice that the quality of the experimental data was not sufficient to refine the oxygen parameter due to texture effects and/or nonisotropic powder averaging. So we cannot determine the pressure dependence of the Mo-O-Mo bond angle.

B. Change of the transition temperature: μSR

Muon spin rotation measurements under pressure were performed on the GPD instrument of the Paul Scherrer Institute, using high energy incident muons to penetrate the pressure cell. The sample was mounted in a piston cylinder cell inserted in a cryostat. The pressure transmitting medium was a 1-1 mixture of isopropyl alcohol and *N*-pentane. The signal from the pressure cell (about 70% of the total asymmetry) was fitted by a Gaussian Kubo-Toyabe depolarization function. The sample was first measured in the pressure cell at ambient pressure in the T range 3.2–130 K, then the cell was pressurized and the experiment repeated. The pressure was determined by measuring the superconducting transition of an indium wire inside the pressure cell, yielding a value of 1.3 GPa. Below T_C it was difficult to extract any information from the μSR spectra at small times (the 2/3 term), due both to the large background of the pressure-cell and to the fast depolarization of the 2/3 term. Hence, below T_C we fitted only the 1/3 term with an exponential depolarization function. Figure 9 compares the temperature dependence of the

relaxation rate at ambient pressure and under 1.3 GPa. The sharp peak in $\lambda_Z(T)$ clearly moves towards lower temperatures under pressure. It reflects a very strong decrease of the transition temperature—from 70 to 38 K, when the pressure increases from ambient pressure to 1.3 GPa.

C. Change of the spin correlations: Magnetic neutron diffraction

Neutron diffraction measurements under pressure were performed on the spectrometer G6-1 of the Laboratoire Léon Brillouin with an incident wavelength of 4.741 Å, in the high pressure version.[34] The sample was loaded in a sapphire anvil cell with 80% in volume of Al powder. The Al powder was used as a pressure transmitting medium, which ensures a pressure homogeneity within ±5%, without bringing additional Bragg peaks. It also decreases the sample absorption. Measurements were performed at pressures 0.5, 1.2, 1.9, and 2.7 GPa, between 1.5 and 90 K. Pressure was measured by the ruby fluorescence technique. The magnetic diffraction patterns were obtained by subtracting a pattern at 90 K (paramagnetic phase). The magnetic intensity was scaled to the integrated intensity of the (222) Bragg peak. This procedure allows us to compare diffraction patterns measured at different pressures and temperatures.

Figure 10(a) shows magnetic diffraction patterns at 1.2 GPa. The pattern at 1.5 K shows that magnetic long range (LRO) and short range (SRO) orders coexist in the sample. Small Bragg peaks are clearly visible, with a width limited by the experimental resolution. An intense scattering is also observed at low q values. This small angle neutron scattering (SANS), which was absent in the ambient pressure data, shows the onset of ferromagnetic correlations with a mesoscopic length scale. With increasing temperature, the (111) peak disappears at about 20 K, whereas the (222) peak vanishes at a higher temperature close to 38 K, the transition temperature determined by μSR for this pressure. It suggests that the spin reorientation observed in the ordered state at ambient pressure still persists under pressure. The short range ferromagnetic correlations persist slightly above the transition.

At 1.9 GPa, a very small ordered component remains at the Bragg positions. At 2.7 GPa, the magnetic Bragg peaks have completely disappeared, and only magnetic short range order is present [Fig. 10(b)]. Short range magnetic correlations are clearly shown at 1.5 K, yielding a strongly modulated magnetic background. Here, the SANS signal coexists with a diffuse peak centered around 1.1 $Å^{-1}$. With increasing temperature, the diffuse peak flattens and vanishes around 20 K, whereas the ferromagnetic correlations persist up to 40 K.

In Fig. 11(a), we compare diffraction patterns at 1.5 K for several pressures. With increasing pressure, the decrease of the Bragg intensity coincides with the growing of the diffuse magnetic peak, showing that the relative contributions of SRO and LRO vary in opposite way. The SANS signals flattens with increasing either T or P, showing that the ferromagnetic correlation length decreases.

To analyze the pressure data we proceeded as follows. The long range magnetic order was analyzed within the collinear ferromagnetic model, by refining the Bragg peaks using Fullprof. In this procedure, the diffuse scattering and SANS signal were treated as a background. The magnetic peaks were scaled to the nuclear Bragg peak (222) measured in the paramagnetic range. The calculated patterns are shown in Fig. 11(a). The ordered moments are plotted versus pressure in Fig. 11(b). The Gd^{3+} moment strongly decreases with increasing pressure. The Mo^{4+} moment is expected to decrease too, but being much smaller, its variation is less visible.

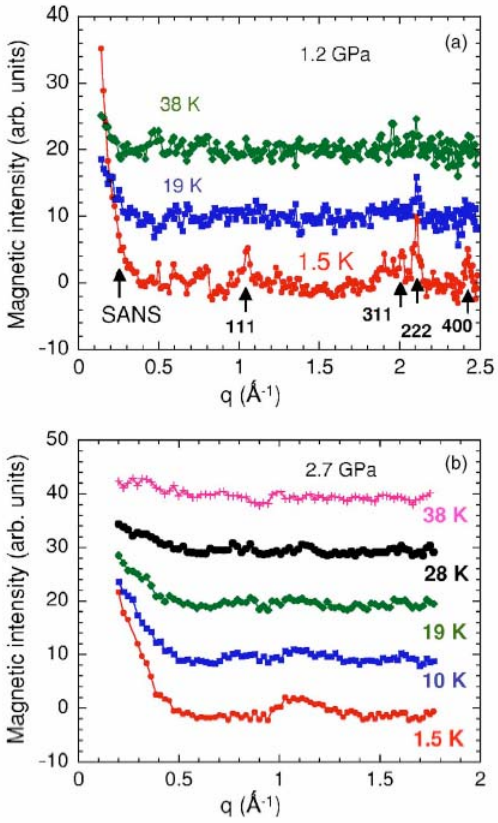

FIG. 10. (Color online) Magnetic diffraction patterns in $Gd_2Mo_2O_7$ under pressure versus the scattering vector $q = 4\pi \sin\theta/\lambda$. (a) $P=1.2$ GPa; (b) $P=2.7$ GPa. The diffraction patterns are corrected by a pattern in the paramagnetic range (90 K) and scaled to the nuclear intensity of the (222) Bragg peak.

To get information about the short range correlations yielding the diffuse magnetic signal at 2.7 GPa, we used the model proposed by Bertaut and Burlet[35] for spin glasses and applied by Greedan *et al.*[36] to the pyrochlore system. A fit of the diffuse magnetic scattering by the sum of radial correlation functions was performed, giving information on the spin-spin correlation parameters γ (Fig. 12). We considered correlations up to the fourth neighbor shell (~7.3 Å). The correlation coefficients γ deduced from this fit at 2.7 GPa are plotted in the inset of Fig. 12. The Gd-Gd correlations are F ($\gamma_{1,3,4}>0$), while the Gd-Mo are AF ($\gamma_2<0$). The AF Mo-Mo correlations responsible for the frustration in the SG state[28] cannot be detected, their contribution being about 50

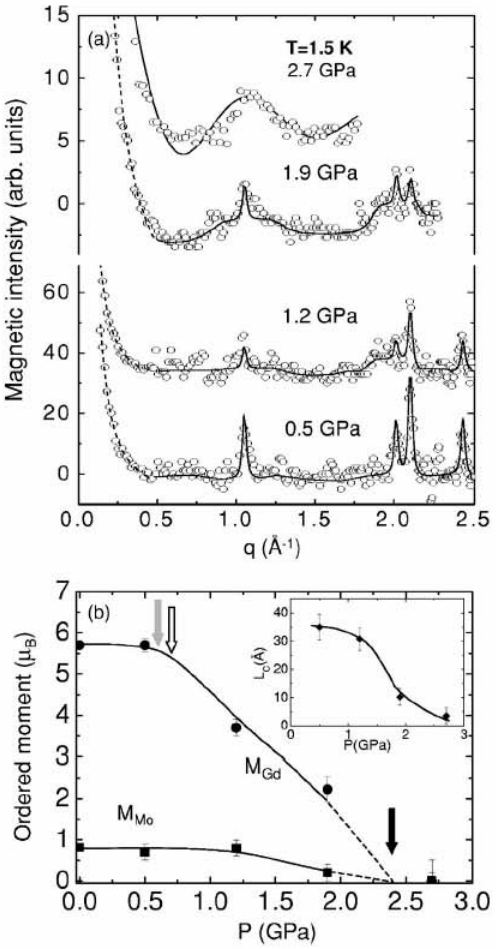

FIG. 11. (a) Magnetic diffraction patterns measured in $Gd_2Mo_2O_7$ at 1.5 K for several pressures. Solid lines are fits of the Bragg peaks (0.5, 1.2, and 1.9 GPa, $q>0.5$ Å^{-1}) and of the diffuse peaks (2.7 GPa), respectively. The dashed lines are fits of the SANS signal (0.5, 1.2, and 1.9 GPa, $q<0.5$ Å^{-1}). All fits are described in the text. (b) Variation of the ordered moments versus pressure. Error bars are given by Fullprof. The arrows indicate the critical pressure as determined from susceptibility (Ref. 14) (0.6 GPa, gray), chemical pressure (Ref. 3) (0.7 GPa, white), and resistivity (Ref. 16) (2.4 GPa, black). In inset: the variation of the correlation length L_C versus pressure at 1.5 K, as obtained by fitting the SANS with a Lorentzian.

times smaller than the Gd-Gd ones due to the smaller Mo moment.

We outline that in the intermediate pressure range ($0<P<2.7$ GPa) neither the ordered ferromagnetic model nor the short range magnetic model can describe the SANS signal in a proper way. This is because the mesoscopic length scale of the SANS is intermediate between the fourth neighbor shell (7 Å) and the domain size associated with the Bragg peaks (400 Å or above, taking into account the experimental resolution). Considering the relative magnitude of the Mo and Gd local moments and the fact that Mo-Mo and Mo-Gd correlations are AF, we attribute the SANS signal to

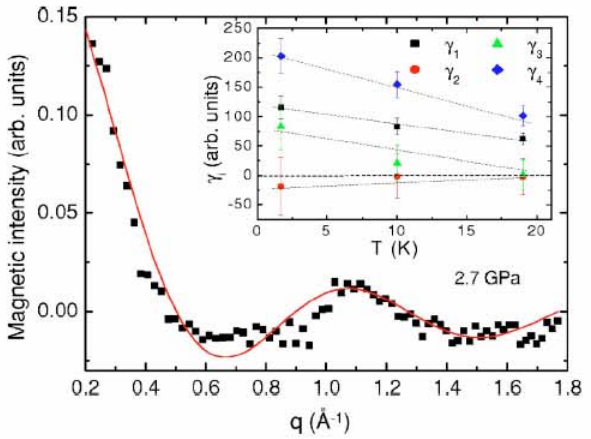

FIG. 12. (Color online) Magnetic intensity in $Gd_2Mo_2O_7$ at 1.5 K and $P=2.7$ GPa. The fit is made with the short range model described in the text. In the inset the temperature dependence of the correlation coefficients. Dashed lines are guides to the eye.

ferromagnetic Gd-Gd correlations. To get an insight into their correlation length L_C, we have fitted the SANS with a Lorentzian function $A\kappa/[\pi(\kappa^2+q^2)]$ where A and κ are the norm and half width half maximum of the Lorentzian curve respectively, with $\kappa=1/L_C$. The correlation length L_c is about 35 Å at 0.5 GPa and 1.5 K. It decreases with increasing pressure [inset Fig. 11(b)] and temperature.

V. DISCUSSION

In this section, we discuss the main results in comparison with other experimental data and existing theories. At ambient pressure, the ordered ground state in $Gd_2Mo_2O_7$ is a collinear ferromagnet, in contrast with $Nd_2Mo_2O_7$, where the Nd^{3+} free ion anisotropy induces a spin ice configuration of the Nd^{3+} moments.[7,37]

A collinear ground state is expected in $Gd_2Mo_2O_7$ from the band structure[6] and from the spin only character of Gd^{3+} ion. It could explain why there is no giant anomalous Hall effect, in contrast with $Nd_2Mo_2O_7$. The ordered magnetic state is, however, strongly abnormal, even at ambient pressure. It coexists with strong fluctuations, which we probe by μSR, and which persist down to 27 mK according to Mössbauer data.[10] These fluctuations could be responsible for the strong reduction of the ordered moments. The Gd^{3+} moment is reduced by 20%, and the Mo^{4+} moment by 60% with respect to the free ion values. Spin fluctuations likely play a role in the spin noncollinearity above 20 K. The origin of these fluctuations needs to be clarified. Low temperature collective fluctuations are widely observed in geometrically frustrated magnets and seem to be a key feature of geometrical frustration.[38] However, in $Gd_2Mo_2O_7$ at ambient pressure, the ferromagnetic Gd-Gd and Mo-Mo first neighbor interactions should be frustrated only by the Gd or Mo anisotropy. This anisotropy is very small, and obviously does not play a key role to select the ground state. A possible source of frustration could come from the Mo orbital degen-

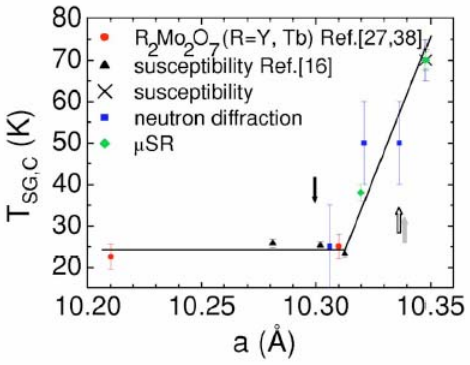

FIG. 13. (Color online) Curie and spin-glass transition temperatures T_C and T_{SG} versus lattice constant in $Gd_2Mo_2O_7$: (crosses) from susceptibility, (squares) neutron diffraction, and (diamonds) μSR (this work); (triangles) from susceptibility under pressure (Ref. 16). The T_{SG} values of $Y_2Mo_2O_7$ (a=10.21 Å) and $Tb_2Mo_2O_7$ (a=10.31 Å) from Refs. 28 and 40 are plotted for comparison. The arrows indicate the critical lattice constant as determined from susceptibility (Ref. 14) (gray), chemical pressure (Ref. 3) (white), and resistivity (Ref. 16) (black), using our compressibility data.

eracy of the t_{2g} levels, and the coupling between spin and orbit degrees of freedom.[39] One could also speculate that the abnormal fluctuations come from the proximity of the threshold and the metal-insulating instability. Taking them into account in the band structure is a challenge for theory.

The ferromagnetic state is strongly unstable under pressure, so that a small pressure of 0.5 GPa induces important changes in the magnetic correlations and strongly decreases the T_C value. Actually in $Gd_2Mo_2O_7$ our neutron data show that the magnetic order gradually evolves from F to SG in the pressure range of 0.5–2.5 GPa: in this region, both SG and F contributions coexist and their relative amounts change with pressure.

Initial measurements in the substituted series[3] $(RR')_2Mo_2O_7$ support a unique threshold from a ferromagnetic metal to an insulating spin-glass state for a lattice constant $a_c \sim 10.33$ Å. Using the equation of state found above, it yields a chemical critical pressure of 0.7 GPa. Actually, macroscopic measurements on $Gd_2Mo_2O_7$ under pressure show a more complex situation. Magnetic measurements under pressure[14,16] suggest a transition from ferromagnetic to spin-glass state already at 0.6 GPa. On the other hand resistivity measurements[16] on *insulating* $Gd_2Mo_2O_7$ crystals, show that they become metallic at a much higher pressure of 2.4 GPa. It suggests that the ferromagnetic-spin glass transition could be disconnected from the metal-insulating one. We notice that all threshold values belong in the pressure range of coexistence deduced from our neutron data.

In Fig. 13, we have plotted the transition temperature T_C measured in $Gd_2Mo_2O_7$ versus the lattice constant, by combining our magnetization, neutron, muon and x-ray data. We also plotted the spin glass transition temperatures T_{SG} corresponding to the susceptibility anomalies under pressure.[16] These T_{SG} values are in the temperature range 20–25 K, in good agreement with the values found at ambient pressure in

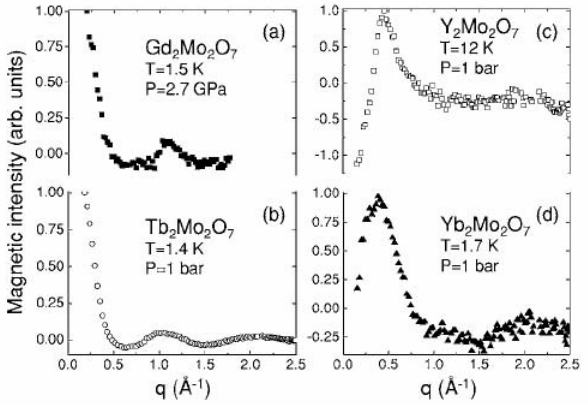

FIG. 14. Magnetic intensity of $R_2Mo_2O_7$ (R=Gd, Tb, Y, and Yb) versus the scattering vector q. A pattern in the paramagnetic phase was subtracted.

$Tb_2Mo_2O_7$ and $Y_2Mo_2O_7$ spin glasses with a smaller lattice constant.[28,40] The temperature for the onset of short range correlations in the spin-glass state is noticeably higher (around 30–40 K at 2.7 GPa) as it often occurs in spin glasses. The whole set of data provides a precise description of the magnetic transition in the instability region.

By comparing the magnetic pattern of $Gd_2Mo_2O_7$ at 2.7 GPa with patterns of $R_2Mo_2O_7$ compounds with small ionic radii (R=Tb, Y, and Yb) at ambient pressure, we can get a general insight on the different types of spin correlations in the spin-glass phase. For this purpose we measured the Y, Tb, and Yb compounds at ambient pressure (Fig. 14). Our results for R=Tb and Y agree with previous results.[28,36,40] We can also follow the evolution of the Mo-Mo, Gd-Mo, and Gd-Gd correlations with pressure from the ferromagnetic to the spin-glass phase.

In the collinear ground state found in $Gd_2Mo_2O_7$ at ambient pressure, all correlations are ferromagnetic. With increasing pressure, Mo-Mo interactions become AF and frustrated by the lattice geometry yielding the SG phase. Neutron scattering cannot probe the Mo-Mo correlations in the SG phase of $Gd_2Mo_2O_7$ since their contribution is much smaller than the Gd-Gd and Gd-Mo ones due to the smaller Mo moment. But these correlations can be directly evidenced in $Y_2Mo_2O_7$ where only the Mo ions are magnetic and the lattice constant (a=10.21 Å from Ref. 28) is equivalent to $Gd_2Mo_2O_7$ at 6.7 GPa. In $Y_2Mo_2O_7$, AF correlations with a scale of about 5 Å forming a four sublattice structure[28] yield a peak in the diffuse scattering at q=0.44 Å^{-1}. A similar structure is observed in $Yb_2Mo_2O_7$ [a=10.1689(7) Å], where the contribution of the Yb^{3+} moments (around 1 μ_B) is much lower than for Tb and Gd.

Concomitantly with the change in the Mo-Mo correlations, the Gd-Mo correlations become AF. The Gd-Gd correlations remain ferromagnetic, but their correlation length decreases with increasing pressure. The comparison of $Gd_2Mo_2O_7$ with $Tb_2Mo_2O_7$ suggests that ferromagnetic R-R correlations are a general feature of the $R_2Mo_2O_7$ series. The length scale of these correlations is reduced by pressure, which enhances the AF interactions. Our measurements on

$Tb_2Mo_2O_7$ under pressure,[41] show that it is also the case for Tb.

From our data, one can evaluate the first neighbor exchange interactions $\mathcal{J}$ and their contribution to the energy balance. One naturally expects $\mathcal{J}_{\text{Mo-Mo}} > \mathcal{J}_{\text{Gd-Mo}} > \mathcal{J}_{\text{Gd-Gd}}$. At ambient pressure, the three interactions are likely all ferromagnetic. Dominant Mo-Mo interactions stabilize the ferromagnetic order but are sensitive to orbital degeneracy and band instability. Gd-Mo ferromagnetic interactions account for the *F* alignment of Gd and Mo moments. Gd-Gd interactions cannot be measured. One can speculate that their ferromagnetic character stabilizes the collinear state at low temperature.

We first estimate the exchange energy per ion (Mo or Gd) for the three interactions. For the Mo-Mo exchange, one can state that $E_{\text{Mo-Mo}} \sim T_C \sim \theta_{CW} = -70$ K where θ_{CW} is the Curie-Weiss constant. For the Gd-Mo exchange, we use the exchange field acting on Gd, determined by fitting the temperature dependence of the ordered Gd moment (Fig. 5): $H_{ex} = 10.8$ T; then: $E_{\text{Gd-Mo}} = -M_{Gd} H_{ex} \sim -45$ K. Finally, to estimate the order of magnitude of the Gd-Gd exchange/dipole energy, we use the θ_{CW} value in $Gd_2Ti_2O_7$ or $Gd_2Sn_2O_7$, where there is no $3d/4d$ magnetic metal ion: $E_{\text{Gd-Gd}} \sim -10$ K. Thus Gd-Mo and Gd-Gd interactions may play a role to determine the ground state in the ferromagnetic phase and threshold region.

In order to estimate the exchange integrals, we make the following assumptions: the exchange between a pair of ions *A* and *B* is written $E_{ex} = -\mathcal{J}_{A-B} S_A S_B$, where S_A and S_B are the true spins of the *A* and *B* ions. Then, the exchange energy per ion is $E_{A-B} = -z\mathcal{J}_{A-B} S_A S_B$, where *z* is the number of nearest neighbors ($z=6$ in the pyrochlore lattice for all exchange bonds). Although an ionic description is not fully appropriate for the Mo ion in $Gd_2Mo_2O_7$, we assume $S=1$ for Mo, and for Gd^{3+}, we use $S=7/2$ as there is no crystal field splitting. Then, we obtain the following exchange integrals: $\mathcal{J}_{\text{Mo-Mo}} \sim 12$ K, $\mathcal{J}_{\text{Gd-Mo}} \sim 2$ K, and $\mathcal{J}_{\text{Gd-Gd}} \sim 0.14$ K.

Under applied pressure, we find that the Mo-Mo exchange interaction changes sign and become AF. Calculated phase diagrams for given values of the exchange interactions[36] show that AF Mo-Mo interactions may stabilize a degenerate ground state whatever the sign of the Gd-Mo interactions. Mo-Mo interaction involves Mo t_{2g} orbitals, which are very sensitive to electron correlations. Pressure is expected to increase the intrasite electron correlation energy *U*. At ambient pressure, our estimation of $\mathcal{J}_{\text{Mo-Mo}}$ (12 K) is lower than the theoretical estimation of about 5 meV (58 K), obtained by Solovyev[6] in the mean field Hartree-Fock approach, taking the onsite Coulomb interaction $U=2.5$ eV between Mo($4d$) electrons. The model predicts that $\mathcal{J}_{\text{Mo-Mo}}$ strongly decreases as *U* increases, although it does not change sign as in $Y_2Mo_2O_7$. Gd-Gd interactions between localized Gd moments are expected to be less sensitive to pressure.

The change in sign of the Mo-Mo interaction is connected with the aperture of a Mott-Hubbard gap in the Mo t_{2g} band, so that theory[6] predicts the spin glass state to be insulating. The is actually true for the spin glasses with small ionic radii (R=Y, Ho, Dy), but not for the pressure induced spin-glass state. Resistivity measurements[16,42] in $Gd_2Mo_2O_7$ and $Sm_2Mo_2O_7$ show that the spin-glass state induced under pressure is actually metallic. With respect to chemical pressure, an applied pressure should not only increase the electron correlations responsible for the Mott-Hubbard gap, but also increase the bandwidth. This should naturally favor electron delocalization as a dominant feature. Optical measurements could also check the evolution of conduction properties under pressure.

VI. CONCLUSION

We have observed an abnormal ferromagnetic phase with strong spin fluctuations in $Gd_2Mo_2O_7$. By applying pressure, we can tune the change of this ferromagnetic phase into a spin-glass phase. The fact that an applied pressure is equivalent to a chemical pressure to induce the ferromagnetic spin-glass transition supports a mechanism mostly controlled by Mo-Mo interactions. The combination of three microscopic probes under pressure allows us to follow the evolution of magnetism with the lattice constant with great precision throughout the threshold and to evaluate the role of the rare earth interactions in the energy balance.

ACKNOWLEDGMENTS

We thank U. Zimmerman for the μSR measurements on GPD (PSI) and M. Mezouar for the x-ray measurements on ID27 (ESRF). We are indebted to J. Rodríguez-Carvajal for many useful discussions and for providing programs to analyze the neutron diffraction data. We also thank I. Solovyev for an interesting discussion.

[1] S. T. Bramwell and M. J. P. Gingras, Science **294**, 149 (2001).
[2] J. E. Greedan, J. Mater. Chem. **11**, 37 (2001).
[3] T. Katsufuji, H. Y. Hwang, and S.-W. Cheong, Phys. Rev. Lett. **84**, 1998 (2000).
[4] Y. Moritomo, S. Xu, A. Machida, T. Katsufuji, E. Nishibori, M. Takata, M. Sakata, and S. W. Cheong, Phys. Rev. B **63**, 144425 (2001).
[5] J. S. Kang, Y. Moritomo, S. Xu, C. G. Olson, J. H. Park, S. K. Kwon, and B. I. Min, Phys. Rev. B **65**, 224422 (2002).
[6] I. V. Solovyev, Phys. Rev. B **67**, 174406 (2003).
[7] Y. Taguchi, Y. Oohara, H. Yoshizawa, N. Nagaosa, and Y. Tokura, Science **291**, 2573 (2001).
[8] Y. Taguchi, T. Sasaki, S. Awaji, Y. Iwasa, T. Tayama, T. Sakakibara, S. Iguchi, T. Ito, and Y. Tokura, Phys. Rev. Lett. **90**, 257202 (2003).
[9] N. P. Raju, E. Gmelin, and R. K. Kremer, Phys. Rev. B **46**, 5405 (1992).
[10] J. A. Hodges *et al.*, Eur. Phys. J.: Appl. Phys. **33**, 173 (2003).
[11] J. E. Greedan, M. Sato, Naushad Ali, and W. R. Datars, J. Solid State Chem. **68**, 300 (1987).

[12] W. Schnelle and R. K. Kremer, J. Phys.: Condens. Matter **16**, S685 (2004).
[13] I. Kézsmárki, N. Hanasaki, D. Hashimoto, S. Iguchi, Y. Taguchi, S. Miyasaka, and Y. Tokura, Phys. Rev. Lett. **93**, 266401 (2004).
[14] J. G. Park *et al.*, Physica B **328**, 90 (2003).
[15] K. Miyoshi, Y. Takamatsu, and J. Takeuchi, J. Phys. Soc. Jpn. **75**, 065001 (2006).
[16] N. Hanasaki, M. Kinuhara, I. Kezsmarki, S. Iguchi, S. Miyasaka, N. Takeshita, C. Terakura, H. Takagi, and Y. Tokura, Phys. Rev. Lett. **96**, 116403 (2006).
[17] D. Schmitt and B. Ouladiaff, J. Appl. Crystallogr. **31**, 620 (1998).
[18] J. Rodríguez-Carvajal, Physica B **192**, 55 (1993). For a recent version of Fullprof, see: CPD Newsletters **26**, 12 (2001), available at http://journals.iucr.org/iucr-top/comm/cpd/newsletters
[19] E. F. Bertaut, Acta Crystallogr., Sect. A: Cryst. Phys., Diffr., Theor. Gen. Crystallogr. **24**, 217 (1969).
[20] Y. A. Izyumov, V. E. Naish, and R. P. Ozerov, *Neutron Diffraction on Magnetic Materials* (Consultants Bureau, New York, 1991).
[21] J. Rodríguez-Carvajal, BasIreps, URL: ftp://ftp.cea.fr/pub/llb/divers/BasIreps
[22] J. D. M. Champion, S. T. Bramwell, P. C. W. Holdsworth, and M. J. Harris, Europhys. Lett. **57**, 93 (2002).
[23] S. E. Palmer and J. T. Chalker, Phys. Rev. B **62**, 488 (2000).
[24] K. Tomala, G. Czjzek, J. Fink, and H. Schmidt, Solid State Commun. **24**, 857 (1977).
[25] E. Dormann, in *Handbook on the Physics and Chemistry of Rare Earths*, edited by K. A. Gschneider, Jr. and L. Eyring (Elsevier, New York, 1991).
[26] P. Dalmas de Réotier, P. C. M. Gubbens, and A. Yaouanc, J. Phys.: Condens. Matter **16**, S4687 (2004).
[27] P. Dalmas de Réotier and A. Yaouanc, Phys. Rev. B **52**, 9155 (1995).
[28] J. S. Gardner, B. D. Gaulin, S. H. Lee, C. Broholm, N. P. Raju, and J. E. Greedan, Phys. Rev. Lett. **83**, 211 (1999).
[29] P. Bonville *et al.*, Hyperfine Interact. **156-157**, 103 (2004); Proceedings of the XXXVIII Zakopane School of Physics, edited by E. Görlich, K. Krolas, A. Pedziwiatr (Institute of Physics, Krakow, Poland, 2003), p. 53.
[30] F. Bert, P. Mendels, A. Olariu, N. Blanchard, G. Collin, A. Amato, C. Baines, and A. Hillier, Phys. Rev. Lett. **97**, 117203 (2006).
[31] P. Dalmas de Réotier *et al.*, Phys. Rev. Lett. **96**, 127202 (2006).
[32] S. R. Dunsiger *et al.*, Phys. Rev. B **54**, 9019 (1996).
[33] A. Apetrei, I. Mirebeau, I. Goncharenko, D. Andreica, and P. Bonville, Phys. Rev. Lett. (to be published), e-print cond-mat/0604627.
[34] I. Goncharenko, Rev. High Pressure Sci. Technol. **24**, 193 (2004).
[35] E. F. Bertaut and P. Burlet, Solid State Commun. **5**, 279 (1967).
[36] J. E. Greedan, J. N. Reimers, C. V. Stager, and S. L. Penny, Phys. Rev. B **43**, 5682 (1991).
[37] Y. Yasui *et al.*, J. Phys. Soc. Jpn. **72**, 865 (2003).
[38] S. Bramwell *et al.*, Phys. Rev. Lett. **87**, 047205 (2001).
[39] M. W. Kim, Y. S. Lee, T. W. Noh, J. Yu, and Y. Moritomo, Phys. Rev. Lett. **92**, 027202 (2004).
[40] B. D. Gaulin, J. N. Reimers, T. E. Mason, J. E. Greedan, and Z. Tun, Phys. Rev. Lett. **69**, 3244 (1992).
[41] A. Apetrei, I. Mirebeau, I. Goncharenko, D. Andreica, and P. Bonville, *Proceedings of the International Conference on Highly Frustrated Magnetism*, edited by Z. Hiroi and H. Tsunetsugu, J. Phys.: Condens. Matter (HFM2006, Osaka, Japan), to be published.
[42] K. Miyoshi, T. Yamashita, K. Fujiwara, and J. Takeuchi, J. Phys. Soc. Jpn. **72**, 1855 (2003).

Available online at www.sciencedirect.com
ScienceDirect
Journal of Magnetism and Magnetic Materials 310 (2007) 919–921
www.elsevier.com/locate/jmmm

Magnetic transition induced by pressure in $Gd_2Mo_2O_7$ as studied by neutron diffraction and μSR

I. Mirebeau[a,*], A. Apetrei[a], I. Goncharenko[a], D. Andreica[b], P. Bonville[c]

[a]*Laboratoire Léon Brillouin, CEA-CNRS, CE-Saclay, 91191Gif-sur-Yvette, France*
[b]*Laboratory for Muon Spin spectroscopy, Paul Scherrer Institute, 5232 Villigen-PSI, Switzerland*
[c]*Service de Physique de l'Etat Condensé, CEA-CNRS, CE-Saclay, 91191 Gif-Sur-Yvette, France*

Available online 10 November 2006

Abstract

$R_2Mo_2O_7$ compounds show a ferromagnetic metal-insulating spin glass transition tuned by the radius of the rare earth ion R^{3+}. We have studied $Gd_2Mo_2O_7$ situated just above the threshold, by neutron diffraction and μSR, at ambient and under applied pressure. A ferromagnetic state with strong fluctuations is stabilized at ambient pressure. Under pressure, the Curie temperature strongly decreases, from 70 K at ambient pressure to 38 K at 1.3 GPa. The intensity of the Bragg peaks decreases, whereas mesoscopic correlations appear. At 2.7 GPa, magnetic long-range order completely breaks down and a spin glass-like state is stabilized, with only short-range correlations. The study provides a microscopic characterization of the magnetic correlations and spin fluctuations throughout the transition.

PACS: 71.30.+h; 71.27.+a; 75.25.+z

Keywords: Frustration; Pyrochlore; Neutron diffraction; μSR; Pressure

In $R_2Mo_2O_7$ compounds, the rare earth R^{3+} and Mo^{4+} ions both occupy a geometrically frustrated lattice of corner sharing tetrahedra. These compounds undergo a ferromagnetic-spin glass transition with decreasing the rare earth ionic radius, which is accompanied by a metal–insulator transition [1]. The systematic change of the electrical properties suggests a quantum phase transition at a threshold close to the ionic radius value of Gd^{3+}. The origin of this transition comes from the aperture of a Mott–Anderson gap at the Fermi level due to increasing strength of electronic correlations. $Gd_2Mo_2O_7$, the most suitable compound to investigate the quantum transition, was intensively studied theoretically [2] and experimentally [3–5]. However, up to now, the type of magnetic order has not been investigated by neutron diffraction since $Gd_2Mo_2O_7$ strongly absorbs neutrons.

We present here the first neutron and μSR measurements in $Gd_2Mo_2O_7$. At ambient pressure, our measurements allow to clarify the nature of the magnetic phase just above the threshold. Moreover, by applying pressure, we induce a transition towards a spin glass phase, as previously inferred from magnetic measurements [6]. Tuning the transition by pressure allows us to study the evolution of the spin correlations and spin fluctuations in a continuous way throughout the threshold region. A detailed description of the results is given in Ref. [7].

Powder neutron diffraction measurements were performed on a sample with isotopically enriched ^{160}Gd at ambient pressure on the D20 diffractometer of the Institut Laüe Langevin (ILL) and under pressure on G6-1 diffractometer of the Laboratoire Léon Brillouin (LLB). μSR measurements were performed at the Swiss Muon Source at the Paul Scherrer Institute (Villigen, Switzerland) at ambient pressure on GPS and under pressure on GPD instruments. Magnetization measurements show a ferromagnetic transition at $T_C = 70$ K. Fig. 1 shows typical neutron diffraction patterns at low temperature ($1.5\,K \ll T_C$), showing the evolution of the magnetic ground state versus pressure.

*Corresponding author. Tel.: +33 1 69 08 60 89; fax: +33 1 69 08 82 61.
E-mail address: mirebeau@dsm-mail.saclay.cea.fr (I. Mirebeau).

0304-8853/$ - see front matter © 2006 Elsevier B.V. All rights reserved.
doi:10.1016/j.jmmm.2006.10.142

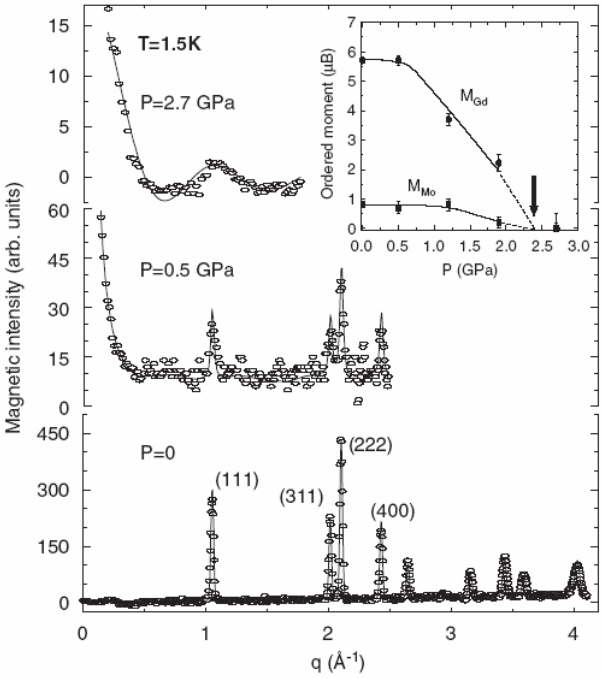

Fig. 1. Magnetic neutron diffraction patterns of $Gd_2Mo_2O_7$ measured at 1.5 K at ambient and under applied pressure. A pattern measured in the paramagnetic phase (90 K) was subtracted. Solid lines are fits to the data. In the inset, the variation of the Mo and Gd ordered moments with pressure. The arrow shows the critical pressure from recent resistivity data [5].

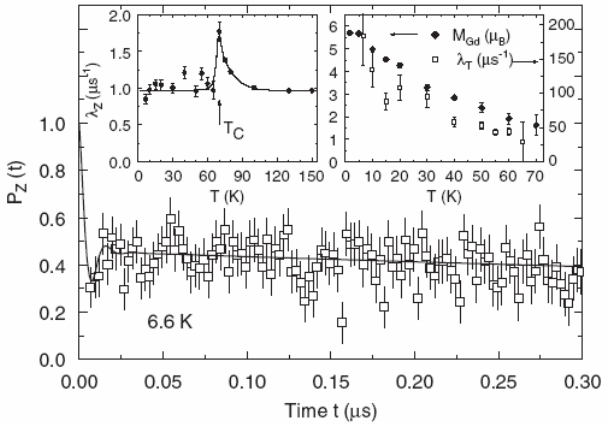

Fig. 2. Muon spin depolarization function in $Gd_2Mo_2O_7$ at ambient pressure ($T = 6.6$ K). The solid line is a fit to the data. In the insets, the longitudinal and transverse relaxation rates λ_Z and λ_T versus temperature. The Gd moment measured by neutron scales to λ_T.

At ambient pressure a collinear ferromagnetic state is stabilized at low temperature, up to about 20 K. The ordered magnetic moments at 1.5 K deduced from Rietveld refinements are parallel and equal to 5.7(5) and 0.8(2) μ_B for Gd and Mo, respectively. Between 20 and 70 K, the experimental spectra start to deviate from those calculated with the collinear ferromagnetic model. A complex spin reorientation, which likely involves noncollinear and/or nonequivalent Gd moments seems to occur.

The ferromagnetic order at ambient pressure coexists with strong fluctuations probed by μSR. This is seen in Fig. 2, showing the μSR depolarization function $P_Z(t)$ at 6.6 K. Below T_C, $P_Z(t)$ shows a rapidly damped oscillation at early times due to the onset of static magnetic order. $P_Z(t)$ decays exponentially at long times, showing that spin fluctuations persist down to the lowest temperature. $P_Z(t)$ was fitted as in Ref. [9], yielding the longitudinal and transverse relaxation rates λ_Z and λ_T plotted versus temperature in the insets. λ_Z, which probes the spin fluctuations, does not decrease to zero as $T \to 0$, as it does in standard ferromagnets due to the coupling to spin waves. It shows a cusp at T_C and remains constant below. The transverse relaxation rate λ_T, assigned to the distribution of local fields, is much larger than λ_Z below T_C and scales with the ordered Gd moment.

The ferromagnetic state is strongly unstable against pressure. μSR measurements show that T_C decreases from 70 K at ambient pressure down to 38 K at 1.3 GPa. Neutron diffraction patterns under pressure show that the Bragg peaks start to decrease at 0.5 GPa, whereas mesoscopic ferromagnetic correlations (with a lengthscale of 30−40 Å) appear at low angles. The ordered magnetic moments decrease with increasing pressure. The Bragg peaks fully disappear at 2.7 GPa and a spin glass-like state is stabilized, with only short-range correlations, yielding a diffuse scattering with broad modulations. An analysis of the diffuse scattering within a short-range order model [8] shows that Gd–Gd spin correlations remain ferromagnetic with a correlation length limited to about four neighbours or 7 Å at 2.7 GPa, whereas Gd–Mo spin correlations turn to antiferromagnetic.

In conclusion, we have observed an abnormal ferromagnetic state with strong spin fluctuations in $Gd_2Mo_2O_7$ at ambient pressure. The spin fluctuations which persist down to $T \to 0$ recall those observed in spin liquid or antiferromagnetically ordered phases of geometrically frustrated magnets. In $Gd_2Mo_2O_7$ at ambient pressure, ferromagnetic interactions between almost isotropic moments are not frustrated, so the abnormal fluctuations likely come from the proximity of the quantum transition. Under pressure, the ferromagnetic phase transforms into a spin glass phase with only short-range correlations. This spin glass-like phase strongly resembles that observed at ambient pressure in $Tb_2Mo_2O_7$, where the Tb^{3+} ionic radius is smaller than the Gd^{3+}one [8,9]. Therefore, by applying pressure, we show that an applied pressure is equivalent to a chemical pressure and we can tune the quantum transition. The change of sign of the Gd–Mo correlations which become antiferromagnetic under pressure supports a mechanism controlled by Mo–Mo interactions, turning from F to AF as previously inferred.

Acknowledgements

We thank A. Forget, D. Colson and J.P. Sanchez for providing the sample, A. Amato and E. Suard for their help in the measurements at PSI and ILL, respectively.

References

[1] T. Katsufuji, H.Y. Hwang, S.W. Cheong, Phys. Rev. Lett. 84 (2000) 1998.
[2] I.V. Solovyev, Phys. Rev. B 67 (2003) 174406.
[3] J.A. Hodges, et al., Eur. Phys. J. B 33 (2003) 173.
[4] I. Kézsmárki, et al., Phys. Rev. Lett. 93 (2004) 266401.
[5] N. Hanasaki, et al., Phys. Rev. Lett. 96 (2006) 116403.
[6] J.G. Park, et al., Physica B 328 (2003) 90.
[7] I. Mirebeau, et al., cond-mat/0606420, to appear in Phys. Rev. B.
[8] J.E. Greedan, et al., Phys. Rev. B 43 (1991) 5682.
[9] A. Apetrei, et al., cond-mat/0604627, to appear in Phys. Rev. Lett.

IOP Publishing Journal of Physics: Condensed Matter

J. Phys.: Condens. Matter **19** (2007) 376208 (10pp) doi:10.1088/0953-8984/19/37/376208

Crystal structure under pressure of geometrically frustrated pyrochlores

A Apetrei[1], I Mirebeau[1], I Goncharenko[1] and W A Crichton[2]

[1] Laboratoire Léon Brillouin, CEA-CNRS, CE-Saclay, 91191 Gif-sur-Yvette, France
[2] European Synchrotron Radiation Facility, BP 220, 38043 Grenoble, France

E-mail: isabelle.mirebeau@cea.fr

Received 28 March 2007, in final form 1 July 2007
Published 22 August 2007
Online at stacks.iop.org/JPhysCM/19/376208

Abstract

We have studied by x-ray synchrotron diffraction under high pressure five pyrochlore compounds: $Tb_2Ti_2O_7$ (up to 42 GPa), $Tb_2Sn_2O_7$ and $Tb_2Mo_2O_7$ (up to 35 GPa), $Gd_2Mo_2O_7$ and $(Tb_{0.8}La_{0.2})_2Mo_2O_7$ (up to 10 GPa). At ambient pressure all compounds crystallize in the cubic $Fd\bar{3}m$ symmetry group. This structure is stable for all compounds in the investigated pressure range. All three compounds having Mo as transition metal are described by the same equation of state, with the same bulk modulus $B_0 = 149$. The bulk modulus is smaller in the Mo pyrochlores than in the Ti and Sn ones, in contrast with *a priori* expectations.

1. Introduction

In pyrochlore oxides $R_2M_2O_7$ the rare earth ion R^{3+} and the transition or sp metal ion M^{4+} both occupy three-dimensional lattices of corner sharing tetrahedra. In recent years these systems have attracted great attention because their lattice can lead to geometrical frustration of the first neighbor magnetic interactions. Since such systems possess an enormous degeneracy of the ground state, they cannot order magnetically in a classical way. They show exotic magnetic ground states, short range ordered, which are called spin liquids, spin ices and spin glasses due to their striking similarities with the states of condensed matter [1]. In practice, the degeneracy of the ground state is generally lifted by a perturbation like pressure, which changes the energy balance between first neighbor exchange interaction, dipolar interaction and rare earth anisotropy and consequently induces new magnetic orders.

We first consider pyrochlores with non-magnetic M^{4+} ion, such as the 3d Ti^{4+} ion or the sp Sn^{4+} ion. These compounds are insulators and frustrated. Among them we studied those with R = Tb. $Tb_2Ti_2O_7$ is a well known example of a spin liquid where short range correlated magnetic moments fluctuate down to the lowest measured temperature of 70 mK [2]. Under applied pressure combined with stress it undergoes antiferromagnetic order [3, 4]. Replacing Ti by Sn yields a lattice expansion. Neutron diffraction measurements show that $Tb_2Sn_2O_7$ orders even at ambient pressure. It forms an 'ordered spin ice' state, coexisting with magnetic

0953-8984/07/376208+10$30.00

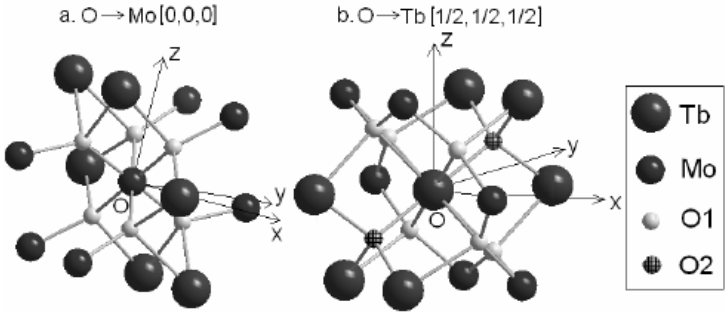

Figure 1. Crystal structure of $R_2M_2O_7$ showing the oxygen environment of an M^{4+} site (left) and an R^{3+} site (right). The structure is drawn for $Tb_2Mo_2O_7$.

fluctuations which persist down to the lowest temperatures [5–7]. Therefore, in $Tb_2Ti_2O_7$ and $Tb_2Sn_2O_7$, the variation of the interatomic distances under applied or chemical pressure changes the energy balance and induces very different magnetic ground states. It is important to know whether these effects are connected with changes in the crystal structure or oxygen position parameter, which can modify the superexchange interaction between Tb ions. This motivated the study of their crystal structure under pressure.

In $R_2Mo_2O_7$ pyrochlores where Mo^{4+} ions are magnetic, the variation of interatomic distances affects not only the magnetic but also the conduction properties. This variation may may be tuned by varying the mean ionic radius r of the rare earth R [8, 9]. Compounds with $r < r_C \sim 1.047$ Å (R = Y, Dy or Tb) are spin glasses and insulators (SGIs), whereas those with $r > r_C$ (R = Gd, Sm or Nd) show ferromagnetic metallic (FM) behavior. All $(RR')_2Mo_2O_7$ show the same variation of the magnetic properties and transition temperature versus the lattice constant, showing the dominant role of Mo–Mo interactions, although the influence of the rare earth cannot be excluded. Chemical pressure and applied pressure stabilize the spin glass state in the same way, as shown by the evolution of their magnetization [10–12], as well as by neutron and muon data [13–15]. However, their effects on the conduction properties are different, since the pressure induced spin glass state remains metallic [16]. This motivated our pressure study of the crystal structure in the critical region.

The crystal structure of $R_2M_2O_7$ pyrochlores of $Fd\bar{3}m$ symmetry is described as follows. The cubic unit cell of lattice constant a contains eight $R_2M_2O_7$ units, where R and M ions occupy two independent lattices of corner sharing tetrahedra. The oxygen environment is different for the R and M ions (figure 1). A given R^{3+} ion, corresponding to the 16d site (1/2, 1/2, 1/2) of the $Fd\bar{3}m$ space group, is surrounded by six oxygen O1 (48f sites) with position $(3/8, 3/8, 1-u)$ and equivalent positions, and two oxygen O2 (8b sites) with fixed positions (3/8, 3/8, 3/8) and (5/8, 5/8, 5/8). The R^{3+} oxygen environment is a puckered ring of six O1 ions with long R–O1 distances (2.54 Å in $Tb_2Mo_2O_7$) and a linear O2–R–O2 unit with short R–O2 distances (2.23 Å in $Tb_2Mo_2O_7$), normal to the average plane of the puckered ring. In contrast, the oxygen environment of a M^{4+} ion, on the 16c site (0, 0, 0), consists of six oxygens O1 with equal M–O1 distances (2.01 Å in $Tb_2Mo_2O_7$). Besides the lattice constant a, the crystal structure is then controlled by the oxygen parameter u only. At ambient pressure the u values found for the pyrochlores studied here range between 0.32 and 0.34. They are intermediate between the value $u = 3/8 = 0.375$ corresponding to eight equal R–O distances for the R site and the value $u = 5/16 = 0.3125$ corresponding to a non-distorted octahedral environment for the M site.

The crystal structure of some $R_2M_2O_7$ pyrochlores was recently investigated under pressure by several groups. In $Gd_2Ti_2O_7$, Raman studies and and x-ray diffraction [17]

Table 1. Ambient pressure and temperature structural parameters of $R_2Mo_2O_7$ (R = Tb, Gd, (Tb, La)) and $Tb_2M_2O_7$ (M = Ti and Sn): the cubic lattice parameter a and positions of O 48f sites $[u, 1/8, 1/8]$. The bulk modulus B_0 as obtained from the fit using the Murnaghan equation (1) is also indicated. The pressure derivative of the bulk modulus was first fixed at $B_1 = 6$, when the fit takes into account the whole pressure range for all samples. Then we fixed $B_1 = 4.5$ and took into account the whole pressure range for $Tb_2Ti_2O_7$ and the 0–10 GPa interval for $R_2Mo_2O_7$ and $Tb_2Sn_2O_7$. The error bar on B_0, taking into account statistical and systematic errors, is estimated to be ±3%.

Compound	a (Å) ambient pressure	u (units of a) ambient pressure	B_0 (GPa) $B_1 = 6$	B_0 (GPa) $B_1 = 4.5$
$Tb_2Mo_2O_7$	10.312(1)	0.334(3)	154	149
$Gd_2Mo_2O_7$	10.348(1)	0.334(1)	154	149
$(Tb_{0.8}La_{0.2})_2Mo_2O_7$	10.378(2)	0.331(1)	154	149
$Tb_2Ti_2O_7$	10.149(2)	0.328(2)	173	191
$Tb_2Sn_2O_7$	10.426(1)	0.336(1)	207	198

suggested a slight distortion at about 9 GPa. X-ray diffraction performed up to higher pressures [18, 19] concluded the presence of anion disorder in $Gd_2Ti_2O_7$ (above 38 GPa) and $Sm_2Ti_2O_7$ (above 40 GPa), and the onset of an amorphous phase above 51 GPa. In $Cd_2Nb_2O_7$, a pressure induced structural distortion from defect fluorite structure was found at 14 GPa, followed by a second transition towards monoclinic/orthorhombic then to amorphous state at about 27 GPa [21]. Similar results [20] were found in $Tb_2Ti_2O_7$ and $Tb_2Sn_2O_7$ with the first transition occurring at 51 and 37 GPa respectively, and the second one at 58 and 91 GPa, above the pressure range studied here. High pressure x-ray data were also obtained in $Nd_2Mo_2O_7$ up to 10 GPa [22].

Using high pressure x-ray synchrotron diffraction, we have studied five pyrochlore compounds and determined the equation-of-state parameters. First, for the same 4d transition metal M = Mo, we varied the rare earth ion and chose three compounds corresponding to the three regions of interest of the phase diagram: $Tb_2Mo_2O_7$ (in the SGI region, with $r < r_C$), $(Tb_{0.8}La_{0.2})_2Mo_2O_7$ (in the FM region, $r > r_C$) and $Gd_2Mo_2O_7$ (located on the verge of the transition, $r \sim r_C$). Then, vice versa, we fixed the rare earth R = Tb and compared $Tb_2Sn_2O_7$ with $Tb_2Ti_2O_7$ and $Tb_2Mo_2O_7$. By analyzing the crystal structure under pressure, we show that to the highest measured pressures there is no structural phase transition and that all compounds keep the ambient pressure cubic $Fd\bar{3}m$ symmetry group. The equation of state changes when changing the M metal (from sp to 3d and 4d). We also study the pressure dependence of the oxygen parameter u in all compounds.

2. Experimental details

All experiments were performed on powdered samples. Their crystal structure at ambient pressure was investigated by combining x-ray and neutron diffraction. Neutron diffraction measurements were performed on 3T2 ($Tb_2Sn_2O_7$ and $Tb_2Ti_2O_7$) and G61 ($Tb_2Mo_2O_7$ and $(Tb_{0.8}La_{0.2})_2Mo_2O_7$) diffractometers of the Laboratoire Léon Brillouin (LLB). Due to the huge absorption of natural Gd, neutron experiments on $Gd_2Mo_2O_7$ were done using a isotopically enriched ^{160}Gd and the high resolution–high flux diffractometer D2B of the Institute Laüe Langevin (ILL). The structural parameters at ambient pressure are given in table 1. X-ray synchrotron diffraction measurements under pressure at ambient temperature were performed on the ID27 beam line of the European Synchrotron Radiation Facility (ESRF). The incident wavelength was $\lambda = 0.3738$ Å. We used a diamond-anvil cell. The transmitting

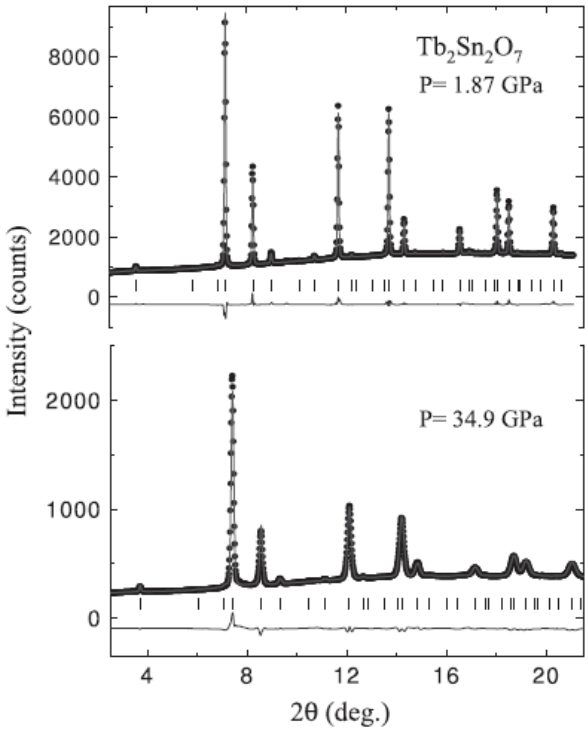

Figure 2. $Tb_2Sn_2O_7$: x-ray diffraction intensity versus the scattering angle 2θ at ambient temperature at $P = 1.87$ and 31.8 GPa, respectively. The incident x-ray wavelength is $\lambda = 0.3738$ Å. Solid lines show the best Rietveld refinement with cubic $Fd\bar{3}m$ symmetry ($R_B = 6.09\%$ and 6.91%, respectively) and the difference spectrum (bottom). Tick marks show the Bragg peak positions.

medium and the maximal pressure are as follows: $Tb_2Mo_2O_7$ (nitrogen, $P_{max} = 35$ GPa), $Gd_2Mo_2O_7$ (ethanol–methanol mixture, $P_{max} = 10$ GPa), $(Tb_{0.8}La_{0.2})_2Mo_2O_7$ (ethanol–methanol mixture, $P_{max} = 10$ GPa), $Tb_2Ti_2O_7$ (neon, $P_{max} = 42$ GPa) and $Tb_2Sn_2O_7$ (ethanol–methanol mixture, $P_{max} = 35$ GPa).

For $Tb_2M_2O_7$ (M = Mo, Ti or Sn) we went to higher pressures in order to compare the effects of M substitution on the equation of state. Per contra, for the other two molybdenum pyrochlores ($Gd_2Mo_2O_7$ and $(Tb_{0.8}La_{0.2})_2Mo_2O_7$) we used a maximum pressure of 10 GPa, which goes well beyond the F–SG transition.

3. Results

The crystal structure at ambient and under applied pressure was determined by Rietveld refinements of x-ray and neutron diffraction patterns, using the crystallographic programs of the FullProf suite [23]. Refinements of ambient pressure patterns show that all samples crystallize in the $Fd\bar{3}m$ space group, yielding a lattice parameter a and an oxygen position parameter u as indicated in table 1.

Under pressure, to the highest pressure value, there is a peak broadening, but neither additional peaks nor a splitting of the existing ones. This shows that the crystal structure remains cubic with $Fd\bar{3}m$ space group in the whole pressure range.

Figure 2 shows two x-ray diffraction patterns of $Tb_2Sn_2O_7$ at ambient temperature for two typical pressures, in the low and high pressure ranges. It clearly shows that there is no structural phase transition.

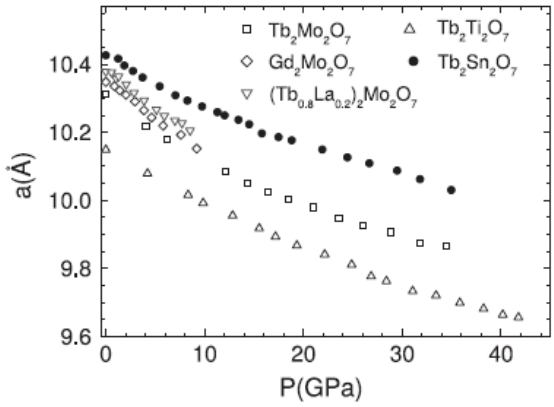

Figure 3. Variation of the lattice parameter a deduced from the structural analysis, versus pressure at ambient temperature for the five samples: $Tb_2Mo_2O_7$ (□), $Gd_2Mo_2O_7$, (◇), $(Tb_{0.8}La_{0.2})_2Mo_2O_7$ (▽), $Tb_2Ti_2O_7$ (△) and $Tb_2Sn_2O_7$ (●).

The evolution of the structural parameters a and u with pressure was determined as follows. For each sample we made the following analysis. First we fitted some selected Bragg peaks, yielding the pressure dependence of a only but with high accuracy. Then we analyzed the whole patterns using Fullprof in the profile matching mode, with no constraint on the peak intensities. Finally, we performed a structure analysis with Fullprof, allowing the determination of both a and u. A Thompson–Cox–Hastings pseudo-Voigt peak shape function was used (for details see [23, 24]). The determinations of a agree for the three analyses. Its evolution with pressure is shown in figure 3 for all samples.

The equation of state was determined by fitting the Murnaghan equation to the data:

$$\frac{V}{V_0} = \left(P\frac{B_1}{B_0} + 1\right)^{-\frac{1}{B_1}} \tag{1}$$

with V_0, B_0 and B_1 the volume at zero pressure, the bulk modulus and its first pressure derivative, respectively.

In a first step, when fitting, we took into account the whole experimental pressure range for all samples, no matter what the pressure transmitting medium. We performed systematic fits using different values for the first pressure derivative of the bulk modulus, B_1. Then we fixed the value $B_1 = 6$, which allows a reasonable fit for all samples in the whole pressure range. As clearly seen in figure 4, for $R_2Mo_2O_7$ the variation of V/V_0 versus pressure is independent of the mean ionic radius of the rare earth r. $Tb_2Mo_2O_7$ ($r < r_C$), $Gd_2Mo_2O_7$ ($r \sim r_C$) and $(Tb_{0.8}La_{0.2})_2Mo_2O_7$ ($r > r_C$) are described by the same equation of state. The values of the bulk modulus B_0 deduced from this fit are listed in 1.

The high B_1 value found in the above analysis may reflect some non-hydrostaticity above 10 GPa, considering the fact that different transmitting media were used, and only neon is believed to be fully hydrostatic at high pressure. The non-hydrostaticity of nitrogen (used for $Tb_2Sn_2O_7$) and ethanol–methanol (used for $Tb_2Mo_2O_7$) with respect to neon (used for $Tb_2Ti_2O_7$) is confirmed by a strong increase of the peak width above 10 GPa, as shown by the pressure dependence of the parameter Y (inset of figure 5), which corresponds to the Lorentzian component of the Thompson–Cox–Hastings pseudo-Voigt peak shape function [23, 24]. This prevents giving a physical meaning to the high B_1 value. So in a second step, we took as reference $Tb_2Ti_2O_7$ measured with the neon transmitting medium. As shown in figure 5, a good fit of the $Tb_2Ti_2O_7$ data can be obtained with a more reasonable value of the bulk modulus derivative, $B_1 = 4.5$. An independent fit of B_0 and B_1 yields the values $B_0 = 187$ GPa and

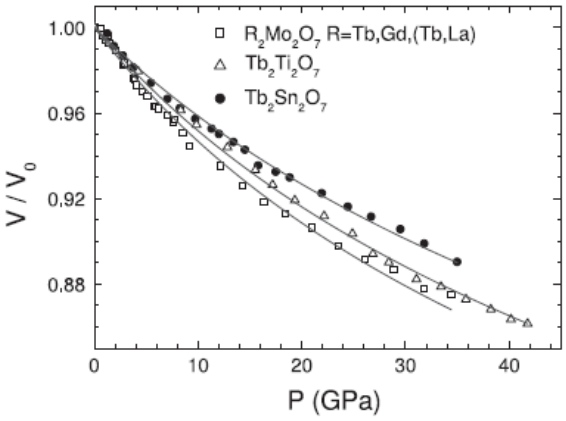

Figure 4. Pressure dependence of V/V_0, with V_0 the unit cell volume at ambient pressure. Lines correspond to fits using the Murnaghan function with fixed $B_1 = 6$ in the whole pressure range for all samples. The corresponding values of B_0 are indicated in table 1.

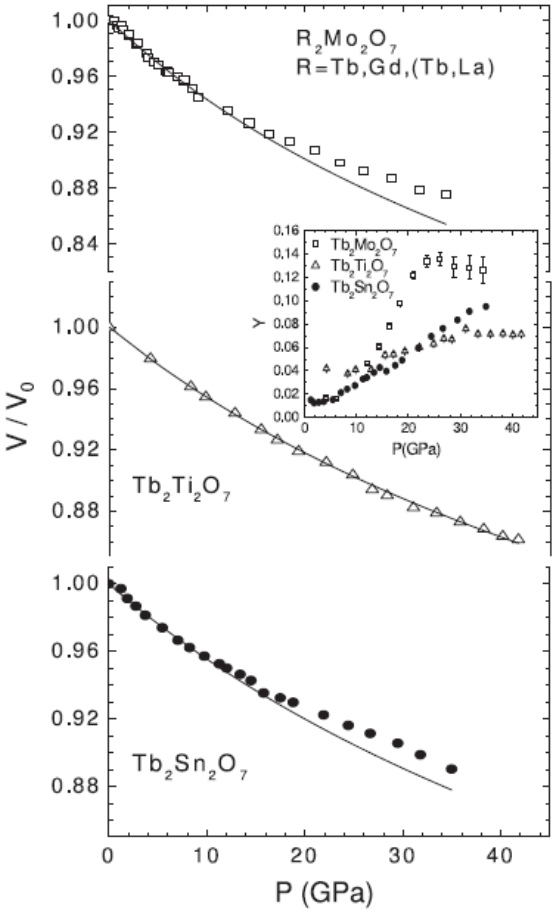

Figure 5. Pressure dependence of V/V_0. Lines correspond to fits using the Murnaghan function. The bulk modulus was fixed: $B_1 = 4.5$. For $Tb_2Ti_2O_7$ the fit was done in the whole pressure range, while for $R_2Mo_2O_7$ and $Tb_2Sn_2O_7$ the fit corresponds to the 0–10 GPa interval. The corresponding values of B_0 are also indicated in table 1, last column. Inset, the variation of the parameter Y, related to the intrinsic peak width, with pressure. Data for $Tb_2Ti_2O_7$ are the only ones which correspond to a fully hydrostatic pressure in the whole pressure range.

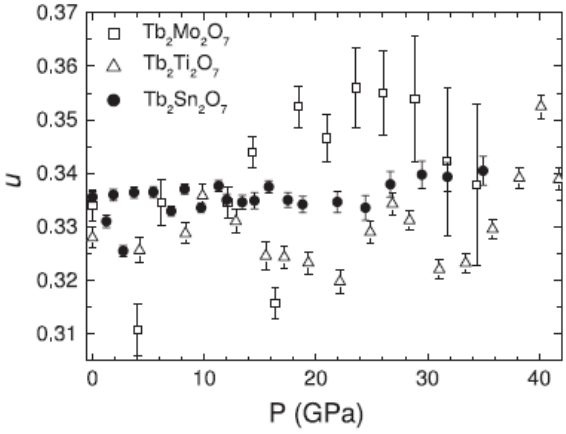

Figure 6. Oxygen position parameter u versus pressure at ambient temperature for Tb pyrochlores: $Tb_2Mo_2O_7$ (□), $Tb_2Ti_2O_7$ (△) and $Tb_2Sn_2O_7$ (●).

$B_1 = 4.8$. We then fitted the data of the other samples, $R_2Mo_2O_7$ and $Tb_2Sn_2O_7$, by fixing $B_1 = 4.5$ and limiting the fitted pressure range to 10 GPa, an interval where ethanol–methanol mixture or nitrogen provide hydrostatical pressure conditions. The corresponding values of B_0 are listed in table 1, last column. We consider these values as the most reliable, since they fit well the $Tb_2Ti_2O_7$ data in the whole pressure range and also the region of interest 0–10 GPa of the molybdenum pyrochlores. Therefore we used them in the following to obtain the equation of state.

As shown in table 1, the bulk modulus increases in the sequence $B_0(\mathrm{Mo}) < B_0(\mathrm{Ti}) < B_0(\mathrm{Sn})$. This remains true whatever the value fixed for B_1.

The determination of the oxygen coordinate u is more intricate. It is directly related to the integrated intensities of the Bragg peaks, which may be partly affected by either texture effects or non-isotropic powder averaging for very small samples. Since it is the only structural parameter (besides a), we still obtained reasonable values (figure 6). For each sample, the average u value agrees with the ambient pressure determination within less than ±1%. The influence of the scatter in u values on the determination of the interatomic distances for a given sample under pressure is evaluated in the worst case ($Tb_2Mo_2O_7$). For $a = 10.112$ Å ($Tb_2Mo_2O_7$ at 10 GPa), the scatter in u of 0.33(1) corresponds to a d (Mo–O1) distance of 1.96(4) Å and an Mo–O1–Mo angle of 131(5)°.

In figure 6, the oxygen coordinate u is shown versus pressure when varying the metal, M = Mo, Ti and Sn. In each case u is independent of applied pressure in the error bar limits. The u values for $Tb_2Ti_2O_7$ are systematically lower than for $Tb_2Sn_2O_7$, whereas the value for $Tb_2Mo_2O_7$ seems to be slightly higher. Our results for Ti and Sn samples agree with previous results [20], which show that the cubic crystal structure is stable and u is independent of pressure in this pressure range.

Figure 7 shows the evolution of u with the lattice constant for the Mo pyrochlore samples: $Tb_2Mo_2O_7$ ($a < a_c \sim 10.33$ Å), $Gd_2Mo_2O_7$ ($a \sim a_c$) and $(Tb_{0.8}La_{0.2})_2Mo_2O_7$ ($a > a_c$), in the pressure range 0–10 GPa. A pressure of 10 GPa is well beyond the values needed to induce the F–SG transition for both Gd and $(Tb_{0.8}La_{0.2})_2Mo_2O_7$ samples, where the critical pressure lies in the range 0.6–2.4 GPa ([14] and references therein) and around 2.1 GPa [13], respectively. The threshold pressures correspond to a critical value of the lattice constant $a_c \sim 10.33$ Å. Within the accuracy of our measurements we cannot evidence any systematic variation of u throughout the threshold. Our results are reported together with ambient pressure data on several samples

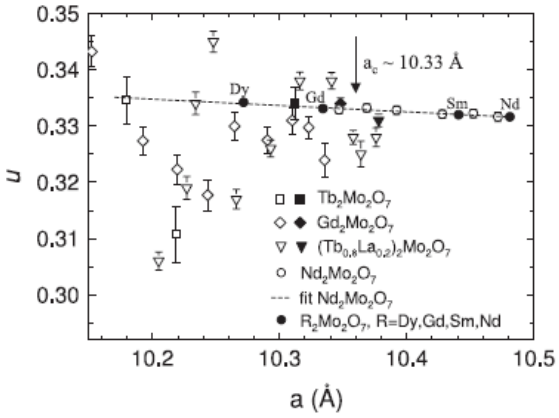

Figure 7. Oxygen coordinate against lattice parameter for the three Mo pyrochlores: $Tb_2Mo_2O_7$, $Gd_2Mo_2O_7$ and $(Tb_{0.8}La_{0.2})_2Mo_2O_7$. Open symbols (□, ◇, ▽) correspond to data under pressure, while the solid symbols indicate the ambient pressure data. For comparison the behavior of $Nd_2Mo_2O_7$ (○) under applied pressure is shown, as cited from [22]. The dashed line is a linear fit of these data. The effect of rare earth substitution as in [9] is also shown (●). a_c is the critical value of the lattice constant as in [13, 14].

with mean ionic radius encompassing the threshold (our data and from [9], as well as high pressure x-ray data on $Nd_2Mo_2O_7$ obtained up to 10 GPa [22]), where the powder averaging seems to be better than here. Our determination of u is situated in the expected range. The very small increase observed under chemical pressure and in [22] (the dashed line in figure 5 corresponds to an increase from 0.3315 to 0.3348, namely about 1% when a varies from 10.5 to 10.2 Å) is beyond the accuracy of the present pressure data.

4. Discussion

The determination of the crystal structure under pressure in rare earth pyrochlores is important since it governs their magnetic and electric properties, which strongly vary under pressure. In all samples, we find that the cubic structure with $Fd\bar{3}m$ symmetry is stable up to the highest measured pressure of 40 GPa, in agreement with previous results.

Considering the good stability of the crystal structure, the only parameters are the lattice constant a and oxygen parameter u. The determination of the equation of state $a(P)$ shows that the bulk modulus B_0 changes when changing the sp or d ion, whereas it does not change with the rare earth ion. One naturally expects that a change in the R ion should have much smaller effects on B_0 than a change in the sp or d ion, since the changes in the atomic radius are smaller, and the localized 4f shells do not participate in the atomic bonding.

We first consider the $Tb_2M_2O_7$ pyrochlores (M = Sn, Ti, Mo). One notices that $Tb_2Mo_2O_7$ has a larger unit cell than $Tb_2Ti_2O_7$, and also the smallest value of the bulk modulus of all compounds. This is not *a priori* expected from the variation of the ionic radius, evaluated in the periodic table as 0.71, 0.68 and 0.68 for Sn^{4+}, Ti^{4+} and Mo^{4+} ions respectively. The softening observed for the Mo compound may be related to the proximity of an insulating–metal transition [25, 26].

The oxygen parameter $\langle u \rangle$, averaged in the range 0–40 GPa, decreases from 0.335(2) for Sn to 0.325(3) for Ti. The decrease of $\langle u \rangle$ corresponds to a decrease of the trigonal compression of the oxygen octahedra around the M atom along the $\langle 111 \rangle$ axis, (the non-distorted case yielding $u = 5/16 = 0.312$). In [22], the small increase of u under applied pressure was explained by the fact that with decreasing a the MO_6 octahedron should become more trigonally

compressed, the O1 oxygen on the 48f sites going away from the Mo tetrahedron to compensate the volume compression. This argument obviously does not hold for chemical pressure induced by Ti/Sn substitution. One also notices that the substitution of Sn by Ti corresponds to chemical pressures of about 7 and 21 GPa respectively, well below the maximum pressures investigated. So the decrease of u when going from Sn to Ti may arise from another reason than the lattice contraction. The influence of the crystal field of the Tb^{3+} ion, which is strongly different in the Ti and Sn compounds [27], could play a role.

We then consider the $R_2Mo_2O_7$ pyrochlores, when we vary the rare earth ion. Here the variations of both B_0 and $\langle u \rangle$ are much smaller and beyond the accuracy of our measurements. We find the same equation of state on both sides of the SG–F threshold, and we did not observe any variation u either under pressure, within the accuracy of our measurements. A very small systematic variation of u with a ($\sim$1% within the whole $R_2Mo_2O_7$ family) is found at ambient pressure under chemical substitution [9] and in the high pressure data of [22]. Our neutron diffraction data on $(Tb_{1-x}La_x)_2Mo_2O_7$ samples, to be published later, where we investigated the threshold region in details at ambient pressure, confirm this effect. The small variation of u scales with a in a unique curve for all rare earth ions. The change in the Mo–O–Mo bond angle is about negligible in the threshold region.

This suggests that the only structural parameter which controls the ferromagnetic–spin glass and insulating–metal transition, or at least the change in sign of the Mo–Mo magnetic interactions, is the Mo–Mo distance and not the Mo–O–Mo bond angle. This result may be considered with regards to band structure calculations. In [28], the stability of the ferromagnetic phase was related to the variation of the bond angle. Our data rather support the picture of [29], which argues that the key parameter in this transition is not the Mo–O–Mo angle, which controls Mo(t_{2g}) orbitals mediated by O(2p) states, but the Mo–Mo distance, directly related to the lattice constant, which controls the direct interactions between the extended Mo (4d) orbitals.

5. Conclusion

By means of high pressure x-ray synchrotron diffraction we have studied the crystal structure of $Tb_2Mo_2O_7$, $Gd_2Mo_2O_7$, $(Tb_{0.8}La_{0.2})_2Mo_2O_7$, $Tb_2Ti_2O_7$ and $Tb_2Sn_2O_7$ pyrochlore compounds. We have shown that there is no structural phase transition to the highest applied pressure. The pressure dependence of lattice and oxygen position parameters was investigated since these two parameters determine the crystal structure and hence the electronic and magnetic properties of the pyrochlores. In $Tb_2M_2O_7$ (M = Mo, Ti, Sn) the bulk modulus increases when varying the transition metal from Mo to Ti and then to the sp metal Sn. In contrast, $R_2Mo_2O_7$ pyrochlores are all described by the same equation of state, whatever their electric or low temperature magnetic state.

Acknowledgments

We thank M Mezouar and M Hanfland for their help in the x-ray measurements under pressure on ID27, and A Forget and D Colson for the sample preparation.

References

[1] Greedan J E 2001 *J. Mater. Chem.* **11** 37
[2] Gardner J S, Dunsiger S R, Gaulin B D, Gingras M J P, Greedan J E, Kiefl R F, Lumsden M D, MacFarlane W A, Raju N P, Sonier J E, Swainson I and Tun Z 1999 *Phys. Rev. Lett.* **82** 1012

[3] Mirebeau I, Goncharenko I N, Cadavez-Peres P, Bramwell S T, Gingras M J P and Gardner J S 2002 *Nature* **420** 54
[4] Mirebeau I, Goncharenko I, Dhalenne G and Revcolevschi A 2004 *Phys. Rev. Lett.* **93** 187204
[5] Mirebeau I, Apetrei A, Rodríguez-Carvajal J, Bonville P, Forget A, Colson D, Glazkov V, Sanchez J P, Isnard O and Suard E 2005 *Phys. Rev. Lett.* **94** 246402
[6] Bert F, Mendels P, Olariu A, Blanchard N, Collin G, Amato A, Baines C and Hillier A D 2006 *Phys. Rev. Lett.* **97** 117203
[7] Dalmas de Réotier P, Yaouanc A, Keller L, Cervellino A, Roessli B, Baines C, Forget A, Vaju C, Gubbens P C M, Amato A and King P J C 2006 *Phys. Rev. Lett.* **96** 127202
[8] Katsufuji T, Hwang H Y and Cheong S-W 2000 *Phys. Rev. Lett.* **84** 1998
[9] Moritomo Y, Xu S, Machida A, Katsufuji T, Nishibori E, Takata M, Sakata M and Cheong S W 2001 *Phys. Rev.* B **63** 144425
[10] Park J G, Jo Y, Park J, Kim H C, Ri H C, Xu S, Moritomo Y and Cheong S W 2003 *Physica* B **328** 90
[11] Kim H C, Jo Y, Park J G, Ri H C and Cheong S W 2003 *Acta Phys. Pol.* B **34** 1429
Kim H C, Jo Y, Park J G, Ri H C and Cheong S W 2005 *Physica* B **359** 1246
[12] Miyoshi K, Takamatsu Y and Takeuchi J 2006 *J. Phys. Soc. Japan* **75** 065001
[13] Apetrei A, Mirebeau I, Goncharenko I, Andreica D and Bonville P 2006 *Phys. Rev. Lett.* **97** 206401
[14] Mirebeau I, Apetrei A, Goncharenko I, Andreica D, Bonville P, Sanchez J P, Amato A, Suard E and Crichton W 2006 *Phys. Rev.* B **74** 174414
[15] Apetrei A, Mirebeau I, Goncharenko I, Andreica D and Bonville P 2007 *J. Phys.: Condens. Matter* **19** 145214
[16] Miyoshi K, Yamashita T, Fujiwara K and Takeuchi J 2003 *J. Phys. Soc. Japan* **72** 1855
[17] Saha S, Muthu D V S, Pascanut C, Dragoe N, Suryanarayanan R, Dhalenne G, Revcolevschi A, Karmakar S, Sharma S M and Sood A K 2006 *Phys. Rev.* B **74** 064109
[18] Zhang F X, Manoun B, Saxena S K and Zha C S 2005 *Appl. Phys. Lett.* **86** 181906
[19] Zhang F X and Saxena S K 2005 *Chem. Phys. Lett.* **413** 248
[20] Kumar R S, Cornelius A L, Nicol M F, Kham K C, Cheetham A C and Gardner J S 2006 *Appl. Phys. Lett.* **88** 031903
[21] Zhang F X, Lian J, Becker U, Ewing R C, Wang L M, Boatner L A, Hu J and Saxena S K 2006 *Phys. Rev.* B **74** 174116
[22] Ishikawa H, Xu Sh, Moritomo Y, Nakamura A, Ohishi Y and Kato K 2004 *Phys. Rev.* B **70** 104103
[23] Rodríguez-Carvajal J 1993 *Physica* B **192** 55
For a recent version of FullProf, see Rodríguez-Carvajal J 2001 *CPD Newslett.* **26** 12 available at http://journals.iucr.org/iucr-top/comm/cpd/newsletters
[24] Finger L W, Cox D E and Jephcoat A P 1994 *J. Appl. Crystallogr.* **27** 892
[25] Kesmarki I, Hanasaki N, Hashimoto D, Iguchi S, Miyasakoa S and Tokura Y 2003 *Phys. Rev. Lett.* **67** 174406
[26] Kim M W, Lee Y S, Noh T W, Yu J and Moritomo Y 2004 *Phys. Rev. Lett.* **92** 27202
[27] Mirebeau I, Bonville P and Hennion M 2007 *Phys. Rev.* B submitted
[28] Kang J-S, Moritomo Y, Xu S H, Olson C G, Park J H, Kwon S K and Min B I 2002 *Phys. Rev.* B **65** 224422
[29] Solovyev I V 2003 *Phys. Rev.* B **67** 174406

RESUME

Dans les oxydes $R_2M_2O_7$, les deux ions R^{3+} (terre rare ou Y) et M^{4+} (M= métal sp ou de transition) occupent des réseaux pyrochlores géométriquement frustrés. Cette étude a pour objet l'analyse de deux types de systèmes: (i) $Tb_2Sn_2O_7$, composé isolant dans lequel l'équilibre en énergie et l'état fondamental sont contrôlés par les interactions magnétiques entre les ions Tb^{3+} et (ii) la série $(Tb_{1-x}La_x)_2Mo_2O_7$ (x=0-0.2), caractérisée par la présence du magnétisme localisé du Tb^{3+} et de celui partiellement itinérant du Mo^{4+}. Nous avons étudié l'ordre magnétique principalement par diffraction de neutrons et rotation et relaxation de spin du muon (μSR), qui grâce à leur complémentarité fournissent une information microscopique précise à la fois sur les corrélations statiques et les fluctuations de spin. Sous l'effet de la substitution chimique et/ou de la pression appliquée nous avons observé une grande variété de comportements magnétiques en variant la température: des ordres à courte portée (liquides et verres de spin), ordre à longue portée original ("glace de spin ordonnée") ou des phases mixtes. Nous avons tenté de comprendre dans chaque cas le rôle du magnétisme de la terre rare et/ou celui du métal de transition afin de déterminer comment les interactions magnétiques favorisent un état magnétique spécifique.

Mots clés: magnétisme, frustration géométrique, pyrochlores, liquides de spin, glaces de spin, verres de spin, diffraction de neutrons, μSR, pression.

ABSTRACT

In the oxides $R_2M_2O_7$, both R^{3+} (rare earth or Y) and M^{4+} (M= sp or transition metal) form geometrically frustrated pyrochlore lattices. The object of the present study is the analyse of two types of systems: (i) $Tb_2Sn_2O_7$, an insulating compound where the energy balance and the ground state are controlled by the magnetic interactions between Tb^{3+} ions only and (ii) $(Tb_{1-x}La_x)_2Mo_2O_7$ (x=0-0.2) series, having both localized Tb^{3+} and partially itinerant Mo^{4+} ions magnetism. We have studied the magnetic order mainly by neutron diffraction and Muon Spin Rotation and Relaxation (μSR), which due to their complementarity yield a microscopic picture of both static spin correlations and spin fluctuations. Under the effect of chemical substitution and/or applied pressure we have observed a great variety of magnetic behaviours when varying temperature: short range orders (spin liquids or spin glasses), original long range order ("ordered spin ices") or mixed phases. We have tried to understand in each case the role played by the rare earth and/or the transition metal ions in order to determine how the magnetic interactions favour a particular magnetic ground state.

Keywords: magnetism, geometrical frustration, pyrochlores, spin liquids, spin ices, spin glasses, neutron diffraction, μSR, pressure.